Structural and stratigraphic controls on mineralization at the George Fisher Zn-Pb-Ag Deposit, Northwest Queensland, Australia

Thesis submitted by

Travis E. Murphy

B.App.Sc. (Hons) University of Technology, Sydney

in October, 2004,

for the degree of Doctor of Philosophy

in the School of Earth Sciences,

James Cook University

Statement of Access

I, the undersigned, author of this thesis, understand that the following restriction placed by me on this thesis will not extend beyond the date specified.

"I wish to place restriction on access to this thesis for a period of two years as per the confidentiality agreement with MIM Ltd (now Xstrata)"

After this period has elapsed I understand that James Cook University will make this thesis available for use within the University library and make this thesis available via the Australian Digital These network, for use elsewhere. All users consulting this thesis will have to sign the following statement:

"In consulting this thesis I agree not to copy or closely paraphrase it in whole or in part without written consent of the author, and to make proper written acknowledgement for any assistance which I obtained from it"

Travis E. Murphy Date

Statement of Sources

Declaration

I declare that this thesis is my own work and has not been submitted in any form for another degree or diploma at any university or other institution of tertiary education. Information derived from the published or unpublished work of others has been acknowledged in the text and a list of referees is given.

Travis E. Murphy   Date

Electronic Copy

I, the undersigned, author of this work, declare that the electronic copy of this thesis provided to the James Cook University Library is an accurate copy of the print thesis submitted, within the limits of the technology available.

Travis E. Murphy

Date

Acknowledgements

This project has been possible thanks to financial support from MIM/Xstrata who have provided access to required data, drill-core, facilities, and the mine at George Fisher.

The initial concept of this study was developed by Alice Clark and Tim Bell. Andrew Allibone, Tom Blenkinsop, and Tim Bell are thanked for their supervision of respective parts of this thesis. Andrew Allibone, in particular, is thanked for guiding this research and for enthusiastic editing of several drafts of the thesis.

Myles Johnston, Ann Mawdesley, Alison Morley, Brad Cox and other geologists from both the Mt Isa and George Fisher offices are thanked for providing logistical support during my stays in Mt Isa on fieldwork. Communication with Allen Shaw proved invaluable due to his intimate knowledge of the stratigraphy at George Fisher.

Paul Whelan (Metech) kindly provided the MineSight software package for use in this study. Andrew Allibone, Roger Taylor, Kylie Prendergast, and Gavin Clark donated some of the samples used in Part C of this study and are thanked for discussions related to the same. Alan Chappell, Gordon Warria, and Kevin Blake provided supervision and support of various stages of laboratory work in the Advanced Analytical Centre at JCU.

Rhenium-Osmium isotopic analysis was possible thanks to funding and support from the PMD-CRC and the efforts of Lucy Chapman were integral in making this happen. Reid Keays, Bruce Schaeffer, Rachelle Hubregtse and other VIEPS personnel conducted this analytical work, and Reid Keays is thanked for his role in this collaborative work.

Finally, I would like to thank Rebecca, my wife, for encouragement to undertake this PhD study, support during my candidature, and patience while I came to blows with this computer whilst producing the thesis.

ABSTRACT

Sediment-hosted stratiform Zn-Pb-Ag deposits have been interpreted as forming during exhalative hydrothermal activity synchronous with the deposition of host rocks and during either syn-diagenetic or syn-metamorphic veining and replacement of the host-rocks later in their orogenic history. This study analyzes the distribution metal and ore-types at the George Fisher deposit and investigates spatial and temporal relationships between high-grade mineralization and structures at all scales throughout the deformation history. The study aims to determine whether remobilization and upgrading of syn-sedimentary and/or syn-diagenetic proto-ore or primary syntectonic mineralization are involved in the formation of economic mineralization. Analysis of the kinematic controls on any Zn-Pb-Ag mineralization which is structurally controlled may enable other prospective structures in the near-mine region to be identified.

The George Fisher Zn-Pb-Ag deposit is located 22km north of Mt Isa in Queensland, Australia; and is hosted by Proterozoic sedimentary rocks of similar age and lithology to the Mt Isa and adjacent Hilton Zn-Pb-Ag deposits. The host-rocks at George Fisher preserve a structural history comprising four distinct ductile deformations with concomitant faulting and younger brittle faults which cut the ore-bearing sequence. The first, D_1 is manifest as an open fold (F_1) with an approximately east-west striking axial plane and was overprinted by F_2 folding and a pervasive slaty/solution cleavage (S_2) during the regionally extensive D_2 episode. An episode of sub-vertical shortening/sub-horizontal extension (D_3) followed this main phase of sub-horizontal shortening which formed folds with sub-horizontal axial planes and gently-dipping crenulations of the S_2 cleavage and bedding. D_3 features are overprinted by sub-vertical crenulations (S_4) and minor folds (F_4) with sub-vertical axial planes.

Ore shoots that comprise high-grade and thicker mineralization plunge parallel to the F_1 fold axes and are largely confined to the short-limb of this fold. Subsidiary ore shoots are coincident with areas of more intense F_2 folding, and trend parallel to both F_2 and F_4 fold axes in longitudinal projection.

Vein-hosted sphalerite and medium-grained galena breccia are the main sources of Zn and Pb metal in the deposit, respectively. Logged widths of each form shoots of thicker mineralization which are broadly coincident with high-grade shoots defined by the assay

data. Sulphide textural studies and vein - host-rock fabric cross-cutting relationships suggest that both postdate D_2.

Empirical relationships between ore shoot geometry and the structural framework of the deposit imply a D_4 control on metal distribution. This is supported by the interpretation of a dominantly syn-D_4 relative timing of the vein-hosted sphalerite and medium-grained galena breccia based on development of these mineralization-types in unique structural settings and the apparent lack of deformation of their constituent sulphides. Potential pre-F_2 mineralization types include some disseminated sphalerite and fine-grained sphalerite-galena breccias which do not currently constitute economic mineralization and account for ca. 10% of the Zn+Pb in the deposit. Remobilization of proto-mineralization is supported by the Zn assay data which indicates that more than one population of Zn grades exists and that a higher grade population is unique to the economic ore-horizons. However, this qualitative observation does not discriminate between upgrading of a pre-F_2 or syn-/post-F_2 sulphide accumulation during D_4.

Re-Os isotopic analysis of sphalerite and galena at George Fisher define an isochron whose slope indicates an age of 1423±130Ma indicating closure of the Re-Os system postdates host-rock deposition by ~100-360Ma.

A mantle source of Pb and Zn is interpreted from the Re-Os isotopic analysis based on the initial $^{187}Os/^{188}Os$ ratio of 0.077±0.071. This differs from previous studies of Proterozoic Zn-Pb-Ag deposits which infer scavenging of metal from within the sedimentary basin or from the basement rocks immediately underlying the sedimentary basin. Proximity to a regional fault zone such as the Mount Isa-Paroo Fault system, interpreted to be part of a fault-network linked to a major mid-crustal shear zone, is considered necessary to bring metal-bearing fluids from depth into contact with prospective host-lithologies at George Fisher.

At the George Fisher deposit, it is inferred that the F_1 fold focussed diagenetic hydrothermal activity and alteration and also acted as a heterogeneity focussing dilation and final sites of mineralization later in the deformation history. The F_1 fold may be the upper level expression of a reactivated basement fault thereby accounting for the longevity of the hydrothermal system responsible for alteration and mineralization at George Fisher. It is possible that diagenetic processes prepared the host-rock for later mineralization at George Fisher.

TABLE OF CONTENTS

PART B. DISTRIBUTION OF ZN-PB-AG MINERALIZATION AND ITS RELATIONSHIP TO STRUCTURAL DOMAINS AT THE GEORGE FISHER MINE, NORTHWEST QUEENSLAND, AUSTRALIA.

PART C. THE RELATIONSHIP BETWEEN THE FRACTAL DIMENSION OF SPHALERITE GRAIN BOUNDARIES AND SULPHIDE DEFORMATION: APPLICATION OF THE COASTLINE METHOD IN MICROSTRUCTURAL STUDIES.

PART D. ORE CHARACTERISTICS, CROSS-CUTTING RELATIONSHIPS, AND TIMING RELATIVE TO DEFORMATION AT THE GEORGE FISHER DEPOSIT, NORTHWEST QUEENSLAND, AUSTRALIA.

PART E. RHENIUM-OSMIUM ISOTOPIC ANALYSIS OF MINERALIZATION AT THE GEORGE FISHER DEPOSIT, NORTHWEST QUEENSLAND, AUSTRALIA: IMPLICATIONS FOR THE ABSOLUTE AGE OF MINERALIZATION AND THE SOURCE OF METALS.

PART F. TECTONOSTRATIGRAPHIC SETTING AND CONTROLS ON STRATIFORM BASE METAL MINERALIZATION IN THE WESTERN FOLD BELT OF THE MT ISA INLIER, AUSTRALIA: COMPARISON OF THE MT ISA, GEORGE FISHER - HILTON, LADY LORETTA, AND CENTURY ZN-PB-AG DEPOSITS.

LIST OF TABLES

LIST OF FIGURES

PART B.

PART C.

PART D.

PART E.

PART F.

INTRODUCTION

The George Fisher Zn-Pb-Ag deposit is located 22 kilometres north of Mt Isa in the north-western region of Queensland, Australia. Mineralization at George Fisher is hosted by Proterozoic sedimentary rocks within the Mt Isa Inlier and shows many similarities to the adjacent Hilton (2 kilometres south from George Fisher) and nearby Mt Isa base metal deposits. Mineralization is dominantly stratiform and stratabound (Valenta, 1994; Chapman, 2004) and is hosted exclusively by the Urquhart Shale unit which comprises pyritic siltstones and carbonaceous siltstones interbedded with dolomitic mudstones (Chapman, 2004). Some galena has been remobilized during deformation (Chapman, 2004). George Fisher has subtle differences from the Hilton and Mt Isa deposits such as its relatively Zn-rich, Ag-poor resource and the absence of significant copper mineralization. The Mt Isa deposit is relatively Pb-rich and has lower Zn grades than George Fisher. Significant copper mineralization is located adjacent to the Pb-Zn orebodies at Mt Isa. The George Fisher deposit therefore represents a Zn-rich, Cu and Ag-poor end-member of the three world-class lead-zinc-silver deposits in the Mt Isa district (Chapman, 2004).

World class base metal deposits can be divided into two categories: giant and super-giant (Singer, 1995). Giant Zn deposits (largest 10% of deposits) comprise >1.7 Mt of Zn and super-giant (largest 1% of deposits) >12 Mt of contained metal (Singer, 1995). Of the eight super-giant Zn deposits in the world, five are in Australia; and include George Fisher and the adjacent Hilton deposits (Large et al., 2002). The George Fisher deposit had a pre-mining resource of 108 Mt grading 11.1% Zn, 5.4% Pb, and 93g/t Ag (MIM Ltd : Report to shareholders – 1998) and qualifies as a giant deposit (Singer, 1995) for both Pb and Ag.

Stratiform lead-zinc deposits are, by definition, conformable with their bedded sedimentary host-rocks. At the broader scale this can be interpreted as indicating concurrent sedimentation and processes of mineralization, however, textural analysis of the mineralization-types often reveals that replacement and veining are important mechanisms of sulphide deposition, therefore indicating mineralization subsequent to deposition of the host-rock sequence. This may occur during diagenesis or later in the deformation history of the rocks. Determination of the timing of mineralization with respect to host-rock formation, diagenesis, and episodes of subsequent deformation has significant implications on the types of exploration models employed in order to discover further Zn-Pb-Ag resources.

Several genetic models have been developed for the sedimentary-hosted Zn-Pb-Ag deposits of the Mt Isa Inlier. The syn-sedimentary or SEDEX genetic model involves hydrothermal fluids carrying metals in solution being expelled from a vent, which are typically inferred to be faults active during rift-associated extension, and sulphides deposited on the seafloor contemporaneous with sediment deposition (e.g. Russell et al., 1981; Sawkins, 1984; Hancock and Purvis, 1990; Cooke et al., 2000). The conformity of mineralization within the sedimentary sequence and stacked geometry of orebodies has been interpreted as a result of episodic expulsion of ore-fluid and precipitation punctuated by periods of sedimentation during which little or no sulphides were formed (Sawkins, 1984; Valenta, 1994). Zn-Pb-Ag mineralization at Mt Isa and Hilton/George Fisher has also been interpreted as having formed during diagenesis (Neudert and Russell, 1981; Valenta, 1988, 1994, Chapman, 1999, 2004). This differs from SEDEX models in that mineralization occurs below the seafloor and occurs as replacement and cavity infill of specific sedimentary sequences. Chapman (1999) interpreted chemically distinct phases of carbonate alteration associated with Zn-Pb-Ag mineralization as diagenetic in origin. Precipitation of sulphides during syntectonic replacement of lithified and deformed sediments has been inferred by Blanchard and Hall (1942), Perkins (1997, 1998), and Perkins and Bell (1998). The spatial correlation and parallelism of high-grade mineralization and fold axes at Mt Isa have been interpreted as supporting the syntectonic genetic model for Zn-Pb-Ag mineralization (Wilkinson, 1995; Perkins, 1997; Davis, 2004).

Previous interpretations of the George Fisher/Hilton deposit infer that the Zn-Pb-Ag mineralization records the same deformation history as the host-rocks (Valenta 1988, 1994) and initial mineralization has been interpreted as predating much of the deformation history. Chapman (1999, 2004) inferred that the George Fisher Zn-Pb-Ag deposit formed during diagenesis with remobilization of galena in the later stages of the deformation history. The key observations linking mineralization with diagenesis include:

- low temperature bitumens interpreted to be of diagenetic origin and cogenetic with sphalerite,
- spatial coincidence of the Zn-Pb-Ag deposit within a carbonate alteration system interpreted as pre-stylolitization and diagenetic, and
- isotopic evidence that the interpreted fluids responsible for Zn-Pb-Ag mineralization are distinct from the Cu (D_4) mineralizing fluids.

This study benefits from the wealth of studies into the stratigraphy, structure, alteration and mineralization processes in the Mt Isa – George Fisher – Lake Moondarra area. Fewer studies have been undertaken on the George Fisher deposit itself, principally due to the lack of mine development pre-1998. The key studies of the George Fisher deposit and environs include comprehensive analysis of the mineralization and alteration paragenesis (Chapman, 1999) and structural analysis of the adjacent Hilton deposit (Valenta, 1988). The purpose of this study is to make detailed structural observations of the George Fisher deposit host-rocks and mineralization from thin-section to deposit-scale and assess whether areas of higher-grade and thicker mineralization are systematically related to deformational features or a unique structural setting. This requires analysis of grade and sulfide distribution and interpretation of the relative timing of textural varieties of mineralization within the framework of the structural history of the deposit. The results of this analysis are likely to be significant guides for within-mine definition and near-mine/extensional exploration for Zn-Pb-Ag mineralization at George Fisher. Absolute ages from rhenium-osmium isotopic data collected from the sulfide samples will assist in refining the timing of mineralization relative to deformation episodes and the isotopic signature can indicate the source of metals which comprise the deposit. Comparison of the interpreted controls on the setting of the George Fisher Zn-Pb-Ag deposit with other significant deposits of the Western Fold Belt in the latter part of this study aims to add to the knowledge base on metallogenic processes in the Mt Isa Inlier and is intended as an aid to exploration for further Zn-Pb-Ag mineralization.

Thesis Structure

This thesis is presented as six sections (A-F), each written in journal article format and summarized below:

Part A. The structural features observed from mine-scale through to micro-scale at the George Fisher deposit are described and their overprinting relationships demonstrated. Emphasis is placed on micro-scale observations as the foliations are not mappable at the exposure-scale. Areas which have unique geometric relationships of overprinting structures and more intense foliation and/or fold development are indicated.

Part B. Grade distribution of constituent metals and the cumulative thickness of mineralization is evaluated enabling definition of ore-shoot orientations and geometry. Ore-shoot locations and orientations correlate with identified structures and domains in Part A and is suggestive of some mine-scale remobilization/syntectonic mineralization.

Part C. Criteria for determining the deformation history of sphalerite through fractal analysis of grain boundary geometry is established. Undeformed, deformed, and recrystallized sphalerite can be distinguished using these criteria and conventional microscopic analysis.

Part D. Distinction and relative timing of mineralization-types is established through mine-scale distribution, mapping at exposure to hand-specimen scale, and microtextural analysis. Interpretation of the range of mineralization types includes both pre- and post-deformation sulphide deposition.

Part E. Re-Os isotopic analysis of the ore-sulphides and some host-rocks suggests that Zn and Pb have a common source from a mantle-derived fluid. An age estimate is obtained but does not indicate a specific deformation episode controlling later mineralization as the uncertainty is large.

Part F. Utilizing interpretations from Parts A-E, comparison is made with other large Zn-Pb-Ag deposits in the Western Fold Belt to determine whether there are consistent controls on the location of these deposits.

References

Blanchard, R. and Hall, G., 1942. Mt Isa ore deposition: Economic Geology, v. 32, p. 1042-1057.

Chapman, L.H., 1999. Geology and genesis of the George Fisher Zn-Pb-Ag deposit, Mount Isa, Australia. (Unpublished PhD thesis – James Cook University, Townsville).

Chapman, L.H., 2004. Geology and mineralization styles of the George Fisher Zn-Pb-Ag deposit, Mount Isa, Australia: Economic Geology, v. 99, p. 233-255.

Cooke, D.R., Bull, S.W., Large, R.R., and McGoldrick, P.J., 2000. The importance of oxidized brines for the formation of Australian proterozoic stratiform sediment-hosted Pb-Zn (Sedex) deposits: Economic Geology, v. 95, p. 1-18.

Davis, T.P., 2004. Mine-scale structural controls on the Mount Isa Zn-Pb-Ag and Cu orebodies: Economic Geology, v. 99, p. 543-559.

Hancock, M.C. and Purvis, A.H., 1990. Lady Loretta Silver-Lead-Zinc Deposit, In: Hughes, F.E. (Ed.), Geology of the mineral deposits of Australia and Papua New Guinea. p. 943-948, (The Australasian Institute of Mining and Metallurgy: Melbourne).

Large, R., Cooke, D., and Davidson, G., 2002, What is a world class deposit?: Abstracts of the 16th Australian Geological Convention, p. 266.

Neudert, M.K. and Russel, R.E., 1981. Shallow water and hypersaline features from the middle Proterozoic Mount Isa sequence: Nature, v. 293, p. 284-286.

Perkins, W.G., 1997. Mount Isa lead-zinc orebodies: Replacement lodes in a zoned syndeformational copper-lead-zinc system?: Ore Geology Reviews, v. 12, p. 61-110.

Perkins, W.G., 1998. Timing of formation of Proterozoic stratiform fine-grained pyrite: Post-diagenetic cleavage replacement at Mount Isa?: Economic Geology, v. 93, p. 1153-1164.

Russell, M.J., Solomon, M., and Walshe, J.C., 1981. The genesis of sediment-hosted, exhalative zinc and lead deposits: Mineralium Deposita, v. 16, p. 113-127.

Sawkins, F.J., 1984. Ore genesis by episodic dewatering of sedimentary basins: Application to giant Proterozoic lead-zinc deposits: Geology, v. 12, p. 451-454.

Singer, D.H., 1995, World Class Base and Precious Metal Deposits – A Quantitative Analysis: Economic Geology, v. 90, p. 88-104.

Valenta, R.K., 1988. Deformation, fluid flow and mineralization in the Hilton area, Mt Isa, Australia. (Unpublished PhD thesis – Monash University, Melbourne).

Valenta, R.K., 1994, Deformation in the host rocks and stratiform mineralization in the Hilton Mine area, Mt Isa: Australian Journal of Earth Sciences, v. 41, p. 429-443.

Wilkinson, D.L., 1995. Structural termination of 8 orebody and its implications for the genesis of lead-zinc-silver mineralisation, Mount Isa, Queensland: Unpublished Hons thesis, James Cook University, Townsville, Australia.

PART A

Structural development of host rocks to Zn-Pb-Ag mineralization at the George Fisher Mine, Northwest Queensland, Australia.

Abstract

The host rocks to base-metal mineralization at the George Fisher Mine, NW Queensland; record the effects of four discrete episodes of ductile deformation during the Isan orogeny (~1610 – 1510Ma). Initial north-south directed shortening (D_1) produced east-west oriented folds and was followed by the main phase of east-west directed horizontal shortening characteristic of this orogeny (D_2). This produced district-scale upright folds with approximately north-south trending axes. In the George Fisher Mine, the effects of D_2 are recognized as a pervasive slaty foliation (S_2) and the majority of mesoscale folds in the mine are F_2. Subsequent sub-vertical shortening during D_3 resulted in the development of asymmetric crenulation of S_2 and bedding, and rotation/flattening of F_2 folds into inclined and recumbent attitudes. Ongoing east-west directed horizontal shortening produced a crenulation of the composite S_0/S_{0c}(compaction)/S_2 fabric and cross-cuts S_3 crenulations. Formation of sub-vertical D_4 fold axial planes and crenulations is restricted to areas affected by the D_3 deformation which rotated vertical and west-dipping older D_1-D_2 fabrics/structures into inclined orientations. In areas of little or no D_3 strain, D_4 results in the reuse of the earlier S_2 fabric and reactivation of bedding. The structural features observed at George Fisher are consistent at micro-, meso-, exposure-, and macro scales.

1. Introduction

Valenta (1988, 1994) and Chapman (1999, 2004) present part or all of a structural history for the Hilton and George Fisher deposits, respectively (George Fisher referred to as Hilton North in Valenta, 1988, 1994). Both recognize a main episode of folding and slaty cleavage development during D_2 with axial planes and cleavage striking north to north-northwest. Valenta (1988, 1994) correlated this slaty cleavage at Hilton (S_2) with the axial planar cleavage associated with district-scale F_2 folding immediately east of the George Fisher and Hilton deposits in the Lake Moondarra region (Winsor, 1982, 1983, 1986; Bell, 1983). Both Valenta and Chapman observed minor folds with sub-horizontal axial planes post-dating F_2 folds. Valenta (1988, 1994) observed gently dipping spaced crenulations (S_3) associated with this deformation. D_4 is interpreted to have resulted in northeast and northwest trending chevron-like folds associated with shear-zones at the Hilton deposit (Valenta, 1988, 1994) and small-scale north-northwest/northwest trending folds with an axial planar cleavage, S_4, at George Fisher (Chapman, 1999, 2004). Correlation of these interpretations with other structural analyses in this part of the Mt Isa Inlier is presented following the description and interpretations of structures in this study.

This paper represents part of a structural analysis of the George Fisher mineralization and host-rocks. Significant mine development has occurred in the George Fisher deposit since the studies by Valenta and Chapman and has enabled detailed mapping and collection of oriented samples in areas which previously could only be interpreted from unoriented diamond-drill core. A detailed microstructural study of both mineralized and unmineralized rocks has been undertaken to determine the sequence of deformation events and the kinematics associated with each. Data from oriented thin sections is presented as a series of deposit-scale form-line maps. The aim of this study is to provide a framework within which the timing of mineralization can be determined and to develop an understanding of the kinematics of each deformation phase which may elucidate key controls on the location of any mineralization that formed during each deformation phase.

2. Geological Setting

2.1 Regional geology

The George Fisher, Hilton, and Mt Isa Zn-Pb-Ag deposits are hosted by polydeformed metasedimentary rocks which form the Leichardt River Fault Trough in the Western fold belt of the Proterozoic Mt Isa Inlier (Figure 1). These sediments were deposited during intracontinental extension between 1780Ma and 1590Ma (Blake and Stewart, 1992; O'Dea et al., 1997a,b; Southgate et al., 2000; Betts and Lister, 2002). The present configuration of the Leichhardt River Fault Trough represents overprinting extensional events (the Leichhardt/Myally Rift Event and Mt Isa Rift Event) with intervening basin formation due to thermal subsidence (Betts et al., 1998). Extension and basin development was terminated prior to the formation of oceanic crust due to the ensuing period of east-west directed shortening associated with the Isan Orogeny (Blake et al., 1990). The Leichardt River fault trough, contains extensive N to NW trending macroscale folds which formed during the Isan orogeny between 1610Ma and 1510Ma (Page and Bell, 1986), and is distinct from the lesser deformed Lawn Hill Platform (Williams, 1998). The Western fold belt is unconformably overlain by the sedimentary rocks of the South Nicholson Basin to the north and bound by a faulted contact with basement rocks of the Kalkadoon-Leichardt Belt to the east.

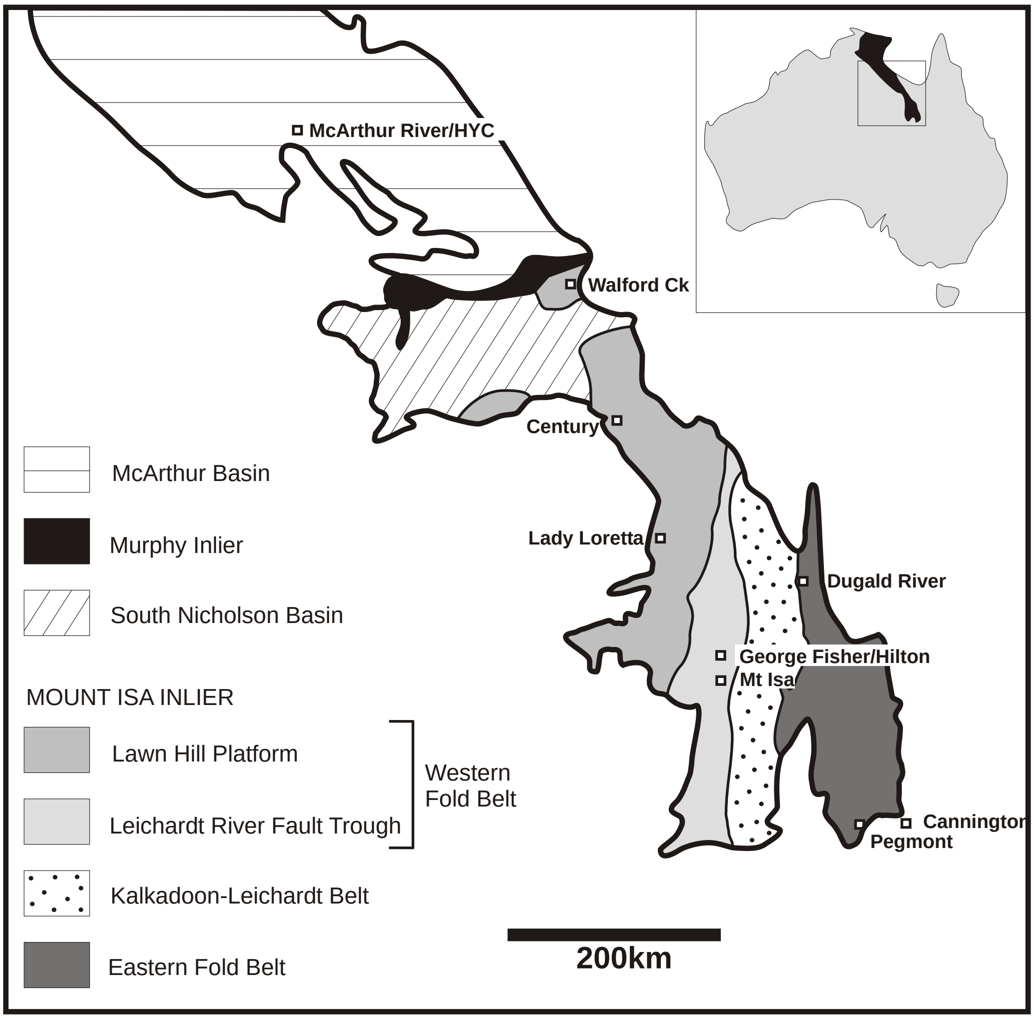

(after Williams, 1998)

Figure 1. Map of the Proterozoic McArthur and Mt Isa Inliers showing location of the major Pb-Zn deposits in the region, including George Fisher.

Major lithostratigraphic units and structures in the vicinity of the George Fisher deposit are illustrated in Figure 2. Large, kilometre-scale folds between George Fisher and Lake Moondarra dominate the structural fabric. The Haslingden Group (Figures 2 and 4) comprises the Mount Guide/Leander Quartzite, basaltic lavas and subordinate sediments of the Eastern Creek Volcanics, and these are overlain by feldspathic and quartz sandstone of the Myally subgroup (Blake and Stewart, 1992). The Haslingden Group was deposited from 1780 to 1760Ma (Blake and Stewart, 1992). Reverse thrusting on the Mt Isa – Paroo Fault system has brought these older rocks in contact with the younger (~100my) Mt Isa Group. The George Fisher deposit is hosted by the Urquhart Shale formation in the upper Mt Isa Group (Figure 2) which is dominated by rhythmically laminated siltstones, pyritic siltstones and mudstones metamorphosed to subgreenschist facies (Chapman, 1999, 2004). U-Pb ages of zircons hosted by interbedded tuffaceous marker horizons within the sedimentary sequence yield an age of 1655±4Ma (Page et al., 2000). The lower Mt Isa Group comprises quartz-rich shale, siltstones and a basal quartz-sandstone/quartzite layer (O'Dea et al., 1997a).

The Sybella batholith to the west of George Fisher (Figures 2 and 3) was emplaced during rifting between 1660±4Ma and 1655±5Ma (Connors and Page, 1995). Emplacement may have continued during deposition of the Mt Isa Group sediments (Connors and Page, 1995). The Sybella batholith is a multistage felsic plutonic complex (Figure 3) implicated in the formation of a high strain zone in the George Fisher area (Valenta, 1988). However, microgranite occurring immediately to the west of the Mt Isa-Paroo fault near the George Fisher deposit (Figure 3) has been interpreted as genetically unrelated to the main-phase and β-quartz phase of intrusion (Figure 3) (Wyborn et al., 1988).

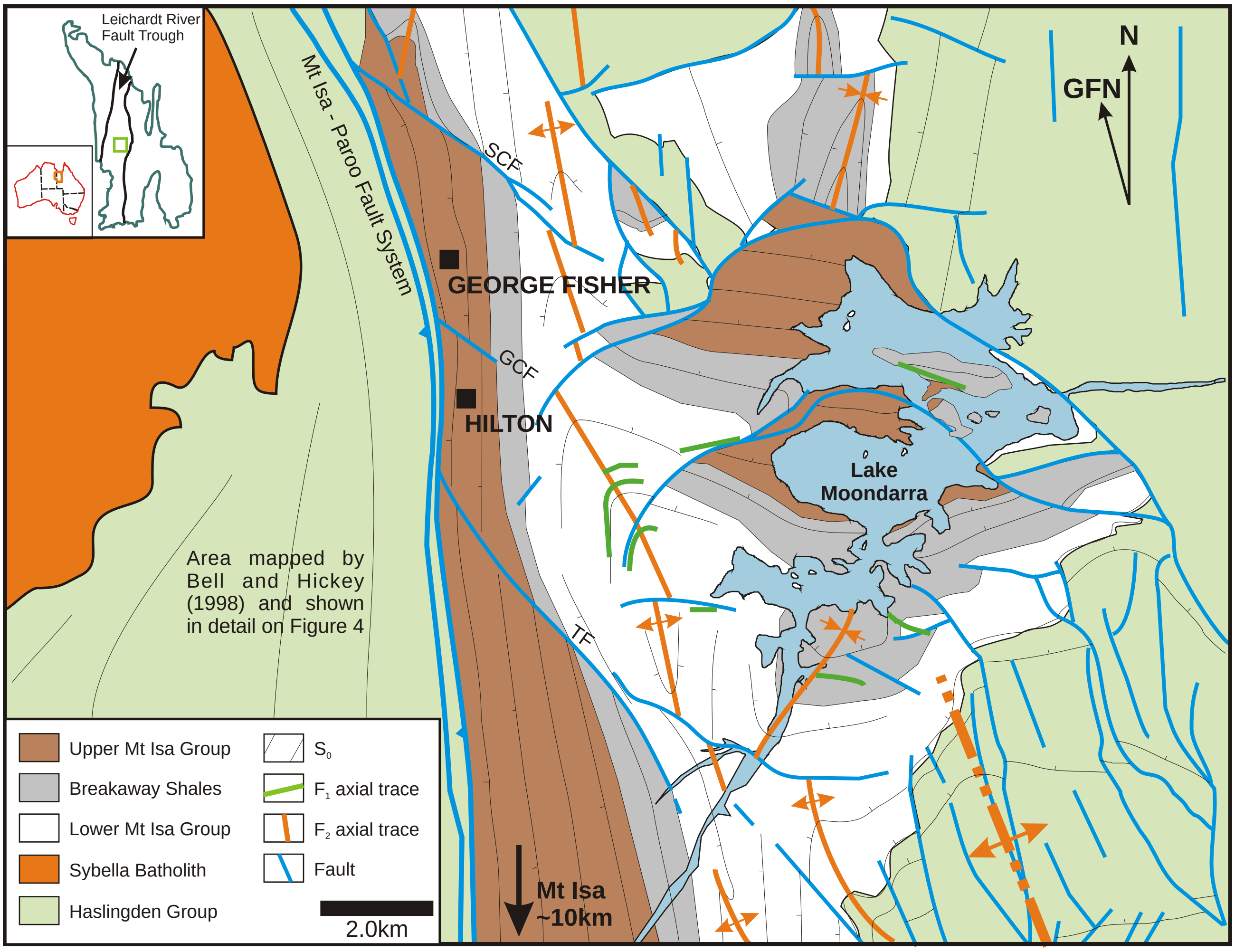

After Winsor (1986), Blake (1987), and Bain et al. (1992)

SCF - Spring Creek Fault

GCF - Gidyea Creek Fault

TF - Transmitter Fault

Figure 2. District-scale geological map showing key geological units and structural features. Note the F_2 folding in the Lake Moondarra area which dominates the structural grain of the Leichardt River fault trough. The thick dashed axial trace in the southeast corner of the map is an approximate location of the regional 20km$^+$-wavelength F_2 fold from Bain et al. (1992).

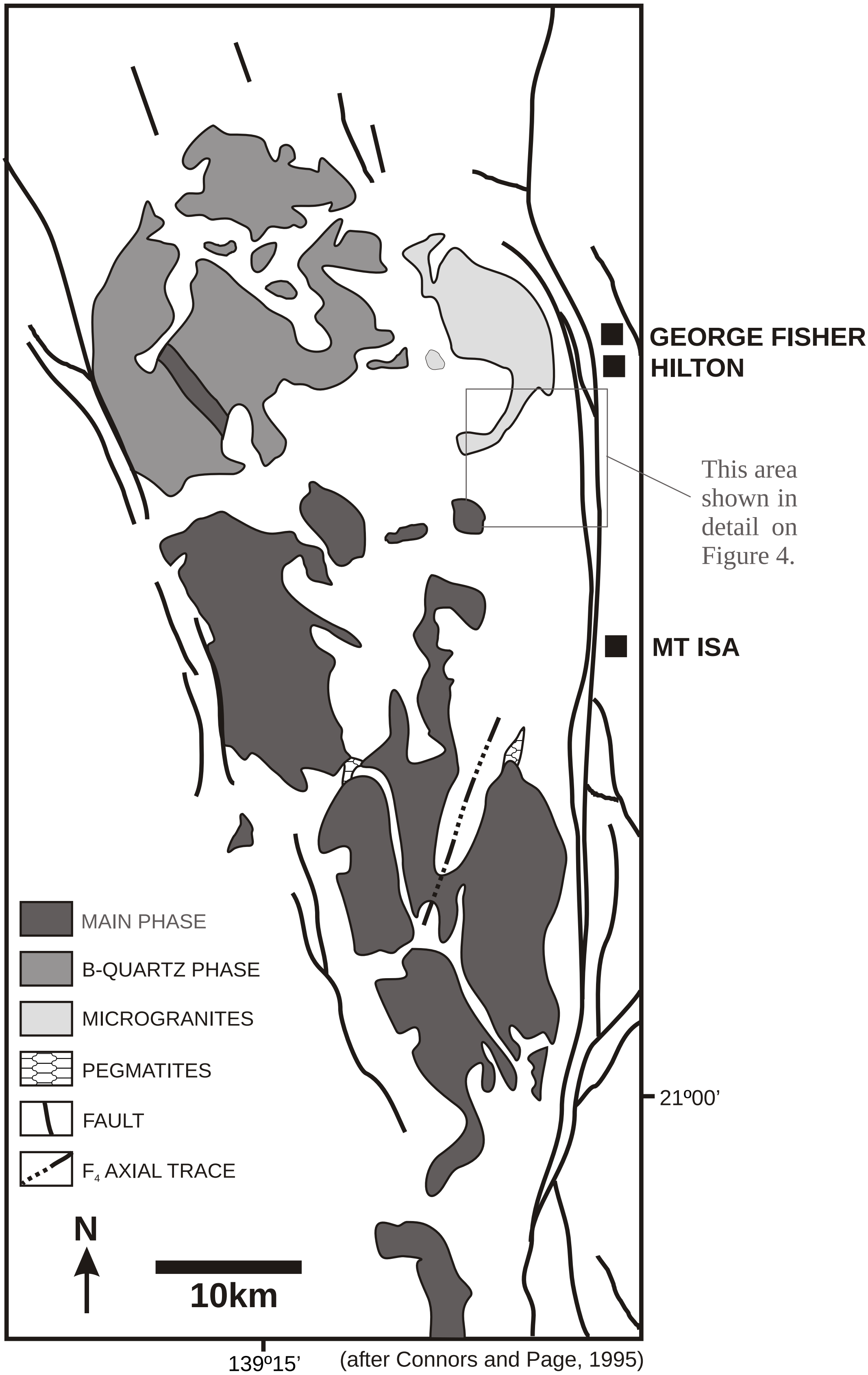

Figure 3. Map of the Sybella Batholith showing the distribution of different phases of the batholith and surrounding faults.

Dissimilarity in sub-surface geometry of the microgranite intrusion as compared to the main batholith supports a differing timing/genetic relationship. The microgranite constitutes approximately 10% of the batholith (Connors and Page, 1995) and has been dated at 1510±10Ma (Page and Bell, 1986). Foliation form-line trends have been constructed from mapping by Bell and Hickey (1998) in the area immediately south of the microgranite (Figures 3 and 4). S_2 form-lines intersect this part of the intrusion at a high angle suggesting that the microgranite post-dates D_2, whereas S_4 form-lines are generally sub-parallel to the district-scale margins of the batholith suggesting the intrusion pre-dates D_4 (Figure 4).

The George Fisher deposit is situated approximately 200m east of the regional scale Mt Isa-Paroo fault system (Figure 2, 3) and is situated between two large scale northwest trending D_4 faults, the Transmitter and Spring Creek faults (Figure 2). The locally significant Gidyea Creek Fault separates the Hilton and George Fisher deposits (Figure 2). Major faults of the Mt Isa – George Fisher – Sybella Batholith region are focussed near the margin of the batholith (Figure 3).

Rocks of the Leichardt River Fault Ttrough record the effects of the Isan orogeny which was active from 1610±13Ma (D_1) to 1510±13Ma (D_3, D_4 this study) (Page and Bell, 1986). The main phase of deformation responsible for regional scale folding and basin inversion in the Leichardt River Fault Trough occurred during D_2 at 1544±12Ma (Page and Bell, 1986).

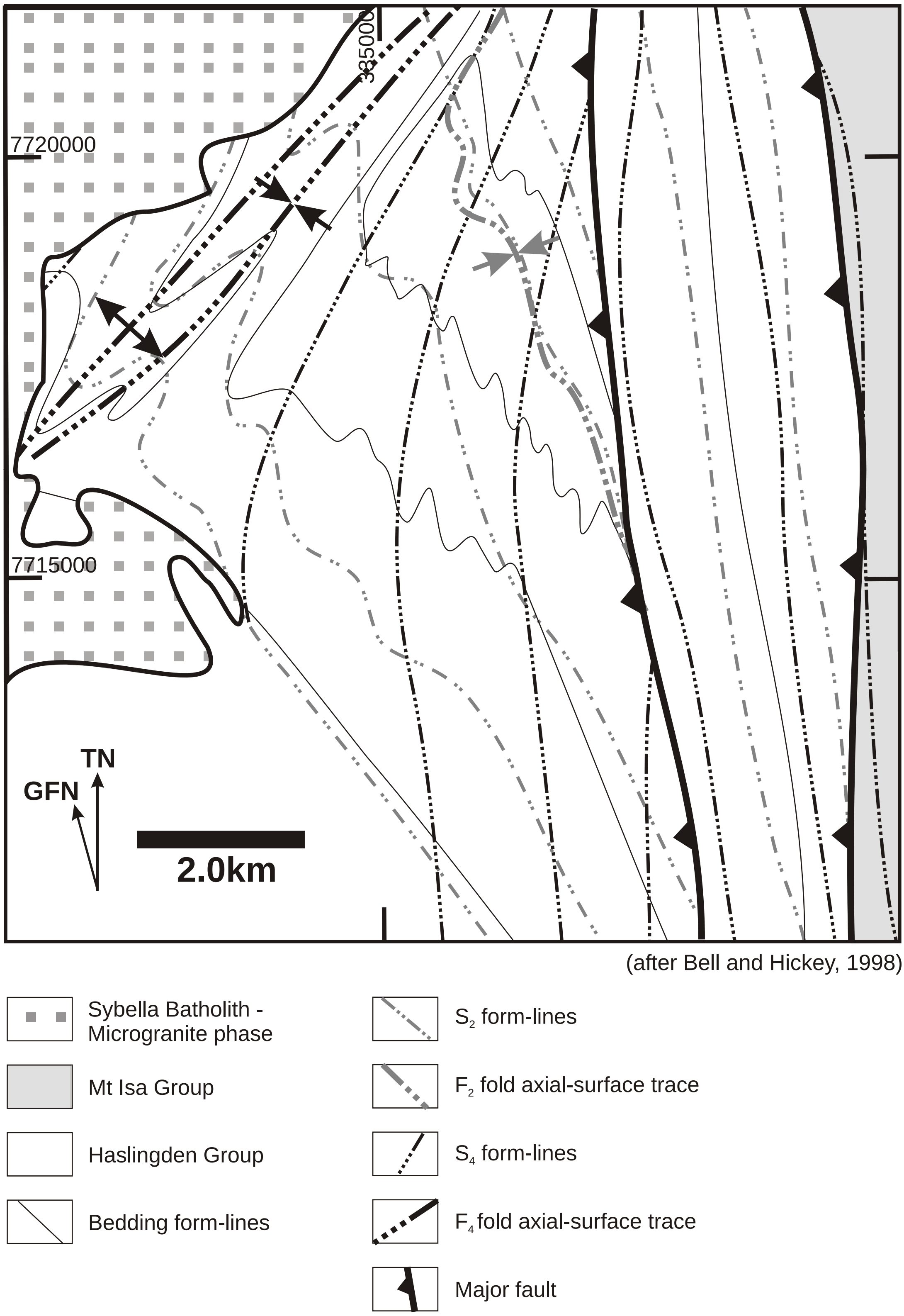

Figure 4. Simplified geological map of the region southwest of George Fisher and west of the Mt Isa - Paroo Fault (see Figures 2 and 3).

Peak metamorphism during the Isan Orogeny is interpreted to have occurred at 1532±7Ma based on the overprinting relationships of syn-D_2 pegmatites to cleavages and the interpretation that the pegmatites were derived from partial melting during peak metamorphism (Connors and Page, 1995). Peak metamorphism and main phase deformation therefore occur synchronously at approximately 1540Ma. The Mt Isa Group lithologies which host mineralization at George Fisher have been metamorphosed to subgreenschist facies and analysis of bitumen reflectance indicates a maximum temperature of ~200°C during D_2 and ~280°C locally during D_4 (Chapman, 1999, 2004). Peak metamorphic temperatures in the Mt Isa Group rocks at Mt Isa are higher than George Fisher at ~350°C to 300°C (Rubenach, 1992).

2.2 Local geology

The geology of the George Fisher area is dominated by the Upper Mt Isa Group metasedimentary rocks. This group comprises the Breakaway Shale, Native Bee Siltstone, Urquhart Shale, and Spears Siltstone (Figure 5). Zn-Pb-Ag mineralization is hosted exclusively by Urquhart Shale at George Fisher. Rock-types which host mineralization at George Fisher comprise laminated siltstones, laminated pyritic siltstones and dolomitic mudstones (Chapman, 1999, 2004). Folding at the local scale comprises approximately east-west oriented open folds and north-south oriented east-verging closed folds (Figure 5). These are parallel to the F_1 and F_2 folds observed in the Lake Moondarra region, respectively (Winsor, 1986, Figures 2 and 5).

In the underground mine, extensive mine development has enabled recognition of the several faults which cross-cut the ore-horizons. Northeast striking dextral normal faults

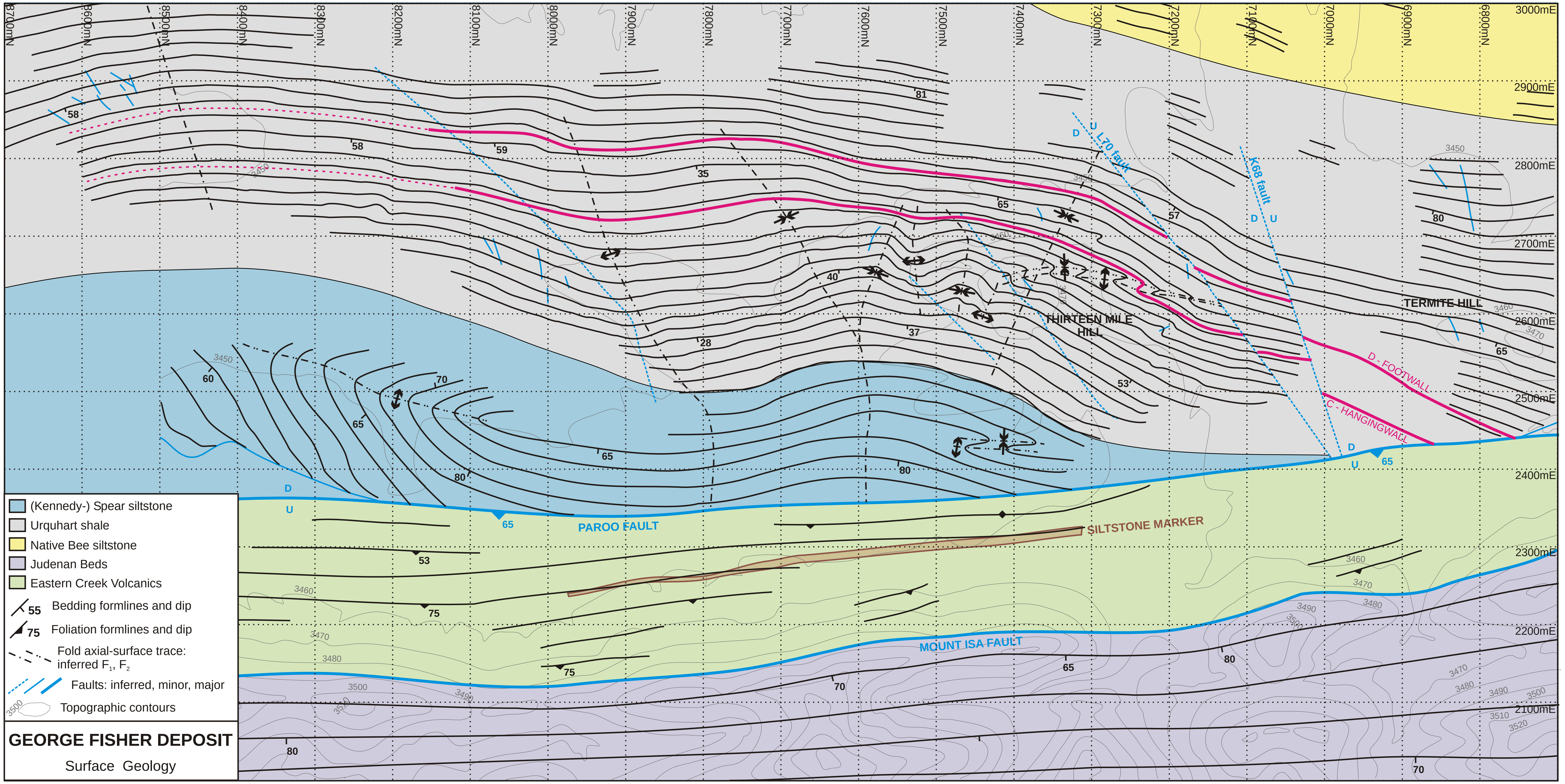

Figure 5. Simplified geological map illustrating the main geological features at the surface above the George Fisher Mine. Open folds with ENE and ESE trending axial traces and westerly plunges dominate the structure of the Urquhart Shale at surface and a tight fold with northerly plunge occurs in the Spear Siltstone at 8200mN/2500mE . The Paroo Fault forms the contact between the Mt Isa Group rocks and the Eastern Creek Volcanics. (Bedding formlines constructed from 1:600 and 1:2500 Hilton Mine Geological Maps, lihological data is from the 1:2500 Hilton Mine Geological Map and the George Fisher drill-hole database).

dominate the structure of the underground orebodies and the Paroo Fault is located approximately 150-200m west of the underground workings at George Fisher (Figure 6).

Mineralization occurs as stratabound concentrations of sulphides separated by barren mudstones (Figure 6). The ore-horizons (Figure 6) represent laminated siltstones and pyritic siltstones with variable amounts of ore-sulfides. Intervening layers of massive dolomitic mudstone are barren of mineralization. Ore-grade mineralization can be continuous for up to one kilometre along strike at George Fisher. Equivalent stratigraphic intervals are also mineralized at the Hilton Pb-Zn-Ag deposit approximately 2 kilometres to the south (Valenta, 1988; Tolman et al., 2002). The ore zones at George Fisher form an en echelon stacked arrangement both along-strike and down-dip, the encompassing surface of which transgresses stratigraphy (Chapman, 1999).

The dominant mineralization styles at George Fisher are stratabound (confined to a package of stratigraphy) and stratiform (having the form of strata, i.e. tabular, bedding parallel occurrence) bedding-parallel sphalerite-dominant accumulations with vein-like characteristics and galena breccias which are locally discordant to bedding but are still stratabound on the larger scale (Chapman, 1999, 2004). Galena and sphalerite occur as both texturally distinct and mixed mineralization styles (Chapman, 1999, 2004). Distribution of the respective ore-types is heterogeneous within the deposit. Details of the mineralization styles and relative timing are discussed in Part D.

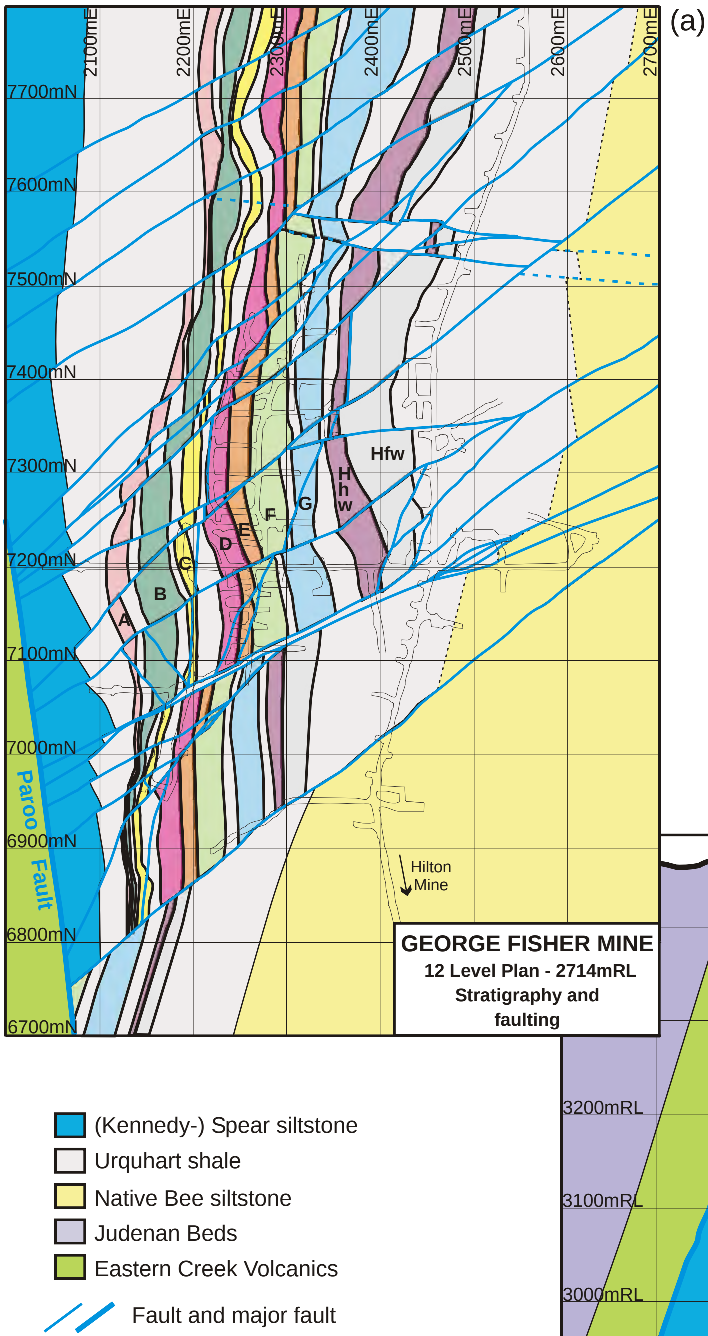

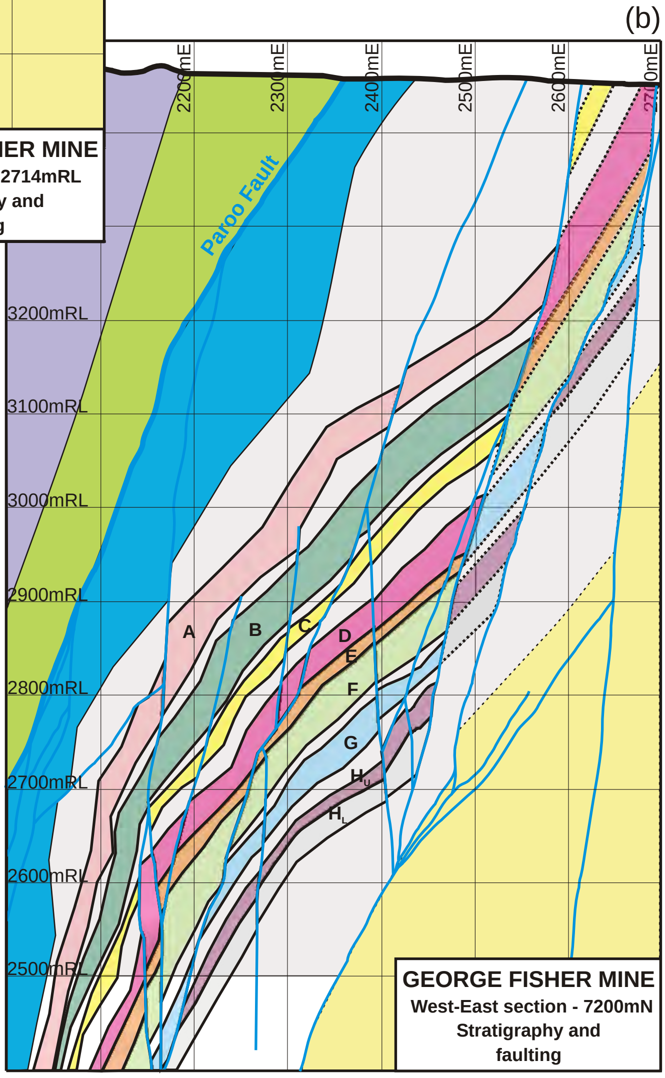

Figure 6. Simplified geology and stratigraphic units of the George Fisher deposit in plan view, (a), and west-east cross-section, (b). The Urquhart Shale is divided into 'ore-horizons' as indicated by labels A-H.

3. Primary Layering – Bedding

Bedding (S_0) in siltstones at George Fisher is defined by compositional and grainsize variation. Individual beds are generally <10cm thick and can be traced for several kilometres (Tolman et al., 2002). Bedding planes often exhibit strong parting and polished graphitic surfaces. Slickensides and foliation intersection lineations are most readily identified on bedding planes.

Sedimentary structures such as cross-bedding and load-casts are present but not a common feature. Graded bedding is observed occasionally in meso- and micro-scale analysis. The stratigraphy at George Fisher youngs to the west.

Bedding within the deposit strikes between northwest and northeast (Figure 7a), north-south in the broader context of the Mt Isa valley (Figure 2). The dip of bedding is generally between 40° and 70° toward the west at George Fisher as a result of regional-scale north-south trending D_2 folding (Winsor, 1986).

A bedding-parallel foliation is widely developed. This fabric commonly occurs as bedding-parallel, discontinuous pressure-solution seams and stylolites (Figure 7b). Folds with bedding-parallel axial planes which may account for the foliation are not observed in the George Fisher area (cf. Valenta, 1988, 1994; Chapman, 1999, 2004). A period of stylolitization associated with diagenesis has been interpreted by Chapman (1999). This episode predates deformation associated with the Isan orogeny (Chapman, 1999). Bedding-parallel stylolites are overprinted by younger fabrics (Figure 7b) which correlate with the S_2 of Valenta (1988, 1994) and Chapman (1999, 2004). The bedding-parallel

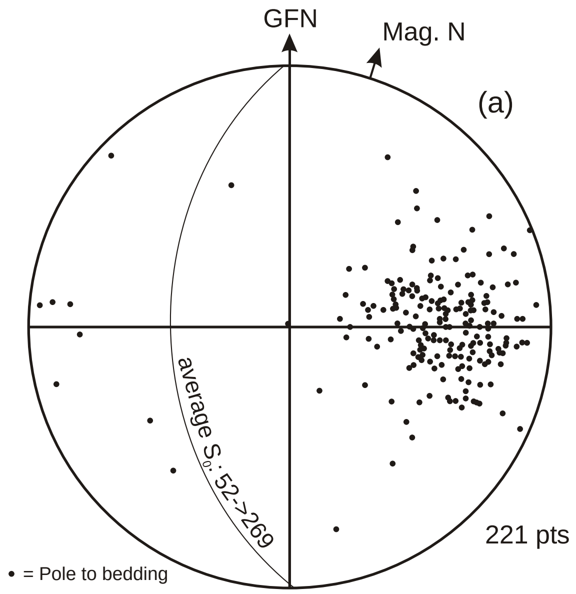

Figure 7. (a) Poles to bedding (S_0) measurements plotted on an equal area lower hemisphere stereonet, (b) S_{0c} occurring as pressure solution seams or stylolites in a phyllosilicate-poor mudstone, a larger carbonate grain is bounded by two seams to the right of 'A'. Sample 1111-4. (c) S_{0c} deformed by the pervasive S_2 fabric, note the z-shaped asymmetry of deformed pressure solution seams to the right of 'B'. Sample 0512-3. Both photomicrographs are in ppl.

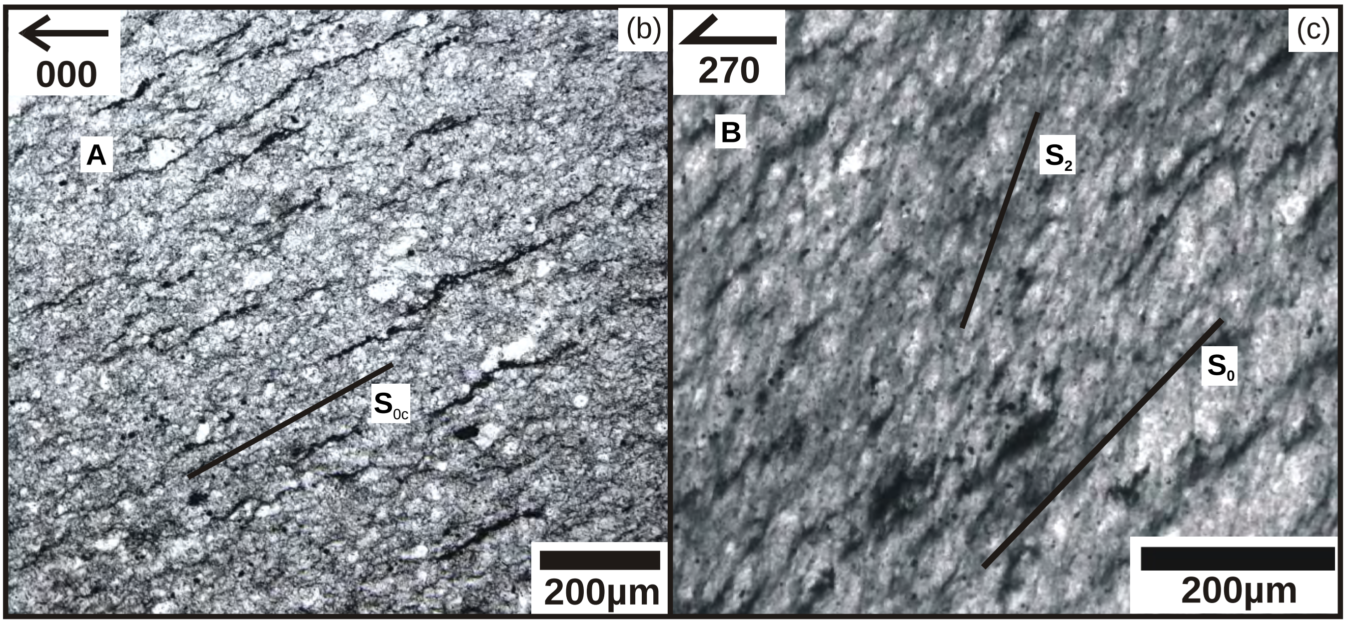

Deformation Event	Form Surfaces	Generated Elements	Folds Formed	Comments
D_1	S_0, S_{0c}	S_1	F_1 ($F^{0\|\|0c}{}_1$)	$S_0\|\|S_{0c}$, S_1 very localized
D_2	S_0, S_{0c}	S_2, $L^0{}_2$	F_2 ($F^{0\|\|0c}{}_2$)	Principal deformation event
D_3	S_0, S_{0c}, S_2	S_3, $L^0{}_3$	F_3 ($F^{0\|\|0c}{}_3$) $F^2{}_3$	Localized in areas of F_2 folding
D_4	S_0, S_{0c}, S_2, S_3	S_4, $L^0{}_4$	F_4 ($F^{0\|\|0c}{}_4$) $F^2{}_4$, $F^3{}_4$	Localized in areas of F_2 folding affected by D_3 deformation
Post-D_4	S_0, S_{0c}, S_2, S_3, S_4	S_5, S_6	Only microscale crenulations observed	Localized in areas of F_2 folding affected by D_3 and D_4 deformation

Table 1. Fabric Catalogue of recognized ductile deformation features

stylolitic foliation is therefore interpreted to have developed during compaction as part of the process of diagenesis rather than a product of secondary tectonism. Stylolites with orientations orthogonal to bedding have been recognized and may be associated with dissolution during subsequent deformations and therefore the interpretation of formation during diagenesis applies only to the bedding-parallel variety. The foliation will be referred to as S_{0c}, representing the foliation derived from compaction and lithification of bedding features. S_1 will be retained for the nomenclature of foliation resulting from the initial episode of deformation, D_1.

4. Deformation history

A fabric catalogue (Table 1) of the recognized structural elements at George Fisher has been constructed. The following description of deformation events describe the broader observations of each episode.

4.1 Description and interpretation of D_1 structures

A weak foliation (S_1) is observed in vertical west-east striking and horizontal thin-sections preserved in the strain-shadow of nodular carbonate grains (Figure 8). Later foliations destroy S_1 outside strain shadows adjacent to the nodules. Crenulation of a pre-existing fabric, termed S_{0c}, occurs in embayments of the nodule (Figure 8). This S_1 crenulation cleavage has a dextral sense of shear (Figure 8) and an average strike of 076° although rotation by subsequent deformations has resulted in the foliation striking 040° - 055° in places.

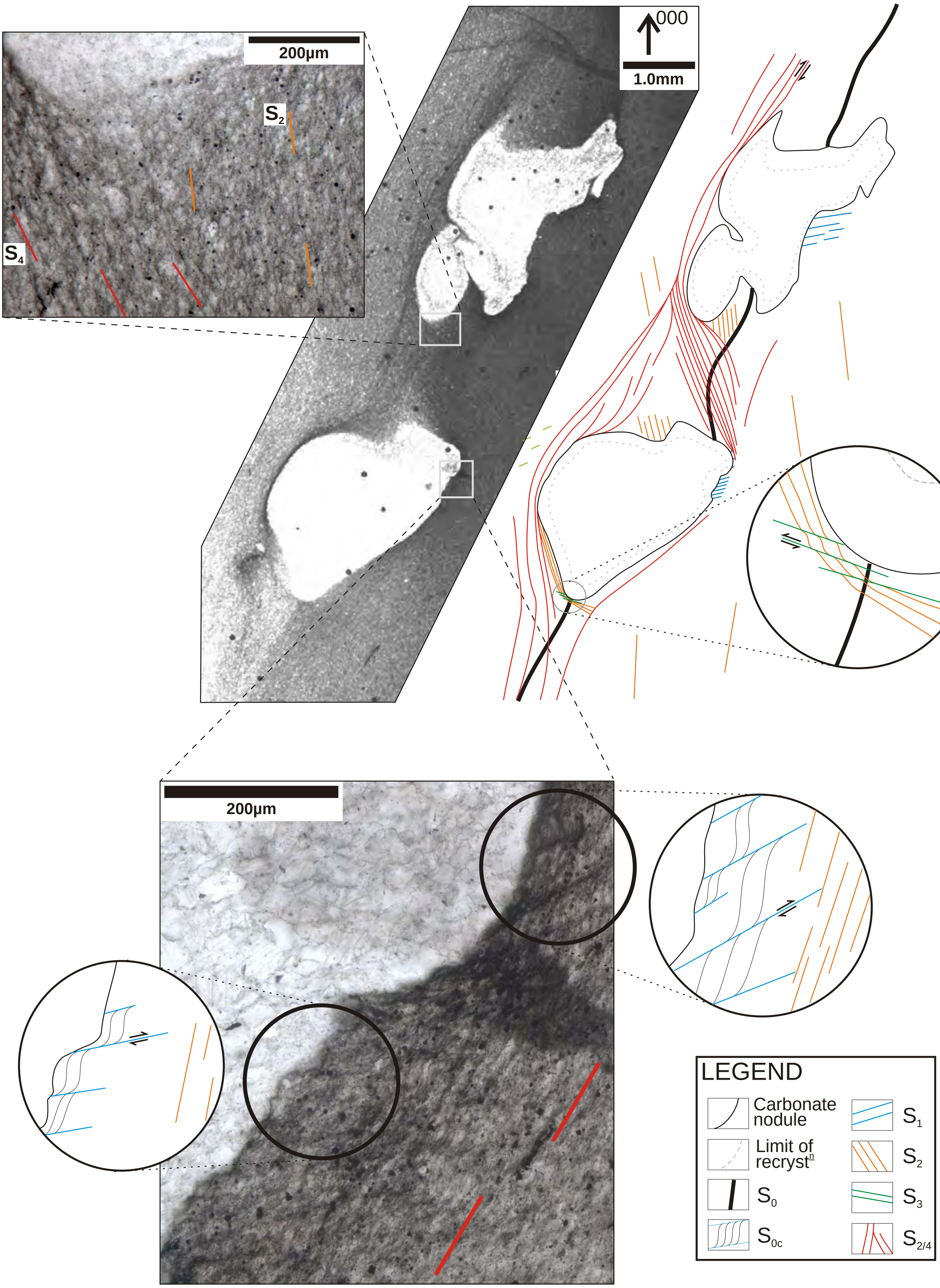

Figure 8. Photomicrographs and accompanying sketch in plan view demonstrating the preservation of interpreted earlier fabrics adjacent to carbonate nodules. Development of pervasive S_2/S_4 fabric around the nodules destroys the earlier fabric outside of the strain shadows. Sample 1412-3.

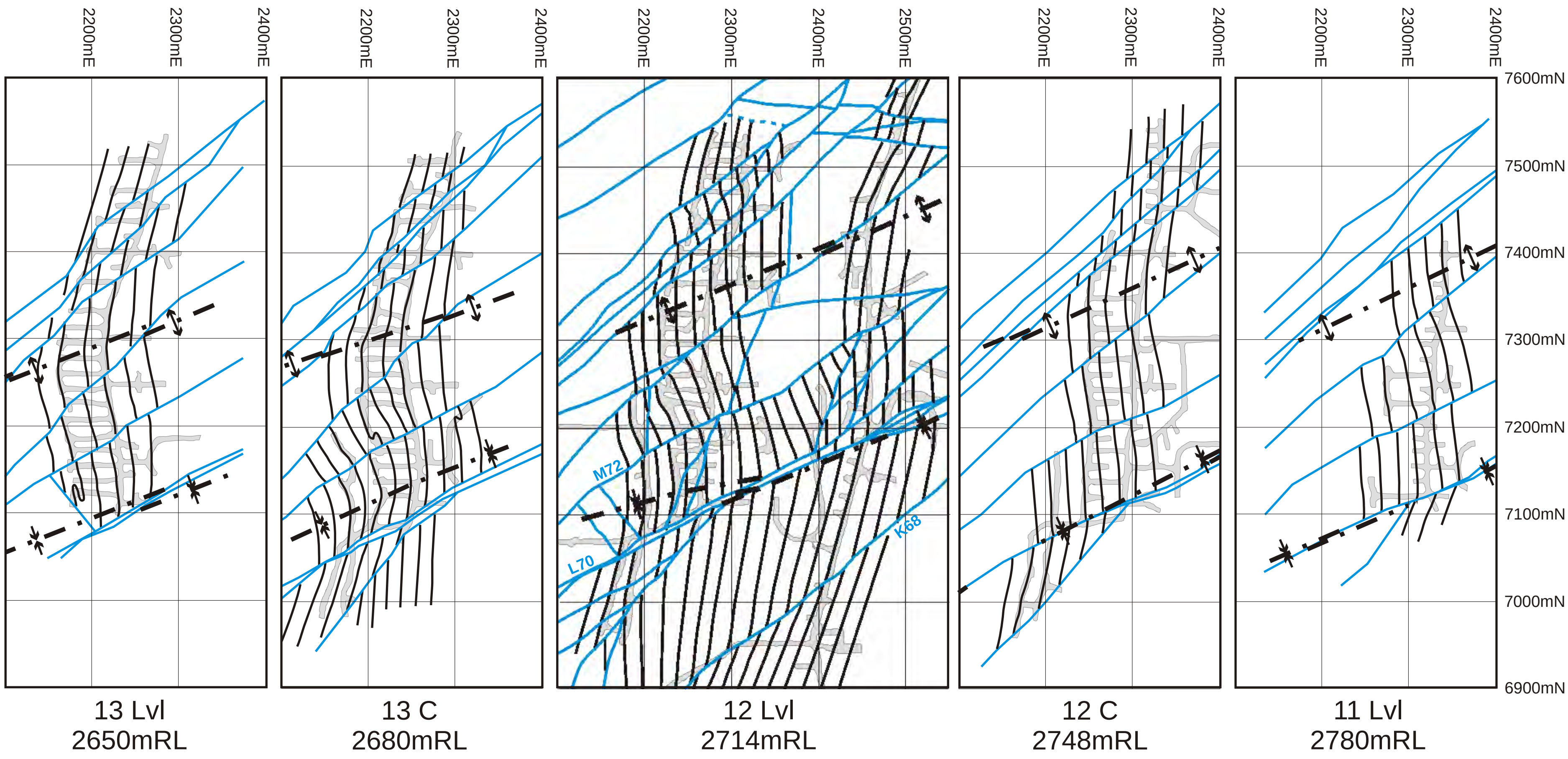

Figure 9. Bedding form-lines (black), faults (blue), and F_1 axial trace (dashed) over five levels of the mine. The extent of workings is illustrated with grey fill. The broad s-shaped flexure in bedding is interpreted as an F_1 fold. See text for discussion.

Minor ENE-WSW trending folds with moderate plunges (20°-50°) to the south-southwest (averaging 230°) occur within the George Fisher workings. The folds are open and axial planes of the folds are sub-vertical to steeply dipping to the southeast. The largest fold of this type occurs in the centre of the George Fisher workings (Figure 9). Bedding form-lines constructed for the five current levels of the George Fisher Mine show an open ‘s’-shaped flexure, particularly on the map of level 13C in Figure 9. The open fold is monoclinal in geometry and is defined by single antiformal and synformal axes. The half-wavelength or distance between synformal and antiformal axes of this fold is approximately 250m (wavelength not quoted as neither synformal nor antiformal axes are repeated along strike). The steep/sub-vertical dip of the fold axial planes is illustrated by the similar position of the axial planes on the five level plans over a 130m depth range (Figure 8). A flexure with the same orientation and vergence occurs at the surface approximately 700m above the George Fisher deposit between ~7700 and 7950mN (Figure 5). This flexure is up-plunge from the flexure in the George Fisher workings and is spatially co-incident with the Pb-Zn bearing gossans on Thirteen Mile Hill which first indicated the presence of Mt Isa style mineralization at George Fisher.

This large flexure is not a product of faulting, either through fault-drag folding, rotation, or ‘apparent’ folding via differential displacement on the cross-cutting faults. The orientation of bedding is only affected by fault-drag phenomena within 0.5 to 1.0 metre of the cross-cutting faults (Figure 10a and b). The M72 fault illustrated in Figure 10a has a displacement in the order of 5m with normal-dextral sense of movement. The drag folding associated with this fault only affects the surrounding rock within 0.5m either side of the fault. Similarly, the K68 fault which has a dextral displacement in the order of

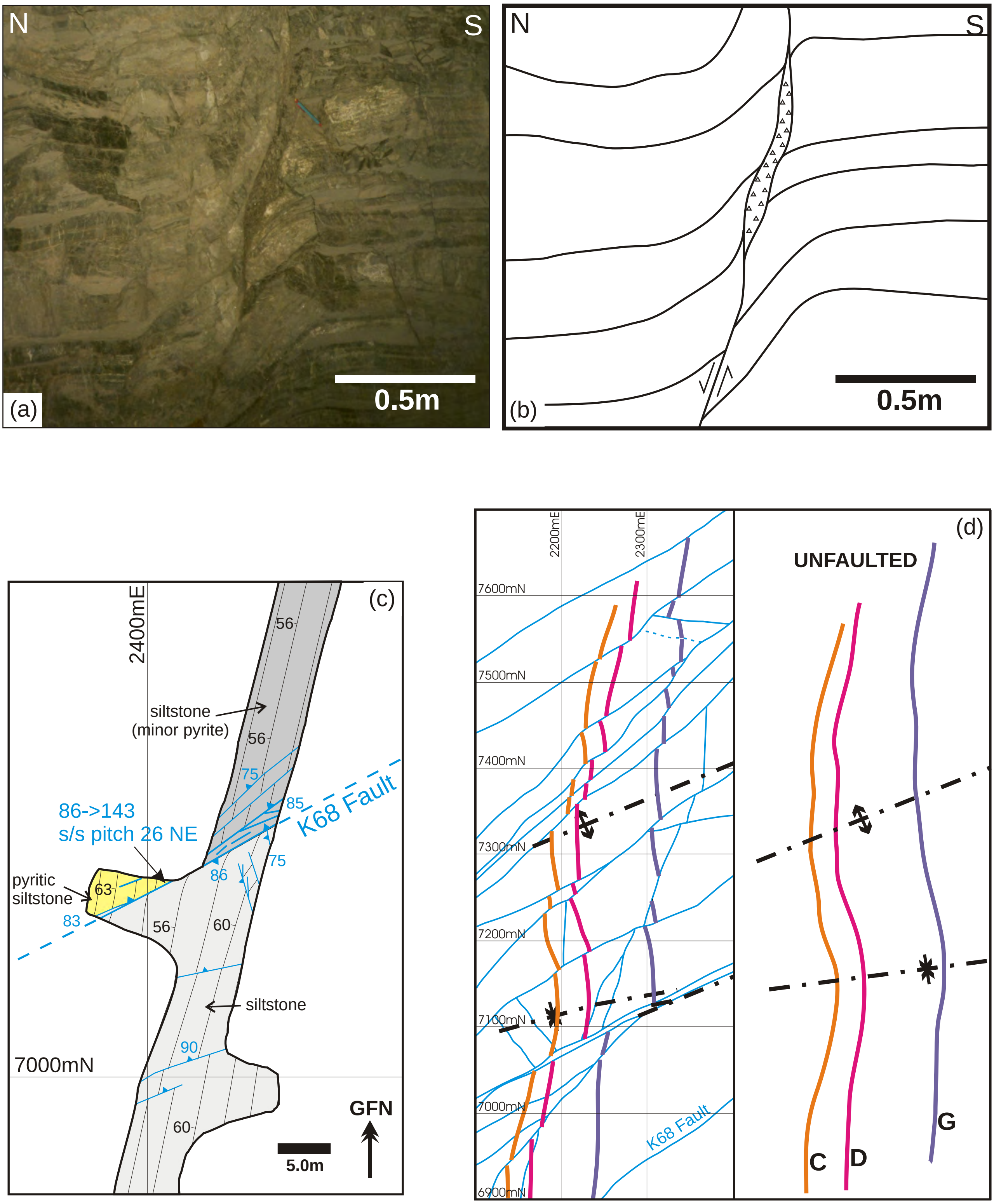

Figure 10. Photograph, (a), and line diagram, (b), of the M72 fault in the mine development. The patterned area is a zone of fault gouge development in a restraining bend in the fault. (c) Mapping of development on 12L in the area of the K68 fault. Note the negligible drag folding or change of bedding orientation on either side of this major fault. (d) Plan view of C, D, and G ore-horizon hangingwall traces in their present faulted geometry (left) and with the strike-slip component of the offset removed (right). The open s-shaped flexure is not an artifact of fault offset.

150m and is a significant, deposit-bounding fault at the southern end of George Fisher (Figure 6a) has negligible associated drag folding (Figure10c). Bedding adjacent to the K68 fault (Figure 10c) does not change in strike or dip across the fault. This observation is not consistent with rotational displacement on the fault plane whereby dip and strike of bedding would change significantly across the fault. Also, larger scale curvature of bedding orientations is not always consistent with the displacement vector and the expected vergence of any drag-folds related to the dextral faults. This is observed on Figure 9 (level 12) at 7250mN/2200mE. The curvature of bedding immediately south of the M72 fault at this location would suggest sinistral sense of shear if related to drag on the fault. However, this is inconsistent with other indicators of the movement direction on the fault such as localised drag folding, slickensides and steps on the fault plane which indicate a dextral sense of shear.

Faults are not often spatially coincident with the inflexion points or hinge zones of these open flexures and the antiformal axis of the open flexure is not coincident with a fault on any of the mine levels (Figure 9). Bedding form-lines (Figure 9) illustrate the spatial coincidence of faulting to the synformal axis on the 11lvl, 12C, and 12lvl plans. However, this relationship does not exist on the 13C level plan where the synformal axis is clearly separated from the fault.

The plunge of the large open flexure/fold couplet is to the SW whereas the dominant NE-striking faults dip to the NW. The fold axial planes and faulting will therefore diverge with a change in RL. This is the case at the surface where the fold axial planes are no longer spatially co-incident with faulting as in the underground workings and the K68 fault occurs further south away from the flexure (compare Figures 5 and 9).

Unfaulting of the stratigraphy by removing the normal, strike-slip movement on NE trending faults results in a tighter F_1 fold (Figure 10d). Together, the various lines of evidence indicate that the broad open fold is not a product of the late brittle faulting. The deposit-scale curvature of bedding is therefore inferred to be a result of folding that pre-dates the faulting event.

The sample described in Figure 8 (a-c) is located on the south limb of the F_1 flexure. Note that the dextral sense of shear observed in thin-section is consistent with the bulk shear expected at this location on the broad fold structure. Dextral shear at this location indicates that the synformal axis is north from this position. The observation that the interpreted S_1 foliation is sub-parallel in strike to the axial plane of the broad F_1 flexure and has a sense of shear consistent with the development of the fold suggests that the foliation described is S_1.

The S_1 foliation, associated with these open folds, is not well preserved in the rocks at George Fisher. This may be due to the folds associated with this deformation being open flexures and it is therefore probable that an intense foliation did not develop. Also, following D_1, the onset of the east-west directed shortening involved regional scale folding and pervasive fabric development, thereby strongly overprinting any weakly developed, east-west oriented S_1 outside strain shadows.

D_1 is interpreted as the manifestation of north-south horizontal compression preceding the dominant east-west shortening associated with the Isan orogeny. East-west striking faults and folds are folded by macroscale F_2 folding in the Lake Moondarra area (Winsor, 1986) as shown in Figure 2. A pre-D_2 timing of these east-west oriented structures is consistent with the interpretation of the micro-scale features described above and S_2 form-lines described below.

4.2 Description and interpretation of D_2 structures

A weak to moderately developed pervasive slaty cleavage is the dominant foliation in the rocks at George Fisher (Figure 11). This cleavage is interpreted to destroy rare S_1 crenulations (Figure 8) and is itself overprinted by subsequent deformation fabrics. This cleavage is therefore interpreted as the fabric formed during the second deformation (D_2) and is termed S_2. S_2 is oblique to sub-parallel to bedding and dips more steeply than bedding indicating anticline-east vergence (Figure 11a and b). In plan view, the S_2 strikes north-northwest compared to the dominantly north striking bedding (Figure 11c) and the vergence of S_2^S_0 indicates an antiform to the east. S_2 occurs as discontinuous graphitic seams around detrital quartz grains, similar to those described by Gray (1978) in deformed psammitic rocks, and more commonly as closely-spaced, anastomosing, semi-continuous graphitic seams and crenulation of the pre-existing bedding parallel S_{0c} fabric. Differing nature of S_2 relative to host-rock is commonly observed (Figure 11). The spacing and intensity of the fabric can vary significantly according to the mineralogy and bedding characteristics of the host-rock. Finely laminated lithologies commonly preserve more intense S_2 development than those that are more coarsely crystalline (Figure 11a-d). The S_2 fabric is only weakly developed in the Urquhart Shales and is not mappable at

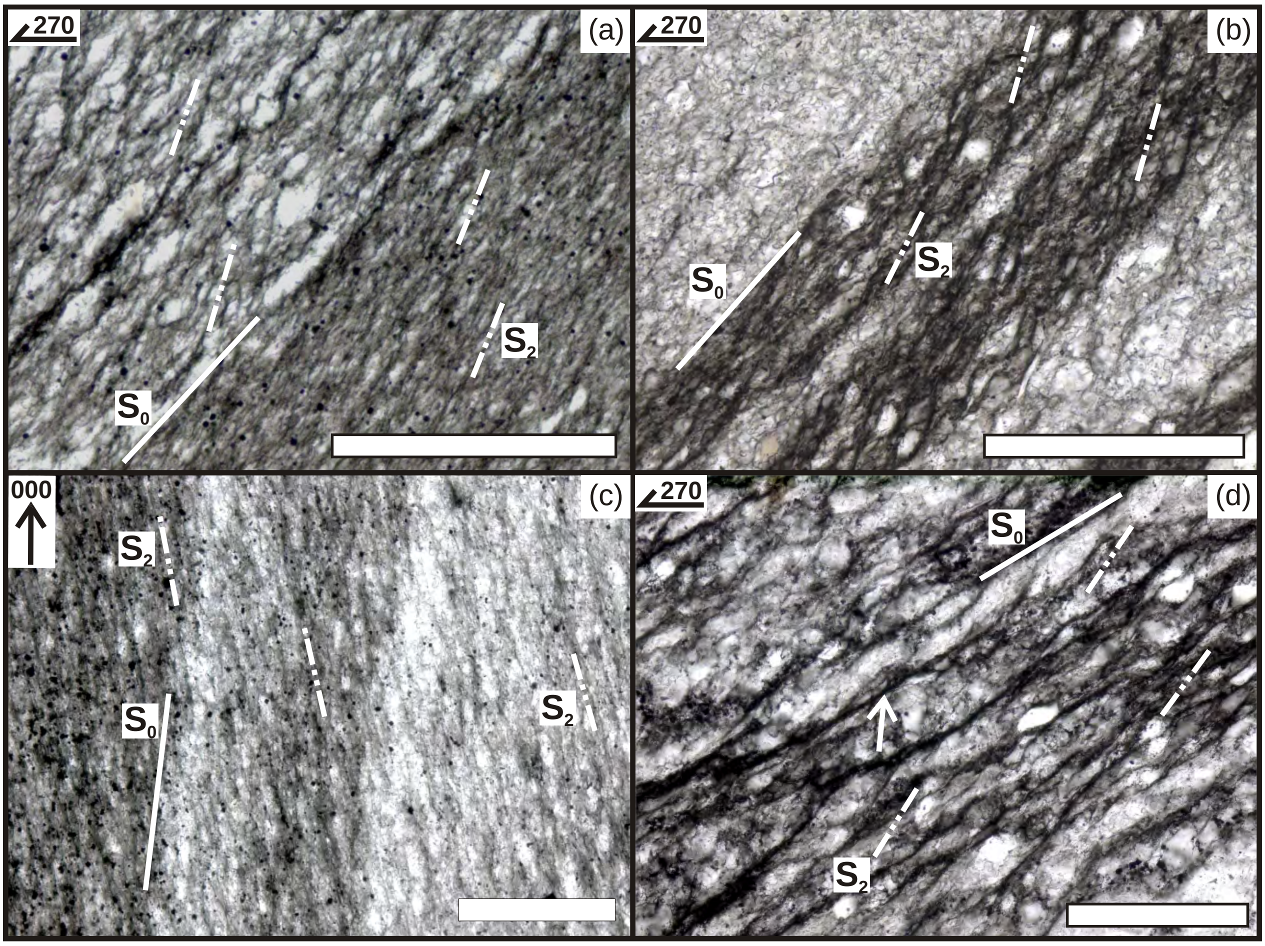

Figure 11. Photomicrographs displaying the S_2 foliation in bedded Urquhart Shale. Scale bars are 200µm and photomicrographs are taken in plane polarized light. (a), (b), and (d) are vertical sections looking north, (c) is a plan view. (a) S_2 is more steeply dipping than bedding indicating the anticlinal axis is to the east (see Figure 2). The S_2 cleavage occurs as a fine slaty cleavage in the fine-grained shale (lower right hand side) and a spaced anastomosing cleavage in the coarser siltstone (upper left hand side). Sample 1311-2. (b) More intense S_2 development occurs within the finely laminated and carbonaceous layer (dark) and is weak to absent in the massive carbonate mudstone (pale). Sample 2810-1. (c) S_2 has a NNW strike compared with bedding which strikes NNE, again demonstrating anticline-east asymmetry. Sample 0512-3. (d) Anastomosing S_2 cleavage in a siltstone layer. Development of bedding-parallel cleavage (indicated by white arrow) is interpreted as D_2 reactivation of an earlier bedding parallel foliation (possibly stylolitic) and curvature of S_2 into the bedding-parallel seams is consistent with west-side-up bedding reactivation during D_2. Sample 1012-6.

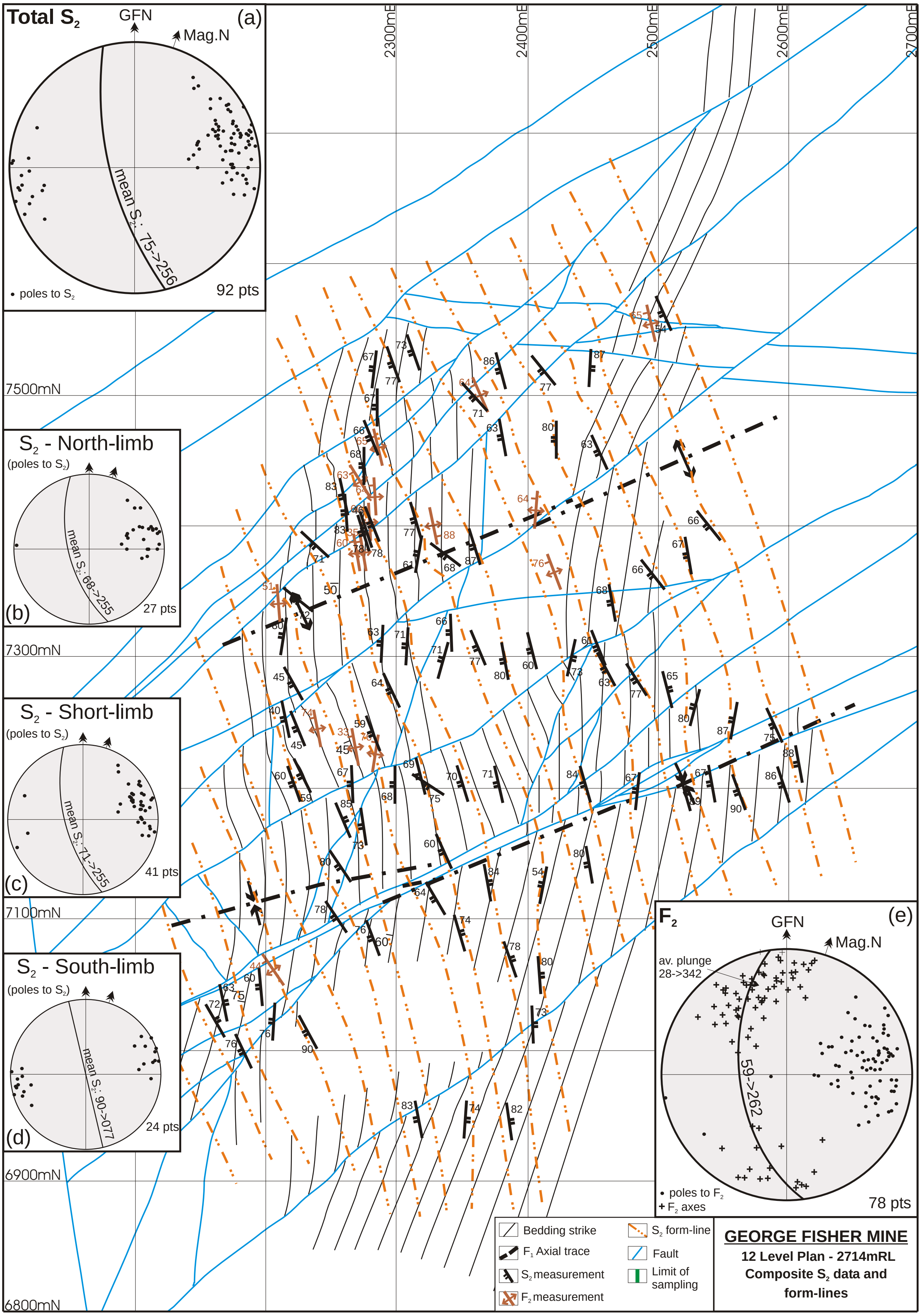

Figure 12. S_2 and F_2 data projected onto 12 Level of the George Fisher Mine. See text for discussion.

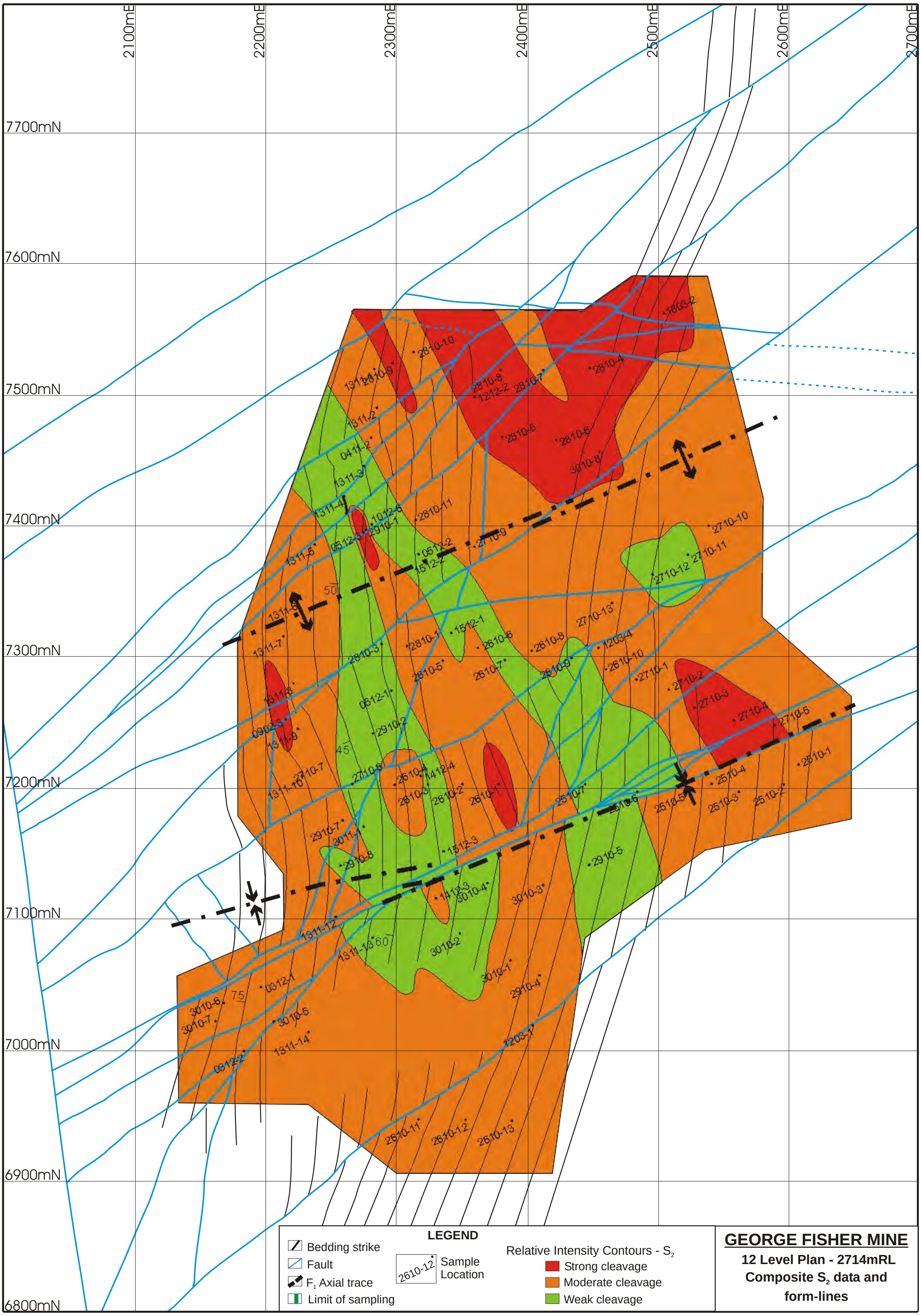

Figure 13. Variation in the intensity of the S_2 foliation. See text for discussion.

exposure and hand-specimen scale thereby requiring all S_2 data in this study to be recorded from oriented thin-sections. Figure 12 displays S_2 data projected onto 12 level at George Fisher. The composite S_2 data clearly exhibits the north-northwest trend, such that bedding-foliation vergence at the deposit-scale again requires a district-scale antiform to the east. Relative intensity contours (Figure 13) of the data from Figure 12 indicate weak north-northwest trends consistent with the average orientation of S_2. Some of the variation in the intensity may be due to lithological variation in samples and resultant variability in the development of S_2 but the host-rock control on foliation development does not control the deposit-scale variation in S_2 intensity (Figure 13). The location of the F_1 folds has no apparent effect on the intensity of the pervasive S_2 fabric.

The S_2 foliation dips to the west from 25° to 80° and the strike of S_2 varies between north and northwest, the average orientation being 75°→256° (Figure 12a). The S_2 foliation maintains consistent strike through each limb of the F_1 fold (compare Figures 12b,c,d) but the dip changes from 90° to 68° moving north. Note that the strike of bedding swings on average 20° between the south limb of the F_1 fold and the short-limb. S_2 is not folded by the east-west trending deposit-scale open flexure and is therefore interpreted as a younger fabric. The consistent orientation of S_2 across the antiformal and synformal F_1 folds is considered as further support for the D_1 timing of the flexure.

The S_2 foliation is often difficult to identify in horizontal section due to the steep, south-pitching extension direction/stretching lineation (Winsor, 1986; Valenta, 1988, 1994). That is, for grains elongated to rod-like or elliptical shape during deformation, a vertical w-e section will cut the steep west dipping ellipsoidal grains lengthways and the result is

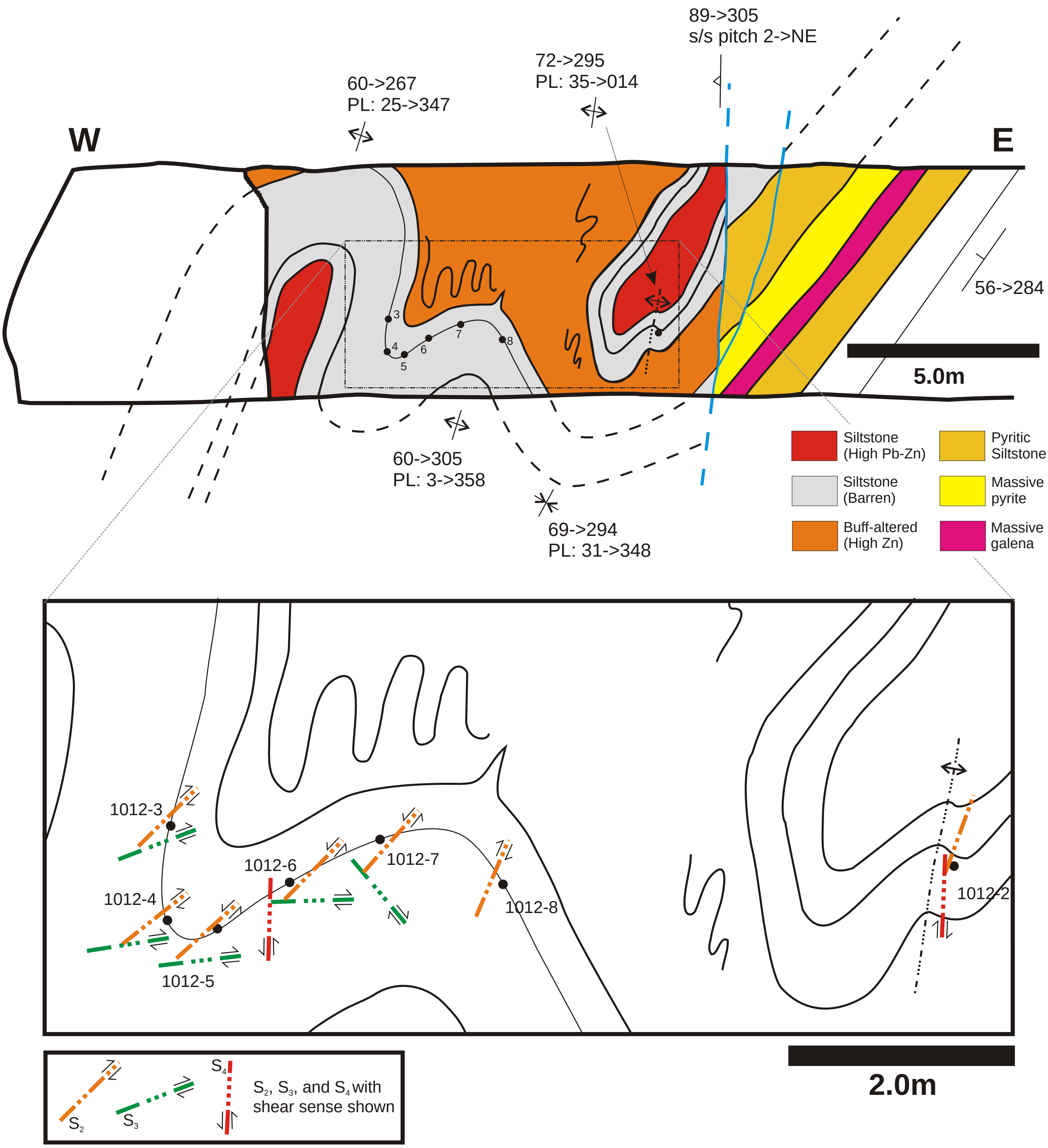

Figure 14. Mapping of 739 cross-cut on level 12C George Fisher. The observed change in the sense of shear on S_2 at sample locations around the fold illustrated indicates that the fold is an F_2 fold. Also, the overprinting S_3 and S_4 foliations are not axial planar to the larger folds.

<u>**Explanation of symbols:**</u> 69->294 PL: 31->348 syncline with axial plane dipping 69º toward 294º and plunging 31º toward 348º

1012-2 oriented hand-specimen location and sample number

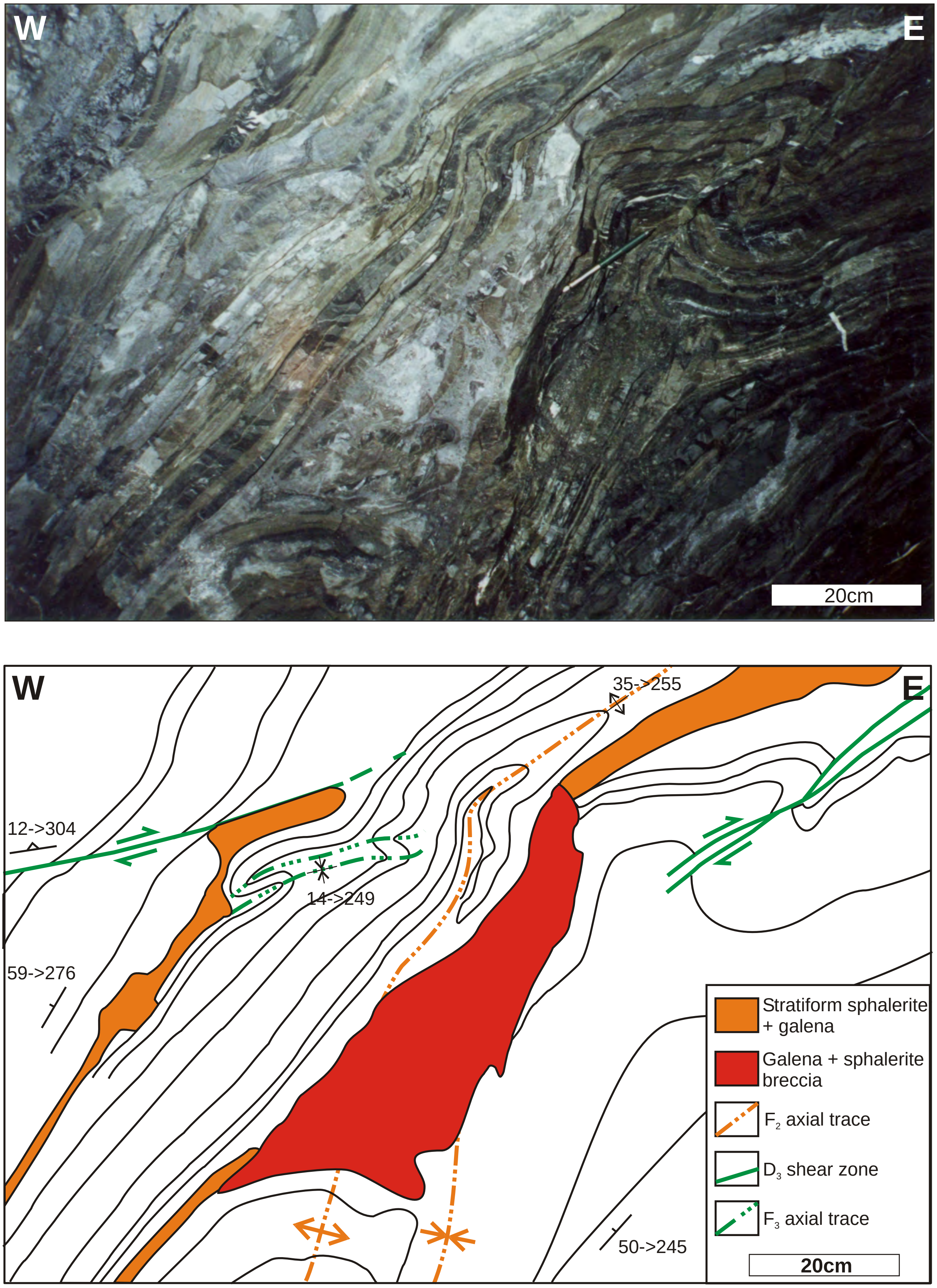

Figure 15. Photograph and line drawing of part of D orebody in 723 stope development, 12L. An F_2 fold is rotated within a D_3 high strain zone in the top half of the diagram. Note the F_3 folds with opposite vergence to F_2 folds and galena-rich brecciation focussed on the F_2 fold

a well-developed foliation in cross-section. When viewed in horizontal sections, the end-sections of the grains are observed and a through-going fabric is more difficult to detect.

Folds which have axial planes parallel to the S_2 orientation occur at scales ranging from millimetre to 5.0 metre amplitude and wavelength (Figure 14). The folds are often inclined and have closed to tight cross-sectional geometry (Figure 15). A change in the sense of shear on S_2 and the bedding-foliation vergence across drive-scale folding indicates that these folds developed during D_2 and are F_2 folds (Figure 14). F_2 folds have moderately dipping axial planes with an average orientation of 59°→262°. These folds plunge to the north-northwest at approximately 30° (Figure 12e). The attitude of gentle north-plunging F_2 fold-axes is consistent with a steep extension direction plunging toward the south (Winsor, 1986; Valenta, 1988, 1994). Subsequent deformation has not resulted in high enough strain to cause significant rotation of F_2 fold axes into the extension direction of the overprinting folds. The orientation of F_2 axes therefore approximates their original orientation.

F_2 folds have been observed with wavelength ranging from 5mm-15m at George Fisher and these folds are the dominant structural feature in the George Fisher deposit (Figure 16). Repetition of stratigraphy at the 10's of metres scale such as that observed in the southern half of the mapping in Figure 16 has significance for mine operations as this causes a thickening of the ore-sequence and larger stope sizes are required in these regions. The relationship between structural features and metal/ore-distribution is discussed in detail in Part B.

Rotation of F_2 folds by subsequent deformation can result in parasitic F_2 folds becoming overturned and rotated to sub-horizontal attitudes in extreme cases (Figure 15). This occurs via a sub-vertical shortening event (discussed below) and causes rotation of F_2 folds about their axes. East-verging parasitic fold geometries and previously discussed bedding-foliation vergence indicate that a larger-scale anticline is situated to the east of George Fisher. Mapping by Winsor (1986), indicates that a significant anticlinal F_2 axial region is approximately 2.5 kilometres east of the George Fisher workings and the regional-scale F_2 fold axial trace projects to approximately 5km east of George Fisher (Figure 2).

D_2 structural elements are the result of east-west horizontal shortening during the Isan orogeny. Regional-scale folds of D_2 timing (Winsor, 1986) dominate the regional structural grain of the Mt Isa-George Fisher-Lake Moondarra area (Figure 2). The moderate westerly dip of stratigraphy at George Fisher is a result of macroscale F_2 folding and the S_2 foliation is generally weakly developed but pervasive. Orientations of the S_2 fabric and F_2 parasitic folds at George Fisher are parallel with the orientation of macro-scale folding in the George Fisher-Hilton-Lake Moondarra area.

4.2.1 Thermal and stress history of the D_2 deformation

D_2 is interpreted to occur approximately synchronous with the peak of metamorphism in this part of the Mt Isa Inlier. Analysis of the Sybella felsic igneous complex to the west of the Mt Isa-Paroo Fault indicates that pegmatites (Figure 3), interpreted to be derived from partial melting during peak-metamorphism, are of D_2 timing (Connors and Page, 1995). Zircons from the pegmatites yield ages of 1532±7Ma (Connors and Page,

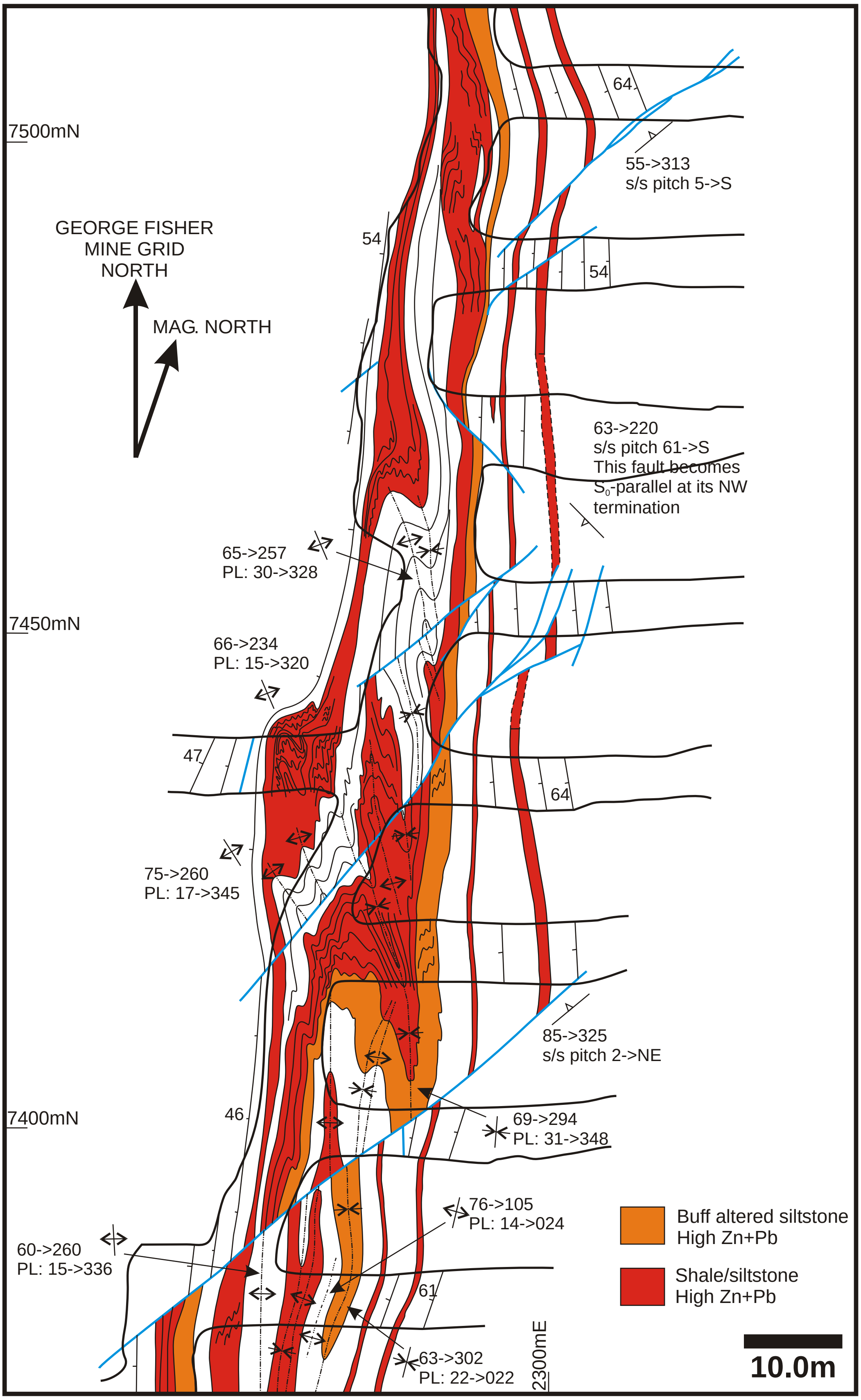

Figure 16. Mapping of the northern section of mine development on level 12C, George Fisher. The mapping represents geology at floor level. See text for discussion. Fold measurements consist of dip and dip-direction of axial plane and plunge (PL) of the fold axis.

1995) which is within limits of uncertainty of the 1544±12Ma age for D_2 deformation proposed by Page and Bell (1986). Metasomatism during D_4 resulted in higher temperatures (~280°C) in areas of copper mineralization (Chapman, 1999) and the following discussion aims to define the maximum temperature of deformation as opposed to metasomatism.

Calculation of the maximum temperature of deformation by quantifying the irregularity of deformed quartz-quartz grain-boundaries is possible using the data collected by Kruhl and Nega (1996). Kruhl and Nega observed a statistical relationship between the fractal dimension of grain-boundaries and the temperature of deformation of metamorphic and igneous rocks (Figure 17a). Samples of deformed quartz-veins in quartzite (Figure 17b) from the Lake Moondarra area have been analysed in light of Kruhl's deformation-thermometer. The fractal dimension of the grain-boundaries as shown in Figure 17(b) are plotted on Figure 17(a) and indicate a temperature of deformation in the order of 270±50°C which is within error of the 200-220°C maximum temperature inferred from bitumen-reflectance (Chapman, 1999).

A classification scheme linking twin geometry with deformation temperature has been developed by Burkhard (1993) and is displayed in Figure 18a. Calcite twins in samples from throughout the George Fisher deposit reflect type I and II twins as defined in Figure 18b-d. Ultra-thin-sections were not used in this study and therefore estimated widths of twins are likely to overestimate the true width. However, thickness of the thin-section does not affect observation of twin shape and geometry which are integral in determining the temperature history of the calcites. The absence of thick, curved, twinned twins,

(a)

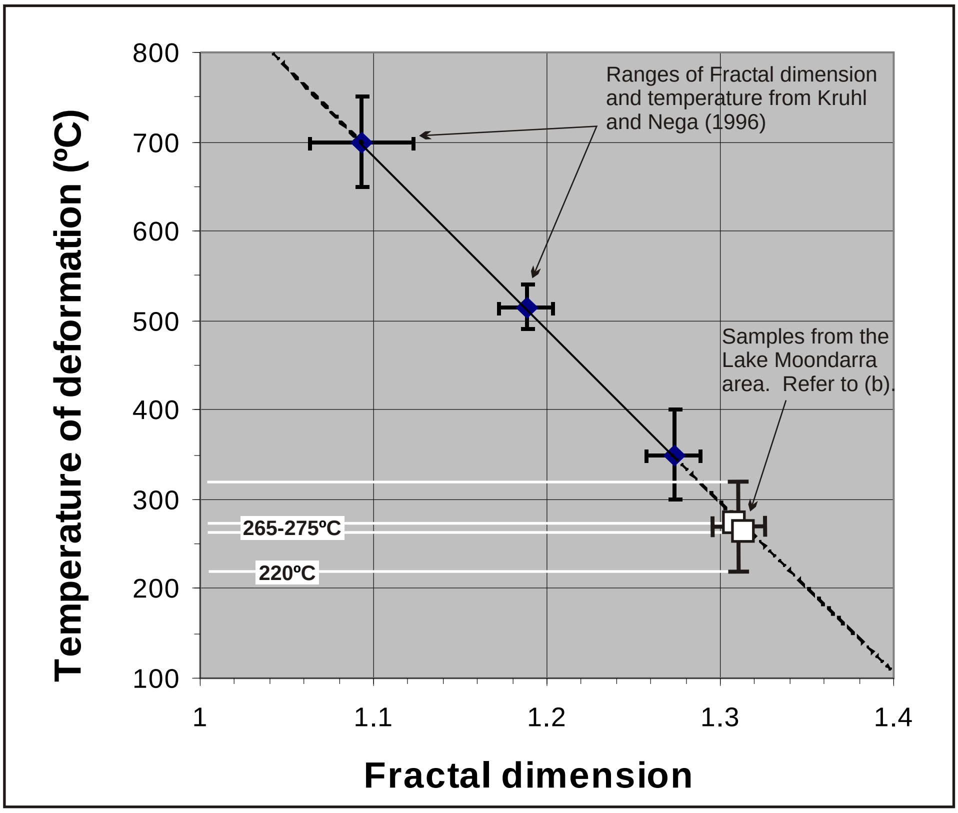

(b)

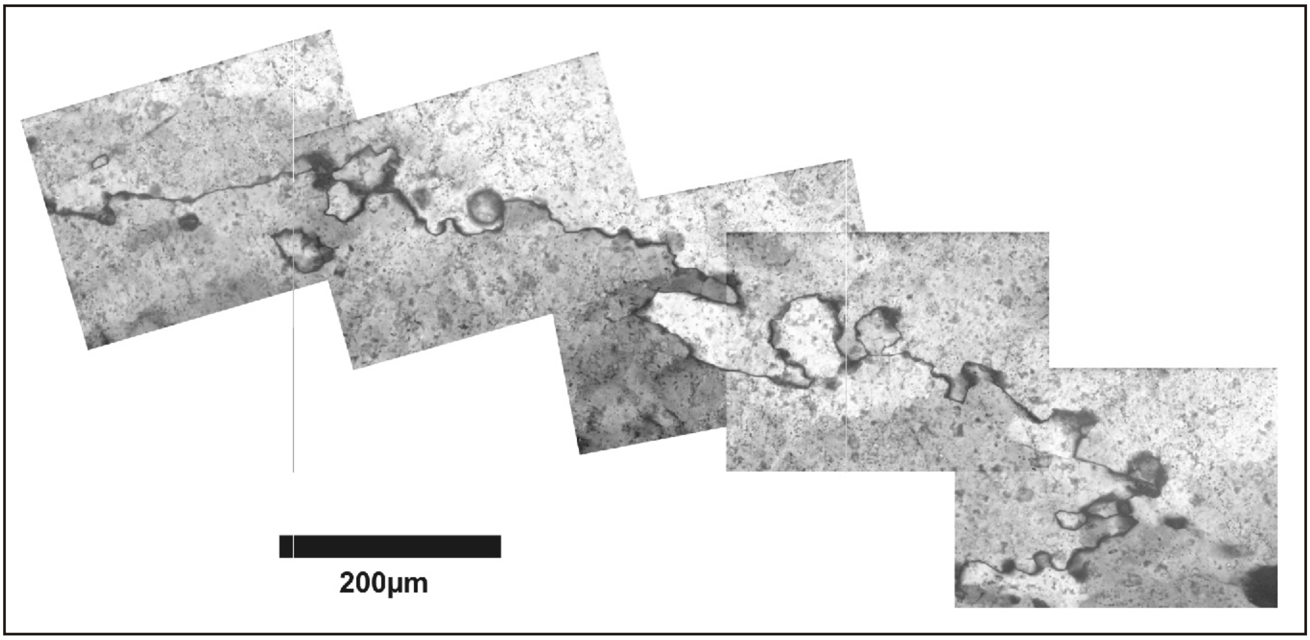

Figure 17. (a) Graph after Kruhl and Nega (1995) showing the relationship between fractal dimension of deformed quartz grain-boundaries and temperature of deformation. (b) Grain-boundary from deformed quartz vein in the Lake Moondarra area. The fractal dimension of this quartz-quartz grain-boundary is approximately 1.32 and is plotted on (a) to give a deformation temperature of 270±50ºC.

Appearance in thin-section	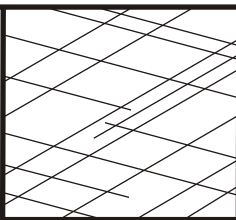	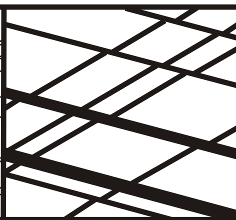		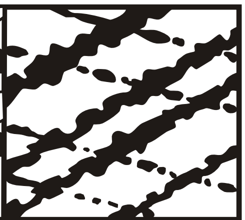
Type	**I**	**II**	**III**	**IV**
Description of twin geometry	thin, straight, 1 to 3 sets per crystal	thick (>>1µm), straight, slightly lense shaped	thick, curved, twinned twins, completely twinned crystals	thick. patchy, sutured boundaries, trails of remnant twins
Interpretations	weak deformation, post-metamorphic/late-tectonic	moderate deformation, syn- or post-metamorphic	strong deformation, syn-metamorphic	strong deformation, dynamic recrystalliza-tion, pre- or syn-metamorphism
Temperature	< 200ºC	150 - 300ºC	> 200ºC	> 250ºC

Figure 18. (a) Diagram from Burkhard (1993) showing the correlation between calcite twin geometry and temperature of deformation.

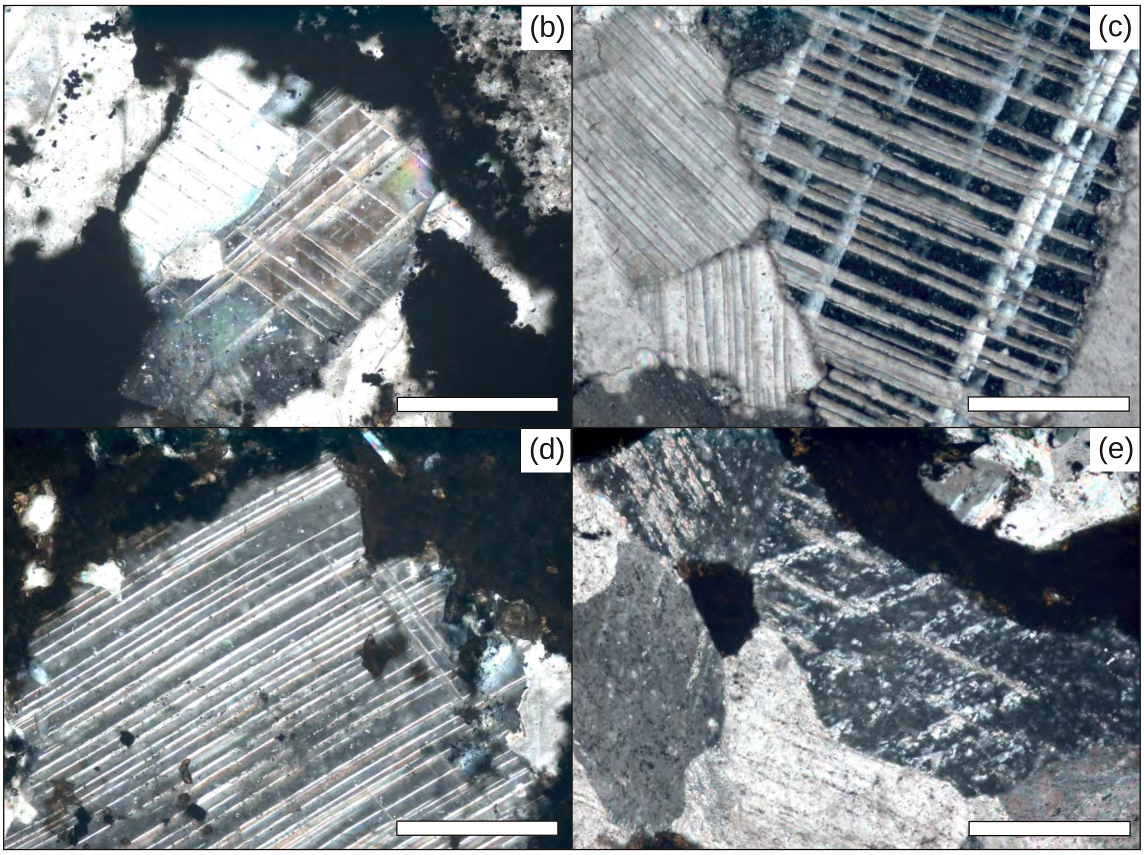

Figure 18. (b),(c),(d) Calcite from mineralized veins at George Fisher. Scale bars are 200µm. The dominant twin type, after the classification in (a), is Type I reflecting <200ºC temperature of deformation. Samples 0512-3, H748EH1, 1311-6, respectively. (e) Calcite within a mineralized vein containing twins which resemble Type IV twins as described by Burkhard (1993) and indicate a temperature of deformation in the order of 250ºC or higher. Sample 1012-2.

sutured twin boundaries, and rare occurrences of trails of remnant twins/irregular-shaped twins (Figure 18e) indicate a temperature of deformation less than 250°C (possibly <200°C) which is consistent with bitumen reflectance estimates of maximum temperature (Chapman, 1999) and within error of temperatures estimated from deformed quartz-quartz grain boundaries.

Calcites are variably twinned in veins and mineralization at George Fisher. The degree of twinning can be used qualitatively to distinguish between deformed and relatively undeformed calcite. A sample which has cross-cutting vein relationships and bedding-parallel sphalerite mineralization is illustrated in Figure 19a as a photomicrograph and isometric diagram of the piece of half core from which the section was obtained (Figure 19b). Calcite in the mineralized layer and the gently-pitching vein are generally less-twinned and have more regular grain-shapes (Figure 19c and d). The steeply pitching veins are comprised of dolomite which is strongly twinned and has irregular grain-shapes (Figure 19e). The interpretation of the timing of these features relative to deformation is that the steeper, more obviously deformed veins are pre/syn-D_2 deformation whereas the calcites in the mineralized layer and gently-pitching vein post-date the main D_2 deformation. Carbonate in the steeply-pitching veins and mineralized veins are chemically distinct (Figure 19f) and this supports the interpretation of cross-cutting relationships. Application of the calcite palaeopiezometer of Rowe and Rutter (1990) to the carbonates from each of the deformed vein, mineralised layer, and late vein result in differing palaeo-differential stress estimates for the deformed vein relative to the interpreted younger features. Note that dolomite from the deformed vein has been analysed using the method calibrated for calcite and therefore the results for this vein may

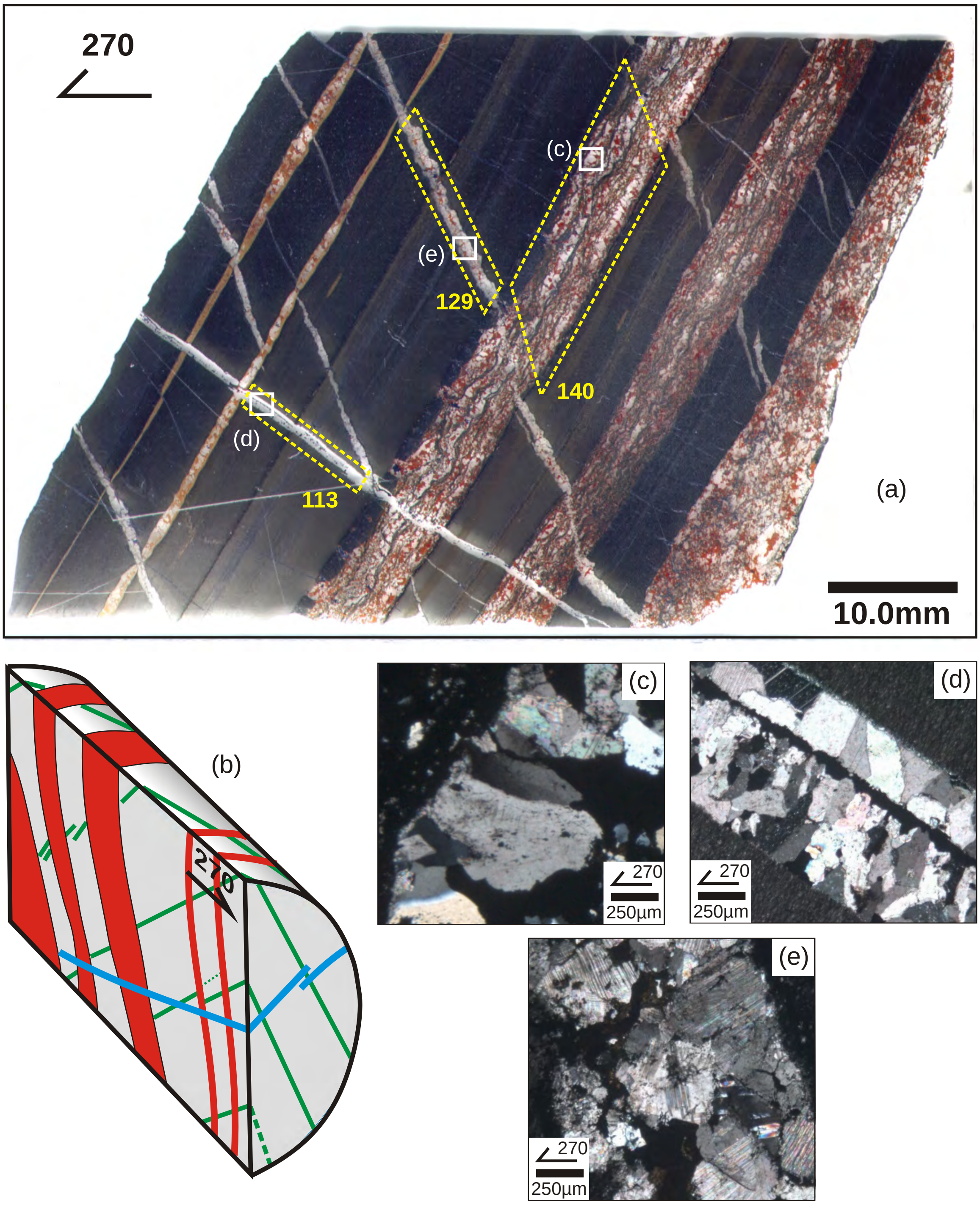

Figure 19. (a) Thin-section and (b) isometric view of piece of half-core containing bedding-parallel sphalerite mineralization, a set of steeply dipping dolomite veins which are cross-cut by mineralization, and a late, gently dipping calcite vein. The diagram in (a) indicates areas analyzed with the palaeostress estimation technique from Rowe and Rutter (1990), number of grains analysed from each area (yellow), and locations of photomicrographs (c), (d), and (e). Calcite in the mineralized vein (c) and late vein (d) are not significantly twinned whereas dolomite in the steeply dipping veins is intensely twinned as seen in (e). See text for discussion. Sample 960519.

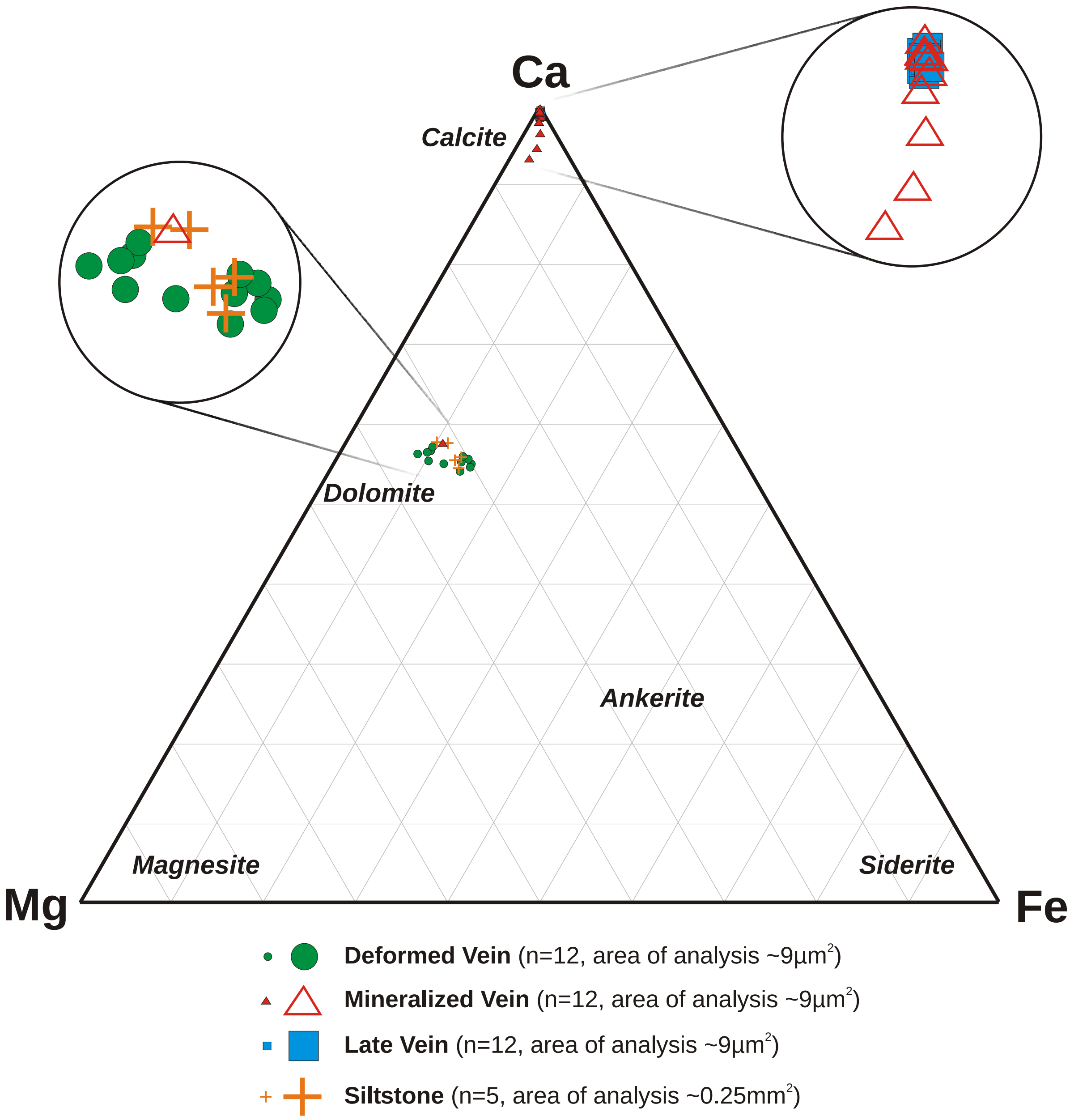

Figure 19. (f) Electron microprobe analyses of the vein and matrix carbonates (Figure 19a-e). Bulk analyses of the barren siltstone are included in the diagram. The analyses form two clusters within which the deformed veins (steeply pitching on Figure 19a, Figure 19e) and host-rock are chemically indistinguishable dolomite. Carbonates from the mineralized vein (Figure 19a and c) and the late cross-cutting vein (Figure 19a and d) are chemically indistinguishable and are calcite. One carbonate analysis taken near the edge of the mineralized layer has chemistry consistent with dolomite, however the rest of the data suggests that the main carbonate phase in the mineralized veins is calcite. All Ca, Fe, and Mg in the siltstone samples is assumed to be associated with constituent carbonate minerals for purposes of representation on the ternary plot, however, the analysis of the siltstones incorporated minor amounts of other mineral species including sphalerite, pyrite, quartz, and feldspar.

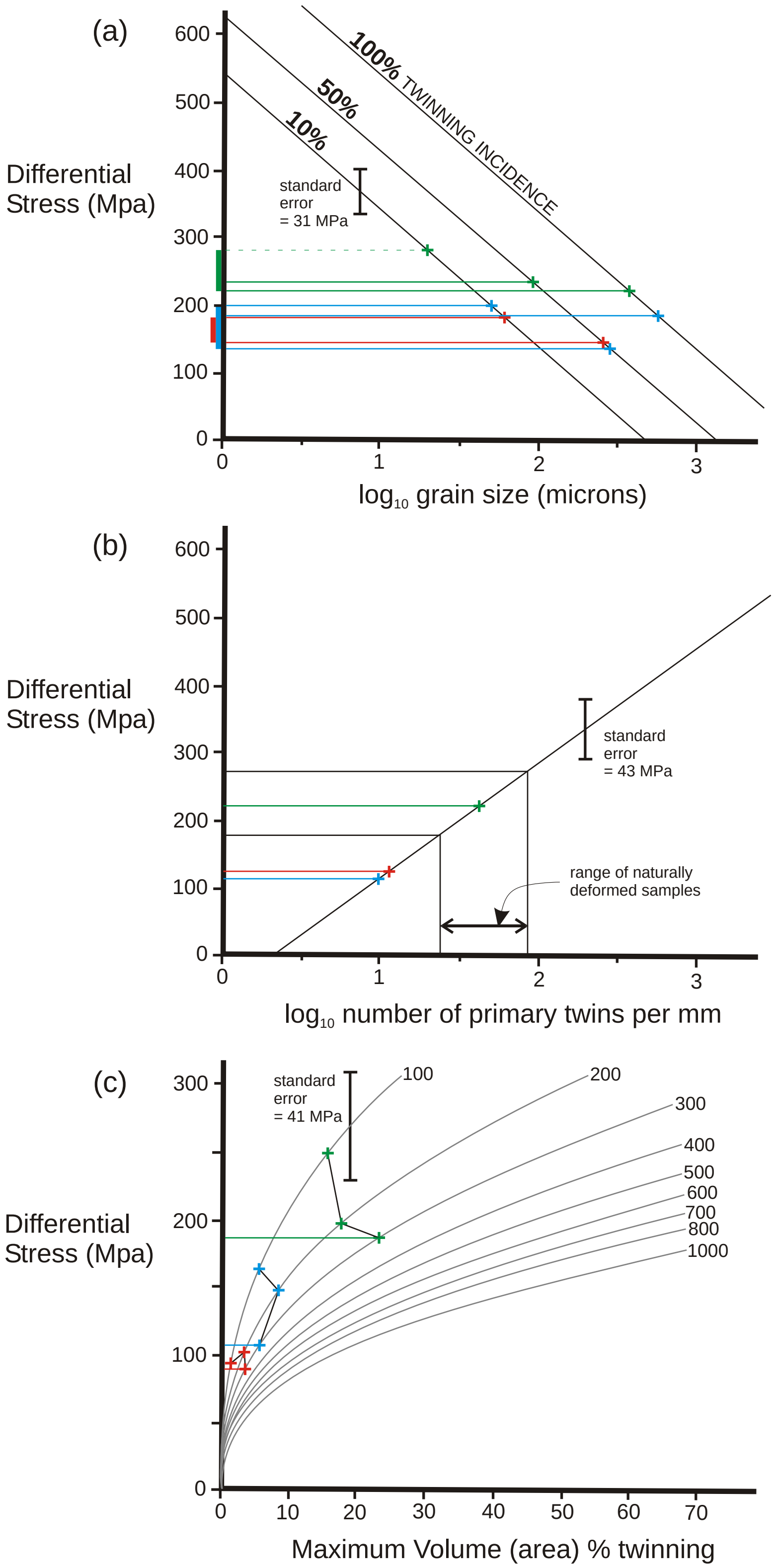

Palaeotress Estimates ±31 MPa
250
165
170

Palaeotress Estimates ±43 MPa
220
125
115

Palaeotress Estimates ±41 MPa
187
90
110

Average Palaeotress Estimates ±43 Mpa
219
127
132

Figure 20. Data plotted onto the palaeostress estimation charts from Rowe and Rutter (1990). Green = deformed vein, red = mineralized vein, and blue = late, non-deformed vein. (a) twin incidence by grain-size category, (b) twin density, (c) volume (area) % twinning by grain-size category. See text for discussion.

not be valid. Both Calcite and Dolomite are rhombohedral however they differ with respect to slip systems (Wenk, 1985). Twinning occurs in both minerals at low temperatures. In the range of deformation temperature 200-250°C at George Fisher, Calcite will develop twins from 10MPa and Dolomite from 100Mpa (Barber et al., 1981). Charts of twinning data in the same format as that published by Rowe and Rutter (1990) are displayed in Figure 20. Three palaeostress estimations are obtained from subsets of the collected data. The subsets are: twin incidence, twin density, and volume % twinning (area % used in this study) as described in Rowe and Rutter (1990). Average palaeostress measurements for the deformed, breccia-vein, and late-vein are 219±43, 127±43, and 132±43 MPa respectively. The differential stress of 219±43 MPa is interpreted to represent the difference between σ_1 and σ_3 during D_2 and is comparable with differential stress estimates from the Santa Lucia and Portilla tectonic wedges from the Somiedo Nappe in northern Spain (Rowe and Rutter, 1990). The breccia-vein and late-vein estimations of approximately 130±43 MPa represent the differential stress post-D_2. As with the study by Rowe and Rutter (1990), stress estimates from twin incidence and vol % twinning data overestimated (25%, 12% [Rowe and Rutter, 1990]) and underestimated (-20%, -20% [Rowe and Rutter, 1990]) the average palaeostress respectively, and the twins/mm data yielded the estimation closest to the average (-5%, 9% [Rowe and Rutter, 1990]).

The interpreted order of veining and deformation from this sample is as follows:

1. steeply-pitching veins pre- to syn-D_2 folding
2. mineralized vein (sphalerite+calcite+quartz+k-feldspar) cross-cuts steep veins

3. gently pitching calcite vein cross-cuts both earlier vein types and negligible change in the magnitude of stress occurs post mineralized-vein development.

4.3 Description and interpretation of D_3 structures

Spaced, asymmetric kink-like crenulations of S_0, S_{0c} and S_2 cleavage occur and a composite $S_0/S_{0c}/S_2$ fabric forms in the short-limbs of interpreted S_3 crenulations (Figure 21). The S_3 crenulations at George Fisher correspond to the Type 2 crenulation cleavage of Bell and Rubenach (1983) in that earlier fabrics are continuous across the crenulations and there is no mineralogical differentiation from limb to hinge in the crenulation folds. As with the S_2 foliation, development of S_3 is not of sufficient intensity to enable mapping in outcrop/exposure in the George Fisher Mine. In oriented thin-section, S_3 dominantly dips gently toward the southeast, however, as illustrated on Figure 22, S_3 dips about the horizontal toward both the northwest and southeast. The average of measurements for S_3 is 8°→147° (Figure 22a). S_3 crenulations characteristically have top-to-the-east asymmetry at George Fisher, causing rotation of bedding and S_2 into more-gently west-dipping attitudes. This deformation is interpreted to be responsible for the inclined to recumbent F_2 fold attitudes observed at George Fisher (Figure 14, 15).

The S_3 foliation is not developed as pervasively through the deposit as S_2 and relatively intense fabric development occurs only within the short-limb of the deposit-scale F_1 fold (Figure 23). A possible explanation for this observation is that the short-limb zone is comprised of more gently-dipping bedding which is more resistant to west-side-down reactivation during D_3. This results in the preferential development of S_3 in this zone.

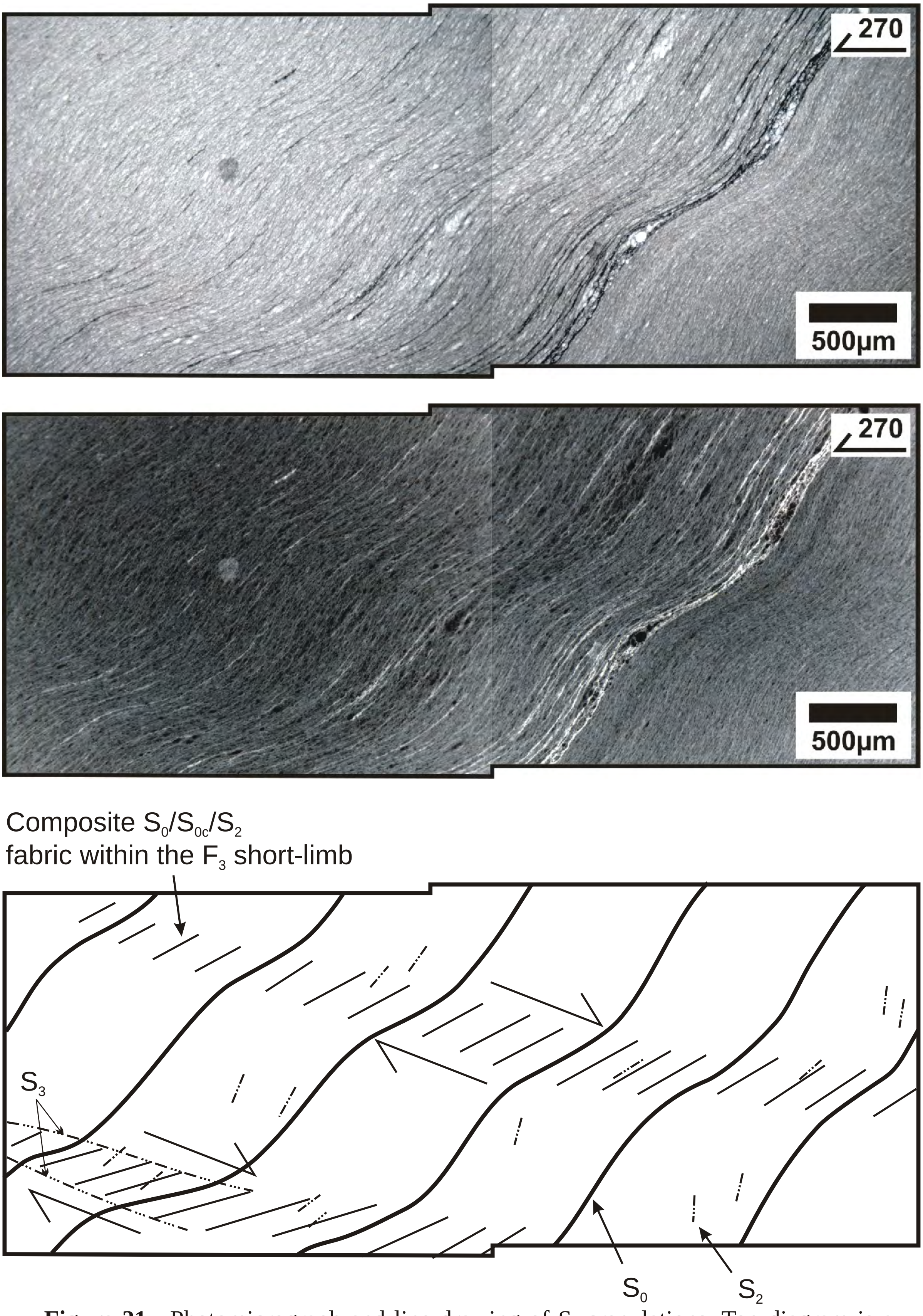

Figure 21. Photomicrograph and line drawing of S_3 crenulations. Top diagram is a photomicrograph taken in plane polarized light and the middle diagram is the same photomicrograph as a negative image for clarity. The lower diagram is a line-diagram of the observed microstructural relationships. Sample 2710-7.

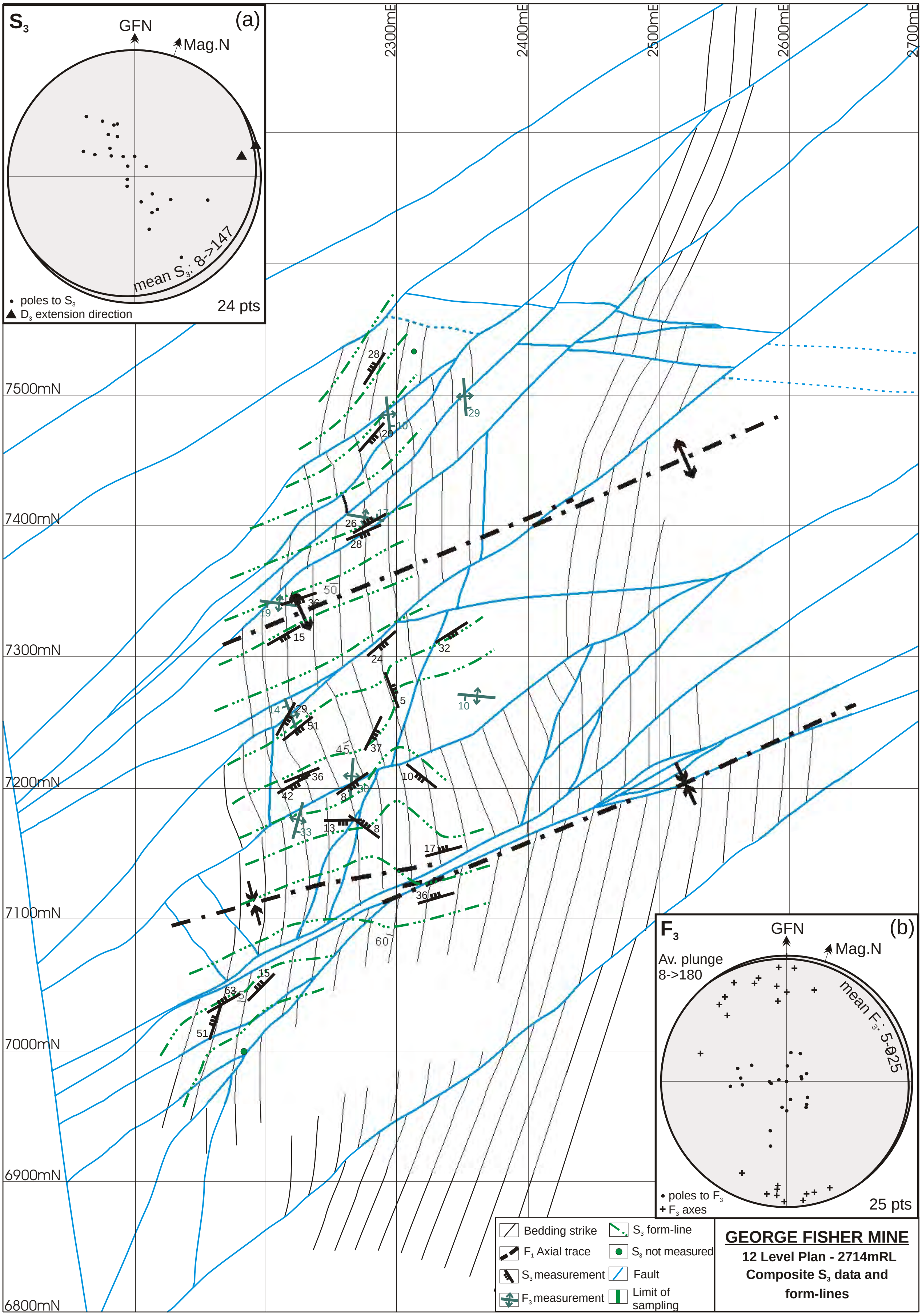

Figure 22. S_3 and F_3 data projected onto 12 Level of the George Fisher Mine. See text for discussion.

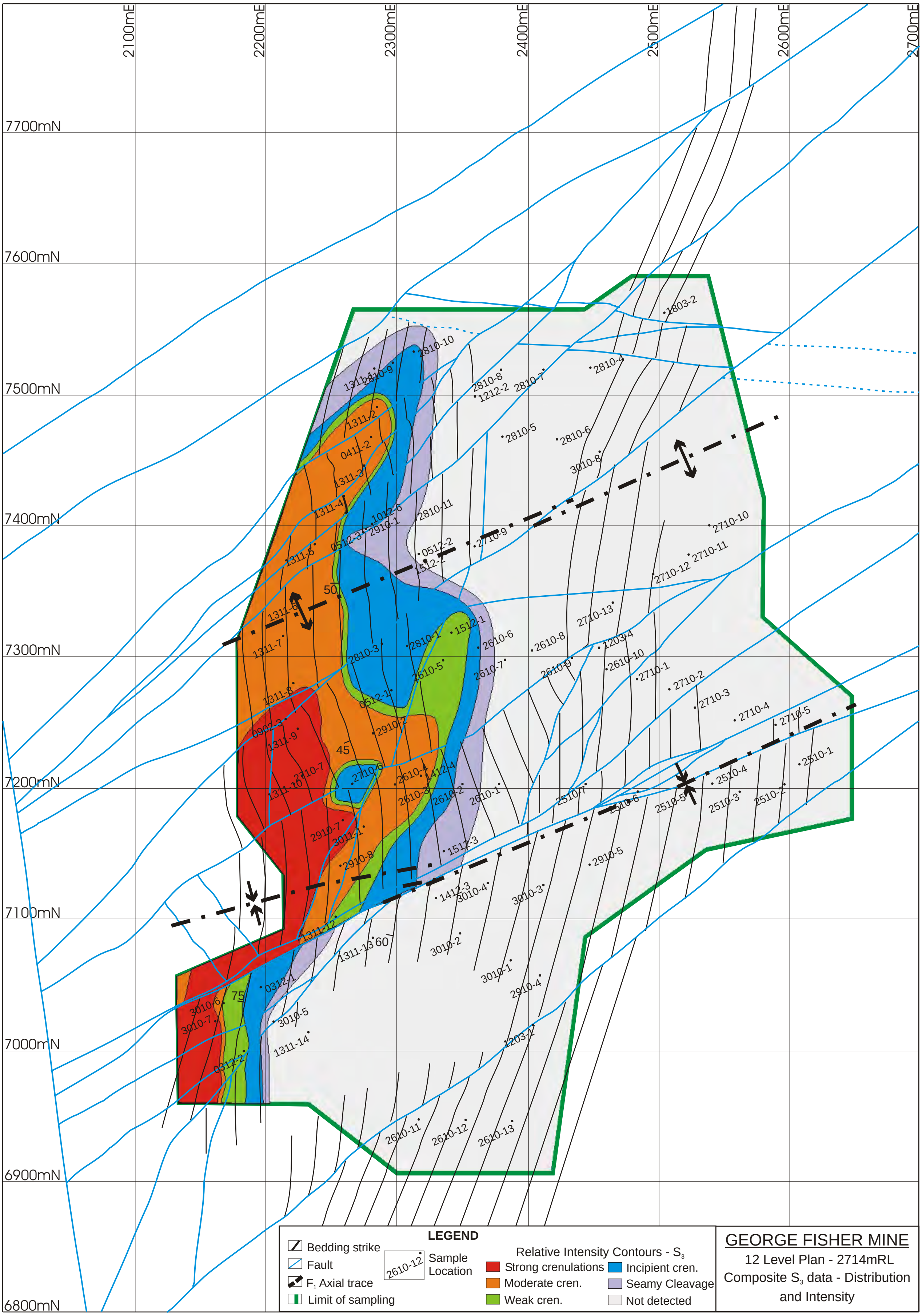

Figure 23. Variation in the intensity of the S_3 foliation. See text for discussion.

Observation of the S_3 fabric is limited to the area within the contours on Figure 23; outside this region, S_3 is absent and S_2 remains steeply-dipping (Figure 12). The restriction of relatively intense S_3 to mid- to hangingwall stratigraphic positions implies partitioning of D_3 strain into a specific stratigraphic package. This region correlates with the more strongly mineralized portion of the sequence (see Part B).

Estimates of the direction of extension during D_3 have been obtained by measuring the plunge of S_3 crenulation hinges or asymmetry-swaps using multiple oriented thin-sections from samples. The direction of extension is assumed to be perpendicular to the plunge of the crenulation hinges within the plane of S_3 (Figure 24). The calculated direction of extension of approximately 7°→076° is an indication only as two samples is insufficient to derive a statistically meaningful measurement. Lack of suitable samples has restricted the number of measurements performed. This estimated direction of extension during D_3 is perpendicular to the average orientation of S_2 and F_2 folds (Figure 12).

Reactivation of pre-existing fabrics (see Bell, 1986) during D_3 results in apparent normal movement on bedding surfaces and west-dipping S_2. Figure 25 displays a photo-mosaic and line-diagram showing subtle D_3 reactivation of bedding and S_2. West-side-down shear has occurred in the darker layer evident in the offset and attenuation of the flat-lying carbonate veins. This direction of reactivation is consistent with the top-to-the-east sense of shear and sub-vertical shortening during D_3. Note that reactivation of S_0/S_2 only occurs in the darker layer where S_2 is well-developed. Reactivation during the younger D_4 event has caused reverse movement on minor chloritic shears and precipitation of sphalerite in micro-dilational jogs is inferred to have occurred at this time. Sphalerite

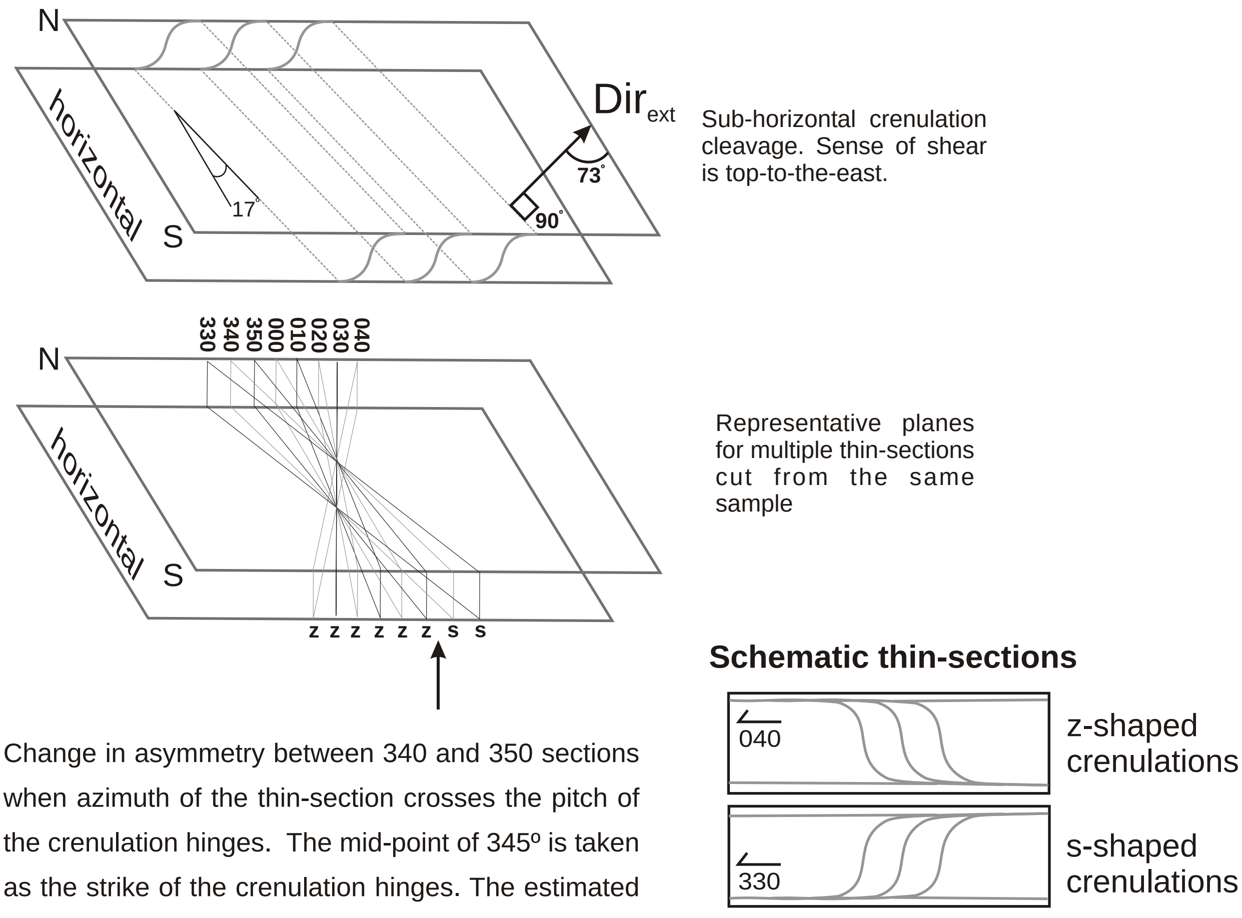

Figure 24. Method of calculation of extension direction in the plane of the S_3 foliation

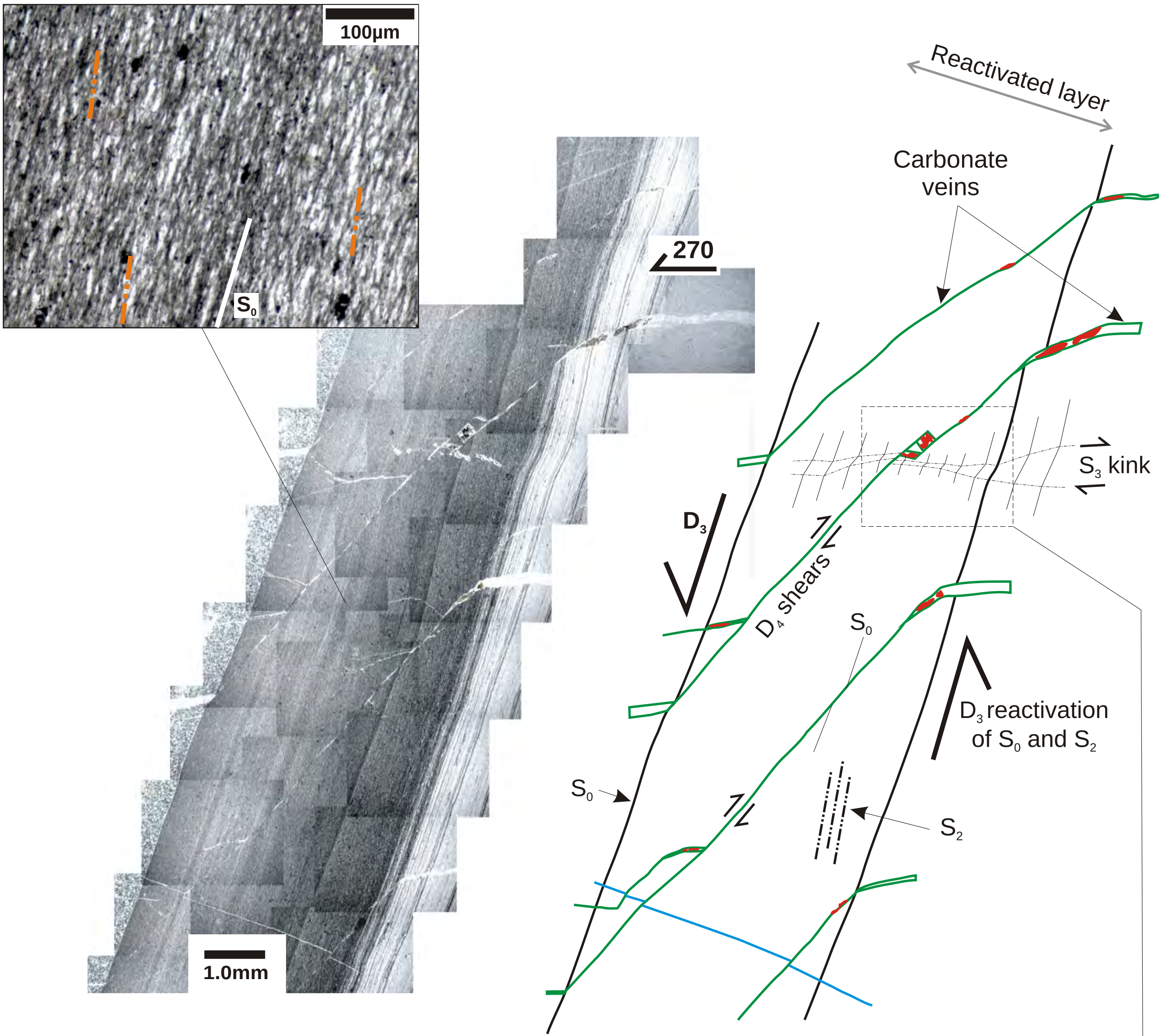

Figure 25. D_3 reactivation of bedding and S_2 illustrated in photomicrograph mosaic and line-diagram. Attenuation of the carbonate veins within the reactivated layer occurs during west-side-down sense of shear. Minor chloritic shears cross-cut S_0, S_2, and S_3 kinks, and sphalerite+carbonate occurs in dilational jogs formed during west-side-up deformation. Areas with red fill represent sphalerite occurrence. See text for discussion. Sample 1311-14.

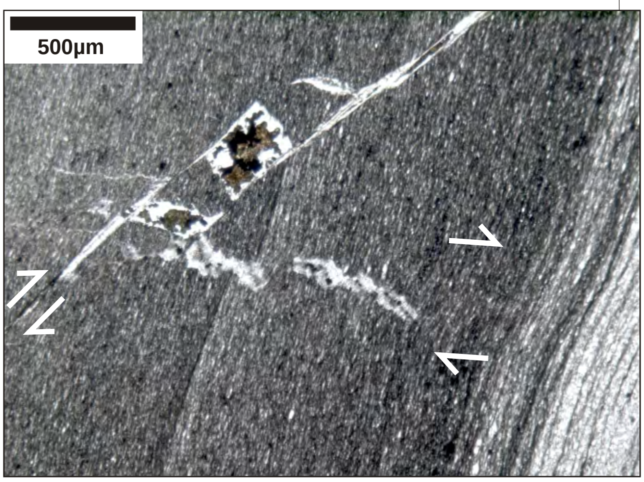

The dilational jog is spatially coincident with a weak S_3 kink. The kink has acted as a heterogeneity during D_4 reactivation of S_0 and S_2 causing stepping of the chloritic shears.

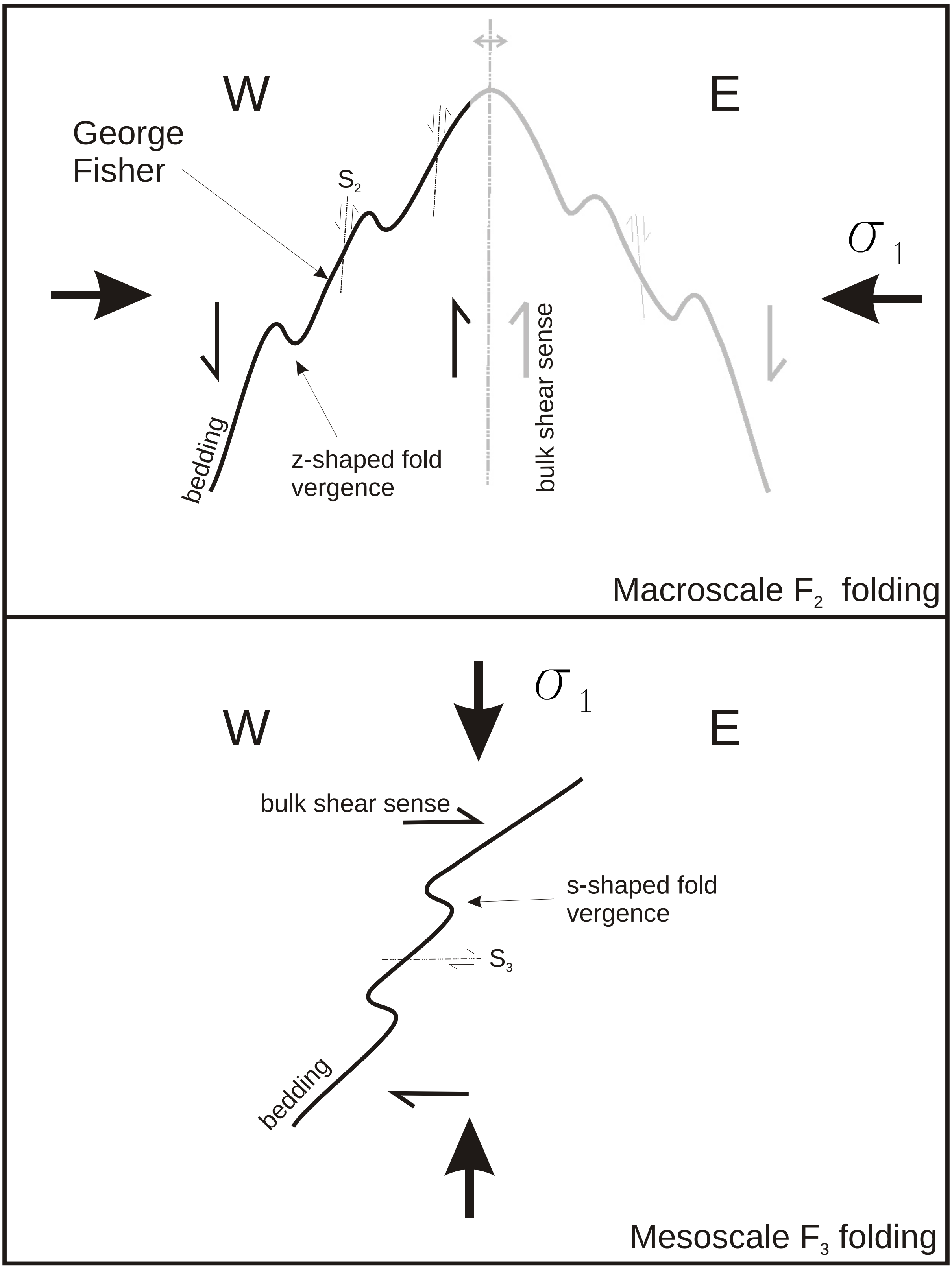

Figure 26. Fold vergence relationships observed at George Fisher. F_2 folds have z-shaped asymmetry and dominant west-side-down sense of shear on S_2 cleavage. F_3 folds have opposing asymmetry with s-shaped geometry and top-to-the-east sense of shear on S_3 crenulations. F_4 folds have the same asymmetry as F_2 folds.

also occurs at the change in dip of the carbonate veins from moderately west-dipping to sub-horizontal attitudes due to micro-brecciation during the D_4 west-side-up reactivation.

F_3 folds are often of the scale of 1cm to 1.0m in amplitude, have asymmetric geometry, and are of monoclinal fold-type or minor folds with vergence opposite to that of F_2 and F_4 parasitic folds (Figure 26). F_3 folds have sub-horizontal to gentle east-dipping axial planes and plunge gently to both the north and south (Figure 22b). Top-to-the-east shear on S_3 and small-scale shears have rotated F_2 folds into inclined to recumbent geometries (Figure 15). Although both F_3 and rotated-F_2 folds have similar axial plane orientations, the fold generations can be distinguished by their opposing vergence.

Formation of a sub-horizontal crenulation cleavage requires a sub-vertical maximum principal stress and sub-horizontal minimum principal stress. Sub-horizontal extension is indicated by the estimated direction of extension of 7°→076° (Figure 22a), sub-horizontal fibres in sub-vertical quartz-carbonate veins parallel to the S_2 orientation (Figure 27) and mineralized bedding-parallel veins which have sub-horizontal quartz fibres. D_3 therefore represents a minor episode of sub-vertical shortening/horizontal extension relative to the major horizontal east-west compression that occurred during D_2.

4.4 Description and interpretation of D_4 structures

A fabric which crenulates the composite $S_0/S_{0c}/S_2$ fabric and cross-cuts S_3 crenulations and is interpreted as S_4 (Figure 28). S_4 crenulations are non-differentiated and correlate with Type 2 crenulations of Bell and Rubenach (1983). S_4 commonly has an en-echelon distribution when viewed in west-east vertical section. As with S_2 and S_3, S_4 is not

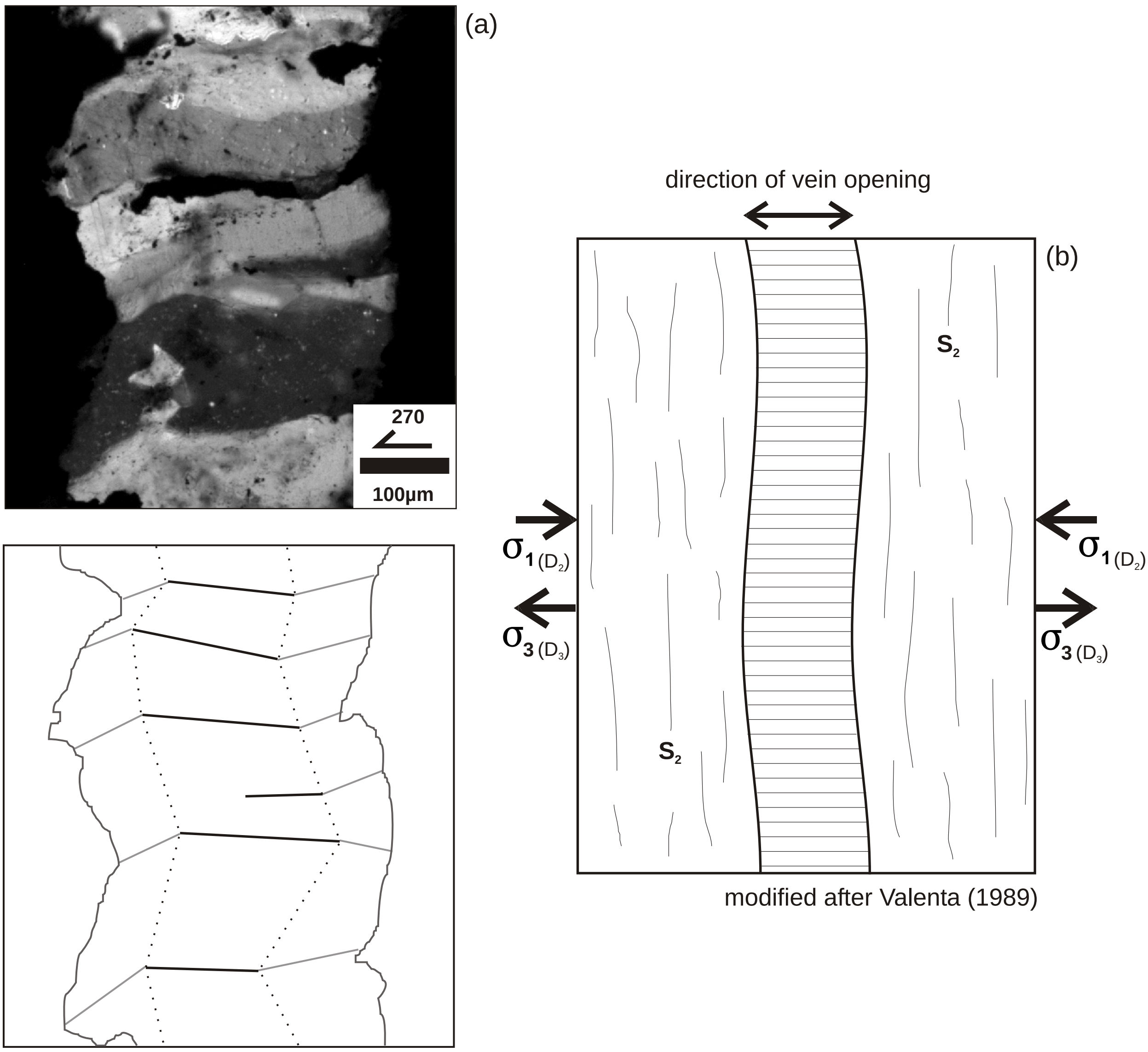

Figure 27. (a) S_2-parallel quartz-carbonate veins contain fibres which are subhorizontal to gently pitching indicating horizontal extension. Note that there are two fibre orientations preserved suggesting a change in the stress-field during vein formation. This sample lacks any other indications of D_3 deformation. Sample 0512-3. (b) Schematic diagram of an S_2-parallel vein with horizontal fibres as illustrated in (a). Valenta (1989) recognized extension parallel to the regional shortening direction and interpreted this phenomenon as the result of fluid overpressuring within an abnormal local stress framework. The vein formation can also be explained in terms of minor sub-vertical shortening exploiting the vertical S_2 foliation during D_3.

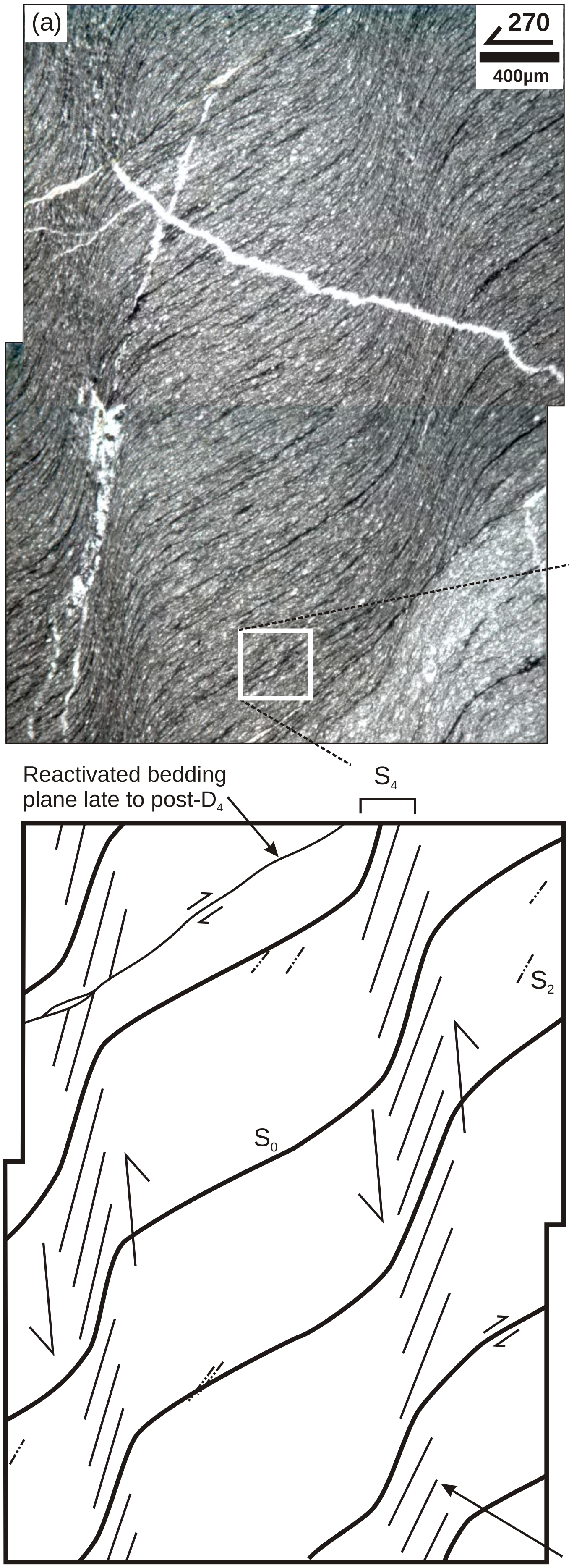

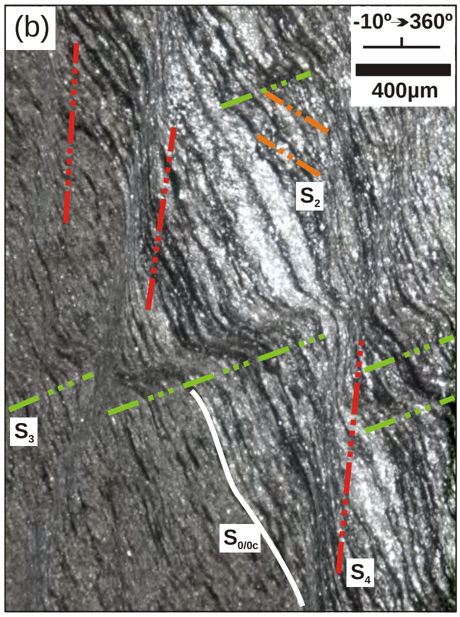

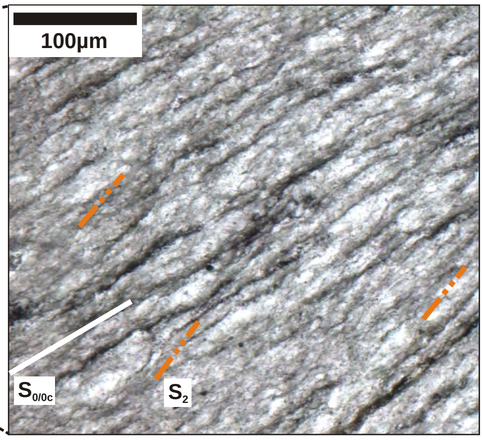

Figure 28. (a) Photomicrograph and line-drawing of S_4 crenulations in vertical section looking north. Note the reactivation of bedding with a reverse sense of shear which has occurred late- or post-D_4. S_2 (see enlarged area) is weakly developed and sub-parallel to S_0. (b) In this plan view, S_4 crenulations with dextral shear sense offset S_3 crenulations. Sample 1311-10.

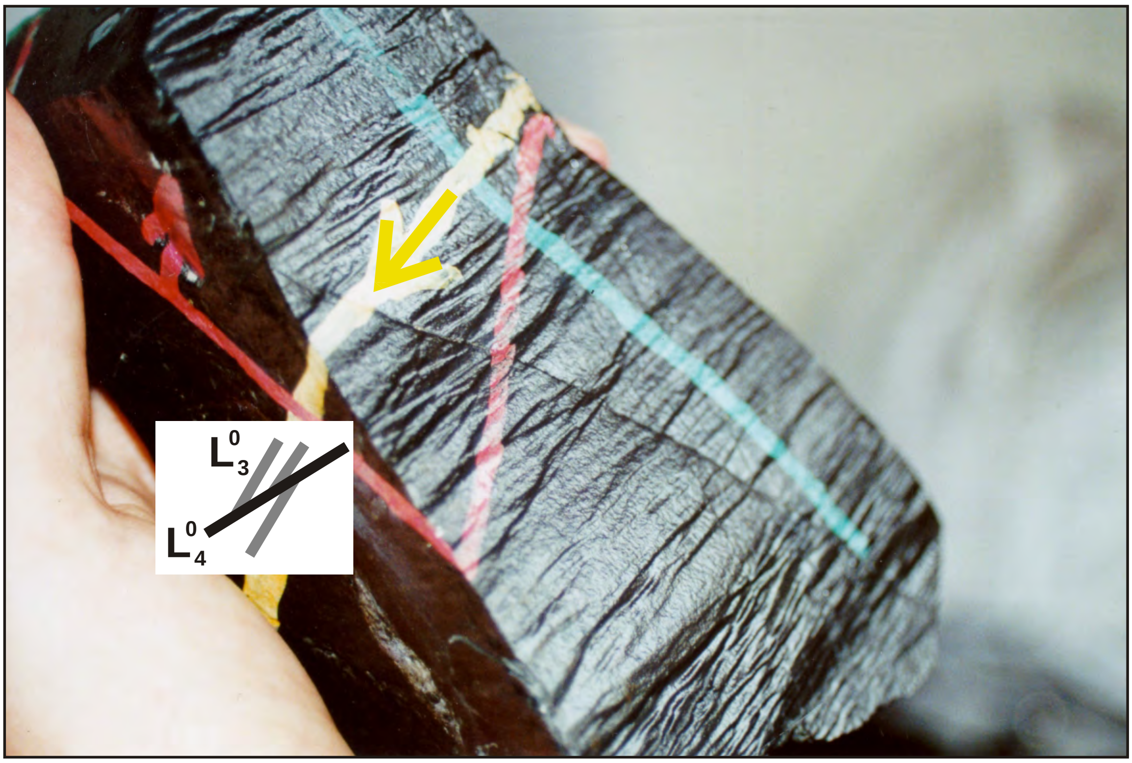

Figure 29. Foliation-bedding intersection lineations preserved on graphitic bedding plane. Yellow arrow indicates north and the red line is the horizontal on this oriented sample. Samples such as this are found only within the F_1 short-limb zone and zones of relatively strong F_2 folding, and are indicators of higher D_3/D_4 strain.

developed to a sufficient intensity to enable mapping in the underground mine or on surface at George Fisher. However, L_4^0 intersection lineations are prominent in areas of higher S_4 intensity (Figure 29). As a result, all foliation orientation data and descriptions of S_4 in this study are from oriented thin-sections.

S_4 crenulations are commonly sub-vertical and where east-dipping, are distributed in an en echelon arrangement within a vertical envelope. The S_4 crenulations have a consistent west-side-down sense of shear (Figure 28). The sense of shear in vertical section is the same as S_2, however, in plan view, the asymmetry of S_4 indicates dextral sense of shear as opposed to the sinistral sense of shear on S_2. S_4 crenulations are morphologically similar to the S_3 crenulations and can appear identical except for orientation and asymmetry. At the intersection between S_4 and S_3 crenulations, unfolding of S_3 crenulations occurs due to the opposing sense of shear on S_4 (Figure 30). The overprinting effect of sub-vertical S_4 crenulations on the sub-horizontal S_3 crenulations also results in a ‘pseudo’-boudinage in competent layers. The sense of shear on each of the foliations is such that the net-effect is bedding-parallel extension when viewed in vertical west-east section.

S_4 and S_4 form-lines strike north to north-northeast (Figure 31). The average orientation of S_4 is 79°→104° and crenulation development is spatially focussed in the F_1 short-limb zone (Figure 29). Relative intensity contours of S_4 (Figure 32) indicate that the most intense crenulation development also occurs within the F_1 short-limb. This relationship is interpreted to be due to the high angle of intersection between S_4 and S_0 compared with areas outside the F_1 short-limb (Figure 33). Comparison of Figures 31 and 32 indicates that areas of high angle of obliquity of S_4 to bedding correlate with the more intensely

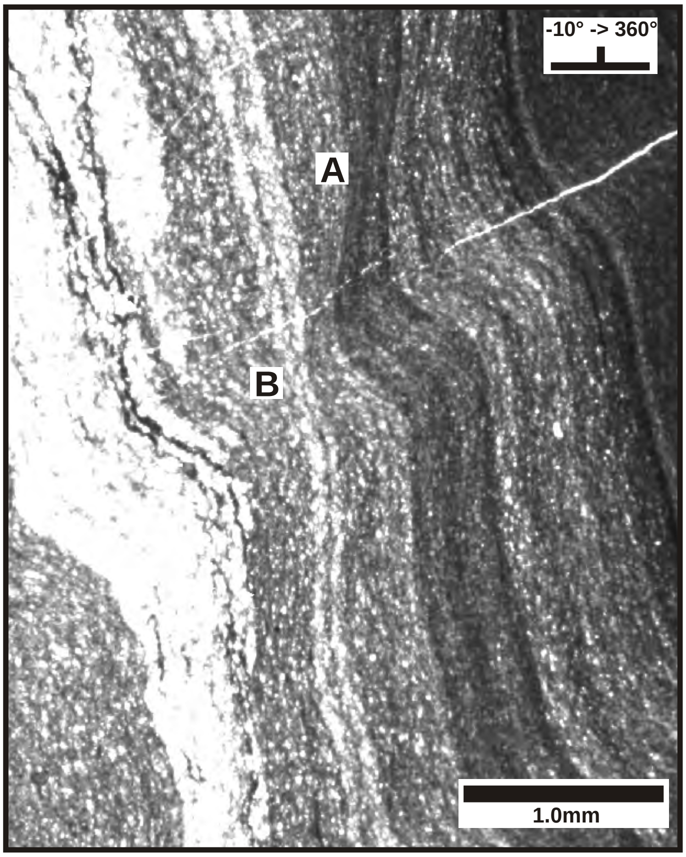

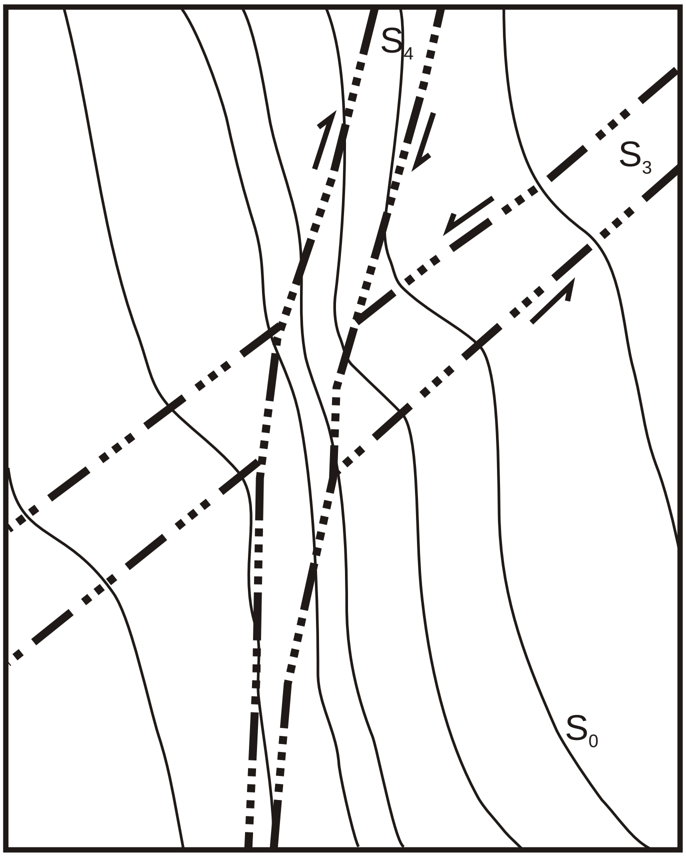

Figure 30. Decrenulation of S_3 by an overprinting zone of D_4 strain. This strain causes attenuation of the dark layer to the right of point 'A' and unfolding of the pale layer at the intersection of S_3 and S_4 crenulations at point 'B' due to the opposing sense of shear. Sample 1311-10.

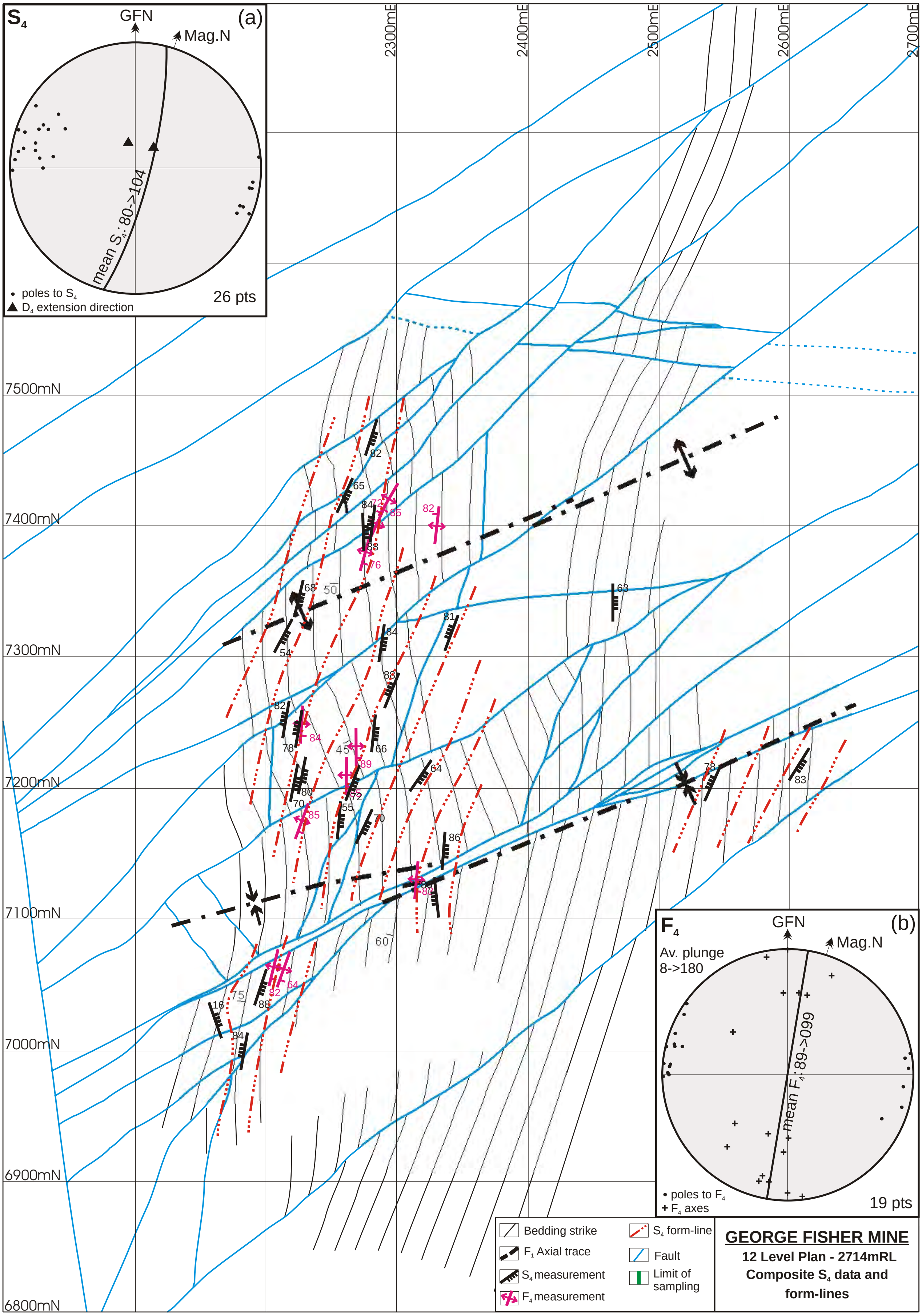

Figure 31. S_4 and F_4 data projected onto 12 Level of the George Fisher Mine. See text for discussion.

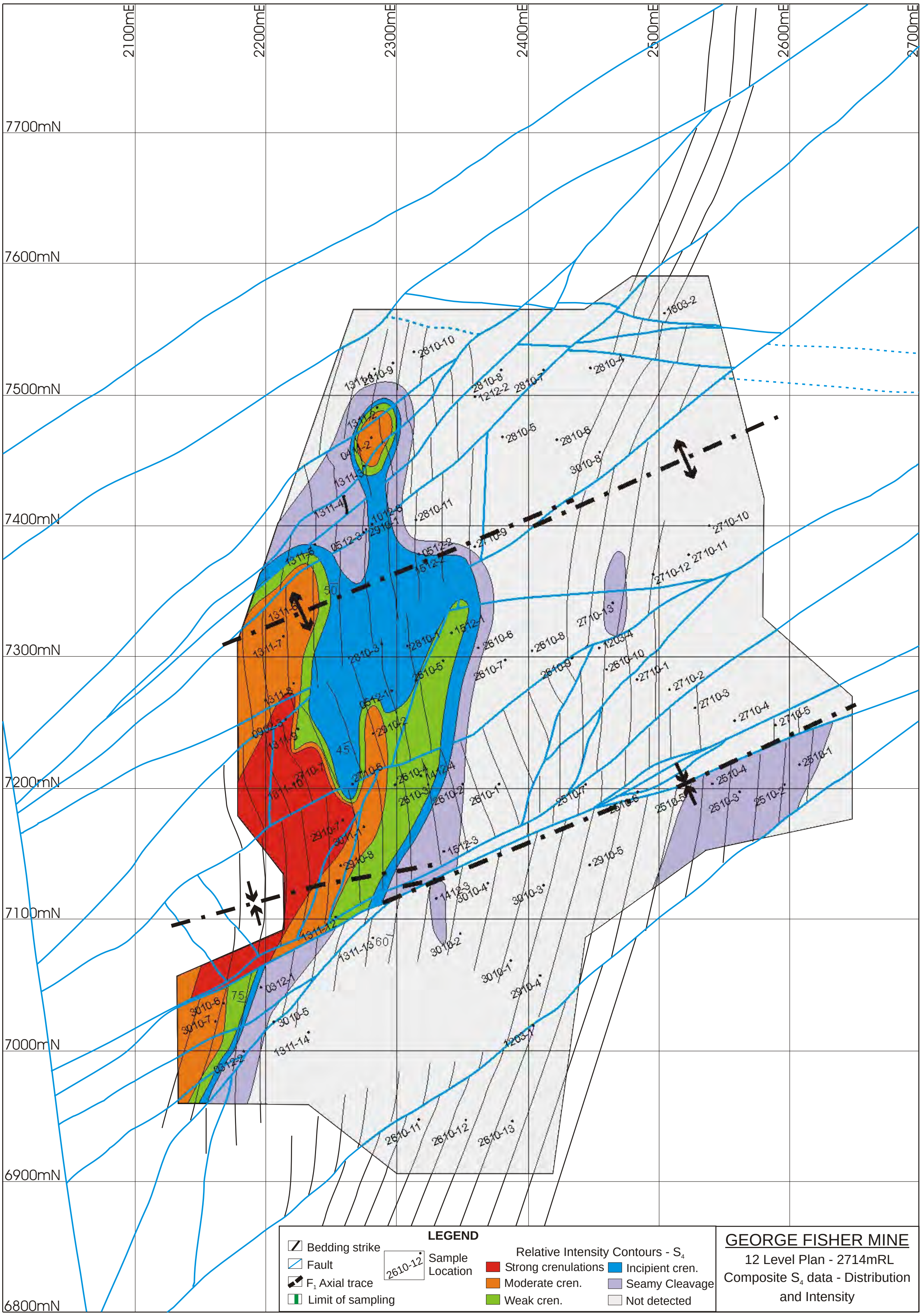

Figure 32. Variation in the intensity of the S_4 foliation. See text for discussion.

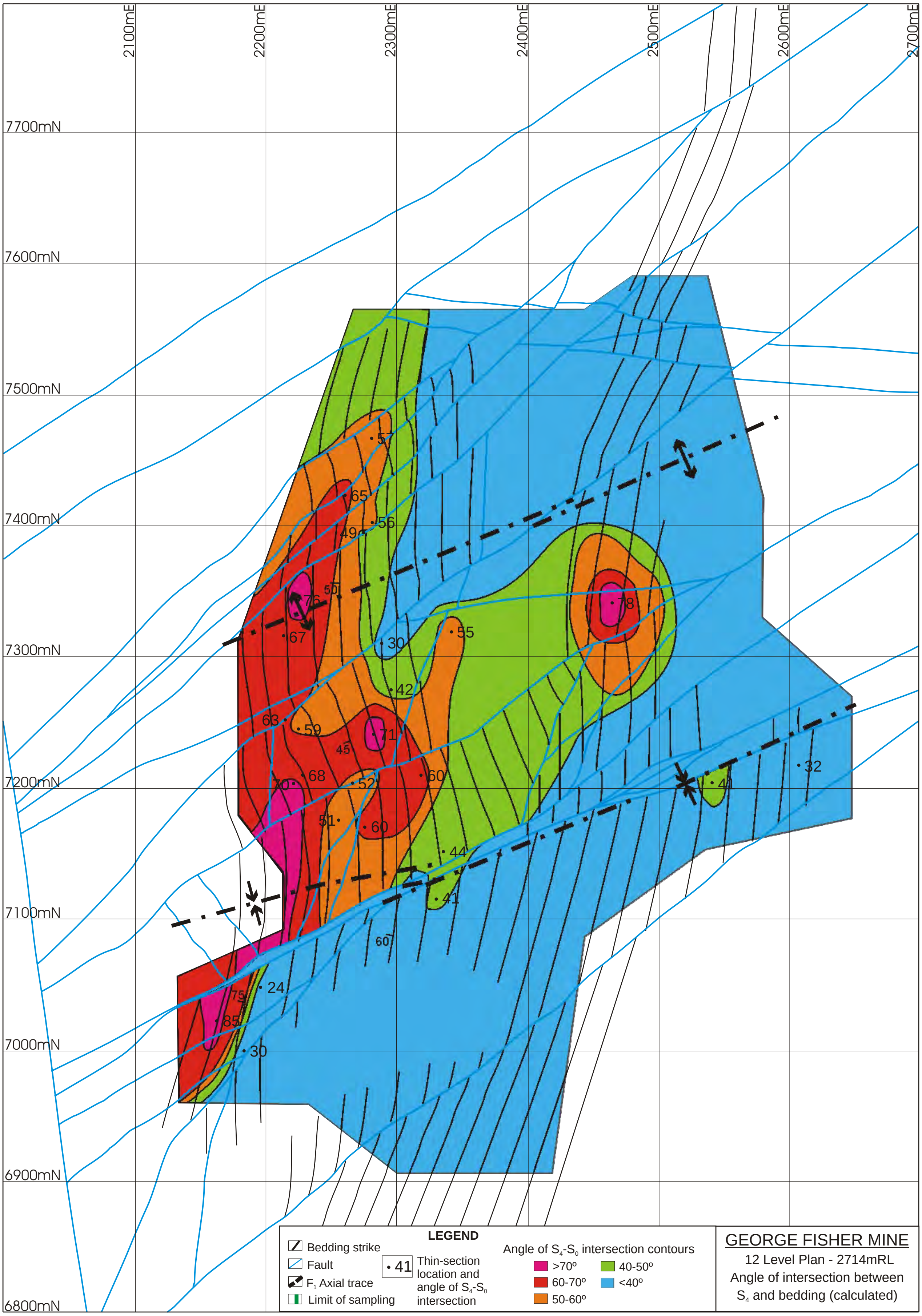

Figure 33. Contours of the angle of intersection between S_4 and S_0 (calculated in 3-dimensions) from thin-section data.

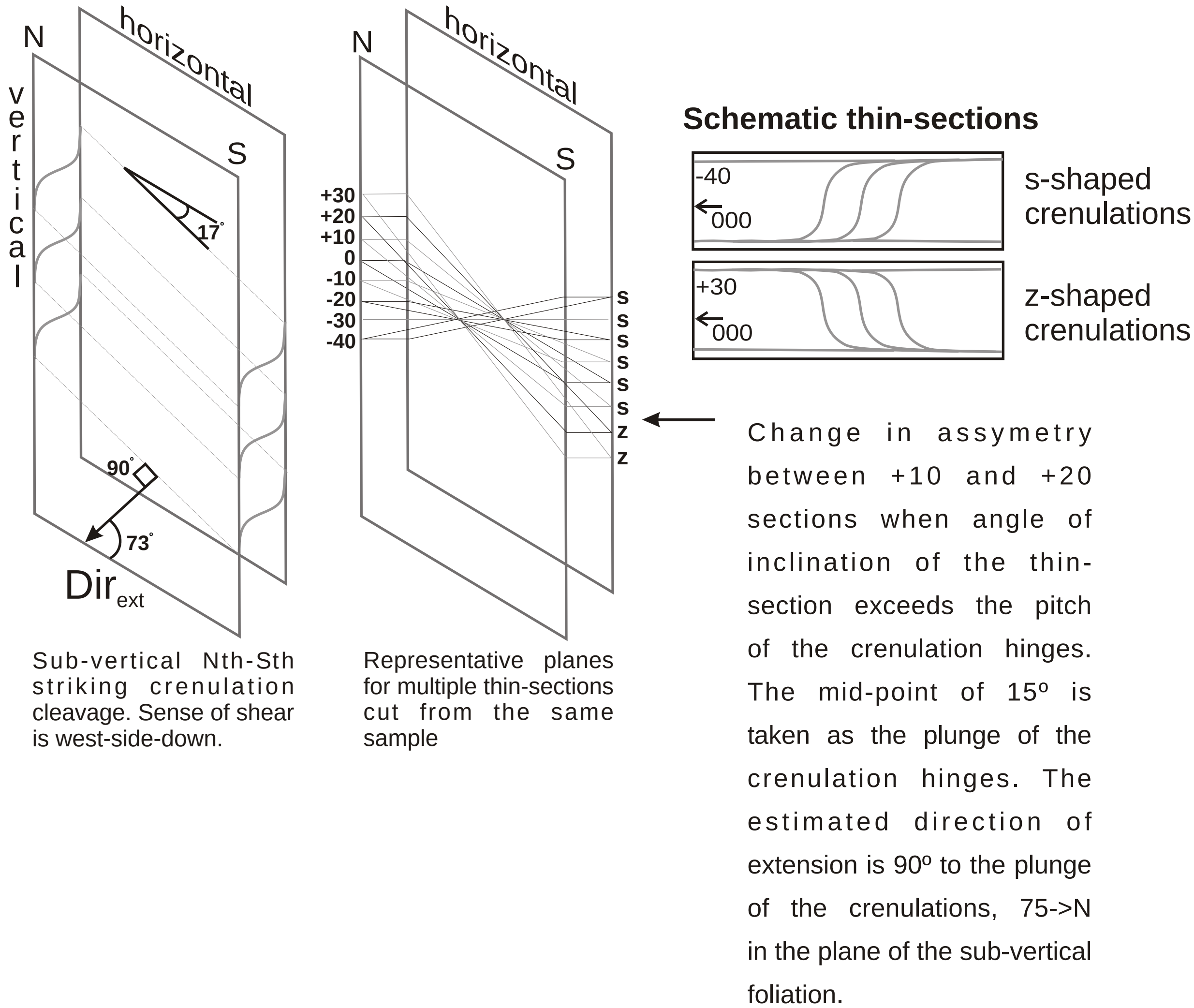

Figure 34. Method of calculation of extension direction in the plane of the S_4 foliation

developed crenulations. On the northern and southern long-limbs of the F_1 fold, D_4 deformation is interpreted to have resulted in reactivation of S_2 and bedding as opposed to S_4 development. The near-parallelism of the strike of S_4 to bedding in the long-limbs of the F_1 fold support this interpretation.

Estimation of the direction of extension in the plane of S_4 has been undertaken using the method described for S_3 by cutting several thin-sections perpendicular to S_4 in order to find the switch in the sense of shear (Figure 34). The estimated direction of extension is steeply dipping to the north and has average plunge of 74°→014° (Figure 31a). This is consistent with the observed west-side-down and dextral (in the horizontal plane) sense of shear on S_4. Also, the intensity of S_4 crenulations varies from more intense in vertical section to weaker in horizontal section suggesting a steep direction of extension.

D_4 formed minor symmetrical upright folds which have vertical axial planes and strike N to NNE (Figure 28b). These folds overprint sub-horizontal F_3 and inclined F_2 folds (Figure 35). F_4 folds and the associated S_4 crenulation cleavage are only recognisable where D_3 folding and cleavage are present and where the D_3 structural elements have rotated F_2 folds into inclined to recumbent attitudes, allowing formation of the new S_4 crenulation rather than re-using the existing S_2 cleavage. The absence of D_3 structural features and their effects means that the S_2 cleavage is sub-vertical and was likely re-used during D_4 horizontal shortening. This is evident in Figure 35 where D_3 strain is focussed into the sub-vertical short-limb of a larger F_2. Bedding planes on this limb of the larger fold cannot reactivate during D_3 kinematics (sub-vertical shortening, top-to-the-east sense of shear) and results in rotation of F_2 folds and minor F_3 fold development. The western

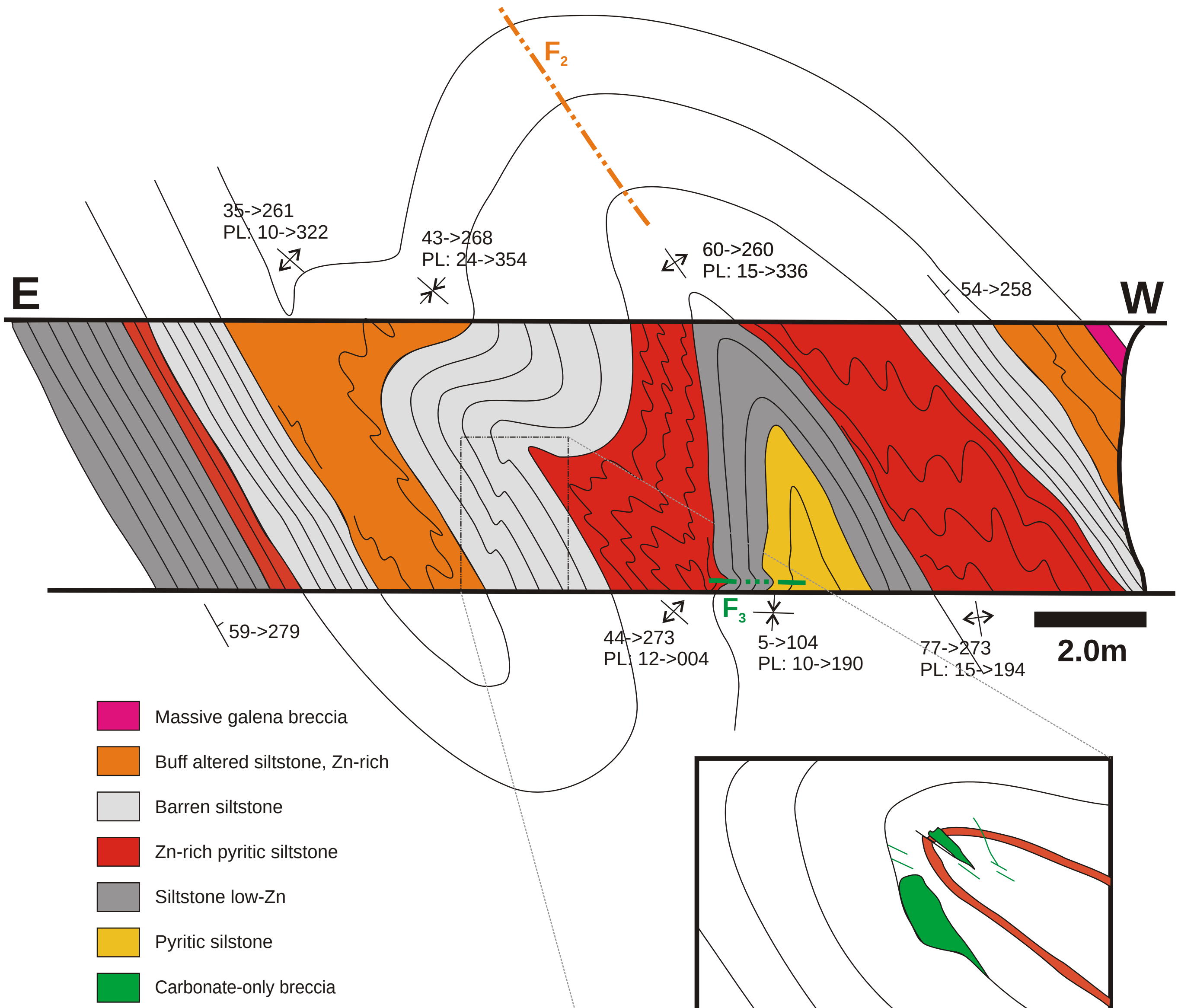

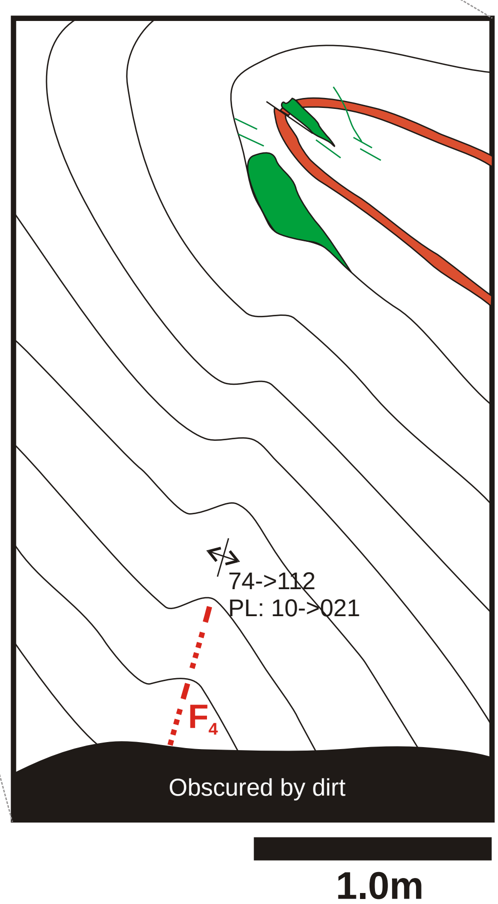

Figure 35. Mapping of part of D-orebody in 737 cross-cut, 12C, looking south. Significant F_2 folding has caused repetiton of stratigraphy and complex overprinting fold relationships. A minor F_3 fold is observed near floor level east of the axial region of the F_2 anticline. Rotation of smaller F_2 folds into inclined orientations occurs on the vertical limb of the large F_2 fold during D_3. A minor F_4 fold occurs in the F_2 short-limb with opposing vergence to the parasitic F_2 folds in this limb. See text for discussion.

limb of the F_2 fold shows little effects of D_3 as this limb is favourably oriented for normal (west-side-down) reactivation of bedding. Subsequent west-side-down bulk shear during D_4 resulted in the formation of a small F_4 fold in the zone of D_3 strain. The F_4 fold occurs in a position where west-side-up reactivation of bedding is inhibited due to a relict F_2 fold. Note that the vergence of the small F_4 fold is inconsistent with it being a parasitic F_2 fold. The enlarged mapping indicates syn-/post-D_4 brecciation and associated infill carbonate occurred at the intersection of F_4 and F_2 folds (Figure 35). Brecciation occurs at this location where neither fold propagation (due to bedding paralleling the F_4 axial plane) nor bedding reactivation (due to the restricting F_2 hinge) can occur. This brecciation overprints a band of stratabound sphalerite mineralization.

Reactivation of earlier formed fabrics and bedding during D_4 is interpreted to be the dominant manifestation of D_4 strain in the George Fisher area. Lack of significant F_4 folding supports this interpretation, as reactivation of S_0 and S_2 (where steeply dipping), has prevented formation of F_4 folds. Exceptions exist where reactivation was locally inhibited by the geometry of early-formed structures (Figure 35).

Evidence for reactivation of the S_3 crenulation in D_4 kink-bands is shown in Figure 36. S_3 is folded by the steeper S_4 fabric with characteristic west-side-down sense of shear. Where S_4 crenulations are less-developed, S_3 retains a steeper dip. In regions of more intense S_4 development, the east-dipping S_3 crenulation is rotated to sub-horizontal and the intensity of the S_3 crenulation is increased due to synthetic reactivation on S_3. These 'corridors' of intensification of S_3 (named S_{3r}) pitch at 50-70° west in vertical W-E sections and strike sub-parallel to the S_4 orientation. The S_4 crenulation cleavage

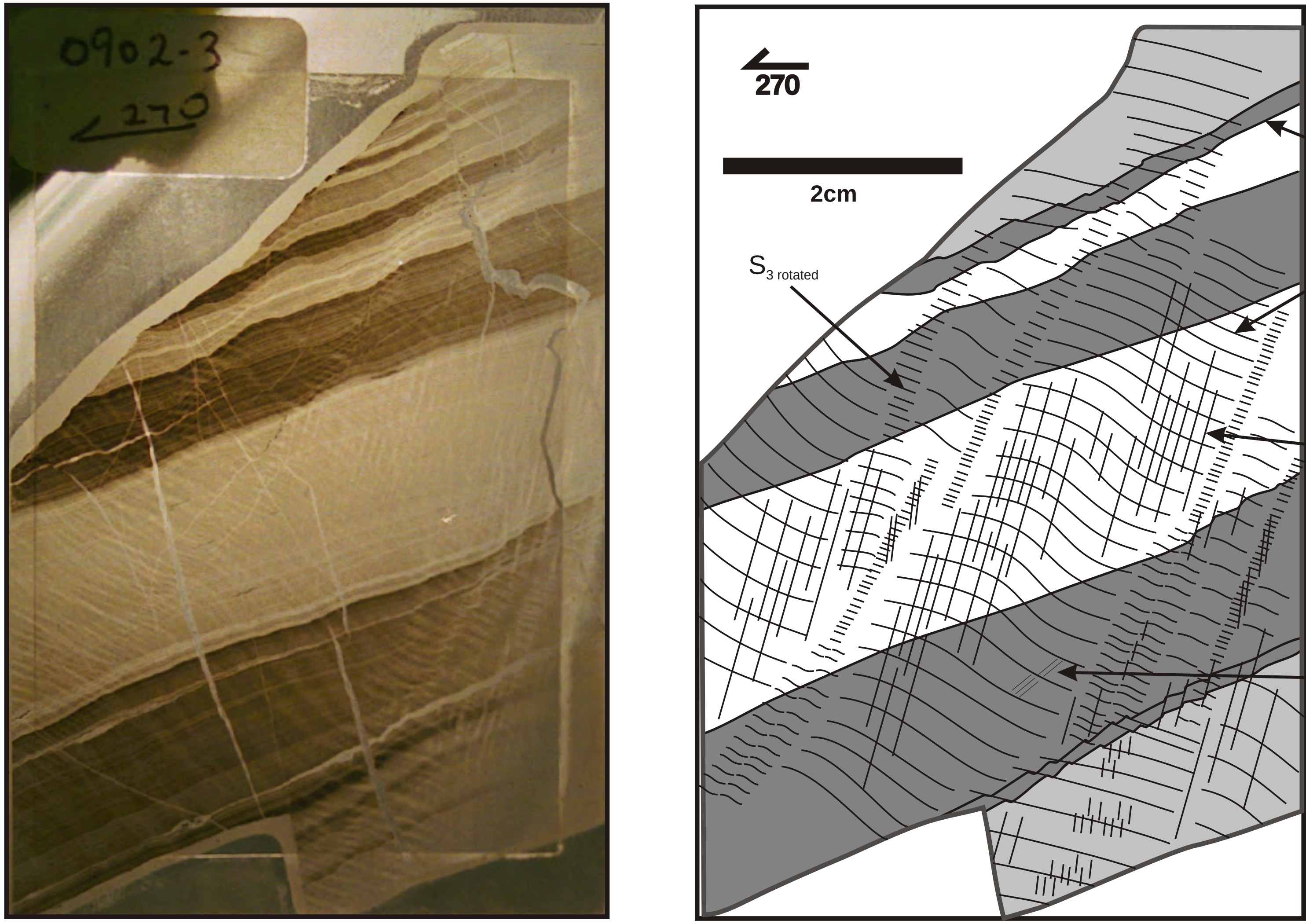

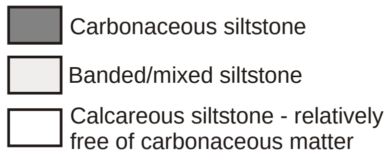

Figure 36. Photograph and line-drawing of a thin-section detailing foliations in non-mineralised siltstone. Veining and some bedding omitted so that foliation relationships are clear. Note the intensification of S_3 crenulations where overprinted and reactivated by S_4. Vertical section looking north. See text for discussion. Sample 0902-3.

overprints S_3 structures outside the S_{3r} 'corridors' but, within S_{3r} and S_4 are mutually cross-cutting. This relationship indicates that rotation of S_3 in the S_{3r} 'corridor' and development of S_4 crenulations was synchronous. Note that S_4 is more intense within the more massive calcareous siltstone than the laminated carbonaceous siltstones as represented on the line diagram (Figure 36). This relationship suggests that crenulation development is suppressed in the more finely bedded lithologies due to the availability of more heterogeneities such as carbonaceous seams and bedding planes for reactivation, whereas S_4 crenulation development is more intense in the relatively massive siltstones that have fewer heterogeneities.

D_4 represents further east-west horizontal shortening, after a period of horizontal extension during D_3, but of apparently lesser magnitude than the east-west shortening during D_2 episode. Morphological characteristics of the foliations suggest that D_4 was of similar intensity to the preceding D_3 episode in the George Fisher area. However, given that an unknown amount of strain was manifest as bedding reactivation, the intensity of D_4 may have been greater than D_3.

4.5 Description and interpretation of Post-D_4 minor fabrics

Post-D_4 fabrics are rare at George Fisher and therefore insufficient data is available to incorporate later features in the structural framework. However, in some samples, gently dipping non-differentiated crenulations (S_5) occur which cross-cut S_4 crenulations and a vertical non-differentiated crenulation has also been observed in samples where the S_4 crenulations have been rotated from vertical to steeply dipping attitudes (Figure 37). The minor vertical crenulation overprints the interpreted S_5 and is inferred to be the youngest

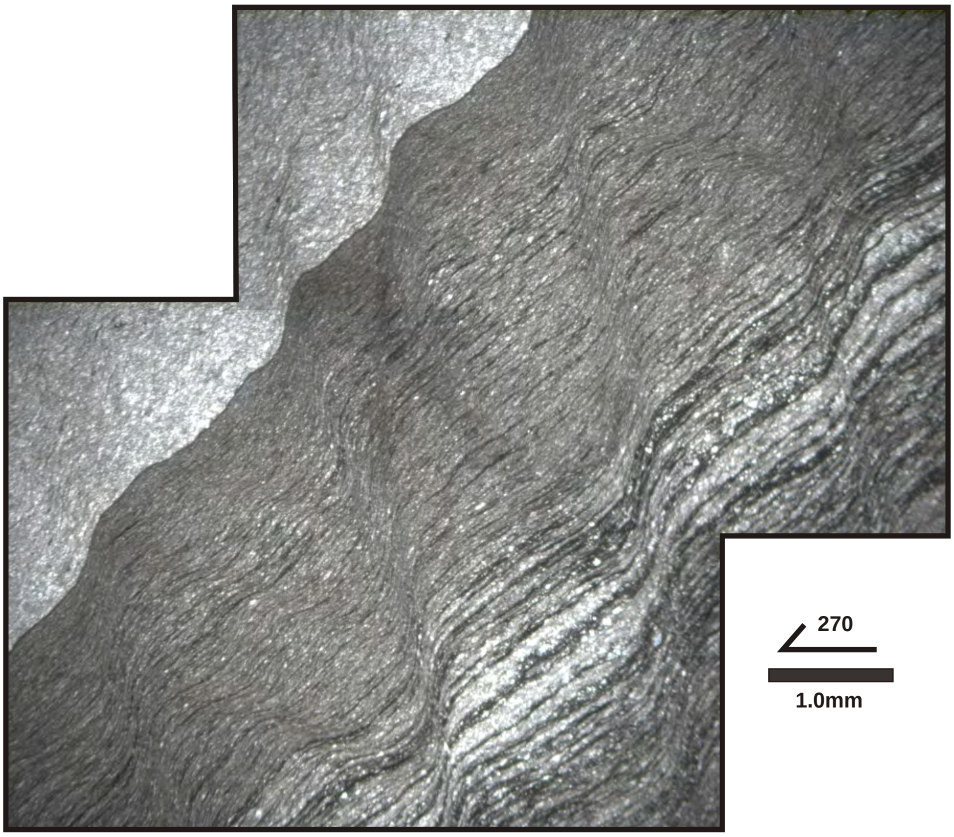

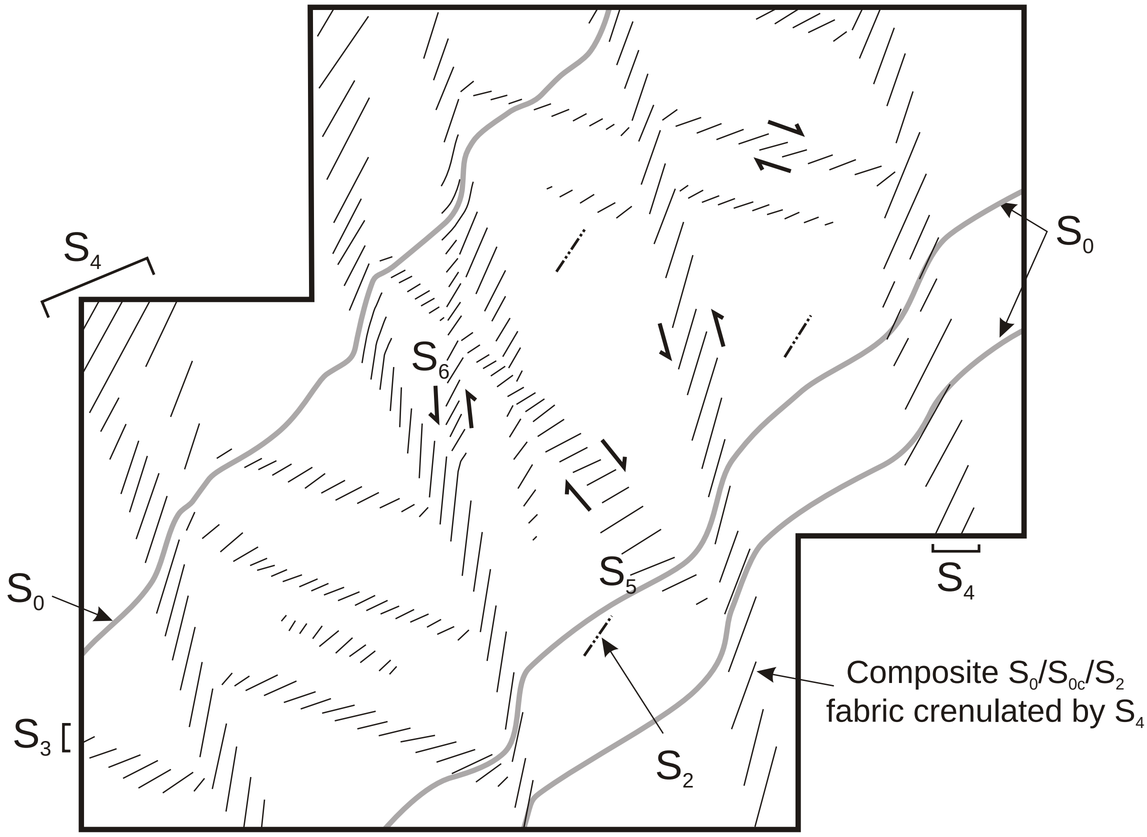

Figure 37. Photomicrograph and line-drawing illustrating the foliations from S_2 to S_6. Interpreted S_5 and S_6 crenulations are weakly developed and are rarely detected in samples, therefore the possibility that S_5 and S_6 are conjugate crenulations cannot be excluded. Note the apparent boudinage (S_0-parallel extension) of layering where crenulations intersect. Sample 1311-10.

fabric observed (S_6). The sense of shear on both pairs of gently-dipping (S_3 and S_5) and steeply dipping (S_4 and S_6) crenulations is consistent (Figure 37). More observations of these younger minor crenulations (S_5 and S_6) is required to determine whether they are conjugate crenulations or cross-cutting like the S_3 and S_4 crenulations.

4.6 Description and interpretation of late kink folding

Angular, kink-like folds occur in the northern and southern areas of the George Fisher deposit (Figure 38). These folds occur on scales from 3cm to 1.0m wavelength and are dominantly located in the mineralized layers. Their axial planes are sub-vertical and they strike east-west. A weak axial planar slaty cleavage is present only in the hinge-zones of these folds. Folding of meso-scale F_2/F_4 folds and S_2 in thin-section is observed and supports a post-D_4 late timing of these folds.

4.7 Description and interpretation of brittle faulting

Several generations of brittle faults occur in the vicinity of the George Fisher deposit. Different fault generations are distinguished by their cross-cutting relationships, orientation, and direction of displacement. Five main fault sets are recognised in the deposit and its immediate surrounds (four of these are illustrated in Figure 39). These are:

1. N-S reverse faults with oblique slip e.g. Paroo fault
2. E-W faults e.g. J75 fault
3. NNE striking, sub-vertical reverse faults e.g. G72
4. NNW striking sinistral faults e.g. Gidyea Creek Fault, Spring Creek fault (refer Figure 2)

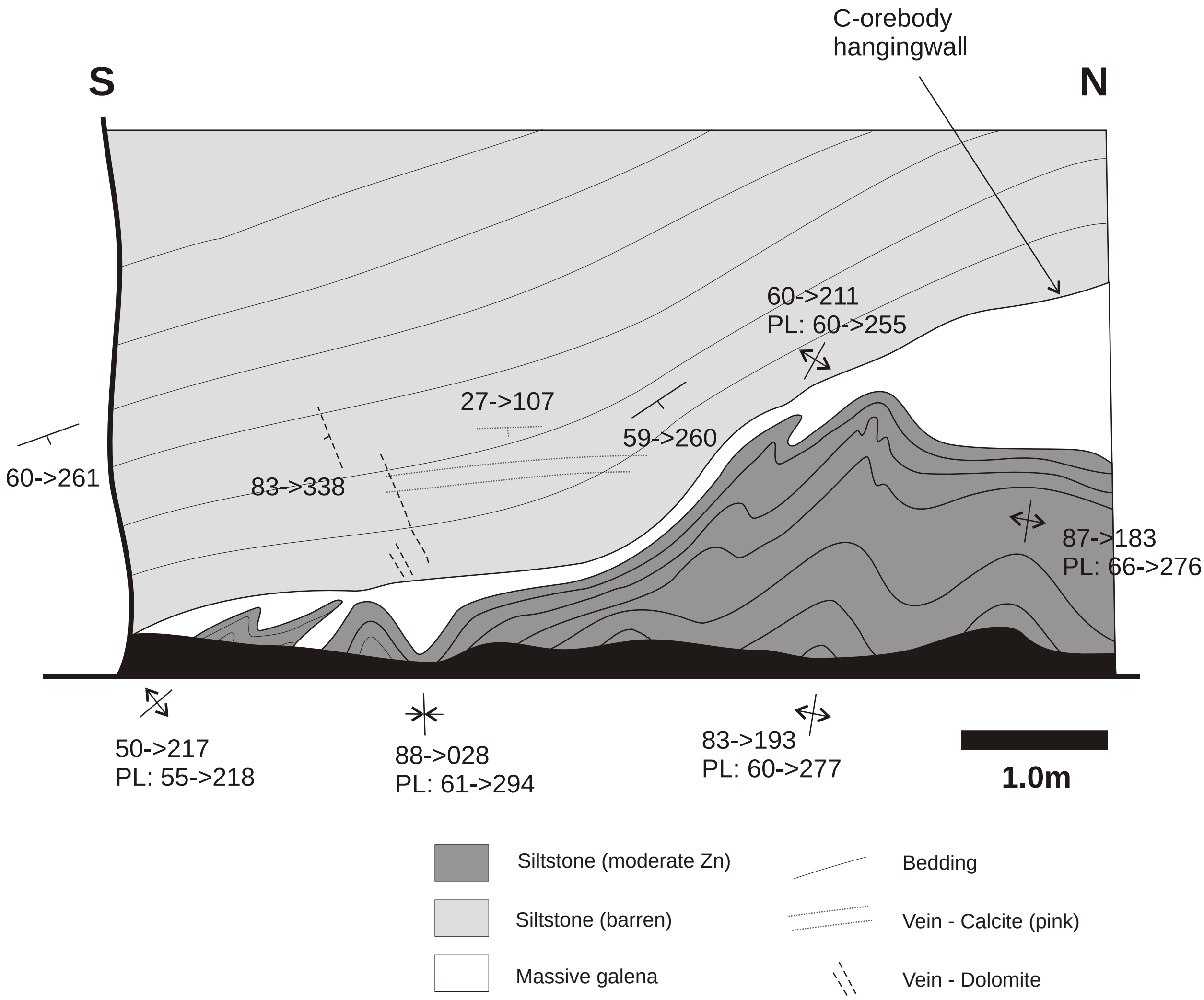

Figure 38. Mapping of the west wall of CN71, 11L. This is the hangingwall of C-orebody and is dominated in this locality by folds with subvertical axial planes and westerly plunges. Cross-cutting relationships that suggest this folding post-dates S_2/F_2 include refolding of F_2/F_4 folds and microscale kink-folds with the same orientation as mapped above fold the S_2 cleavage.

Explanation of symbol: 88->028 PL: 61->294 — Synformal fold with axial plane dipping 88º toward 028º and plunging 61º toward 294º.

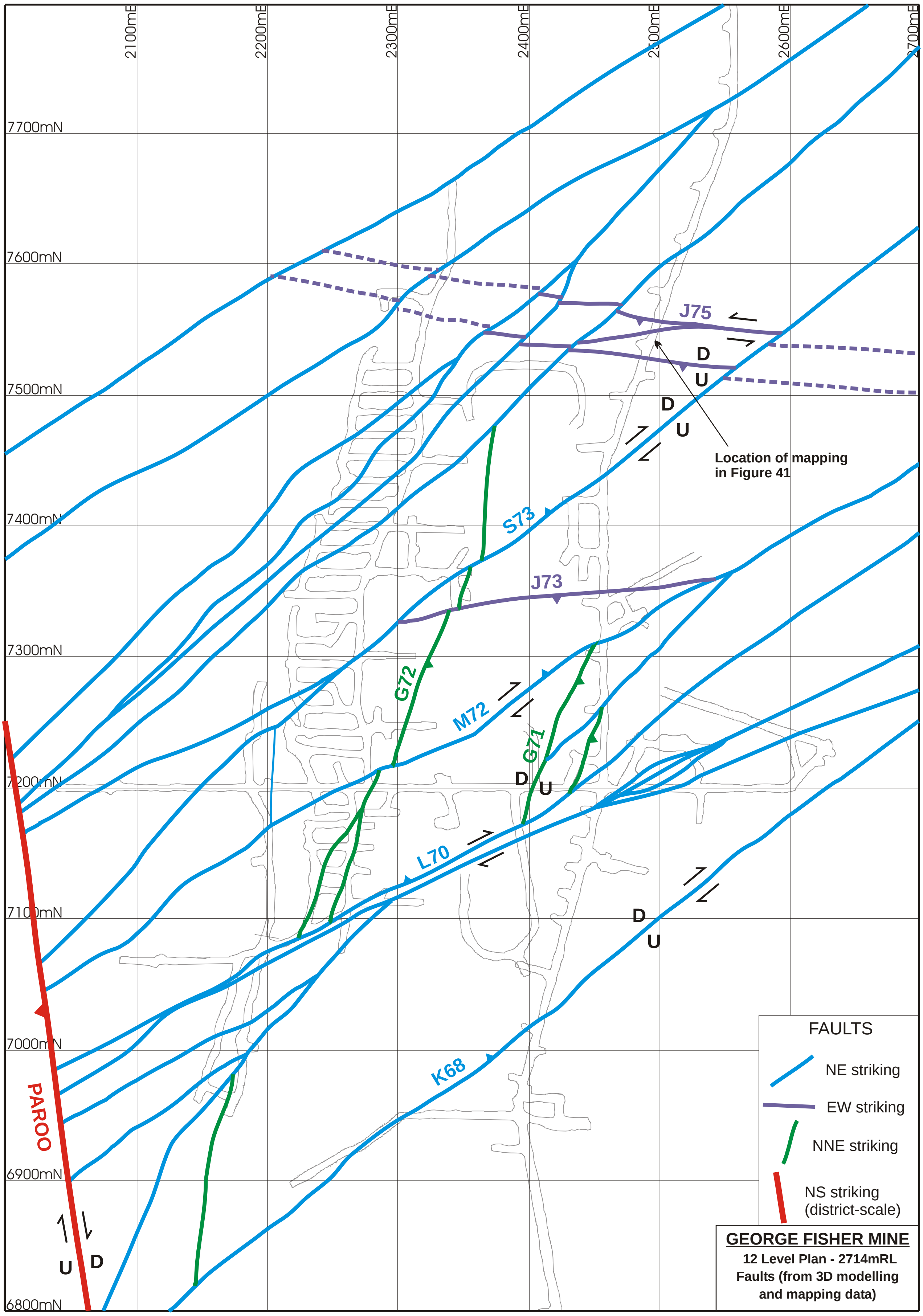

Figure 39. Main fault sets at George Fisher. See text for discussion.

Figure 40. Cataclasite from the Paroo Fault. 'Clasts' from the fault breccia have well polished/slickensided surfaces.

5. NE striking dextral faults with normal slip e.g. L70

4.7.1 North-South reverse faults with oblique slip

West-dipping faults of this type include the Paroo fault (Figure 39) to the west of the George Fisher deposit. This regionally significant fault is characterized by a 200m high-strain zone (Valenta, 1988) that contains cataclasite (Figure 40) and graphitic fault gouge. Valenta (1988) recorded steeply pitching mineral lineations and s-c fabrics displaying west-side-up shear sense in the Paroo fault zone indicating reverse dip-slip movement on the fault. This movement direction is consistent with the dominant east-west horizontal shortening expected during the Isan Orogeny. The presence of s-c fabrics indicates that the fault/shear was active during ductile deformation and was reactivated during progression into brittle deformation. The Paroo Fault is interpreted to represent a bounding fault to a half-graben formed during the rifting which predates the deposition of the Mt Isa Group sediments (Betts and Lister, 2002). The fault is therefore likely to have been active throughout the Isan Orogeny (D_1-D_4).

4.7.2 East-West striking faults

These faults (including J75, J74) are less numerous than other fault types (Figure 39) and occur as wide brittle fault zones in the eastern footwall drive at 12 Level George Fisher (Figures 39 and 41a). The faults generally have only minor (<10m) normal (north-side-up) displacement, although reverse drag folding is observed on some faults. The high strain/fracture zone and folding suggest that these faults are long-lived and may be associated with the D_1 event. Winsor (1986) mapped east-west trending D_1 faults in the Lake Moondarra area to the east of George Fisher (Figure 2) which had normal

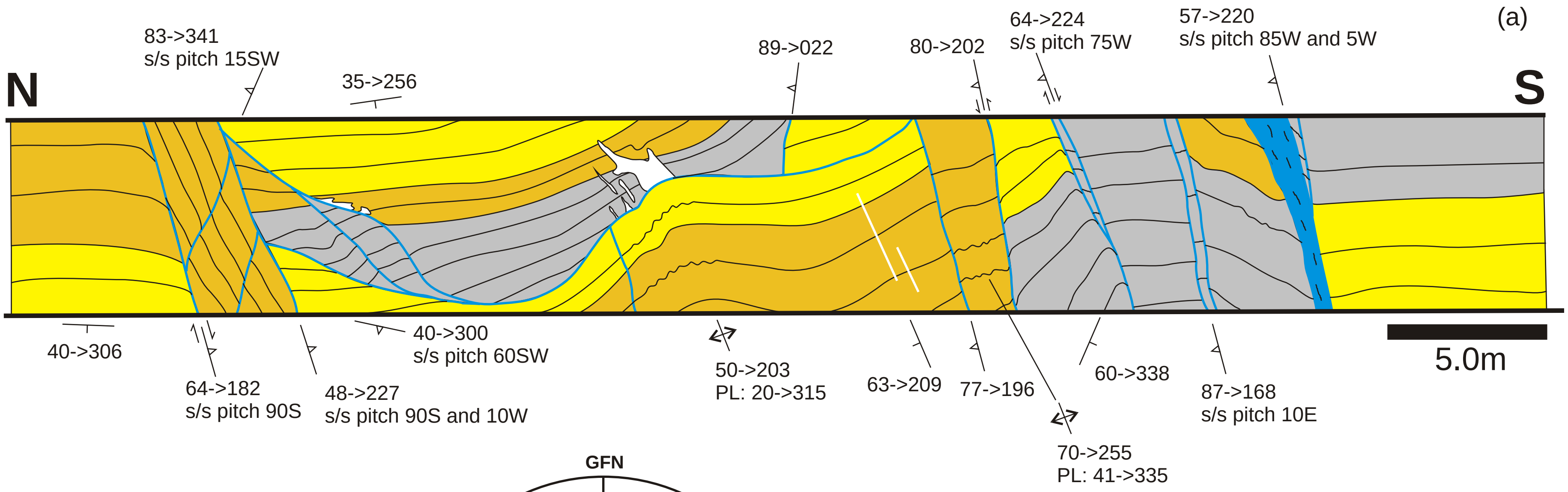

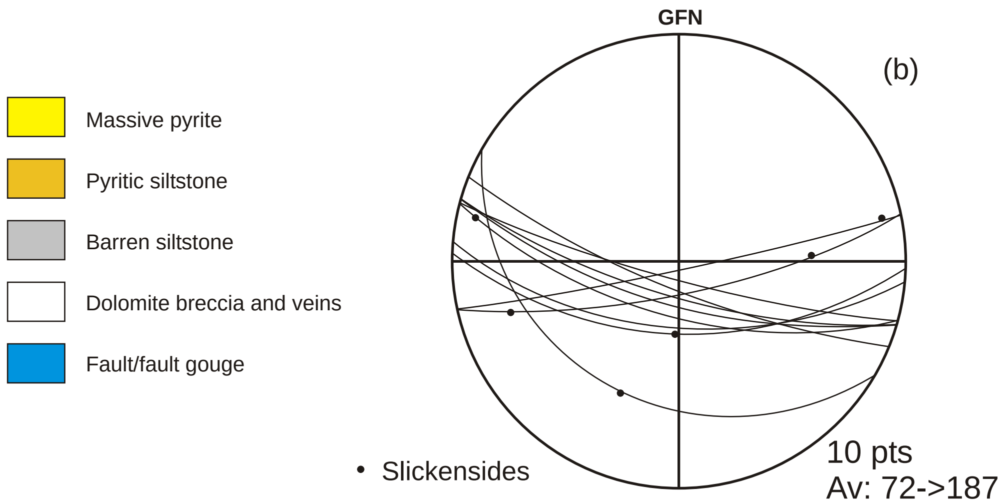

Figure 41. (a) Mapping of the east wall of the IJ69 drive, 12L George Fisher. The east-west striking faults have dip directions between 168º and 227º as labelled on the above diagram. These faults commonly contain fault gouge. (b) Slickensides and fault drag folding indicate normal and reverse movement and both dip and strike-slip. This suggests a long movement history and reactivation of the faults during repeated movement episodes.

displacement and an associated E-W slaty foliation. These faults have sinistral offset (Figure 2) which is consistent with reactivation of the faults during D_2/D_4 east-west shortening. Steep and gently pitching slickensides on these faults suggest reactivation during subsequent deformations (Figure 41b).

4.7.3 North-Northeast striking, sub-vertical reverse faults

These are a less abundant fault type with small offset (<5m) and minor reverse movement as indicated by drag folding immediately adjacent to the faults. The orientation and sense of shear on these faults is consistent with that of S_4 crenulations suggesting that these faults may be a late-D_4 transition into more brittle deformation. Some faults have a component of strike-slip movement as preserved by gently pitching slickensides (Figure 42). Strike-slip movement on these faults may have occurred as a younger phase of movement associated with north-east striking dextral faults discussed below. Minor, discontinuous faults of this type have been observed as syn-galena brecciation but they are not a significant control on mineralization (Figure 42).

4.7.4 North-Northwest striking, west-dipping sinistral faults

The district-scale Transmitter, Gidyea Creek, and Spring Creek faults are examples of this fault set which cross-cut macro-scale F_2 folds (Figure 2). Minor faults of this type change strike and become bedding parallel fault zones when heterogeneities such as pre-existing folds are absent (see 7475mN on Figure 16). The orientations of faults of this type are displayed in Figure 43a. These faults are minor at the scale of the George Fisher workings but are significant district-scale structures (Figure 2). Interpreted as D_3 faults

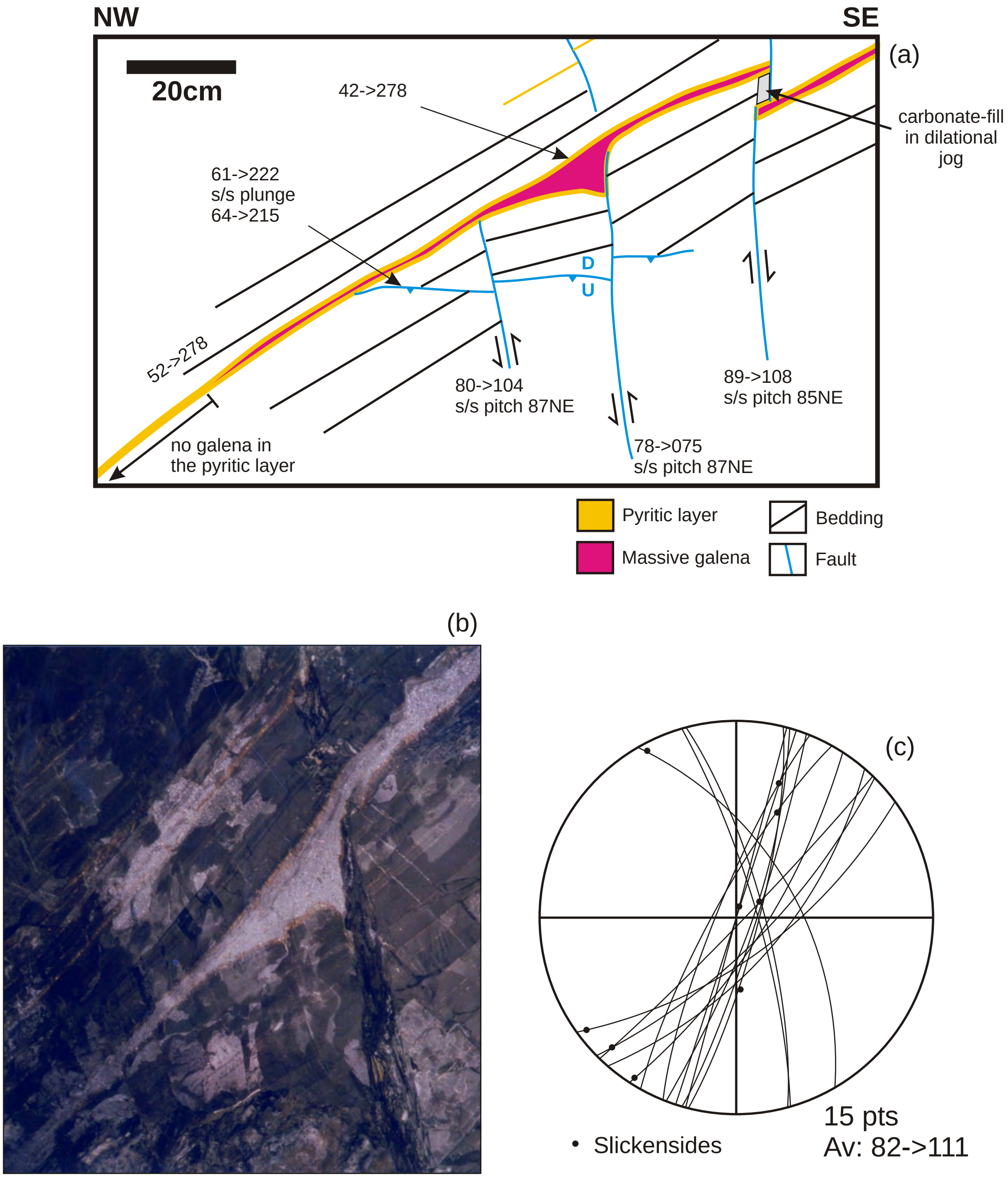

Figure 42. (a) Mapping of east-dipping faults with minor east-side-up displacement and potentially synchronous galena mineralization. (b) Photograph of the same exposure as in (a) but taken at a different angle. Note the brassy pyrite 'rim' to the galena mineralization. Down-dip from the galena occurrence, only a brassy pyrite layer remains (see (a)). (c) Data for east-dipping faults measured in the George Fisher mine. Both dip-slip and strike-slip movement senses are indicated by slickensides.

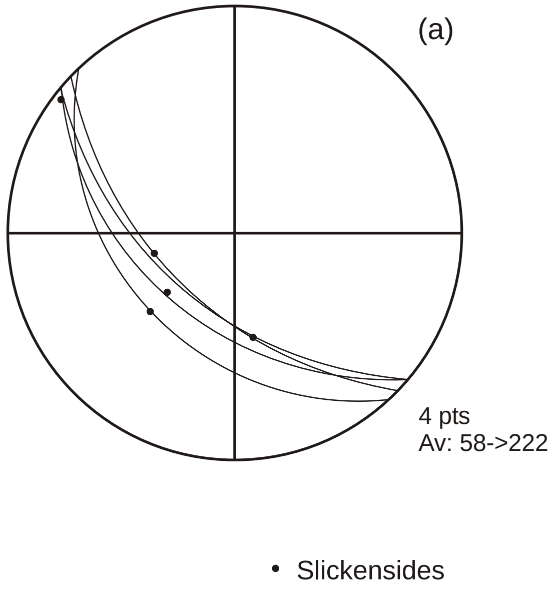

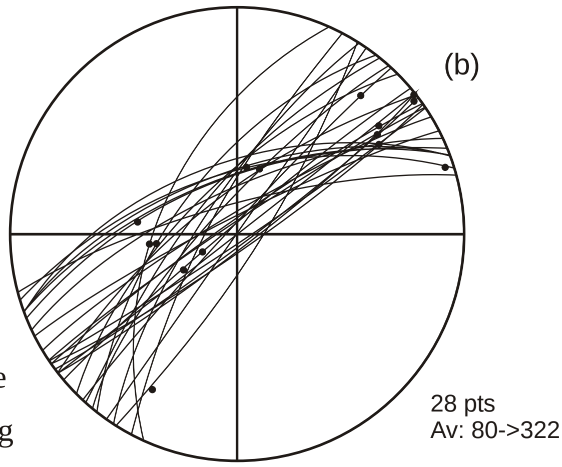

Figure 43. Fault orientation and slickenside data, (a) NW trending faults, (b) NE trending dominant fault set at George Fisher.

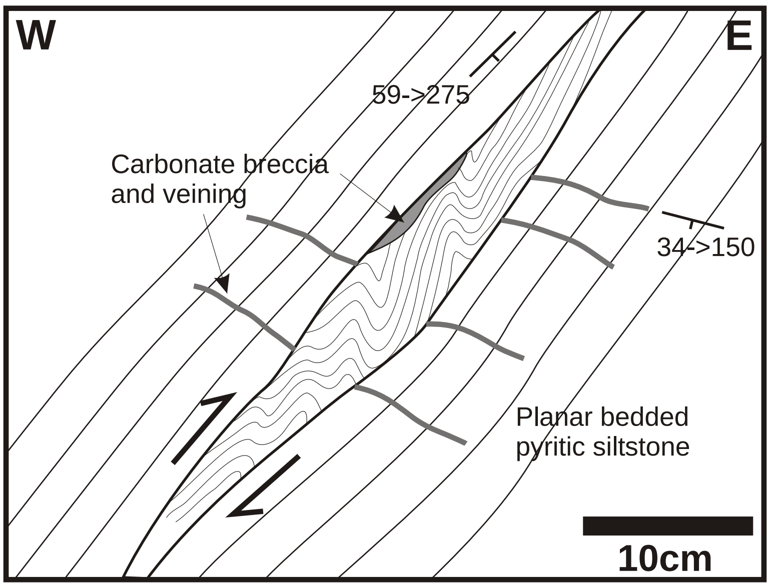

Figure 44. Sketch of bedding-parallel fault with kink-like folding and tension veining indicating reverse sense of shear.

(D_4 - this study) by Valenta (1988; D_4 this study) as they displace macro scale F_2 folds east of the George Fisher and Hilton deposits, these major faults have a strike-slip component of movement which is consistent with ongoing east-west horizontal shortening during D_4. Note that minor faults of this orientation have dip-slip movement indicators at George Fisher (Figure 43a).

4.7.5 Northeast striking dextral-normal faults

These faults have the most significant impact on the George Fisher deposit as they occur in relatively high abundance and can have significant offset (2 to >100m). Sense of movement is characteristically north block down and to the east (normal-dextral) and orientation and slickenside data are presented on Figure 43b. Note some slickensides data indicates dip-slip movement. These faults cross-cut F_2 folds and offset D_4 higher-strain zones (Figure 31) and often have minor fault-drag folding affecting approximately 1.0m of the country-rock on either side of the fault (Figure 10). They are therefore related to the transition from ductile to brittle deformation and from vertical extension to north-south directed extension. The abundance of faulting of this type in the deposit environs may be due to the F_1 fold acting as a local heterogeneity during brittle deformation. This generation of faulting causes both vertical and north-south extension in the George Fisher – Hilton region (Valenta, 1994).

4.7.6 Bedding-parallel faults

Bedding parallel faults (west-dipping) are locally significant structures and are more significant at the adjacent Hilton deposit than at George Fisher. These faults are likely to have had a long movement history during the east-west horizontal shortening of the Isan orogeny. A bedding-parallel fault which displays west-side-up movement and the formation of kink-like folds in the zone of cataclasis is illustrated in Figure 44. Where folding is not present within the fault, these bedding-parallel faults are difficult to detect in the shale/siltstone lithologies.

5. Discussion

5.1 Comparison with previous structural interpretations

Regions which have previously been studied in a structural context are indicated on Figure 45 and the corresponding findings of the studies on Table 1. Colours on Table 1 indicate probable correlations of deformation episodes between individual structural interpretations.

Common to most analyses is the observation of early, approximately east-west oriented deformation features associated with the D_1 episode. D_1 strain is manifested as south-verging folds (Winsor, 1986; Bain et al, 1992**;** Stewart, 1992) (Table 1) with approximately east-west trending axial planes. The interpreted F_1 fold central to the George Fisher deposit also has south-verging asymmetry. The synclines accompanying east-west faults are interpreted as drag-folds in a thrust-duplex system by Bell (1983, 1991). Alternatively, D_1 faults are interpreted as the reactivation of basement faults active during early rifting in the Leichhardt River Fault Trough (O'Dea et al., 1997a,b; Betts and Lister, 2002) and associated folds occur due to buttressing of sediments against basement horsts during basin inversion (Betts and Lister, 2002). A component of north-south shortening is required in both interpretations. East-west trending faults with evidence for both dip-slip and strike-slip movement post-date the F_1 folding in the Lake

Author	Location	Pre D_1	D_1	D_2	D_3	D_4	D_5	D_6	D_7
Swager, 1983	**1** Mt Isa		Small scale parasitic folds with opposite assymetry to later F_3 folds	No mesoscopic F_2 folds. S_2 occurs as pervasive, weakly developed N-S cleavage seams	Macroscopic, east-verging F_3 fold zones with sub-vertical axial planes and NNW trending strike and plunge. S_3 occurs as both crenulation and seamy cleavage.				
Winsor; 1986	**2** Lake Moondarra		Macroscopic folds trending E-W with sinistral vergence. S_1 occurs as a slaty cleavage.	Macroscopic, N-S trending folds with northerly plunges. S_2 occurs as a vertical N-S striking slaty cleavage with mineral elongation direction 76->160. S_2 strikes NNW in the George Fisher region.	Folds/flexures trending NNW at a low angle to F_2 folds. S_3 occurs as a slaty cleavage dipping 88->072 with stretching direction 74->122.				
Valenta; 1988, 1994	**3** Hilton Mine	Bedding parallel foliation of compaction/-diagenetic origin	No folding observed	Upright N to NNW-trending folds with shallow axes. S_2 occurs axial planar to F_2 folds as a solution/slaty cleavage. Steep stretching lineations.	NNW trending, inclined to recumbent folds which form in association with earlier folding and have north-south plunging axes. Neutral vergence. S_3 occurs as flat-lying, spaced crenulations and S_2-similar cleavage with steep stretching direction (?)	F_4 folds occur as chevron-like conjugate kinks with steeply plunging axes and axial surfaces trend NE and NW. Restricted in occurrence to areas near shear zones.			
Nijman et al.; 1992a,b	**4** Paroo Range, and Hero/Paroo/Western fault intersection		Flower structures and drape folds	Low angle thrusting	Major N trending upright folds with horizontal to moderate plunges. S_3 varies in intensity from spaced cleavage through to pervasive foliation and averages 90->260.	E-W trending folds/flexures interpreted to cross-cut main-stage folding.	N and NNE trending upright folds with steep northerly plunges. S_4 is sub-vertical and strikes 023 in Western Fault region		
Stewart, 1992	**5** Horse's Head Thrust		W-plunging South-verging upright folds. S_1 occurs as a spaced to slaty cleavage.	N-plunging upright folds. S_2 occurs as axial planar slaty cleavage.	Local NW-plunging upright folds, with open to tight geometry. S_3 not observed.	E-W normal faults (spatial association with F_1?)	N trending folds with horizontal to steep northerly plunges associated with strike slip faulting		
Xu, 1996	Dugald River		E-W trending folds and flexures. S_1 is locally preserved.	Macroscopic, tight to isoclinal, N trending folds. S_2 occurs as a pervasive slaty cleavage.	Small-scale folds with gently dipping axial planes. S_3 occurs as a weak crenulation cleavage.	Outcrop-scale upright folds trending NW. S_4 occurs as NNW trending penetrative crenulation and fracture cleavage.	Kink folds with sub-horizontal axial planes.	E-W trending open folds.	
Bell & Hickey, 1998	**6** Mt Isa - Hilton		E-W, near vertical foliation, thrust repetition of stratigraphy, N-S mineral elongation lineation in bedding parallel S_1	Regional folding with steeply dipping NW to N trending axial planes. S_2 is the dominant schistosity and the mineral elongation lineation pitches steeply to the south.	Referred to as $D_{2.5}$ (equivalent of D_3 - this study), this event produced meso- to macroscale folds with sub-horizontal axial planes. S_3 occurs dominantly as rotation of earlier foliation. During D_3 (equivalent of D_4 - this study), localized folding with steeply dipping, NNW to NE trending axial planes. S_3 is only locally developed and can occur as a pervasive fabric containing a steeply south-pitching elongation lineation	Rare flat-lying kinks	Weak, steeply dipping crenulations striking NW-SE		
Chapman; 1999, 2004	**7** George Fisher	Bedding parallel foliation of compaction/-diagenetic origin		Upright N-S trending folds with 0.5 to 2.0m amplitudes. S_2 occurs as an axial planar crenulation cleavage	Folds with sub-horizontal axial planes. S_3 not observed.	Small-scale NNW/NW trending folds. S_4 occurs as axial planar foliation.			
This study	**8** George Fisher	Bedding parallel foliation of compaction/-diagenetic origin commonly occurring as pressure-solution seams	Open s-shaped fold/flexure with steeply dipping E-W trending axial planes.. S_1 is weak to absent	Open to closed folds with NW (NNW wrt GF mine grid) trending axial planes and steep to reclined westerly dips. F_2 folds generally plunge gently to the NW (NNW wrt GF mine grid). S_2 occurs axial planar to F_2 folds and is the dominant, pervasive slaty/solution, cleavage.	Minor folds with sub-horizontal axial planes and top-to-the-east vergence. S_3 is domainal at deposit-scale and parallels the axial planes of F_3 folds. S_3 occurs as crenulations of S_0, S_{0c} and S_2.	Minor folds with sub-vertical axial planes and gently-plunging axes trending N (NNE wrt GF grid). S_4 is domainal at deposit-scale and parallels the axial planes of F_4 folds. S_4 occurs as crenulations of the composite $S_0/S_{0c}/S_2$ fabric and cross-cuts S_3.	Rare, minor, gently dipping crenulation development only	Very rare, minor, vertical crenulation development	Kink-folds with moderate south-west plunging fold axes.

Table 2. Previous structural interpretations in the Mt Isa - George Fisher - Lake Moondarra area. Numbers in ***Location*** field refer to Figure 45.

Moondarra area (Winsor, 1986). Repetition of the stratigraphic sequence in the Lake Moondarra region (Bain et al., 1992) and Mt Gordon Arch north of George Fisher (Bell, 1983) has been interpreted to be due to north over south thrusting pre-D_2. At the Mt Isa Mine, Bell (1991) recognised a sub-vertical east-west oriented foliation which was attributed to D_1 and a stretching lineation on bedding parallel foliation surfaces which trends N-S and has sub-horizontal plunge. These features support north-south directed thrusting prior to the main D_2 phase of folding. Valenta (1988, 1994) did not observe D_1 folds at the adjacent Hilton Mine but recognised a bedding-parallel schistosity, which he termed S_1, developed in rocks rich in phyllosilicates and which was folded around F_2 folds. This schistosity was interpreted to have developed during compaction as part of the process of diagenesis as the foliation is not associated with macro-scopic folds. Chapman (1999) recognized stylolites which predate the formation of fine-grained pyrite which is interpreted as diagenetic. The stylolites therefore also have a diagenetic origin and represent compaction/solution features. The stylolitic seams have therefore been referred to as S_{0c} (bedding parallel compaction) in this study (see Figure 7).

Most workers have attributed macroscale folding and pervasive slaty cleavage development to the D_2 episode (Winsor, 1986; Valenta, 1988; Stewart, 1992; Xu, 1996; Bell and Hickey, 1998). The dominant slaty cleavage at George Fisher (S_2) is interpreted to be of D_2 timing based upon cross-cutting relationships, and is parallel to the axial planes of district-scale F_2 folds in the George Fisher – Lake Moondarra area (see Figure 2, 45).

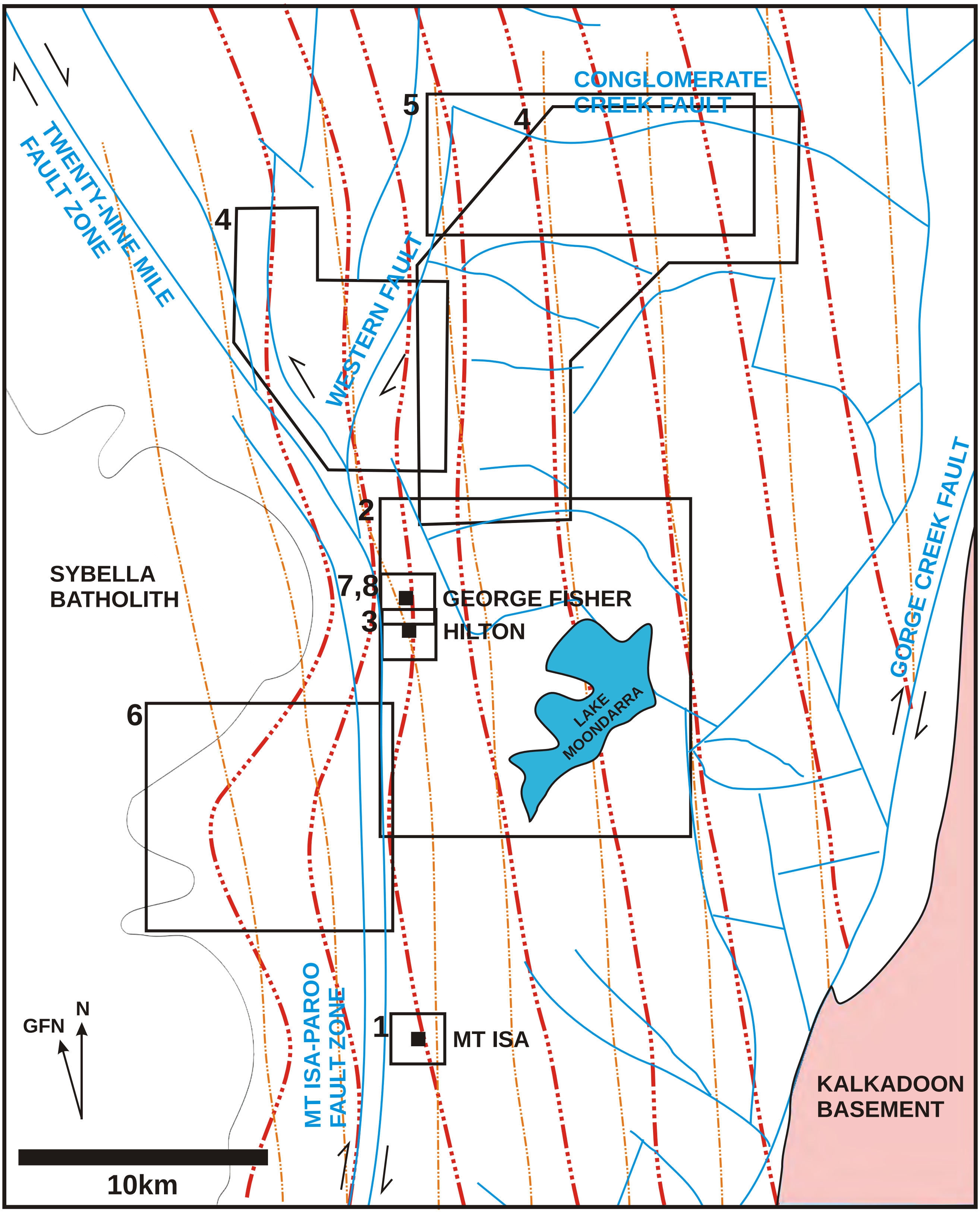

Figure 45. District-scale map displaying major geological features (after Nijman et al, 1992b) and areas of previous structural analysis (numbered boxes corresponding with Table 1). The strike of D_2 structural formlines (orange) and D_4 structural formlines (red) are shown and discussed in the text.

The near flat-lying S_3 fabric and F_3 folds were first observed in the Hilton Zn-Pb-Ag deposit by Valenta (1988) (Table 1), and have since been recognized in the Mt Isa mine (Davis, 2003 pers. comm.), west of the Mt Isa-Paroo fault between Mt Isa and George Fisher (Bell and Hickey, 1998), and F_3 were recognized by Chapman (1999) at George Fisher (Table 1). Valenta (1988) observed gently-dipping crenulations of S_0, S_1, and S_2 and inclined to recumbent folding of bedding at the Hilton mine and correlated this foliation with the steeply-dipping S_3 (S_4 this study) of Winsor (1986) due to the similarity of strike of the foliations (Valenta, 1994). However, a difference in dip of approximately 60° exists between the S_3 of Winsor (1986) and the S_3 of Valenta (1988, 1994). East of George Fisher in the Lake Moondarra region, Winsor (1983) did not observe a fabric associated with D_3 (this study) but recorded sub-horizontal fibres in quartz veins oriented parallel to S_2. This was interpreted as relaxation post-D_2 folding by Winsor (1983). In the context of the structural history of the George Fisher area, these vein/fibre relationships are inferred to represent syn-D_3 sub-vertical shortening/horizontal extension and resultant gaping on S_2 with sub-horizontal quartz fibres recording the horizontal extension associated with D_3. At the George Fisher deposit, the effects of D_3 are interpreted to include formation of folds with gently dipping axial planes and vergence opposing that of the F_2 and F_4 folds, development of domainal crenulations of $S_0/S_{0c}/S_2$ and rotation/flattening of F_2 folds consistent with the top-to-the-east sense of shear on S_3. The lack of documentation of other occurrences of D_3 structures is possibly due to district-scale partitioning of strain resulting in a domainal nature of D_3 zones of higher strain.

D_4 resulted in localized, small-scale folding (Stewart, 1992; Xu, 1996; Bell and Hickey, 1998; Chapman, 1999) and/or reuse of existing S_2 and F_2 features (Winsor, 1986) (Table

1). At George Fisher, F_4 folding is minor and folds have wavelength less than 1.0m. D_4 folding to the south near Mt Isa and west adjacent to the Sybella Batholith (Bell and Hickey, 1998) has produced significant F_4 folds and F_4 fold corridors the scale of which are not present at George Fisher. Winsor (1986) interpreted the regional scale fold to the east of George Fisher to be a composite F_2/F_4 fold produced through reuse of the earlier S_2 fabric during D_4. S_4 is domainal at the George Fisher deposit-scale and crenulates the $S_0/S_{0c}/S_2$ composite fabric and S_3. S_4 (this study) does not correlate with the S_4 of Valenta (1988, 1994)) which was observed only in close proximity to shear zones. Bell and Hickey (1998) interpreted the stretching lineation on S_3 (S_4 – this study) as steeply plunging to the south. Findings of this study suggest that the stretching direction is steeply north plunging to sub-vertical in the George Fisher area. The direction of extension during D_4 is a critical piece of the structural/mineralisation framework as it indicates the direction that pre-existing structures or bedding, if oriented in suitable orientations, will gape during D_4 deformation, possibly providing fluid channel ways. D_4 deformation at George Fisher is interpreted to have been accommodated largely by reactivation of existing foliations and bedding surfaces rather than formation of significant F_4 folds.

A swap in the asymmetry of the S_2/S_4 relationship occurs between Mt Isa and George Fisher (Figures 45 and 46) (compare Swager, 1983; Davis, 2004; and this study). Figure 45 displays form lines for D_2 and D_4 features, as documented by previous workers. Variation in the orientation of S_2/F_2 is minimal across the district and intersects the region of microgranite (Figure 3) in the Sybella Batholith at a high angle in area 6 (Figure 45) mapped by Bell and Hickey (1998). Mapping of S_4 in this region (Figure 4) indicates that

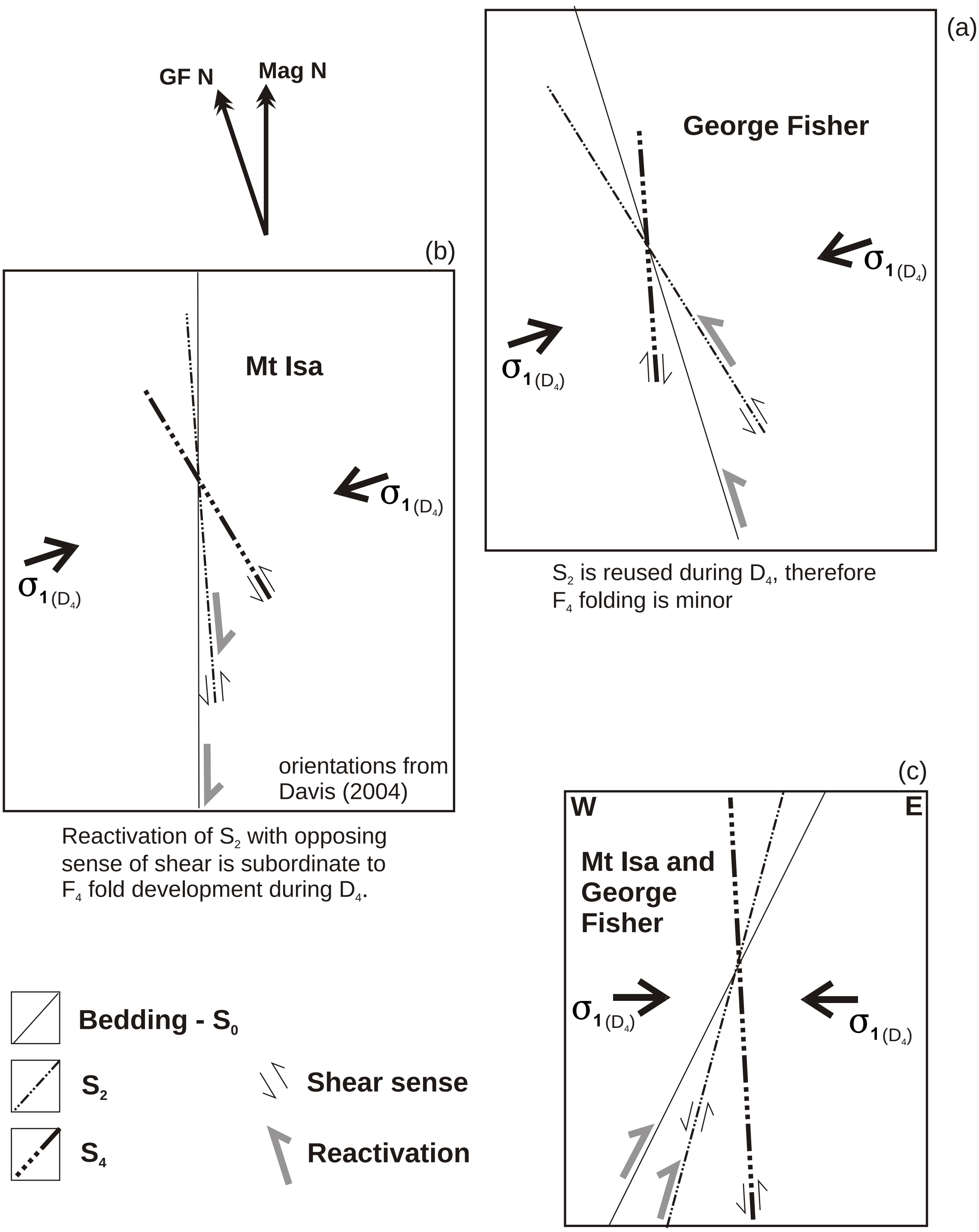

Figure 46. Schematic diagrams (plan view) of the geometric relationships of bedding (S_0), S_2 and S_4 at the (a) George Fisher Mine and (b) Mt Isa Mine. The change in asymmetry results in opposite sense of shear on S_0 and S_2 during D_4 reactivation between the George Fisher and Mt Isa deposits. The result may include reuse of S_2 at George Fisher during D_4. D_4 reactivation of S_2 at the Mt Isa Mine has opposing shear sense to that of S_2 and S_4 is at a higher angle to S_0 than at George Fisher. S_4 development and associated F_4 fold formation proceed to a greater intensity than observed at George Fisher. (c) In vertical section, D_4 causes west-side-up reactivation on bedding and S_2 at both George Fisher and Mt Isa.

S_4 is sub-parallel to the margin of the Sybella Batholith and the main F_4 fold mapped has a northeast strike. The S_2/S_4 asymmetry observed by Bell and Hickey (1998) is consistent with that observed at George Fisher (S_2 strikes NNW and S_4 strikes NNE). The opposite relationship is observed at Mt Isa where S_2 strikes N and S_4 strikes NNW. Also, a significant F_4 fold situated approximately 15 km southwest of Mt Isa (see Figure 3) has a NNE striking axial plane (Connors and Page, 1995; Bell and Hickey, 1998) which is different from the NNW trending Mt Isa Fold and subsidiary F_4 folds at the Mt Isa Mine (Davis, 2004). The variation in the orientation of the S_4/F_4 structures suggests that the geometry of the Sybella Batholith influenced the orientation of later formed D_4 deformation features in close proximity to the contact, whereas the regionally pervasive S_2/F_2 features maintain consistent orientation (Figure 44). The buttressing effect of the Sybella Batholith and its relationship to D_4 features on a local scale has previously been suggested by Bell and Hickey (1998). The swap in the geometric relationship of S_0, S_2, and S_4 between George Fisher and Mt Isa (Figure 46) may indicate why F_4 folding is only minor at George Fisher yet F_4 are the dominant fold type at Mt Isa (Davis, 2004). In the absence of the effects of D_3 strain, S_2 is reused at George Fisher during D_4 (Figure 46). At the Mt Isa Mine, S_4 is at a high angle to bedding and D_4 would cause dextral reactivation of S_2 opposing the dominant sinistral shear that occurred during D_2. S_4 and associated F_4 folds are likely to have developed under these conditions at Mt Isa (Figure 46). Note that the reactivation of both bedding and S_2 are in opposing directions between Mt Isa and George Fisher (Figure 46).

5.2 *Discrete episodic foliation development vs conjugate crenulations*

The S_3 and S_4 crenulations observed at George Fisher have opposing sense of shear and generally intersect at an angle of 50º to 90º. The geometrical relationship of these crenulations needs to be discussed in terms of conjugate crenulation development. Tewksbury (1986) interpreted conjugate crenulations and folds in Precambrian rocks of the Needle Mountains in Colorado, USA. In photomicrograph (fig 5c, Tewksbury, 1986), the crenulations are differentiated, intersect at angles of 30º to 50º, and have opposing sense of shear. At points of cross-cutting crenulations, displacement is negligible despite significant rotation of an early slaty cleavage. Hobbs, Means, and Williams (1976) state that conjugate cleavage development is most likely to occur where an early well-developed cleavage or schistosity is overprinted. The pre-existing schistosity will be oriented such that it bisects the angle between the overprinting crenulation cleavages. Cosgrove (1976) investigated the development of conjugate kink and crenulation structures in materials of varying anisotropy and at different angles to the direction of shortening. Conjugate geometries develop in materials with moderate to high anisotropy where the direction of shortening is either parallel or normal to the pre-existing schistosity (Cosgrove, 1976). This is the case with the crenulations in Tewksbury (1986) and in the sample from George Fisher displayed in Figure 35. In this 2-dimensional image S_2 is sub-parallel to S_0, but the 3-dimensional orientations of S_2, S_3, and S_4 are such that S_2 is not the bisector of these crenulations (compare Figures 12, 22, and 30). Steeply-dipping S_4 crenulations overprint and displace gently dipping S_3 crenulations at George Fisher and unfolding of the earlier S_3 crenulation has also been observed (Figure 29). This indicates that the crenulations are not contemporaneous conjugates. Also, fold geometries associated with conjugate crenulations and conjugate folding are characteristically box or anvil-shaped (Tewksbury, 1986; Tobisch and Fiske, 1976). Both F_3 (Figure 15) and F_4 (Figure 35) folds have regular fold geometry and F_4 folds refold F_3 folds and F_2 folds rotated/flattened during D_3. The S_3 and S_4 foliations are therefore interpreted to have formed at different times and are the result of episodic crenulation development.

5.3 Origin and significance of D_3 structures

Having interpreted the S_3 and S_4 crenulations as non-conjugate, the near orthogonal geometry of the foliations must be addressed. The gently dipping S_3 crenulation (Figure 21) and F_3 folds with sub-horizontal axial planes (Figure 15) at George Fisher indicate formation under conditions of sub-vertical shortening and sub-horizontal extension. This sub-horizontal extension is recorded in the L_3^3 extension direction (perpendicular to the axial planes of F_2 folds, see Figures 22 and 12), flattening and rotation of bedding, S_2, and F_2 folds with a top-to-the-east sense of shear, and growth of sub-horizontal quartz fibres in S_2-parallel veins (Figure 16; Valenta, 1989). Rotation of F_2 folds to inclined to recumbent attitudes could be interpreted as the result of non-coaxial simple shear during west over east thrusting (Figure 47a). However, the district-scale folds in the Leichardt River Fault Trough to the east of George Fisher have sub-vertical axial planes (Valenta, 1988, 1994) and the S_2 cleavage is sub-vertical in the Lake Moondarra area (Winsor, 1986) thereby suggesting that formation of F_2 folds did not include a component of top-to-the-east shear and the rotated F_2 geometries observed at George Fisher are not observed at larger scales. Extension parallel to the regional direction of shortening is problematic and implies that either localized heterogeneous strain development has

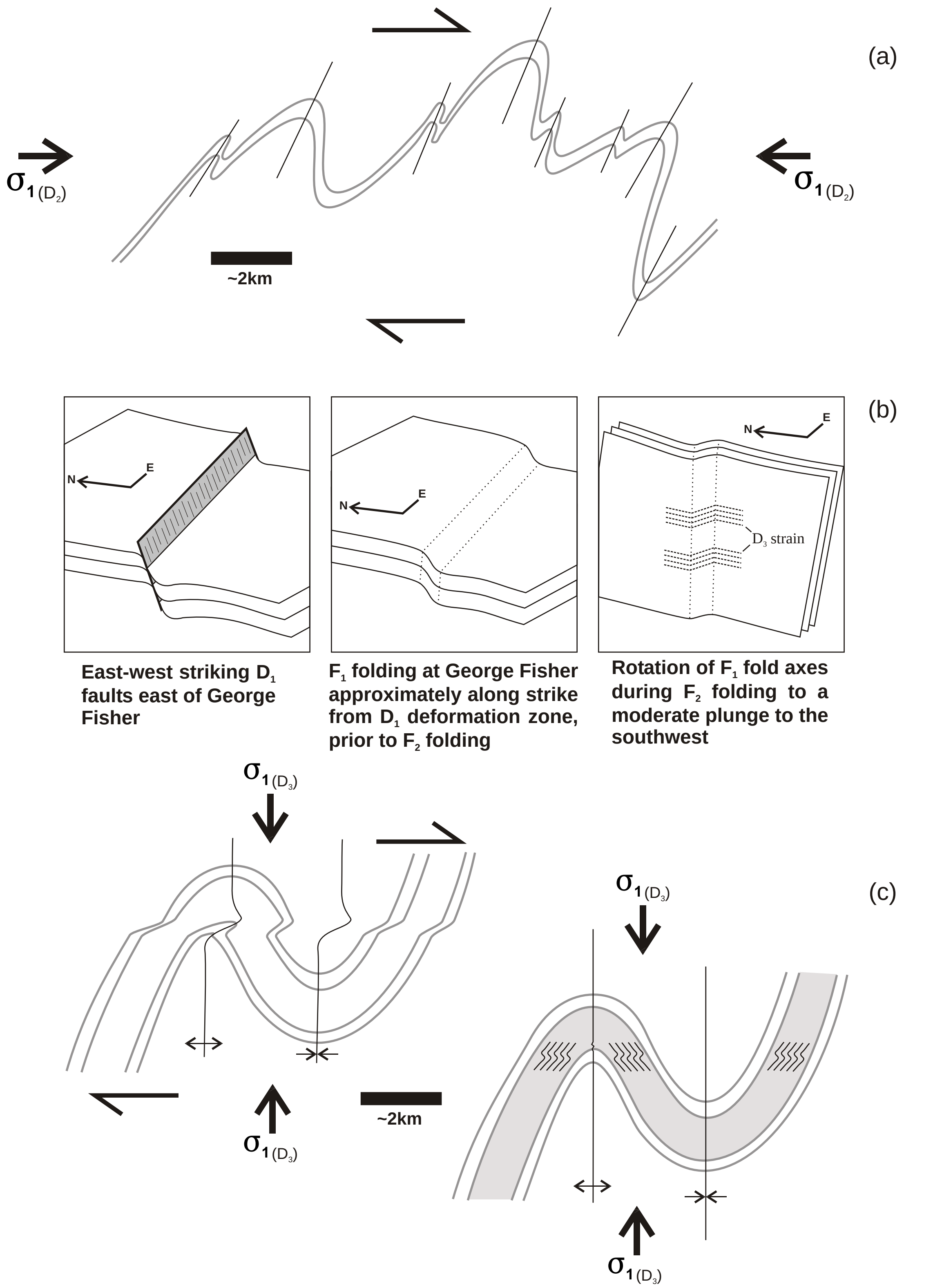

Figure 47. Possible explanations for observed D_3 deformation features. (a) Non-coaxial simple shear during D_2, (b) heterogeneous strain development in the F_1 short-limb during D_2 folding, and (c) Subvertical shortening. Note that the left hand diagram illustrates a component of simple shear whereas the right hand diagram represents coaxial deformation preferentially accommodated by a weaker sedimentary unit (grey).

occurred during D_2, or a discrete deformation phase has occurred after regional D_2 deformation.

Folding of the F_1 fold from a pre-D_2 orientation where fold axes are inferred to have been approximately horizontal and east-west trending, to the current F_1 axis orientation of 50° to the south-southwest occurred during D_2 (Figure 47b). Development of domainal S_3 strain was subsequently focussed into the F_1 short-limb zone due to the heterogeneity of the flexure in bedding. This may have occurred due to the s-shaped F_1 fold acting as a restraining bend to bedding reactivation during D_2. However, S_3 crenulations overprint S_2 cleavage and F_2 folds are rotated in zones of D_3 strain indicating that D_3 is distinct from the D_2 episode and is not heterogeneous development of localized strain during the district-scale folding. Alternatively, D_3 deformation represents an episode of sub-horizontal shortening with a component of top-to-the-east shear immediately following and in part overlapping with macroscale F_2 fold development (Figure 47c).

The D_3 deformation at George Fisher is interpreted as a period of vertical shortening/east-west extension late in D_2 or subsequent to D_2 folding. While Valenta (1989) suggested that S_2 parallel veins opened parallel to the direction of shortening due to fluid overpressuring, this model does not account for the gently dipping S_3 crenulations or rotation of F_2 folds (Valenta, 1994). The Western Fold Belt and its constituent terranes has been a locus of repeated episodes of intra-cratonic crustal extension which have resulted in basin formation due to rifting and thermal subsidence (sag) (Betts and Lister, 2002; O'Dea et al., 1997). These episodes both predate and include deposition of the host-rocks at George Fisher. Extension of this type was terminated by the onset of the

Isan Orogeny (Blake et al., 1990) which has been the focus of this paper. D_3 at George Fisher represents a minor phase of horizontal extension parallel to the direction of this orogenic shortening and intervening episodes of east-west shortening (D_2 and D_4). This weak deformation is implicated in the development of younger F_3 folds (F_4 – this study) and has been recognized in the George Fisher – Hilton region both east and west of the Mt Isa – Paroo Fault (Bell and Hickey, 1998). The formation of sub-horizontal folds and crenulations was interpreted as the result of episodic sub-vertical and sub-horizontal directed shortening during orogenesis (Bell and Hickey, 1998; Bell and Johnson, 1989). Gently-dipping folds and crenulation of older, steep foliations in the Eastern Goldfields Province of the Yilgarn Craton in Western Australia (Davis and Maidens, 2003) are interpreted as the result of vertically-directed contraction during an episode of gravitational collapse (Davis and Maidens, 2003). The D_3 features described at George Fisher can be interpreted as sub-vertical shortening immediately post-dating district-scale F_2 folding and are analogous to the features described by Bell and Hickey (1998) and Davis and Maidens (2003).

D_3 at George Fisher was a low strain deformation episode which resulted in subtle structures and overprinting of existing structures. Despite this, the D_3 deformation is significant in that it is a control on the distribution and intensity of D_4 deformation features. This is evident in Figures 28, 36, and 37 and where D_4 deformation is likely to have reactivated the S_2 cleavage and bedding except S_3 crenulation has created microscale heterogeneity which inhibited reactivation/reuse of the pre-existing fabrics. At the larger scale, rotation of F_2 folds facilitates F_4 development, though this folding event at George Fisher was very minor (Figure 35). The distribution and intensity of S_4 crenulation development is almost identical to that of S_3 (Figures 23 and 32). Apparent partitioning of D_3 strain into that part of the stratigraphy containing the C and D ore-horizons (Figure 23) may be due to subtle rheological contrast amongst the Urquhart Shale or spatial correlation with more abundant F_2 folding. A possible rheological control on the location and intensity of D_3 strain may result in preferential accommodation of the deformation in the Urquhart Shale relative to the adjacent Spear Siltstone and Native Bee Siltstone which both lack the degree of bedding and lithological heterogeneity observed in the Urquhart Shale.

6. Conclusions

The structural history of the host-rocks to base-metal mineralization at the George Fisher deposit involves the development of four fold and foliation generations and concomitant ductile shear zones progressing into a period of brittle faulting.

Predominantly east-west directed shortening during the Isan orogeny has resulted in the north-south structural grain of the Leichardt River Fault Trough. At George Fisher, this deformation is preserved as a dominant pervasive slaty foliation (S_2) and exposure-scale (0.1-5m amplitude) folding (F_2) in the deposit which is situated on the west limb of a district-scale F_2 fold. These D_2 features strike NNW and overprint a large but subtle flexure/open fold (F_1) central to the George Fisher deposit. S_1 is rarely preserved at George Fisher.

Subsequent to macroscale F_2 fold formation (1000m+ amplitude) a period of sub-vertical shortening / horizontal shortening resulted in the formation of gently dipping crenulations and folds with sub-horizontal axial planes. These folds have vergence opposite to that of F_2 and later F_4 folds. Non-coaxial strain during D_3 is evident in the consistent top-to-the-east shear on asymmetric S_3 crenulations and resultant rotation and flattening of earlier formed structures and bedding.

Rotation of vertical and west-dipping structures and bedding creates heterogeneity for development of sub-vertical D_4 deformation features. S_4 crenulations and F_4 folds are strongly partitioned on the mine-scale into the F_1 short-limb and pre-existing F_2 folds. Areas of more intense D_4 strain have been indicated. Significant F_4 folds occur elsewhere in the Leichardt River fault trough and their absence from the George Fisher area is interpreted to be due to preferential reactivation of S_0 and S_2 rather than initiation of new F_4 fold development.

The local geological setting is dominated by faulting of various orientations. The regionally significant Mt Isa – Paroo Fault System is located 200-300m west of the George Fisher deposit and comprises an intense fracture zone which encompasses the hangingwall stratigraphy of the Urquhart Shale. This fault has had a prolonged movement history and may have been active as early as D_1. NW striking sinistral faults are significant on the local scale, separating the George Fisher and Hilton ore deposits. These faults postdate the main phase (D_2) deformation. NE-striking faults with normal and dextral movement are most abundant and cause disruption of the ore-bearing sequence. These faults are at a high angle to bedding and the orebodies and create complexities in mining even though they dominantly only offset the orebodies in the order of five metres or less. This faulting post-dates D_4.

Structural observations are consistent over micro-, meso-, exposure-, and macroscales. The development of structural histories provides the necessary framework for development of predictive strategies in locating and defining structures of potential economic interest.

References

Bain, J.H.C., Heinrich, C.A., and Henderson, G.A.M., 1992, Stratigraphy, structure, and metamorphism of the Haslingden Group, east Moondarra area, Mount Isa: a deformed and mineralised Proterozoic multistage rift-sag sequence: Detailed studies of the Mount Isa Inlier – BMR Bulletin 243, p. 125-136.

Barber, D.J., Heard, H.C., and Wenk, H.R., 1981. Deformation of dolomite single crystals from 20-800°C: Physics and Chemistry of Minerals, v. 7, p. 271-286.

Bell, T.H., 1983, Thrusting and duplex formation at Mount Isa, Queensland, Australia: Nature, v. 304, No, 5926, p. 493-497.

Bell, T.H., 1986, Foliation development and refraction in metamorphic rocks: reactivation of earlier foliations and decrenulation due to shifting patterns of deformation partitioning: Journal of metamorphic Geology, v. 4, p. 421-444.

Bell, T.H., 1991, The role of thrusting in the structural development of the Mount Isa Mine and its relevance to exploration in the surrounding region: Economic Geology, v. 86, p. 1602-1625.

Bell, T.H. and Hickey, K.A., 1998, Multiple deformations with successive subvertical and subhorizontal axial planes in the Mount Isa region: Their impact on geometric development and significance for mineralization and exploration: Economic Geology, v. 93, p. 1369-1389.

Bell, T.H. and Johnson, S.E., 1989, Porphyroblast inclusion trails: the key to orogenesis: Journal of Metamorphig Geology, v. 7, p. 279-310.

Bell, T.H. and Rubenach, M.J., 1983, Sequential porphyroblast growth and crenulation cleavage development during progressive deformation: Tectonophysics, v. 92, p.

Betts, P.G. and Lister, G.S., 2002. Geodynamically indicated targeting strategy for shale-hosted massive sulfide Pb-Zn-Ag mineralisation in the Western Fold Belt, Mt Isa terrane: Australian Journal of Earth Sciences, v. 49, p. 985-1010.

171-194.

Betts, P.G., Lister, G.S., and O'Dea, M.G., 1998. Asymmetric extension of the middle Proterozoic lithosphere, Mount Isa terrane, Queensland, Australia: Tectonophysics, v. 296, p. 293-316.

Blake, D.H. and Stewart, A.J., 1992. Stratigraphic and tectonic framework, Mount Isa inlier: Australian Geological Survey Organization Bulletin 243, p. 1-11.

Blake, D.H., Etheridge, M.A., Page, R.W., Stewart, A.J., Williams, P.R., and Wyborn, L.A.I., 1990. Mount Isa Inlier – Regional Geology and mineralisation, In: Hughes, F.E. (ed.), Geology of the Mineral Deposits of Australia and Papua New Guinea, Australasian Institute of Mining and Metallurgy Monograph 14, p. 915-925.

Burkhard, M., 1993, Calcite twins, their geometry, appearance and significance as stress-strain markers and indicators of tectonic regime: a review: Journal of Structural Geology, V. 15, Nos 3-5, p. 351-368.

Chapman, L., 1999, Geology and genesis of the George Fisher Zn-Pb-Ag deposit, Mount Isa, Australia. (Unpublished PhD thesis – James Cook University, Townsville).

Chapman, L.H., 2004. Geology and mineralization styles of the George Fisher Zn-Pb-Ag deposit, Mount Isa, Australia: Economic Geology, v. 99, p. 233-255.

Connors, K.A. and Page, R.W., 1995, Relationships between magmatism, metamorphism and deformation in the western Mount Isa Inlier, Australia: Precambrian Research, v. 71, p. 131-153.

Cosgrove, J.W., 1976. The formation of crenulation cleavage: Journal of the Geological Society of London, v. 132, p. 155-178.

Davis, B.K. and Maidens, E., 2003. Archaean orogen-parallel extension: evidence from the northern Eastern Goldfields Province, Yilgarn Craton: Precambrian Research, v. 127, p. 229-248.

Davis, T.P., 2004. Mine-scale structural controls on the Mount Isa Zn-Pb-Ag and Cu orebodies: Economic Geology, v. 99, p. 543-559.

Gray, D.R., 1978. Cleavages in deformed psammitic rocks from southeastern Australia: Their nature and origin: Geological Society of America Bulletin, v. 89, p. 577-590.

Hobbs, B.E., Means, W.D. and Williams, P.F., 1976, An outline of structural geology: eds John Wiley and sons, 571p.

Kruhl, J.H. and Nega, M., 1996, The fractal shape of sutured quartz grain boundaries: application as a geothermometer: Geol. Rundsch, v. 85, p. 38-43.

Nijman, W., Mijnlieff, H.F., and Schalkwijk, G., 1992, The Hero Fan delta (Lower Mt Isa Group) and its structural control: deformation in the Hero/Western Fault Zone and Paroo Range compared, Proterozoic, Mount Isa Inlier, Queensland, Australia: Detailed studies of the Mount Isa Inlier – BMR Bulletin 243, p. 75-110.

Nijman, W., van Lochem, J.H., Spliethoff, H., and Feijth, J., 1992, Deformation model and sedimentation patterns of the Proterozoic of the Paroo Range, Mount Isa Inlier, Queensland Australia: Detailed studies of the Mount Isa Inlier – BMR Bulletin 243, p. 29-74.

O'Dea, M.G., Lister, G.S>, Betts, P.G>, and Pound, K.S., 1997a. A shortened intraplate rift system in the Proterozoic Mount Isa terrane, NW Queensland, Australia: Tectonics, v. 16, p. 425-441.

O'Dea, M.G., Lister, G.S., MacCready, T., Betts, P.G., Oliver, N.H.S., Pound, K.S., Huang, W., and Valenta, R.K., 1997b. Geodynamic evolution of the Proterozoic Mount Isa terrain, In: Burg, J.-P. and Ford, M. (eds), Orogeny Through Time. Geological Society Special Publication No. 121, p. 99-122.

Page, R.W. and Bell, T.H., 1986, Isotopic and structural responses of granite to successive deformation and metamorphism: Journal of Geology, v. 94, p. 365-379.

Page, R.W., Jackson, M.J., and Krassay, A.A., 2000, Constraining sequence stratigraphy in north Australian basins: SHRIMP U-Pb zircon geochronology between Mt Isa and McArhur River: Australian Journal of Earth Sciences, v. 47, p. 431-459.

Rowe, K.J. and Rutter, E.H., 1990, Paeaeostress estimation using calcite twinning: experimental calibration and application to nature: Journal of Structural Geology, v. 12, No. 1, p. 1-17.

Rubenach, M.J., 1992. Proterozoic low-pressure/high-temperature metamorphism and an anticlockwise P-T-t path for the Hazeldene area, Mount Isa inlier, Queensland, Australia: Journal of Metamorphic Geology, v. 10, p. 333-346.

Southgate, P.N., Bradshaw, B.E., Domagala, J., Jackson, M.J., Idnurm, M., Krassay, A.A., Page, R.W., Sami, T.T., Scott, D.L., Lindsay, J.F., McConachie, B.A., and Tarlowski, C., 2000. Chronostratigraphic basin framework for Palaeoproterozoic rocks (1730-1575Ma) in northern Australia and implications for base-metal mineralisation: Australian Journal of Earth Sciences, v. 47, p. 461-483.

Stewart, A.J., 1992, Geology of the Horse's Head structure, north of Mount Isa, and its bearing on the 'roof thrust + imbricate stack' hypothesis, Mount Isa Inlier, Queensland: Detailed studies of the Mount Isa Inlier – BMR Bulletin 243, p. 111-124.

Swager, C.P., 1983. Microstructural development of the silica-dolomite and copper mineralization at Mount Isa, NW-Queensland, with special emphasis on the timing and mechanism of mineralization. Unpublished PhD thesis – James Cook University, Townsville. 258p.

Tewksbury, B.J., 1986, Conjugate crenulation cleavages in the Uncompahgre Formation, Needle Mountains, Colorado: Journal of Structural Geology, v. 8, No. 2, p. 145-155.

Tobisch, O.T. and Fiske, R.S., 1976, Significance of conjugate folds and crenulations in the central Sierra Nevada, California: Geological Society of America Bulletin, v. 87, p. 1411-1420.

Tolman, J., Shaw, A., and Shannon, K., 2002, Stratigraphic relationships between stratiform polymetallic base metal deposits within the Mount Isa Inlier, NW Queensland, Australia: Australasian Institue of Mining and Metallurgy Conference Proceedings Volume 6/00.

Valenta, R.K., 1988, Deformation, fluid flow and mineralisation in the Hilton area, Mt Isa, Australia. (Unpublished PhD thesis – Monash University. Melbourne).

Valenta, R.K., 1989. Vein geometry in the Hilton area, Mount Isa, Queensland: implications for fluid behaviour during deformation: Tectonophysics, v. 158, p. 191-207.

Valenta, R.K., 1994, Deformation in the host rocks and stratiform mineralization in the Hilton Mine area, Mt Isa: Australian Journal of Earth Sciences, v. 41, p. 429-443.

Wenk, H.-R., 1985. Carbonates. In: H.-R. Wenk (ed), Preferred orientation in deformed metals and rocks: An introduction to modern texture analysis, p. 361-384.

Williams, P.J., 1998, Metallogeny of the McArthur River – Mount Isa – Cloncurry Minerals Province: Economic Geology, v. 93, p. 1119-1131.

Winsor, C.N., 1982. The structural geology of the Lake Moondarra area, Mount Isa, Australia, with particular reference to the relationship between folding and faulting: Unpublished PhD thesis, James Cook University, Townsville, Australia, 149 p.

Winsor, C.N., 1983, Syntectonic vein and fibre growth associated with multiple slaty cleavage development in the Lake Moondarra area, Mount Isa, Australia: Tectonophysics, v. 92, p. 195-210.

Winsor, C.N., 1986, Intermittent folding and faulting in the Lake Moondarra area, Mount Isa, Queensland: Australian Journal of Earth Sciences, v. 33, p. 27-42.

Wyborn, L.A.I., Page, R.W. and McCulloch, M.T., 1988, Petrology, geochronology, and isotope geochemistry of the post-1820 Ma granites of the Mount Isa Inlier: mechanisms for the generation of proterozoic anorogenic granites: Precambrian Research, v. 40/41, p. 509-541.

Xu, G., 1996, Structural geology of the Dugald River Zn-Pb-Ag deposit, Mount Isa Inlier, Australia: Ore Geology Reviews, v. 11, p. 339-361.

.

PART B

Distribution of Zn-Pb-Ag mineralization and its relationship to structural domains at the George Fisher Mine, Northwest Queensland, Australia.

Abstract

Shoots comprised of thicker, high-grade mineralization are recognized in the analysis of Zn, Pb, and Ag grades of C, D, and G ore-horizons, in north-south longitudinal projections at George Fisher. These shoots correlate with the location and orientation of structures described in Part A. The F_1 short-limb appears to be the site of preferential Zn-Pb-Ag mineralization and the main shoot is located in this area and plunges parallel to the F_1 fold axes. Subsidiary ore shoots are parallel to F_2 and F_4 fold axes. The obliquity of the S_4 foliation to bedding and the associated intensity of the S_3 and S_4 foliations also correlate with areas of higher-grade, such that the intersection of structures of different ages is inferred to be a control on the location and orientation of ore shoots. The kinematics associated with each deformation phase are interpreted and maximum dilatancy and potential for fluid flow in the F_1 short-limb is achieved during D_4 as the D_4 stress field orientation is appropriate for sinistral-reverse reactivation of bedding in the F_1 short-limb. Sulphide mineralization is interpreted to have occurred at least partly during D_4 based on empirical geometric relationships between sulphide distribution and structural features. The location of other structures with similar geometry within the prospective Urquhart Shale is considered important for locating any further high-grade Zn-Pb-Ag ore.

1. Introduction

At George Fisher, mineralization occurs as stratiform (*having the form of strata*) and stratabound (*restricted to a stratigraphic package*) sphalerite accumulations and stratiform galena occurrences that are locally discordant to bedding. Stratabound ore lenses have economic limits up and down-dip and have restricted along strike extent (Figure 1). They are therefore isolated occurrences of sulphides within a laterally continuous stratigraphic horizon and barren equivalents of the mineralized sequence occur along strike from the deposit (Figure 1). The Hilton mine stratigraphy and ore positions can be correlated with that of George Fisher (Chapman, 2004) although rare transgression of stratigraphic markers (tuffaceous beds) by mineralization between the two deposits has been identified (Allen Shaw - pers. comm., 2001). The Mt Isa Pb-Zn deposit is also hosted by stratigraphy of similar age (Domagala et al., 2000; Chapman, 2004) and is situated at a similar level below surface as the Hilton and George Fisher deposits despite district-scale north-plunging folding. Controls on localization of the George Fisher deposit within the 30km strike continuation of the Urquhart shales north from the Mt Isa mine, have not previously been determined. Elucidation of these larger scale controls would be of significant advantage in exploration for further George Fisher style Zn-Pb-Ag mineralization as it could add a predictive component to the empirical process of exploration which currently employs stratigraphic, geophysical, and geochemical methods.

In Part A, the structure of the host rocks to mineralization was discussed and their deformation history established. This paper assesses the geometry of orebodies and their location relative to structures described in Part A in order to determine whether a

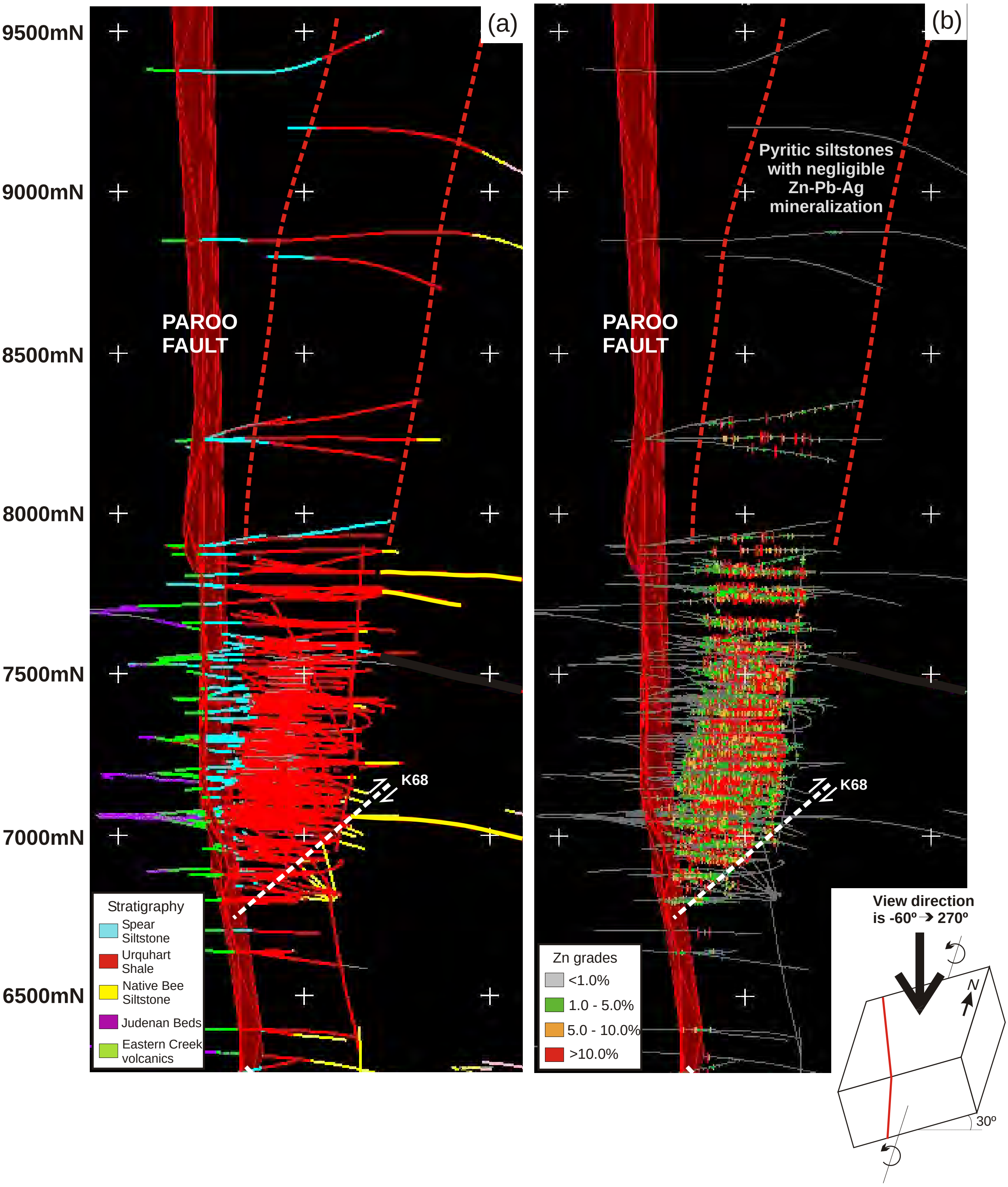

Figure 1. Rotated plan views (see inset) of the Paroo Fault and George Fisher drill-holes displaying (a) stratigraphic unit and (b) Zn assay data looking down the intersection of the Paroo Fault and Urquhart shale. The Urquhart Shale is continuous to the NNE in (a) however, Zn grades diminish considerably in more widely spaced drilling to the north of the deposit. The K68 fault (white dashed line) forms the southern boundary to mineralization at George Fisher and has offset the mineralized stratigraphy to the west, on the southern side of the fault.

relationship exists. Incorporated in this study is an analysis of metal distribution, assessment of the geostatistical distribution of grades in order to determine whether more than one population exists, and integration of the observed ore shoot geometries and orientations within a kinematic framework utilizing the work in Part A.

The relationship of metal distribution to structure has been studied at Mt Isa where high-grade shoots and the boundary to economic Pb-Zn mineralization are interpreted to be parallel to F_4 fold axes and the location of the deposit is apparently controlled by larger scale structure (Perkins, 1997; Davis, 2004). At George Fisher, metal ratios for the respective ore-horizons were studied (Chapman, 1999) showing an increase in the Zn/Pb ratio from west to east across the deposit. However this method of analysis did not reveal the geometry of high-grade ore shoots.

2. Metal Distribution

2.1 Methods for analyzing metal grade distributions

The distribution of higher grade material was analyzed by determining the average grade over the full width of drill-hole intersections through each ore horizon of interest. The metal distribution at George Fisher has been assessed using longitudinal projection of the average grade of intersections for the three main C, D, and, G ore-horizons. The average grade of intersections has been calculated by compositing the intersection assays in the Minesight software package. The intercept points are then viewed on a North-South vertical section such that all intersections in a given ore-horizon can be displayed on a single diagram (Figure 2a). Contours on longitudinal projections in this study have been manually drawn.

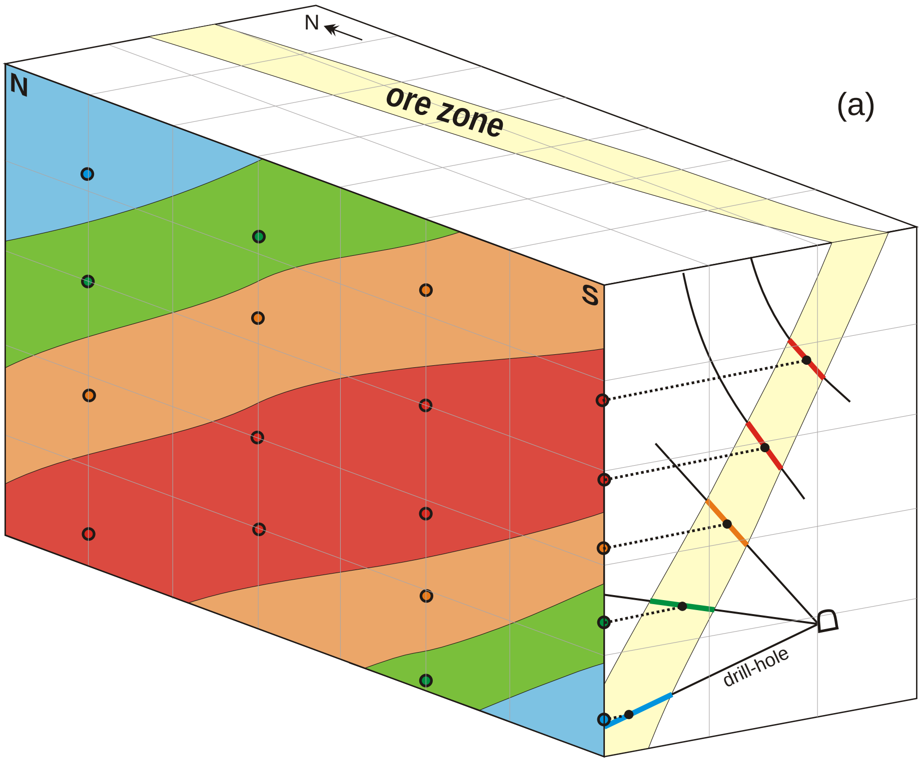

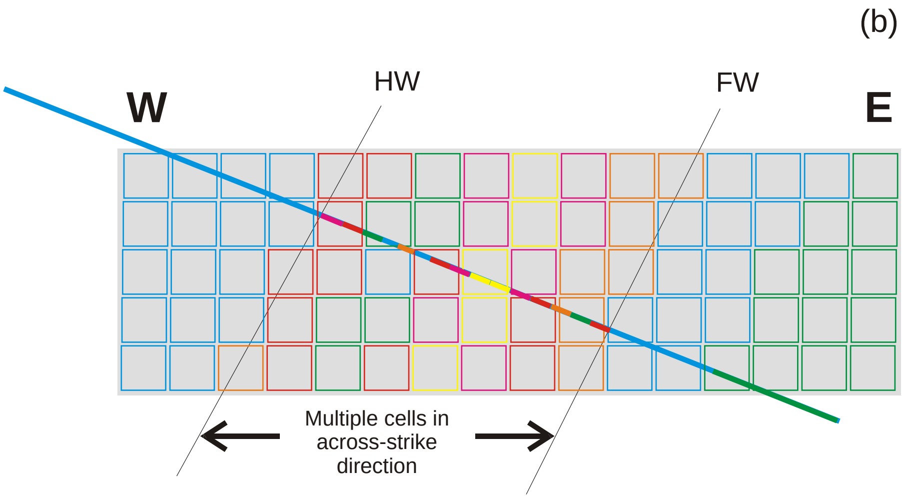

Figure 2. (a) Schematic diagram illustrating construction of a longitudinal projection for use in defining ore-shoot location and geometry. Average grade of drill-hole intercepts are projected onto a vertical north-south plane from which contouring of all intersections in the ore zone can be constructed. (b) Schematic diagram of a block model with cell colour representing a specific grade range. Grades have been interpolated up/down-dip of the intersection in this example. The drill-hole is coloured with the same hypothetical grade ranges. An average of the estimated grades of the cells in the across-strike direction is required to construct a longitudinal projection from the block model as opposed to a weighted average of the actual assay grades in (a).

Grade contours in plan and section view have been constructed from a block model created by George Fisher Mine personnel. Block models consist of a network of three-dimensional cells which are assigned a grade (and other variables such as rock type, specific gravity, RQD) (Figure 2b) based on their proximity to drill-hole intersections and interpolation of grades within specific parameters including search ellipse and search distance derived from geostatistical analysis. A block model can be constructed from cells constrained within three-dimensional solids or wireframes (as at George Fisher) or unconstrained cells where there are no hard boundaries for grade interpolation. The block model used in this study (GF0115.028 – March, 2002) consists of individual wireframes for the respective ore-domains (defined by stratigraphic markers, Figure 3) which prevent erroneous interpolation of grades across stratigraphy. The block model can be interrogated in plan and section view and provides more automated smoothed grade contours for assays in drill-hole intersections. The block model, however, cannot readily produce longitudinal projections due to the requirement for multiple cells in the across-strike direction (Figure 2b). An average grade of the cells across the ore zone (Figure 2b) would be required to produce a longitudinal projection as in Figure 2a.

The stratabound nature of mineralization at George Fisher (Valenta, 1988; Chapman, 1999, 2004) requires grade distribution to be analyzed in particular stratigraphic horizons (Figure 3) separately. The stratigraphy at George Fisher dips moderately to the west and strikes approximately north-south on the local mine-grid (Mine Nth is 342° Mag.). The stratigraphy is divided into ‘ore-horizons’ that comprise siltstones and pyritic-siltstones (Figure 3) which host mineralization (Part A – Figure 6). Intervening stratigraphy consists of barren massive mudstones (Figure 3). Cross-sections, plans, and longitudinal

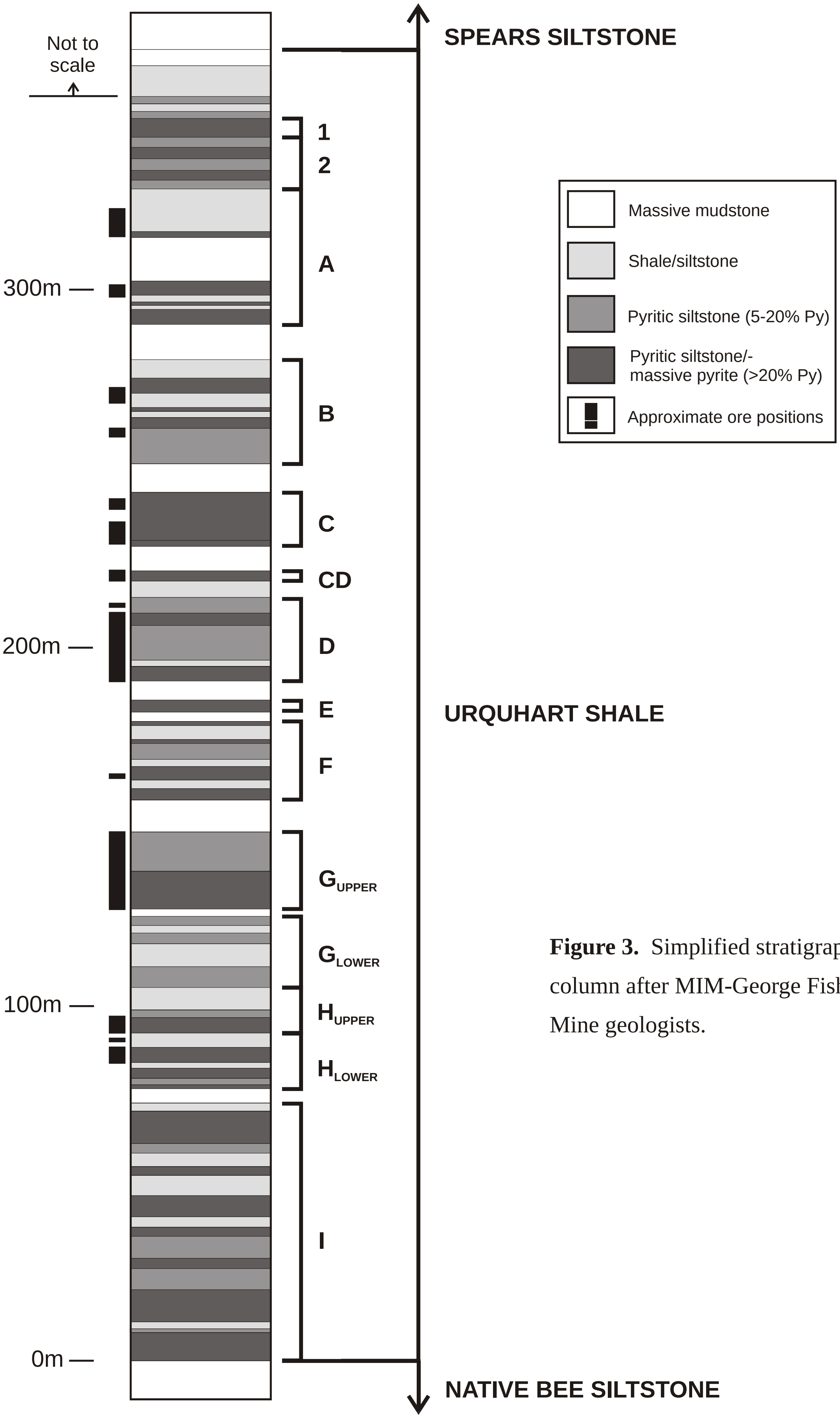

Figure 3. Simplified stratigraphic column after MIM-George Fisher Mine geologists.

projections in this study are annotated with the respective ore-horizon nomenclature as summarized on Figure 3.

2.2 Deposit-wide correlations between metal grades and structure in plan and section

The mine-scale distribution of Zn, Pb, and Ag metal grades at George Fisher are represented in cross-sections (Figures 4-6) and plans (Figures 7-9). The contours in each diagram have been constructed from the mine block-model (GF0115.028 – March, 2002). Stratigraphic control is applied to the block-modelling process and this results in a concordance between the contoured grades in Figures 4-9 and the orientation of stratigraphy.

Wider zones of higher Zn grades correlate with more gently dipping stratigraphy in the central part of the deposit (Figure 4). Mineralization containing >20% Zn is restricted to the more gently dipping host rocks. At the northern and southern ends of the deposit, stratigraphy dips more steeply and the width of higher grade Zn mineralization diminishes. Particularly high Zn grades (>12%) occur in the gently dipping strata on 7200mN in the C ore-horizon.

Higher Pb grades (>4% Pb), when viewed in west-east sections (Figure 5), display a more restricted distribution than Zn. However, as with Zn, higher Pb grades are preferentially concentrated in the more gently-dipping stratigraphy in the central part of the deposit (Figure 5 – 7200 and 7400mN sections). Widths of higher Pb grades are also greatest in this part of the deposit and narrow significantly towards the south (7000mN) and north

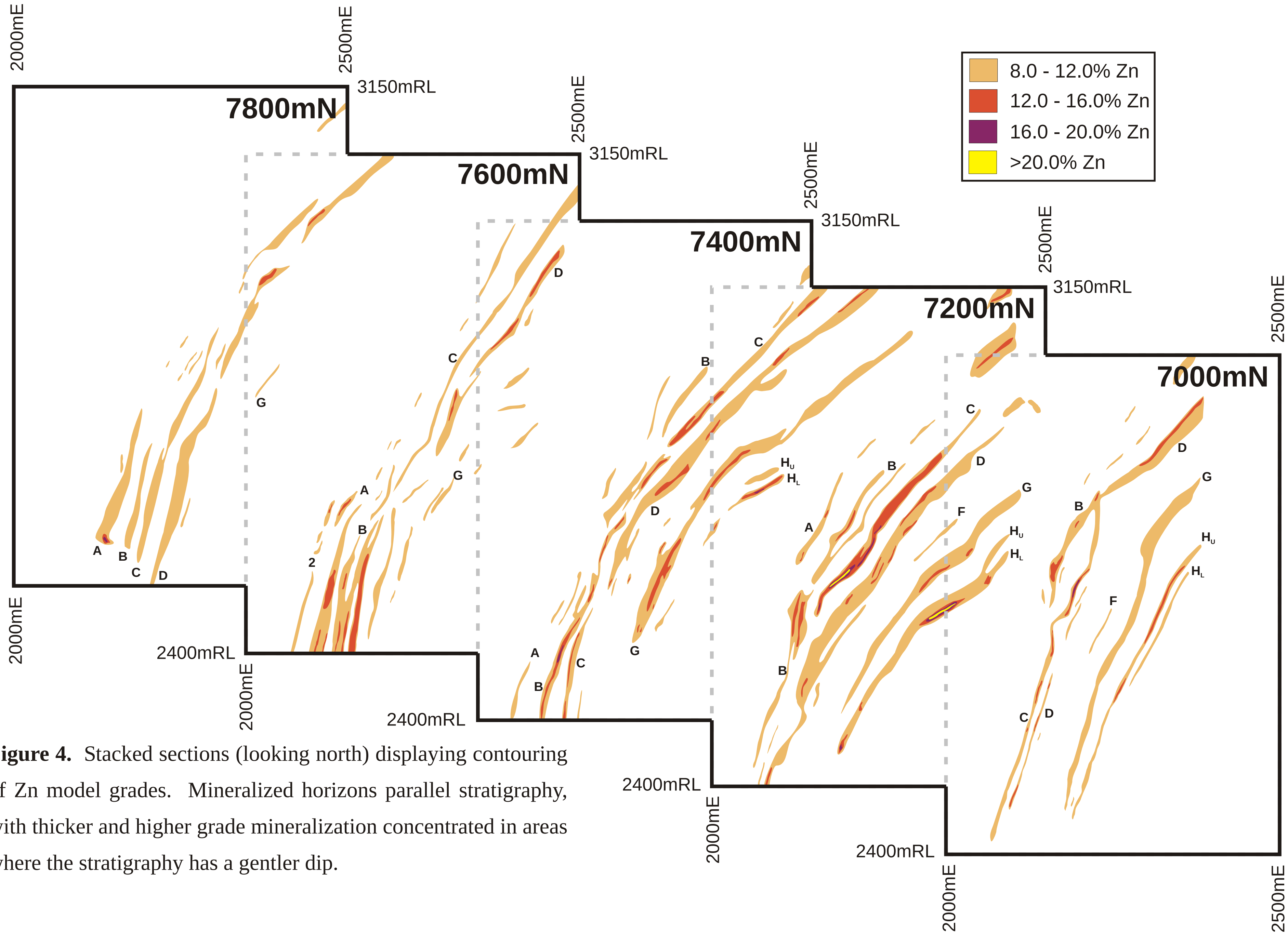

Figure 4. Stacked sections (looking north) displaying contouring of Zn model grades. Mineralized horizons parallel stratigraphy, with thicker and higher grade mineralization concentrated in areas where the stratigraphy has a gentler dip.

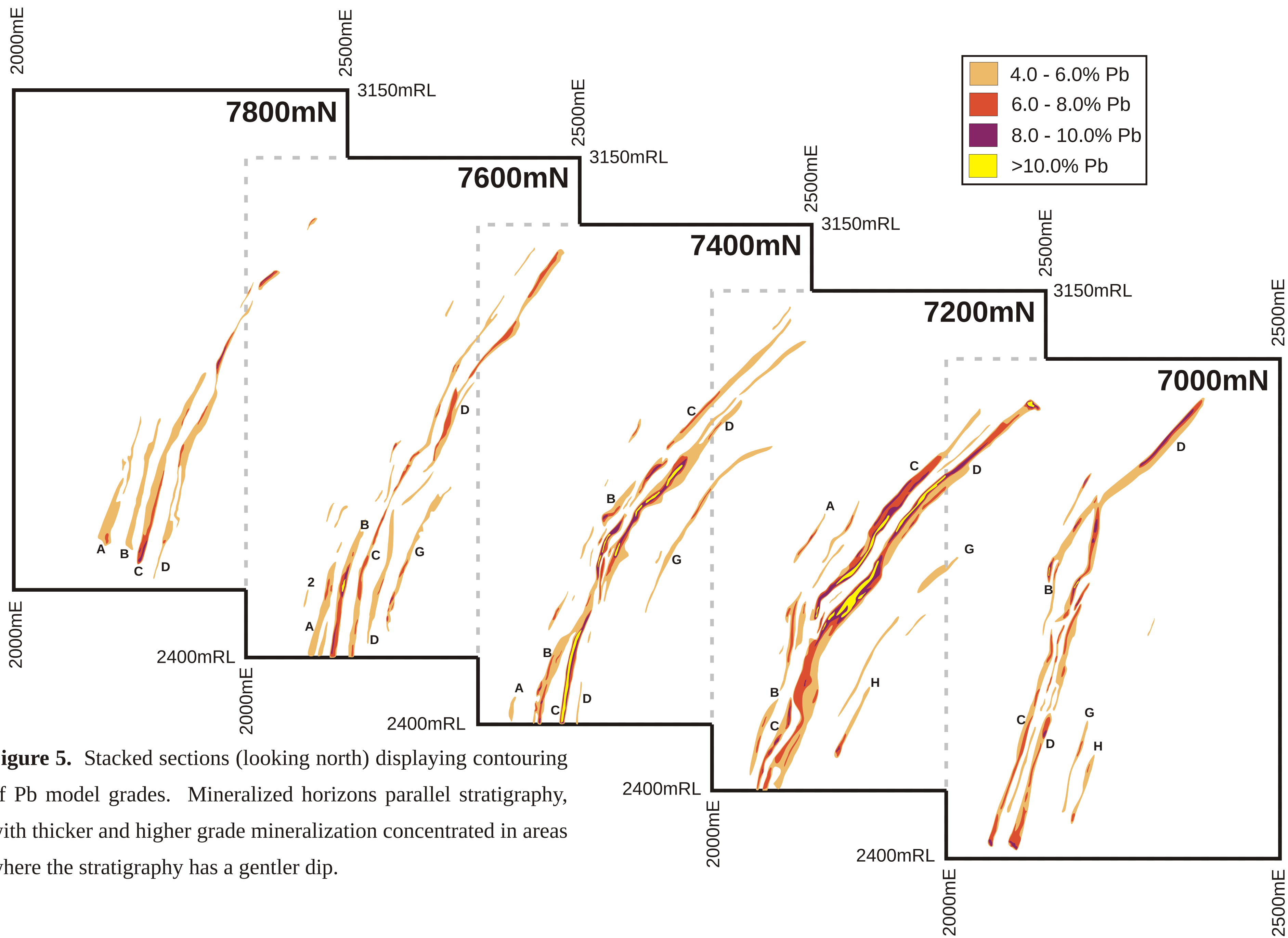

Figure 5. Stacked sections (looking north) displaying contouring of Pb model grades. Mineralized horizons parallel stratigraphy, with thicker and higher grade mineralization concentrated in areas where the stratigraphy has a gentler dip.

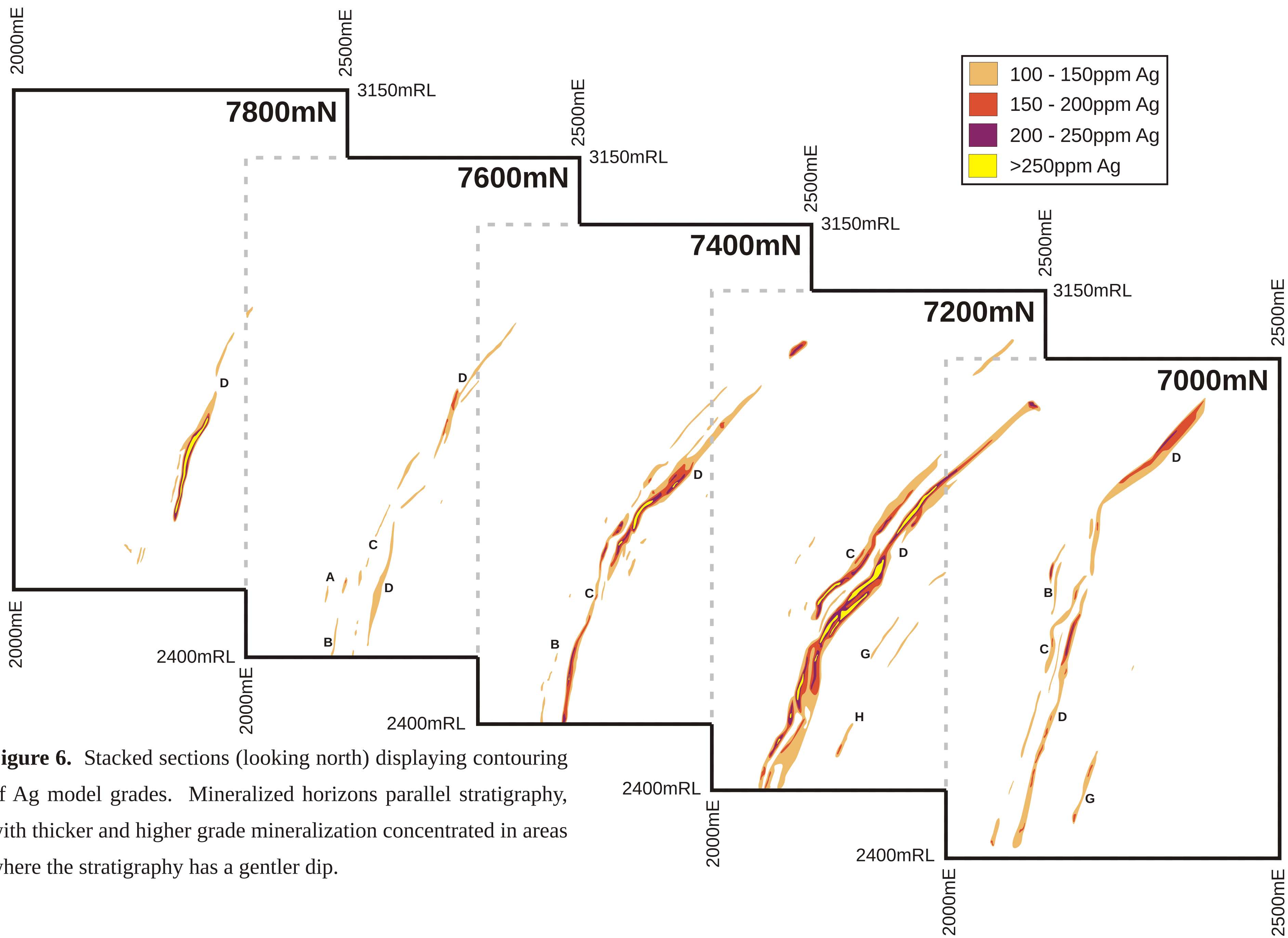

Figure 6. Stacked sections (looking north) displaying contouring of Ag model grades. Mineralized horizons parallel stratigraphy, with thicker and higher grade mineralization concentrated in areas where the stratigraphy has a gentler dip.

(7600 and 7800mN) where the dip of stratigraphy increases. Grade continuity in the central sections is greater than the northern and southern sections where the higher grade zones break-up and are less-continuous (Figure 5).

Higher Ag grades show the most restricted distribution (Figure 6). As with Zn and Pb, the widest zones of higher Ag grades (>200ppm Ag) are located within the more gently-dipping stratigraphy in the central part of the deposit. On section 7800mN, high Ag grades also occur in steeply dipping strata. This is not consistent with trends in Pb or Zn grades in this region and may represent isolated native Ag occurrences. Thickness and continuity of high-grade Ag ore is greatest in the central region of the deposit at 7200mN.

Wider zones and higher Zn, Pb, and Ag grades are preferentially hosted by the more gently-dipping stratigraphy in the central part of the mine. This location coincides with the short-limb of a deposit-scale F_1 fold between approximately 7150mN and 7350mN (Part A – Figure 8). More gently-dipping stratigraphy (~45°) is confined to the short-limb of the F_1 fold while more steeply dipping bedding occurs on the longer northern and southern limbs (~60 and 75° respectively).

Similar relationships are observed in plan view (Figures 7-9). Higher Zn grades (>8%) (Figure 7), form wider zones in the F_1 short-limb and higher Zn grades within C and H ore-horizons are largely restricted to the F_1 short-limb zone. Continuity of the higher Zn grades is highest within the short-limb area for all ore-horizons. As recognized in the sectional views, higher Pb grades are more restricted than higher Zn grades. There is a clear decrease in the grade of Pb mineralization within ore-horizons with increase in

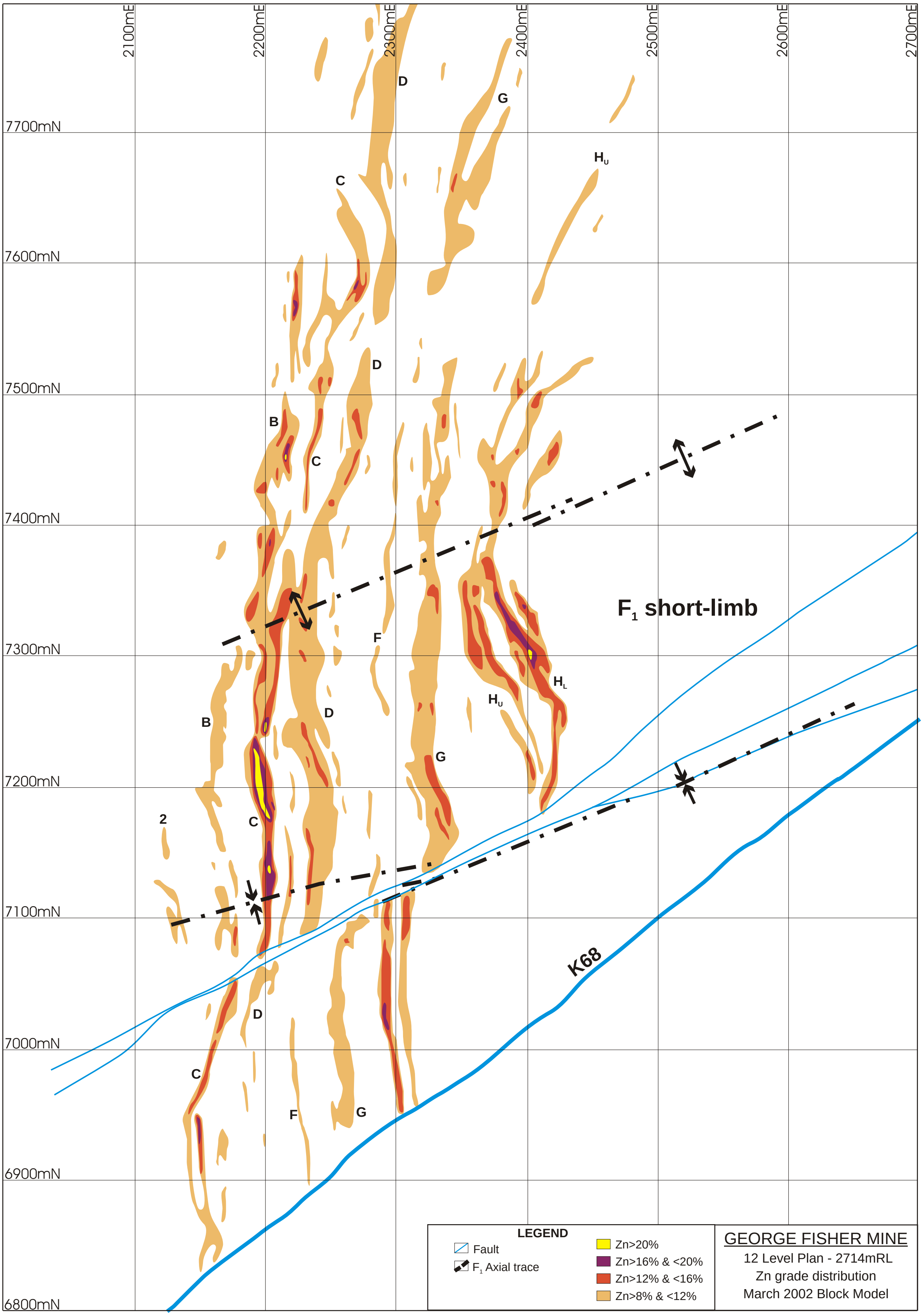

Figure 7. Zn grade distribution - 12 Level (2714mRL). Higher Zn grades are concentrated in the F_1 short-limb where stratigraphy strikes NNW rather then N.

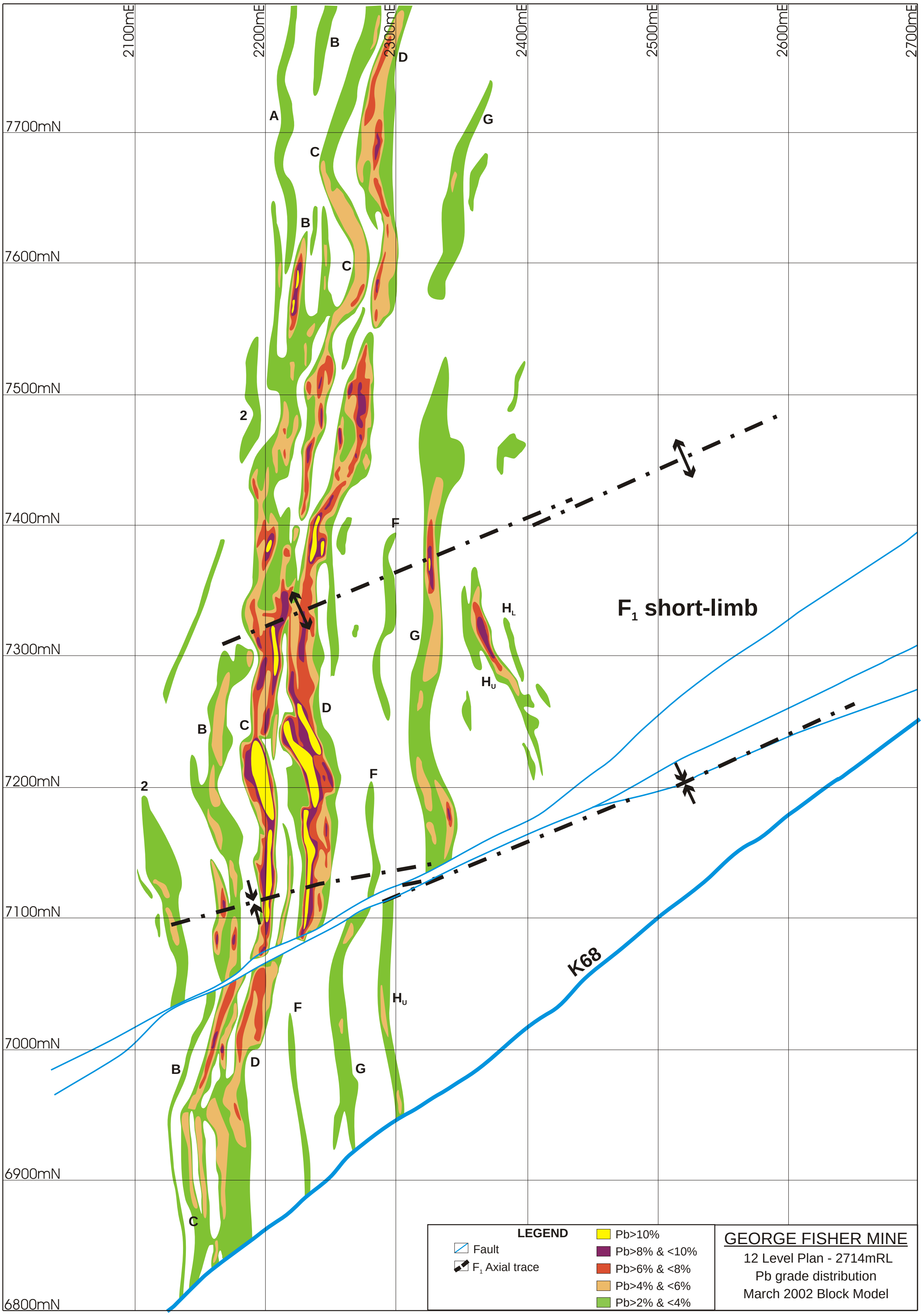

Figure 8. Pb grade distribution - 12 Level (2714mRL). Higher Zn grades are concentrated in the F_1 short-limb where stratigraphy strikes NNW rather then N.

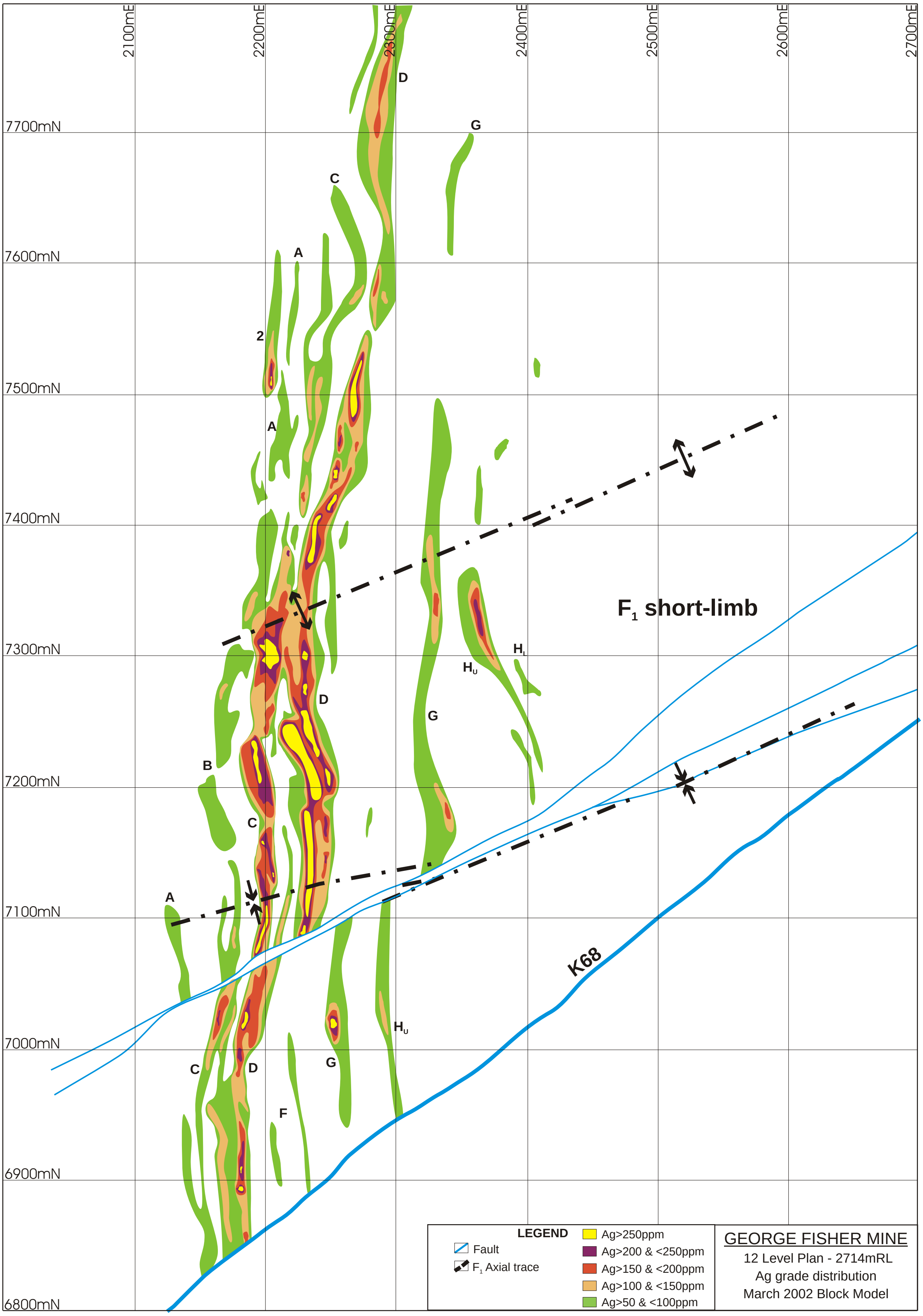

Figure 9. Ag grade distribution - 12 Level (2714mRL). Higher Zn grades are concentrated in the F_1 short-limb where stratigraphy strikes NNW rather then N.

northing, as recognized in sectional view (Figure 5). As with Zn grades, higher Pb grades are widest and display the maximum continuity in the F_1 short-limb (Figure 8), and therefore the distribution of higher Pb grades suggests preferential mineralization within the F_1 short-limb (Figure 8). Ag distribution (Figure 9) shows the most restricted distribution with >250ppm Ag ore almost exclusively localized in the F_1 short-limb.

2.3 Distribution of metal ratios

Whereas high Zn grades (>8%) occur throughout the prospective stratigraphy, high-grade Pb and Ag mineralization are restricted to the hangingwall part of the sequence and in particular, C and D ore-horizons (Figures 4-6). This produces an apparent metal zonation across the deposit from a Zn-rich footwall to a Pb-rich hangingwall, a feature previously recognized by Chapman (1999) who analyzed spatial trends in metal ratios. This study has analysed the distribution of different metal grades, as opposed to metal ratios, in order to determine whether deposit-scale higher-grade shoots are present. Recognition of the correlation between higher-grade ore and the position of the F_1 short-limb is not possible using analysis of metal ratios in longitudinal projection as the metal ratios do not change across the fold (fig. 18a [Part B] – Chapman, 1999) and metal ratios do not reveal areas of higher Zn, Pb and Ag mineralization.

Zn grades are generally double the accompanying Pb grades in the same sample (Figure 10). This is consistent with the pre-mining resource grades of 11.1% Zn and 5.4% Pb (MIM Ltd : Report to shareholders – 1998). The dataset displayed in Figure 10 consists of over 69,500 assays from non-composited raw drill-hole data. Trends in the data distribution in Figure 8a are highlighted in Figure 10b. Green data points represent

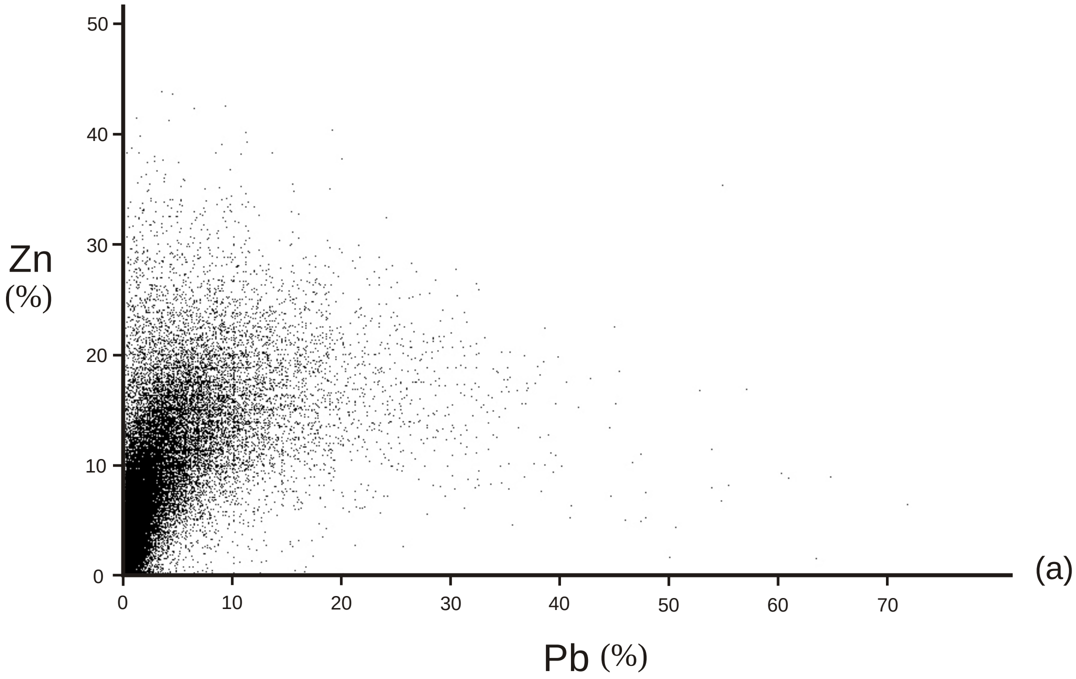

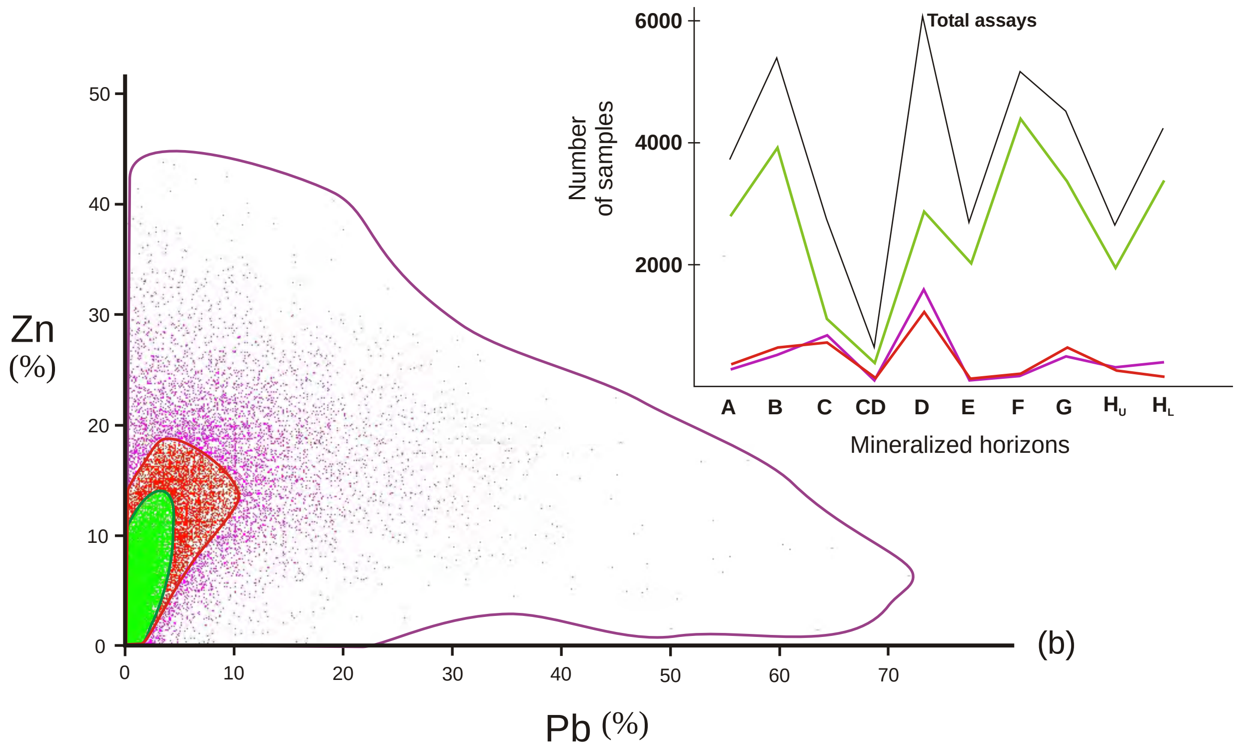

Figure 10. Zn and Pb assay data for all George Fisher sampling (~69500 samples). (a) raw data, Zn vs Pb; (b) trends in the spread of data and accompanying line graph indicating the source ore-horizons for each dataset. Colours on the bar charts indicate the dataset analysed.

barren to low grade assays, red data points reflect a higher-grade trend, and magenta data points indicate the high to very high-grade assays. A steeper trend characterizes the lower grade samples. The graph in Figure 10b shows the distribution of high and low grade assays compared with the number of total assays per ore-horizon. Variation in the total number of assays per ore-horizon (black line in line graph) is a function of their width, that is, the narrow ore-horizons will account for fewer samples than the wider ore-horizons. Coloured lines correspond to the sub-divisions used in the scatter-plot. From these charts it is clear that ore-horizons C, D, and G include a greater proportion of the higher-grade assays than the other horizons. Together they account for 62% of the high-grade magenta-coloured data-points (Figure 10b).

High-Zn assays are almost exclusively from the footwall horizons (G_U to H_L) whereas the high-Pb assays are concentrated in the hangingwall horizons (A-G_U) and dominantly in C and D ore-horizons (Figure 11). Pb:Zn ratio plots for individual ore-horizons at George Fisher are displayed on Figure 12. There are key differences in the population of assays between ore-horizons comprising economic concentrations of Pb-Zn ore (e.g. A, C, D, and G_U) and those which do not (e.g. E, F, and H_L). In those horizons that contain economic concentrations of Zn and Pb, a skewed distribution of Zn:Pb ratios is apparent in higher grade material. The 2Zn:1Pb relationship seen in the lower grade and less economically attractive horizons begins to break down. This suggests that the economic concentrations of ore in C, D, and G_U ore-horizons are a result of the addition of a second population of samples as opposed to just being larger amounts of, or more continuous concentrations of the same material as the uneconomic horizons. The implications of these data, with respect to remobilization, are discussed later.

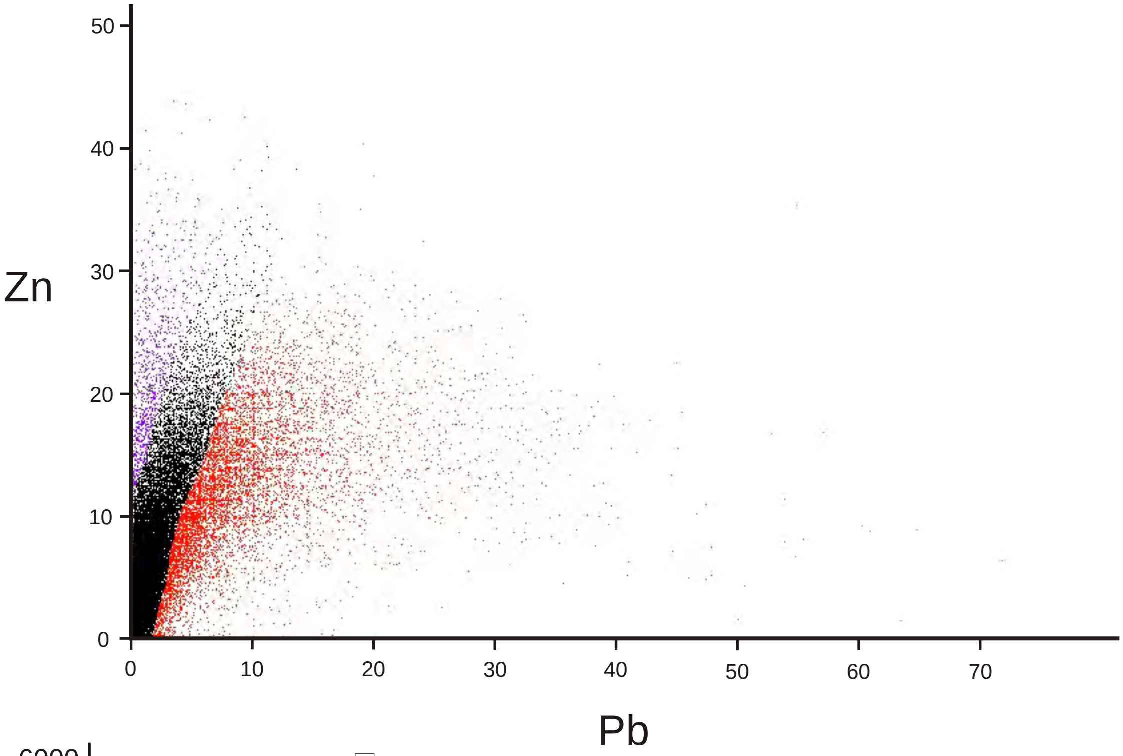

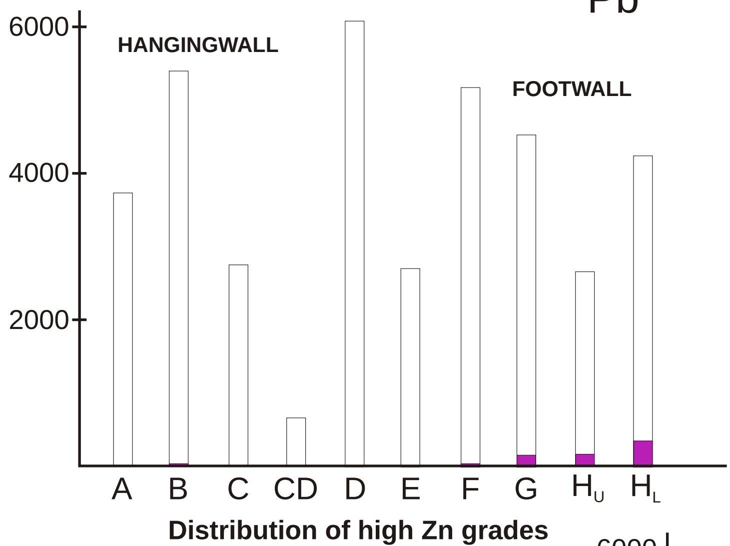

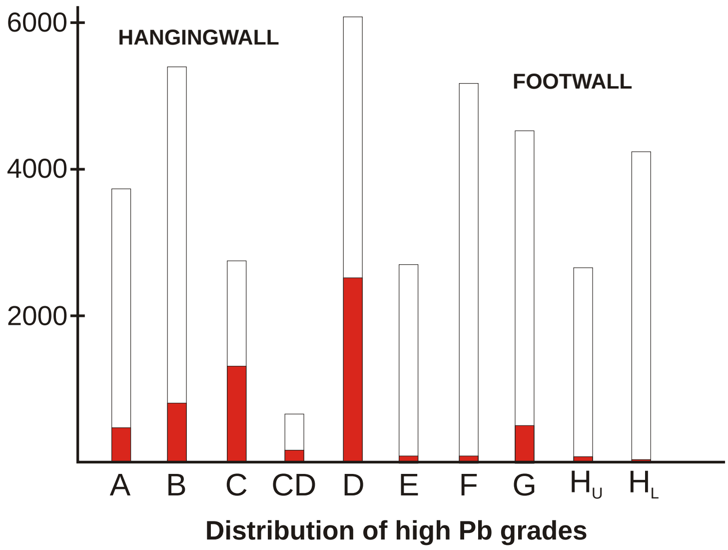

Figure 11. Distinction of high-Zn and high-Pb populations. Frequency histograms indicate the source ore-horizons for each population.

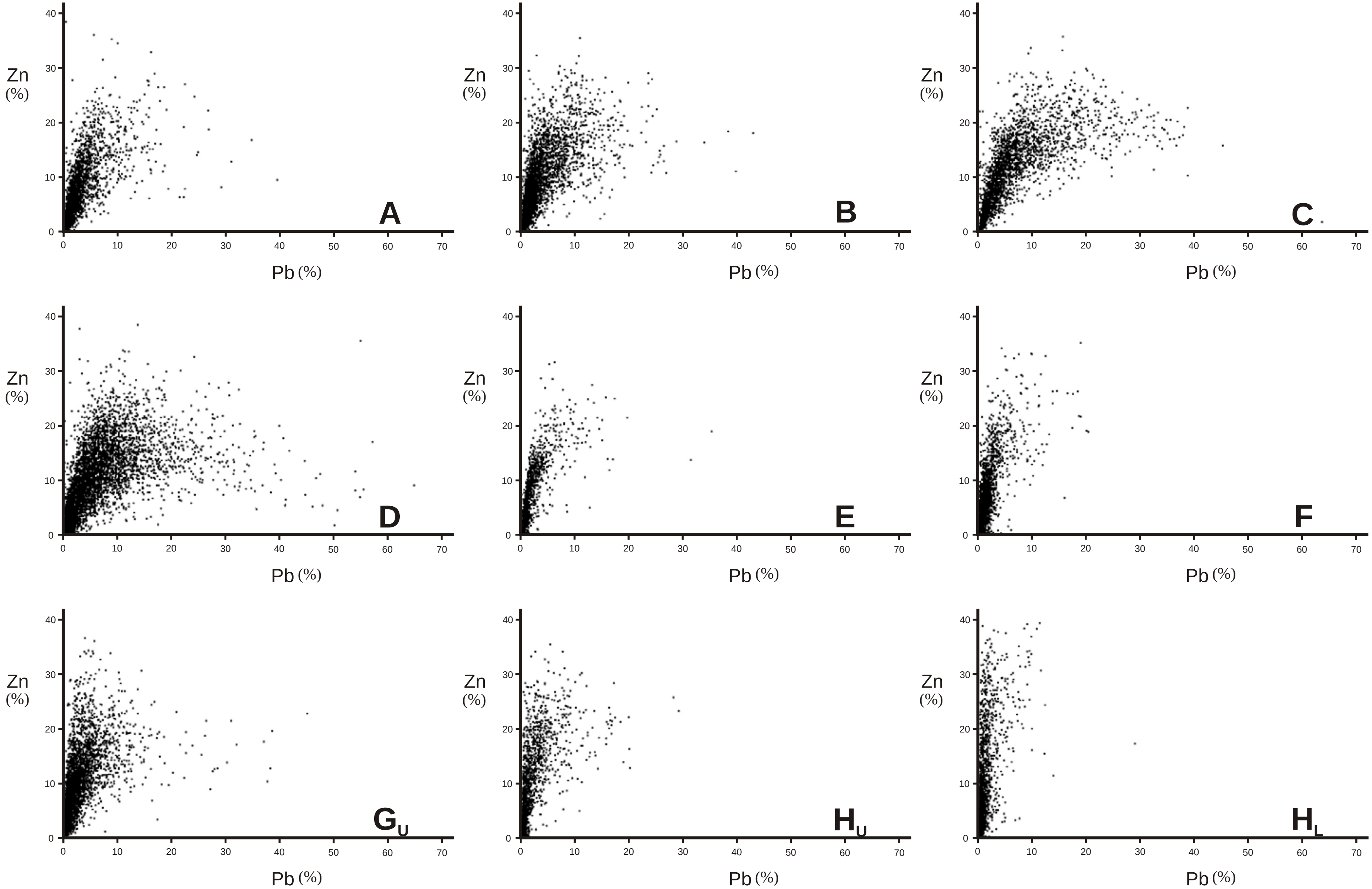

Figure 12. Zn vs Pb plots for each individual ore-horizon. See text for discussion.

'C', 'D', and 'G' ore-horizons (Figures 4-6) have been selected for intensive study as these units constitute 68% of the resource and 88% of the reserve at George Fisher (MIM George Fisher Mine November 2001 - Resource/Reserve estimates) and there is sufficient underground access to study these units. Given the moderate westerly-dip of stratigraphy, analysis of all data for a given ore-horizon is best achieved using north-south longitudinal projections as described in section 2.1.

2.4 Mineralization and grade distribution in C ore-horizon

C ore-horizon is situated in the hangingwall of the deposit, above D and G ore-horizons (Figures 4-6). It is a narrow, often semi-massive sulphide occurrence bounded by barren mudstones (Figure 3). The ore within C orebody is highly pyritic and the footwall portion of the orebody consists of a massive pyrite band approximately 1.0m wide. The economic ore zone is commonly 3 to 5 metres wide. Pb:Zn ratios for C ore-horizon (Figure 12) display a steep trend for Zn<15% and Pb<5%. The distribution of high Pb grades (>20%) occurs as a more gentle trend and correlates with Zn grades of approximately 20% Zn (Figure 12).

Higher-grade Zn mineralization shows elements of a gentle northerly plunge parallel to L^0_2 and a steep southerly plunge parallel to L^0_1 (Figure 13a). Higher grade mineralization is broadly distributed, although the majority of >14% Zn intersections are within or in close proximity to the F_1 short-limb. The distribution of Zn in C ore-horizon is also centred on the short-limb of the F_1 fold.

Figure 13. Longitudinal projections (looking East) of Zn, Pb, and Ag average grades in C ore-horizon (a) Zn distribution, (b) Pb distribution, and (c) Ag distribution. Contours are constructed from the average grade of diamond drill-hole intercepts. Yellow lines indicate the F_1 axial traces and are solid where locations are interpreted from mapping and dashed where projected up/down-plunge. Intersection lineation orientations for the various fold generations are also shown.

The distribution of Pb differs significantly from that of Zn, in that a greater proportion of the higher grade Pb is situated within the short-limb of the F_1 fold (Figure 13b). Higher Pb grades (>8% Pb) form a steeply south-pitching ore-shoot that broadly coincides with the short-limb of the F_1 fold. High-grade (>10% Pb) ore is coincident with the antiformal axis of the F_1 fold. Further moderate to high-grade intersections define a secondary ore-shoot orientation that again pitches gently toward the north parallel to L^0_2.

Higher Ag grades are also concentrated in the F_1 short-limb where they define a steeply plunging coincident shoot (Figure 13c). Again, a gentle, north-pitching secondary trend occurs that is approximately parallel to the F_2 axes.

2.5 Mineralization and grade distribution in D ore-horizon

D ore-horizon includes the main ore-zone (D orebody) at George Fisher and is situated in the middle of the mineralized package of Urquhart Shale (Figures 4-6). The D ore-horizon comprises siltstones and pyritic siltstones (Figure 3) and a 'buff'-coloured K-feldspar altered zone which has significant enrichment in sphalerite. Barren mudstones bound the mineralized siltstones (Figure 3). The ore-zone ranges in width from 15 to 30m. Pb:Zn ratios for D ore-horizon (Figure 12) display a steep trend for Zn<15% and Pb<5% and a maxima for high-Pb grades occurs at approximately 10-15% Zn.

Zn distribution in D ore-horizon (Figure 14a) displays a general north-pitching trend in longitudinal projection similar to that in the C ore-horizon (Figure 14a). The difference in grade between the two horizons reflects the incorporation of more sub-grade rock in the D ore-horizon stratigraphic package and does not reflect the actual resource/reserve

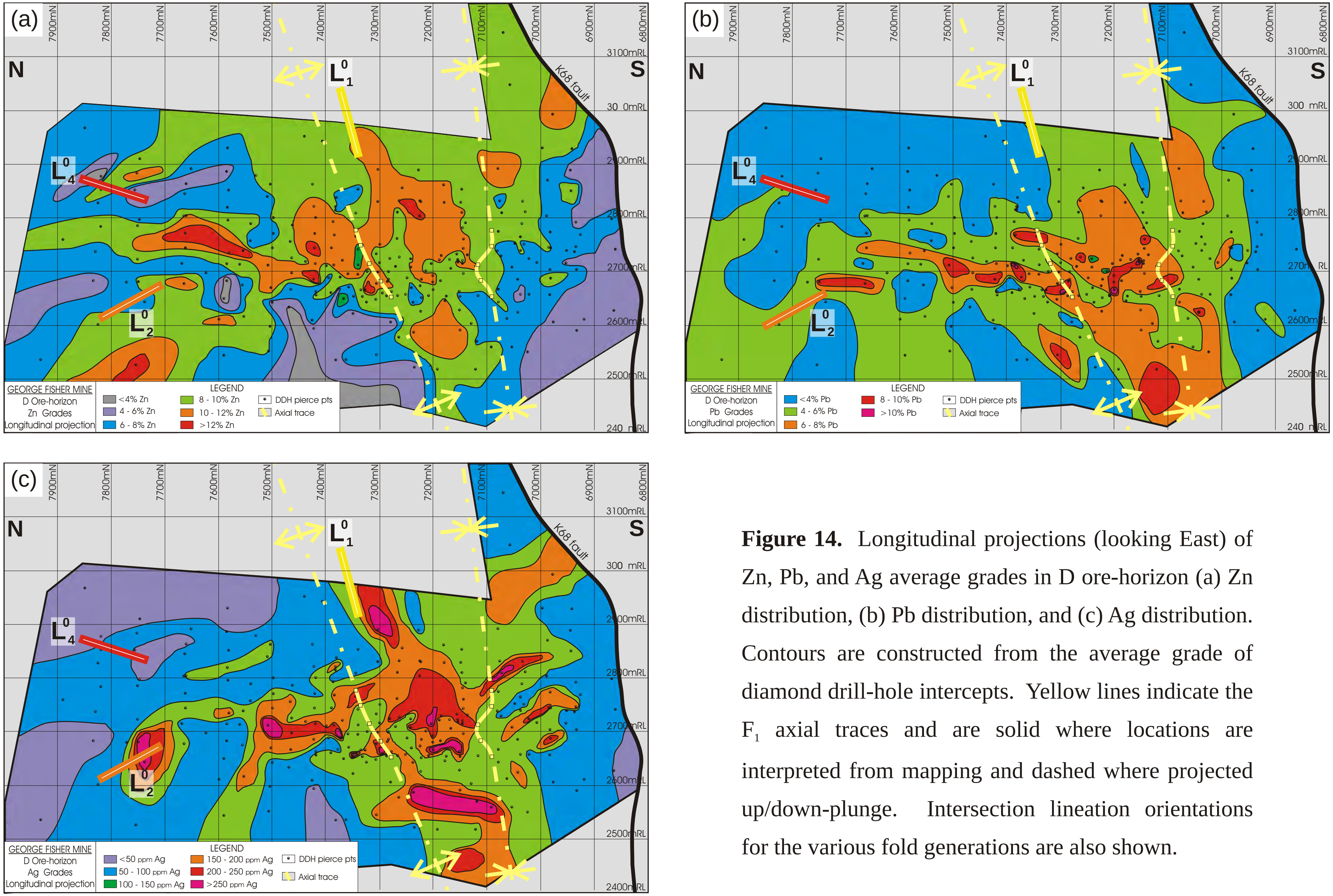

Figure 14. Longitudinal projections (looking East) of Zn, Pb, and Ag average grades in D ore-horizon (a) Zn distribution, (b) Pb distribution, and (c) Ag distribution. Contours are constructed from the average grade of diamond drill-hole intercepts. Yellow lines indicate the F_1 axial traces and are solid where locations are interpreted from mapping and dashed where projected up/down-plunge. Intersection lineation orientations for the various fold generations are also shown.

grades. The F_1 short-limb and distribution of higher Zn grades show a weak correlation with a steeply pitching ore shoot recognizable. Between northings 7400mN and 7700mN, a gently south-pitching shoot is apparent. This orientation is parallel to the trend of F_4 fold axes (or the L^0_4intersection).

Higher Pb grades (>6% Pb) show a close correlation with the F_1 short-limb where they form a steeply-pitching shoot parallel to L^0_1 (Figure 14b). Gently south-plunging/pitching high-grade zones centred on the 2700mRL occur within a broad, gentle, north-plunging/pitching envelope. This gently plunging mineralization coincides with a similar gently plunging high-grade shoot of Zn mineralization (Figure 14a), and is again parallel to the intersection between S_4 and bedding (L^0_4 intersection), and F_4 axes.

As with Ag in C ore-horizon (Figure 13c), Ag in D ore-horizon (Figure 14c) has the most restricted distribution of the three metals and most clearly defines the two main ore shoot orientations, parallel to the F_1 short-limb, and the gently north-plunging F_2 axes. The intersection of these two orientations is coincident with the main mining area (between 2650mRL – 2800mRL and between 7100mN – 7500mN).

2.6 Mineralization and grade distribution in G ore-horizon

G ore-horizon is approximately 100m into the footwall from C ore-horizon (Figures 4-6). G ore-horizon stratigraphy is dominated by a highly pyritic unit at the base of the G-upper package (Figure 3). Barren mudstone units delineate the hangingwall and footwall of the ore-bearing stratigraphy. Ratios of Pb:Zn for the G_U ore-horizon for Zn<18% and Pb<5% define a steep trend (Figure 12). The higher Pb grades reach a maximum at approximately 15% Zn. Note that longitudinal projections of G-upper ore-horizon are contoured at different intervals to those used for the previously discussed C and D ore-horizons. This is necessary as Pb and Ag grades in G-upper ore-horizon are low and the contour intervals are constructed at appropriate thresholds so as to indicate anomalism within the lower grade mineralization.

The distribution of Zn in G ore-horizon (Figure 15a) shows a weak correlation with the F_1 short-limb zone. The F_1 short-limb is still the geographical centre of the spread of Zn metal and the antiformal axis is potentially associated with the higher grade material (>10% Zn). Elements of a steeply-pitching and gently, north-pitching shoot are recognizable. Note the distinct reduction in grade at approximately 7500mN (Figure 15a).

Pb distribution in G ore-horizon (Figure 15b) is focused around the F_1 short-limb. The >2% Pb contours have dominantly steeply pitching boundaries that are sub-parallel to the F_1 fold-axes. A gentle, north-pitching high-grade trend is again recognizable.

Ag distribution (Figure 15c) is very similar to that of Pb and displays steep, gentle south-pitching, and gentle north-pitching trends. As with Zn and Pb, there is a sharp reduction in grade north of 7500/7600mN where contours have a very steep pitch to the south.

3. Deposit-scale sulphide distribution

Sulphide thickness data was obtained for each of the C, D, and G ore-horizons by measuring the cumulative thickness of galena and sphalerite mineralization in diamond-

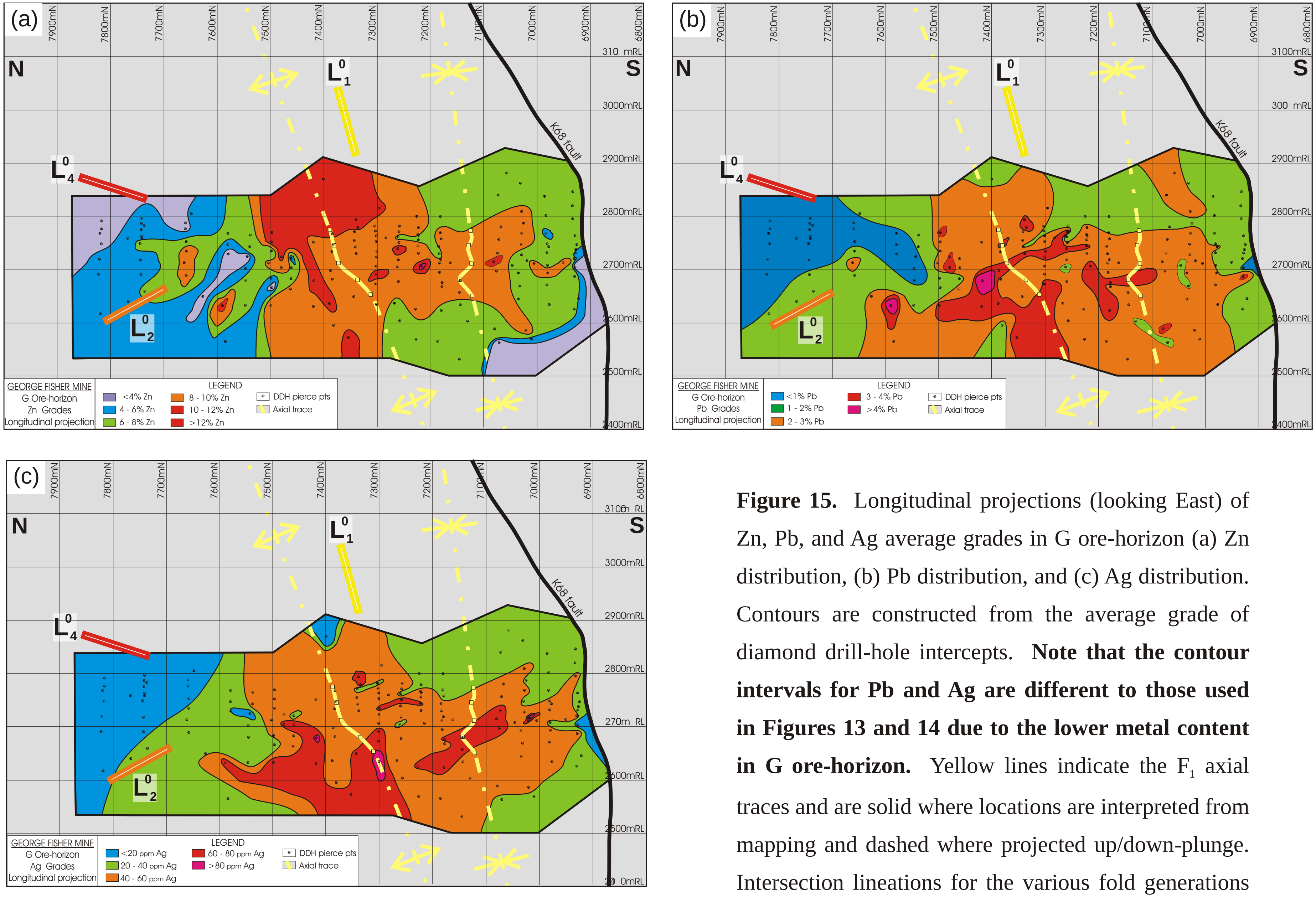

Figure 15. Longitudinal projections (looking East) of Zn, Pb, and Ag average grades in G ore-horizon (a) Zn distribution, (b) Pb distribution, and (c) Ag distribution. Contours are constructed from the average grade of diamond drill-hole intercepts. **Note that the contour intervals for Pb and Ag are different to those used in Figures 13 and 14 due to the lower metal content in G ore-horizon.** Yellow lines indicate the F_1 axial traces and are solid where locations are interpreted from mapping and dashed where projected up/down-plunge. Intersection lineations for the various fold generations are also shown.

drill hole core for C, D, and G ore-horizons. Drill holes used in this study are a approximately 150m apart in C and D ore-horizons and ~100m in G ore-horizon. The drill holes selected cover an area up to 1.0km in strike and 0.5km vertical. Data obtained from this process is displayed as north-south longitudinal projections.

3.1 C ore-horizon

Variation in the cumulative thickness of sphalerite ore-types in the C ore-horizon are displayed on Figure 16a. The thicker mineralization forms a steeply pitching shoot which coincides with the F_1 short-limb discussed previously. The along-strike extent of Zn-rich mineralization thicker than 3.0m is limited to ca. 50-100m. Note the thicker ore in the northern-upper corner of the contouring in Figure 16a. The inferred setting of this mineralization is discussed later in this paper.

The thicker zone of galena mineralization has a broader distribution than sphalerite but is still centred on the steeply-pitching F_1 short-limb (Figure 16b). Thicker galena mineralization occurs in the deeper part of the C ore-horizon and in close proximity to the F_1 antiformal axis which has been recognized as the locus for high-grade Pb mineralization (Figure 13b).

The total ore-sulphide thickness for C ore-horizon shows the close spatial correlation between thicker mineralization and the F_1 short-limb, although the thickest sulphide occurrence is situated just north of the antiformal axis at 2500mRL (Figure 16c). Note that the position of the F_1 fold axial traces are projected 200m down-plunge from the deepest accessible exposure to this location, and this particularly thick intersection may

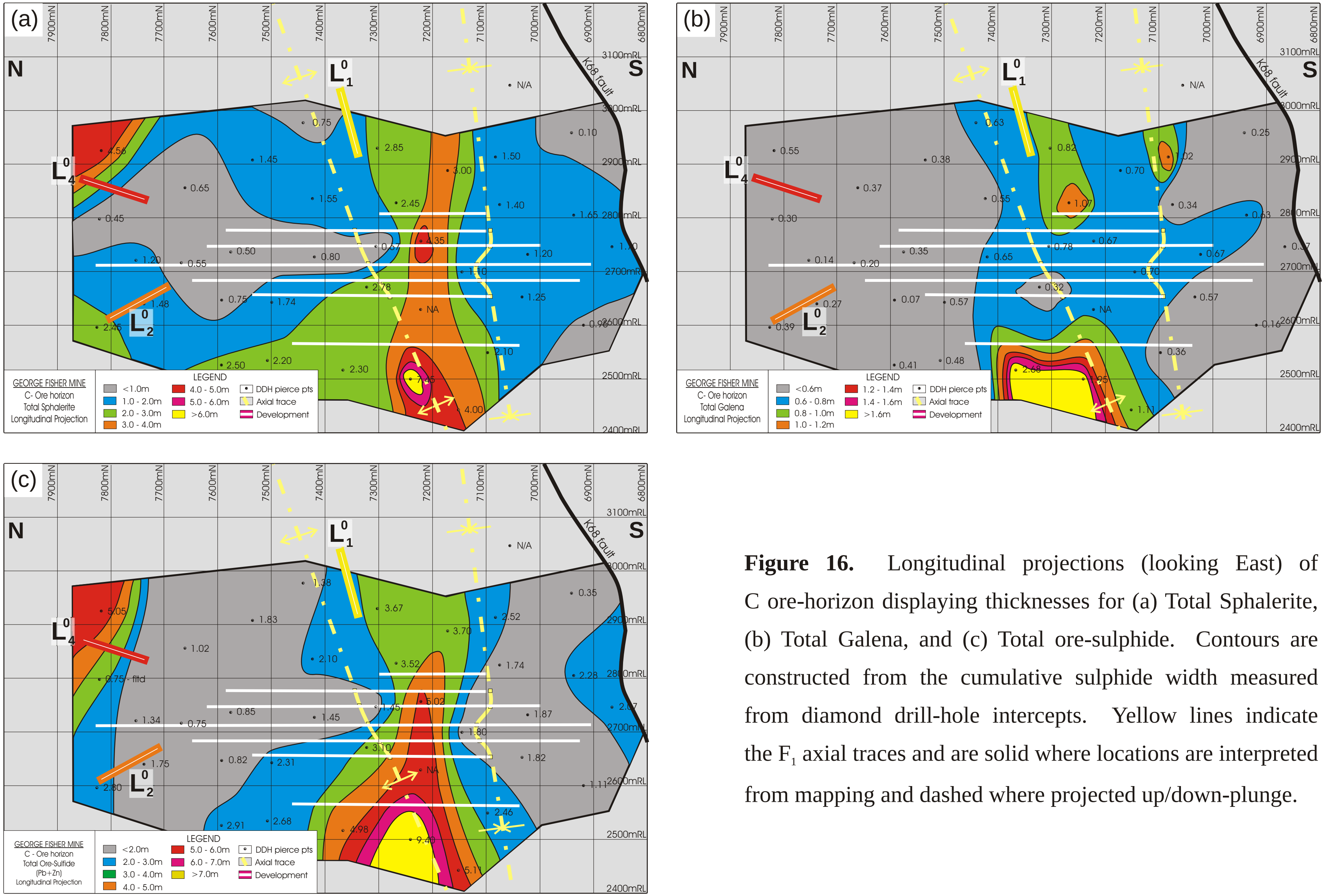

Figure 16. Longitudinal projections (looking East) of C ore-horizon displaying thicknesses for (a) Total Sphalerite, (b) Total Galena, and (c) Total ore-sulphide. Contours are constructed from the cumulative sulphide width measured from diamond drill-hole intercepts. Yellow lines indicate the F_1 axial traces and are solid where locations are interpreted from mapping and dashed where projected up/down-plunge.

therefore be within the short-limb of the F_1 fold if the axes curve ca 30° with depth.

3.2 D ore-horizon

A strong correlation between thicker sphalerite mineralization and the location of the F_1 short-limb also occurs in D ore-horizon (Figure 17a). At the northern extent of the data, similar thickening of sphalerite mineralization occurs as that seen in the C ore-horizon (Figure 16a and c) and will be discussed later (p152). The average width of ore-sulphides outside the F_1 short-limb is approximately 2.5m (Figure 17a) and approximately 5.0m within representing a twofold apparent thickening of sphalerite in the F_1 short-limb.

Galena distribution is very similar to sphalerite in that the thicker ore is clearly spatially associated with the F_1 short-limb (Figure 17b). Thicker intercepts of galena that occur at the northern extent of the data are coincident with the thicker sphalerite (Figure 17a). A gentle north-plunging trend in galena cumulative thickness (0.8-1.0m contour interval, Figure 17b) coincides with a zone of intense F_2 folding and similar trends can be seen in Pb grade distribution in Figure 14b again indicating a link between high-grade and thicker mineralization.

The incidence of thicker total ore-sulphides shows a very strong correlation with the position of the F_1 short-limb in D ore-horizon (Figure 17c). Anomalous ore-thickness occurs north of 7700mN but does not have the continuity of the trends observed in the F_1 short-limb.

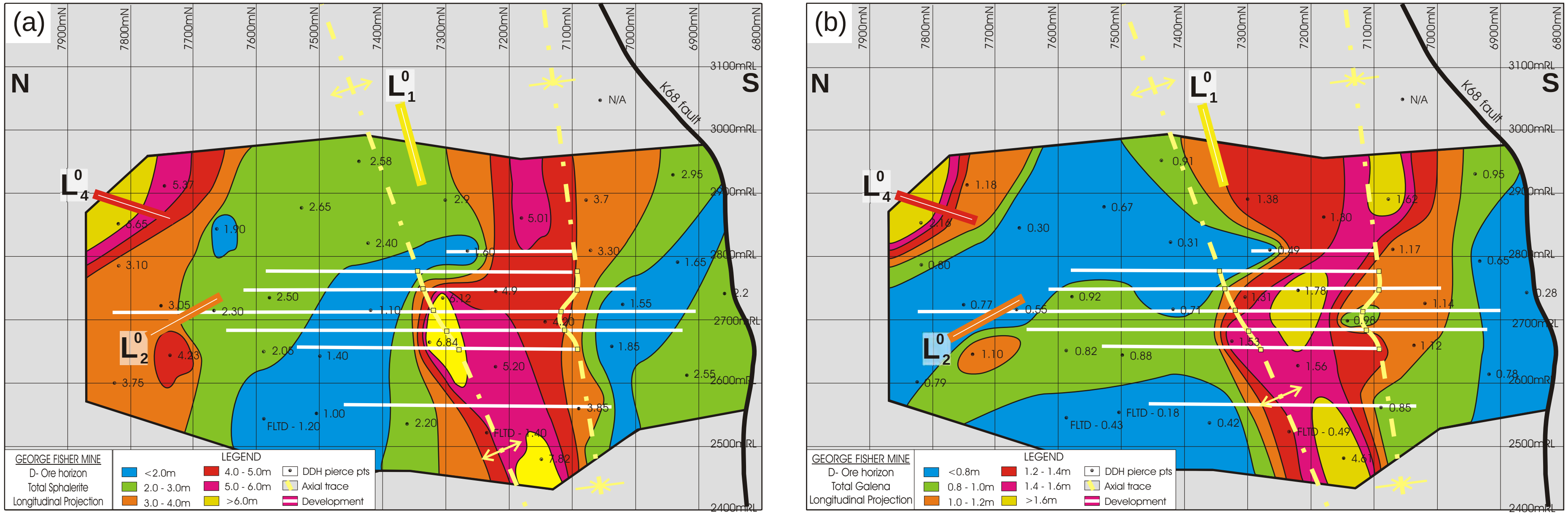

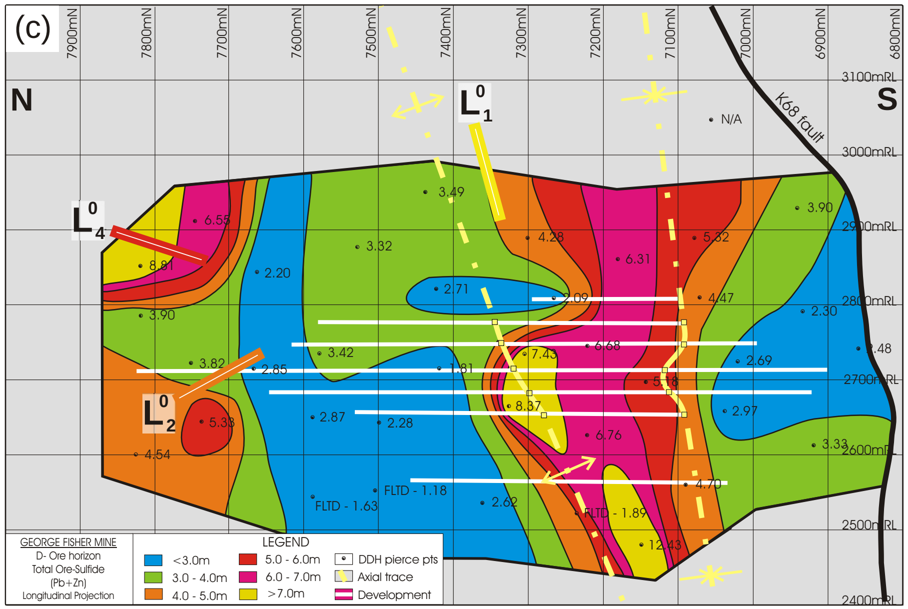

Figure 17. Longitudinal projections (looking East) of D ore-horizon displaying thicknesses for (a) Total Sphalerite, (b) Total Galena, and (c) Total ore-sulphide. Contours are constructed from the cumulative sulphide width measured from diamond drill-hole intercepts. Yellow lines indicate the F_1 axial traces and are solid where locations are interpreted from mapping and dashed where projected up/down-plunge.

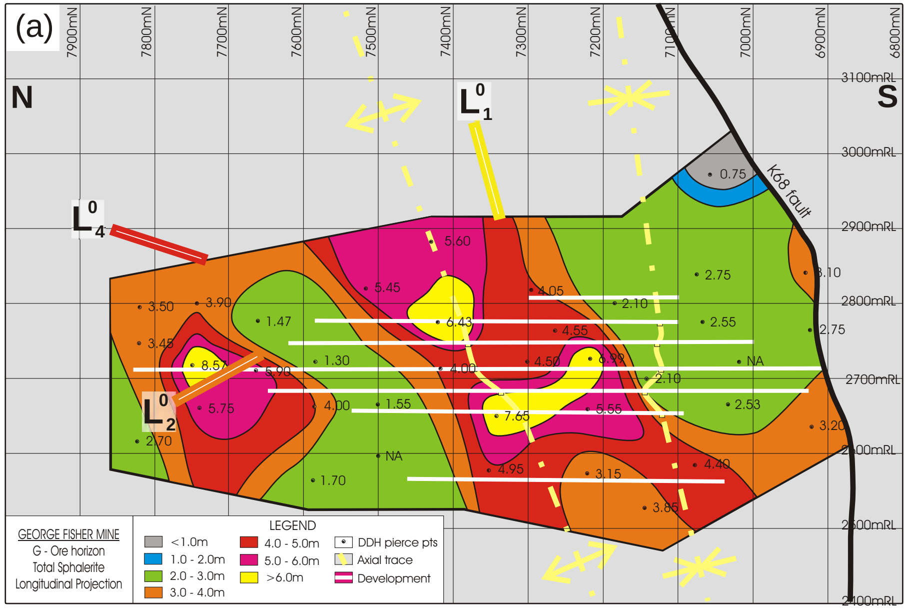

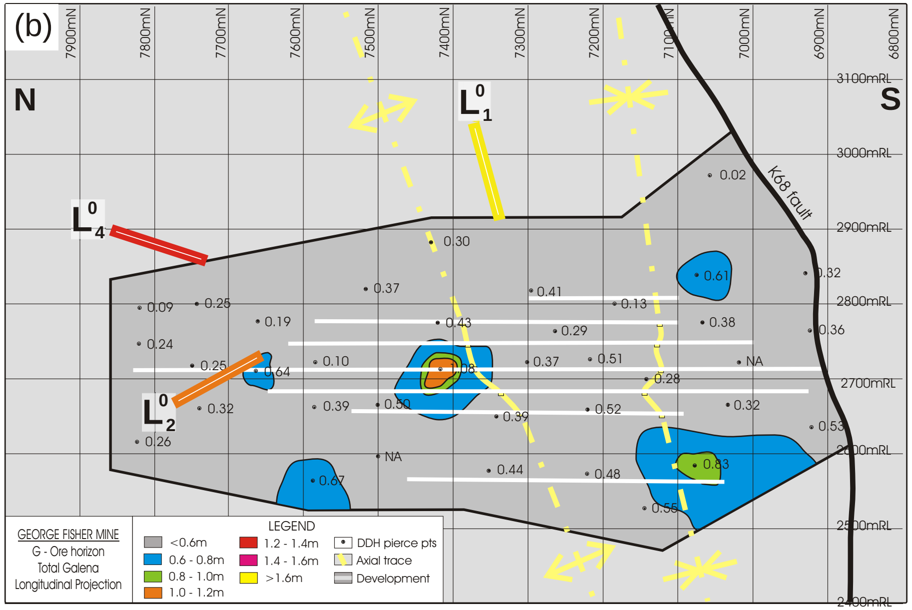

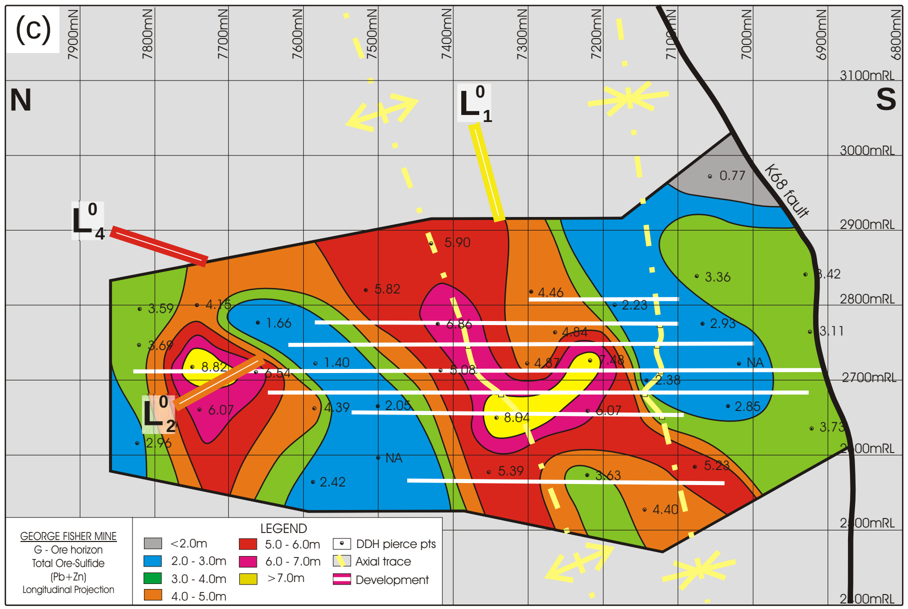

Figure 18. Longitudinal projections (looking East) of G ore-horizon displaying thicknesses for (a) Total Sphalerite, (b) Total Galena, and (c) Total ore-sulphide. Contours are constructed from the cumulative sulphide width measured from diamond drill-hole intercepts. Yellow lines indicate the F_1 axial traces and are solid where locations are interpreted from mapping and dashed where projected up/down-plunge.

3.3 G ore-horizon

The main shoot of greater total sphalerite-ore thickness within G ore-horizon has a more-gentle pitch than C and D ore-horizons (Figure 18a). This is interpreted to be due to the more-gently dipping bedding in the footwall stratigraphy which in turn results in a more-gently plunging intersection between G ore-horizon stratigraphy and the F_1 axial planes.

Thicker ore is situated dominantly within the F_1 short-limb and extends slightly north of the F_1 antiformal axis. The antiformal axis is spatially coincident with the greatest thickness of sphalerite ore. A second thick ore shoot occurs to the north of the short-limb and may be associated with the thicker Zn and Pb ores observed at ca. 7700mN in plots of C and D ore-horizon data (Figures 16c and 17c). The thicker ore between 7600mN and 7800mN is more Zn-rich than that in C and D ore-horizons but unlike C and D, the thicker ore is not open up-dip and along-strike. There is no corresponding increase in metal grades at this northing on the longitudinal projections in Figures 13-15. This may be a factor of the broader drill-hole spacing of this sulphide thickness study as opposed to the complete drill-hole dataset as plotted in Figures 13-15. This suggests that isolated thicker pods of mineralization occur (as seen in Figure 18c at ~ 7700mN) but break up when more data is collected through closer spaced drilling.

G ore-horizon lacks economically significant Pb mineralization, with only narrow isolated intersections obtained (Figure 18b). Total ore-sulphide thickness (Figure 18c) is therefore dominated by sphalerite thickness. The distribution of thicker ores is similar to that observed in the C and D ore-horizons which are consistently located within and/or adjacent to the F_1 short-limb.

3.4 Combined ‘C+D’ and ‘C+D+G’ data

Combining the ore-sulphide thickness data in the C and D ore-horizons further demonstrates the strong spatial correlation of the zones of thicker mineralization and the F_1 short-limb (Figure 19a). Thicker ore in the combined C and D ore-horizons forms a single steeply-pitching shoot, approximately 300m wide, in the mine area. At the northern extent of the data, thicker ore occurs in a second steeply pitching shoot whose full extent is not yet defined. Anomalous thickness of ore-sulphides between 7650mN and 7850mN has a steep pitch parallel to the main ore shoot but lacks continuity of thicker ore intersections.

Combination of data for C, D, and G ore-horizons results in the distribution of ore-sulphide thickness displayed in Figure 19b. The striking relationship between the distribution of combined Zn and Pb ore thickness and the F_1 short-limb emphasizes the key role that this structural feature has played in localizing economic mineralization at George Fisher.

4. Discussion

4.1 Correlations between the geometry, orientation, and location of ore shoots and structural features

Previous interpretation of the distribution of ore-types and metal ratios (Chapman, 1999) has been interpreted to represent the primary fluid-flux at George Fisher and remobilization of ore-sulphides has occurred on the micron to metre scale (Chapman, 1999). Local remobilization of galena and minor sphalerite breccia inferred to have occurred late in the deformation history did not significantly affect the 100m+ distribution

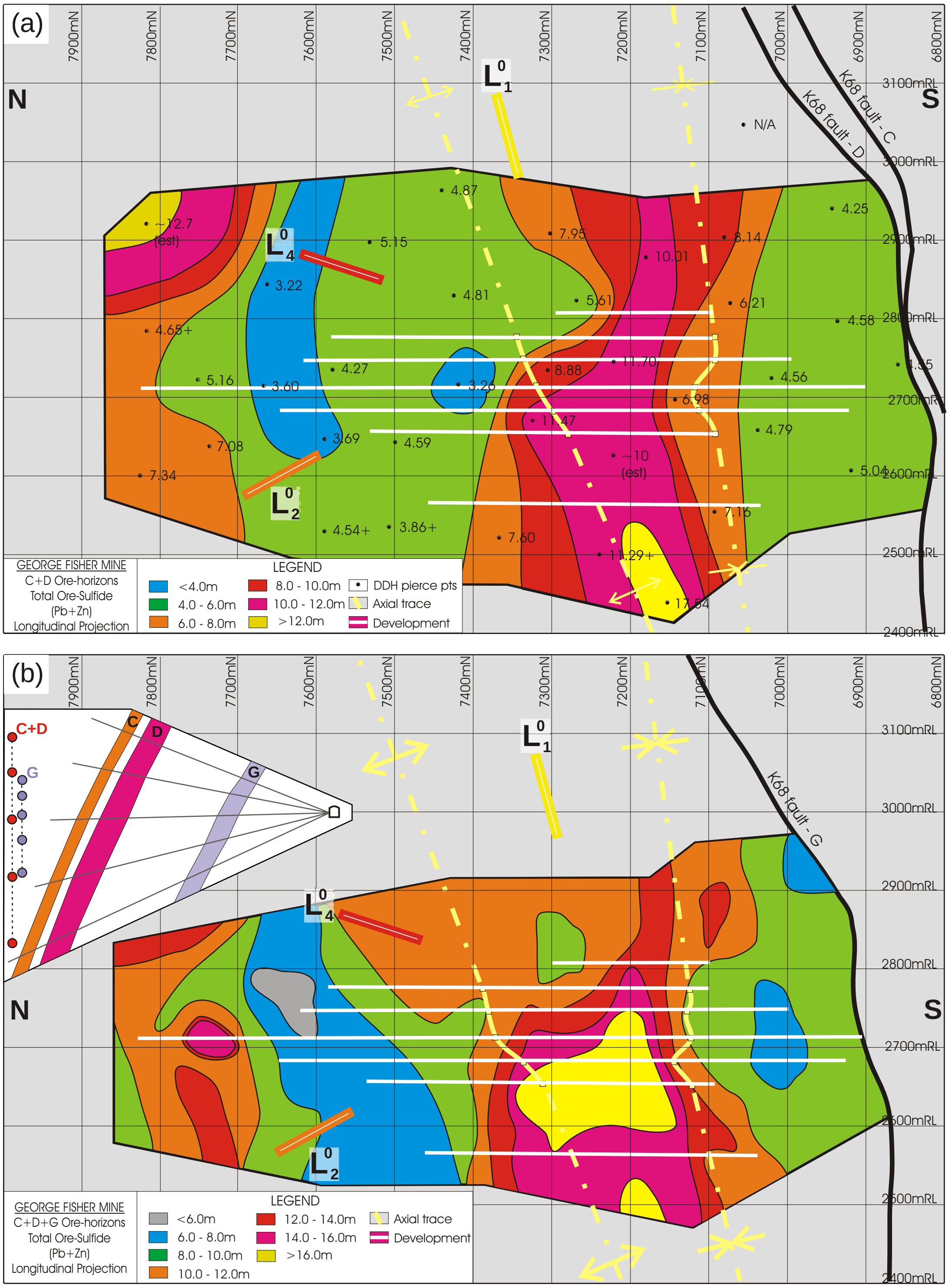

Figure 19. Longitudinal projections (looking East) displaying thicknesses for (a) Total ore-sulphide (C+D ore-horizons). Contours are constructed from the cumulative sulphide width measured from diamond drill-hole intercepts. (b) Total ore-sulphide (C+D+G ore-horizons). Contours are constructed by addition of contours in (a) with contours from Figure 18c. The inset schematic diagram illustrates why the use of a single pierce point per drill-hole is problematic when displaying sulphide width data from C, D, and G ore-horizons on a longitudinal projection as the fanned drill-holes result in G ore-horizon intercepts at closer spacing than the combined C and D ore-horizon intercepts (c.f. Figure 2a).

of sulphides at George Fisher (Chapman, 1999, 2004). Macroscopic and mesoscopic ore-thickness variations, interpreted to be spatially associated with cross-cutting brittle faults, have been interpreted as the result of strain incompatibility between brittle host rocks and more ductile ore layers and have played a major role in the present geometry and thickness of ores at Hilton (Valenta, 1994). Recognition of ore-shoots within the deposit as part of this study and the correlation with structural domains suggests significant remobilization (in the order of 200m+) and/or syn-deformational mineralization were involved in the formation of the orebodies at George Fisher. The role of remobilization at George Fisher is discussed in Part D in the context of the relative timing and overprinting relationships of mineralization types.

Consistent ore shoot locations and orientations have been recognized for metal distribution over several stratigraphic packages which indicate that the distribution of metal at George Fisher correlates with structural domains described in Part A. The dominant shoot comprises high-grade mineralization and thicker ore-sulphides with the deposit-scale F_1 short-limb (Figure 20a). This is consistent across the ca. 100m of stratigraphic package, which hosts the C and G ore-horizons. A trend in higher grades and thicker mineralization therefore exists almost orthogonal to the strike of stratigraphy but parallel to the axial planes of the F_1 fold pair. Within the current extent of drilling and mine development, no bedding-discordant mineralized faults or facies changes in the host-rocks have been recognized which may account for the location of the recognized ore shoots. This supports the interpretation of localization of higher-grade mineralization in the short-limb during either D_1 or later deformation. The kinematics involved in this process are discussed later.

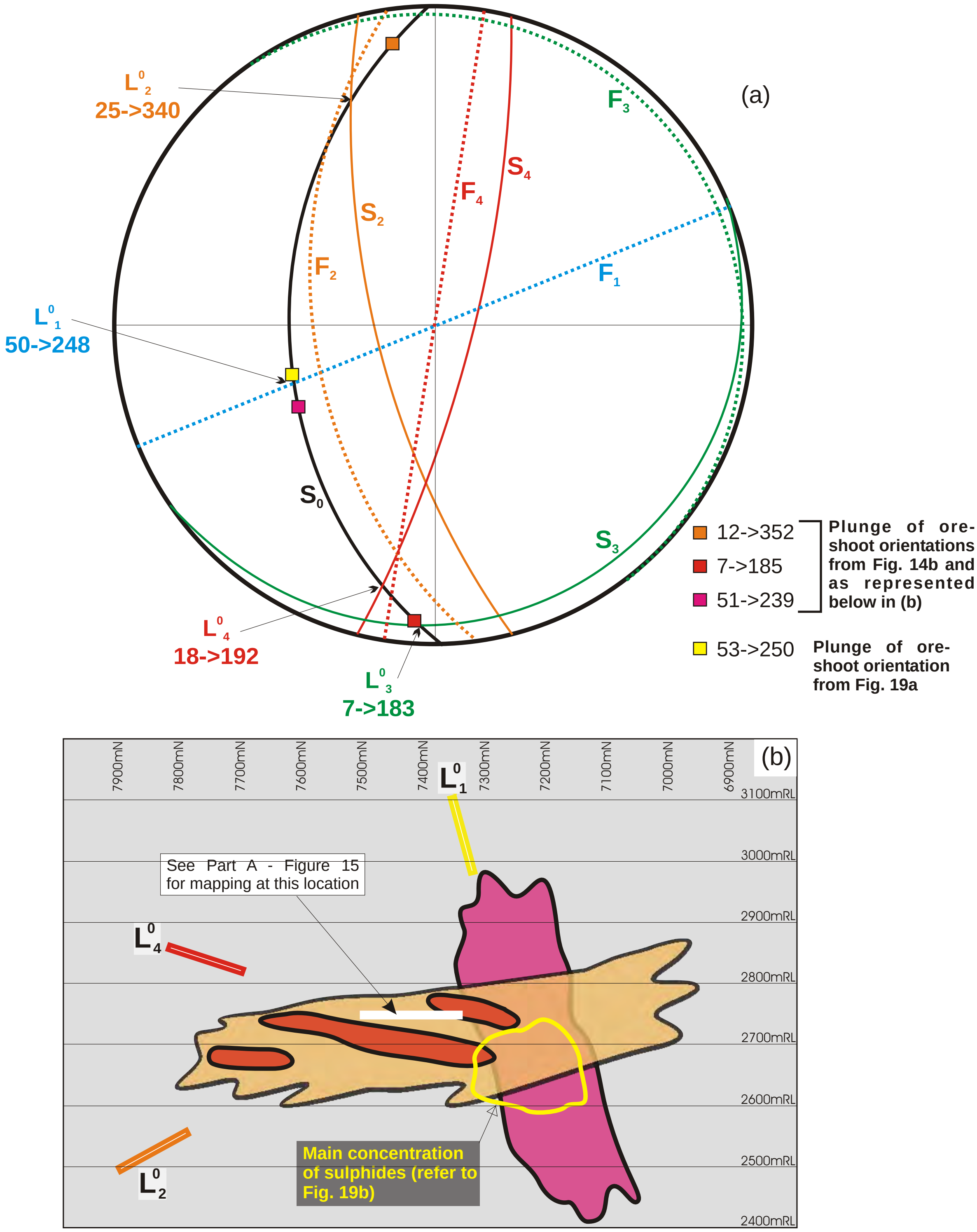

Figure 20. (a) Stereographic projections of the average orientations of structural features and their intersection lineation with average bedding orientation. The intersections of D_1, D_2, D_3 and D_4 structures correlate with ore-shoot orientations defined within the D ore-horizon. (b) generalized ore-shoot orientations. Note that the L^0_3 orientation is approximately coincident with the gentle, south-pitching shoot orientation in (a), however the intersection of F_3 folding with average bedding orientation is north-plunging. The L^0_4 and F_4/S_0 intersections both plunge gently to the south and are also sub-parallel to this shoot orientation.

A secondary shoot orientation occurs parallel to the axis of F_2 folds (L^0_2 - Figure 20a an b) and is spatially associated with a zone of more intense F_2 folding (Figure 20b). This shoot occurs as a gently, north-pitching zone of higher Zn, Pb, and Ag grades but an equivalent increase in the ore-thickness coincident with this shoot orientation is not recognized.

Within the north-pitching L^0_2 trend in metal distribution, a sub-horizontal to very gentle, south-pitching trend occurs (Figure 20b). This south-pitching trend is parallel to F_4 fold axes (L^0_4 - Figure 20a) but is restricted to the C and D ore-horizons. The lack of shoots with this trend in the G ore-horizon is consistent with weak S_4 development in this area (Part A – Figure 32).

Correlation between the orientation of shoots defined by thicker accumulations of sulphides or higher grade material with each of the F_1, F_2, and F_4 orientations suggests that either mineralization predates deformation and has subsequently been remobilized during each deformation episode or that mineralization occurs late and exploits earlier structures which have acted as heterogeneities in the Urquhart shale host rocks. Timing of the main ore-types relative to each other and the main phases of folding is determined in Part D which will assist in testing each of the above hypotheses.

High-grade mineralization does not occur along the full extent of the F_1 short-limb, that is, there is an upper limit to economic mineralization within the F_1 short-limb. This is observed in longitudinal projections of grade data (Figures 13-15) and the absence of relatively thick, high-grade mineralization in shallow intersections illustrated on Figure

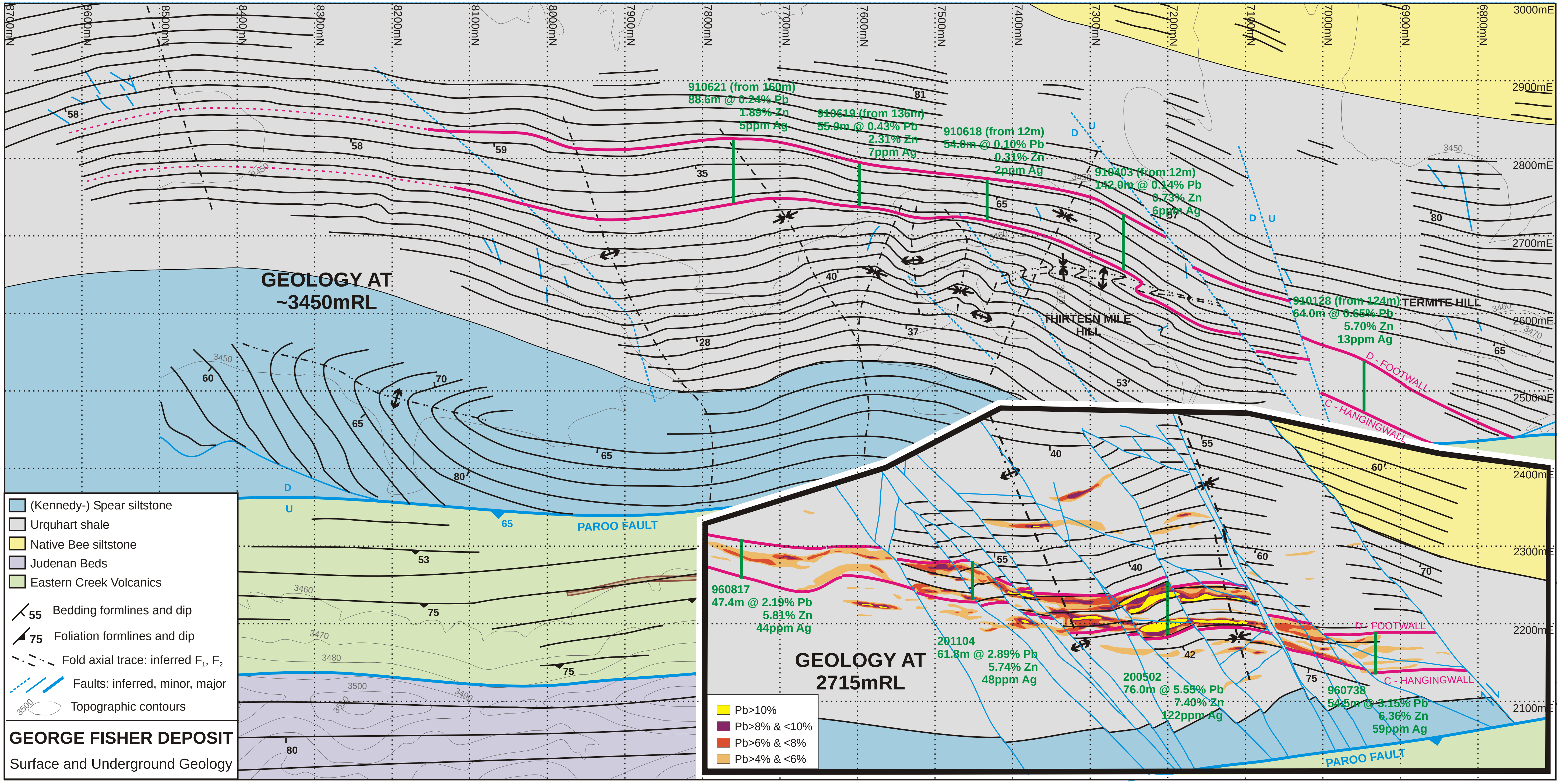

Figure 21. Simplified surface geological map above George Fisher Mine and inset area illustrating the main geological features and Pb contours at 12 Level in the underground mine. Folding at surface has the same vergence, shape, and orientation as the open east-west trending F_1 fold recognized in the underground mine. The s-shaped fold between 7700 and 7950mN in the highlighted C-D stratigraphy, occurs approximately in the up-plunge projected position from the F_1 fold in the mine. Intersections for the total C and D ore-horizon stratigraphy are plotted for both near surface and underground positions. The intersections, which occur at variable depth, are projected to 3450mRL and 2715mRL respectively. There is anomalous mineralization in the near-surface intersections but they are of significantly lower grade than the equivalent intersections shown for the underground part of the deposit. A higher grade intersection occurs near surface to the south where the C-D stratigraphy intersects the Paroo Fault. This represents an upthrown block south of the K68 fault. (Bedding formlines constructed from 1:600 and 1:2500 Hilton Mine Geological Maps, lihological data is from the 1:2500 Hilton Mine Geological Map and the George Fisher drill-hole database)

21. The presence of approximately east-west open folds at the surface up-plunge from the F_1 identified in the underground mine does not automatically indicate ore grade mineralization although sub-grade intersections and associated gossans are focussed in this area (Figure 21). Coincidence of thicker high-grade mineralization within a zone of stronger S_4 development in the short-limb in the underground mine implies some D_4 control on the localization of fluid and mineralization at the intersection of the F_1 short-limb and the F_2/F_4 fold corridor which forms the locus for the bulk of the economic ore at George Fisher (compare Figure 20 and Figure 17b). Explanation for this empirical relationship is offered in the following section. The zone of D_4 strain coincident with high-grade mineralization in the F_1 short-limb in the underground mine (Part A – Figure 30) is not exposed at surface as it is truncated by the Paroo Fault (Figure 21). The full extent of this zone of D_4 strain is unknown.

4.2 Comparison with the structural setting of ore shoots within the Mt Isa and Hilton Zn-Pb-Ag deposits

At the Mt Isa mine, studies of the location and orientation of high-grade Zn+Pb shoots have recognized a parallel relationship between the shoots and associated folds interpreted to be of D_3 (D_4 in Davis, 2004 and this study) equivalent age (Wilkinson, 1995; Perkins, 1997; Davis, 2004). Two distinct centres of Zn-Pb mineralization occur on each side of the D_4 Mt Isa fold. (Perkins, 1997; Davis, 2004). A relationship between bedding orientation and grade is recognized at Mt Isa such that grade diminishes rapidly where the strike of bedding changes from north-northeast - south-southwest to north-south (Davis, 2004). Each study recognizes the diminution of grade approaching the Mt Isa fold, whilst Davis (2004) illustrates higher and lower-grade trends within ore-shoots parallel to F_4 fold axes. The coincidence of F_2 and F_4 folding is interpreted to have promoted enhanced fluid flow and formation of high-grade shoots whereas F_4 folding alone did not produce high-grade shoots of Zn-Pb mineralization (Davis, 2004). Mineralization occurs preferentially on the long-limbs between F_4 hinge zones (Wilkinson, 1995; Perkins, 1997; Davis, 2004) with an apparent 'bounding' effect of the hinge zones on Zn-Pb sulphide distribution. This is interpreted as the concentration of mineralizing fluids, resulting in more intense mineralization, in the limbs between F_4 hinge zones which are inferred to have acted as aquicludes during D_4 deformation (Figure 22) (Wilkinson, 1995; Myers et al., 1996). At the exposure scale, apparent folding of mineralization may be the result of replacive alteration and sulphide deposition parallel to the fold axes (discussed in Part D description of ore textural types).

Discontinuous lateral continuity of Zn-Pb ore in the 4-pod at the Hilton mine (Perkins and Bell, 1998) was interpreted as heterogeneous replacement of host stratigraphy and has not been correlated with deposit-scale folds of a particular generation. This may be partly due to the complex post-mineralization faulting which has affected the deposit. A relationship between high Cu metal ratios and proximity to the 'hangingwall-fault' and dyke system (Wilson, 1992; Valenta, 1994) also applies to Pb:Zn ratios where Pb:Zn ratio decreases with distance from the fault (Perkins and Bell, 1998) implies that this syn- to post-D_2 fault (Valenta, 1994) was a conduit to both Cu and Pb+Zn mineralizing fluids.

Ore shoot locations and orientations recognized at George Fisher do not correlate directly with observations from the Mt Isa deposit. The F_1 fold is interpreted to be the main focus of fluid/mineralization at George Fisher and subsidiary ore shoot orientations occur

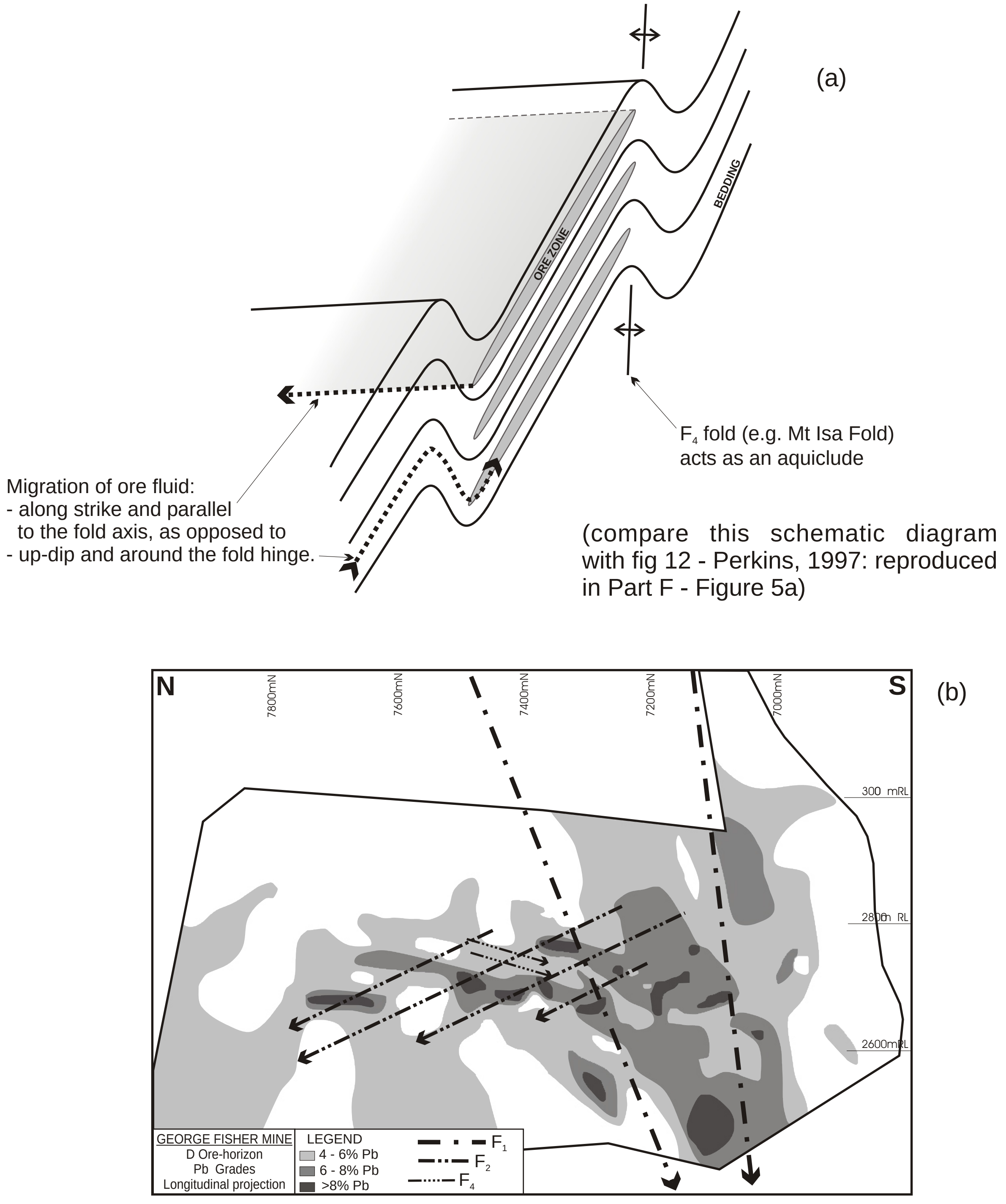

Figure 22. (a) Schematic diagram illustrating the termination of ore zones coincident with F_4 folds as inferred by Wilkinson (1995), Perkins (1997), and Davis (2004). Mineralizing fluids are interpreted by Wilkinson (1995) and Myers et al. (1996) to migrate dominantly along strike. (b) Longitudinal projection of contoured Pb grades from D ore-horizon in the George Fisher Mine. While the steeply pitching F_1 fold is considered to be the main fluid conduit, mineralization occurring within more gently dipping shoots is coincident and parallel to both the dominant F_2 folds and minor F_4 folding. It is inferred that the F_2 fold zones acted as sites for brecciation and along-strike fluid flow during subsequent deformations. The final sites for high grade mineralization are interpreted to be controlled by D_4 kinematics at George Fisher.

parallel to F_2 and F_4 folds (Figure 22b). There is significant contrast in the intensity of D_4 strain between the Mt Isa and George Fisher deposits in terms of the abundance and magnitude of F_4 folds. While F_4 folds dominate the structural grain of the Mt Isa deposit (Davis, 2004), F_2 are the dominant folds at George Fisher and F_4 development is very minor. The swap in S_0/S_4 and S_2/S_4 vergence between Mt Isa and George Fisher may explain why significant F_4 folding has not occurred at George Fisher (refer to Part A). Alternatively, D_4 strain may simply have been heterogeneous throughout the Leichhardt River Fault Trough and, as a result, developed more intense F_4 folding in the Mt Isa area as compared to the George Fisher – Hilton area . The dominant F_4-parallel ore shoot orientation at Mt Isa is therefore not recognized at George Fisher although discrete high-grade shoots are interpreted to parallel F_4 axes (Figure 14b). A similar relationship between high-grade shoots and overprinting fold generations (F_4 on F_2) at Mt Isa (Davis, 2004) is also inferred at George Fisher. The high-grade shoots which parallel F_4 axes in Figure 14b are only mineralized within an envelope which parallels F_2 axes and contains abundant F_2 folding. Note that the F_2/F_4 intersection (L^2_4) at Mt Isa plunges north and defines high grade shoots (Davis, 2004) whereas this intersection plunges approximately 28°→189° at George Fisher (Figure 20a) and does not correlate with an ore shoot orientation. The coincidence of more-intense S_3 and S_4 development in the F_1 short-limb with higher-grade mineralization (Figure 26) implies that the overprinting of the F_1 fold by D_4 deformation features is linked to development of high-grade mineralization. Alternatively, it could be the influence of rheology on the distribution of structure and structural intensity. This is evaluated further in terms of textural and isotopic analyses of George Fisher mineralization in the following parts of the thesis.

4.3 Kinematics controlling ore-sulphide concentration : Implications for extensional and near-mine exploration

Both grade and ore-sulphide thickness data indicate that the higher-grade ore and thicker accumulation of ore-sulphides is spatially coincident with the short-limb of the deposit-scale F_1 fold. Explanation of this empirical relationship incorporating relative structural timing of ore-types will be discussed in later chapters. The relationship will be discussed here in terms of the structural history detailed in Part A.

The F_1 short-limb has a NNW strike relative to the N/NNE striking long-limbs to the north and south (see Part A – Figure 8). Bedding in the F_1 short-limb is sub-parallel to S_2 at George Fisher (Part A – Figure 12) and the D_2 principal compressive stress is sub-orthogonal to the short-limb. The short-limb was therefore a site of high normal-stress during the main-phase of folding, D_2 (Figure 23). Reactivation of bedding with reverse movement may have caused the gently dipping stratigraphy to be dilational in late-D_2. In plan view however, the F_1 short-limb is a restraining bend during late-D_2 reactivation of bedding (Figure 23). Dilation on the F_1 short-limb may have occurred late in D_2 when the F_1 fold was rotated into an orientation favourable for gaping on bedding planes in the D_2 stress-field.

During D_3, top-to-the-east shear and sub-vertical shortening resulted in the reactivation of bedding with a normal sense of shear (Figure 23, Part A - Figure 25). The direction of extension in the plane of S_3 is estimated to be 7°→076° which is sub-parallel to the strike of the F_1 axial planes (Part A – Figure 8). The vector of reactivation, defined by the intersection of bedding with the plane containing both the principal compressive stress

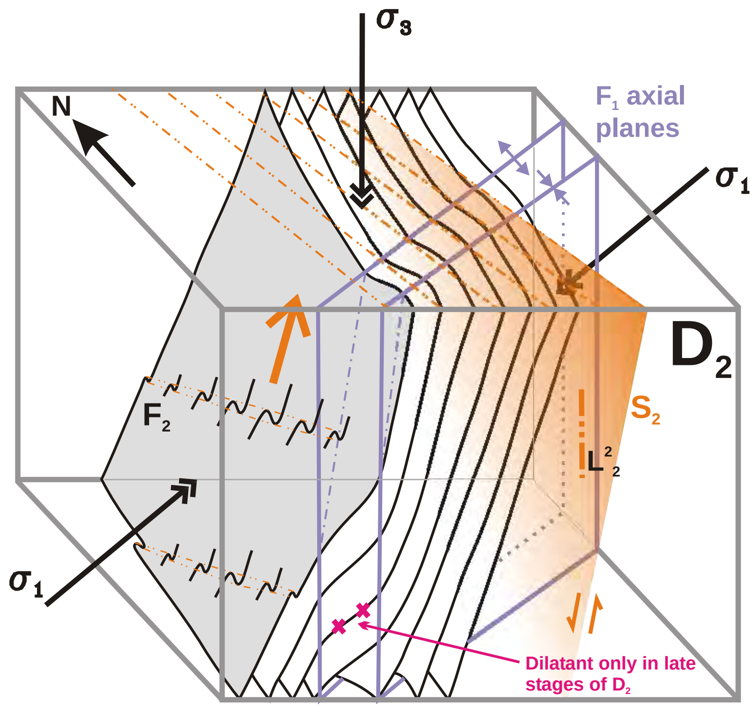

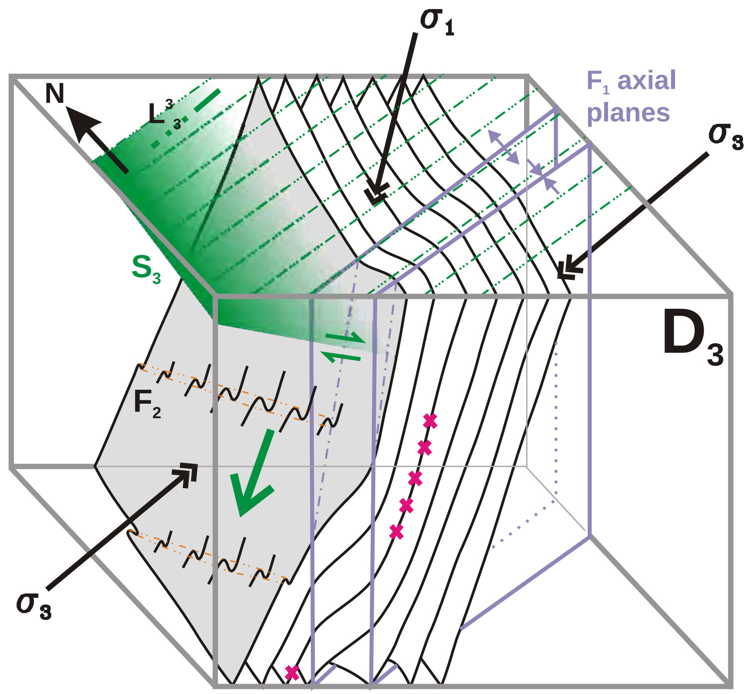

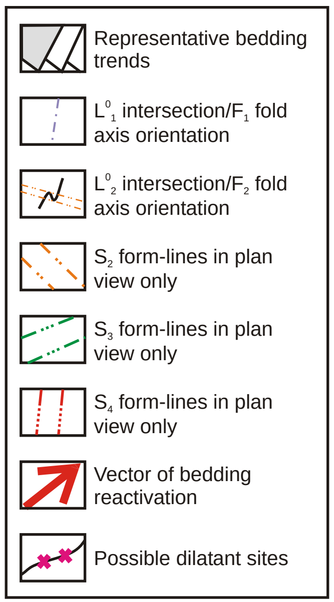

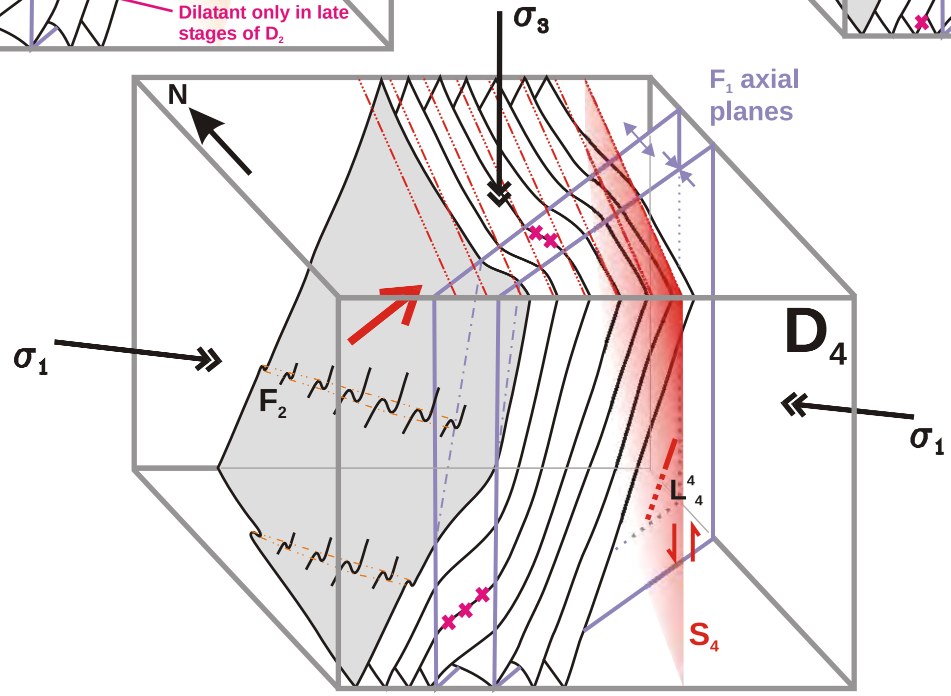

Figure 23. Schematic block diagrams of major structural features at George Fisher and the resultant reactivation of bedding during deformation episodes D_2-D_4. The vector of reactivation of bedding is defined by the intersection of the plane containing σ_1 and the direction of extension (e.g. L^4_4), with bedding.

direction and the direction of extension in the respective foliation, and is sub-parallel to the F_1 fold axes (Figure 23). This geometry results in no dilation where bedding changes strike in the short-limb. Normal reactivation of bedding in the area of the short-limb zone will only induce gaping on bedding planes where bedding has steeper dip and where F_2 folds inhibit bedding reactivation (Figure 23). This results in minor gaping of bedding planes and/or micro-brecciation. This deformation event is of particular low strain and it is likely that any brittle deformation during D_3 reflects this subtlety. Minor sub-horizontal quartz and carbonate fibres in mineralized ‘layers’ (Part A – Figure 18c) indicate that gaping has occurred on bedding during D_3. Unfolding and concomitant brecciation of F_2 folds (Figure 24) results in further brecciation and mineralization.

The effects of D_4 reactivation of bedding results in low stress in the short-limb and D_4 kinematics are also conducive to gaping of bedding in the F_1 short-limb (Figure 23 and 24). The change in strike and dip of bedding in the short-limb, relative to the northern and southern long-limbs, means that the F_1 short-limb has the potential to act as a dilational bend within the D_4 stress field (Figure 24). Predicted syn-D_4 horizontal and vertical components of displacement along bedding planes result in dilation in the F_1 short-limb (Figure 24), mimicking the distribution of high-grade mineralization in vertical section (Figures 4-6) and in plan view (Figures 7-9). F_2 folds may further focus dilation during subsequent deformation, as they act as a heterogeneity which focuses deformation through obstruction of bedding reactivation in the gentle, north-plunging shoots parallel to L^0_2 observed on longitudinal projections of metal grades (Figures 14b and c). This is discussed in more detail in Part D.

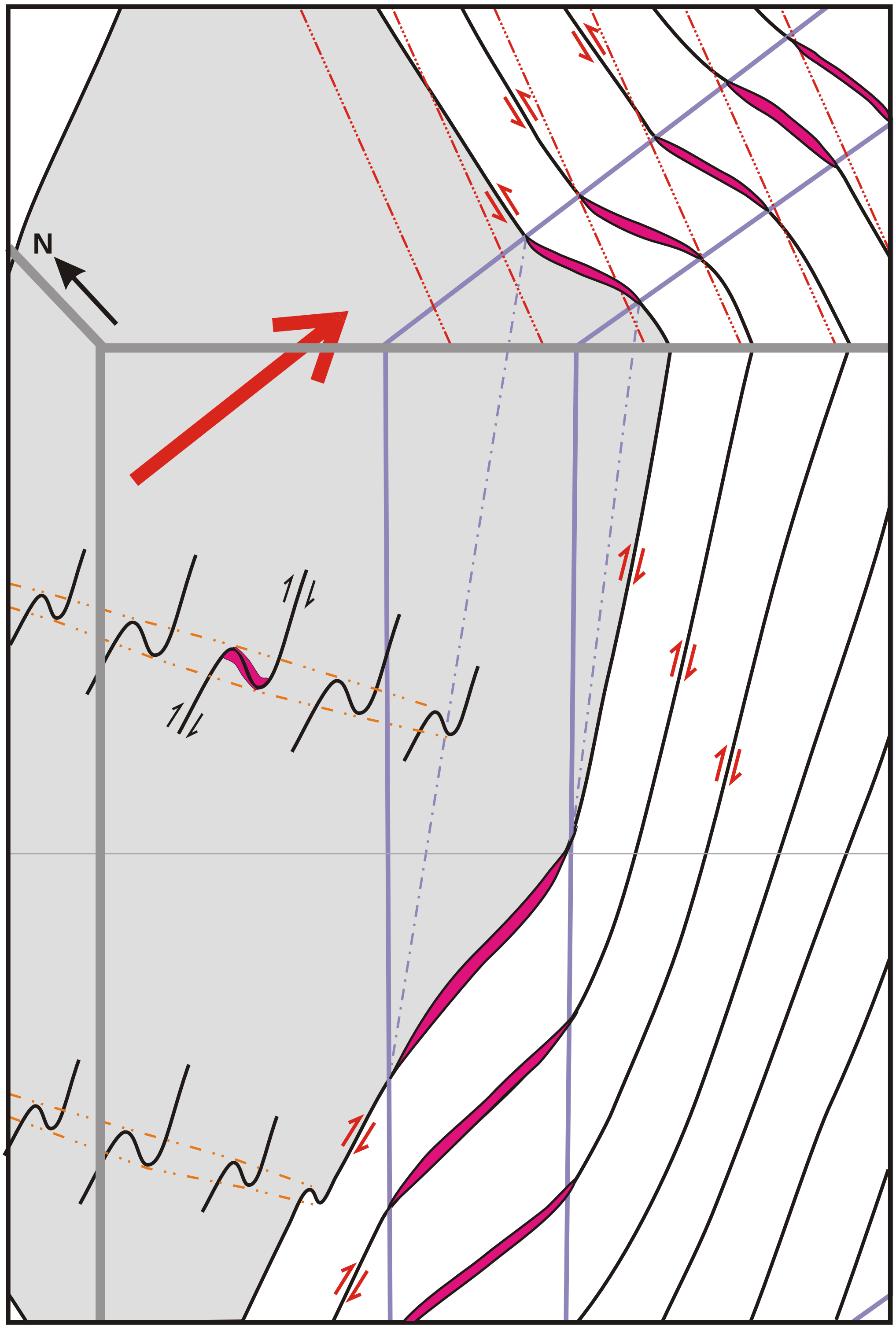

Figure 24. Enlarged portion of Figure 22 displaying the effects of D_4 reactivation of bedding on the F_1 short-limb. Note that dilation (magenta-coloured areas) occurs in the short-limb due to both horizontal and vertical components of displacement.

Distribution of thicker and higher-grade ore appears to be a function of the tightness of the F_1 fold. That is, where the fold is tightest and the angle between short and long-limbs (see Part A - Figure 8) is greatest (e.g. C ore-horizon, Figure 16c) the sulphide concentrations have the most restricted along-strike distribution. Conversely, where the fold opens and becomes a weak flexure in bedding the along-strike distribution of ore-sulphides is at its greatest (e.g. G ore-horizon, Figure 18c). D ore-horizon is situated midway between C and G ore-horizons and both the tightness of fold and distribution of sulphides are consistent with this and form the mid-point. When considering the dilational-bend hypothesis discussed previously, the tightness of the F_1 fold is critical in controlling the net-dilation in the short-limb zone during bedding-plane reactivation. Assuming consistent displacement during bedding-plane reactivation, greater dilation will occur in areas of tighter folding than in areas where the F_1 fold is an open flexure in bedding (Figure 25). Width of the fluid-channel or strike-extent may affect the relative intensity of mineralization. The region of low stress/maximum dilation (correlating with the short-limb-zone) in C and D ore-horizons has a smaller area than that of G ore-horizon. Focussing of fluids through a smaller portion of the stratigraphy may result in higher-grade ore whereas a greater strike-extent may result in higher-tonnage but lower grades. This is observed with respect to Pb mineralization when comparing C, D, and G ore-horizons (Figures 8, 13, 14, 15).

Also, a relationship between intensity of later foliations and the geometry or ‘tightness’ of the F_1 fold is observed. The intensity of S_3 and S_4 crenulations is contoured on Figure 25. The areas of moderate to high relative intensity crenulation development correlate strongly with the high-grade mineralization on the corresponding level plan of Pb grades

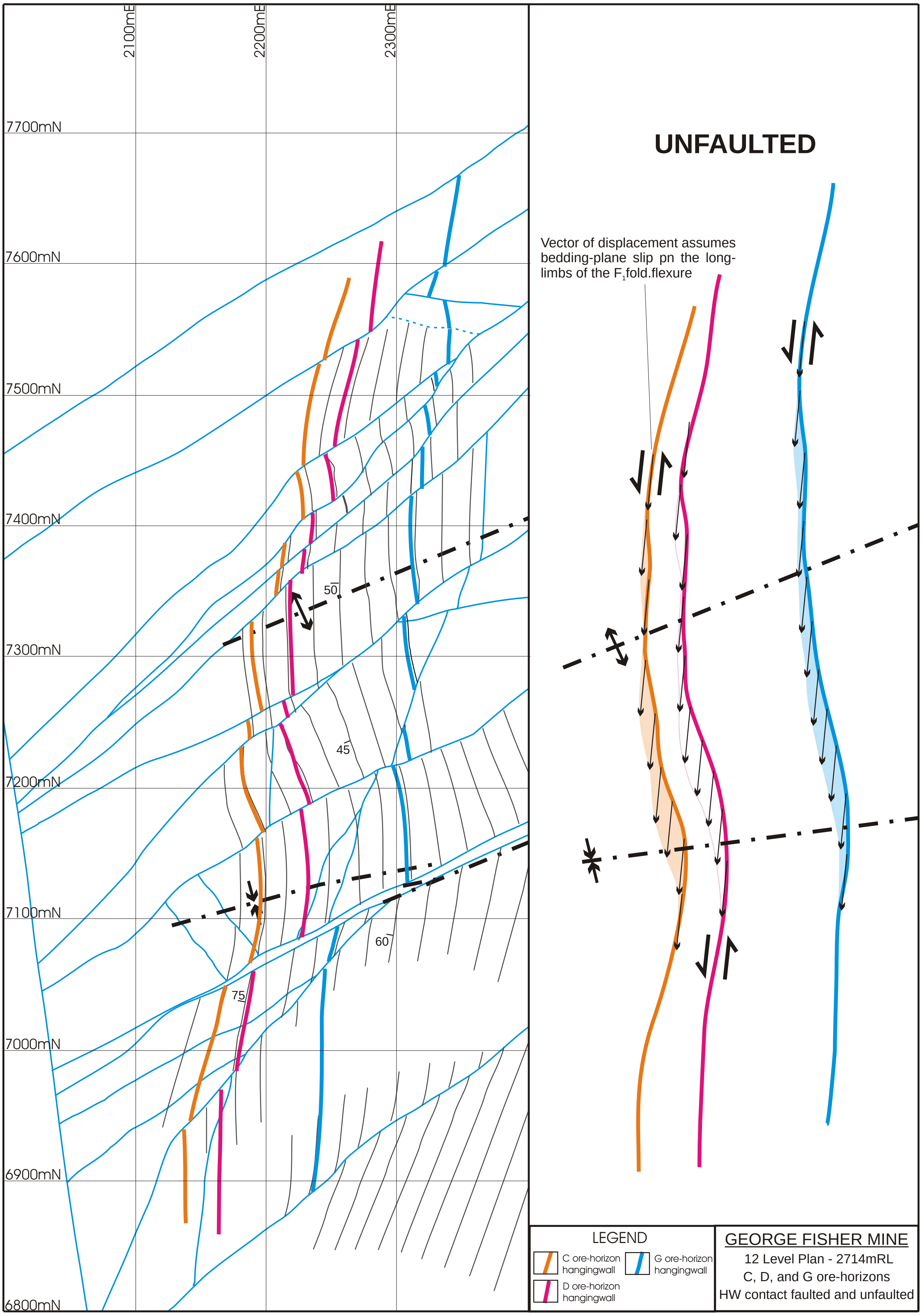

Figure 25. Unfaulting of the C, D, and G ore-horizon hangingwall positions and net-dilation during bedding plane reactivation syn-D_4. See text for discussion.

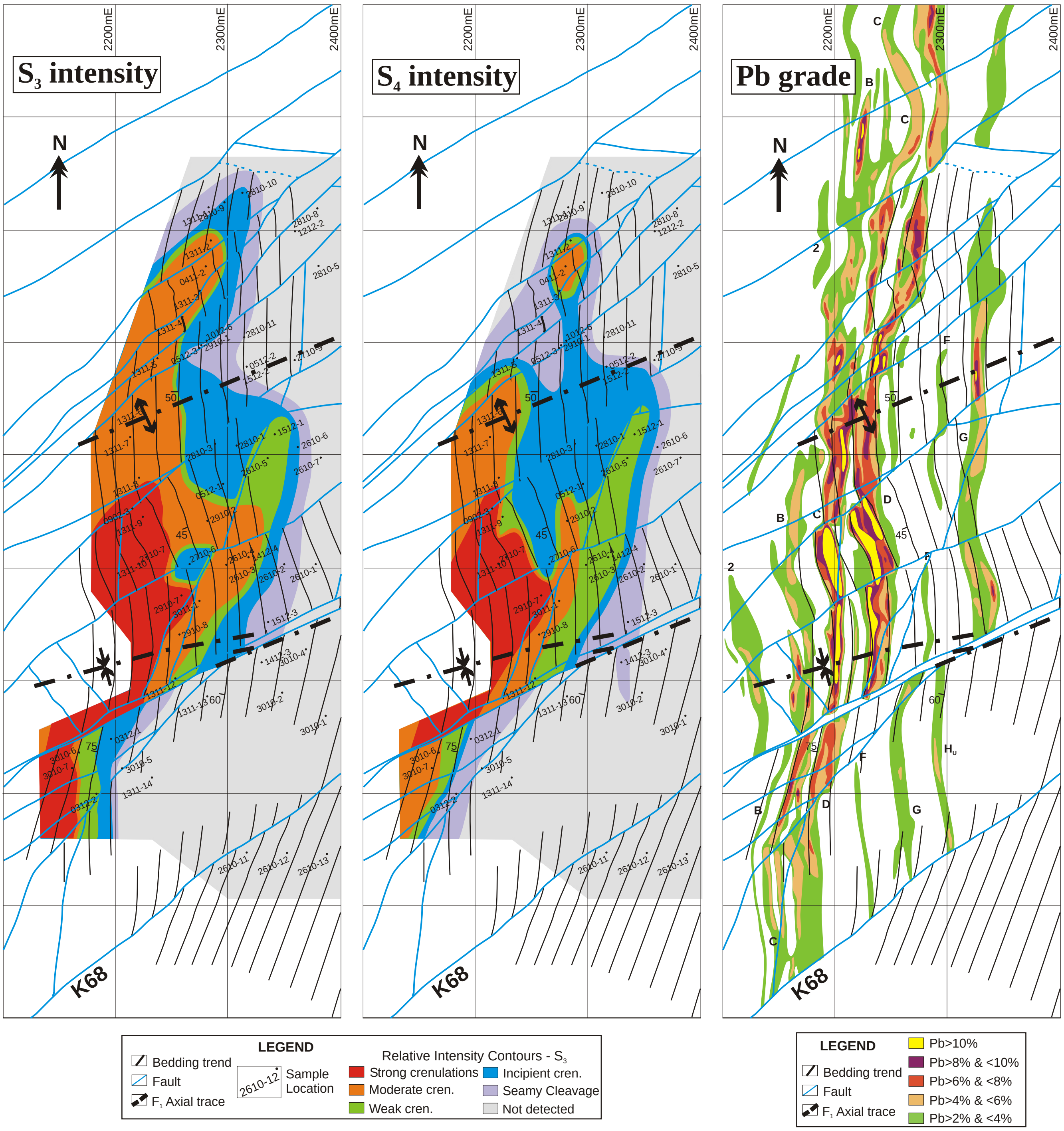

Figure 26. An empirical relationship exists between the location of more intense S_3 and S_4 crenulation development (as judged by visual comparison) and higher Pb grade at 12 level (2714mRL) in the underground mine. Crenulation development is more intense in the F_1 short-limb zone where bedding is more oblique to the overprinting S_3 and S_4 foliations. Note also the correlation of intensity of S_3 and S_4 crenulations. Further detail is shown on Part A: Figures 22 and 30 and Part B: Figure 8.

(Figure 26). Note that the distribution of Zn in this view (refer to Figure 7) does not correlate as strongly as Pb reflecting the broader distribution of Zn observed in longitudinal projections (Figure 13a, 14a, and 15a). The correlation of more intense mineralization occurring in sites of crenulation development during D_3 and D_4 suggests that the orientation of bedding in the F_1 short-limb is such that bedding does not reactivate efficiently and crenulations and minor folds develop. This process would create dilatancy at sites of rheological contrast such as between layers of fine-grained pyrite and massive mudstone and where older folds (F_2) and fabrics are oblique to the younger deformation.

If the F_1 fold is a key element in concentration of ore-sulphides, as suggested by this study, the location of other favourably oriented structures within the prospective Urquhart Shale could be identified. An alternative hypothesis may be that pre-deformational mineralization has focussed F_1 and subsequent deformation, still suggesting that the location and geometry of structures act as a guide to ore. Thicker occurrences of ore-sulphides occur north of the current mining area at George Fisher. This can be recognized in Figures 16c, 17a and c, and 18a and c. The thicker ore-sulphide occurrence does not translate into high-grade intersections in Figures 13 to 15. However, a left-hand bend in the strike of bedding occurs at the same northing as the thicker sulphide occurrence (~7650mN) with the same asymmetry as the F_1 fold at 7100mN (Part A - Figure 30). Exposure of this northern area is limited but it is possible that this left-hand flexure is similar in nature to the F_1 fold in the current mine area. Thickening, mainly in Zn, in C, D, and G ore-horizons (Figures 16c, 17a and c, and 18a and c; respectively) is spatially coincident with this change in strike but does not comprise economic ore possibly due to the weakness of the flexure.

5. Conclusions

Particular structural domains at the George Fisher deposit correlate with higher-grade and thicker accumulations of Zn-Pb-Ag sulphides.

The dominant ore-shoot is located in a deposit-scale F_1 fold, central to the George Fisher workings. This is a region of coincident higher-grade mineralization and thicker accumulation of ore-sulphides. The ore-shoot orientation and F_1 axial planes are parallel to each other in the C, D, and G ore-horizons resulting in a corridor of greater metal concentration across-strike of bedding/stratigraphy.

Another significant trend in grade distribution is sub-parallel to the orientation of F_2 fold axes. This secondary trend pitches gently to the north in longitudinal projections. The main zone of economic ore at George Fisher occurs at the intersection of the steeply plunging F_1 fold and gently plunging F_2 folds.

A minor trend in higher grade, thicker zones of mineralization observed in the D and C ore-horizons parallels the orientation of F_4 fold axes. This ore-shoot orientation is sub-horizontal to very-gently pitching to the south in longitudinal projections.

In order to explain the coincident distribution of metals and structural domains, the kinematics of each deformation event has been analyzed to determine the conditions favourable for enhanced fluid-flow in the F_1 short-limb.

Subhorizontal shortening in late-D_2, subsequent to rotation of F_1 fold axes about macroscale F_2 folds, may be conducive to some dilation on the gently dipping bedding during west-side-up reactivation of bedding. There is little potential for significant strike-slip dilation as the F_1 short-limb is perpendicular to the principal compressive stress in D_2 and the s-shaped F_1 fold is a restraining bend to along-strike bedding reactivation during D_2. Reactivation of bedding is parallel to $L^0{}_1$ and therefore oblique slip on bedding-surfaces, required for dilation in the short-limb, does not occur. D_3 causes reactivation of bedding with a normal sense of shear parallel to the $L^0{}_1$ direction. Gaping during D_3 can only occur where the dip of bedding is steeply dipping or irregular due to F_2 folding. The D_4 stress field orientation is appropriate for sinistral-reverse reactivation of bedding in the F_1 short-limb.

Trends in the obliquity of S_4 to bedding and the associated intensity of the S_3 and S_4 foliations correlate with areas of higher-grade. A relationship between the tightness of the F_1 fold and the potential net-dilation that may have occurred during bedding plane reactivation is inferred. This relationship corresponds to the amount of ore-sulphide accumulation and grade of mineralization.

The F_1 flexure is interpreted to be a key structural control on the location of the deposit and is inferred to have acted as heterogeneity in the overall structural architecture which focussed dilation during subsequent D_2-D_4 deformation thereby promoting brecciation and fluid flow. Sulphide mineralization is interpreted to have occurred at least partly during D_4 based on empirical geometric relationships between sulphide distribution and structural features. The location of other structures with similar geometry within the prospective Urquhart Shale is considered important for locating any further high-grade Zn-Pb-Ag ore.

The structural localization of ore-sulphides at George Fisher demonstrated at the larger scale in this study (meso- to micro-scale analysis in Part D) implies deposition of sulphides in their current position during D_2 to D_4. Correlation of thicker sphalerite and galena ore-types at the deposit-scale suggests a similar control on the deposition of both ore-sulphides. The role of remobilization in formation of the orebodies is discussed in relation to individual textural types and their relative structural timing in Part D. The patterns in metal/ore-distribution recognised as part of this study indicate that mine-scale structural domains control the present-day metal distribution.

References

Chapman, L.H., 1999. Geology and genesis of the George Fisher Zn-Pb-Ag deposit, Mount Isa, Australia. (Unpublished PhD thesis – James Cook University, Townsville).

Chapman, L.H., 2004. Geology and mineralization styles of the George Fisher Zn-Pb-Ag deposit, Mount Isa, Australia: Economic Geology, v. 99, p. 233-255.

Davis, T.P., 2004. Mine-scale structural controls on the Mount Isa Zn-Pb-Ag and Cu orebodies: Economic Geology, v. 99, p. 543-559.

Domagala, J., Southgate, P.N., McConachie, B.A., and Pidgeon, B.A., 2000. Evolution of the Palaeoproterozoic Prize, Gun, and Lower Loretta Supersequences of the Surprize Creek Formation and Mount Isa Group: Australian Journal of Earth Sciences, v. 47, p. 485-508.

Myers, R., Ceremuga, C., Clark, D., McSkimming, D., Price, S., Tuesley, M., and Wilkinson, D. 1996. Mount Isa lead-zinc minerlisation: What controversy? In: Baker, T., Rotherham, J., Mark, G., and Williams, P.J. (eds), New Developments in Metallogenic research: The McArthur, Mt Isa, Cloncurry Minerals Province, p. 33-35. James Cook University Economic Geology Research Unit Contribution 55.

Perkins, W.G., 1997. Mount Isa lead-zinc orebodies: Replacement lodes in a zoned syndeformational copper-lead-zinc system?: Ore Geology Reviews, v. 12, p. 61-110.

Perkins, W.G. and Bell, T.H., 1998. Stratiform replacement lead-zinc deposits: A comparison between Mount Isa, Hilton, and McArthur River : Economic Geology, v. 93, p. 1190-1212.

Valenta, R.K., 1988. Deformation, fluid flow and mineralisation in the Hilton area, Mt Isa, Australia. (Unpublished PhD thesis – Monash University. Melbourne).

Valenta, R.K., 1994. Deformation in the host rocks and stratiform mineralization in the Hilton Mine area, Mt Isa: Australian Journal of Earth Sciences, v. 41, p. 429-443.

Wilkinson, D.L., 1995. Structural termination of 8 orebody and its implications for the genesis of lead-zinc-silver mineralisation, Mount Isa, Queensland: Unpublished Hons thesis, James Cook University, Townsville, Australia.

Wilson, A., 1992. Metal distribution in the Hilton Mine, Mount Isa, and it's genetic implications: Unpublished B.Sc. Honours thesis, Monash University, Melbourne, 159p.

PART C

The relationship between the fractal dimension of sphalerite grain boundaries and sulphide deformation: Application of the coastline method in microstructural studies.

Abstract

Several microstructures in a limited number of geological materials appear to have fractal geometries, which have a number of useful applications. This study demonstrates that sphalerite grain boundaries have fractal geometries which can be related to deformation history when analyzed using etched samples under the optical microscope. The fractal dimension of grain boundaries, determined using the coastline method, of undeformed, deformed, and recrystallized sphalerite grains have average values of 1.01, 1.09, and 1.05 respectively and 95% confidence intervals of their means do not overlap. The fractal dimension increases from the undeformed to the deformed grains because of increasing grain boundary complexity caused by grain boundary migration, and reduces in the recrystallized, strain-free grains due to grain shape equilibration. Quantitative discrimination of the three classes of grains is possible on a log-normal plot of grain size against fractal dimension. These results have potential applications to ore deposit studies where the timing of deformation relative to sulphide mineralization is unclear.

1. Introduction

Several microstructural properties appear fractal. This means that one or more aspect of the microstructures exhibits statistical self-similarity or scale-invariance (Mandelbrot, 1967) which can be quantified by obtaining the fractal dimension. Properties of geological materials investigated using fractal analysis include grain shapes (e.g. Orford and Whalley, 1987), surface geometry (e.g. Kristáková and Kupková, 1994), porosity (e.g. Pape et al., 2000), and particle size distributions of fragmented rocks (e.g. Sammis and Biegel, 1989). Analyses of these fractal properties have been used to constrain a variety of microstructural problems, including geothermometry (e.g. Kruhl and Nega, 1996), strain and strain rate estimation (Tanaka et al., 1998a, 1998b; Takahashi et al., 1998), understanding crystallization (e.g. Jacob et al., 1994; Ortoleva et al., 1994) and fragmentation processes (e.g. Blenkinsop, 1991). It seems likely that there are many other potential applications, but these depend on establishing the fractal nature of microstructural properties.

Sulphide microstructures are the key to understanding sulphide deformation mechanisms (e.g. McClay, 1980; McClay and Ellis, 1983; and Cox, 1987) and essential pieces of evidence in understanding mineralizing processes. For example, the state of sulphide deformation can reveal whether mineralization is pre-, syn- or post-tectonic in deposits where there is ambiguity as to whether syngenetic or epigenetic models of ore genesis are applicable. At the Mt Isa Pb-Zn deposits, mineralization has been interpreted to have occurred synchronous with sediment-deposition (Finlow-Bates and Stumpfl, 1979; Russell et al., 1981; Sawkins, 1984), during diagenesis of the sedimentary pile (Cooke et al., 2000; and Chapman, 2004) and during late orogenic deformation of the sedimentary sequence (Blanchard and Hall, 1942; Perkins, 1997; Davis, 2004). Analysis of sulphide textures and the intensity of deformation of the ores can aid in determining the timing of ore formation and thus potentially lead to a syn- or epigenetic interpretation. However, the interpretation of deformation histories in sulphides is complicated by their propensity for recrystallization (Ewers, 1967; Clark and Kelly, 1976; Stanton and Gorman, 1968; and Cox, 1987), and the opaque character of sulphides, although the latter problem can be solved by electron microscopy (e.g. Boyle et al., 1998; Trimby et al., 2000). Another problem is that microstructures such as grain shapes commonly show intermediate morphologies that do not readily allow samples to be characterized by a dominant deformation mechanism on the basis of qualitative observations. Methods of quantitative microstructural analysis can overcome this difficulty.

This work was undertaken as a preliminary step in assessing whether the use of fractal analysis can assist in microstructural interpretation of sulphides. The aim of this study is investigate whether sphalerite grain boundaries have fractal properties, and whether these can be used to quantify microstructural history, in particular, to provide evidence for deformation and recrystallization. The use of etching and optical microscopy as a simple technique to reveal grain boundary shape and grain size is emphasised (cf. Herwegh, 2000). The fractal dimension is shown to be a sensitive indicator of the degree of sulphide deformation.

2. Method

2.1 Methods of grain boundary characterization

Several methods of object boundary characterisation have been proposed in the literature which are well summarised and compared by Berube and Jebrak (1999). The coastline (Mandelbrot, 1967) or structured walk method, as applied in this study, has several advantages:

- The method has been applied successfully to particle analysis (e.g. Orford and Whalley 1987, Hayward et al., 1989) and grain boundaries (Kruhl and Nega, 1996).
- It can handle closed and open shapes
- A calibration exists for this method which relates temperature of deformation to grain boundary geometry of quartz (Kruhl and Nega, 1996).

The method characterises the complexity of a grain boundary by its fractal dimension, which is obtained from the relationship between the length or perimeter of the grain boundary, P, at differing ruler length or step-size, L (Figure 1). Generally, measurement of a boundary using increasing step sizes results in estimates of the length of the boundary decreasing. The roughness of the grain boundary is characterised by the exponent of the relationship between P and L;

$$P \sim L^{1-D}$$

D is the fractal dimension of the grain boundary. A straight line has a D value = 1, and progressively more complex grain boundary shapes have larger D values. This

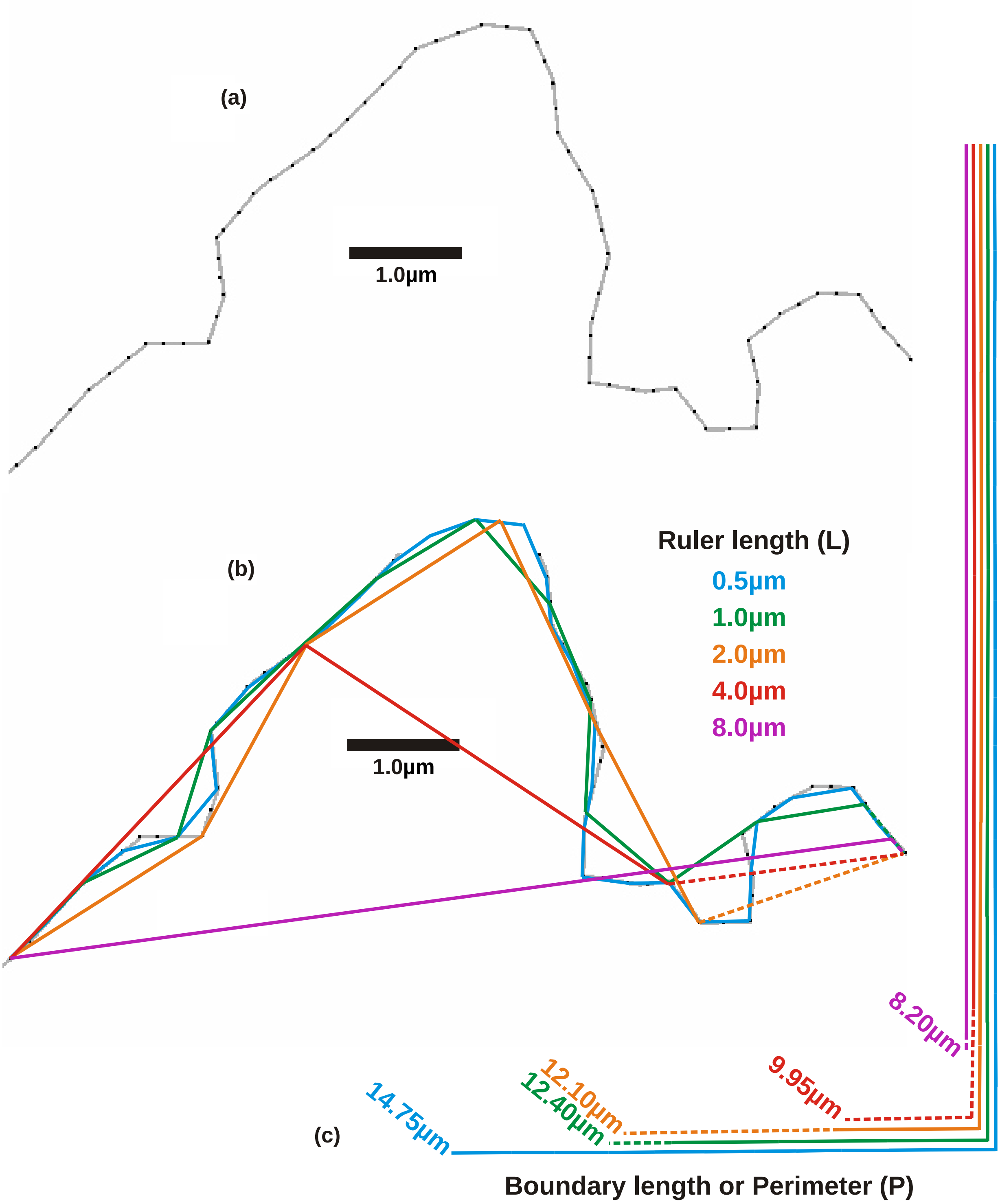

Figure 1. Graphical representation of the coastline algorithm. (a) Grain boundary outline digitized at 0.25μm spacing. (b) Outlines constructed at various ruler lengths showing the different paths taken. Dashed lines indicate the 'remainder'. (c) Comparison of the length of the paths (straightened). The length of the outlines decreases with increasing ruler size. The rate of change of P at varying values of L determines the fractal dimension.

relationship was applied to both whole grains and fragments of grain boundaries in this study. Further explanation of the particular method of fractal analysis employed in this study is described in section *2.3 Procedure*.

2.2 Sample preparation

The samples used in this study were prepared as polished thin-sections for use in optical microscopic analysis. All thin sections were etched with concentrated (55%) Hydriodic acid (HI) (c.f. Stanton and Gorman (1968), Stanton and Gorman-Willey (1971), and Gregory (1978)) for periods of one to five minutes until a suitable depth of etching was achieved. Recognition of microstructures in sulphides examined as polished thin-sections is not possible in detail unless the sulphides are etched (compare Figure 2a, c, e to Figure 2b, d, f). Intracrystalline deformation microstructures such as grain size, grain shape, and shape-preferred orientation can only be determined using optical microscopy after etching (e.g. McDonald, 1970; McClay and Atkinson, 1977; McClay, 1983; Siemes, 1976, 1977; Stanton and Gorman, 1968; and Stanton and Gorman-Willey, 1971; and Cox, 1987. Despite the advice given in Cox (1987), etching is still used less commonly in studies of sulphide mineral deformation than in metallurgical studies. The present study re-emphasises the importance of this etching technique. Suitable etchants are available for most sulphide minerals (e.g. Ramdohr, 1969).

2.3 Procedure

Grain boundaries or parts of grain boundaries were selected for fractal analysis using the following criteria:

- the boundary consists of sphalerite in contact with sphalerite,

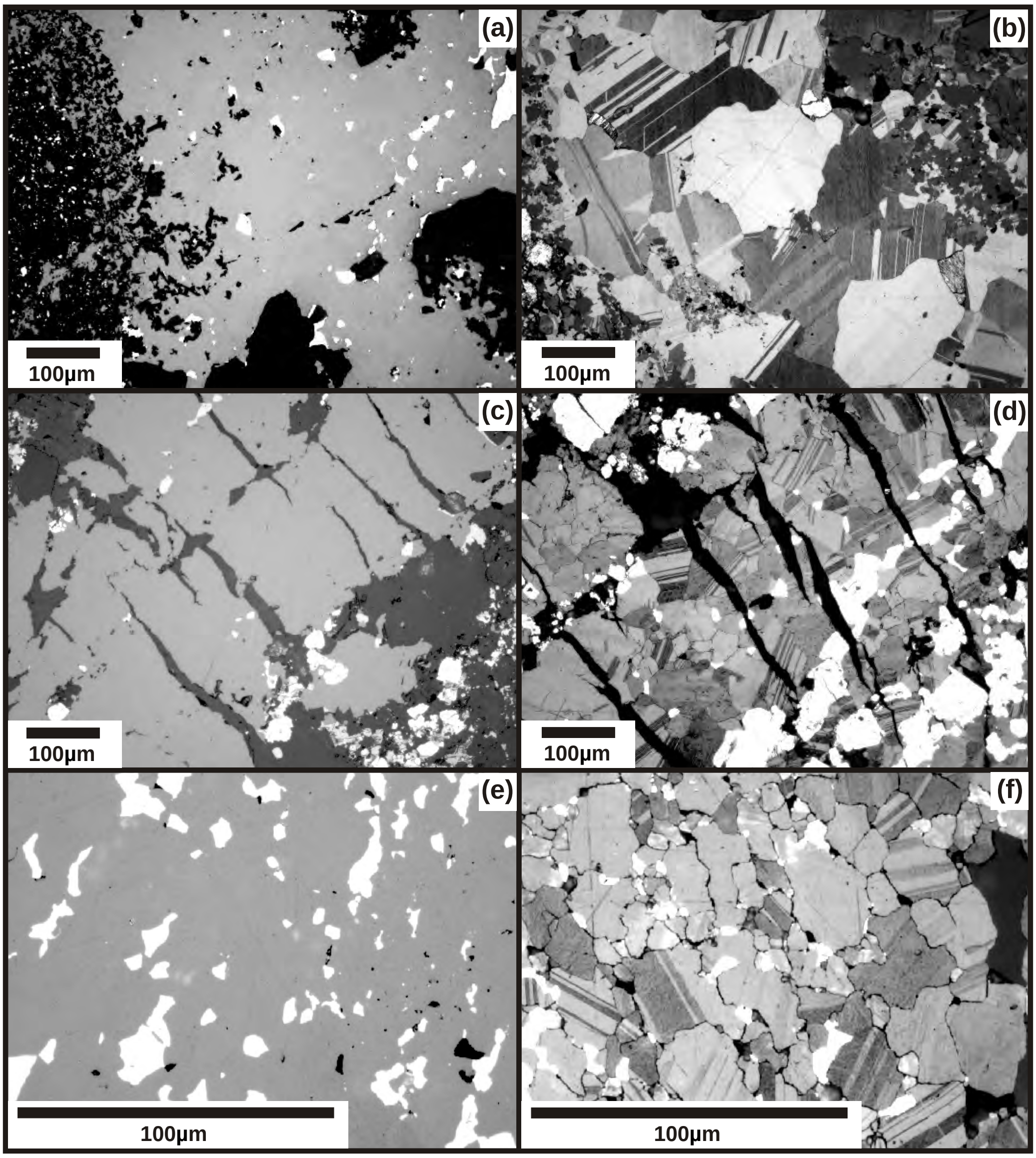

Figure 2. Photomicrographs of polished thin-sections in reflected light, demonstrating the benefit of etching sulphide-rich samples. Sphalerite is the dominant sulphide in each photomicrograph. (a), (c), and (e) are normal polished thin-sections and (b),(d), and (f) are etched portions (etched with conc. HI) of the thin-sections pictured in (a), (c), and (e); respectively. The samples are from the George Fisher deposit, Australia, sample 0103-1 (a and b), Silver Spur deposit, Australia (c and d), and Rammelsberg, Germany (e and f).

- the grain is representative of the population as judged by visual comparison,
- the section is etched deeply enough that the boundary could be traced confidently under high magnification, and
- the boundary is of sufficient length or grains are of sufficient diameter for a suitable amount of data to be collected. This criterion meant that no grains smaller than 10µm were analysed.

Digital photomicrographs of grain boundaries in reflected light were taken under 50x magnification, with the incident light aperture diaphragm adjusted to show high relief, which aided more precise definition of the grain boundary. The etched zone incorporating grain boundaries averaged approximately 0.5µm wide. An outline of the grain boundary was constructed using a 1.00µm (the limit of resolution of the original image whereby the boundary could be traced accurately) segmented line. The outline was digitised at 0.25µm intervals, and the coordinates were processed by a computerized coastline algorithm using ruler lengths from 1.00µm in 0.25µm increments up to the diameter of the grain or the length of the partial grain boundary. The procedure was then repeated from the opposite end of the grain boundary (in the reverse direction) in order to assess sensitivity of the method to starting position (cf. Aviles et al. 1987), and the difference between the forward and reverse measurements is reported as 'coastline error'. Error associated with manual digitizing of points on the grain boundaries has been assessed (Figure 3). This error is negligible and has a magnitude outside the four decimal places that the fractal dimension is reported to in this study.

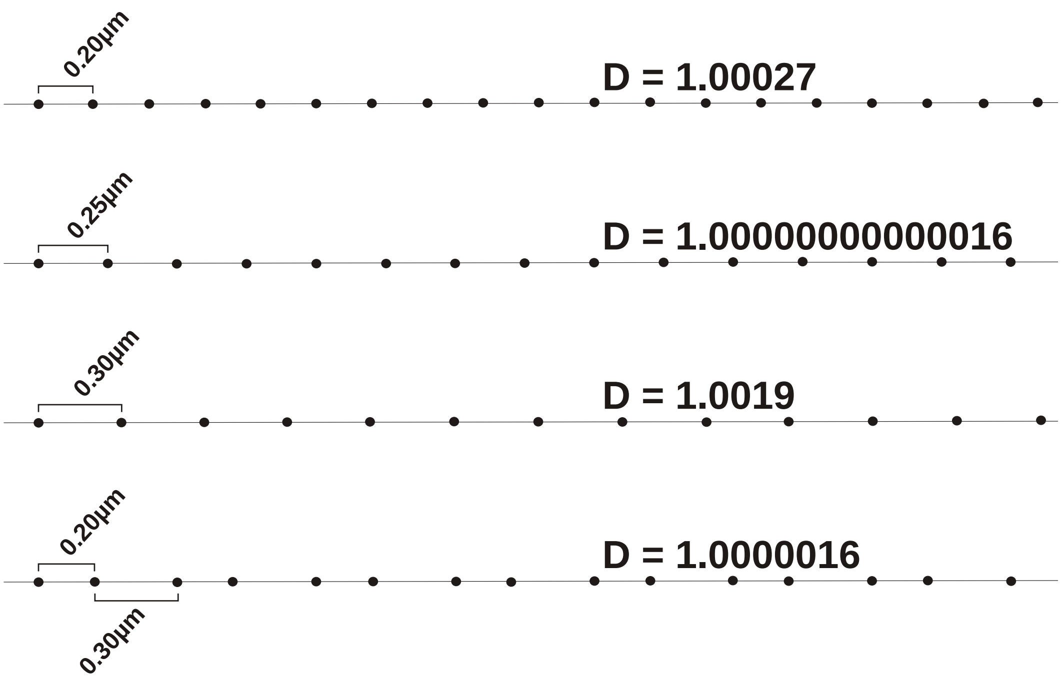

Figure 3. Assessment of the sensitivity of error associated with manual digitizing of points on a boundary. A straight line has been used as the standard for this analysis as it has a theoretical fractal dimension (D) of 1. Fractal dimensions have been calculated for the straight line at varying point spacing. The best approximation (~D=1) is achieved by a 0.25µm spacing as the algorithm incorporates a 0.25µm increase in L with each pass. The last example best represents the actual digitizing whereby point spacing occurred between 0.20 and 0.30µm and averaged at approximately 0.25µm. In this study, D is reported to four decimal places (1.0000 in the bottom example), the effect of digitizing error is therefore considered negligible.

Regression of the logarithmic values of P and L was performed between limits within which the data best fitted a straight line (Figure 4). The upper limit is constrained by the onset of a stepping of the data (Figure 4a, b) whereby P increases with increasing L. This phenomenon is in opposition to the general trend of data where P reduces with increasing L (Figure 4a, c) and is inferred to occur when L approximates the sides of the grain being studied (Figure 4b). The gradient of the line of best fit to the data defines the fractal dimension. The fractal dimension reported is the average of the forward and reverse measurements; standard errors of regression and correlation coefficients were also recorded.

3. Samples studied

A total of 107 grain boundaries have been studied from 18 mostly unoriented samples, including 5 photomicrographs from the literature (Table 1). The selection of samples included obviously deformed, undeformed, and recrystallized sphalerite so as to quantify the D of each. Samples were obtained from 12 deposits/localities, mostly from Australia (Table 1) so as to gain exposure to a broader spectrum of sphalerite textures compared to a single, deposit-specific study. A significant amount of data has been obtained from samples from the George Fisher Zn-Pb-Ag deposit, Mt Isa Inlier, Australia; as this work is part of a larger study investigating the structural history of that deposit.

4. Sulphide microstructures

Within the samples studied, 3 main (A, B, and C) and 2 subordinate (D and E) classes of microstructures were observed.

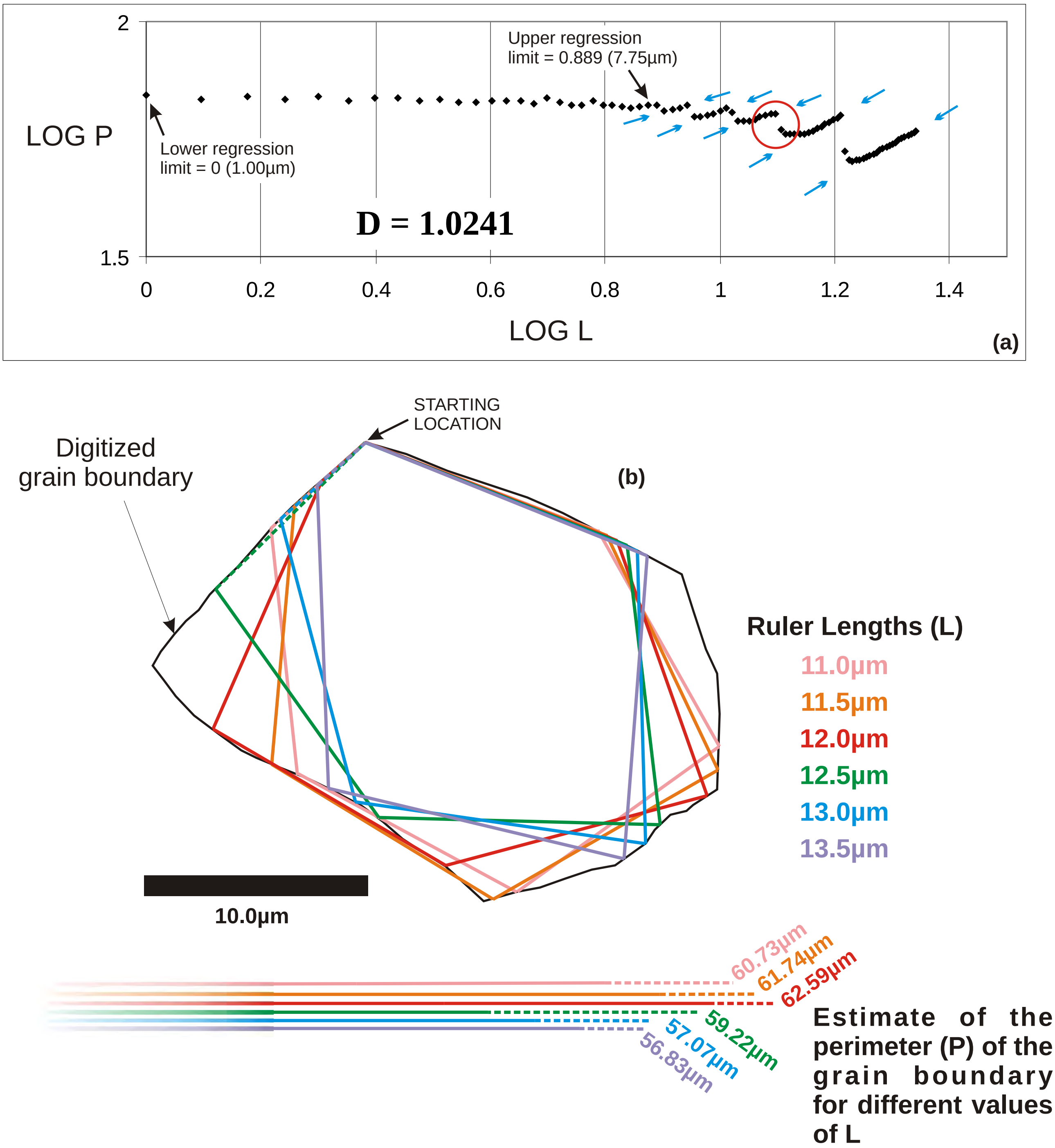

Figure 4. (a) Data displayed on a Log P vs Log L graph. Regression limits are determined by visual observation of the limits within which data is best fitted by a straight line. The upper limit coincides with a stepping of the data (blue arrows) at higher values of L. (b) Grain boundary and paths at different values of L which correspond to the area indicated by a red circle in (a). The estimates of P at the various ruler lengths indicates that P increases with increasing L and reaches a maximum at L=12.0µm and from that point, P decreases with increasing L conforming to the overall trend of the dataset. This step effect occurs where the ruler length (L) approximates the sides of the grain boundary and the sharp decrease in P at L=12µm corresponds with a change from six to five sided polygonal paths.

Deposit	Location	Samples		Images		Total	
		No	Grains	No	Grains	Samples	Grains
George Fisher Zn-Pb-Ag Mine	Queensland, Australia	5	39			5	39
Welcome Au Mine	Queensland, Australia	1	3			1	3
Mt Molloy Cu-Zn Mine[1]	Queensland, Australia	1	3	2	17	3	20
Silver Spur Ag Mine	Queensland, Australia	1	9			1	9
Century Zn Mine	Queensland, Australia	1	1			1	1
Mt Muro Au Mine	Kalimantan, Indonesia	1	2			1	2
Ertsberg Cu-Au Mine	West Papua, Indonesia	1	2			1	2
Rammelsberg Zn-Pb-Cu-Ag Mine	Germany	1	22			1	22
Los Minas dos Ingleses	Brazil	1	2			1	2
Sullivan Zn-Pb Mine[2]	B.C., Canada			1	4	1	4
Rosebery Au-Cu-Pb-Zn Mine[3]	Tasmania, Australia			1	1	1	1
East Tennessee[4]	U.S.A.			1	2	1	2
						18	107

Table 1. Sample locations. (Images were obtained from [1]Gregory, 1978; [2]McClay, 1982; [3]Stanton and Gorman, 1968; [4]Clark and Kelly, 1973)

4.1 Class A

Sphalerite grains in this class are characterised by wide, straight, parallel-sided twins which are free of offsets and that are continuous across the grains (Figure 5a and b). There is no preferred orientation and grain size is approximately 1.0mm. Grain size, in this study, represents an estimate of the diameter of the grain obtained from the average of the length of the long and short axes of the grain. Infill of crystal vughs (Figure 5b) and lack of deformation in the enclosing gangue crystals is observed. The characteristic shape of the grain boundaries is planar to smoothly curved (Figure 5a). These grains are interpreted to represent undeformed sphalerite.

4.2 Class B

Sphalerite grains within this class display irregular grain-shapes (Figure 5c), weak shape-preferred orientation, or bent or dislocated twins (Figure 5d). Truncation of twins (Figure 5c and d) or twins with variable width are also commonly observed. Grain size is approximately 100µm. Larger grains with these microstructures (Figure 5d) exist within a matrix of less-strained equant sphalerite, and are interpreted to be relicts. A bimodal grain size distribution is commonly observed. The grain boundary shape is irregular (Figures 5c and d) as compared with Class A (undeformed) sphalerite (Figure 5a) at the same scale. The commonly accepted interpretation of these microstructures (e.g. Passchier and Trouw, 1996; and Blenkinsop, 2000) indicates that they are the product of intracrystalline plasticity. Class B sphalerite grains represent relics of deformed grains which have not totally recrystallized into new low-strain grains.

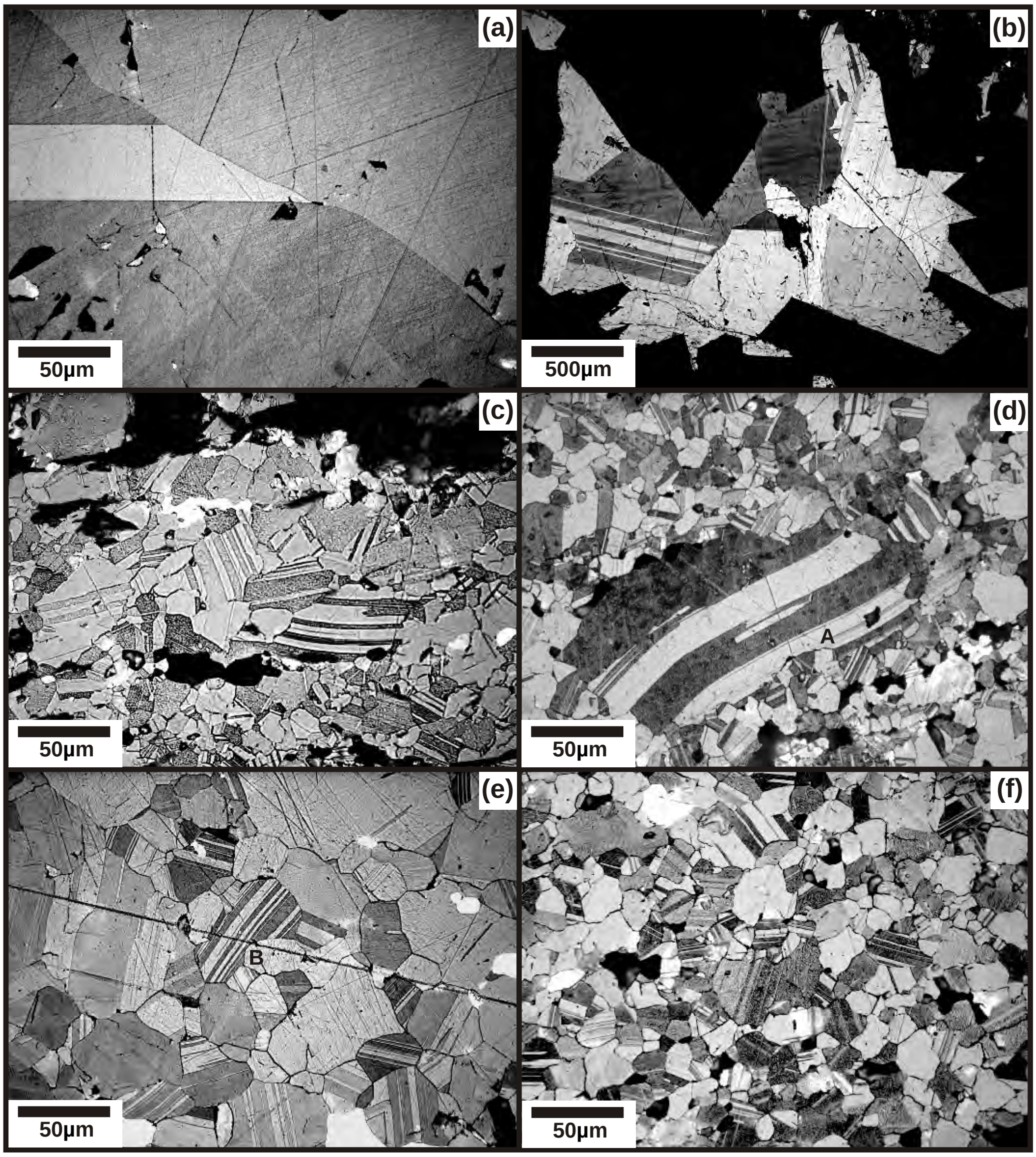

Figure 5. Photomicrographs of polished thin-sections (etched with conc. HI) in reflected light. (a) and (b) represent Class A, infill sphalerite from the Los Minas dos Ingleses and George Fisher deposits respectively. Straight twins with uniform width characterize the Class A samples. Note the smooth, gently curved grain-boundaries. Open-space growth is indicated in (b) where carbonate rhombs (black) define the vugh (note the change in scale in (b)). The larger grains in (c) and (d) represent Class B sphalerite from the Mt Molloy and George Fisher deposits respectively. Class B samples display bent twins and twins truncated mid-crystal. Grain shapes and boundaries of the Class B grains are irregular due to grain-boundary migration and recrystallization along margins. (e) and (f) represent Class C sphalerite from the Silverspur and George Fisher deposits respectively. 120^{o} triple-point junctions, equant grain shapes, and uniform grain-size reflect grain-boundary equilibration. Points ‘A’ and ‘B’, in (d) and (e) respectively, indicate locations where Class C grains overprint twins in older grains.

4.3 Class C

Sphalerite grains in class C have a grain size of approximately 15µm, and equant shapes. The grains commonly have straight, parallel-sided twins and grain boundaries of the crystals meet at ~120° triple-point junctions on average (Figs. 5e and f) indicative of grain boundary equilibration due to surface energy minimization (Smith, 1964). Growth of these grains can be seen to cross-cut early-formed twins in the larger host grains at locations 'A' and 'B' on Figs. 5d and e respectively. The grain boundary shape of Class C grain boundaries is of intermediate irregularity compared to Classes A (undeformed) and B (deformed). The features exhibited by these grains are characteristic of recrystallization of deformed sphalerite grains by grain boundary migration, resulting in strain-free grains which nucleate along grain boundaries and cross-cut deformation features.

4.4 Class D

Class D grains are observed in samples with a tri-modal distribution of grain sizes (Figure 6). They consist of larger grains with bent and dislocated twins (Class B), dominant 20-40µm sized grains with shape-preferred orientation (Class D), and sub-10µm equant grains (Class C). Overprinting relationships occur at localities 'A' and 'B' on Figure 6 where smaller grains truncate the twins of the larger host grains. The dominant 20-40µm (Class D) grains are aligned with the long axis of the large grain in the centre of Figure 6. At point 'A' on Figure 6, these 20-40µm (Class D) grains overprint the growth twins of the large grain and have irregularly shaped grain boundaries, and do not preserve 120° triple-point junctions. The 20-40µm (Class D) grains are in turn overprinted by sub-10µm equant grains at point 'B'. At other locations in the photomicrograph (Figure 6b)

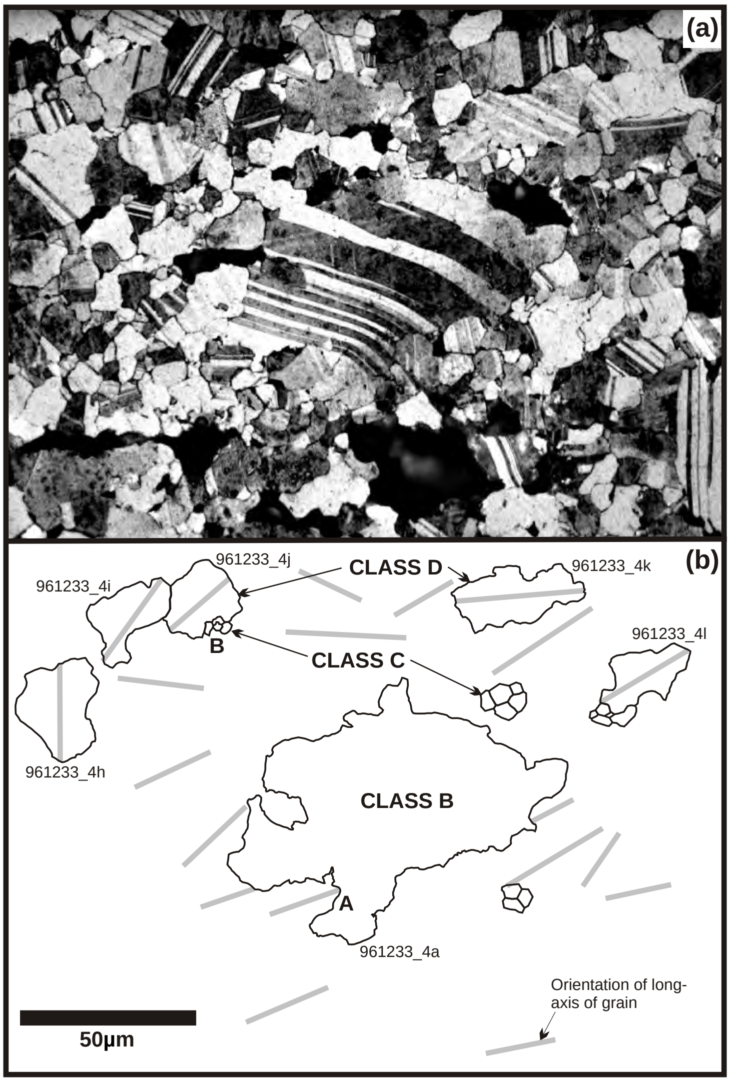

Figure 6. Photomicrograph (a) and line-diagram (b) of a sphalerite-dominant sample in polished thin-section (etched with conc. HI). A tri-modal grain-size distribution is observed consisting of a larger class B (deformed) grain with bent and dislocated twins, dominant 20-40μm grains with a weak shape preferred orientation (class D), and sub-10μm sphalerite occurring as equant grains (class C). These are interpreted as: relict deformed grain, recrystallized and subsequently deformed/recrystallizing, and youngest recrystallized sphalerite; respectively. Recrystallized grains cross-cut twins in the deformed grain at 'A' and the recrystallized/deformed grain at 'B'. Other observations from this sample indicate that larger grains are considerably more deformed than the matrix sphalerite. Grain outlines with annotation (e.g. 961233_4a) have been measured and data for these grain-boundaries can be found in Electronic Appendix IVb. Sample 961233.

the sub-10µm grains exhibit 120° triple-point junctions similar to Class C recrystallized sphalerite grains. The most voluminous 20-40µm (Class D) sphalerite grains in Figure 6 are distinct from grains in Classes A, B, or C, as they have a smaller grain size characteristic of grains in Class C (recrystallized) yet the irregular grain shape and preferred orientation of Class B (deformed) sphalerite grains. These grains are interpreted as deformed sphalerite which has recrystallized and subsequently been deformed and recrystallized a second time.

4.5 Class E

Sphalerite grains which exhibit characteristics common to Class A such as straight, parallel-sided twins; and Class B such as curved to bulging grain boundaries, are recognized and interpreted as weakly deformed sphalerite grains.

5. Results of fractal analysis of sphalerite grain boundaries

Sphalerite grain boundaries were analyzed by the coastline fractal method to investigate whether the grain boundaries have fractal geometries, and whether these can be used to quantify the classification introduced on the basis of the microstructural character of each class above. Results from the three main classes (A – undeformed, B – deformed, C – recrystallized) are summarized in Table 2. Class D and E sphalerite grains are treated as 'transitional' sample-sets as they do not represent end member textural styles. Data for the samples used in this study is available in Appendix IV.

Representative outlines of sphalerite grains (Figure 7) illustrate the difference in grain boundary geometry between undeformed, deformed, and recrystallized sphalerite at the

	D	95% Confidence interval	R	Std Error	Coastline Error	Lower fractal limit (µm)	Upper fractal limit (µm)	Grain diameter (µm)
Undeformed	1.0126	(1.0071,1.0181)	-0.94	3.7E-04	1.9E-04	1.0	62.8	1221.6
Deformed	1.0948	(1.0816,1.1080)	-0.95	3.8E-03	2.2E-03	1.0	26.3	130.5
Recrystallized	1.0485	(1.0442,1.0528)	-0.86	6.0E-03	3.2E-03	1.0	8.1	17.9

Table 2. Descriptive statistics for each dataset (values are averages).

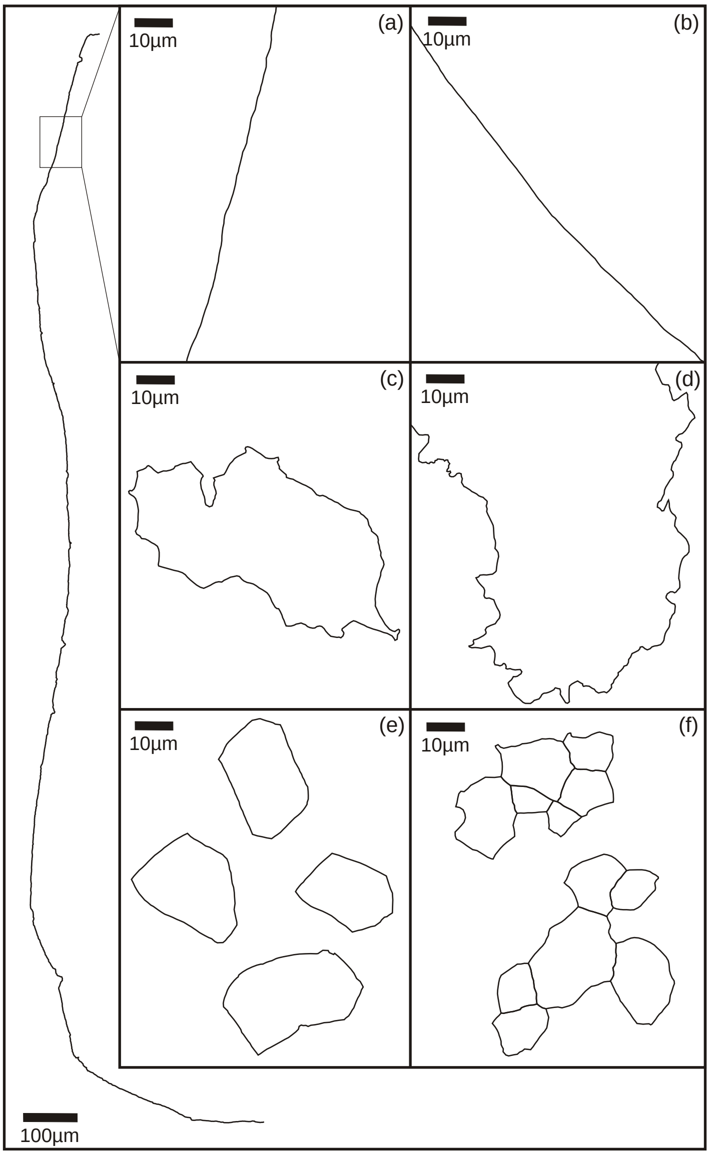

Figure 7. Representative outlines of grain-boundaries as used in the fractal analysis. (a) and (b) are undeformed infill samples *welcome_2* and *gf_late_1* respectively; (c) and (d) are deformed sphalerite grains from samples *mt molloy_3* and *961233_1* respectively and (e) and (f) display recrystallized sphalerite from samples *silverspur_1* and *gf_dyn_recryst.*

same scale of observation. Data from fractal analysis of these and other grain boundaries is displayed in Figure 8. A representative undeformed sphalerite grain boundary (D closest to mean D of sample set) is displayed on Figure 8a. The lines in Figure 8b show the straight lines of best fit to data from undeformed grain boundaries (as in Figure 8a) between the regression limits of L. The deviation of the data from the fractal relationship at large values of L is characteristic of the coastline method as noted by Mandelbrot (1967) and Aviles et al. (1987). The upper regression limit was chosen to exclude this deviation (cf. Aviles et al., 1987). Data for deformed and recrystallized grains are shown in the same format in Figures 8c to f respectively. There is a clear increase in the gradient of the data (Log P/Log L) from undeformed to recrystallized to deformed samples.

The data displayed as lines of best-fit on Figure 8 is plotted as a histogram in Figure 9. Undeformed sphalerite grain boundaries have fractal dimensions in the range 1.0000 to 1.0300, deformed grains 1.0550 to 1.1750, and recrystallized grains 1.0150 to 1.0800. The ranges of fractal dimensions from undeformed and deformed sphalerite grain boundaries do not overlap. The fractal dimensions of the recrystallized grains are intermediate and overlap with the undeformed and deformed ranges.

The 95% confidence intervals of **μ** (mean of the population), assuming a normal distribution of the sample mean and that the standard deviation of the sample approximates that of the population, are plotted beneath the histogram in Figure 9. The 95% confidence intervals do not overlap suggesting that the categorization of undeformed, deformed, and recrystallized sphalerite grain boundaries on the basis of a range of fractal dimensions is statistically valid.

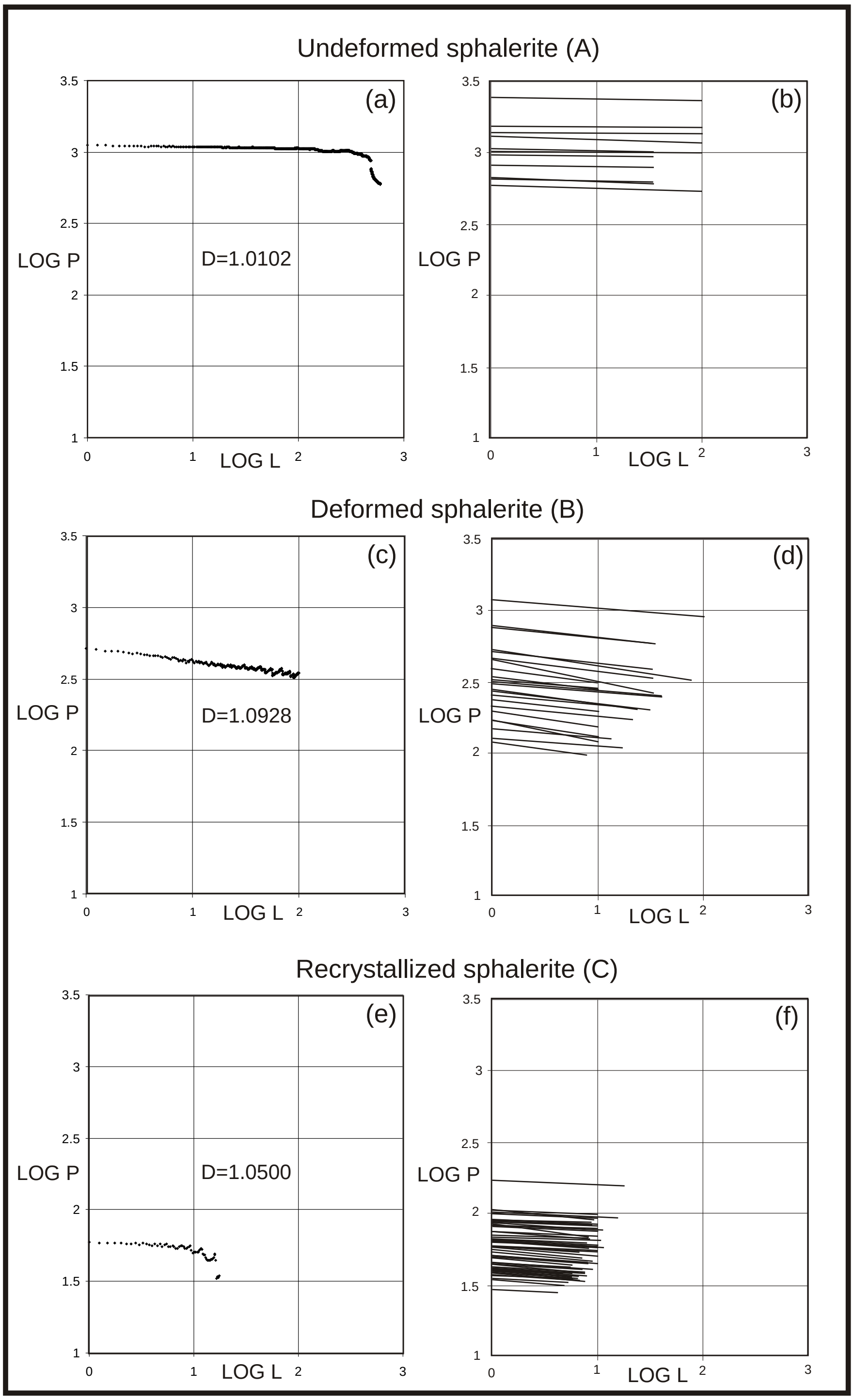

Figure 8. Log P vs Log L plots displaying data for representative samples (a,c,e) and lines of best fit for each sample in the entire dataset (b, d, f) for undeformed (a,b), deformed (c,d), and recrystallized sphalerite (e,f).

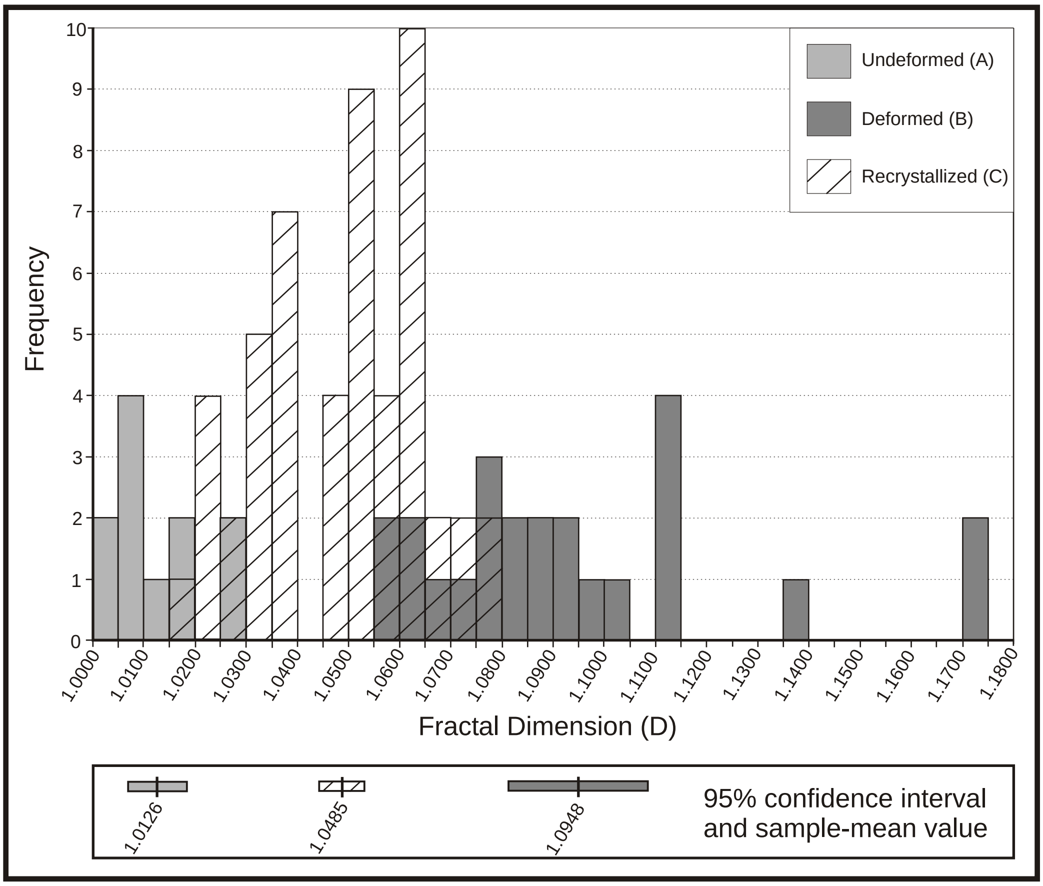

Figure 9. Frequency histogram of data used in this study and the 95% confidence interval for each sub-set. Data from the *transitional* sample sets are excluded for clarity.

The coastline or structured-walk method of fractal analysis resulted in an average error which is less than the average standard error of regression in the data analysis. The difference between the upper and lower fractal limits of L chosen for the lines of best fit for undeformed and deformed grains (Figure 8) is greater than one order of magnitude. The fractal limits of recrystallized grain boundaries studied (1- 8.1µm) is comparable with the study of Tanaka et al. (1998b) where small grains (<20µm) of zinc metal were analyzed and a range of fractal limits of 0.4 – 2.5µm used.

The three categories of undeformed, deformed, and recrystallized sphalerite grains can be discriminated when grain-diameter is plotted against fractal dimension (Figure 10). The data from Figure 9 now plot in exclusive fields due to the order of magnitude difference in grain size between undeformed, deformed, and recrystallized grains. The transitional Class D - recrystallized and subsequently deformed grains and Class E - weakly deformed data plot in intermediate positions.

6. Discussion

6.1 Sulphide microstructural studies

Etching sulphide samples for microstructural analysis, as discussed by Cox (1987), is emphasised as a cheap and simple technique that reveals features which allow robust interpretations of sulphide deformation processes. The etchant used in this study was found to produce consistent, good quality results.

The results of the coastline method establish the fractal nature of the sphalerite grain boundaries. The fractal geometry of quartz and metal grain boundaries have been

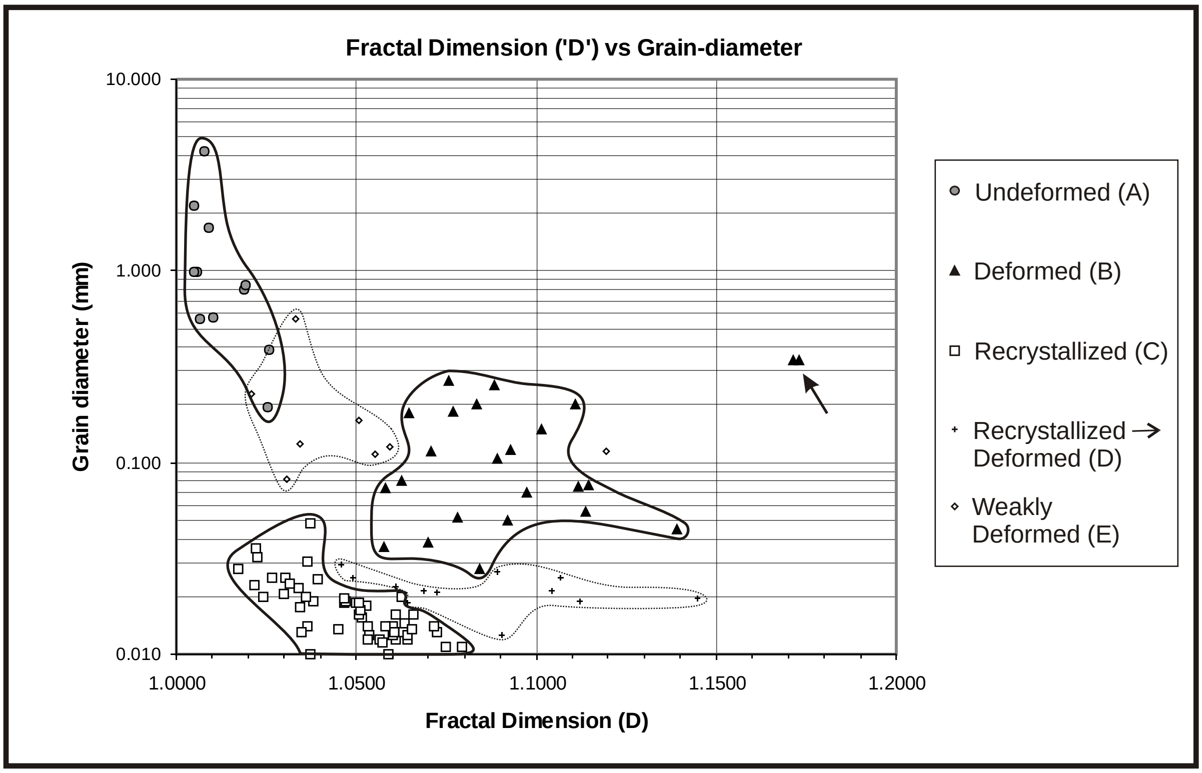

Figure 10. Grain-diameter vs fractal dimension plot for sphalerite grain-boundaries studied. The undeformed, deformed, and recrystallized data plot in exclusive fields while transitional weakly deformed, and recrystallized and subsequently deformed data plot in intermediate positions. Note the points indicated by an arrow are grain-boundaries from experimentally deformed sphalerite published by Clark and Kelly (1973). The outlying nature of these points suggests that the experiments produced realistic grain sizes however the grain boundary geometries are not compatible with naturally deformed sphalerite.

reported (e.g. Kruhl and Nega, 1996; Tanaka et al., 1998a, 1998b) but fractal analysis has not previously been applied to sulphide grain boundaries.

The fractal analysis of sphalerite grain boundaries indicates that this method can be employed to discriminate quantitatively between undeformed, deformed, and recrystallized sulphides when grain boundary geometry and grain size analysis are combined. The ranges of fractal dimensions with distinct confidence intervals for undeformed, deformed, and recrystallized sphalerite are a useful tool to aid microstructural analysis. Although some contribution to the scatter in the fractal dimension from section effects in the unoriented samples cannot be excluded, the 95% confidence intervals for undeformed, deformed, and recrystallized grains do not overlap.

A progression from undeformed to weakly-deformed to deformed grains (Figure 10) involves both a reduction in grain size with increasing deformation and increasing complexity of grain boundary shapes (higher D) due to grain boundary migration. Bulges and serrated grain boundaries reflect strain-induced grain boundary migration. Differences in interfacial energy between neighbouring grains (Stanton and Gorman, 1968) and the requirement to reduce the area of grain boundary contacts thereby reducing both surface and volume free-energy (Smith, 1964; Ewers, 1967; and Cox, 1987), drive the movement of atoms during dynamic recrystallization via grain boundary migration. Recrystallization of deformed grains leads to nucleation of strain-free grains at the expense of the deformed host (Stanton and Gorman, 1968) during grain boundary adjustment. As a result, the recrystallized grains are of inherently smaller grain size (Figure 10) and less complex geometry (lower D). The changes in grain size and grain boundary geometry with deformation are shown schematically in Figure 11. If such data was collected from a single deposit, similar trends may indicate multiple episodes of deformation and recrystallization.

While this method is not intended as a stand-alone classification of sulphide deformation and recrystallization, within the limitations of this dataset, end-members can be distinguished which enable discrimination between undeformed, deformed, and recrystallized sphalerite. Fractal analysis of sulphide grain boundaries can therefore complement conventional microscopic techniques in sulphide deformation studies. Future studies that integrate the approach used in this study with electron microscopy and EBSD may allow for automation of some steps in the procedure applied in this study.

Factors which may affect the fractal dimension of grain boundaries include the deformation temperature, strain, strain rate, and post-strain history. The temperatures of deformation for the deposits from which some of the samples analyzed in this study have been obtained, are as follows:

- Sullivan: 450°C (De Paoli and Pattison, 1995)
- Mt Molloy: 210-280°C (Gregory, 1978)
- Rammelsberg: 225-250°C (Ramdohr, 1953)
- George Fisher: 200-250°C (Chapman, 1999; Part A – this study)

The majority of data for the deformed and recrystallized grains has been obtained from the three deposits: Mt Molloy, Rammelsberg, and George Fisher which are all within the 200-300°C deformation temperature range (Figure 12). The Sullivan orebody has

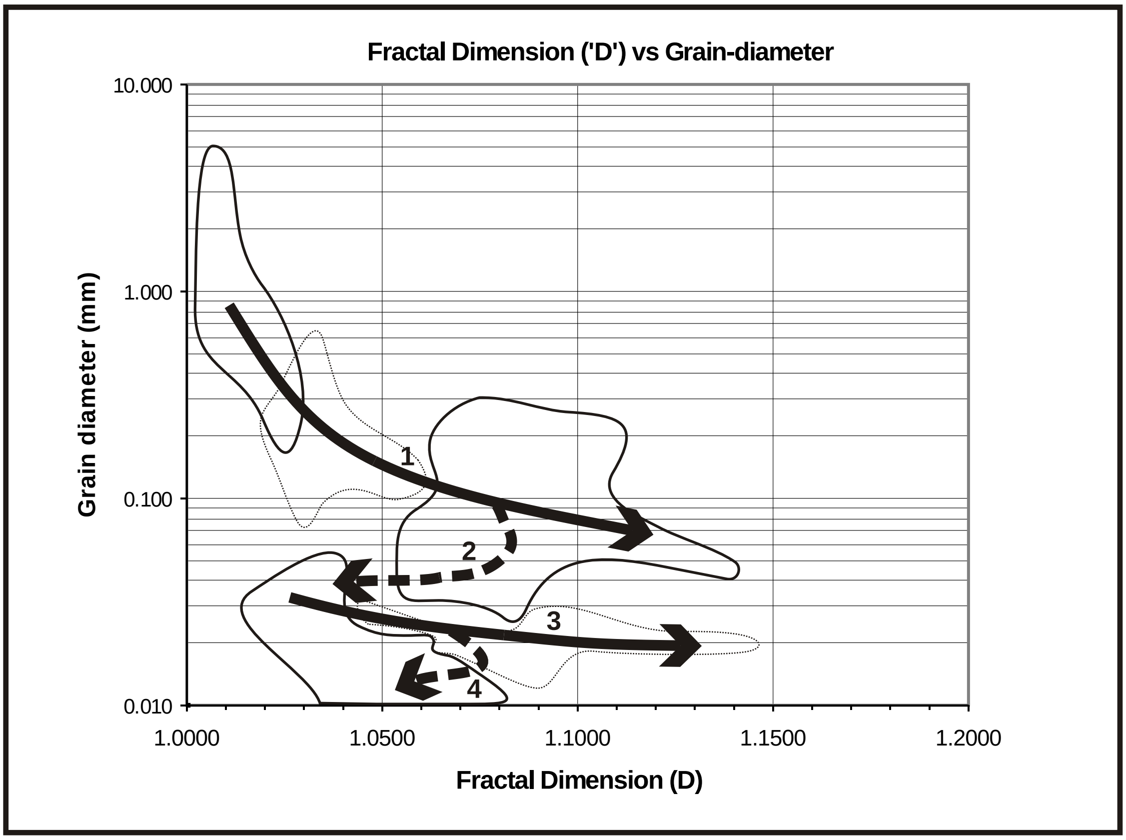

Figure 11. Grain-diameter vs fractal dimension plot displaying the outlines of fields from Figure 10 with data points omitted for clarity. Solid lines with arrowheads indicate deformation paths (i.e. increase in D and grain-size reduction) and dashed lines indicate recrystallization of deforming grains (i.e. reduction in D and further grain-size reduction). The process represented by each path is as follows.

1. Deformation without recrystallization
2. Recrystallization of strained grains
3. Deformation of recrystallized grains
4. Recrystallization to equilibrium texture

These trends are apparent within the limitations of the dataset and other permutations are likely.

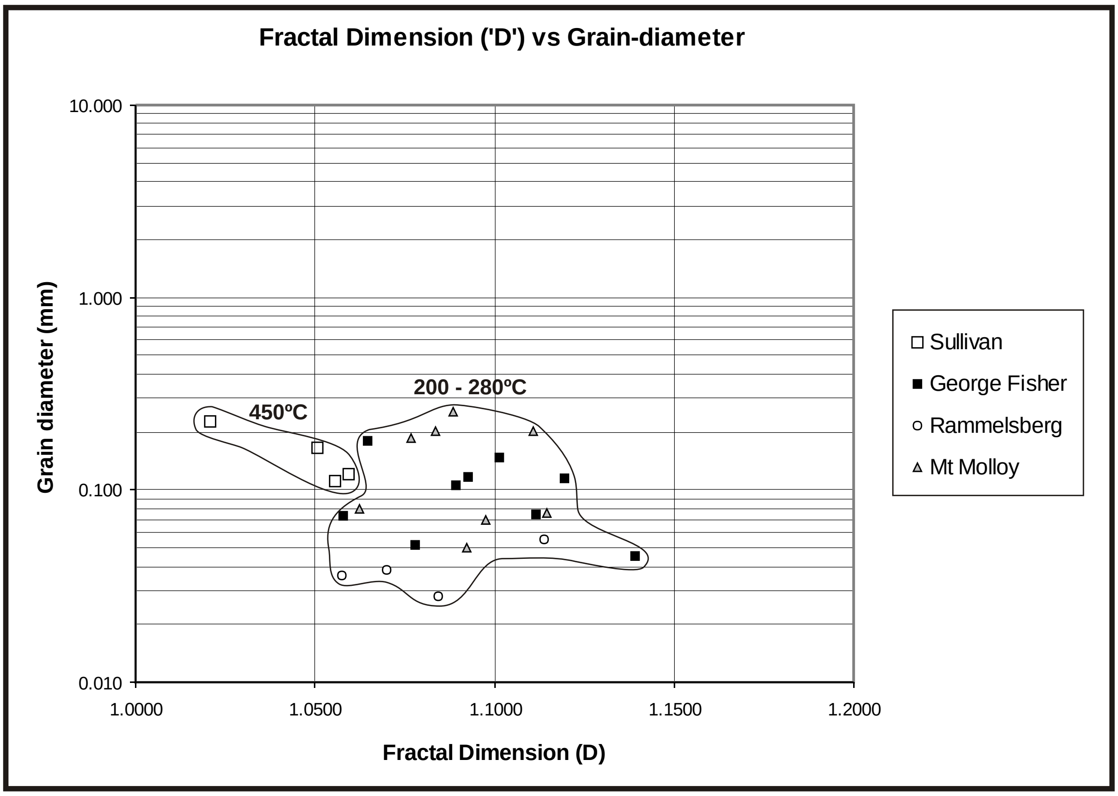

Figure 12. Grain-diameter vs fractal dimension plot for deformed grains only. The data are grouped according to temperature of deformation and an apparent relationship of high temperature to low D and vice versa is illustrated. The same relationship has been observed of quartz grain boundaries (Kruhl, 1995). However, the Sullivan grains studied were classified as only weakly deformed as they did not contain bent growth twins or deformation twins, and it is therefore ambiguous as to whether the lower fractal dimension for the Sullivan data is a function of temperature, strain, or strain rate. Data in the deformed and recrystallized fields (Figure 10) are only representative of the deformation temperature range of approximately 200-300ºC.

undergone higher temperature deformation and sphalerite grain boundaries from this deposit have lower fractal dimensions (Figure 12). The grains analyzed from Sullivan are classified as weakly deformed as growth twins are not bent or dislocated and deformation twins are absent and a lower fractal dimension is therefore expected. The apparent higher temperature-lower fractal dimension relationship of the data is therefore ambiguous in this example. However, Kruhl and Nega (1996) have recognized a relationship between the temperature of deformation and fractal dimension of quartz-quartz grain boundaries such that with increasing temperature of deformation the fractal dimension decreases. The same relationship is likely to be observed in sphalerite.

The measurement of the fractal dimension of zinc metal polycrystals at different strain intensities and constant temperature (Tanaka et al., 1998b) has shown that the fractal dimension of the grain boundaries increases with strain and strain rate. Similarly, experimental deformation of quartz resulted in increasing fractal dimension of grain boundaries with increasing strain rate at constant temperature and increasing fractal dimension with decreasing temperature at a constant strain rate (Takahashi et al., 1998). The deformed field defined in Figure 10 may shift left toward lower fractal dimensions if samples were analyzed from regions deformed at a higher strain rate.

Therefore the data and interpretations of this study may only be applicable to sphalerite deformed in the temperature range from 200-300°C or greenschist facies metamorphism, and at the strain and strain rates which characterize the tectonic history of the studied deposits and which are presently less constrained.

6.2 Implications for ore deposit analysis

Interpretation of the deformation history of sulphides is complicated by their susceptibility to recrystallization (Ewers, 1967; Clark and Kelly, 1976; Stanton and Gorman, 1968; and Cox, 1987) (as observed in this study) and a general lack of preferred orientation and foliation development in sphalerite-rich samples. The technique described here may enable comparison and correlation of the deformation history of sulphides to that of the deposit host rocks and broader region, potentially elucidating the controls on localization of ore. Comparison of sphalerite textures is also possible between deposits of varied age, location, and genesis as long as the temperatures of deformation and strain history of the deposits are similar. Recognition of deformation and recrystallization textures in sphalerite may enable the timing of mineralization to be inferred relative to deformation episodes. This information has significant implications for exploration strategies employed in the search for further orebodies where the timing of deformation relative to mineralization and any structural control on mineralization remain unclear.

7. Conclusions

Etching of sphalerite in polished thin-section has facilitated the analysis of deformation microstructures using optical microscopy. Samples were classified as undeformed. deformed, and recrystallized based upon qualitative mesoscale and microscale features such as relationship to gangue minerals, overprinting relationships, and deformation microstructures. Transitional samples that are either weakly deformed or were deformed and subsequently recrystallized are also recognized. A relationship between the fractal dimension of sphalerite grain boundaries and the degree of deformation and recrystallization is recognized.

Sphalerite grain boundaries, like quartz and metals, have fractal geometries, which allow sensitive and quantitative discrimination of the degree of deformation and recrystallization. Undeformed, deformed, and recrystallized grains have mean fractal dimensions and 95% confidence intervals of $1.0126 \pm 5.5 \times 10^{-3}$, $1.0948 \pm 1.3 \times 10^{-2}$, and $1.0485 \pm 4.3 \times 10^{-3}$ respectively for rocks deformed at low temperatures (200-300°C). The 95% confidence intervals of the means occupy distinct ranges and do not overlap. The three categories of undeformed, deformed, and recrystallized sphalerite grains can be completely discriminated when grain diameter is plotted against fractal dimension on a log-normal plot. Each class occupies an exclusive field due to the order of magnitude difference in grain size. This is considered to be a significant quantitative aid in determining the deformation history of sphalerite.

This technique was developed as a tool to assist in objective determination of the deformation/recrystallization state of sphalerite in an applied ore-deposit study and is relevant to other microstructural studies where sulphide deformation processes are being investigated. The application of this technique is not limited to Zn-Pb-Ag deposits as sphalerite is common to many hydrothermal ore deposits. It has obvious potential for application to other sulphides if fractal dimensions for undeformed, deformed, and recrystallized grains are obtained.

References

Aviles, C. A., Scholz, C. H., Boatwright, J., 1987. Fractal analysis applied to characteristic segments of the San Andreas Fault. Journal of Geophysical Research 92, 331-344.

Bérubé, D., Jebrak, M. 1999. High precision boundary fractal analysis for shape characterization. Computers and Geosciences 25, 1059 – 1071.

Blanchard, R. and Hall, G., 1942. Mt Isa ore deposition: Economic Geology, v. 32, p. 1042-1057.

Blenkinsop, T.G. 1991. Cataclasis and Processes of Particle Size Reduction. Pure and Applied Geophysics. 136, 59-86.

Blenkinsop, T.G., 2000. Deformation microstructures and mechanisms in minerals and rocks. Kluwer Academic, Dordrecht, 164pp.

Boyle, A. P., Prior, D. J., Banham, M. H., Timms, N. E., 1998. Plastic deformation of metamorphic pyrite: new evidence from electron-backscatter diffraction and forescatter orientation-contrast imaging. Mineralium Deposita, 34, 71-81.

Chapman, L.H., 1999. Geology and genesis of the George Fisher Zn-Pb-Ag deposit, Mount Isa, Australia. (Unpublished PhD thesis – James Cook University, Townsville).

Chapman, L.H., 2004. Geology and mineralization styles of the George Fisher Zn-Pb-Ag deposit, Mount Isa, Australia: Economic Geology, v. 99, p. 233-255.

Clark, B.R. and Kelly, W.C., 1973. Sulphide deformation studies: I. Experimental deformation of pyrrhotite and sphalerite to 2000 bars and 500°C. Economic Geology, 68, 332-352.

Clark, B.R. and Kelly, W.C., 1976. Experimental deformation of common sulphide minerals. In: R.J. Strens (ed), The physics and chemistry of minerals and rocks. John Wiley and sons, p. 51-69.

Cooke, D.R., Bull, S.W., Large, R.R., and McGoldrick, P.J., 2000. The importance of oxidized brines for the formation of Australian Proterozoic stratiform sediment-hosted Pb-Zn (Sedex) deposits. Economic Geology, 95, 1-18.

Cox, S.F., 1987. Flow mechanisms in sulphide minerals. Ore Geology Reviews, 2, 133-171.

Davis, T.P., 2004. Mine-scale structural controls on the Mount Isa Zn-Pb-Ag and Cu orebodies: Economic Geology, v. 99, p. 543-559.

De Paoli, G.R. and Pattison, D.R.M., 1995. Constraints on temperature-pressure conditions and fluid composition during metamorphism of the Sullivan orebody, Kimberley, British Columbia, from silicate-carbonate equilibria: Canadian Journal of Earth Sciences, v. 32, 1937-1949.

Ewers, W.E. ,1967. Physico-chemical aspects of recrystallization, Mineralium Deposita, 2, no. 3, 221-227.

Finlow-Bates, T. and Stumpfl, E.F., 1979. The copper and lead-zinc-silver orebodies of Mount Isa Mine, Queensland, products of one hydrothermal system, Annales Soc Geol Belgique, T 102, 497-517.

Gregory, P.W., 1978. Geology of the Mt Molloy and Dianne massive sulphide deposits, Hodgkinson Province, North Queensland. Unpublished PhD thesis – James Cook University, Townsville, Australia.

Hayward, J., Orford, J. D., Whalley, W. B., 1989. Three implementations of fractal analysis of particle outlines. Computers and Geosciences 5, 199-207.

Herwegh, M., 2000. A new technique to automatically quantify microstructures of fine grained carbonate mylonites: two-step etching combined with SEM imaging and image analysis. Journal of Structural Geology, 22, 391- 400.

Jacob, K.-H., Dietrich, S., Krug, H.-J. 1994. Self organization of Mineral Fabrics. In Kruhl, J. H. (Ed.), Fractals and Dynamic Systems in Geoscience, Springer-Verlag, Berlin, pp. 259-268.

Kristáková, Z. and Kupková, M., 1994. Correlation of Fractal Surface Description Parameters with Fracture Toughness. In Kruhl, J. H. (Ed.), Fractals and Dynamic Systems in Geoscience, Springer-Verlag, Berlin, pp. 77-86.

Kruhl, J.H. and Nega, M., 1996. The fractal shape of sutured quartz grain boundaries: application as a geothermometer. Geologische Rundschau, 85, 38-43.

Mandelbrot, B., 1967. How long is the coast of Britain? Statistical self-similarity and fractional dimension, Science, 156, 636-638.

McClay K.R. and Atkinson, B.R., 1977. Experimentally induced kinking and annealing of single crystals of galena. Tectonophysics, 39, 175-189.

Mc Clay, K. R., 1980. Sheared galena: textures and microstructures. Journal of Structural Geology, 2, 227-234

McClay, K.R., 1982. Fabrics in Ores: Sphalerite, Chalcopyrite, Pyrite: in Atlas of Deformational and Metamorphic Rock Fabrics, ed. Borradaile, G.J., Bayly, M.B., and Powell, C.McA., publ. Springer-Verlag, Berlin.

McClay, K.R., 1983. Fabrics of deformed sulphides. Geologische Rundschau, 72, 2, 469-491.

McClay K. R., Ellis P.G., 1983. Deformation and recrystallization of pyrite. Min. Mag. 47: 527-538

McDonald, J.A., 1970. Some effects of deformation on sulfide-rich layers in lead-zinc ore bodies, Mount Isa, Queensland. Economic Geology, 65, 273-298.

Orford, J.D., Whalley, W.B., 1987. The quantitative description of highly irregular sedimentary particles: the use of fractal dimension. In: Marshall, J.R. (Ed.) Clastic Particles, Van Nostrand Reinhold company, New York, pp. 267-289.

Ortoleva, P., Chen, Y., and Chen, W., 1994. Agates, Geodes, Concretions, and Orbicules: Self-organized Zoning and Morphology. In Kruhl, J. H. (Ed.), Fractals and Dynamic Systems in Geoscience, Springer-Verlag, Berlin, pp. 283-306.

Pape, H., Cluaser, C., Iffland, J., 2000. Variation of Permeability with porosity in sandstone diagenesis interpreted with a fractal pore space model. In Blenkinsop, T.G., Kruhl, J., and Kupkova, M. (Eds) Special Issue of Pure and Applied Geophysics, Fractals and Dynamic Systems in Geosciences, 157, pp. 603-620.

Passchier, C.W. and Trouw, R.A.J., 1996. Microtectonics. Springer-Verlag, Berlin, 289pp.

Perkins, W.G., 1997. Mount Isa lead-zinc orebodies: Replacement lodes in a zoned syndeformational copper-lead-zinc system? Ore Geology Reviews, 12, 61-110.

Ramdohr, P., 1953. Mineralbestand, strukturen und genesis der Rammelsberg-Lagerstatte: Geologisches Jahrbuch, v. 67, p. 367-494.

Ramdohr, P., 1969. The ore minerals and their intergrowths. Publ.: Oxford Pergamon [1st edition]

Russell, M.J., Solomon, M., and Walshe, J.C., 1981. The genesis of sediment-hosted, exhalative zinc and lead deposits: Mineralium Deposita, v. 16, p. 113-127.

Sawkins, F.J., 1984. Ore genesis by episodic dewatering of sedimentary basins: Application to giant Proterozoic lead-zinc deposits: Geology, v. 12, p. 451-454.

Sammis, C.G., Biegel, R.L. 1989. Fractals, fault-gouge and friction. Pure and Applied Geophysics, 131, 254-271.

Siemes, H., 1976. Recovery and recrystallization of experimentally deformed galena. Economic Geology, 71, 763-771.

Siemes, H., 1977. Recovery and recrystallization of deformed galena. Tectonophysics, 39, 171-174.

Smith, C.S., 1964. Some elementary principles of polycrystalline microstructure, Metallurgical Reviews, 9, 1-48.

Stanton, R.L. and Gorman, H.G., 1968. A phenomenological study of grain boundary migration in some common sulfides. Economic Geology, 63, 907-923.

Stanton, R.L. and Gorman-Willey, H., 1971. Recrystallization softening and hardening in sphalerite and galena. Economic Geology, 66, 1232-1238.

Takahashi, M. Nagahama, H. Masuda T. Fujimura, A., 1998. Fractal analysis of experimentally, dynamically recrystallized quartz grains and its possible application as a strain rate meter, Journal of Structural Geology, 20, 269-275.

Tanaka, M., Kayama, A., Ito, K., Kato, R., 1998a. Effects of creep deformation on the fractal dimension of the grain boundaries in an austenite steel. Journal of Materials Science, 33, 3351-3359.

Tanaka, M., Kayama, A., Ito, K., Kato, R., 1998b. Change in the fractal dimension of the grain boundaries in pure Zn polycrystals during creep. Journal of Materials Science, 33, 5747-5757.

Trimby, P. W., Drury, M.R. Spiers, C. J., 2000. Misorientations across etched boundaries in deformed rocksalt: a study using electron backscatter diffraction. Journal of Structural Geology, 22, 81-89.

PART D

Ore characteristics, cross-cutting relationships, and timing relative to deformation at the George Fisher deposit, NW Queensland, Australia.

Abstract

The George Fisher Zn-Pb-Ag deposit is comprised of several texturally-distinct mineralization types. Textural description, observations from mapping, and mine-scale distribution of the mineralization types has enabled determination of the relative timing of each variety relative to the deformation history detailed in Part A. Vein-hosted sphalerite and medium-grained galena breccia are the dominant sources for Zn and Pb, respectively. The sphalerite and galena in these mineralization-types, respectively, are shown to be only weakly deformed and their mine-scale distribution in longitudinal projection has similar geometry to ore shoots described in Part B. Vein-hosted sphalerite and medium-grained galena breccia are interpreted to have formed late in the deformation history of the deposit and are located in sites inferred to be dilational within the D_4 stress field. Minor disseminated sphalerite and fine-grained sphalerite+galena breccia mineralization types may be interpreted as pre- to syn-D_2 deformation based on cross-cutting relationships and intensity of strain preserved in the sulphides. If a pre-D_2 Zn+Pb sulphide accumulation was present, it is inferred that this would not constitute economic mineralization. Orebody formation is the result of evolving syntectonic processes during D_4. The separation of syn-D_4 galena and sphalerite into separate paragenetic sites implies two distinct phases of mineralization during D_4. Early in D_4, dilation in the F_1

short-limb occurred mainly due to bedding-slip during reactivation. The bulk of sphalerite mineralization is inferred to have occurred during this time. Later in D_4, F_4 folds developed and bedding reactivation proceeded to the extent that F_2-F_4 folds brecciated and galena mineralization was emplaced at this time. Syn-tectonic mineralization can be interpreted as remobilization within the deposit as medium- and fine-grained galena breccias are almost inversely proportional in mine-scale distribution suggesting redistribution during deformation. Analysis of assay data suggests that more than one population of Zn grades exists and that a higher grade population is unique to the economic ore-horizons. This supports the interpretation of remobilization and upgrading of mineralization. However, this qualitative observation does not discriminate between upgrading of a pre-F_2 or post-F_2 sulphide accumulation during D_4.

1. Introduction

Models of ore-genesis for Mt Isa/Hilton/George Fisher style sediment-hosted Zn-Pb-Ag emphasise synsedimentary (Finlow-Bates, 1979; Russell et al, 1981; Sawkins, 1984; Cooke et al., 2000), syndiagenetic (Valenta, 1994; Chapman, 1999), and syn-deformational (Blanchard and Hall, 1942; Perkins, 1997; Davis, 2004) processes that differ temporally by ~150Ma. The existence of several varied genetic models for these deposits is problematic for ongoing exploration unless different deposits evolved by different processes. If a company has to focus exploration efforts by selecting one of the three general models offered, which ones should they choose in order to successfully locate ore? Common to all three generic models (variations exist within each classification due to the intricacies of the deposit studied and area of focus of the researcher) is the fact that the Urquhart Shale is the host for base-metal mineralization.

The three major deposits discovered to date: Mt Isa, Hilton, and George Fisher occur within a discrete corridor of stratigraphy. With a corridor of prospective stratigraphy defined, what controls the localization of economic sulphides at deposits such as George Fisher within this corridor?

At George Fisher, deposit-scale ore-shoots have been identified which are located in an F_1 fold and parallel to the subsequent F_2 and F_4 fold axes. This indicates a degree of structural control on orebody location (see Part B). The location of these shoots is not coincident with a change in sedimentary facies or the position of a fault active during sediment deposition. A key piece of evidence in the synsedimentary and syndiagenetic models is the strong bedding parallelism of ores from cm to km scale, although the deposit-scale mineralization envelope transgresses stratigraphy at George Fisher (Chapman, 1999; refer to Part B). While some ambiguity in the interpretation of bedding-parallel stratiform ores at exposure-scale exists, this paper incorporates deposit-, exposure-, hand specimen-, and micro-scale observations in order to determine the relative timing of mineralization types and their timing with respect to the deformation history established in Part A.

Analysis of the Zn-Pb-Ag ores from the Hilton and George Fisher (referred to as Hilton North by Valenta) deposits by Valenta (1988, 1994) lead to an interpretation that the mineralization at Hilton records the entire deformation history as observed in the host rocks (Valenta, 1994). This interpretation hinges on the overprinting of coarse-grained pyrite (interpreted to be paragenetically associated with the mineralization) by a bedding-parallel foliation which predates folding in the Hilton-George Fisher area and the fact that the sulphides bands have folded shapes (Valenta, 1994). The bedded and finely banded nature of mineralization is also interpreted as indicating a syngenetic to early diagenetic timing of sulphide deposition (Valenta, 1988). Valenta therefore interprets the bulk of mineralization at Hilton as predating deformation. Deformation of the sulphides associated with the three fabric-forming episodes (D_2, D_3, D_4) was not observed and/or used to support the pretectonic timing of mineralization. Both sphalerite and galena are treated as components of a singular 'stratiform lead-zinc' mineralization type in the study by Valenta.

Chapman (1999, 2004) developed a detailed paragenetic sequence of alteration and mineralization types for the George Fisher deposit (Table 1) and recognized several textural varieties of both sphalerite and galena mineralization, some with overprinting relationships. Chapman recognized intensification of the S_2 foliation in the host rocks at the margins of mineralized sph+qtz+carb veins and used this as evidence for the vein pre-existing regional deformation. This differs from the interpretation of Valenta (1994) in which weaker sulphide-rich layers focus deformation as Chapman's observations imply that the host siltstones rather than the mineralized veins, preferentially focussed strain. This is discussed further in the textural descriptions of George Fisher ores in thin-section. The George Fisher Zn-Pb-Ag deposit is spatially coincident with host-rocks affected by repeated hydrothermal alteration (manifest as dolomite and calcite alteration), much of which is interpreted to have occurred during diagenesis. Chapman (1999, 2004) interpreted sphalerite mineralization as predating regional deformation, and occurring late in diagenesis. Galena mineralization is interpreted to occur dominantly post-regional deformation in sites of mechanical remobilization (Chapman, 1999).

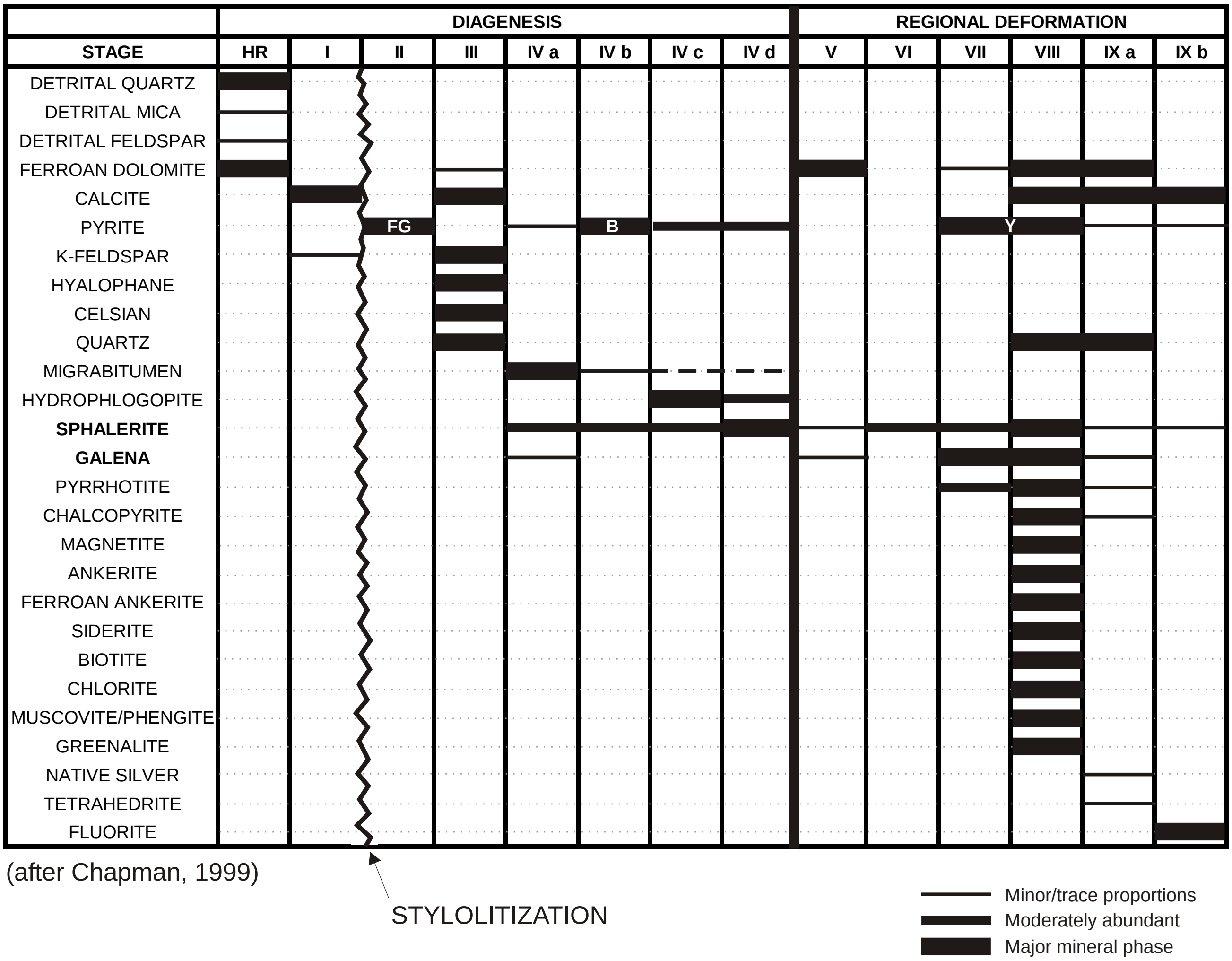

Table 1. Paragenetic sequence of alteration and mineralization developed by Chapman (1999). A summary of the definitions for each of the stages follows.

HR - host rock constituents

I - Calcite alteration and nodule development

II - Fine-grained (FG) spheroidal pyrite

III - Calcite-Quartz ±Celsian±Hyalophane±K-feldspar alteration and vein development

Onset of regional deformation → IV - Sphalerite mineralization, 'brassy' pyrite (B), and migrabitumen (ca. 200ºC)

V - Ferroan dolomite veining

VI - Sphalerite breccia formation

VII - Galena mineralization and 'yellow' pyrite (Y)

VIII - Copper mineralization (ca. 250-300ºC)

IX - Late Stage faulting

Common to both studies is the interpretation of ore formation pre-regional deformation (D_2-D_4). If this is correct, sphalerite and galena should exhibit microstructures consistent with the deformation history of the host rocks and potentially more texturally destructive given that the weak sulphide layers will focus later strain (Valenta, 1994). Sulphides are weaker than silicate minerals and most carbonate minerals at regional metamorphic temperatures and strain rates as sulphides such as galena and sphalerite are in their steady state flow regime as opposed to strain hardening of carbonates and silicates under these conditions (Clark and Kelly, 1973; Marshall and Gilligan, 1987). D_2 was the highest strain episode in the George Fisher area and produced a pervasive slaty/solution cleavage in the host rocks, meso-scale and exposure-scale folds at the George Fisher deposit, and kilometre-scale folds in the district. It must therefore be asked whether or not the ore-sulphides record the effects of D_2? If 'yes' then the pre-D_2 accumulation of sulphides is confirmed, if 'no' then what does this imply regarding the emplacement and distribution of the ore minerals.

Zn-Pb-Ag mineralization at the Mt Isa Mine is interpreted as syn-regional deformation (Blanchard and Hall, 1942; Myers et al., 1996; Perkins, 1997; Davis, 2004). Introduction of ore sulphides is interpreted as syn- to late in the deformation history as replacement of host rock during differential shear on bedding surfaces (Blanchard and Hall, 1942; Perkins, 1997). Apparent terminations of orebodies at F_4 fold hinge zones (Wilkinson, 1995; Myers et al., 1996; Perkins, 1997; Davis, 2004) and parallelism of high-grade shoots with F_4 fold axes (Davis, 2004) implicates the D_4 deformation episode in either syntectonic Zn-Pb-Ag mineralization or remobilization of pre-existing sulphides at Mt Isa.

The following is a description of dominant ore-types at George Fisher and emphasis is placed on those which contribute directly to the orebody-forming economic mineralization as mined and relative timing of these ore-types within the structural framework established in Part A. Comprehensive description of the alteration and mineralization paragenesis is available in Chapman (1999, 2004).

2. Description and interpretation of sphalerite-dominant ore-types

2.1 Vein-hosted sphalerite

Previously described as ‘stratiform’ mineralization (Valenta, 1988) and ‘vein-hosted stratabound’ sphalerite mineralization (Chapman, 2004), this textural variety of mineralization is the dominant source of zinc at the George Fisher deposit. Vein-hosted sphalerite accounts for ~95% of economic mineralization at Hilton Mine (Valenta, 1988) and ~82% of sphalerite ore thickness in drill-hole intersections (C, D, and G ore horizons) at George Fisher. Valenta (1988) interpreted phenomena such as abrupt thickness changes in individual layers, intense brecciation, grainsize coarsening, and strong recrystallization of both sulphides and gangue minerals as representing deformation of the sulphide-rich layers on all scales. However, thickness changes and brecciation do not necessarily resolve timing of the sulphide introduction within the four phase deformation history. Grainsize coarsening in sulphides is temperature dependent (Stanton and Gorman-Willey, 1972) and it has been shown through experimental work that galena recrystallizes at lower temperatures than sphalerite (Stanton and Gorman-Willey, 1971). Galena undergoes grainsize coarsening only above temperatures of approximately 400°C (Stanton and Gorman-Willey, 1972) and it is therefore reasonable to expect sphalerite to coarsen at higher temperatures again. Temperatures of deformation in the Hilton-George

Fisher area during D_2 were approximately 200-250°C (Chapman, 1999, Part A – this study), well below the temperature required to drive grainsize coarsening. Alternative explanation for the presence of coarse-grained sulphides is warranted.

Chapman (1999, 2004) observed euhedral quartz, carbonate, and hydrophlogopite crystals; and bitumens interpreted to be the product of diagenesis, within vein-hosted sphalerite mineralization. Chapman ascribed the euhedral form to mineral growth in open-space infill. Corroded and brecciated gangue minerals are replaced by sphalerite (Chapman, 2004) suggesting a component of sphalerite mineralization postdates earlier-formed quartz-carbonate veining (Chapman, 2004). Crenulation of vein margins and intensification of S_2 in the adjacent host rock were interpreted to represent evidence for pre-F_2 stratabound vein-hosted sphalerite mineralization (Chapman, 2004).

The sphalerite veins are characteristically bedding-parallel and have widths ranging from mm to 10cm, more commonly in the 1 to 3 cm width range (Figure 1 a,b). The veins occur in the order of 10 per metre. While their appearance in hand specimen is of semi-massive sphalerite, sphalerite commonly only comprises approximately 30-50% of the vein (Figure 1c); carbonate and quartz are the dominant gangue minerals. Pyrrhotite and pyrite also occur as accessory sulphide minerals with sphalerite. This mineralization type is dominated by sphalerite with only very minor associated galena.

Microstructure of the sphalerite in vein-hosted ore has been revealed by chemical etching of polished thin sections using concentrated Hydriodic acid (55%) as described in Part C. Comparisons of etched and unetched sphalerite is illustrated in Figures 2a and b.

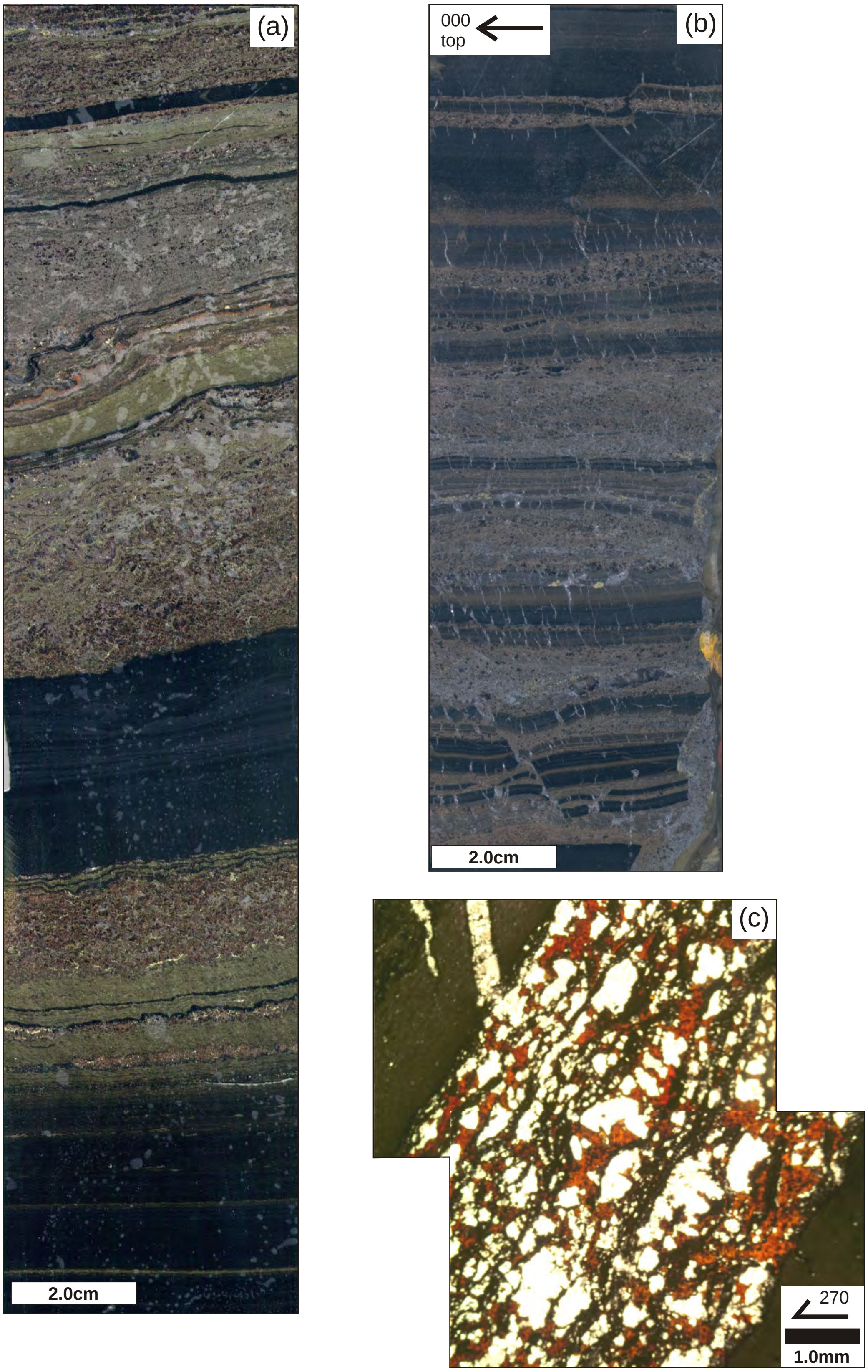

Figure 1. (a) Hand specimen of characteristically bedding-parallel vein hosted sphalerite with galena absent. Sample 960355, (b) galena tension gashes and brecciation overprinting vein-hosted sphalerite. Sample 0103-1, (c) thin section (ppl) of vein-hosted sphalerite, note the absence of fine laminations in the sulphide-rich domains. Sample 960519.

At the micro-scale, the sphalerite grain-size is significantly larger than the host lithologies (~100µm compared to ~10µm). Sphalerite grains form an interlocking crystalline network, compared with the postulation of sphalerite 'spheres' (Mathias et al., 1971) similar to framboidal pyrite. Sphalerite is also commonly twinned as revealed by etching (Figure 2c). These are interpreted as growth twins as they are often broad and extend across the full width of the grain (Figure 2b to f) compared with deformation twins which are commonly discontinuous and have lensatic geometry. Deformation twinning, bending of twins, irregular thickness and non-parallelism of twin-boundaries represent intracrystalline plasticity and reflect deformation of sphalerite grains. Deformation twins were absent in this textural variety of sphalerite mineralization and bending of twins (Figure 2d) where observed, is only weak. Recrystallization of sphalerite has been recognized within these veins (Figure 2e,f) and is characterized by equant grain shapes, 120° triple junctions, and overprinting of growth twins in the host grains. Recrystallization of sphalerite is not pervasive but affects 5-10% of the vein-hosted sphalerite across the deposit as a whole which contrasts with the interpretation of strong recrystallization of sulphides in the adjacent Hilton Mine by Valenta (1988). The recrystallization does not occur as continuous bedding-discordant zones within the veins. Pyrite and more commonly pyrrhotite occur on grain boundaries (Figures 2e,f) rather than as intracrystalline inclusions in the sphalerite. Note the overgrowth of sphalerite twins by euhedral pyrite (white) in Figure 2d. Valenta (1994) interpreted coarse pyrite associated with Pb-Zn mineralization to preserve a foliation which predates folding in the area.

Grain boundaries are generally smoothly curved (Figure 2c,d) although some irregularity associated with recrystallization of larger grains can be recognized (Figure 2e,f). Results

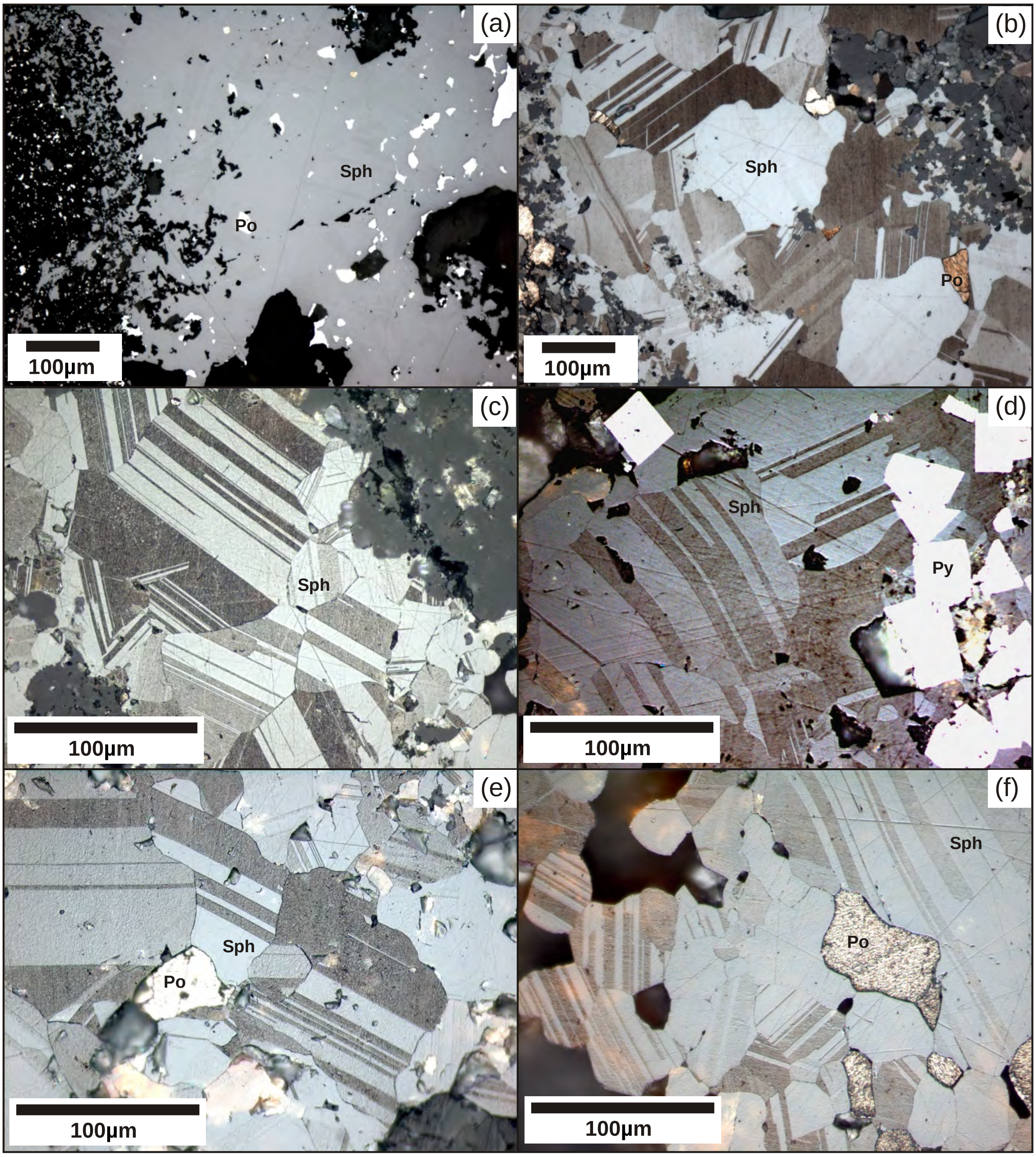

Figure 2. Photomicrographs of polished thin sections, sphalerite (Sph) is the dominant sulphide in each and minor pyrrhotite (Po) and pyrite (Py) also occur in vein-hosted sphalerite. (b) to (f) are polished sections etched with conc. HI. (a) Unetched vein hosted sphalerite and (b) an area of the same sample etched. Note that the grain shape and size, orientation, presence of twinning, and grain boundary irregularity are revealed subsequent to etching. Sample 0103-1. (c) Straight, parallel-sided growth twins in sphalerite. Gently-curved grain boundaries and 120º triple junctions suggest grain-shape equilibration is underway via recrystallization. Sample 0103-1. (d) Weakly bent twins. Sample 960519. (e) Recrystallized grain (centre) cross-cutting growth twins in older grain. Sample 2603-1. (f) Recrystallized sphalerite (left) and large relict grain (right). Sample 1212-1.

from fractal and grain-size analysis of 29 sphalerite grains and 8 recrystallized grains from vein-hosted sphalerite mineralization are displayed on Figure 3a. The gently curved grain boundaries and intermediate grain size results in clustering of the measurements between the infill/undeformed and recrystallized fields for both fractal dimension and grain diameter. This is consistent with the weakly deformed field, although this field is poorly constrained as the study in Part C focussed on end-member undeformed, deformed, and recrystallized grains. Alternatively, the vein-hosted grains represented on Figure 3a may define part of a field for undeformed replacive sphalerite. In such circumstances, grain size is limited due to lack of open-space for growth (as for infill veins) and mild irregularity of the grain boundaries results from impingement of grains during growth and replacement of the host. The mean fractal dimension of the vein-hosted sphalerite is $1.0375 \pm 4.70 \times 10^{-3}$ (95% confidence interval). The 95% confidence interval of the mean for vein-hosted sphalerite does not overlap with that of infill/undeformed and recrystallized sphalerite (Figure 3b). Recrystallized grains within the vein-hosted sphalerite mineralization were also measured and these plot in the well-defined recrystallized field on Figure 3a.

2.1.1 Evidence for replacive sphalerite

Vein-hosted sphalerite occurs as preferential replacement of host lithologies on the micro and meso scale. Replacement of a quartz and calcite vein by sphalerite is indicated by irregular margins of the relict quartz and calcite grains and irregular internal margins of the vein pictured (Figure 4a-c). Sphalerite and pyrite occur central to the vein either as syntaxial (Durney and Ramsay, 1973) addition of material to the vein or brecciation and replacement of the inclusion-rich median line (Durney and Ramsay, 1973). A thin band

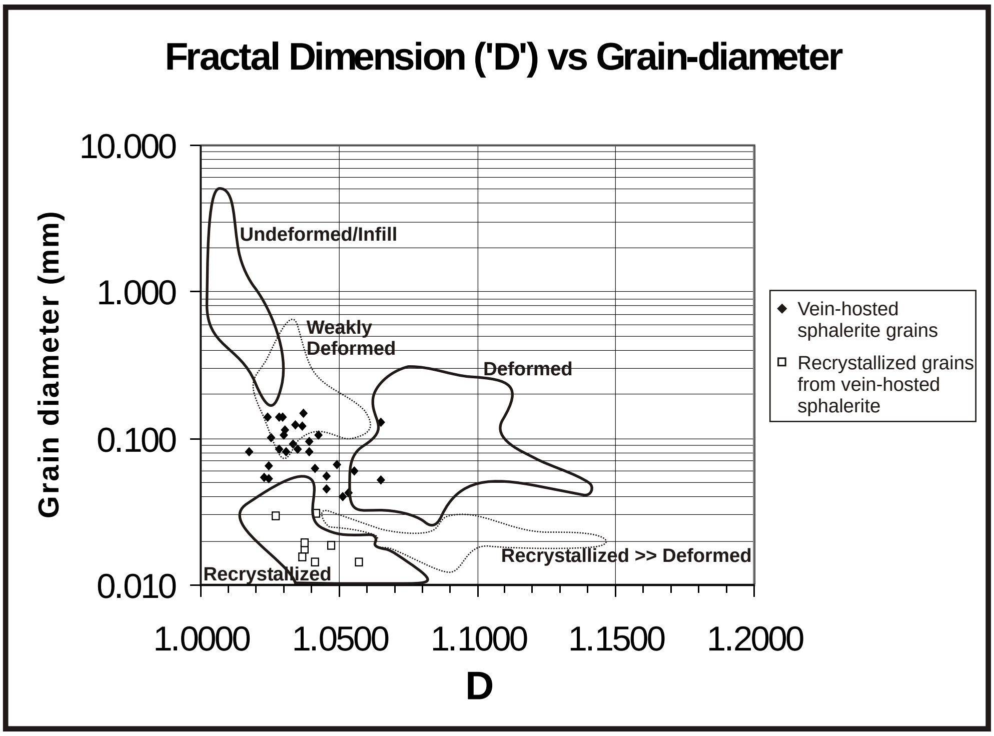

Figure 3a. D vs grain diameter plot with fields established from the study in Part C. Vein hosted sphalerite grains have a tight distribution and their location on the plot is consistent with weakly deformed sphalerite. Recrystallized grains associated with the vein hosted mineralization plot in the recrystallized field.

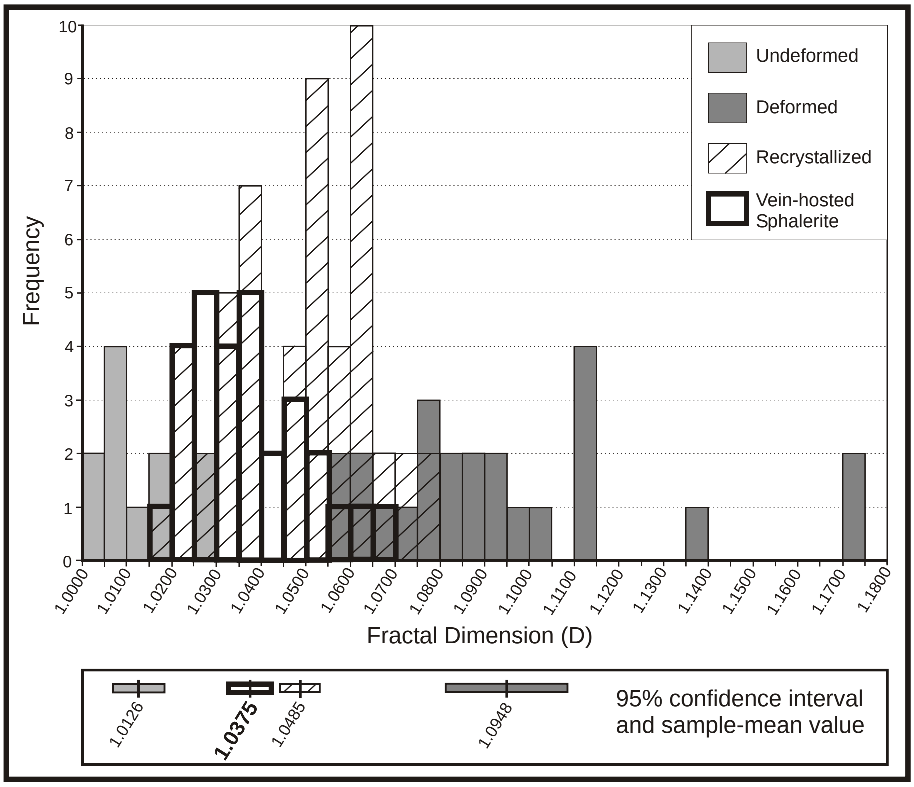

Figure 3b. Frequency histogram displaying the vein-hosted sphalerite data with undeformed, deformed, and recrystallized sphalerite. Note that the 95% confidence interval for the vein hosted sphalerite does not overlap with the undeformed and recrystallized intervals.

of fine-grained pyrite now marks the position of the median line of the vein (Figure 4a and c). Sphalerite replaces quartz and calcite fibres and migrates along fibre grain boundaries (Figure 4a).

Brecciation and replacement of pyritic siltstone host rock is indicated by the presence of displaced and rotated clasts and, as is the case with Figure 5, irregularly shaped and insufficient clast material to reconstruct the proto-layer. The coloured regions on Figure 5b represent clasts that once formed continuous layers which can be traced across the image. Narrow black lines within the clasts indicate layering interpreted as bedding. It is clear that even with the bedding-parallel extension associated with the galena tension gash/boudin necks, there is insufficient volume of clast material to fully reconstruct the pyritic layers. Also, margins of the pyritic ‘clasts’ are highly irregular and often grade into the massive sphalerite indicating replacement. Quartz and calcite grains have ragged margins and are distributed sporadically throughout the mineralized layer suggesting that they are the remnants of a vein now partially replaced by sphalerite. These observations are consistent with the paragenesis developed by Chapman (1999, 2004) as shown on Table 1. Early fine-grained spheroidal pyrite (Table 1, Stage II) and quartz-carbonate alteration/veining (Table 1, Stage III) are cross-cut by sphalerite. This is consistent with evidence of replacement of earlier quartz-carbonate fibre veins (Figures 4 and 6).

Truncation of vein-hosted sphalerite mineralization by cross-cutting features is visible in hand specimen (Figure 6a). In this specimen, typical vein-hosted sphalerite terminates abruptly at a carbonate vein. The protolith on the right hand side of the vein (Figure 6b) is barren. This implies that the sphalerite mineralization occurred later than the cross-

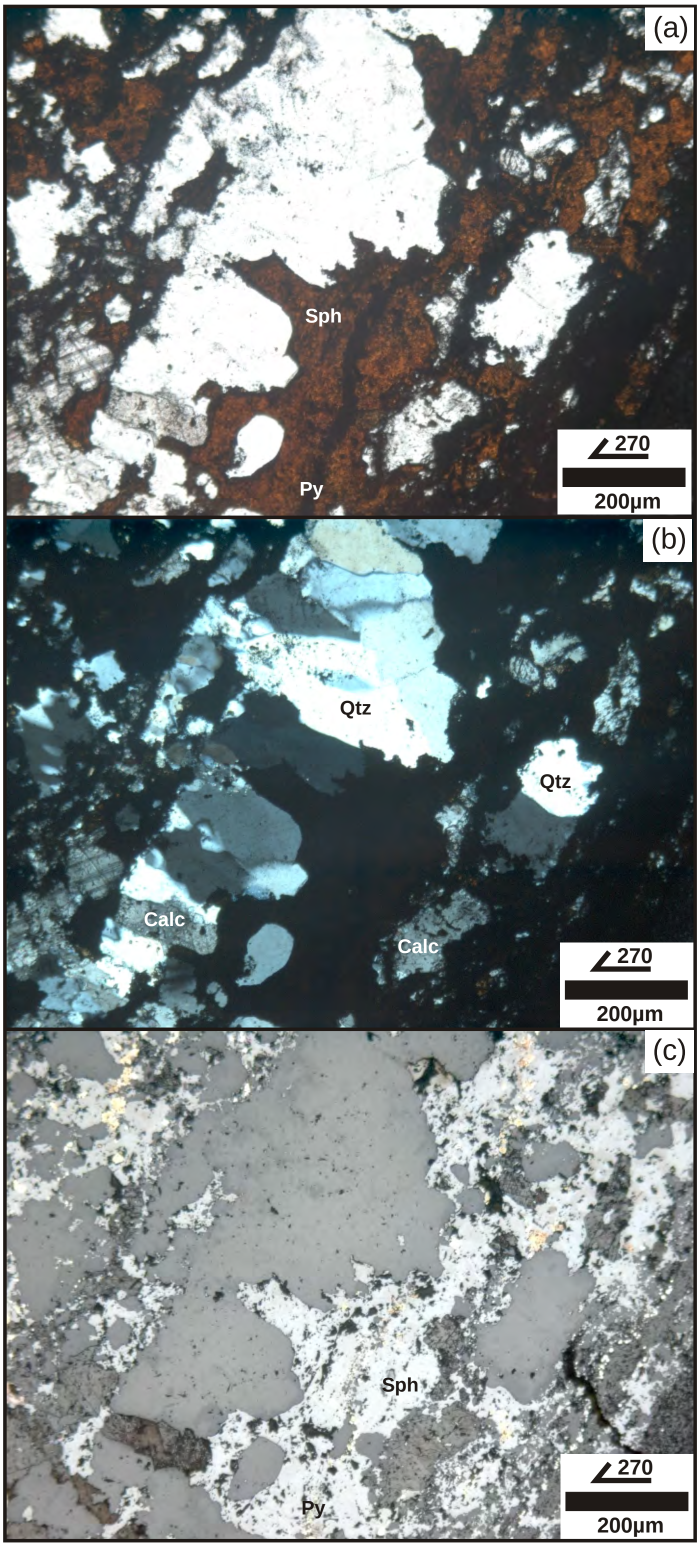

Figure 4. Photomicrographs of vein hosted sphalerite. (a) in plane polarized light, (b) with crossed polarizers, and (c) in reflected light. Sphalerite (Sph) replaces quartz (Qtz) and calcite (Calc) vein material preferentially along fibre contacts. Pyrite (Py) occurs as a narrow band and may represent a replacement of the original median line of the vein or late syntaxial growth. Sample 960519.

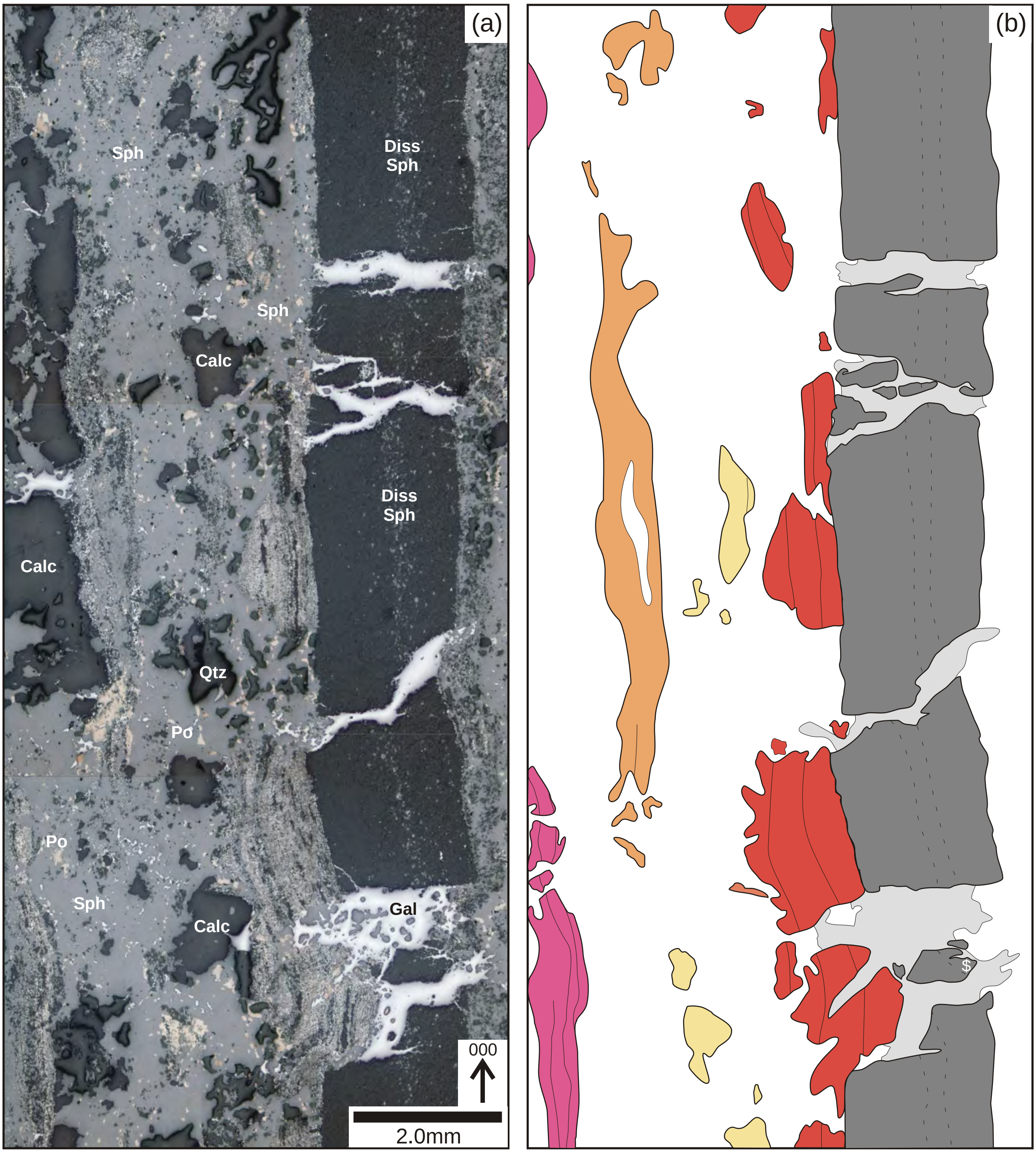

Figure 5. Photomicrograph (a) and line drawing (b) of replacive vein-hosted sphalerite in plan view. Sphalerite (Sph) is the dominant sulphide and is accompanied by abundant small grains of pyrrhotite (Po). Irregular shaped quartz (Qtz) and calcite (Calc) occur as gangue minerals. Galena (Gal) occurs as tension gashes in the adjacent mudstone layer. Coloured regions in (b) indicate pyritic layering brecciated and undergoing replacement by sphalerite. Bedding parallel disseminated sphalerite (Diss Sph) occurs within the mudstone layer. Irregular sphalerite grains in the galena tension gashes/boudin necks indicate replacement by galena, suggesting that the necks were originally dominated by sphalerite. Sample 0103-1, as illustrated in Fig 1(b) and 2(c).

cutting vein and the vein has acted as an impermeable barrier to the ore fluids. Veins with fibres at a high angle to bedding occur on both sides of the later cross-cutting carbonate vein (Figure 6c, d, e). Carbonate fibres dominate on the barren side of the cross-cutting vein (Figure 6c) whereas on the mineralized side of the sample, quartz fibres are well developed (Figure 6d, e). Sphalerite occurs central to the veins and infiltrates along quartz fibre contacts indicating that sphalerite introduction occurred late to post-vein development. Vein formation at this scale has resulted in an increase in width from the barren section (A-A’) to the mineralized section of 14%. The 14% increase in volume, accommodated by vein formation, alone is not sufficient to account for the ~40% increase in sphalerite content of the layer, implying replacement has played a significant role rather than infill sphalerite accounting for all sphalerite deposition in the sample.

Further evidence for replacive sphalerite is seen in Figure 7. Again, sphalerite mineralization terminates on a carbonate vein and the pyritic protolith is preserved on the opposite side of the vein. Weak folding is developed in the mineralized side of the core but is absent from the barren side (Figure 7a,b). A 40% increase in width of the partly mineralized pyritic siltstone layer occurs from barren (A-A’) to mineralized (B-B’) sections in Figure 7a. Primary laminations are destroyed as part of the mineralization process (Figure 7b) and only the mudstone layers are preserved within the sphalerite mineralization. Pyrite content remains the same across the vein that separates barren from mineralized material. Disseminated pyrite in the mudstone layer at ‘A’ in Figure 7c is remobilized and redistributed along the margins of the layer in the mineralized rock (‘B’) indicating that pervasive fluid flow has occurred through the rock.

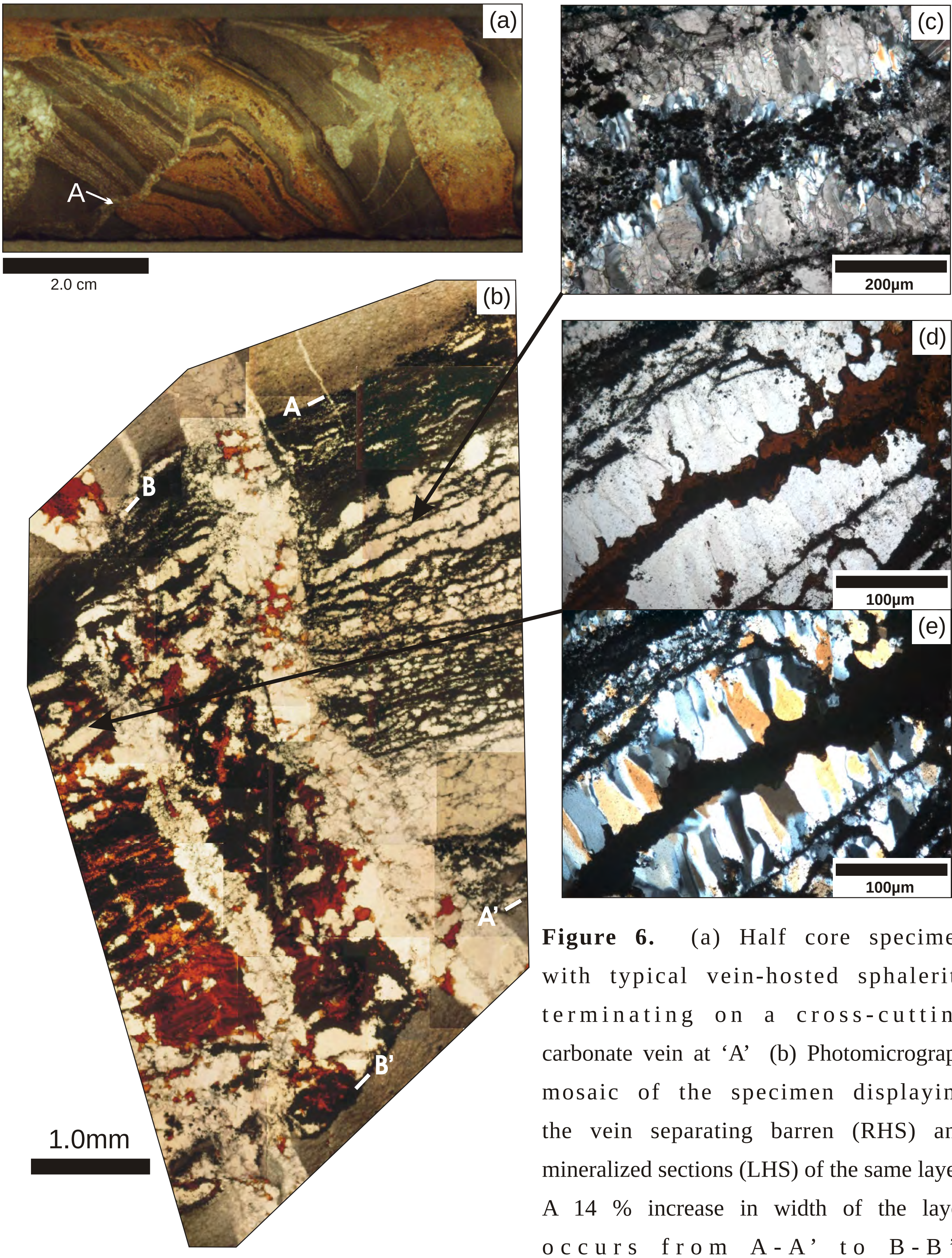

Figure 6. (a) Half core specimen with typical vein-hosted sphalerite terminating on a cross-cutting carbonate vein at 'A' (b) Photomicrograph mosaic of the specimen displaying the vein separating barren (RHS) and mineralized sections (LHS) of the same layer. A 14 % increase in width of the layer occurs from A-A' to B-B'. (c) Carbonate fibres developed in the barren protolith. (d) photomicrograph in plane polarized light and (e) with crossed polarizers of bedding-parallel quartz vein development and sphalerite infiltration on the mineralized side of the dividing vein. Sample H748 EH1.

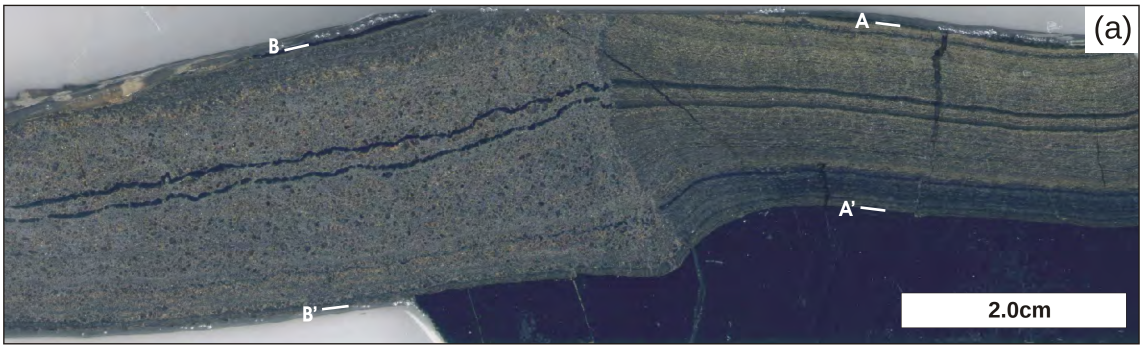

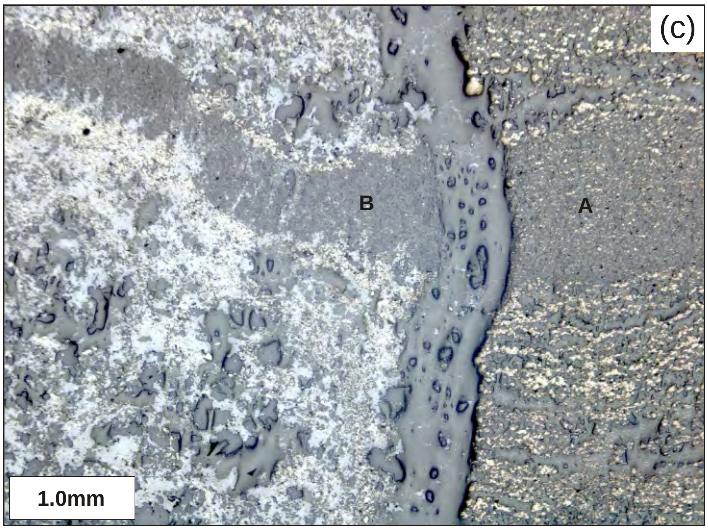

Figure 7. (a) Specimen of half core composed of pyritic siltstone to the right and sphalerite mineralization to the left. A narrow carbonate-quartz vein forms the boundary between the two. Weak microfolding of the mineralized half is visible, however the barren side appears unaffected by this microfolding. Width of the mineralized layer from A-A' to B-B' increases by 40%. (b) Enlarged region of the hand specimen showing the continuity of dark mudstone layers across the bounding vein but destruction of fine pyritic lamellae within the mineralized siltstone. (c) Photomicrograph (reflected light) of the vein dividing barren and mineralized areas. Disseminated pyrite in the mudstone layer at 'A' is remobilized during the influx of mineralizing fluid. Note the reduction in thickness of the mudstone layer from A to B. Sample J754 WD1.

2.1.2 Sphalerite occurring as breccia-infill and replacement of pre-existing veins

Vein-hosted sphalerite mineralization occurs as brecciation and replacement of older bedding-parallel quartz-carbonate veins, an observation also made by Valenta (1988) and Chapman (1999). This is seen in Figure 4 where sphalerite post-dates the formation of sub-horizontal quartz and calcite fibres in a bedding parallel micro-vein. Also, although not oriented, the specimen in Figure 6 contains sphalerite overprinting quartz-carbonate fibres that formed at a high angle to bedding in bedding-parallel micro-veins. The formation of carbonate fibres in the carbonate-rich protolith (Figure 6c) yet lacking in sphalerite mineralization suggests that increments of bedding perpendicular extension occurred prior to the emplacement of cross-cutting vein and later sphalerite mineralization. These fibrous veins have been analyzed in some detail as they provide a potentially important time datum which helps to link mineralization to the history of deformation at George Fisher.

Observations in thin sections of sub-horizontal quartz-calcite fibre relics in vein-hosted sphalerite aid in determining the relative timing of this ore type. Formation of sub-horizontal fibres during bedding-parallel vein development requires extension perpendicular to the bedding surfaces. This process is more likely to occur where there is rheological contrast between adjacent lithological layers or where a planar discontinuity occurs in the rock mass. This is evident in Figure 8a and b where a fibrous quartz-carbonate vein has formed along a stylolitic contact (early diagenetic feature, see Table 1), a mechanism also observed at the adjacent Hilton Mine (Valenta, 1988). Note the gentle pitch (Figure 8a) and ENE strike (Figure 8b) of fibres. Fibres in extensional veins grow parallel to the direction of extension (Ramsay and Huber, 1983) in the stress field at the time of mineral precipitation. Direction of growth of fibres changes as the stress field alters. The subhorizontal attitude of the fibres is consistent with their developing in the D_3 stress field which is inferred to have a subhorizontal, ENE trending extension direction (see Part A) in gently dipping S_3 crenulations. Brecciation and mineralization of these veins (Figure 8c,d) has occurred and sphalerite overprints the gently pitching fibres. Preservation of gently pitching quartz fibres amongst vein-hosted sphalerite is patchy in the image displayed in Figure 8e and f although abundant in the thin section. Steeply pitching fibres, which postdate the gently pitching D_3 fibres and parallel the steep extension direction during D_4, occur in this sample but are much less abundant. Another explanation for the orientation of the fibres is that they developed during F_1 folding and have been rotated into their present orientation during F_2 folding. This possibility cannot be discounted with respect to the samples in Figure 8, however the lack of deformation suggests post-D_2 formation and a sample with subhorizontal fibres spatially related to F_3 microfolds (confirming D_3 vein growth) will be discussed in the next section.

Deformation features preserved in fibres but absent from the mineralization assemblage also give insight as to the relative timing of mineralization to deformation episodes.

Clasts in a vein-hosted sphalerite layer (Figure 9a,b) consist of relict fibres (Figure 9c) with gently pitching attitude which may represent vein formation during incipient F_2 development. The fibres are deformed and have undulose extinction which radiates from a central fracture associated with the sphalerite mineralization (Figure 9d). Two sets of deformation lamellae are observable in the quartz fibres (Figure 9d), however those pitching approximately 42°W dominate (Figure 9e) and are associated with significant

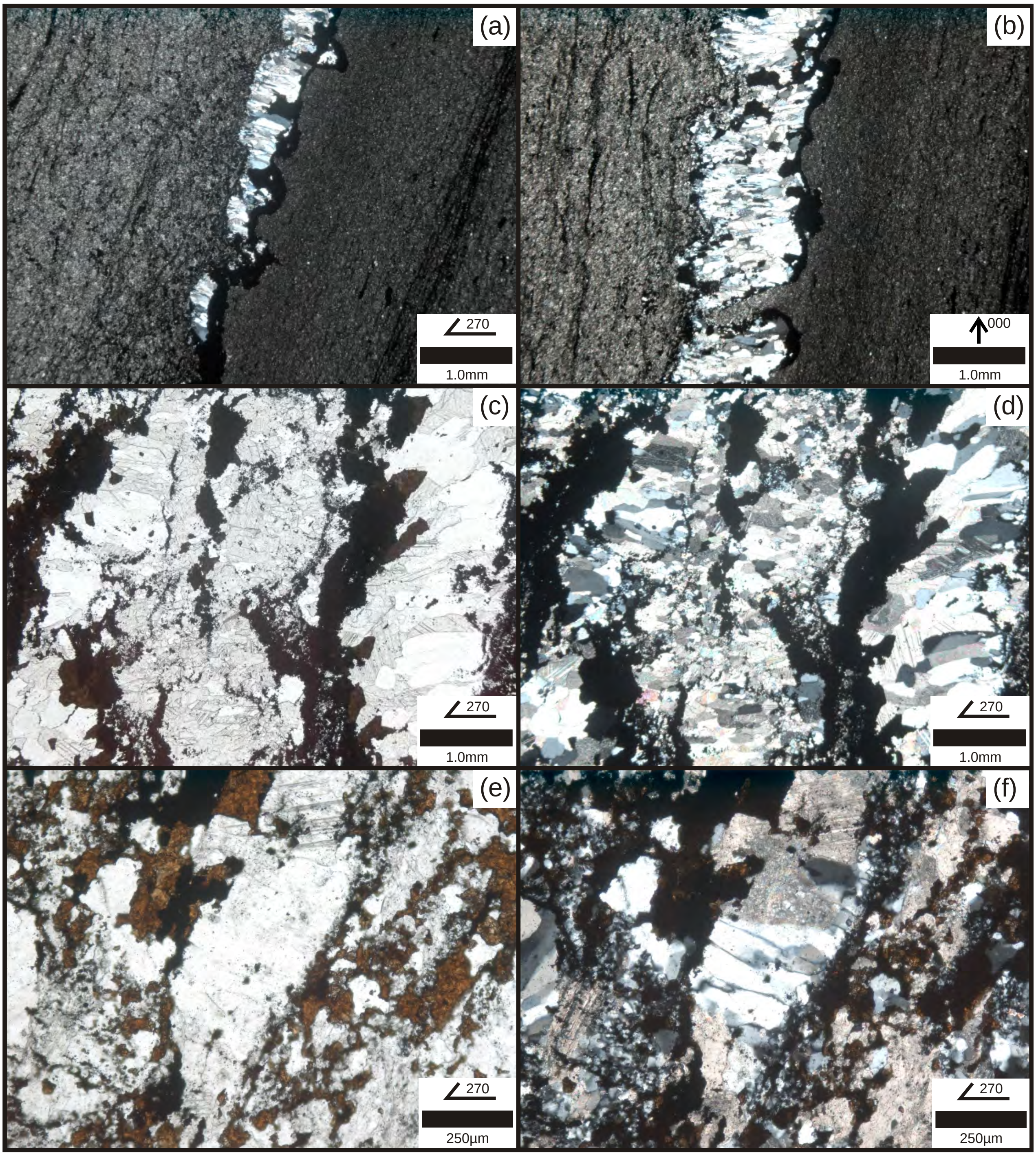

Figure 8. Photomicrographs of quartz-carbonate micro-veins displaying fibrous growth. (a) A vertical section looking north, and (b) a plan view of the same sample under crossed polarizers. The fibrous vein has developed off a stylolitic contact on its RHS. Sample 1311-5. (c), (d) photomicrographs in plane polarized light and under crossed polars of a mineralized vein preserving sub-horizontal fibres. Sample 1311-5 (e), (f) photomicrographs in plane polarized light and under crossed polars of patchy preservation of fibrous relict material in a mineralized vein. Sample 3010-1.

grain boundary migration of the fibre contacts (Figure 9b). The deformation lamellae are likely to reflect D_2 deformation as this level of intensity (Figures 9d and e) is uncharacteristic of the relatively weak D_3 and D_4 episodes. Quartz and calcite associated with the sphalerite mineralization do not exhibit similar deformation features. Quartz occurring as matrix to the relict clasts has straight extinction and smoothly curved grain boundaries (Figure 9f) while calcite grains are not significantly twinned (Figure 9f). The matrix minerals associated with the sphalerite mineralization occur as breccia-fill of the relict fibrous clast and do not have equivalent deformation features. Sphalerite mineralization in this example postdates an earlier veining event (again fibres are potentially sub-horizontal) and occurs syn- to post- deformation of the fibres.

2.1.3 Sphalerite occurring synchronous with vein development

Development of sphalerite mineralization as a distinct veining event, as opposed to brecciation of existing quartz-carbonate veins, is also recognized (Figure 10a). These veins contain euhedral calcite ± hydrophlogopite crystals (as recognized by Chapman, 1999, 2004) within the sphalerite (Figure 10b). The presence of euhedral crystals suggests that the vein includes infill material. This interpretation is supported by the divergence of bedding planes where the vein material is situated (Figure 10a). In these cases veins are inferred to open due to competency contrasts of the adjacent layers and/or differential slip on bedding surfaces. The sphalerite-calcite-quartz vein in Figure 10a has developed due to gaping of a lithological contact during deformation. Note that the vein forms where right-stepping changes in strike of bedding occur.

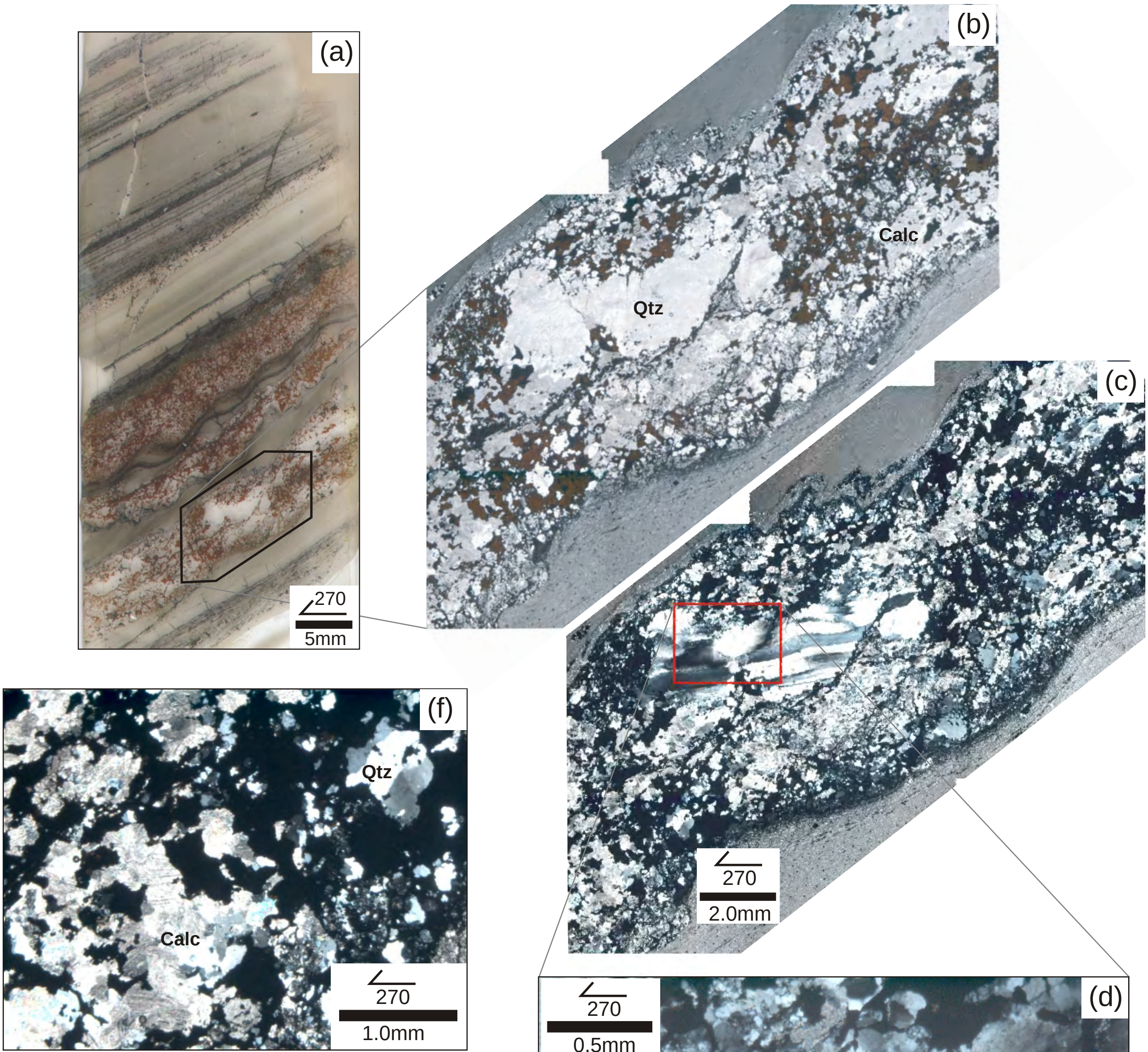

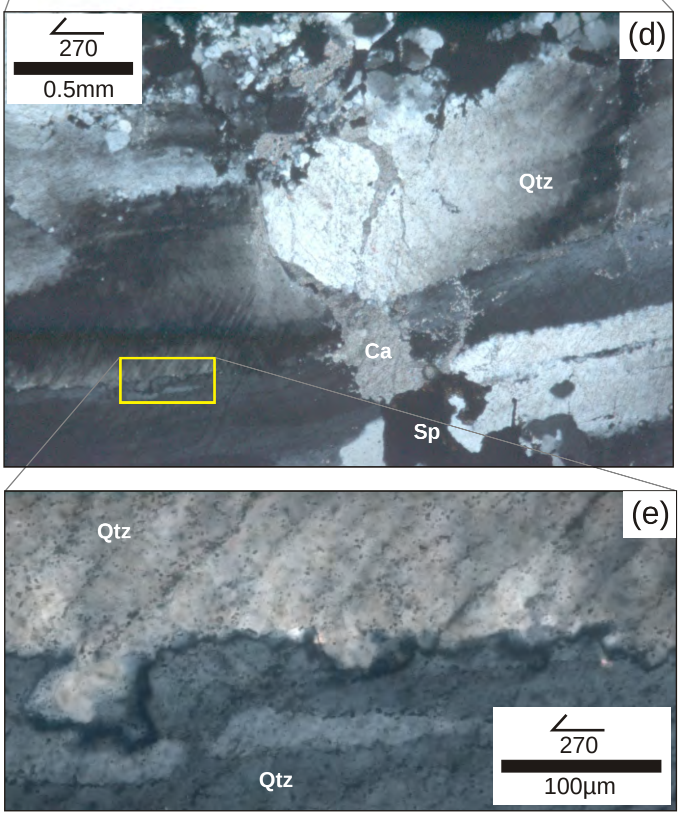

Figure 9. (a) Thin section with bands of vein hosted mineralization. (b) Photomicrograph in plane polarized light revealing larger clast of quartz in sphalerite, quartz, calcite matrix. (c) When viewed under crossed polars, the fibrous nature of the quartz clast is revealed. (d) Undulose extinction radiates symmetrically about a sphalerite+calcite filled fracture through the deformed fibres. (e) Grain boundary migration and inclusion-rich deformation lamellae distort a fibre contact. (f) Quartz and calcite associated with the sphalerite mineralization do not exhibit equivalent deformation. Sample 1012-6.

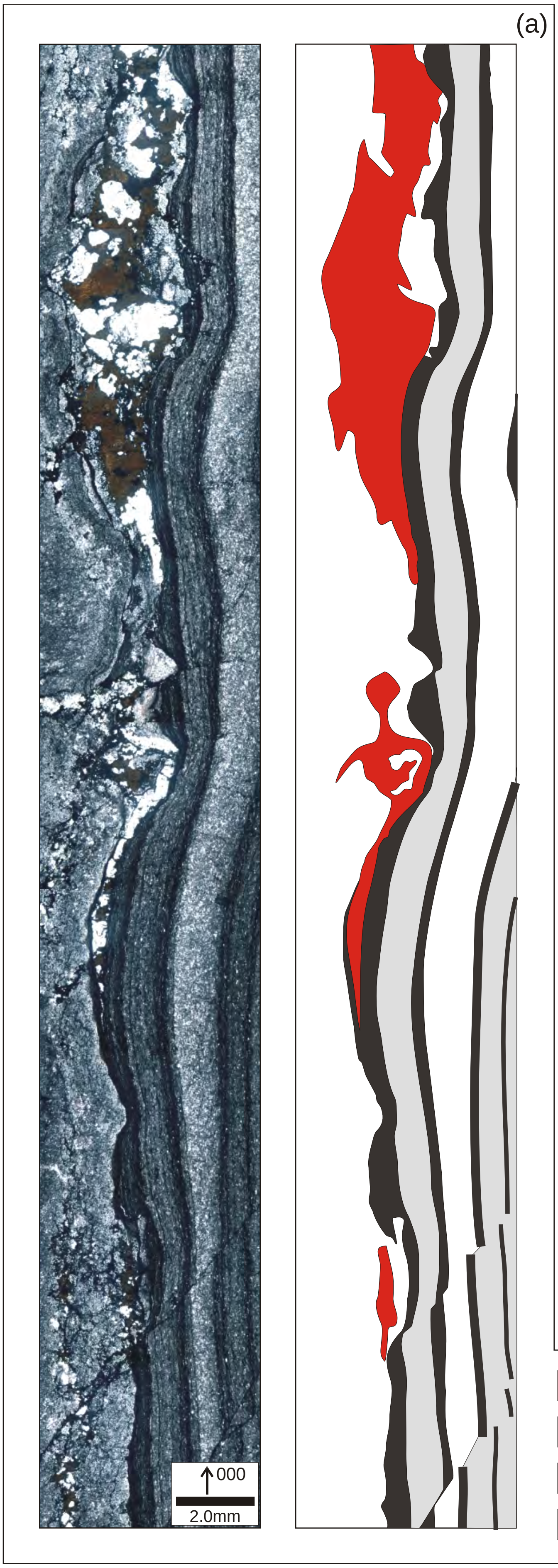

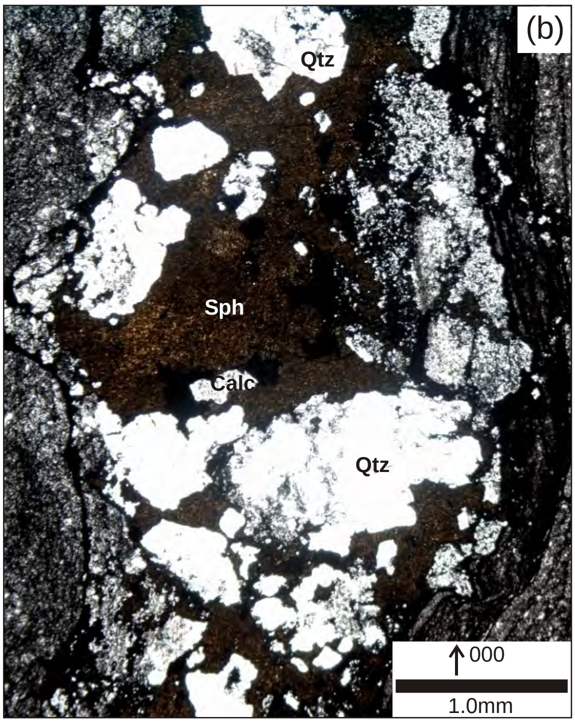

Figure 10. (a) Photomicrograph in plane polarized light and accompanying line diagram. Infill sphalerite (Sph)-quartz (Qtz) -calcite (Calc) veining occurs in dilational sites associated with flexures in bedding. (b) Enlargement of a section of the photomicrograph in (a) displaying sub- to euhedral calcite crystals in sphalerite. Sample 1311-7.

Another example of this type of vein-hosted sphalerite is shown in Figure 11. Sphalerite mineralization occurs almost exclusively on the western limb of an interpreted F_2 fold (Figure 11a) where small-scale F_4 folds (axial planes parallel to S_4 in this sample) have developed. Sphalerite-calcite veins are situated along bedding planes which have focussed dilation during deformation. The axial traces of the F_4 folds have a right-stepping geometry up-section suggesting that a reverse sense of shear has occurred on bedding planes offsetting the axial traces. As a result, the axial traces have a near vertical pitch in the vertical thin section (Figure 11d) as compared to the 76°E pitch of S_4 in the barren host rock away from the reactivated bedding (Figure 11d – white lines). Euhedral calcites (Figure 11c) are abundant in the veins and support interpretations of infill vein development and the undeformed state of the veins. Although the veins are interpreted as infill veins, the thickness of the layer from A-A' to B-B' on Figure 11a undergoes a 19% reduction associated with mineralization. Horizontal shortening of the layer evidenced by the abundant F_4 microfolds in the vicinity of B-B' may explain this. Note that dilation occurs only in the area of F_4 folding and not in the gently dipping eastern limb. West over east shear on bedding planes should have created dilation in the eastern limb, but the lack of mineralization here suggests that sphalerite mineralization is more intimately associated with the F_4 folding in this sample. The absence of F_4 folding in the thicker, less laminated siltstone layer immediately above the sphalerite mineralization equates to an absence of mineralization and confirms the role of the F_4 microfolds in facilitating mineralization of the host rock.

The sample in Figure 12 contains veins with gently pitching fibres that are interpreted to have formed during D_3. The siltstone layers intervening between the

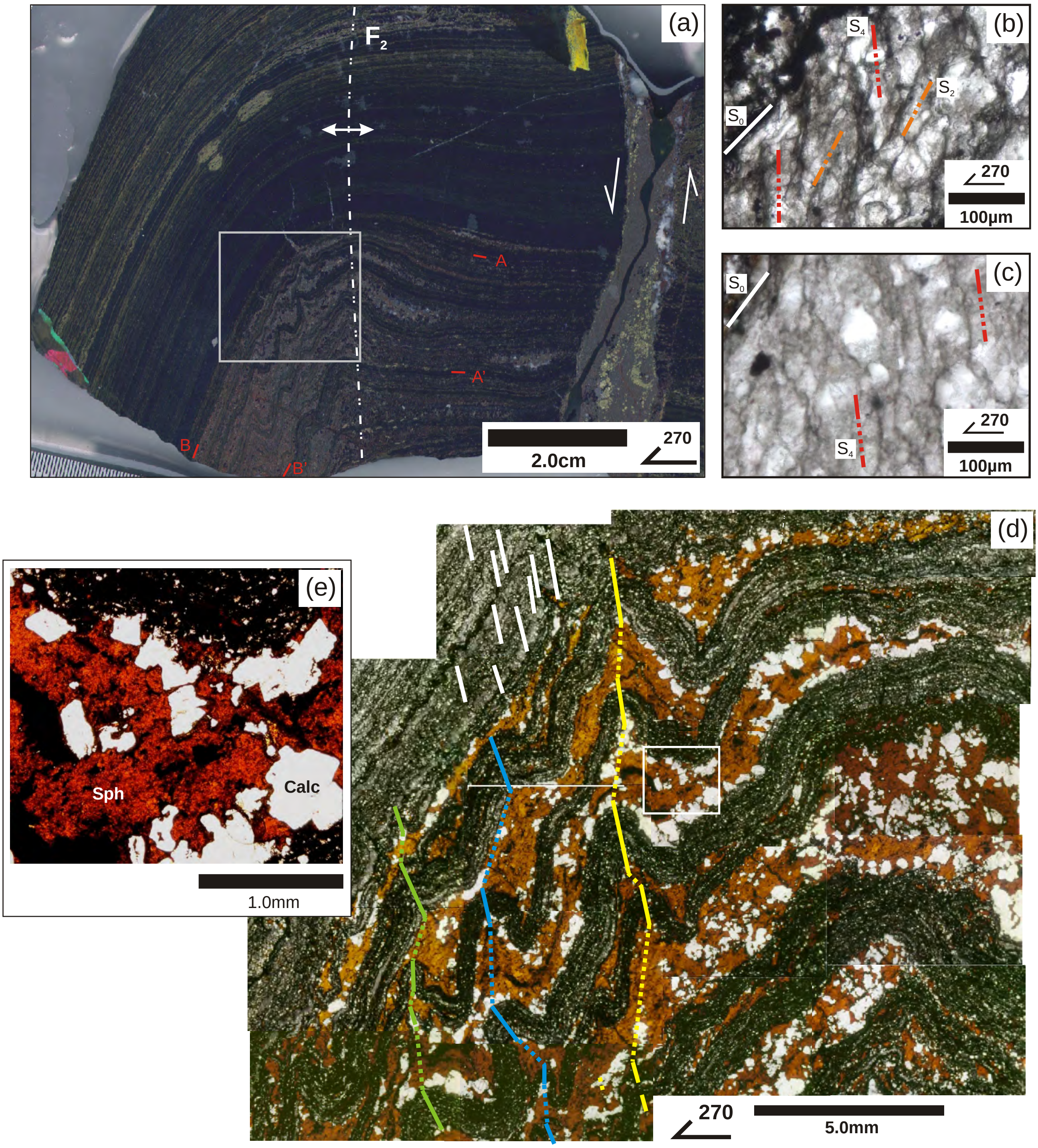

Figure 11. (a) Vertical face of an oriented hand specimen with mesoscale F_2 folding and sphalerite vein-hosted mineralization developed preferentially on the western limb of the fold. The width of the layer where barren (A-A') is 19% less than where significant mineralization occurs (B-B') . (b) and (c) Photomicrographs (plane polarized light) illustrating the bedding and foliation relationships, note that S_4 occurs as dissolution seams as opposed to crenulation of S_2. (d) Photomicrographs of the inset area in (a). Coloured lines indicate F_4 axial traces and white lines indicate S_4 orientation. F_4 axial traces display a right-stepping deviation up-section suggesting reverse slip on bedding. Mineralization occurs in dilational sites where bedding has gaped during late-D_4 deformation. (e) Enlargement of the inset from (d) emphasizing the undeformed euhedral calcites (Calc) developed with this mineralization type. Sample 0203-3.

mineralized veins do not have matching curvature, that is, they do not preserve their pre-veining geometry. This is interpreted to result from unfolding of the earlier fold during bedding reactivation. This is inferred as the mechanism for space creation and fluid focussing and requires west-over-east reactivation of bedding. This is the observed sense of shear on bedding during D_4. Steep fibres that postdate the gently pitching D_3 fibres also occur in the mineralized veins. They are consistent with vein opening during D_4. Note that the carbonate+sphalerite veins in Figure 12 propagate from narrow pyritic layers that, acting as a heterogeneity in the rock mass, focus slip and dilation on bedding planes. Both vein-brecciation/replacement and vein opening/infill are shown to be mechanisms for mineralization which are interpreted to have operated simultaneously during D_4 deformation.

Focussing of fluids into dilational sites in folds can be observed at a larger scale where the short-limb of an F_2 fold is preferentially mineralized (Figure 13a). Numbered sample locations in the mapping (Figure 13a) correlate with images of samples. Slightly overturned, steeply-dipping bedding in the western sample (1012-3) is devoid of sphalerite mineralization. Samples from the gently-dipping F_2 short-limb (1012-5, -6) contain the most sulphide. The steeply dipping bedding in sample 1012-8 from the eastern fold limb is also only weakly mineralized. Sphalerite mineralization is dominantly replacive in these samples as the increase in thickness of the sphalerite-rich zone from sample 1012-3 to 1012-4 (Figure 13b) mimics thickening of the barren layers. Sample location 1012-6 in Figure 13a correlates with the sample studied in detail in Figure 9 (different samples from the same locality) in which sphalerite mineralization is interpreted as postdating earlier fibre vein formation. Microscale brecciation and dilation

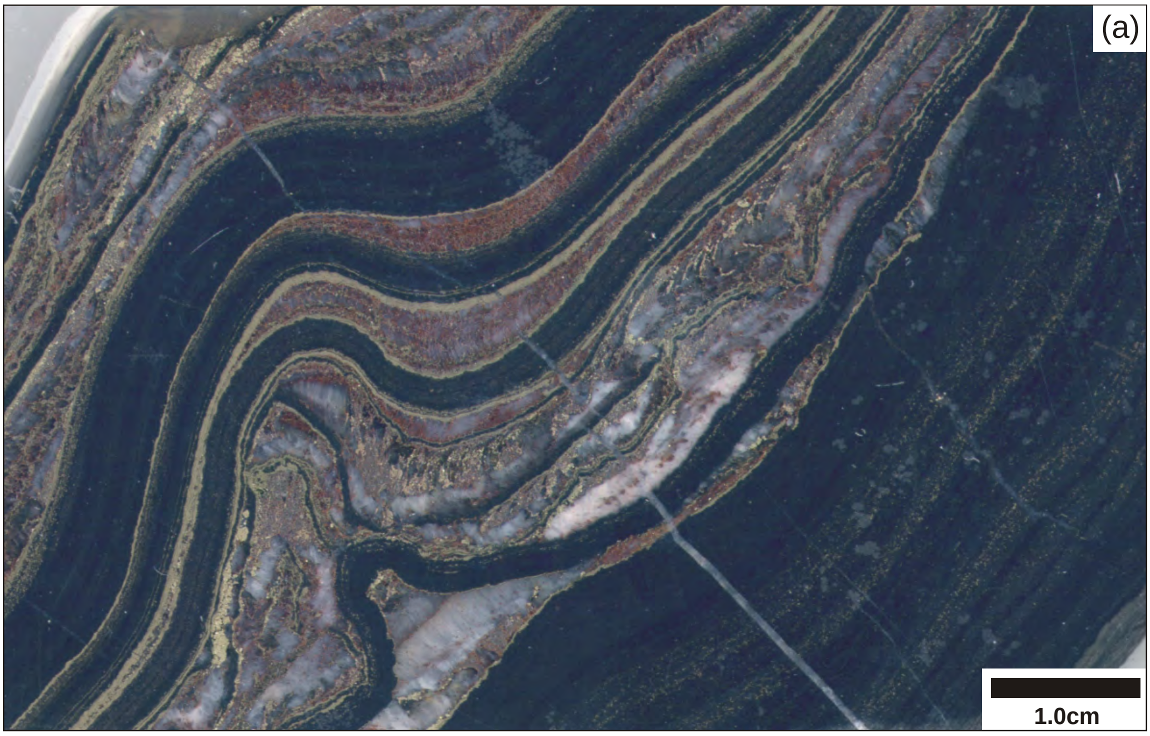

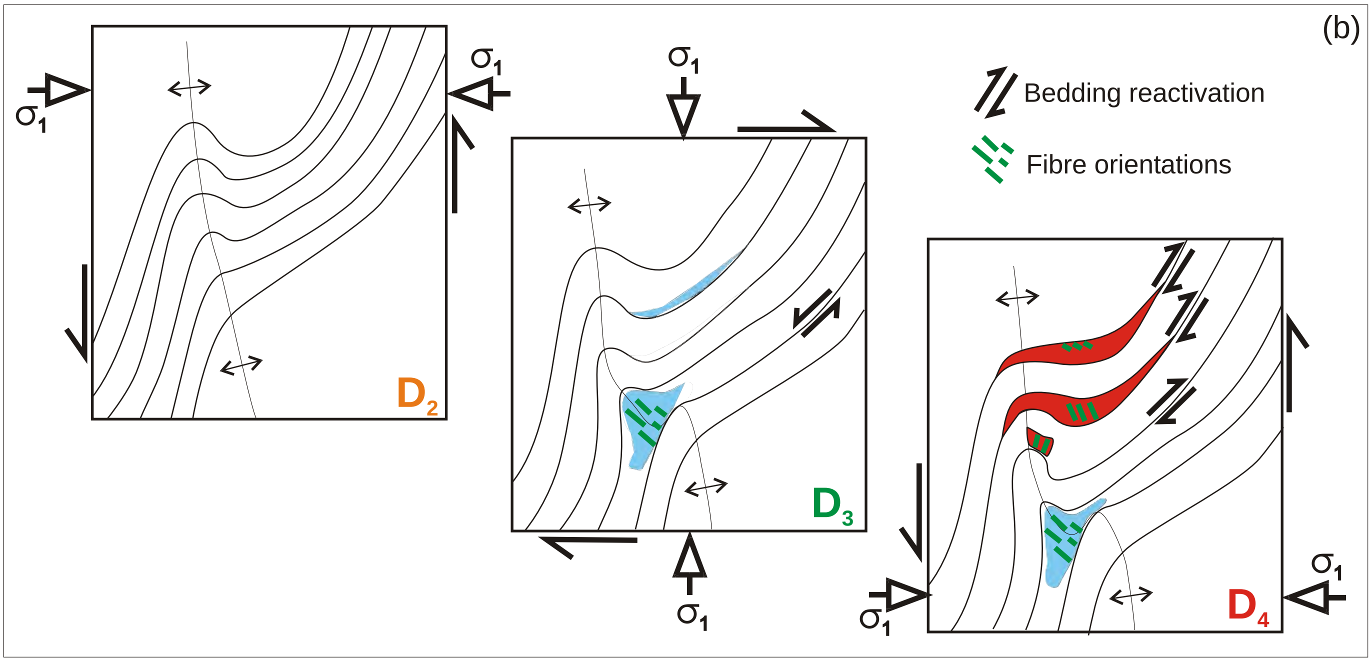

Figure 12. (a) Hand-specimen (unoriented) of bedding-parallel veining within bedded siltstone and minor pyritic siltstone. Pyritic layers (bottom right corner) develop into dilational veins in the short-limb of the small-scale fold (which is probably of D_2 timing) demonstrating how bedding-paralllel veins can nucleate on heterogeneities during folding. (b) Diagrammatic sketches of the development of the veins observed in (a) during the deformation episodes D_2, D_3 and D_4. Fibre orientations preserved in the sample suggest that vein development began during D_3 and these veins continued to gape and were brecciated during the subsequent D_4 episode. Sample 960817_ 125.35m

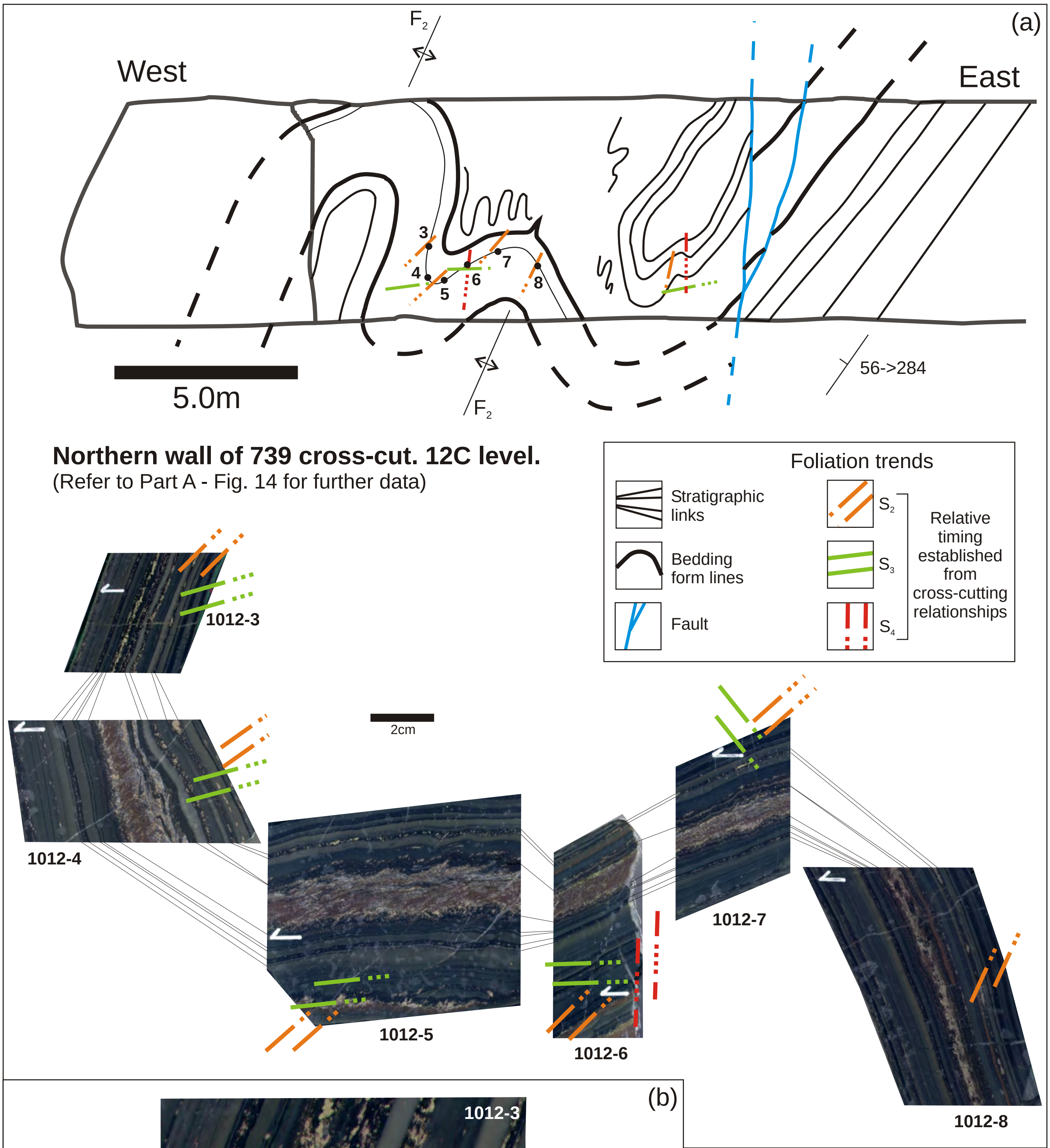

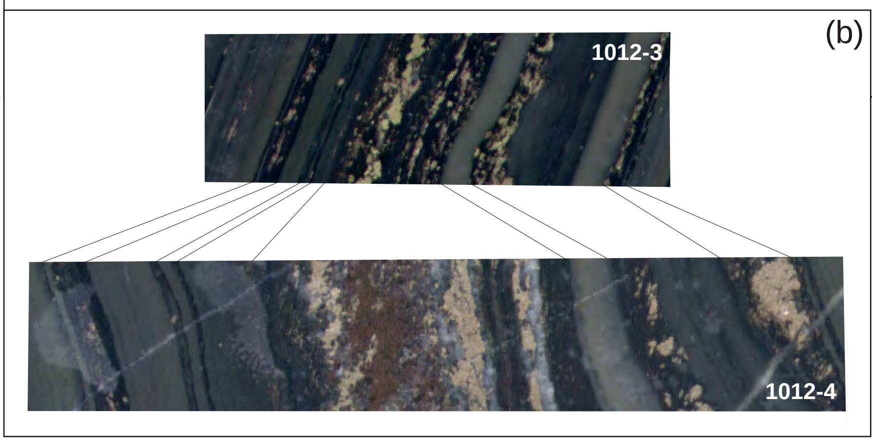

Figure 13. (a) Mapping and samples demonstrating the preferential mineralization of the short-limb of an F_2 fold. Sample locations in line-drawing correlate with images below. (b) Enlargement of the transition from 1012-3 to 1012-4. The increase in the thickness of the mineralized zone is consistent with that of the barren beds. Layering is thinned due to higher strain on the sub-vertical limb of the fold.

of the short-limb of this F_2 fold is therefore interpreted to have occurred subsequent to F_2 folding and resulted in preferential mineralization in the more gently dipping bedding.

Vein-hosted sphalerite samples do not exhibit intense deformation features such as deformation twins, preferred orientation, or pervasive recrystallization in thin section. Folding of bedding in a vein-hosted sphalerite sample is demonstrated in Figure 14a. The folds have an apparent isoclinal geometry which may be a factor of the gently plunging orientation of the folds. Twinning in the sphalerite is straight and parallel sided, and grain boundaries are gently curved with only minor bulging (Figure 14b, c). This suggests that these sphalerite grains have undergone only weak deformation as the microtexture of sphalerite occurring between folded layers is not consistent with intense folding. Despite triple point junctions near 120°, the coarse grain size and absence of relict grains from which those pictured might have recrystallized suggest that there has been no recrystallization and that the fabric represents the primary texture of the ore. There is a lack of timing criteria for the folding in this sample, however, the folds clearly have sub-horizontal fold axes due to the apparent doubly-plunging fold closure in the upper part of the section. The fold axes must therefore be sub-parallel to the horizontal thin section. F_2 folds generally have more moderate plunges and F_4 are gently plunging to sub-horizontal, it is therefore likely that folding in Figure 14a represent the latter. The sphalerite mineralization appears to be largely unstrained and therefore postdates D_2 and may occur syn-/post- F_4 folding. Sub- to euhedral calcite crystals occur within sphalerite in the top right hand corner of Figure 14a as observed in previous samples studied, indicating that the sph+carb assemblage has undergone little strain, supporting a post-D_2 interpretation.

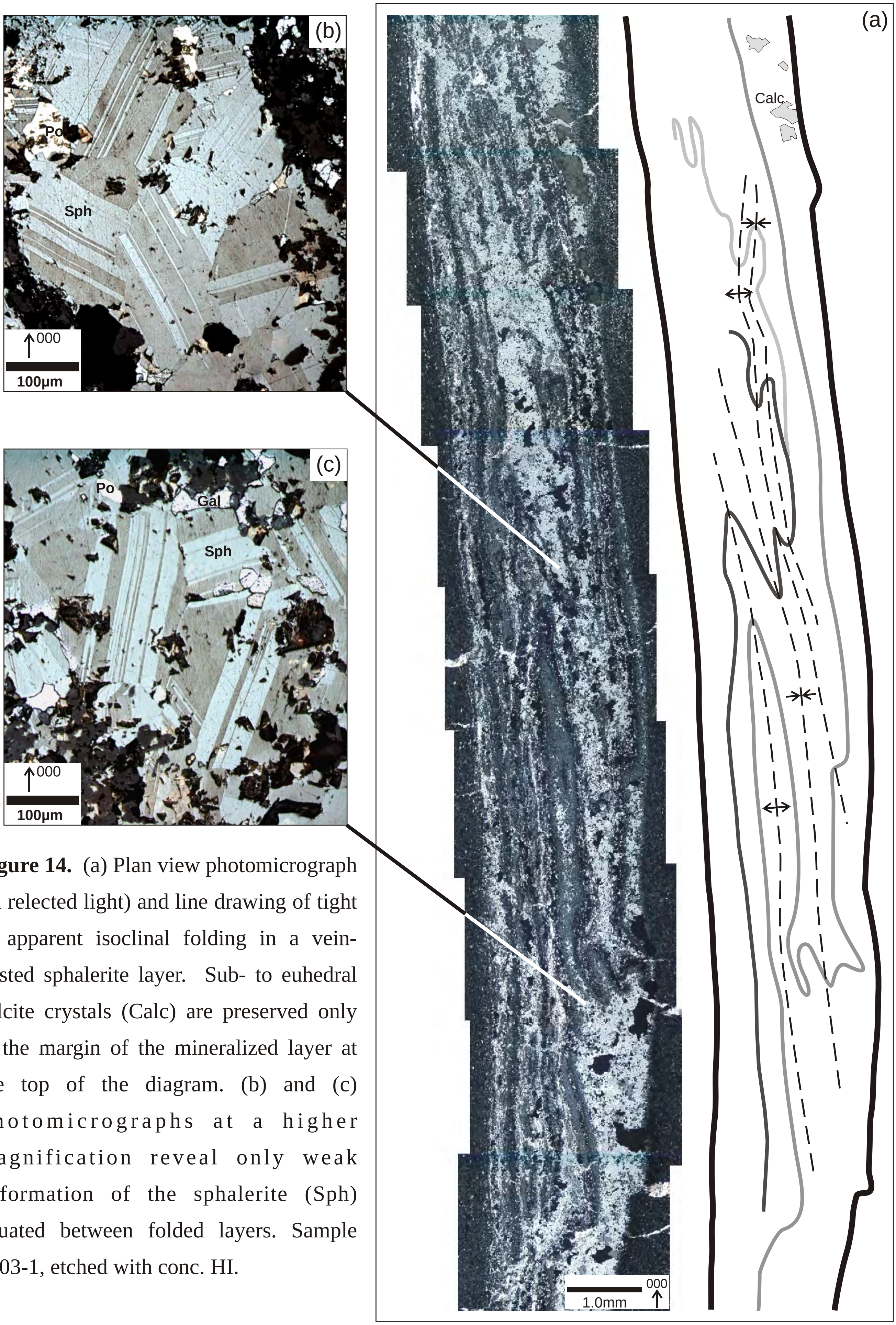

Figure 14. (a) Plan view photomicrograph (in relected light) and line drawing of tight to apparent isoclinal folding in a vein-hosted sphalerite layer. Sub- to euhedral calcite crystals (Calc) are preserved only at the margin of the mineralized layer at the top of the diagram. (b) and (c) Photomicrographs at a higher magnification reveal only weak deformation of the sphalerite (Sph) situated between folded layers. Sample 0103-1, etched with conc. HI.

2.1.4 Implications of cross-cutting relationships and palaeostress estimation

Palaeostress estimates have been obtained from calcite veins in a sample containing vein-hosted sphalerite (Part A – Figure 19, 20) and constrained by overprinting vein relationships. The specimen used for the measurements is displayed in Figure 15a, and palaeostress estimates are annotated. The steep, east-pitching, and variably mineralized dolomite veins are cross-cut by vein-hosted sphalerite layers (Figure 15b) and these two vein generations have been shown to be chemically distinct (Part A – Figure 19f). The mineralized layers are in turn cut by late, gently pitching calcite veins (‘late vein’: Figure 15a). Cross-cutting relationships and continuity of the steeply pitching veins has been established in Part A (refer to Part A – Figure 19b). Relict deformed vein material (blue areas – Figure 15c) can be observed in the vein-hosted sphalerite also supporting the interpreted relative timing relationships. Palaeostress estimates are consistent with the observed vein paragenesis in that the deformed veins (although of dolomite mineralogy) have higher palaeostress than the mineralized and late veins. The fact that the calcites in the ore vein do not record the entire deformation history (i.e. 219Mpa inferred from the deformed dolomite vein) indicates that the mineralization postdates an episode of significant deformation. Orientation of the veins to the stress field is such that the vein-hosted sphalerite layers, had they occurred pre-D_2, would be expected to be significantly deformed as they are oriented favourably for bedding reactivation during this deformation. As discussed in Part A, the orientation of the deformed veins approximates the ac-vein orientation of F_2 folds. The vein-hosted mineralization in this sample can therefore be interpreted as postdating D_2. Similarities in palaeostress estimates between the mineralized vein and cross-cutting late-vein suggest a similar deformation history.

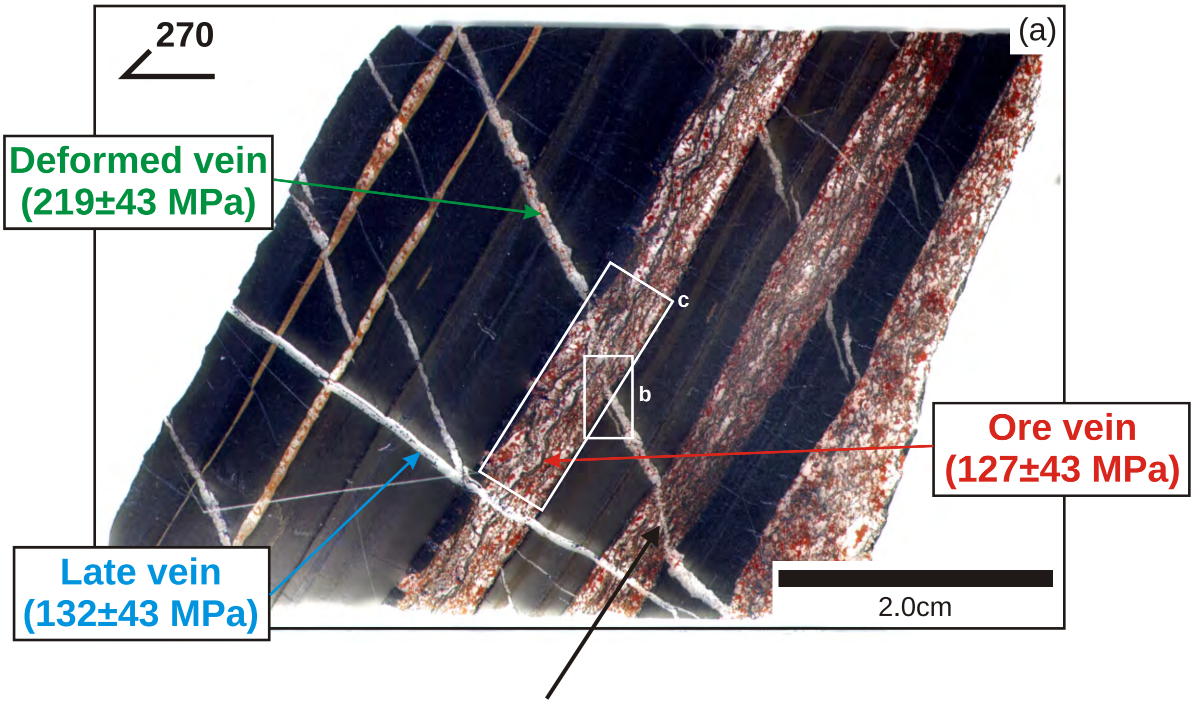

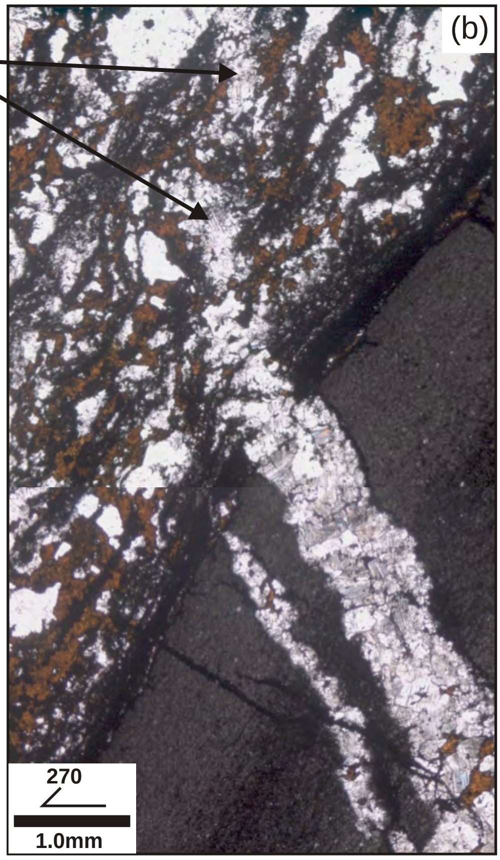

Figure 15. (a) Thin section with estimated palaeostress (differential) annotated on pre-ore deformed, ore-stage, and post-ore carbonate-rich veins. Ore veins overprint the steeply-pitching deformed veins and do not record the same deformation history (127Mpa compared with 219Mpa) indicating a younger age for the vein-hosted sphalerite mineralization. (b) Enlarged inset area demonstrating the cross-cutting relationship between ore-veins and the steeply pitching veins interpreted as D_2 'ac' veins as their orientation is perpendicular to the orientation of F_2 fold axes (see Part A-Fig. 18b). Sample 960519.

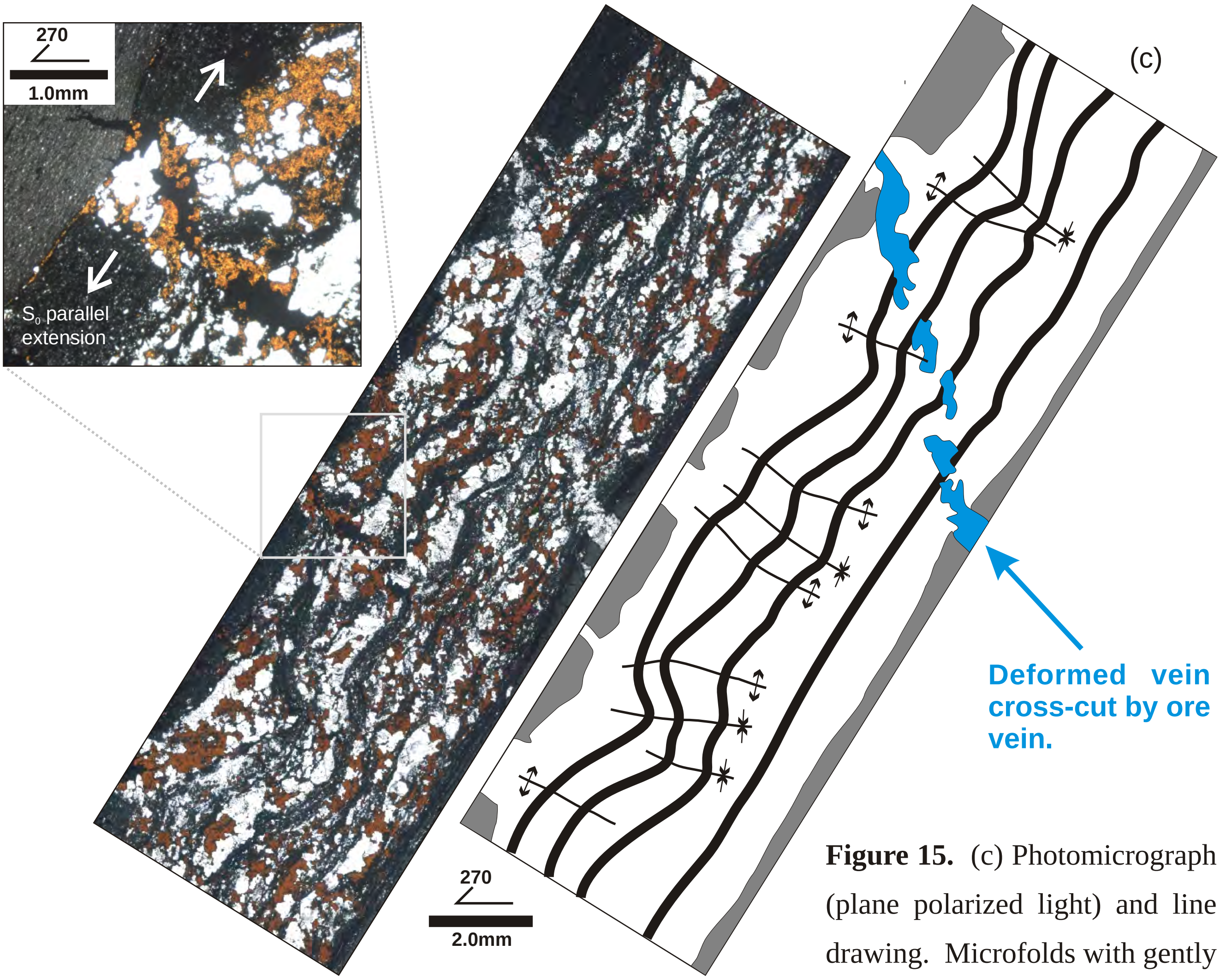

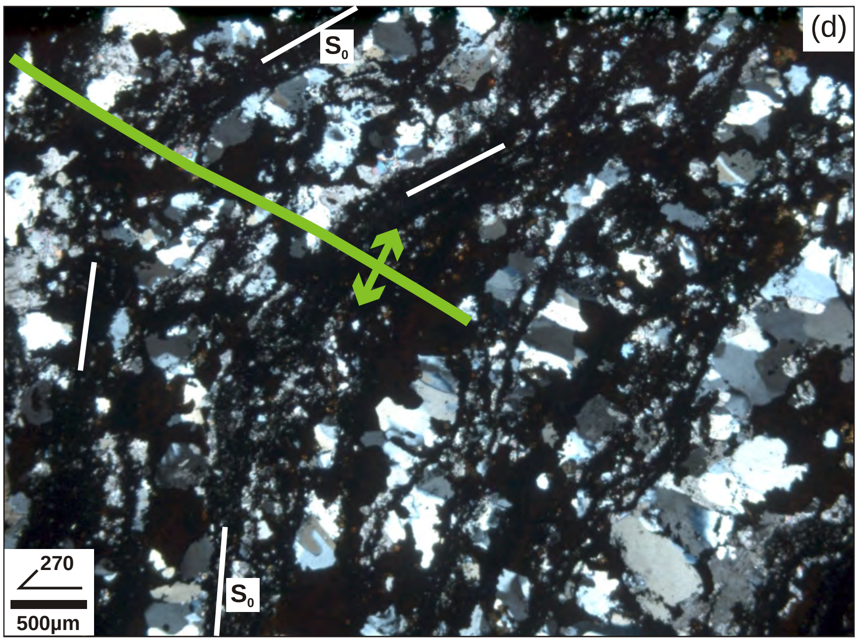

Figure 15. (c) Photomicrograph (plane polarized light) and line drawing. Microfolds with gently pitching axial traces occur only within the mineralized layer and are consistent with F_3 folding. Sphalerite occurs as irregular masses within quartz-calcite microveins and in locations of bedding-parallel extension (see enlargement). (d) Photomicrograph (crossed polars) displaying an F_3 microfold and abundant microveining. Fibres in the microveins are parallel to the axial trace (green) and can be interpreted as forming synchronous with the F_3 microfolds. Sample 960519.

Microfolds with gently pitching axial traces are present only in the mineralized layer (Figure 15c) and there is little evidence for similarly oriented deformation in the adjacent siltstones. This orientation is consistent with D_3 deformation features and the microfolds have the same s-shaped vergence as meso-scale F_3 folds. Quartz and calcite fibres in the ore vein parallel the axial planes of microscale F_3 folds (Figure 15d). As fibres in extension veins parallel the direction of extension (Ramsay and Huber, 1983), parallelism of carbonate fibres with F_3 axial planes therefore suggests cogenesis. Formation of the host microveins is inferred as syn-D_3. Another example of this can be seen in Figure 4 where relict fibres pitch at approximately 20°E compared with the 25°E pitch of F_3 axial traces in Figure 15c. Valenta (1988) records a relationship between the incidence of F_3 folds or subhorizontal S_3 crenulations and bedding parallel vein development and also observed sulphides cross-cutting early fibrous gangue textures in the Hilton deposit. Such textures were interpreted as sulphides post-dating a vein-forming event (Valenta, 1988). Sphalerite replaces D_3 quartz and calcite fibres (Figure 4) and occurs as irregular masses throughout the veined layer with no preferential sites of mineralization relative to F_3 microfolding (Figure 15c). Vein-hosted sphalerite mineralization is texturally continuous with apparent boudin-necks/sites of bedding parallel-extension (Figure 15c – enlarged area). The D_3 stress field is interpreted to have a component of sub-vertical shortening based on the gently dipping fold axial planes and crenulations (see Part A). Extension on bedding planes as illustrated is therefore considered unlikely during D_3 and is more consistent with sub-vertical extension during D_4. These observations suggest post-D_3 timing of sphalerite in this example of vein-hosted sphalerite.

The precursor to the micro-veined mineralized layer is thought to be a laminated shale horizon which, due to competency/rheological contrast, has focussed strain in the form of bedding reactivation within the layers during D_2. Syn-folding micro-vein development during D_3 (as evidenced by the parallelism of fibres and fold axial traces discussed above) is focussed in these layers. The lack of folding or crenulations in the barren siltstones suggests that D_3 strain has been partitioned into the finely laminated layers which alternate with the fine-grained foliated (S_2) siltstones. Although the siltstones are of finer grainsize than the mineralized layer, and would therefore be assumed to be of lower strength, heterogeneity within the mineralized layer is interpreted to have significantly reduced the strength of the veined layer. The heterogeneity is in the form of relict bedding and aggregates of fibrous calcite and quartz, and K-feldspar (see precursor veined layer in Figure 6c). Weak deformation involving bedding reactivation during D_4 caused fracturing of the vein material and sphalerite is deposited as both breccia-fill and replacement of the pre-cursor vein material.

If the sphalerite, calcite, quartz, and K-feldspar assemblage in Figure 15 pre-dated D_2, the mineralized layer should have focussed strain during all subsequent deformations due to this heterogeneity of the sphalerite, calcite, quartz, and K-feldspar assemblage, and the presence of relict bedding. The mixed assemblage of dominantly calcite and sphalerite has a net strength equal to the intermediate strength of the constituents (Marshall and Gilligan, 1987), i.e. the vein will have a net strength stronger than calcite but weaker than sphalerite.

Dolomite is stronger at low temperatures than calcite (Wenk, 1985) due to the fewer twin forms available in the lower symmetry crystal structure of dolomite (Barber and Wenk, 1979). Calcite-rich veining would therefore be weaker than the host dolomitic siltstones. Experimental deformation of sphalerite and carbonate rocks (Figure 16) indicates that at temperatures of deformation in the order of 200-250°C (as interpreted in the George Fisher area) sphalerite is weaker than dolomite at equivalent temperatures and stronger than coarse grained calcite (marble). In terms of the sample in Figure 15, deformation of the sample during D_2 would result in higher strain in the mineralized layer with deformation of the sphalerite and more intense deformation of the calcite associated with the mineralization. Instead, as indicated by visual comparison of their form and microstructure as well as palaeostress measurement (which uses empirical data of twin occurrence, width and density), the calcite associated with sphalerite mineralization is considerably less deformed than the D_2 deformed equivalent (steeply pitching vein – Figure 15). This suggests that the sphalerite, calcite, quartz vein assemblage post-dates D_2.

Lower than expected response of sphalerite layers to folding in the Mt Isa mine (McDonald, 1970) was interpreted to be a function of the thin nature of layers, delicacy of alternating silicate and sulphide laminae in the layer, and the relative strength of the layer constituents. However, thin laminated sulphide and silicate layers are rheological heterogeneities in the siltstone dominated rockmass and, combined with the lower relative strength of the sulfides (Figure 16), would focus deformation (F_3 folding – Figure 15) rather than resist it. An alternative interpretation to that of McDonald (1970) could be that the sulphides post-date the folding.

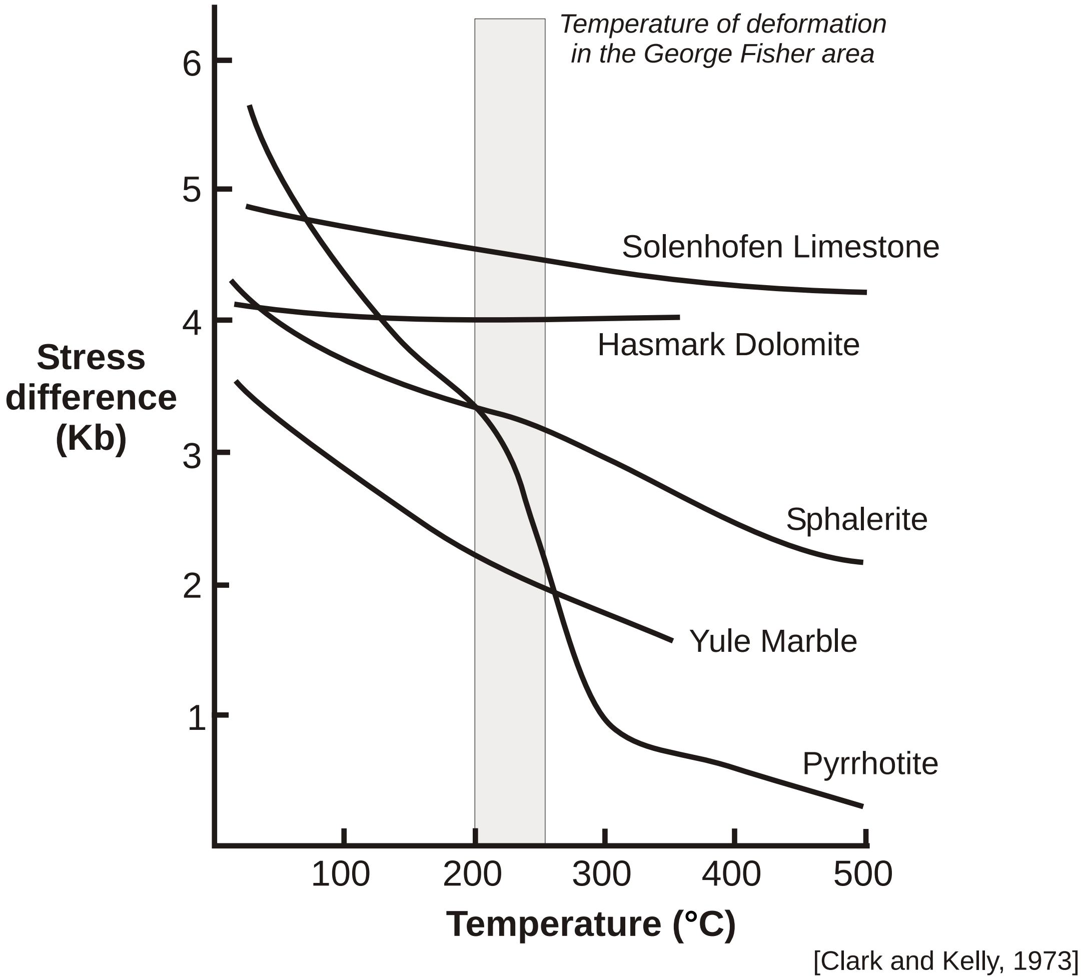

Figure 16. Graph of stress difference (ultimate strength or strength at 10% strain at confining pressure of 1Kb) vs temperature from Clark and Kelly (1973). The maximum temperature of deformation for the George Fisher area is represented as the temperature range from 200-250ºC. At this temperature, Sphalerite is stronger than marble (coarse calcite) yet weaker than dolomite reflecting the contrasting strength of the two carbonate minerals. With respect to George Fisher, an inference of this diagram is that a sphalerite layer or a sphalerite+calcite layer will be weaker than the host dolomitic mudstones and should therefore focus strain during deformation. Grain size and heterogeneity of the respective rock types will also affect their relative strengths.

Deformed vein-hosted sphalerite has been observed within an intense fold zone which records three fold generations; F_2, F_3, and F_4 (Figure 17a). Structural repetition of a mineralized stratigraphic package has occurred (Figure 17a) and samples were obtained (Figure 17b and c) so as to compare the microstructural characteristics both inside and outside the fold zone. Outside the fold zone, in sample 1011-2, grain boundaries are smoothly curved and grains have simple grain shape, twins are parallel sided and straight, and grain-size is uniform; indicating the sample is at most weakly deformed (Figure 17d). Within the folded zone, in sample 1011-7 (Figure 17e), grain boundaries and shapes are irregular but twins are only mildly disrupted, generally still have parallel sides, and variability in grain size is observed, the equivalent of which is not seen in sample 1011-2 (Figure 17d). These observations suggest that the sphalerite has undergone deformation but the lack of preferred orientation of grains or obvious internal strain (e.g bent twins, deformation twins) make a conclusive interpretation difficult. Analysis of selected grains from each sample using the fractal analytical method described in Part C enables independent classification of the samples based on the grain size and irregularity of the grain boundaries, calculated as its fractal dimension (Figure 18). An overall reduction in grain size and an increase in the fractal dimension of the grains, equating to increasing grain boundary complexity is observed when comparing sample 1011-2 to sample 1011-7 (Figures 17 and 18). These samples plot in the ‘weakly deformed’ and ‘deformed’ fields (established in Part C) respectively. This demonstrates the application of fractal analysis of sphalerite grain boundaries in a microstructural study where some ambiguity in qualitative analysis of the microstructures exists.

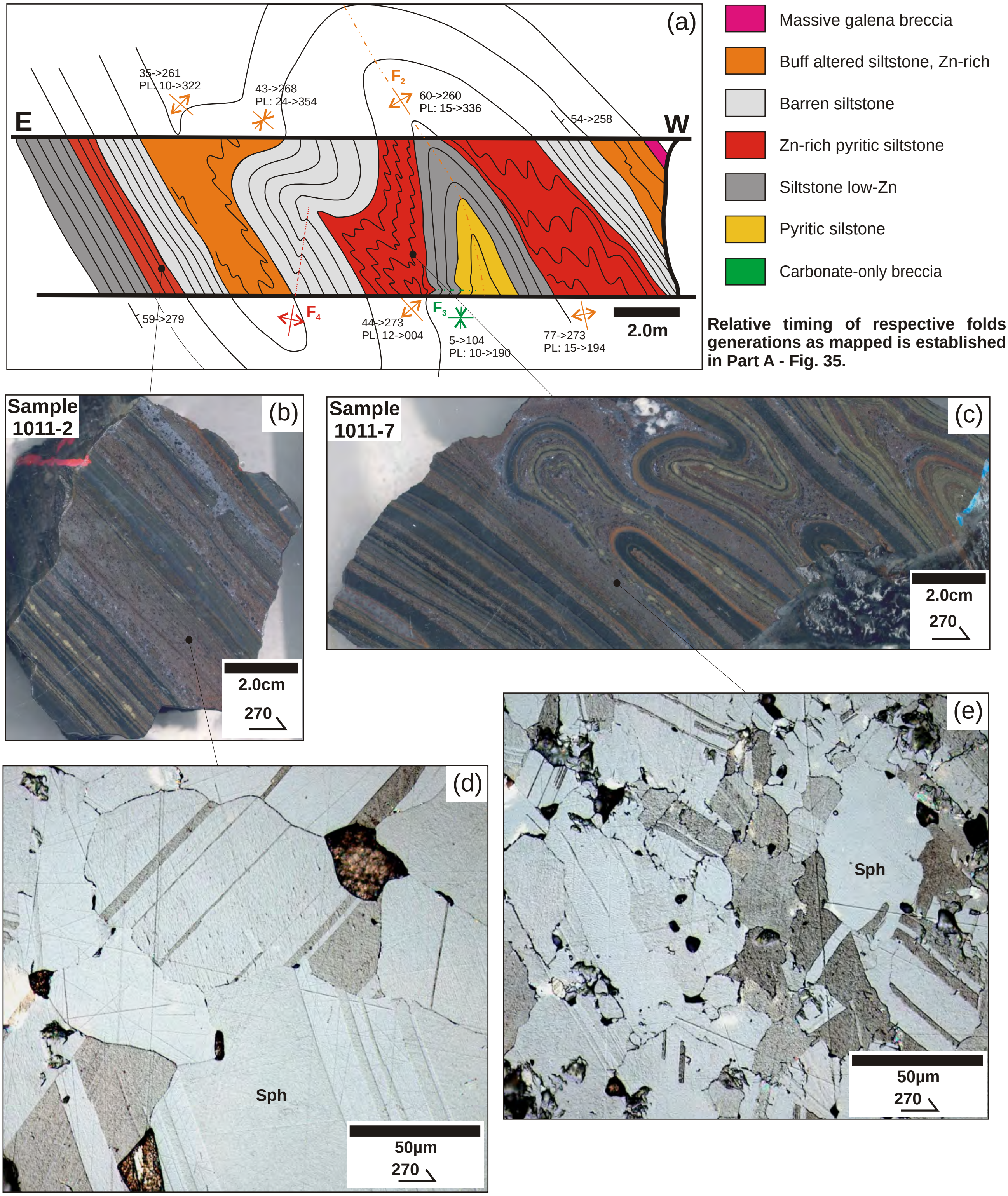

Figure 17. (a) Mapping of 737 cross-cut 12C, samples 1011-2 (b) and 1011-7 (c) from outside and within the fold zone respectively, and photomicrographs (d and e) of each (reflected light, etched with conc. HI) demonstrating the contrasting microstructure of the sphalerite in both samples. Sphalerite from sample 1011-2 (d) has gently-curved grain boundaries, straight and parallel-sided twins, low variability of grain size whereas sample 1011-7 (e) has irregular shaped grain boundaries and grain shape, and greater variability in grain size, but only minor disruption of twins.

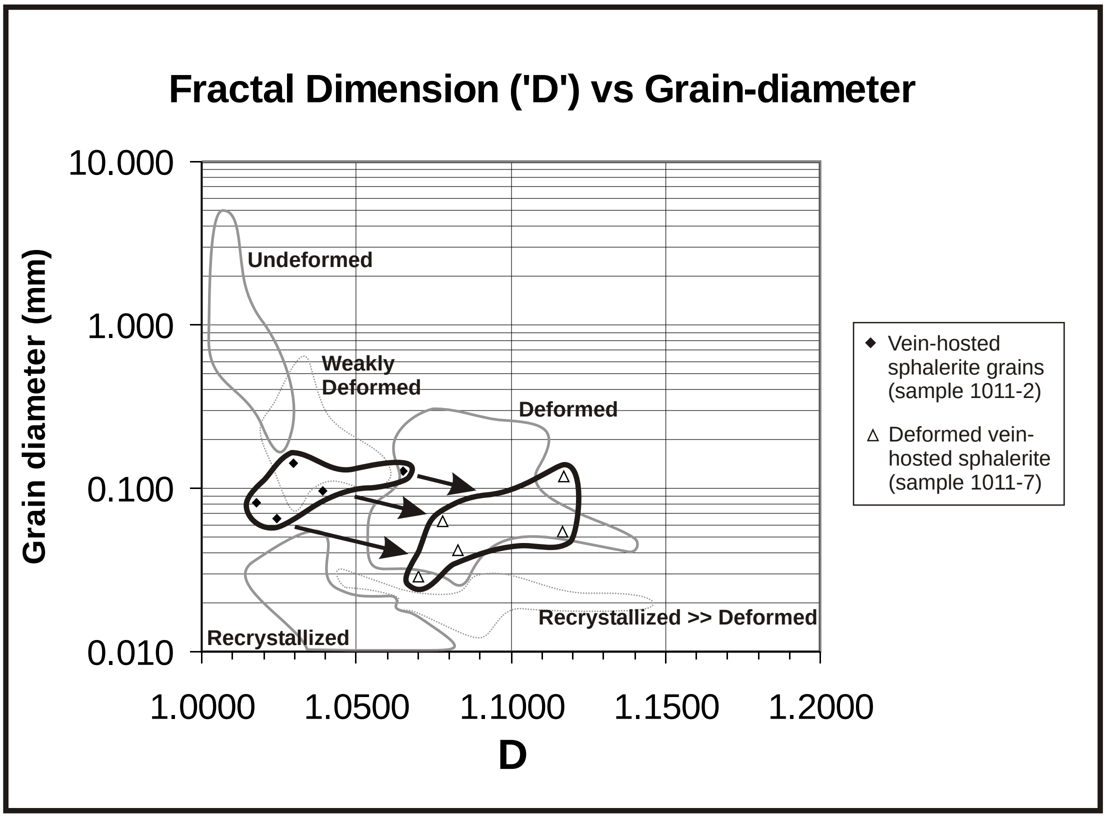

Figure 18. D vs grain size plot with fields established in Part C. Measurements from selected grains in both 1011-2 and 1011-7 (Figure 16) are plotted and their positions are consistent with 1011-2 representing weakly deformed sphalerite and 1011-7 representing deformed sphalerite. Arrows indicate the path from weakly deformed to deformed sphalerite capturing both an increase in the fractal dimension of the grain boundaries and grain size reduction.

As the sphalerite in the deformed sample (1011-7) does not preserve a foliation, it is not possible to directly correlate the microstructures with a distinct deformation episode. However, the stratigraphy hosting both samples 1011-2 and 1011-7 has been affected by pervasive D_2 deformation which has produced the larger scale folds and resulted in the 60° dip of bedding. Only sample 1011-7 is in the vicinity of the smaller scale F_3 and F_4 folds. The disparity of deformation features is inferred to be a result of post-D_2 deformation affecting only sample 1011-7. The lack of deformation in sample 1011-2 suggests that the sphalerite mineralization post-dates the main strain event, D_2. However, these observations do not preclude the development of a strain-free fabric after the D_2 episode.

Cumulative thickness of vein-hosted mineralization in diamond drill-hole intersections were measured for C, D, and G ore-horizons. At the mine-scale, vein-hosted sphalerite is concentrated in the F_1 short-limb zone and plunges parallel to the axes of the mine-scale F_1 folds (Figure 19). There is a trend in the cumulative thickness of vein-hosted sphalerite from smaller to greater thickness from hangingwall (Figure 19a) to footwall (Figure 19c) stratigraphy. The thickness of the stratigraphic packages (C is the narrowest) affects the thickness of mineralization that can be hosted, however, a deposit scale zonation of Pb and Zn grades (Pb-rich hangingwall and Zn-rich footwall) established in Part B also exists. Given that this textural variety of mineralization at George Fisher accounts for approximately 80% of the cumulative thickness of sphalerite ore types in drill-hole intersections, its spatial distribution will determine deposit-scale trends in Zn grade. Deposit-scale controls on the concentration of Zn in the F_1 short-limb

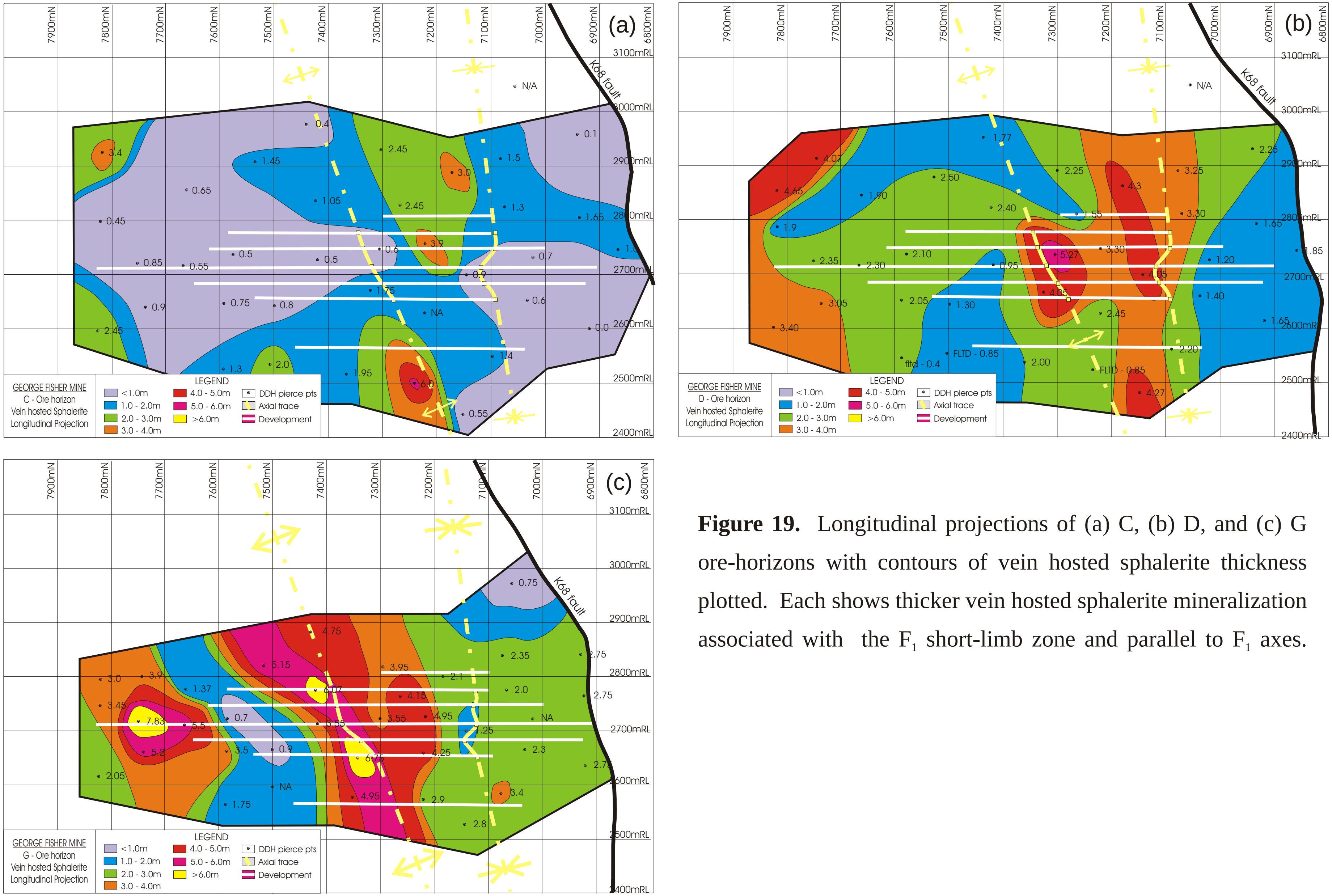

Figure 19. Longitudinal projections of (a) C, (b) D, and (c) G ore-horizons with contours of vein hosted sphalerite thickness plotted. Each shows thicker vein hosted sphalerite mineralization associated with the F_1 short-limb zone and parallel to F_1 axes.

zone (Part B) are consistent with the preferential development of vein-hosted sphalerite in this region. More intense development of S_4 in the short-limb (Part A – Figure 30) is also consistent with increased brecciation and fluid flow in this region during D_4.

2.1.5 Summary and interpretation

Based on microstructural observations, the vein-hosted variety of sphalerite mineralization encompasses two sub-types, considered to have formed contemporaneously involving:

- micro-brecciation and replacement of an existing lithology/quartz-carbonate-K-Feldspar vein by sphalerite±calcite±pyrrhotite, and
- deposition of sphalerite±quartz ±calcite±hydrophlogopite in veins which form due to competency contrasts between adjacent layers and/or in rocks subjected to bedding plane reactivation.

Bedding-parallel migration of fluids through fracture networks and along grain-boundaries has resulted in replacement of gangue minerals. Replacement fronts which are truncated by cross-cutting veins confirm the preferential movement of fluid along favourable lithological units and that this mineralization postdates an episode of vein-formation and associated deformation.

Several independent observations suggest that this textural variety of sphalerite mineralization is relatively unstrained:

- Pervasive recrystallization of sphalerite has not occurred (cf. Valenta, 1988) and lack of preferred orientation, absence of deformation twins, and only minor bending of twins in the sphalerite are interpreted to represent mild modification of the primary ore texture.

- An interpreted pre-D_2 foliation which is overprinted by coarse pyrite associated with sphalerite mineralization (Valenta, 1988, 1994) is not manifest in the sphalerite at George Fisher either as preferred orientation of grain shapes or grain boundaries.
- Fractal and grain size analysis of vein-hosted sphalerite grains indicates that they are only weakly deformed and these grains may define a previously unrecognized field in this scheme representing ‘replacive’ sphalerite.
- Vein-hosted sphalerite cross-cuts deformed veins (Figure 15), overprints syntectonic quartz-calcite fibres in bedding-parallel veins (Figures 4 and 8), and contains clasts of deformed quartz in the lesser deformed matrix (Figure 9). This indicates that vein-hosted sphalerite mineralization postdates a deformation episode interpreted as D_2 based on the intensity of quartz deformation. Pre-mineralization carbonate fibres, distinct from quartz-fibres more closely associated with mineralization, in bedding-parallel veins also indicates deformation prior to vein-hosted sphalerite introduction (Figure 6).
- Euhedral calcites, and less-commonly quartz, which appear undeformed are associated with a variety of vein-hosted sphalerite mineralization.

2.2 Massive sphalerite

Massive sphalerite bands differ from vein-hosted sphalerite due to a lack of significant banding or relict layering in hand-specimen (Figure 20a) and gangue mineral component (Figure 20b and c), compared to vein-hosted sphalerite (e.g. Figure 15). This textural

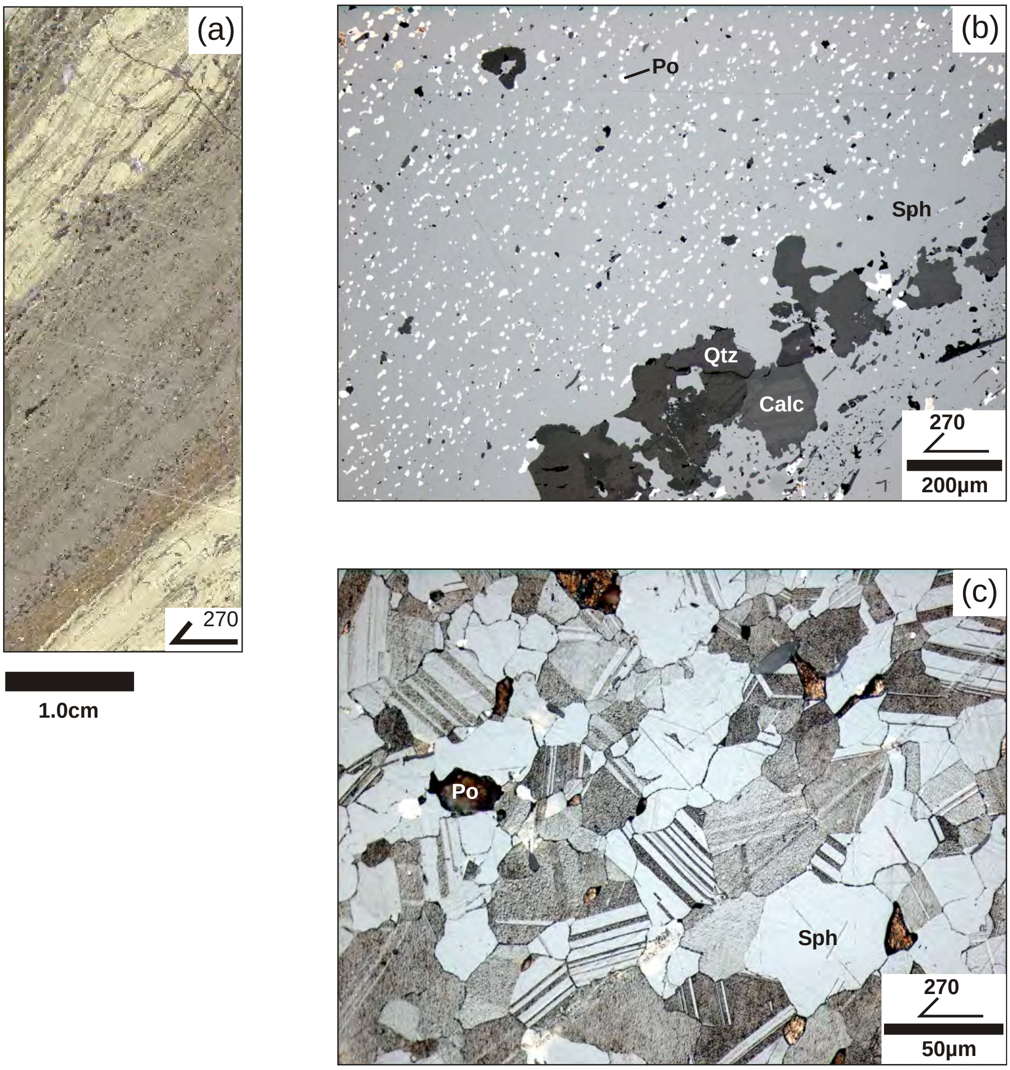

Figure 20. (a) Hand specimen of a massive sphalerite band in a massive pyrite host (sample 0803-1), (b) Photomicrograph (reflected light) displaying the massive nature of the ore (compared to vein-hosted sphalerite) and abundant pyrrhotite inclusions (sample 0803-1), (c) Photomicrograph (reflected light, etched with conc. HI) of the massive sphalerite ore showing sphalerite grains with straight twins and generally smoothly curved to mildly irregular grain boundaries indicating weak deformation (sample 0803-1).

variety accounts for approximately 4% of sphalerite ore thickness in drill-hole intersections in C, D, and G ore horizons. In thin-section, microtextures (Figure 20c) are similar to the vein-hosted sphalerite, except that sphalerite constitutes up to ca. 90% of the mineralization rather than ca. 40% in typical vein-hosted sphalerite, suggesting that massive sphalerite is the result of more advanced replacement of the protolith rock type. The mine-scale distribution of this mineralization, as with vein-hosted sphalerite, correlates with the F_1 short-limb (Figure 21), although distribution varies in detail between adjacent ore horizons (e.g. Figure 21c). Given the similarities in microtexture, general form in hand-specimen, and mine-scale distribution; between massive sphalerite and vein-hosted sphalerite, an equivalent timing and genesis is inferred.

2.3 Sphalerite breccia

Sphalerite breccia is a term used to describe sphalerite mineralization where layers of generally unmineralized host rock, once continuous and planar or folded, now occur as clasts within a sphalerite-dominated matrix (Figures 22a, 23a). The internal texture of the breccia is consistent with durchbewegung structure (Marshall and Gilligan, 1989) and indicates deformation/reworking of sulfides. This textural variety of sphalerite mineralization accounts for approximately 14% of sphalerite ore thickness in drill-hole intersections in C, D, and G ore horizons. Clasts of host rock are variably rotated and are locally sourced. Relict folds, now brecciated, are present (Figure 22a). The breccias generally comprise 80-95% matrix sphalerite and 5-20% clasts (compare Figures 22a and 23a). The clast-rich breccia in Figure 22a contains deformed clasts of host mudstones (Figure 22b) within a sphalerite-pyrrhotite-galena-pyrite matrix. Minor chalcopyrite occurs as very small grains on sphalerite grain boundaries. Pyrrhotite displays a micro-

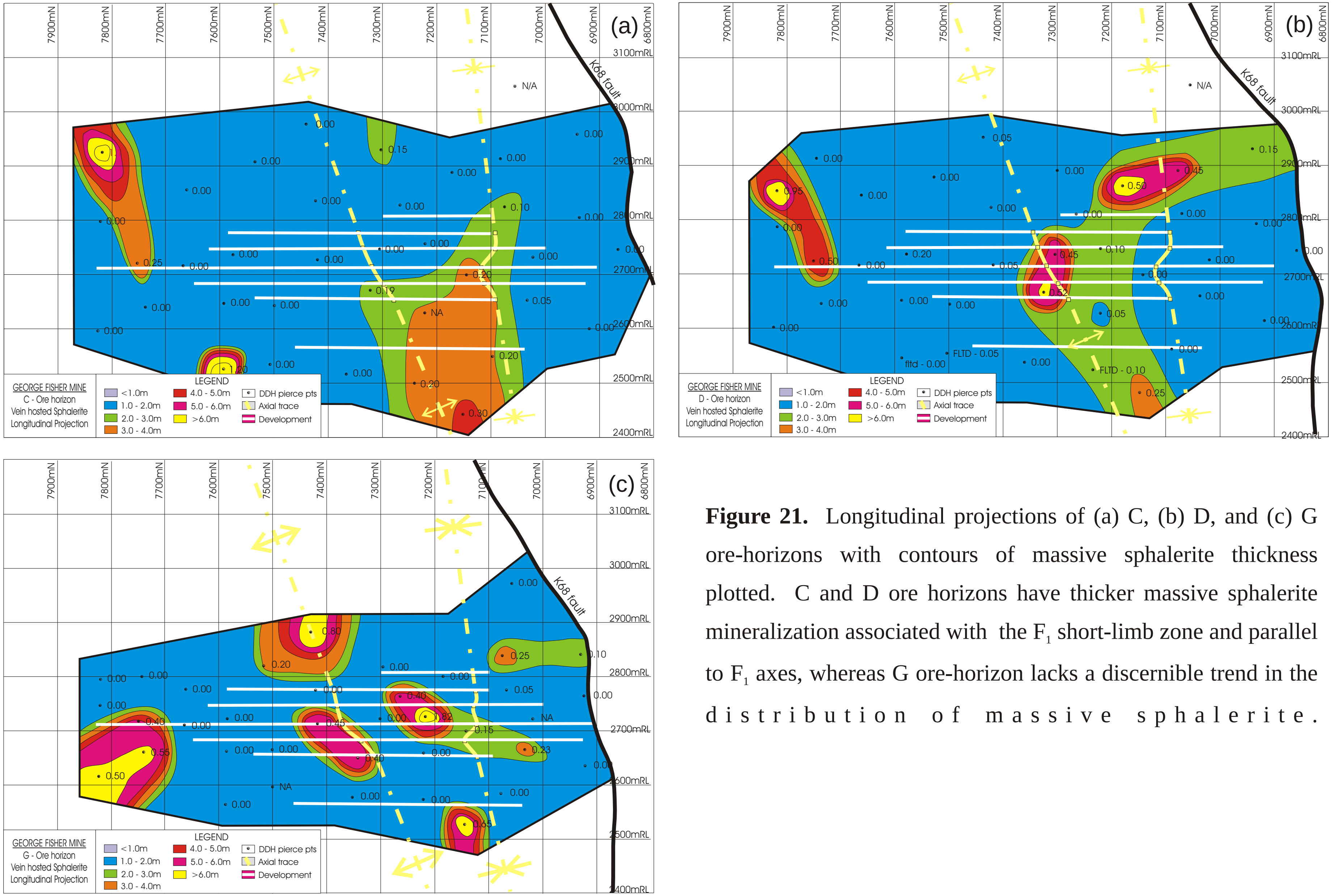

Figure 21. Longitudinal projections of (a) C, (b) D, and (c) G ore-horizons with contours of massive sphalerite thickness plotted. C and D ore horizons have thicker massive sphalerite mineralization associated with the F_1 short-limb zone and parallel to F_1 axes, whereas G ore-horizon lacks a discernible trend in the distribution of massive sphalerite.

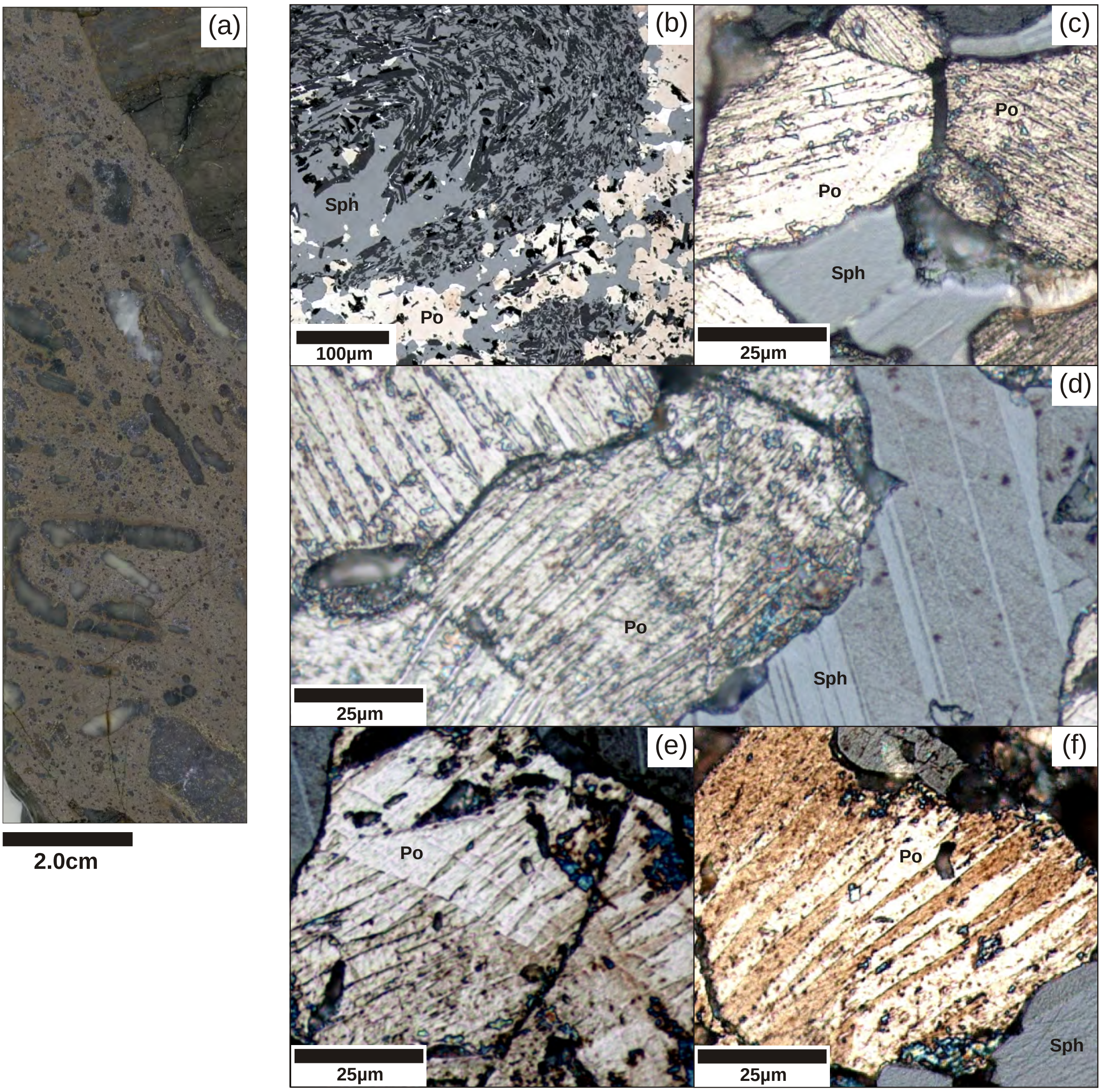

Figure 22. (a) Half core specimen of sphalerite breccia with abundant pyrrhotite. A relict fold is present in the lower part of the image (sample 960436 296.5m). (b) Photomicrograph (reflected light) of the sample in (a) showing folded phyllosilicates in a clast within the sphalerite (Sph)+pyrrhotite (Po)+galena+pyrite matrix. (c) to (f) are higher magnification photomicrographs of the sample in (a) and (b) (etched with conc. HI). Striations in pyrrhotite (c and d) change orientation across grain boundaries. Note the lack of deformation in adjacent sphalerite in (d). The width of the striations in pyrrhotite suggests that they are fine twin lamellae rather than slip lines. This is more evident in (e) and (f) where lensatic twins are developed within pyrrhotite grains.

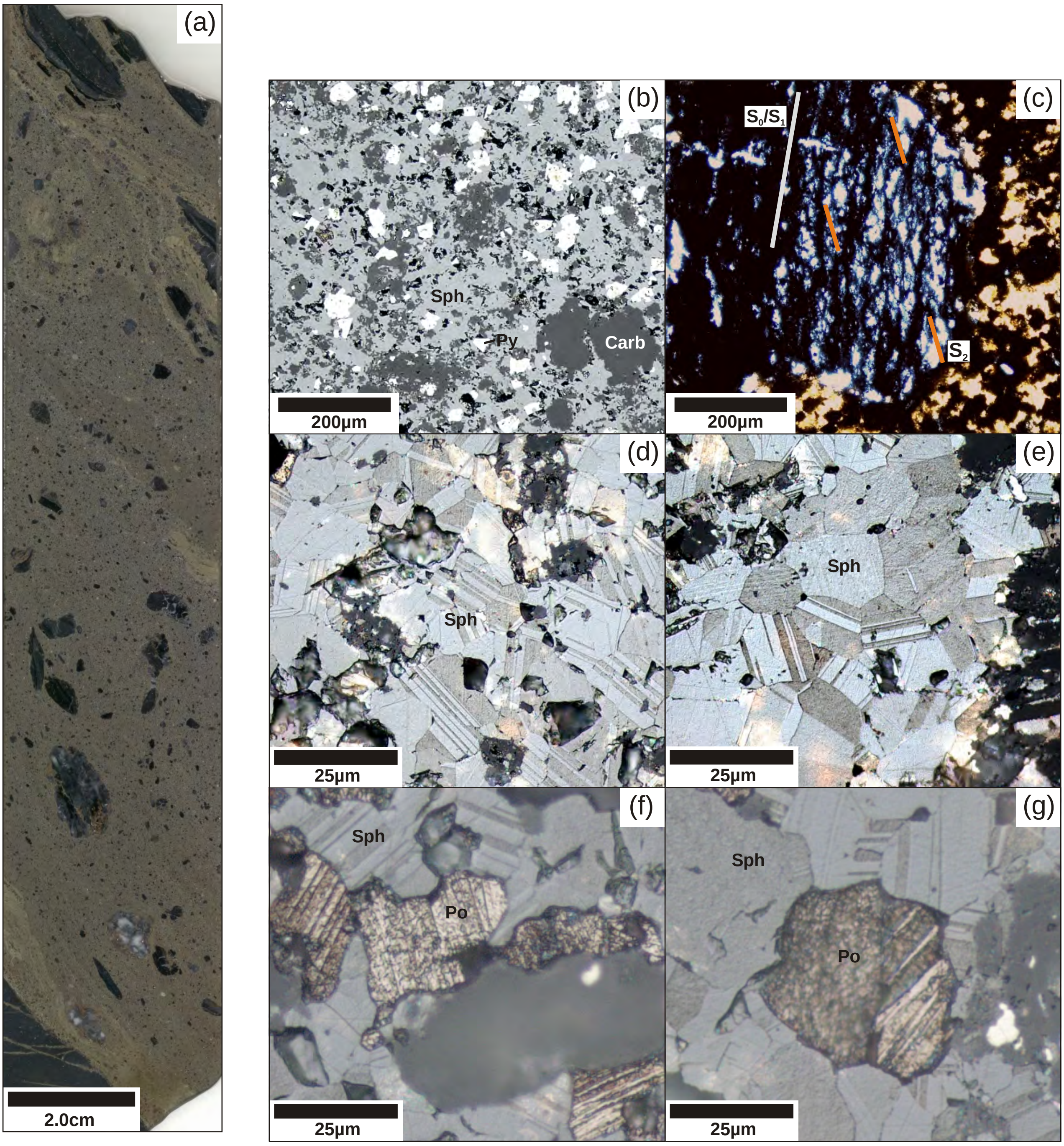

Figure 23. (a) Half core specimen of sphalerite breccia (sample 951033 221.05m). (b) Photomicrograph (reflected light) of the sample in (a). Euhedral pyrite (Py) occurs within the sphalerite (Sph) matrix and pyrrhotite is less abundant. Carbonate (Carb) gangue has highly irregular margins indicative of replacement by sphalerite. (c) Photomicrograph (plane polarized light) of a siltstone clast within the breccia which has a well-developed S_2 foliation (slaty cleavage oblique to bedding) indicating brecciation/mineralization occurred post-D_2. (d) to (g) are photomicrographs of this sample etched with conc. HI. (d) and (e), sphalerite is fine-grained (~20μm) and evidence for recrystallization includes overprinting of twins and development of 120° triple-point junctions. (f) and (g) show twins in pyrrhotite (Po). Adjacent twins in sphalerite are straight and of equal width and therefore undeformed.

structure that consists of fine striations which are visually comparable to slip lines (Clark and Kelly, 1973 - Figure 10). These striations change orientation across grain boundaries (Figure 22c and d) and can attain widths which suggest that they are fine twin lamellae. Lensatic twins (shape characteristic of deformation twins whereby twin boundaries converge at their termination) are observed (Figure 22e and f) which confirm the presence of twinning in the pyrrhotite grains. In a clast-poor breccia (Figure 23a), matrix mineralogy is similar except that pyrrhotite is locally less abundant (Figure 23b).

Evidence for deformation prior to breccia formation includes the well-developed foliation in a breccia clast (Figure 23c). The foliation in the clast shown in Figure 23c is an anastomosing slaty cleavage which is oblique to bedding (~40° angle) and is interpreted to represent the S_2 foliation described in Part A. Note that the S_3 and S_4 foliations occur dominantly as crenulations and not as slaty cleavage. Development of a slaty cleavage in a clast enclosed by sulphides and carbonate gangue is considered unlikely as strain would be concentrated in either the sulphide matrix or at the margins of the clasts. Timing of brecciation/mineralization in this sample is therefore interpreted as late to post-D_2. Folds preserved within the breccia are inferred to be of D_2 timing or younger as mesoscale folds of D_1 age are not observed. Sphalerite in the breccia is fine-grained and preservation of 120° triple-point junctions and twins overprinted by recrystallizing grains (Figure 23d and e) imply recrystallization of some sphalerite.

Twinning in pyrrhotite (Figure 23f and g) provides information as to the deformation temperature as twinning in pyrrhotite develops at temperatures >250°C (Clark and Kelly, 1973, 1976). Twinning in experimentally deformed pyrrhotite is absent below 200°C, and becomes a significant deformation mechanism >300°C (Clark and Kelly, 1973, 1976). Growth twins in adjacent sphalerite grains (Figure 22d and 23f, g) are straight and parallel-sided suggesting that they were not deformed during twin-forming deformation of the pyrrhotite. This is consistent with pyrrhotite being of equivalent strength to, or weaker than sphalerite at temperatures of 200-250°C (Figure 16; Clark and Kelly, 1973). Twins in pyrrhotite (Figures 20c – f, 23f - g) are not strongly developed suggesting a maximum temperature of 250-275°C during deformation. This is a marginally higher temperature the than 200°C - 220°C estimated using bitumen reflectance (Chapman, 1999, 2004) and <250°C temperature estimated from calcite twin geometry (see Part A – Figure 17). However, the temperature is the same as that inferred for the later parts of the paragenesis synchronous with copper mineralization (250-300°C) and associated alteration at George Fisher (Chapman, 1999).

The deposit-scale distribution of sphalerite breccia is illustrated on Figure 24. The thickest sphalerite breccia occurs within the F_1 short-limb zone (Figure 24a, b, c). The thicker occurrence of sphalerite breccia in C and D ore-horizon plunges steeply parallel to the short-limb. However, in G ore-horizon thicker sphalerite breccia distribution has a gentler pitch parallel to the intersection of bedding and the S_4 foliation (L^0_4) (see Part B). Samples illustrated in Figures 22 and 23 are indicated on Figure 24b. These samples occur in the thicker region of sphalerite breccia mineralization in the deeper part of the F_1 short-limb explored to date.

Sphalerite breccias are interpreted to occur post-D_2 based on the presence of disrupted F_2 folds and S_2 foliation in clasts, and distribution in longitudinal projection within and

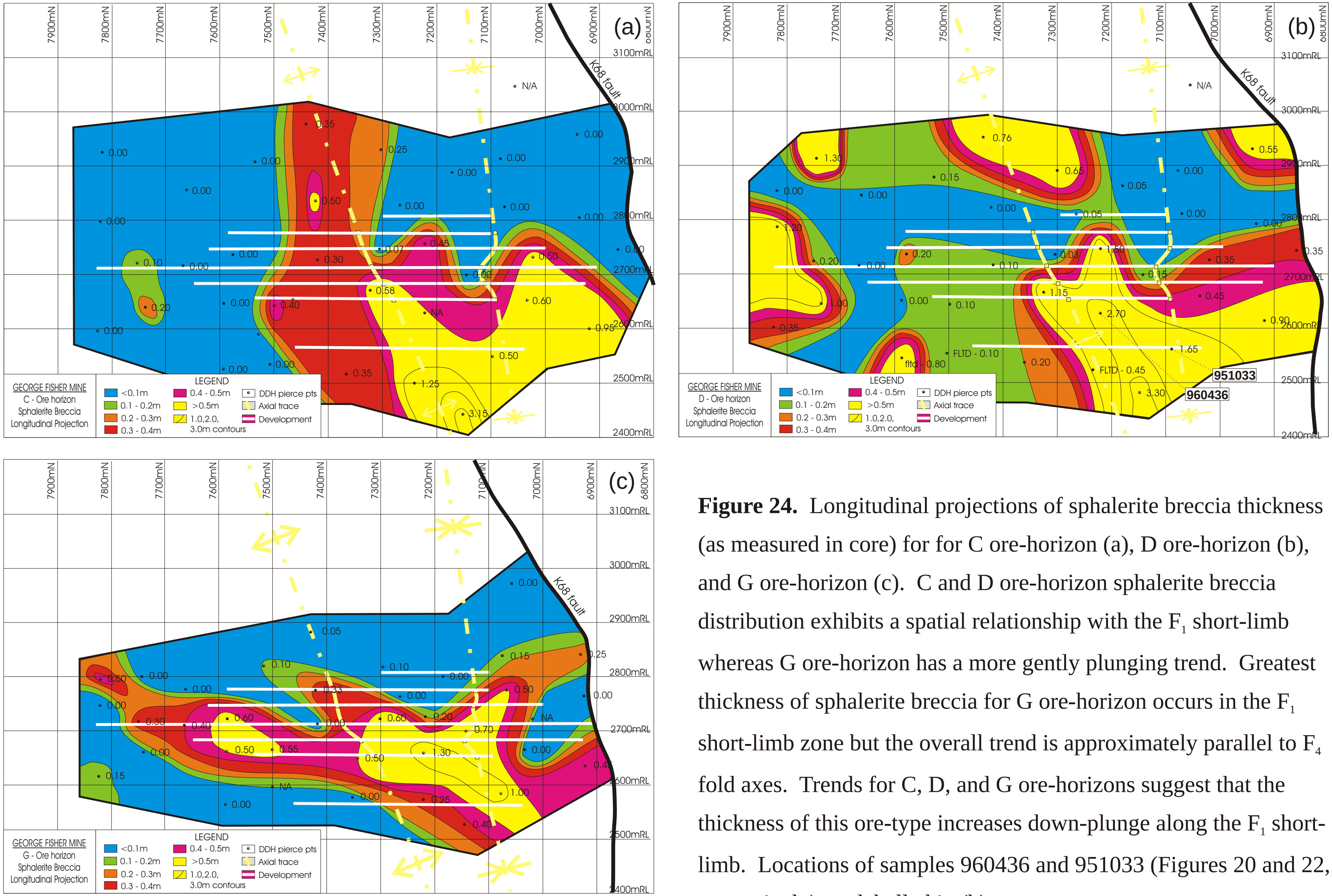

Figure 24. Longitudinal projections of sphalerite breccia thickness (as measured in core) for for C ore-horizon (a), D ore-horizon (b), and G ore-horizon (c). C and D ore-horizon sphalerite breccia distribution exhibits a spatial relationship with the F_1 short-limb whereas G ore-horizon has a more gently plunging trend. Greatest thickness of sphalerite breccia for G ore-horizon occurs in the F_1 short-limb zone but the overall trend is approximately parallel to F_4 fold axes. Trends for C, D, and G ore-horizons suggest that the thickness of this ore-type increases down-plunge along the F_1 short-limb. Locations of samples 960436 and 951033 (Figures 20 and 22, respectively) are labelled in (b).

parallel to the F_1 fold is indicative of post-D_2 mineralization exploiting the short-limb zone (as described in Part B). Chapman (2004) interpreted ***breccia-hosted sphalerite mineralization*** as post-D_2 mechanical deformation of vein-hosted sphalerite mineralization.

2.4 Disseminated sphalerite

Fine-grained disseminated sphalerite occurs dominantly in bedding parallel zones from 1 to 5mm wide (Figures 5 and 25a) although bedding oblique (Figures 25b and c) disseminated sphalerite is also observed. Disseminated sphalerite is not a significant component of economic Zn mineralization at George Fisher. Chapman (2004) interpreted layer-parallel disseminated sphalerite as an alteration selvedge to vein-hosted sphalerite mineralization.

Layer-parallel disseminated sphalerite (Figure 25a) is cross-cut by a carbonate vein interpreted to be deformed during D_2, which is in turn cross-cut by vein-hosted sphalerite. The relative timing indicated by the cross-cutting relationships is:

1. Disseminated sphalerite replacement of host rock.
2. Emplacement of cross-cutting carbonate vein, remobilizing some of the sphalerite from the layer-parallel disseminated sphalerite where they intersect.
3. Formation of vein-hosted sphalerite mineralization.

The relative timing of features in Figure 25a, indicate that not all layer-parallel sphalerite is an alteration selvedge to vein-hosted mineralization (cf. Chapman, 2004). Deformation intensity of the disseminated sphalerite grains cannot be determined due to their fine-

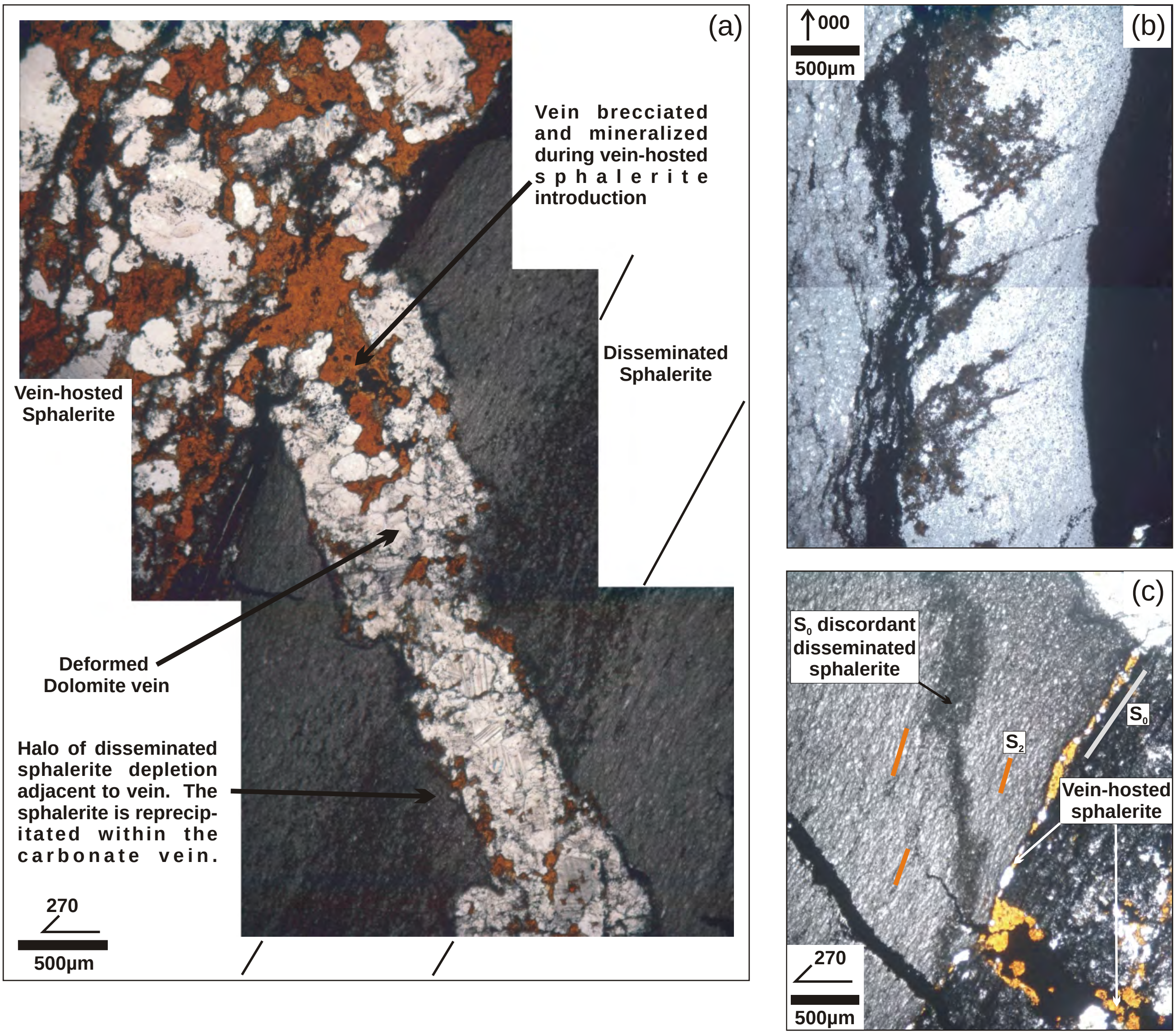

Figure 25. (a) Fine grained layer-parallel disseminated sphalerite cut by a dolomite vein which is in turn cross-cut by vein-hosted sphalerite (sphalerite+calcite+quartz). Photomicrograph in plane polarized light, sample 960519. (b) Fracture-controlled replacive disseminated sphalerite in a crystalline carbonate-dominant layer. Fractures have similar orientation to S_4 and apparent dextral offset is consistent with both sense of shear in S_4 and the expected movement on the oblique fractures during D_4 sinistral reactivation of bedding. Photomicrograph in plane polarized light, sample 2610-6. (c) Disseminated sphalerite discordant to bedding. The 'plume' of disseminated sphalerite appears to parallel the S_2 foliation in the upper and lower parts of the photomicrograph and joined in the middle by S_2-discordant disseminated sphalerite. Photomicrograph in plane polarized light, sample 960519.

grained nature. However, relative timing based on the abovementioned cross-cutting relationships suggests that the disseminated sphalerite may be pre- to early-D_2.

Fracture-controlled sphalerite in a crystalline carbonate layer in Figure 25b illustrates the development of disseminated sphalerite in a bedding-oblique orientation. Dextral offset on the fractures is consistent with D_4 reactivation of bedding during north-south bedding parallel extension. Sphalerite occurs as dendritic replacement of the host lithology adjacent to fractures as opposed to infill of the fractures alone. Bedding-oblique disseminated sphalerite in siltstone is less common presumably as bedding-parallel heterogeneities form more efficient fluid migration paths. However, Figure 25c illustrates two zones of disseminated sphalerite which parallel S_2 connected by further disseminated sphalerite with a vertical pitch parallel to S_4. These relationships suggest that some of the disseminated sphalerite postdates S_2/D_2. Other indications of disseminated sphalerite postdating deformation are illustrated in Figure 26. In this photomicrograph, disseminated sphalerite does not occur as layer-parallel accumulations in the massive carbonate mudstone but is concentrated in the hinges of microfolds in the narrow bedding-discordant carbonate veins. The axial traces of these folds parallel S_2/S_0 and are therefore interpreted to have formed during D_2.

Disseminated sphalerite is dominantly observed in massive layers (without laminations) and this reflects a host-rock control on this mineralization type whereby only sites of restricted fluid flow and possibly less-reactive hosts are available to the mineralizing fluids. Disseminated sphalerite is interpreted to form both pre- and post-D_2 based on cross-cutting relationships and location relative to microstructures. Previous

Figure 26. Photomicrograph (plane polarized light) of folded carbonate veins in a carbonate-dominant siltstone. Bedding-parallel disseminated sphalerite is absent from the layer, however, disseminated sphalerite is concentrated in the hinges of microfolds which parallel the weak bedding-subparallel slaty S_2 foliation in this sample and are interpreted as syn-D_2 folds. The disseminated sphalerite in this sample can therefore be interpreted as having syn- to post-D_2 timing. Sample 1011-2.

interpretation by Chapman (2004) inferred pre-F_2 timing of layer-parallel disseminated sphalerite as sphalerite grains were interpreted as interstitial infill after rhombohedral calcite (interpreted as diagenetic) and variably intergrown with bitumen. Layer-parallel disseminated sphalerite in Figure 25a is also interpreted as early-D_2 however layer-discordant disseminated sphalerite may be younger in age.

2.5 Fine-grained sphalerite-galena breccia

Fine-grained sphalerite+galena breccia occurs as bedding-parallel massive sulphide layers. Galena, pyrite, and pyrrhotite occur in variable quantities. Galena poor mineralization (Figure 27a) occurs as dull-lustred, banded (Figure 27b), fine-grained averaging ~10 to 20µm (Figure 27c). Significant brecciation of layers of host siltstones occurs yet fine-grained pyritic layers are relatively undisturbed (Figure 27b). This suggests that the fine-grained pyrite in Figure 27b occurred syn-mineralization and may not represent a primary feature of the host-rock. The sphalerite exhibits indications of recrystallization, however, grain shapes and boundaries are irregular and an equilibrium or foam texture has not been achieved and/or preserved. Annealing has not occurred and the sphalerite microstructure therefore records a period of deformation.

A more-galena rich sample is illustrated in Figure 28a within which relict bands in the massive sulphide layers exhibit folding (Figure 28a). Again, the fine-grained sphalerite-galena mineralization has a characteristic dull lustre. Sphalerite grains in the sample appear more equant (Figure 28b) but still have irregular grain boundaries and do not represent an equilibrium foam texture. A bimodal grain size distribution is recognized. Coarser grains (~100µm) are characterized by bent twins, irregular shapes and in some

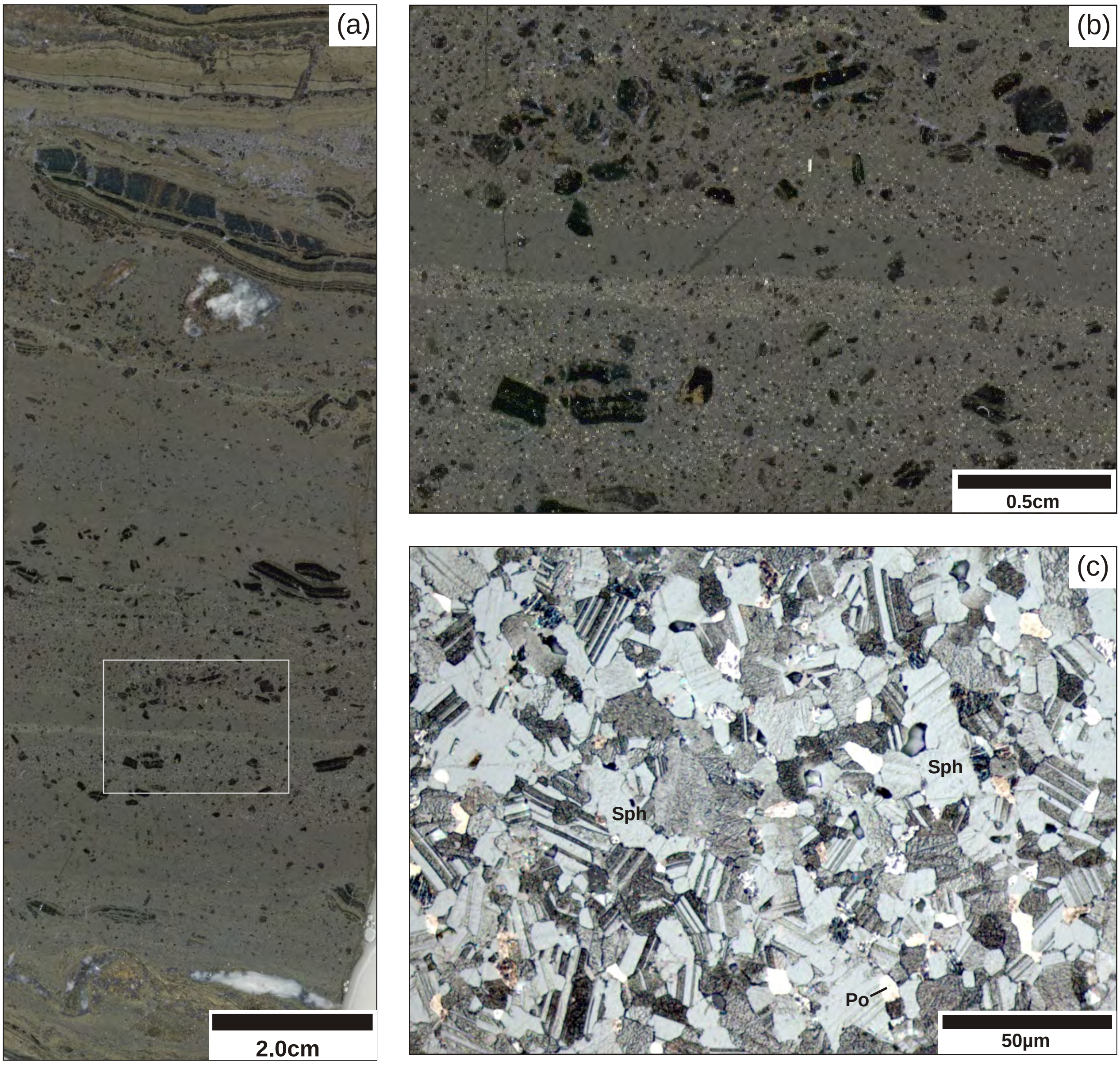

Figure 27. (a) Half-core specimen of fine-grained sphalerite mineralization. Significant brecciation of the host-rock layers is evident, however, pyritic layers (b - enlarged inset area in (a)) are apparently unaffected by the deformation. Many of the siltstone clasts are rotated, some to bedding-orthogonal orientations in (b). (c) Photomicrograph (reflected light, etched with conc. HI) of the fine-grained sphalerite (Sph) and minor pyrrhotite (Po). Significant recrystallization and grain boundary migration has occurred but the texture illustrated does not represent an equilibrium texture resulting from annealing processes. Grains are not equant and do not preserve 120º triple point junctions as characterized by an equilibrium (e.g foam) texture. A weak preferred orientation of grain shapes (bottom right to top left) can be recognized in (c). Sample 960355-389.8m.

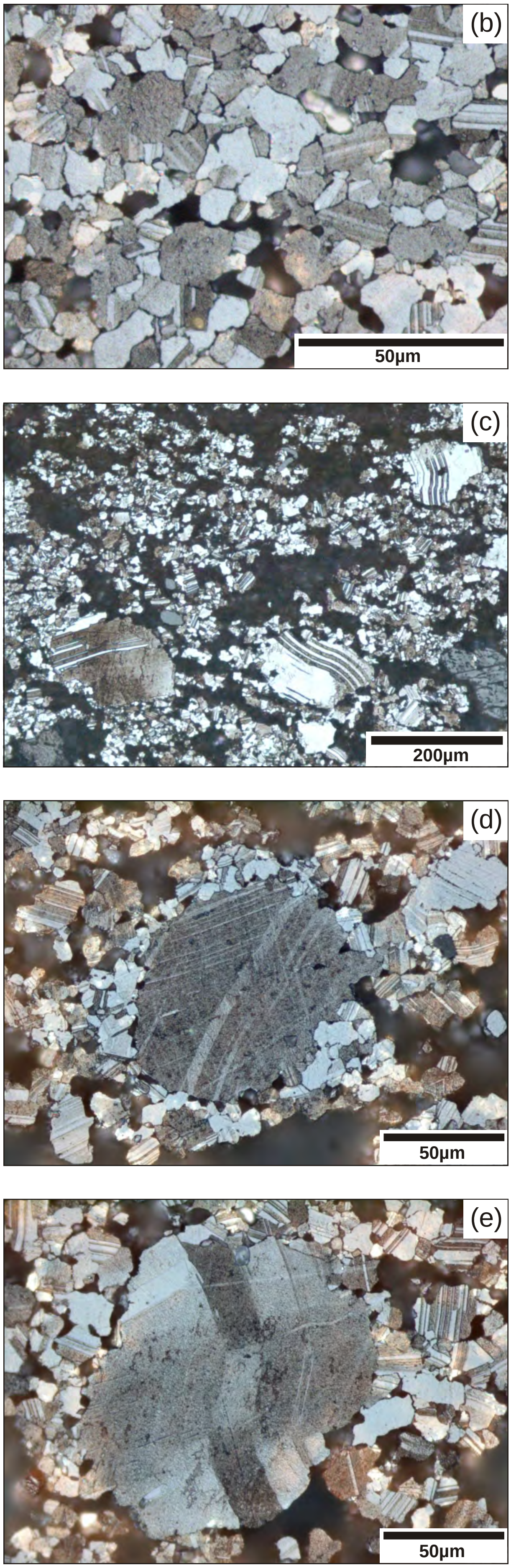

Figure 28. (a) Half-core specimen of sphalerite+ galena mineralization. Folding (white form-lines) indicates that the sulphides are deformed. (b) to (e) Photomicrographs of the sample in (a) in reflected light, etched with conc. HI. Dark areas which are out of focus is galena eroded by HI etchant, sphalerite is the dominant sulphide in each (b) grainsize varies from 5-20µm and is not foam-textured. (c) Bimodal grain size occurs due to the recrystallization of relict deformed grains (d) and (e). Rare deformation twins (gently pitching) occur in the upper part of the large grain in (d). Significant deformation of growth twins is illustrated in (e). Sample 961233 - 80.8m.

cases deformation twinning (Figure 28c). These features indicate that the grains are deformed. Coarser grains recrystallize to form the dominant fine-grained (~10µm) surrounding sphalerite grains (Figure 28d). The fine-grained matrix sphalerite does not exhibit deformation features as seen in the coarser grains.

Fractal dimensions of the grain boundaries of the relict deformed grains are within the deformed range (Figure 29a). Measurements taken from grains interpreted as recrystallized and subsequently deformed/recrystallizing, are appended to the diagram in Figure 29b, these are illustrated and interpretation explained in Part C – Figure 3. The location of measured foam-textured sphalerite is also indicated. The foam textured grains in this sample (Part C – Figure 3) were too small for fractal analysis using the method developed in Part C, the pentagon indicating foam-textured recrystallized sphalerite is located using other samples (Part C). Two stages of deformation and recrystallization are inferred from the trends in Figure 29b. The original grains (similar to vein-hosted sphalerite?) undergo the following changes:

1. Increase in grain boundary irregularity (D) and grain size reduction due to grain boundary migration and the nucleation of new grains at the expense of the larger grains.
2. Recrystallized grains undergo similar grain size reduction and increase in grain boundary irregularity and recrystallize again to even finer-grained foam-textured sphalerite.

It is possible that both deformation/recrystallization paths could occur simultaneously during progressive deformation, that is, during a single deformation episode.

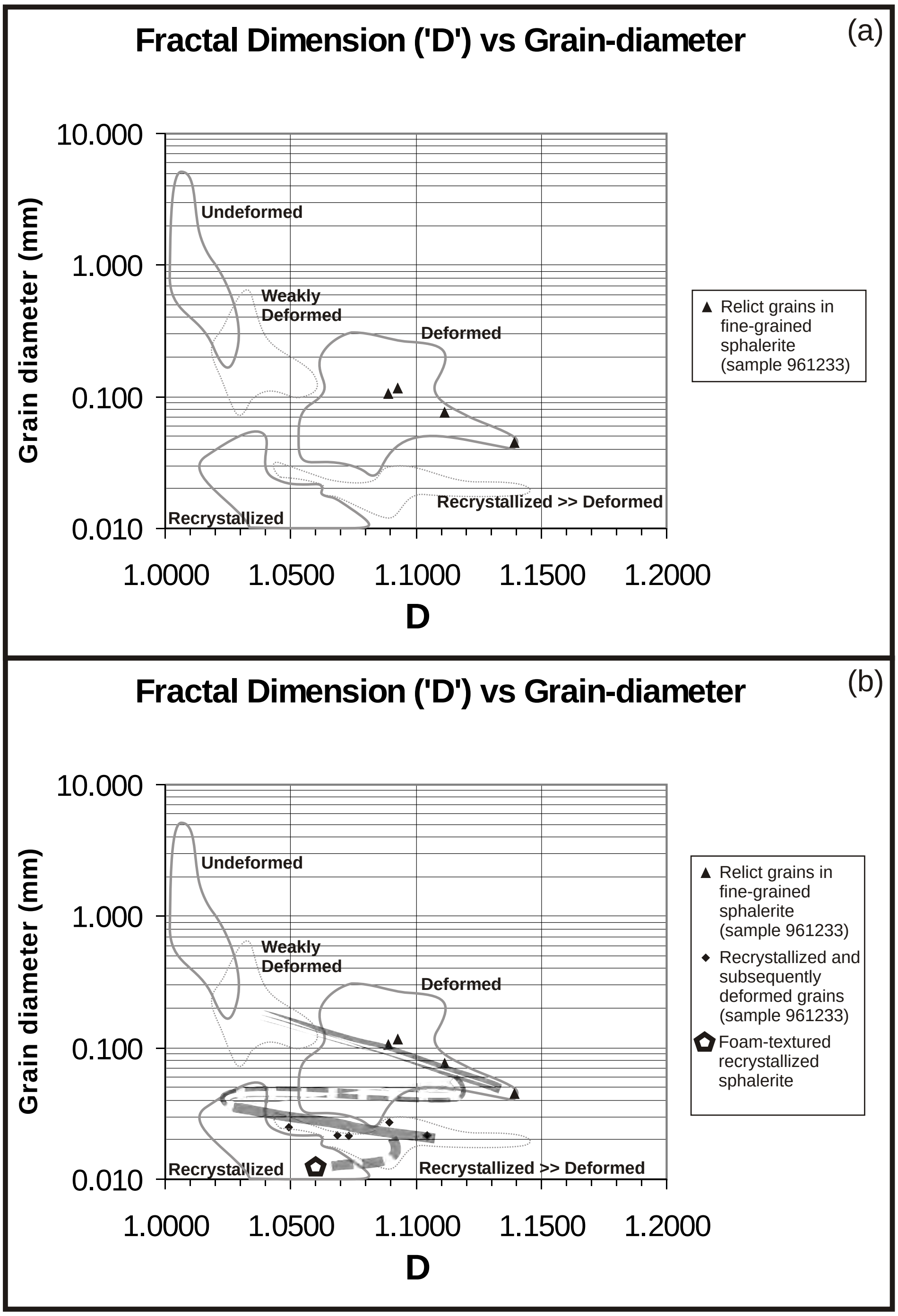

Figure 29. D vs grain size plot with fields established in Part C. (a) Fractal measurements from selected grains in the sample pictured in Figure 27 (some used to define 'deformed field', see Part C) plot in the deformed field. (b) Data from (a) incorporated with measurements from grains interpreted as recrystallized and subsequently deformed/recrystallizing (Part C - Figure 3). The location of foam-textured, recrystallized sphalerite is indicated by a pentagon. Grains exhibiting this texture in Part C-Figure 3 were too small to obtain fractal measurements using the method in this study. The arrows represent deformation/dynamic recrystallization paths, dashed lines indicate formation of recrystallized grains. The trends indicate that two deformation/recrystallization episodes may have occurred in the path from undeformed/weakly deformed/(replacive?) sphalerite to equilibrium textured recrystallized sphalerite.

Fine-grained equilibrium textured sphalerite is the end-point of the process until temperature driven grain-size coarsening occurs. Grain boundary migration of the recrystallized sphalerite can lead to preferential growth of selected grains via discontinuous grain growth (Stanton and Gorman, 1968) where grains impinge on one another.

Deposit-scale distribution of this textural variety of mineralization is noticeably different from the previously described sphalerite ore-types (Figure 30). The thicker occurrences of fine-grained sphalerite+galena mineralization are not spatially related with the F_1 short-limb zone as seen in previous ore-types (Figure 30). C and D ore-horizons (Figures 30a and b, respectively) have an apparent depletion of fine-grained mineralization coincident with the zone of economic mineralization (refer to Part B). This trend is not observed in G ore-horizon (Figure 30c).

Fine-grained sphalerite+galena mineralization exhibits features consistent with significant deformation and the controls on its deposit-scale distribution differ from the previously described sphalerite ore-types. Microstructures observed in this mineralization-type are not observed in other styles which are interpreted as having post-D_2 timing. Based on qualitative observations, the fine-grained ores may therefore pre-date the main deformation phase, D_2.

An alternative explanation for the deformation characteristics observed in the fine-grained breccia as opposed to the vein-hosted sphalerite may be due to partitioning of strain during D_4. D_4 deformation is interpreted to have consisted dominantly of bedding plane

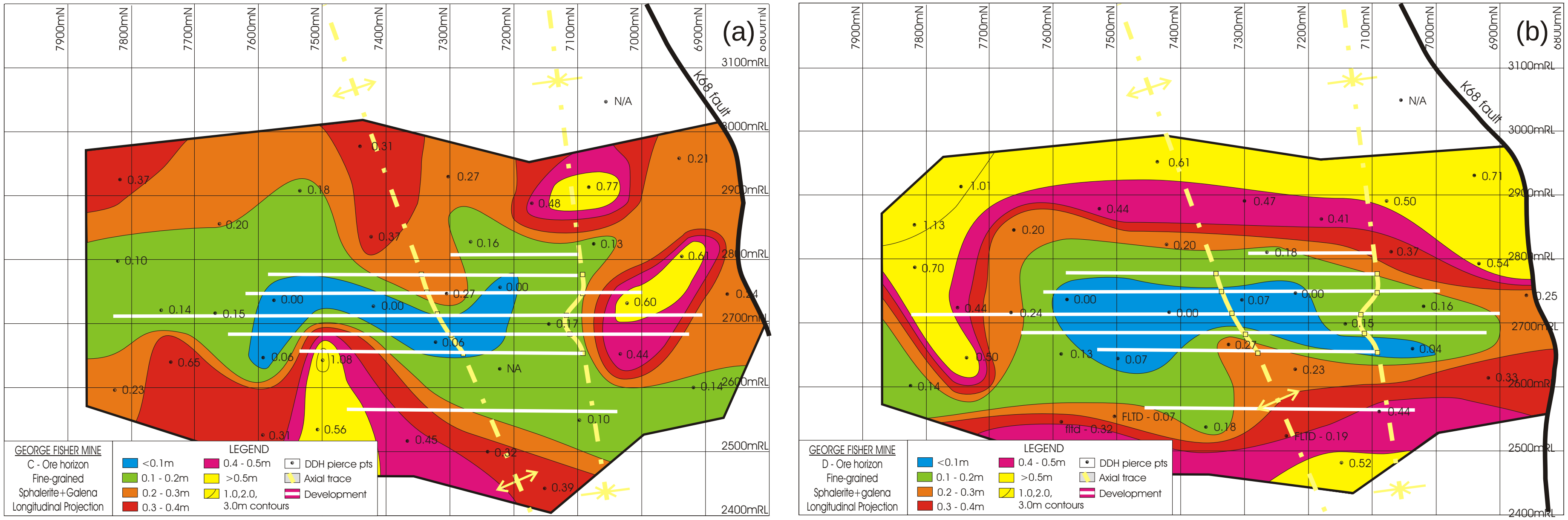

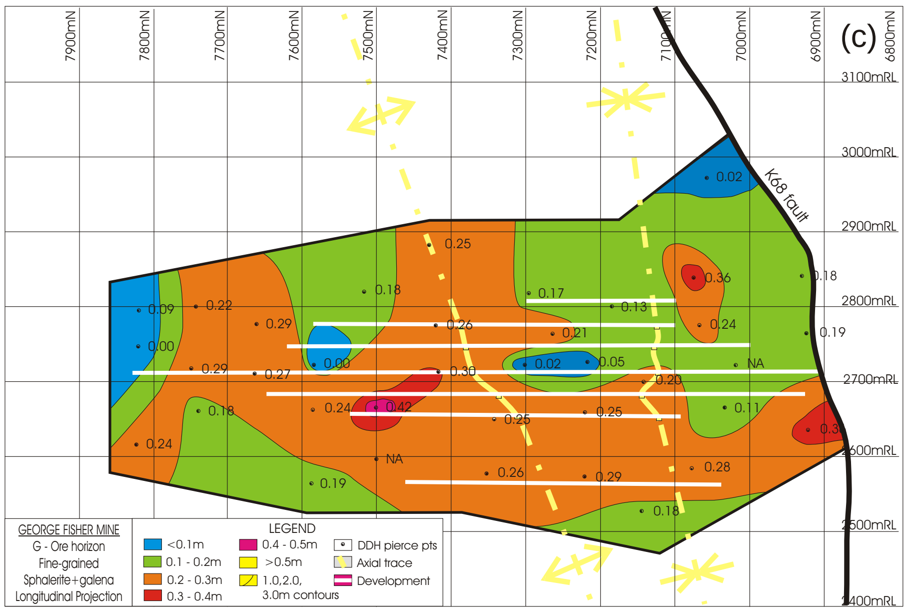

Figure 30. Longitudinal projections of fine-grained sphalerite+galena breccia thickness for (a) C ore-horizon, (b) D ore-horizon, and (c) G ore-horizon. C and D ore-horizons show similar distribution with a region of apparent depletion of fine-grained sphalerite+galena breccia spatially coincident with the area of economic mineralization (see extent of mine development). G ore-horizon does not exhibit this trend. The distribution of fine-grained breccia does not correlate with the F_1 short-limb zone in any of the three main ore-horizons illustrated.

reactivation/shear (refer to Part A). The inferred result of this deformation is dilation in the F_1 short-limb zone and higher shear on the long limbs of this gentle fold (refer to Part B – Figure 24). If the fine-grained breccia is a deformed equivalent of the other ore types observed at George Fisher, higher strain on the long limbs may explain the dominance of this deformed ore type to the north and south of the economic region of the deposit. However, fine-grained ore occurs within the short-limb up and down plunge from the economic zone (Figure 30). This may correlate with unfolding of the F_1 fold up- and down-plunge from the current mine area (see change in tightness of F_1 fold in Part A – Figure 9).

Chapman (2004) recognized preferred orientation of rounded to elongate clasts which resembled paragenetically earlier mineralization styles within fine-grained mixed sulphide breccia. These observations were interpreted as the effects of mechanical remobilization during D_4 (Chapman, 1999). An increase in mesoscopic folding is spatially coincident with fine-grained breccia dominance in the northern part of the deposit (Chapman, 1999, 2004). Despite this deformation, fine-grained breccia maintains planar and parallel margins (Chapman, 2004). Partitioning of strain into the layers now comprised of deformed fine-grained breccia is inferred by Chapman (2004). Other textural varieties of mineralization are found proximal to the fine-grained breccia in drill-core. This indicates that partitioning of D_4 strain as proposed by Chapman (2004) must have occurred on the sub-metre scale so as to not texturally alter other mineralization styles. Alternatively, fine-grained breccia may represent earlier sulphide accumulations from which metal was remobilized during regional deformation. This is discussed further below.

2.6 Some microstructural evidence for sphalerite mobility during D_4

Additional evidence for mobility of sphalerite during D_4 includes the observation of sphalerite inclusions within S_4 crenulations (Figure 31). The only sphalerite in this sample is located within the S_4 crenulation where it intersects a horizon with minor disseminated pyrite. This indicates that the Zn-rich fluid was moving along the cleavage and that a host-rock control on the sites of precipitation exists. The distance of transport of the fluid is unknown. An equivalent relationship between S_2 cleavage and sphalerite mineralization has not been observed. Given that D_2 was approximately synchronous with peak metamorphism and the highest strain event in the region, the lack of sphalerite in the cleavage seams may indicate that sphalerite was not present in the system; however, this is inconsistent with other timing criteria in this study and those of Chapman (1999, 2004) and Valenta (1988, 1994). Another possibility is that the fluids during D_2 were incapable of transporting Zn due to temperature, pH, or salinity constraints. Sphalerite occurring in dilational jogs on the micro-scale is observed in Part A - Figure 25. Dilation in this example is consistent with west-over-east reactivation of earlier formed structures/bedding, a kinematic scenario compatible with D_4. S_3 crenulation of bedding planes is observed in Figure 32a. Reactivation of bedding planes during D_4 with west-over-east shear sense causes dilation in the favourably oriented bends in bedding (Figure 32a and b). Fibrous infill consisting dominantly of chlorite (Figure 32c) with euhedral quartz and sphalerite (Figure 32d) is observed. This is further evidence for mobility of sphalerite in solution during D_4. This mode of metal transport is considered to be secondary to the bedding-parallel focussing of fluid along conduits formed during deformation (Figures 6 and 7).

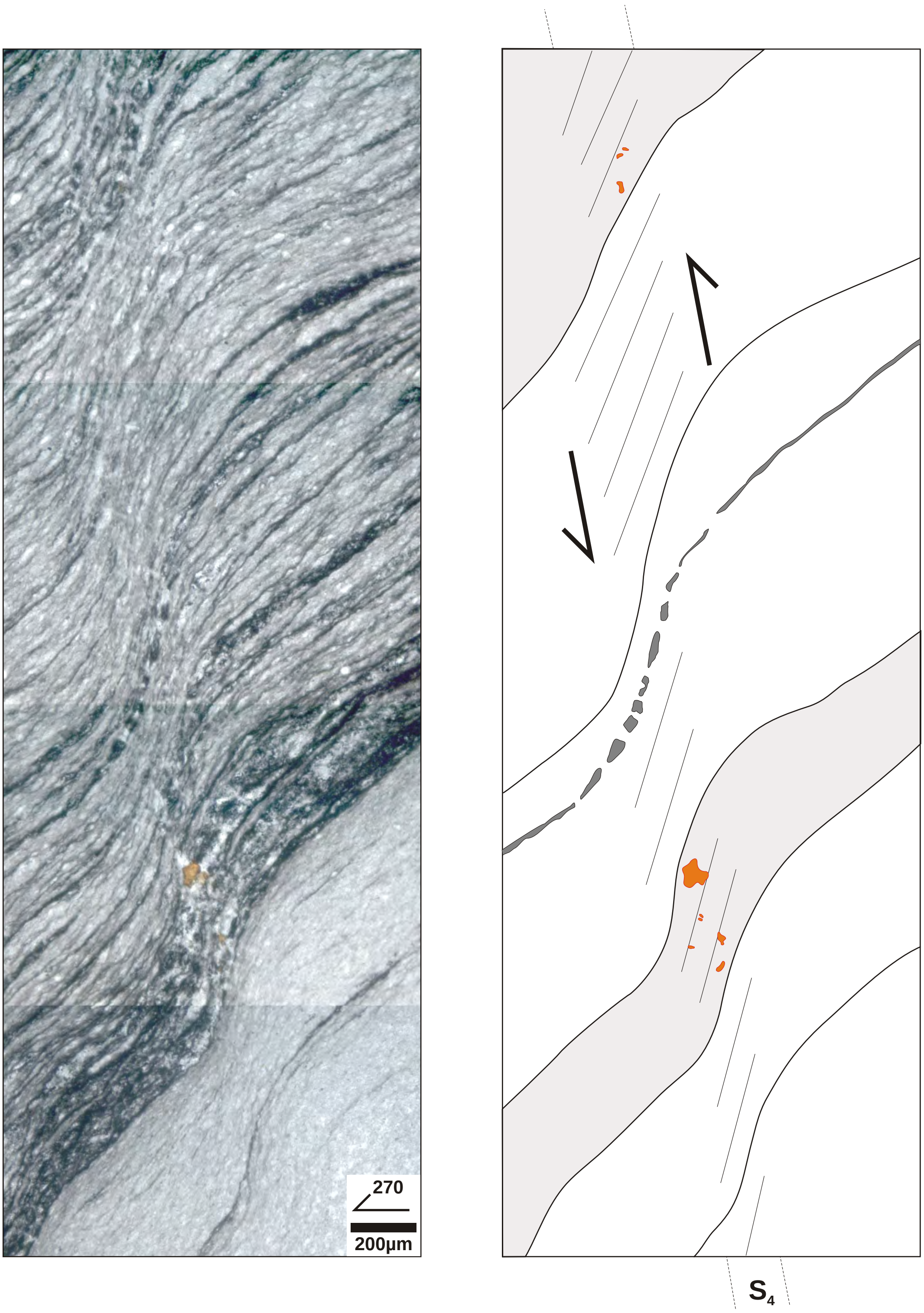

Figure 31. Photomicrograph of a vertical section and line diagram. This section is from a barren sample and the only sphalerite occurrence is as indicated in orange on the right hand diagram. The sphalerite only occurs within an S_4 crenulation and at locations where the crenulation intersects a favourable lithology (which contains fine grained pyrite). Although this is clearly not of ore-forming significance, the relationship does demonstrate that Zn is mobile during D4 and deposition involves both structural and host-rock controls. Sample 1311-10.

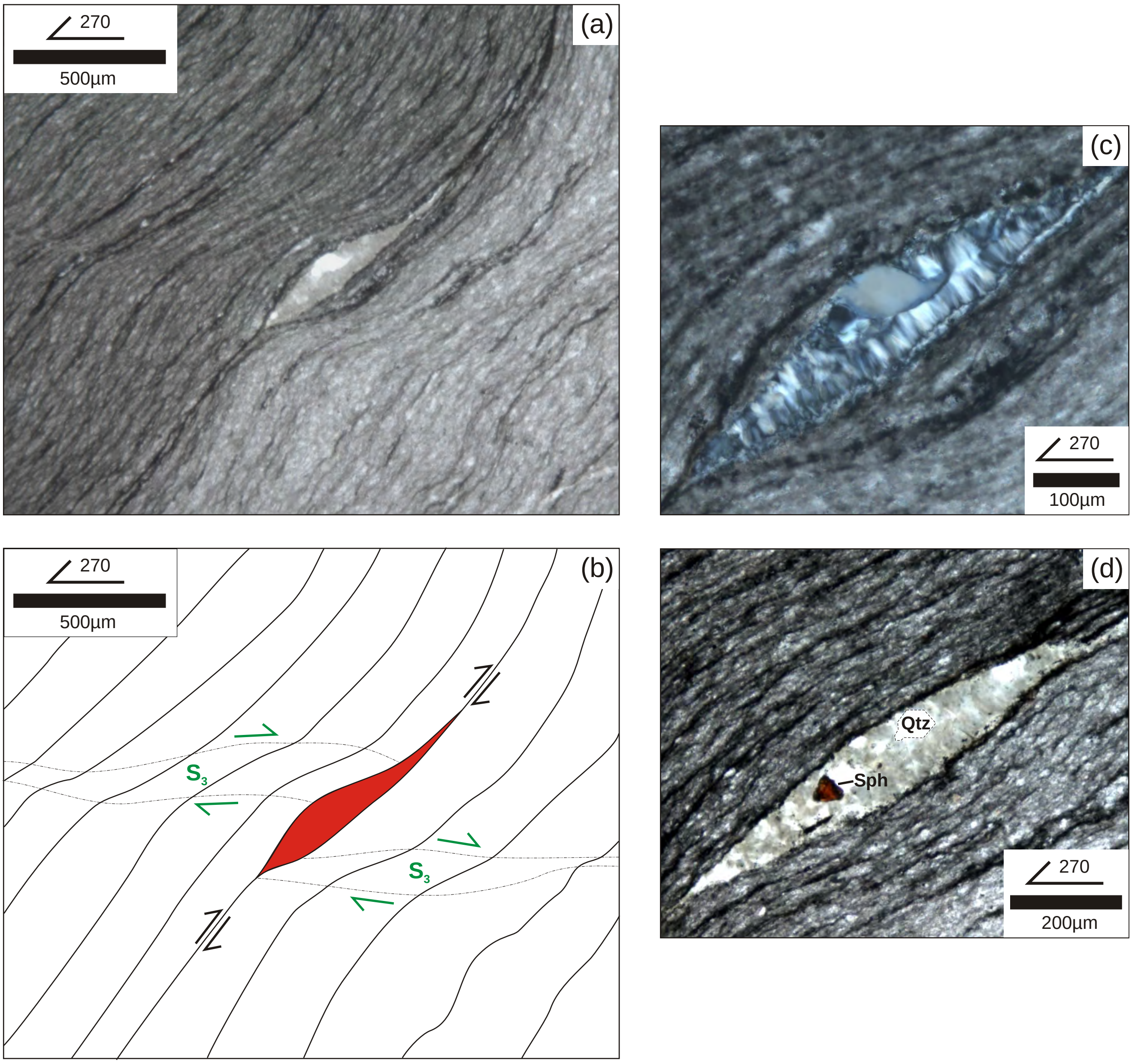

Figure 32. (a) Photomicrograph of a vertical section and (b) line diagram of the same view. A minor chlorite+quartz vein occurs at a lithological contact where bedding becomes more gently dipping. This corresponds with west-side-up displacement (consistent with D_4 reactivation of bedding) of an S_3 crenulation across the same bedding surface. The vein is therefore interpreted as a syn-D_4. (c) Enlargement of the vein in (a) (under crossed polars) illustrating chlorite fibre development in the vein. Fibres developed during 2-dimensional shear as indicated in (b) would have a sub-vertical pitch in vertical section, however the more gently pitching fibres in (c) suggest that there was a component of oblique slip during D_4 bedding reactivation. (d) A photomicrograph (plane polarized light) of a similar vein in the same sample in which euhedral quartz ('Qtz'- outlined for clarity) and sphalerite (sph) are observed. The sphalerite has been deposited synchronous with vein development and D_4 timing is inferred. Sample 1311-10.

3. Description and interpretation of galena-dominant ore-types

3.1 Fine-grained galena-sphalerite breccia

Fine grained galena-sphalerite breccia (galena-rich end member of fine-grained breccias as described above) occur as bedding parallel massive matrix-supported breccia. The sulphides have a dull lustre due to their fine grain size (individual grains not visible with naked eye) and weak sphalerite and galena-dominant banding can be observed. A galena-rich sample is illustrated in Figure 27a. Galena occurs as irregular crystalline aggregates within the sphalerite (Figure 33a) and fine bands where connectivity of aggregates is attained. When viewed at higher magnification after etching with thiourea and HCl (Brebrick and Scanlon, 1957), galena occurs as equant grains which preserve 120° triple point junctions (Figure 33b, c). Sphalerite occurs as both inclusions within galena and as grains on galena grain boundaries (Figure 33b, c). Relic inclusions of sphalerite in the galena grains are suggestive of galena replacing sphalerite.

Deposit-scale distribution of fine-grained sphalerite+galena breccia is illustrated in Figure 30. The apparent depletion of this textural variety in the zone of economic mineralization (see extent of level development – Figure 30) means that fewer observations of this mineralization can be made in the underground workings. There is no discernible relationship of the spatial distribution of this ore-type with the F_1 short-limb zone (Figure 30). Apparent depletion of fine-grained galena+sphalerite ore in the mining area is observed in C and D ore horizons (Figure 30a, b) but not in G ore horizon (Figure 30c).

Galena in fine-grained breccia at George Fisher postdates the associated fine-grained sphalerite mineralization and is interpreted to replace this sphalerite. Recrystallization of

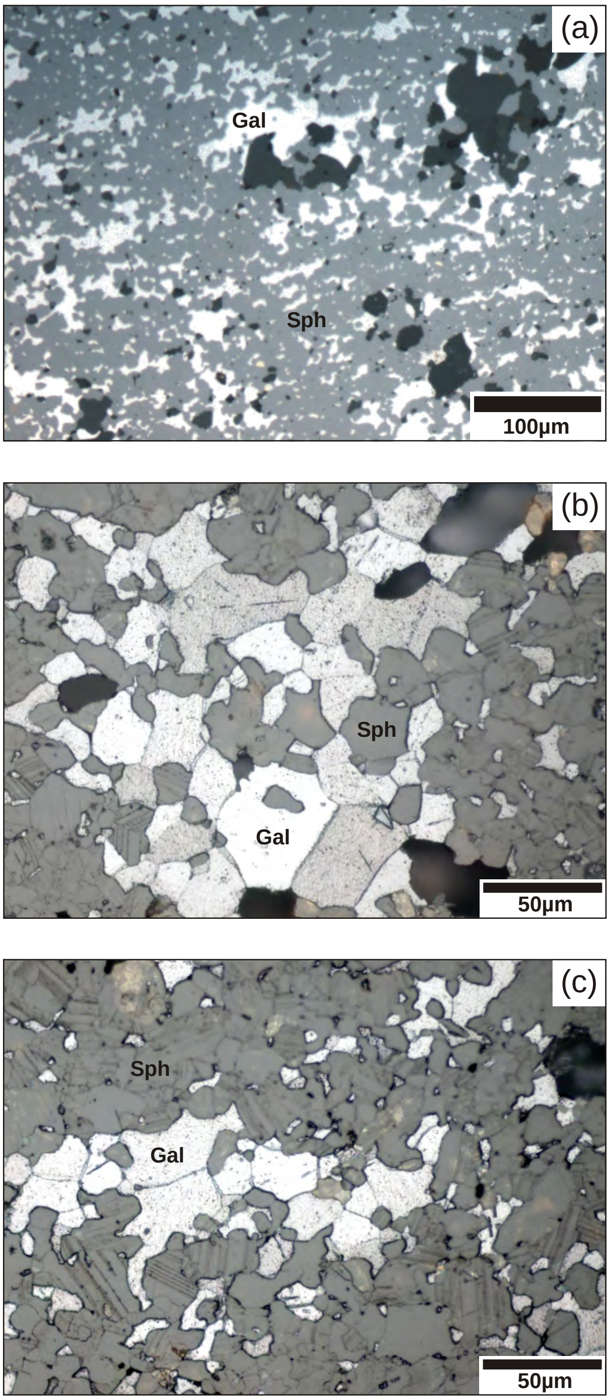

Figure 33. Photomicrographs (reflected light) of galena (Gal) and sphalerite (Sph) in fine-grained breccia. (a) Fine bands of galena (white) within sphalerite matrix (grey). Bands form where individual accumulations of galena become connected. (b) and (c) etched with Thiourea and HCl (Brebrick and Scanlon, 1957). Equant grains and 120º triple point junctions suggest recrystallization of galena has occurred. Replacement of sphalerite is indicated by relict inclusions of sphalerite grains in galena in (b) and galena progressing along sphalerite grain boundaries in (c). Sample 961233.

the galena obscures deformation features which may indicate a relative timing to the main deformation phase (D_2).

3.2 Medium-grained galena breccia

Medium-grained galena (individual grains visible with naked eye) occurs both as parallel and bedding-discordant zones and is generally less continuous in dip and strike than the sphalerite-dominant ore-types. Medium-grained galena has a shiny, metallic lustre in hand specimen (Figure 34) which clearly distinguishes it from the fine-grained variety and occurs in bodies from 2 to 50cm wide. Medium-grained galena is the dominant galena ore-type at George Fisher and accounts for approximately 42% of galena ore thickness in drill-hole intersections in C, D, and G ore horizons. The breccias contain clasts (Figure 34a, b, c) which can include vein-hosted and massive sphalerite (Figure 34a). Galena cross-cuts and brecciates vein-hosted sphalerite in Figures 34b and c (also recognized by Chapman, 1999, 2004) indicating that medium-grained galena breccia mineralization postdates vein-hosted/massive sphalerite mineralization. Relict fold hinges are common in the medium-grained galena breccias indicating that their formation postdates a mesoscale fold-forming deformation, the earliest of which was D_2.

Galena is the dominant sulphide and pyrite and pyrrhotite are common sulphide accessory minerals. Large dihedral angles for galena-pyrrhotite-galena triple-point junctions in the top left of Figure 35a suggest that recrystallization has occurred at low temperatures (<300°C) (Lusk et al., 2002). Galena occurs as inclusions in pyrite (Figure 35b) which parallel sides of the euhedral pyrite. This suggests that galena is replacing relic zoning within the pyrite. Overprinting of twinning in sphalerite by galena (Figure 35c) and

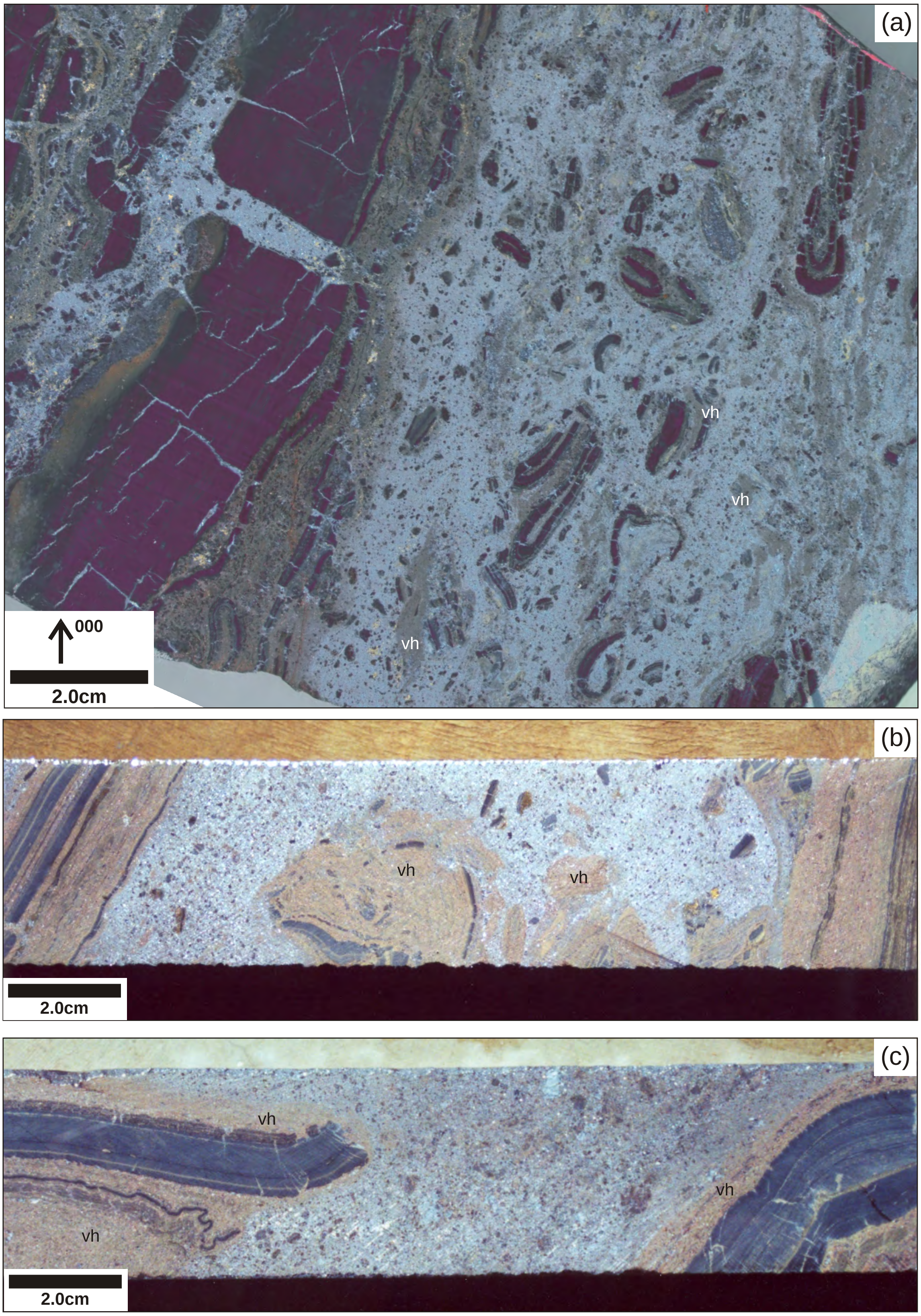

Figure 34. Medium grained galena in hand-specimen. (a) Relict fold hinges occur as clasts and have variable orientations indicating rotation during brecciation. Vein-hosted sphalerite clasts (vh) are abundant. Sample 0803-3. (b) Brecciation of vein-hosted sphalerite by medium-grained galena mineralization. Sample 960817_256.6m. (c) Medium-grained galena cross-cuts vein-hosted sphalerite mineralization. Sample 960932_178.7m.

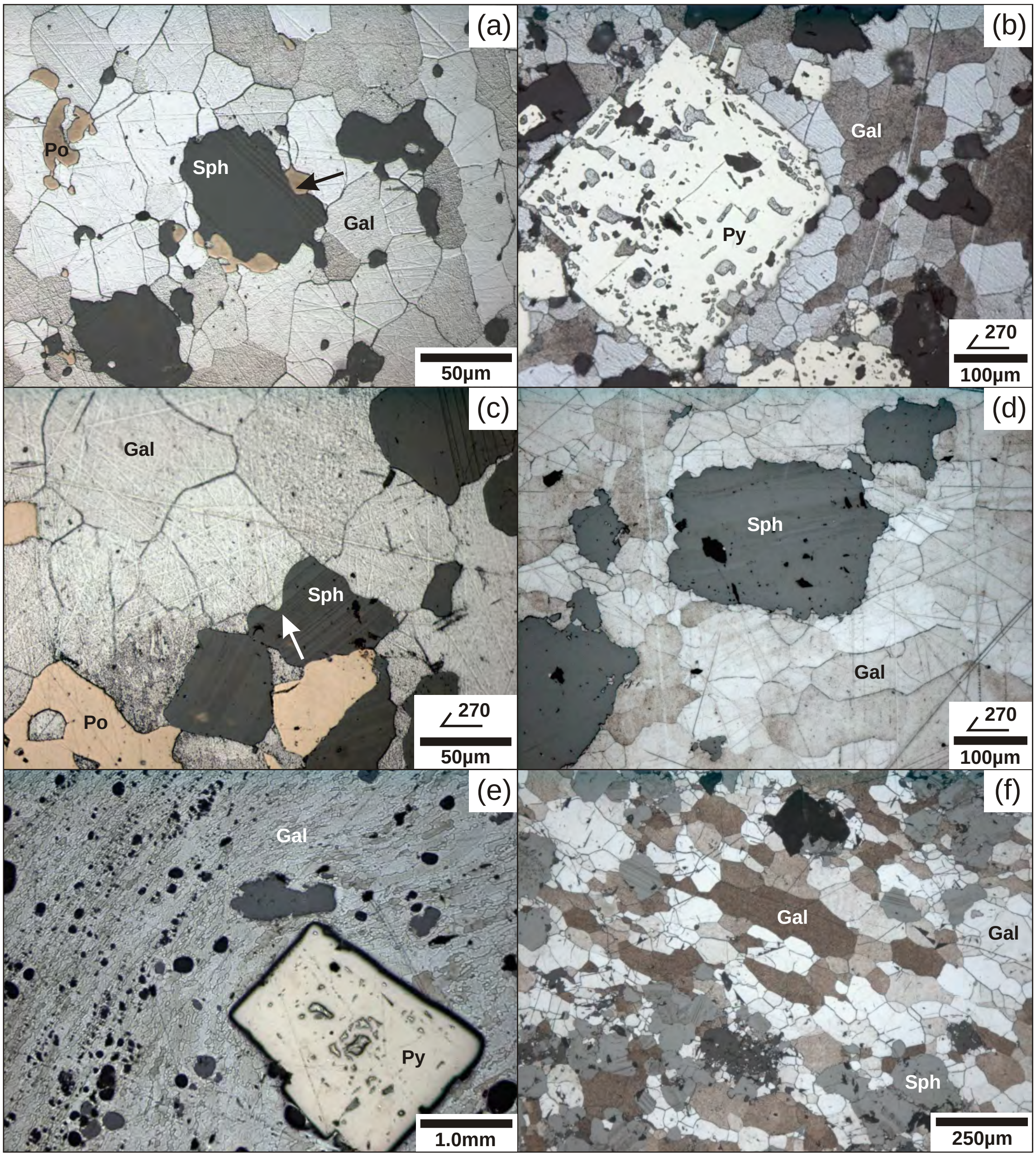

Figure 35. Photomicrographs of medium-grained galena etched using Thiourea and HCl (Brebrick and Scanlon, 1957) (a) Equant galena (Gal) replacing sphalerite (Sph). Although some 120º triple-point junctions occur, an equilibrium or foam texture has not been attained. Growth twins in sphalerite (arrow) are overprinted by a pyrrhotite (Po) grain. Sample 951033. (b) Equant galena occurs as matrix to euhedral pyrite (Py), also undergoing replacement by galena. Sample 2102-3. (c) Galena grains with some weak grain boundary irregularity. Galena overprints twins in sphalerite (arrow). Sample 2602-2. (d) Highly irregular margins of sphalerite clasts indicate replacement by galena. Sample 1302-2. (e) Shape preferred fabric in galena wrapping around euhedral pyrite crystal. Sample 960313. (f) Shape preferred orientation and recrystallization of galena. Sample 960436.

irregular margins of sphalerite clasts (Figure 35d) indicate galena postdates the sphalerite and a component of replacement is inferred. Grain shape preferred orientation is preserved (Figure 35e, f) and elongation of grains is consistent with dislocation glide, the dominant deformation mechanism for galena at lower temperatures and moderate stress (Atkinson, 1976; Cox, 1987).

A relationship between grain boundary geometry and deformation/recrystallization state is illustrated in Siemes (1977) where undeformed galena has smooth to gently curved grain boundaries and experimentally deformed (at 300°C) galena has irregular, serrated grain boundaries due to grain boundary migration. This phenomenon is analogous to the relationship in sphalerite discussed in Part C. Grain boundaries in medium grained galena observed in this study do not preserve an equivalent serrated grain boundary as illustrated in Siemes (1977). This suggests that either the galena postdates D_2 deformation (200°-250°C) or recrystallization and advanced grain boundary migration have pervasively modified the grain boundary geometry.

Galena-filled tension gashes/cracks are common in intervening layers of host rock that separate galena breccias and sphalerite mineralization types within broader mineralized intervals (Figure 36a). Medium grained galena breccia matrix is texturally continuous with these veins. The veins have a dominant ENE (mine grid, NE magnetic) strike. Chapman (1999) observed a conjugate set of these galena veins trending NE and NW and interpreted their formation as syn-D_4 as they cross-cut F_2 and F_3 folds. The veins (as illustrated in Figure 36b, c) can have both sharp and gradational vein walls and do not consistently exhibit mirrored geometry as expected with purely dilational veins.

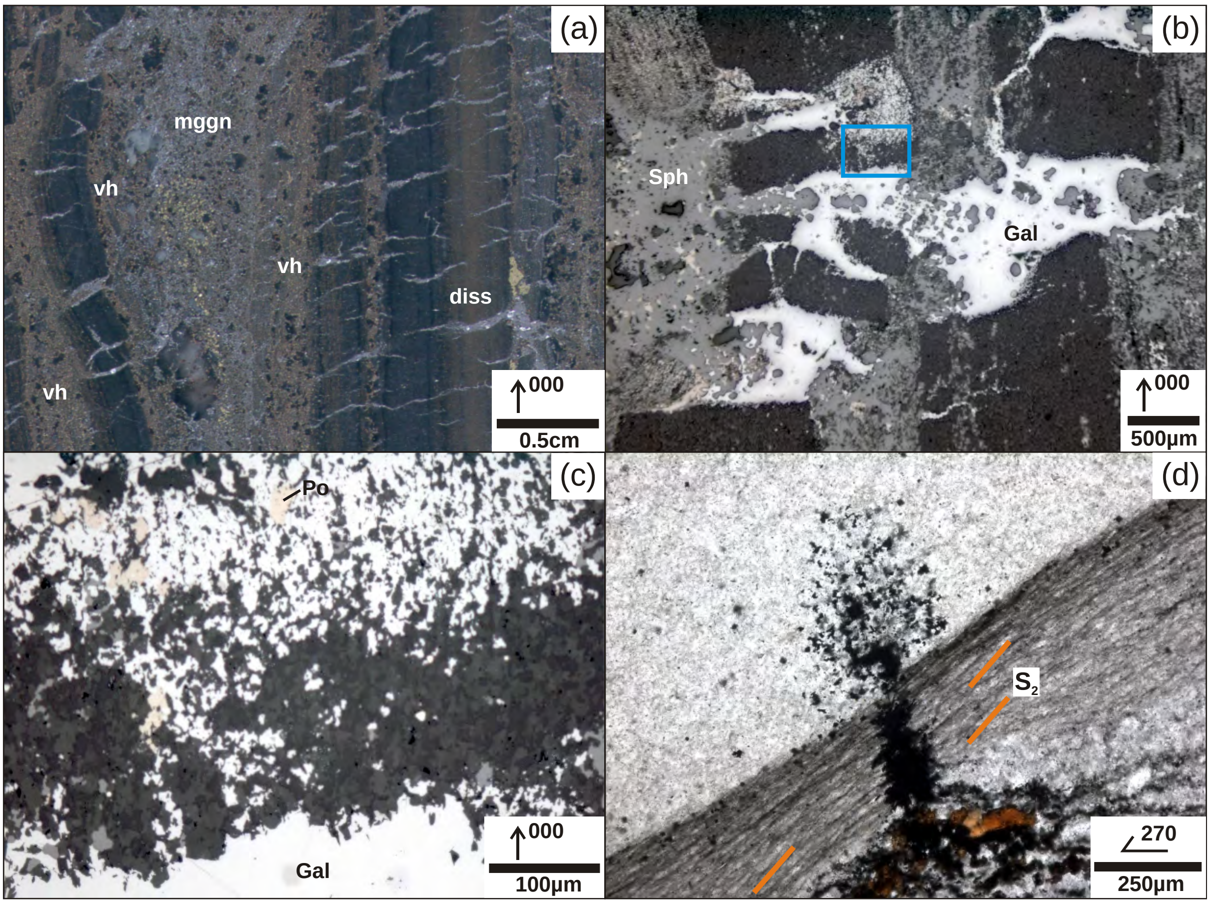

Figure 36. (a) Hand specimen of medium-grained galena breccia (mggn) and galena tension gashes cross-cutting vein-hosted sphalerite (vh) and tension gashes cross-cutting disseminated sphalerite (diss). Sample 0103-3. (b) Photomicrograph of galena (white) occurring as infill and replacement of host siltstone. Galena occurs in locations of bedding-parallel extension. Sample 0103-3. (c) Enlargement of inset in (b) illustrating partial replacement of the host rock at top and complete at bottom of photomicrograph. Sample 0103-3. (d) Galena-filled tension crack in foliated siltstone (darker layer) progresses to diffuse replacement of crystalline carbonate layer (pale layer). Lack of offset of the vein by the S_2 cleavage and the absence of galena along S_2 seams indicates that the galena mineralization in this example postdates D_2. Sample 1012-6.

Evidence for replacement as a process in forming these veins is illustrated in Figure 36c (enlargement of the inset in Figure 36b) in which the galena is inclusion-rich where replacement is not fully advanced as compared to the lower region of Figure 36c where galena is free from inclusions of wall rock. Galena mineralization in a similar tension crack illustrated in Figure 36d exhibits a host rock control on vein morphology as the vein is narrow within foliated siltstone and becomes diffusive where galena replaces the more massive crystalline layer. Galena cross-cuts the S_2 cleavage in this sample suggesting the galena mineralization occurred post-D_2. Galena tension veins are therefore interpreted to form due to a combination of brecciation/dilation and replacement synchronous with medium-grained galena breccia formation.

3.2.1 Relative timing of medium-grained galena breccia formation

Refolding of earlier folds in galena breccia can be used as criteria for timing the brecciation given that galena can preserve a foliation in the form of a preferred orientation of grain shapes. An isoclinal F_2 fold is folded by subhorizontal F_3 folds within galena matrix in Figure 37. A possible F_4 fold (there are no cross-cutting relationships to confirm this but orientation is consistent with F_4) also occurs in this sample. This sample was situated in the hinge region of a five metre amplitude F_2 fold yet no significant foliation is observed in the galena. Clasts of a relict layer can be traced around the flat-lying F_3 folds indicating that brecciation postdates F_3 fold formation. There is no significant foliation in the galena parallel to the axial trace of the F_4 fold, suggesting the galena was introduced syn- to post-D_4.

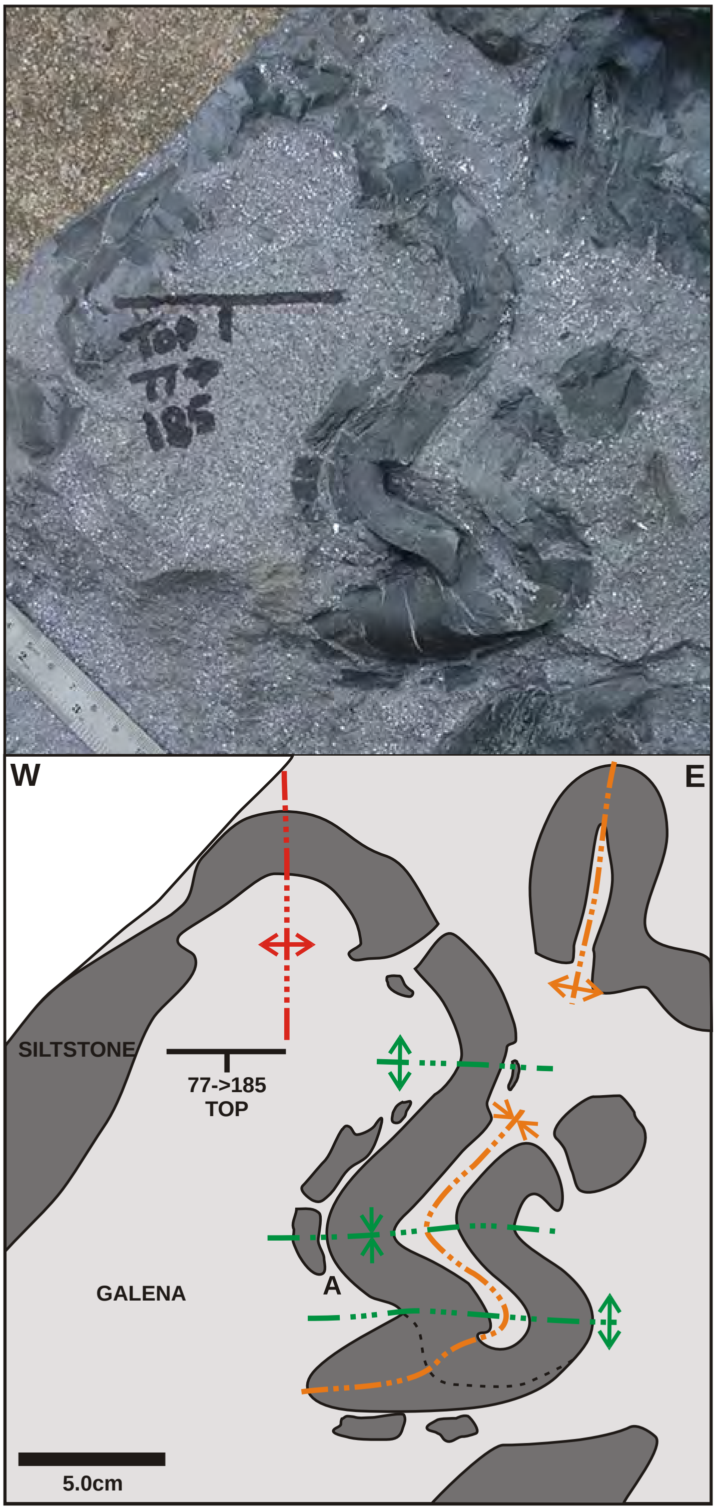

Figure 37. Photograph and sketch (looking north) of a massive medium-grained galena breccia. An isoclinal F_2 fold (orange) is folded by gently dipping F_3 folds (green). An inferred F_4 fold (red) is observed. Brecciation and introduction of the galena postdates F_3 folding as some folded (F_3) layers are invaded/truncated by galena (see location 'A'). Lack of preferred orientation in the galena suggests late to post-D_4 timing. Sample 0611-5.

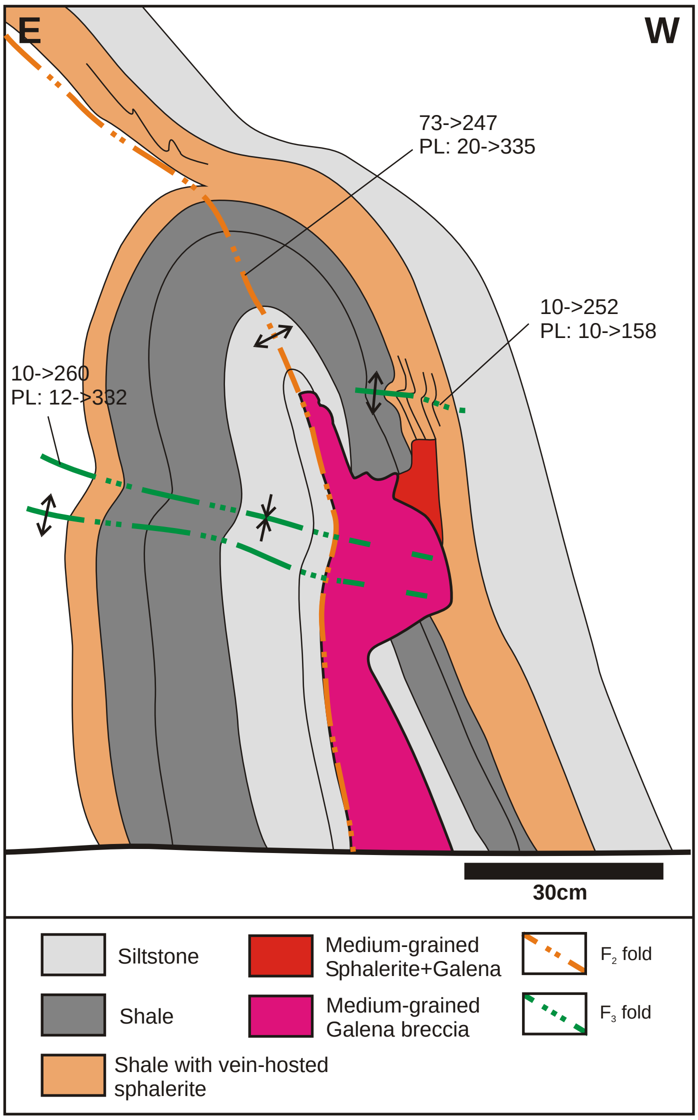

Figure 38. Mapping from 742 cross-cut, 12C level. The main fold in the diagram is an F_2 fold. The F_2 fold is cross-cut by a small fold on the western limb which has vergence that is inconsistent with the main F_2. This, and the gentle dip of the fold are characteristic of F_3 folds at George Fisher. The larger F_3 fold on the eastern limb folds the axial trace of the F_2 fold and its projected location on the western limb is occupied by a medium grained galena breccia. There is no textural variation in the galena breccia from the F_3 position to the F_2 axial region indicating that this is not a piercement structure formed by mechanical remobilization. Brecciation and introduction of the galena is interpreted to have occurred during D_4 reactivation of bedding (west-side-up), during which, the F_3 fold would have inhibited reactivation of bedding at this location and this resulted in local brecciation.

Further evidence for post-D_3 emplacement of the medium-grained galena breccia is illustrated in Figure 38 where the mineralization is located in the projected position of an F_3 fold. F_3 timing of the gently-dipping folds is indicated by the small fold on the western limb having vergence which is inconsistent with its position on the larger F_2 fold and the apparent folding of the F_2 axial plane by the larger F_3 fold (same vergence characteristics as western fold) on the eastern limb. Brecciation of the projected F_3 fold is interpreted to have occurred during D_4 west-side-up reactivation of bedding.

The gently dipping attitude of F_3 folds means that they focus vertical extension/dilation during the later D_4 east-west subhorizontal shortening. Rheological contrast is also important in this process as illustrated on Figure 39a. An F_3 fold (as observed in pyritic siltstone) occurs as a dilated fracture in a massive mudstone layer (Figure 39a). Top-to-the-east deformation during D_3 resulted in an asymmetric crack/vein in the more competent mudstone and folding in the weaker pyritic siltstones. The vein has massive sulphide infill consisting of clasts of vein-hosted sphalerite and wallrock (Figure 39b). Sphalerite bands in the breccia vein are folded and preserve a steep axial trace consistent with D_4 folding (Figure 39c). Clasts of wallrock are rotated such that they parallel the vein margins at its mouth, yet clasts and folding (Figure 39c) are oriented perpendicular to the vein margins toward the tip of the vein. There is no textural variation in the sulphides from the bedding-parallel mineralization into the vein itself which suggests that they formed synchronously. However, parallelism of clasts with the vein margin at the mouth of the vein suggests the vein is a piercement structure (cf. Maiden et al., 1986; Gilligan and Marshall, 1987) that formed post-D_3 and may therefore represent local mechanical remobilization but this is inconsistent with the lack of textural variation in the

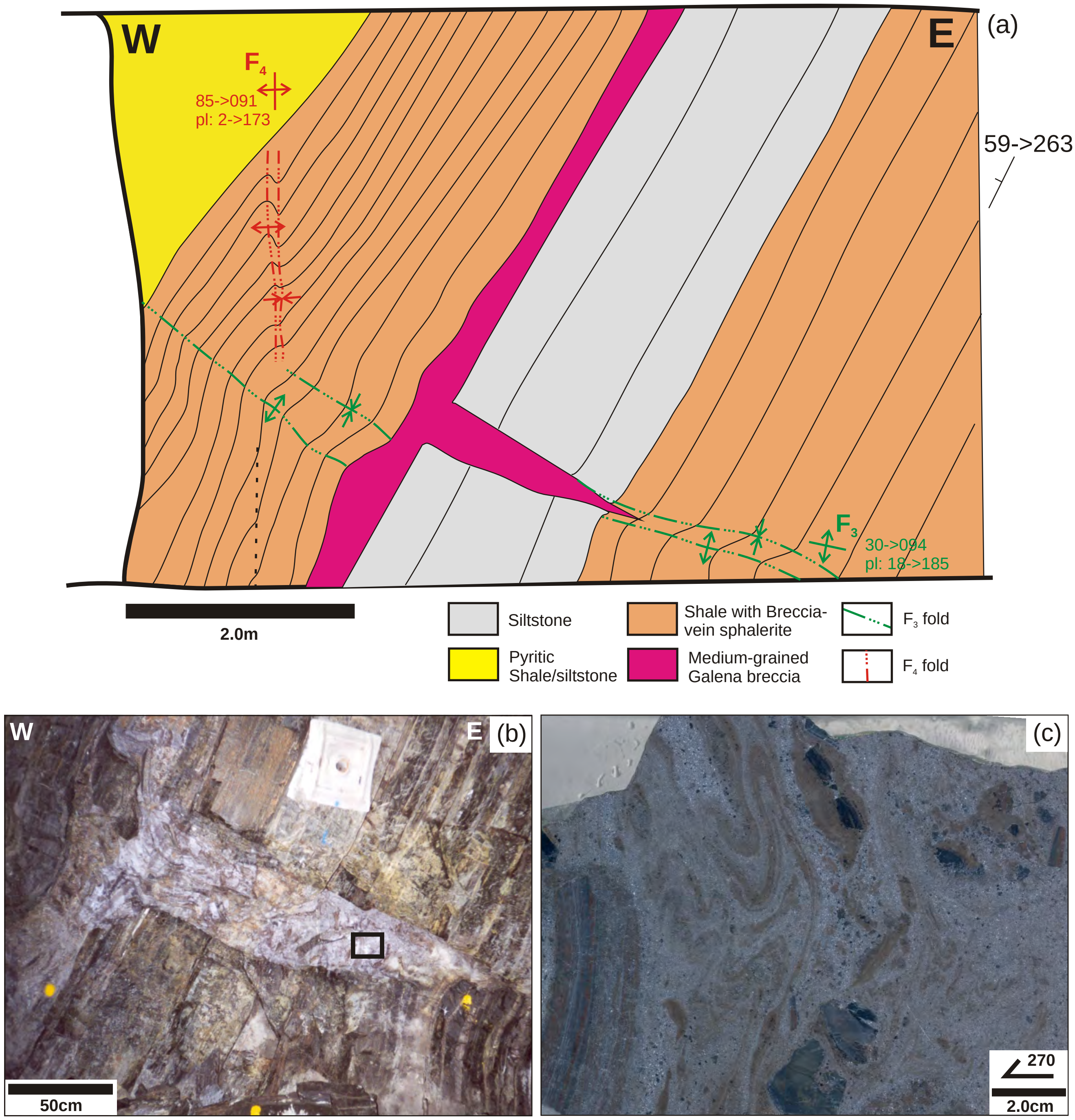

Figure 39. (a) Mapping of 720 cross-cut, 12C. Galena breccia forms a bedding-parallel layer and also occurs as a bedding perpendicular vein which cross-cuts a mudstone layer and extends approximately 2.0m into the footwall. This vein is spatially coincident with a gently dipping F_3 fold which is interpreted as the heterogeneity from which the vein was able to propagate. F_4 folding on the western side of the diagram is coincident with apparent unfolding of the gently-dipping F_3 fold. (b) Photograph of the discordant vein. Clasts, and the bedding within them, are sub-parallel to the walls of the vein near its mouth but discordant to the general orientation of bedding outside the vein. This may indicate that material has been flowed into the vein from the adjacent bedding parallel mineralization. (c) Vertical face looking north from a sample from the area inset in (b). Folds in bedding and sphalerite mineralization with steeply dipping axial planes are preserved in the galena breccia. Sample 0512-6.

sulphide. The timing of medium-grained galena in Figure 40 is less ambiguous. Mapping of this cross-cut wall (looking south) indicates a mineralized sequence with considerable folding bounded by less mineralized planar bedded host rock. F_3 folds in the mineralized sequence have gently dipping axial planes and z-shaped vergence. These are folded by upright F_4 folds with more steeply dipping axial planes (Figure 40). Galena mineralization cross-cuts the F_4 folds and therefore has late to post-D_4 timing.

Local thickening of galena in zones of folding is illustrated in Figure 41a and b. Interpreted F_2 folds cause an apparent thickening of galena in isolated pods connected by narrow bedding-parallel medium-grained galena breccia (Figure 41b). Chaotic folding of narrow layers is observed within the massive galena (Figure 41b) and a preferred orientation is observable in hand specimen (Figure 41c). The foliation dips steeply to the west and strikes 016° (Figure 41d) which is consistent with S_4, and does not parallel the axial trace of fold-clasts (Figure 41c) or the larger scale F_2 folds (Figure 41a, b). An F_4 fold with a steeply dipping axial plane occurs immediately above the galena breccia (Figure 41a, b) and it is possible that the steep foliation observed (Figure 41d) is associated with this deformation. The mineralization is therefore pre- to syn-D_4. The intersection of the F_4 fold with bedding in this locality plunges 8°→177° which is parallel to the trend in high Pb grades recognized in Part B – Figure 14b.

The host-rocks at George Fisher preserve medium-grained galena breccia in sites of extension from micro to exposure-scale. Boudinage of a barren siltstone layer in Figure 42 resulted in the development of carbonate extension veins within the neck region, and these veins were subsequently brecciated by medium grained galena which is laterally

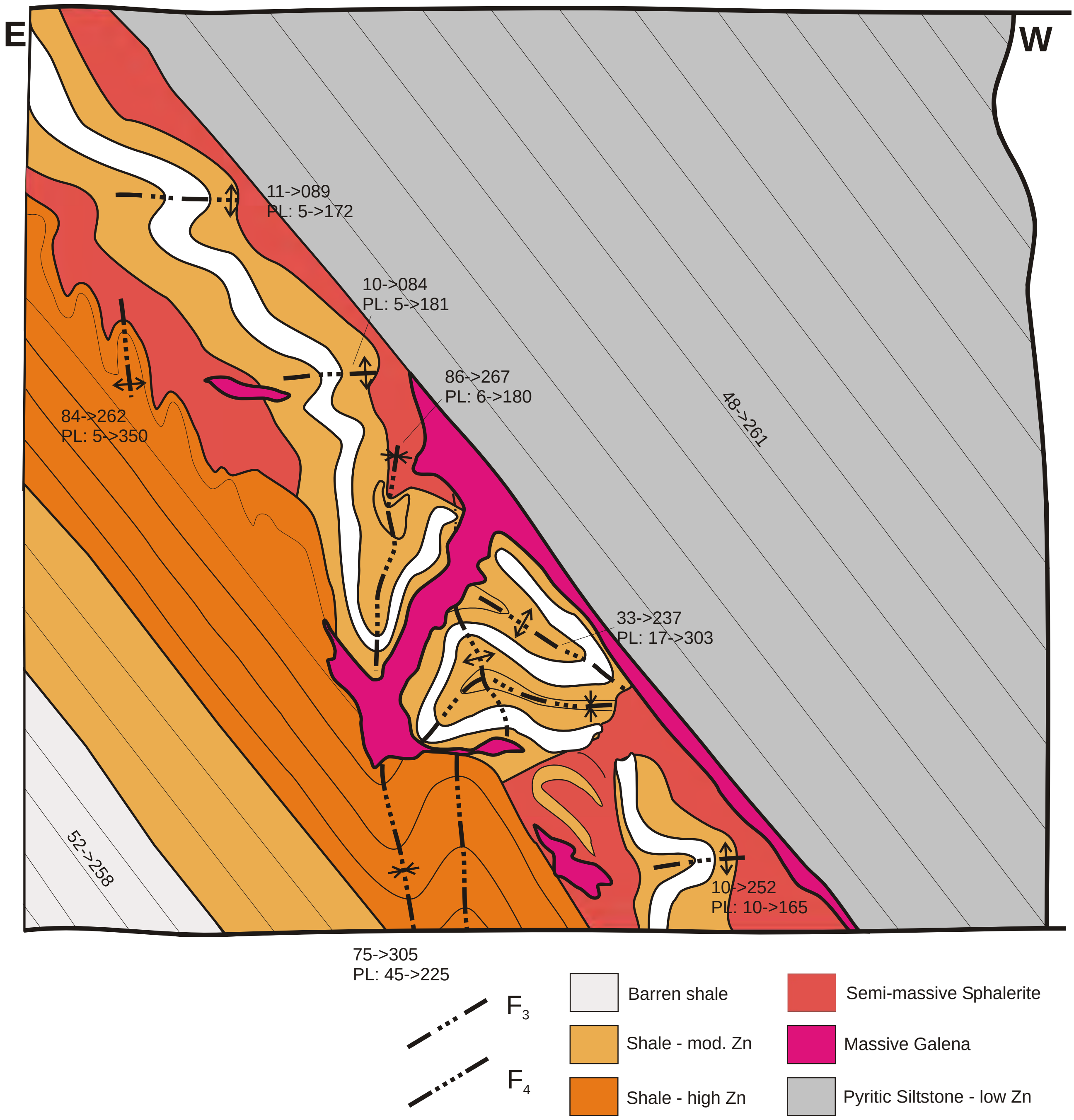

Figure 40. Mapping of 7490 cross-cut, 12C. Galena breccia occurs at the intersection of gently dipping F_3 folds and the later steeply dipping F_4 folding. Note the refolding pattern which indicates the relative timing of fold generations in the exposure. The medium-grained galena breccia cross-cuts the F_4 axial trace suggesting that brecciation in this case is late- to post-D_4.

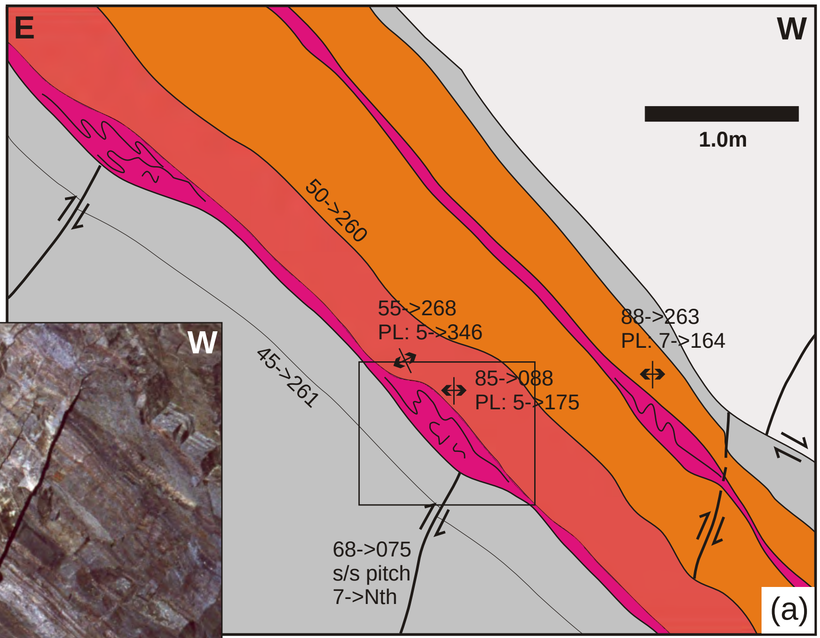

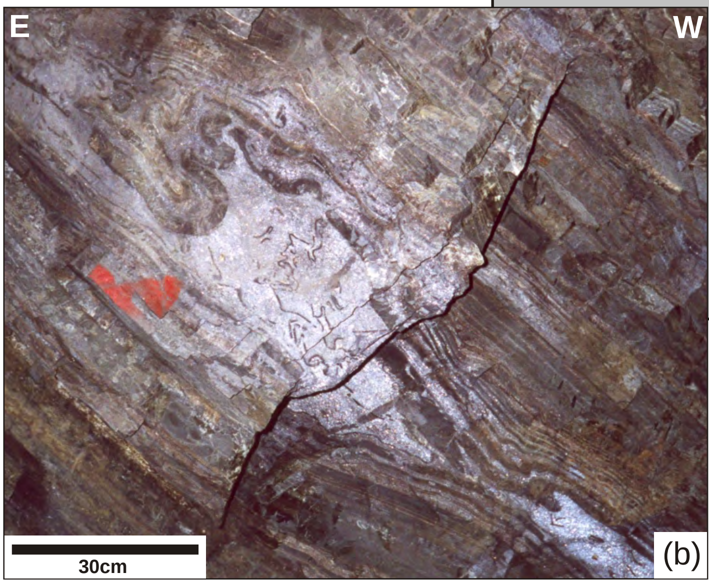

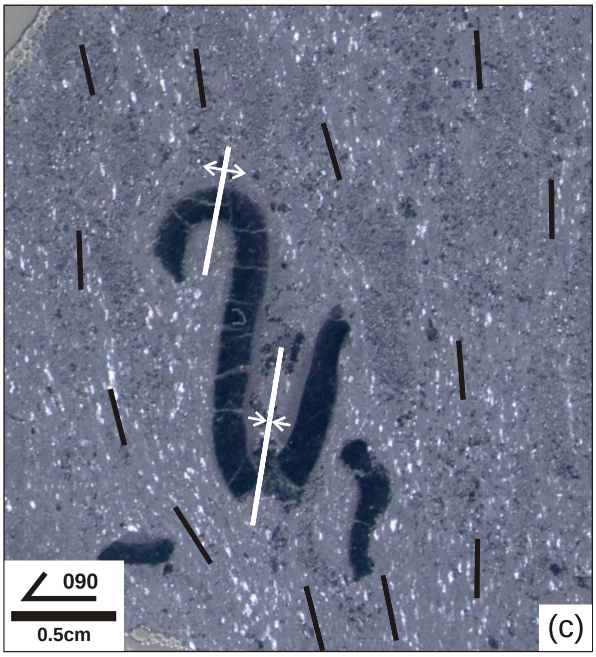

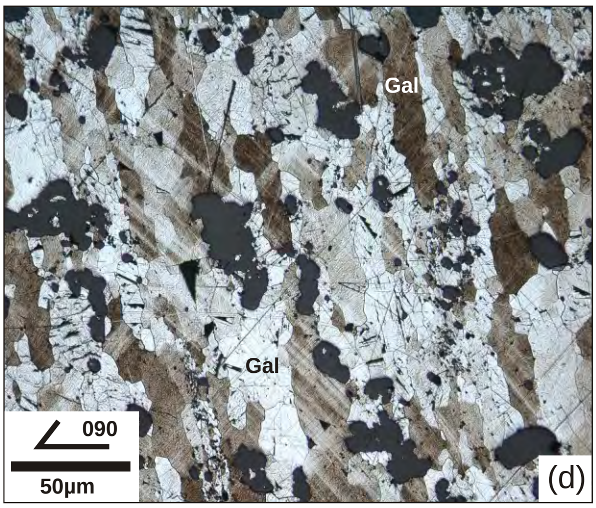

Figure 41. (a) Mapping of 723 cross-cut, 12L. Medium grained galena occurs as thicker pods coincident with folding within a specific stratigraphic horizon. (b) Photograph of the inset area in (a), showing chaotic folding within the mineralization and continuity of bedding above and below the breccia. (c) Vertical face of an oriented hand specimen with a floating fold hinge within the galena dominant matrix. A well-developed foliation in the galena (indicated by black lines) wraps around the fold/clast and is oblique to the axial traces of the relict fold. (d) The foliation in galena (Gal) pitches steeply to the west in vertical section as shown in this photomicrograph and has strike of 016º, which is parallel to the orientation of S_4. Sample 0412-1. **Note that all views are looking south, including photomicrographs.**

Figure 42. (a) Photograph of the back (ceiling) of an ore-drive in D orebody. A barren siltstone layer is boudinaged and medium-grained galena occurs adjacent to and within the boudin neck. 723 stope 12L. (b) Hand specimen from the boudin neck. The orientation of carbonate veins perpendicular to bedding indicates layer-parallel extension during boudinage. Clasts containing the carbonate veins occur within the galena breccia suggesting that the galena postdates some of the layer-parallel extension and was introduced during deformation. Sample 0902-2.

continuous for approximately five metres. The axis of the boudin neck plunges 45°→277° and has a pitch of near 90° in the plane of bedding. Relics of the carbonate extension veins occur within the galena breccia. Subhorizontal, north-south bedding-parallel extension therefore predates galena introduction as evidenced by the breccia containing clasts of carbonate veins. The relative timing of the boudinage is not clear as both D_2 and D_4 could have formed this structure as they are approximately coaxial, however, introduction of the galena breccia postdates at least one episode of deformation, and this is likely to be D_2, and therefore the breccia is of post-D_2 timing.

At the mine-scale, medium grained galena (Figure 43) is concentrated in two shoots, a steeply pitching shoot approximately co-incident with the F_1 short-limb zone and a gently pitching shoot which parallels the L^0_2 orientation. As discussed in Part B, higher grades and thicker sulphides are concentrated in the F_1 short-limb and medium-grained galena exhibits a similar trend in C and D ore-horizons (Figures 43a and b). The trend is not apparent in G ore-horizon (Figure 43c) which generally lacks significant Pb grades (Part B - Figure 15b). F_2 folding is observed in D ore-horizon within the gently pitching trend (Part A – Figure 16) and several of the previously discussed medium-grained galena localities (Figures 37, 38, 39) are located within this fold zone. The F_2 folds are considered to act as heterogeneities which focus D_3 and D_4 deformation. The thickness of medium-grained galena in D and C ore-horizons is almost inversely proportional to the fine-grained sphalerite+galena breccia (Figure 30b). This phenomenon may indicate remobilization of galena from bedding-parallel fine-grained sphalerite+galena layers to the structurally controlled medium-grained galena breccias in areas of folding. The

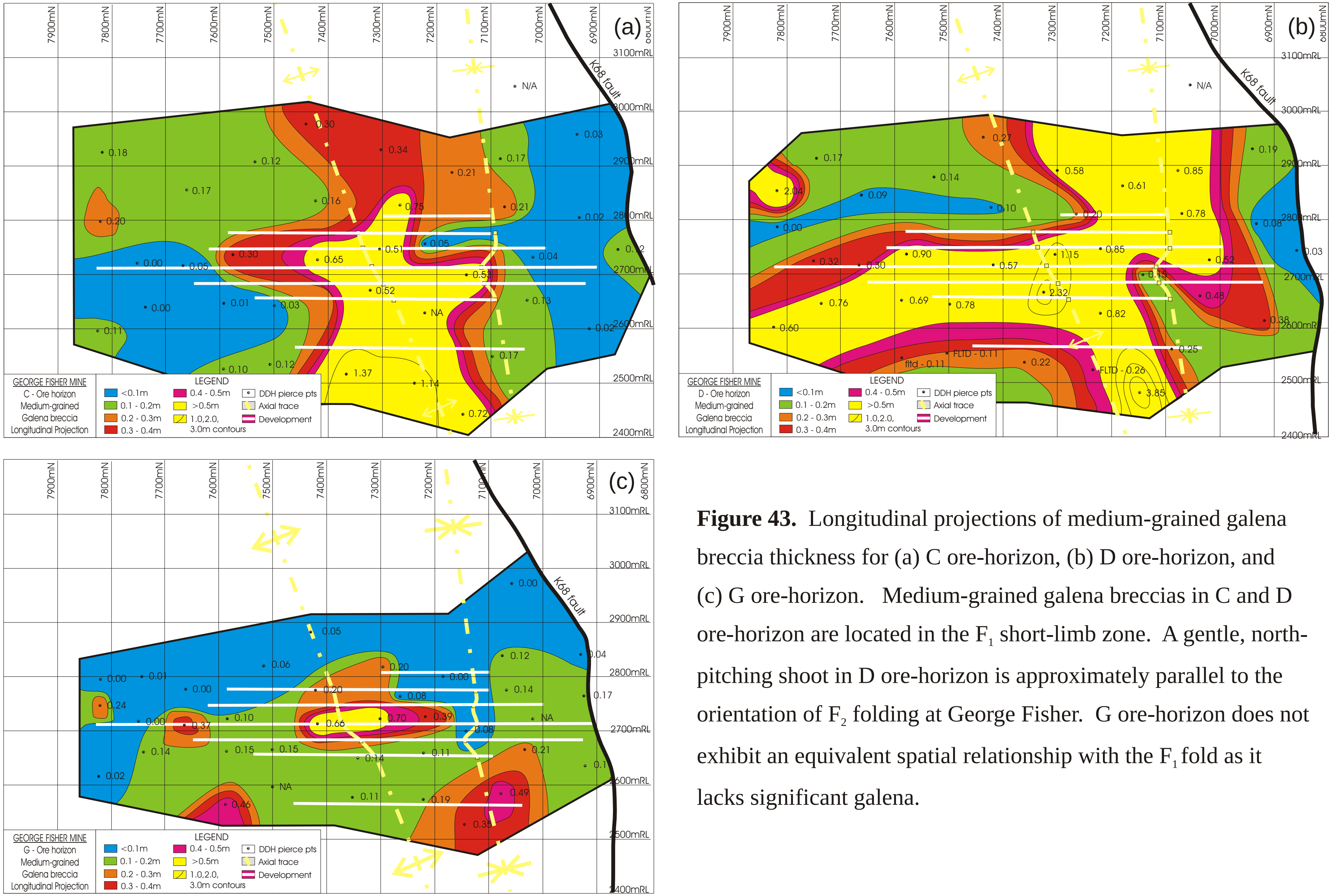

Figure 43. Longitudinal projections of medium-grained galena breccia thickness for (a) C ore-horizon, (b) D ore-horizon, and (c) G ore-horizon. Medium-grained galena breccias in C and D ore-horizon are located in the F_1 short-limb zone. A gentle, north-pitching shoot in D ore-horizon is approximately parallel to the orientation of F_2 folding at George Fisher. G ore-horizon does not exhibit an equivalent spatial relationship with the F_1 fold as it lacks significant galena.

absence of this relationship in G ore-horizon corresponds with a lack of significant Pb mineralization.

This relationship is illustrated in Part B – Figure 26 where G ore-horizon is situated outside the region of more intense S_4 crenulation development and has significantly lower Pb grade than C and D ore-horizons in the area of more intense S_4. This suggests insufficient sites or lack of fluid pathways have largely prevented precipitation of galena in G ore-horizon. Fine-grained galena (+sphalerite) is generally of more uniform thickness (Figure 30) compared to the poddy nature of medium-grained galena consistent with remobilization and upgrading of stratigraphy due to increased galena width on a local scale.

Medium-grained galena is interpreted to occur in sites of bedding parallel extension and brecciation of earlier formed folds. The timing criteria discussed above indicate that the medium-grained galena postdates the main deformation (D_2) and occurs in sites which indicate late-D_4 timing. Mine-scale remobilization from fine-grained breccia to the irregularly distributed and laterally discontinuous medium-grained galena breccia may have occurred during D_4.

3.3 Coarse- grained galena breccia

Coarse-grained galena-dominant breccia is characterized as the name suggests, by coarse crystalline (grains generally > 1mm) aggregates of galena (Figure 44 a and c) with variable amounts of sphalerite and/or pyrite (Figure 44 b and d, Figure 45). Sphalerite occurs as inclusions within galena grains in galena-rich samples (Figure 44c) and as

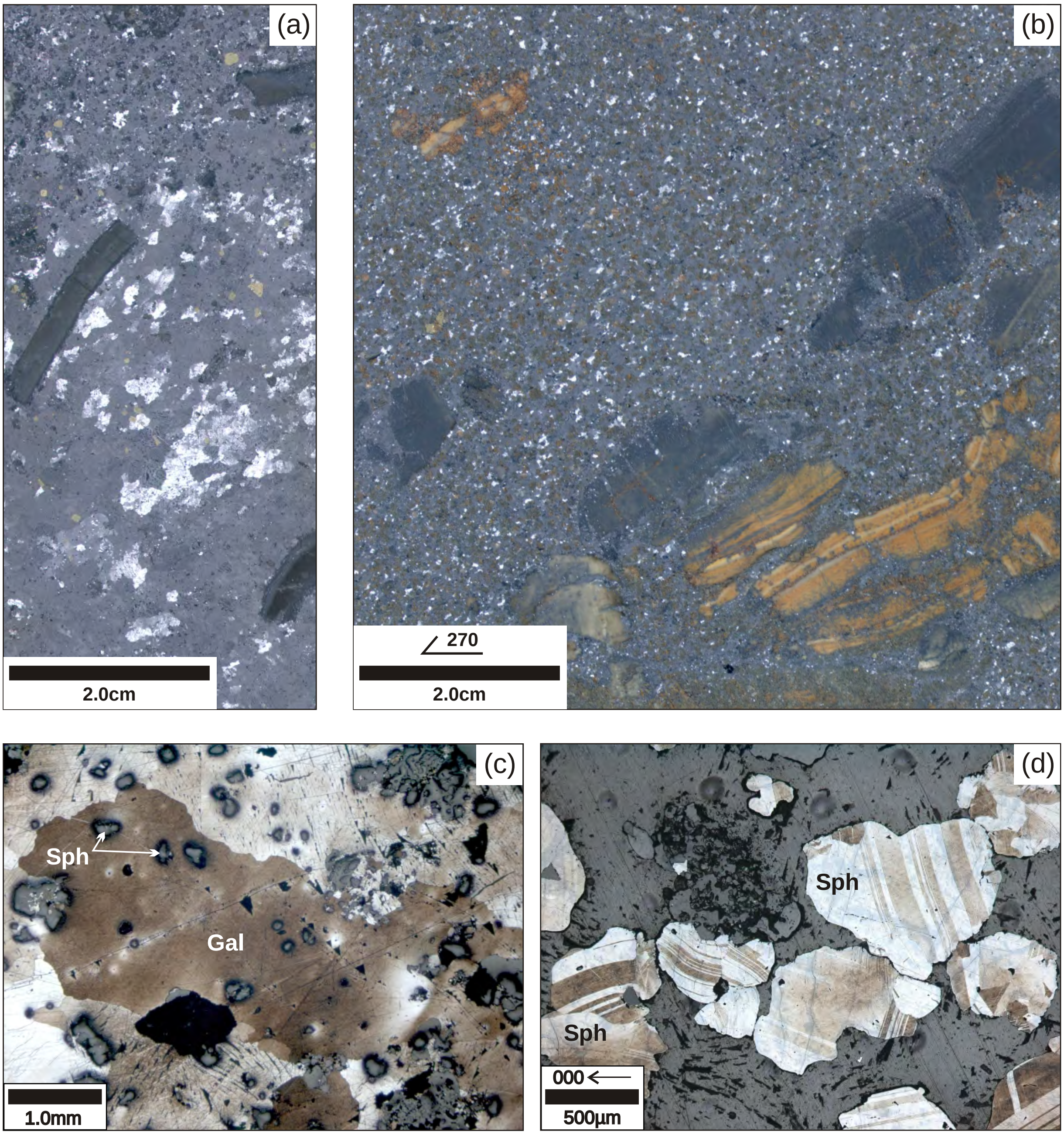

Figure 44. Coarse-grained galena in hand specimen (a & b) and photomicrographs (c & d) of the samples ((c) etched with Thiourea and HCl, (d) etched with conc. HI), respectively. Galena dominant mineralization in (a) has a galena (Gal) grain size of approximately 5mm and sphalerite (Sph) occurs as intragranular inclusions within galena as seen in (c). The sample in (b) is typical of the buff-altered siltstones and sphalerite is more abundant and occurs as clasts with corroded/embayed margins as seen in (d). The dull grey area in (d) represents eroded galena from the thin section during etching with HI. Twins in sphalerite are bent indicating that the clasts are deformed. (a) and (c): sample 960313_380.35m, and (b) and (d): 1712-3.

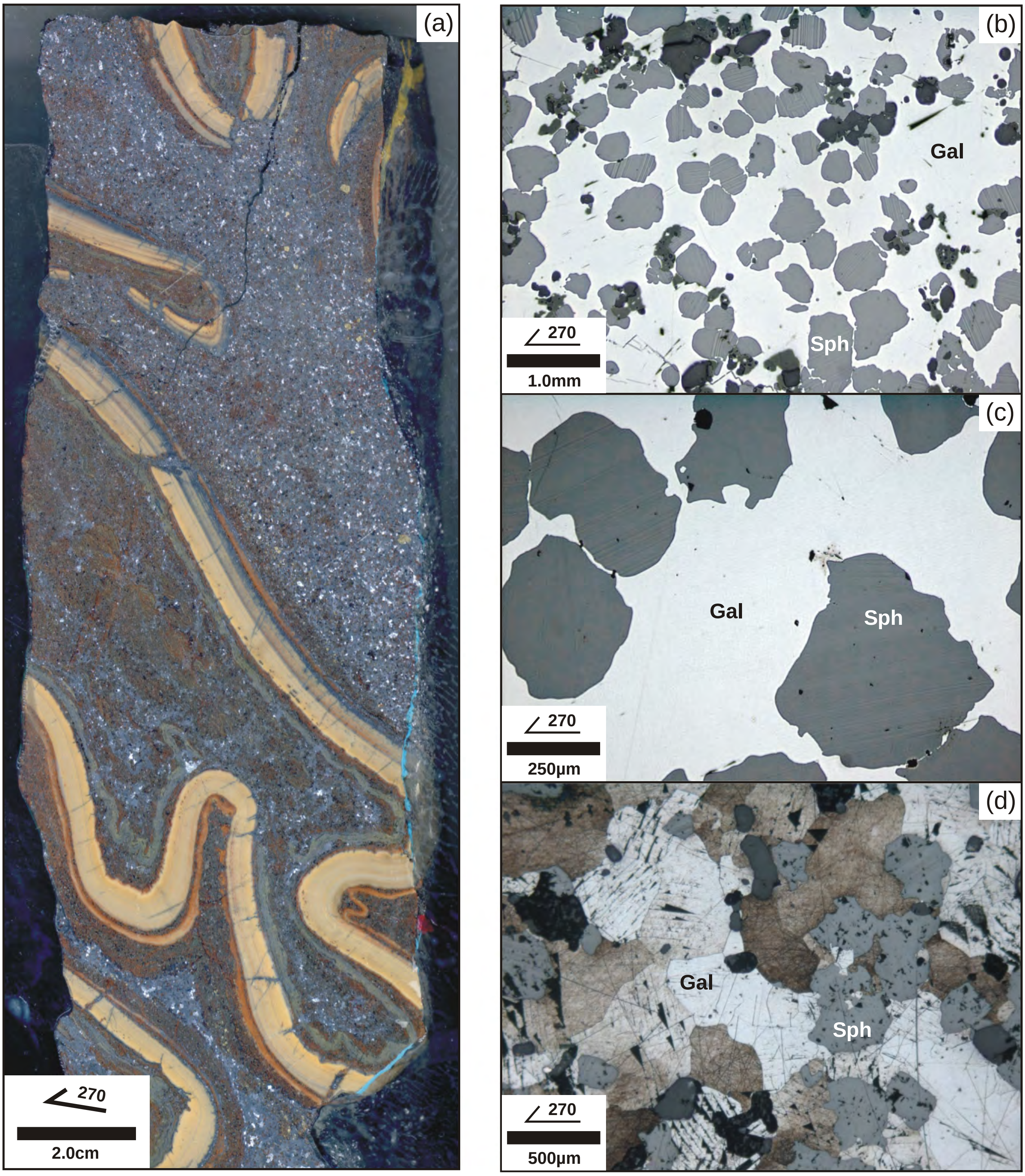

Figure 45. Coarse-grained galena in hand specimen (a) and polished section (b, c, d). (a) The galena does not preserve a preferred orientation in hand specimen despite the degree of folding. (b) Sphalerite (Sph) occurs as isolated clasts within a galena (Gal) matrix. (c) A photomicrograph at higher magnification shows the irregular, embayed margins of sphalerite clasts and galena growth along relict sphalerite grain boundaries. (d) Polished section etched with Thiourea and HCl solution reveals the equant grain shapes and grain size (~300µm) of sphalerite and galena. Sample 1112-6.

intercrystalline grains in more sphalerite-rich samples (Figure 44d, Figure 45 b-d). Sphalerite grains in the latter exhibit bent and discontinuous twins (Figure 44d) which indicate that deformation of pre-existing sphalerite has occurred prior to or synchronous with galena emplacement. Irregular embayed margins of sphalerite grains also suggest replacement of sphalerite by galena (Figure 45b, c, d). Although folding is observed in the sample pictured in Figure 45a, a foliation is not observed within the galena at the microscale (Figure 45d) which may indicate post-folding emplacement of the galena breccia. Exposure scale relationships support this interpretation. Folds with gently dipping axial planes which are the product of D_3 deformation (either F_3 folds or F_2 folds rotated during D_3) are cross-cut by coarse-grained galena+sphalerite breccia (Figure 46). F_3 fold hinges are 'floating' in the galena breccia and a quartz-carbonate-sphalerite vein which cross-cuts the folding is in turn cross-cut by the galena breccia indicating that emplacement of the breccia has occurred post-D_3. Brecciation may have occurred during inferred bedding reactivation associated with D_4.

Relict fold-hinges occur in coarse-grained galena breccia (Figure 47) indicating mineralization post-dating a folding event. The fold in Figure 47 may be of D_2 or D_3 timing. Coarse-grained galena breccia is located in sites of dilation whose shape and position is consistent with their formation during bedding plane slip (Figure 48). Textural continuity of the breccia in the dilational area and bedding-parallel zone suggest that they formed simultaneously. Dilation in this position is unlikely to have occurred during subvertical shortening associated with D_3, but is consistent with the stress fields for both D_2 and D_4.

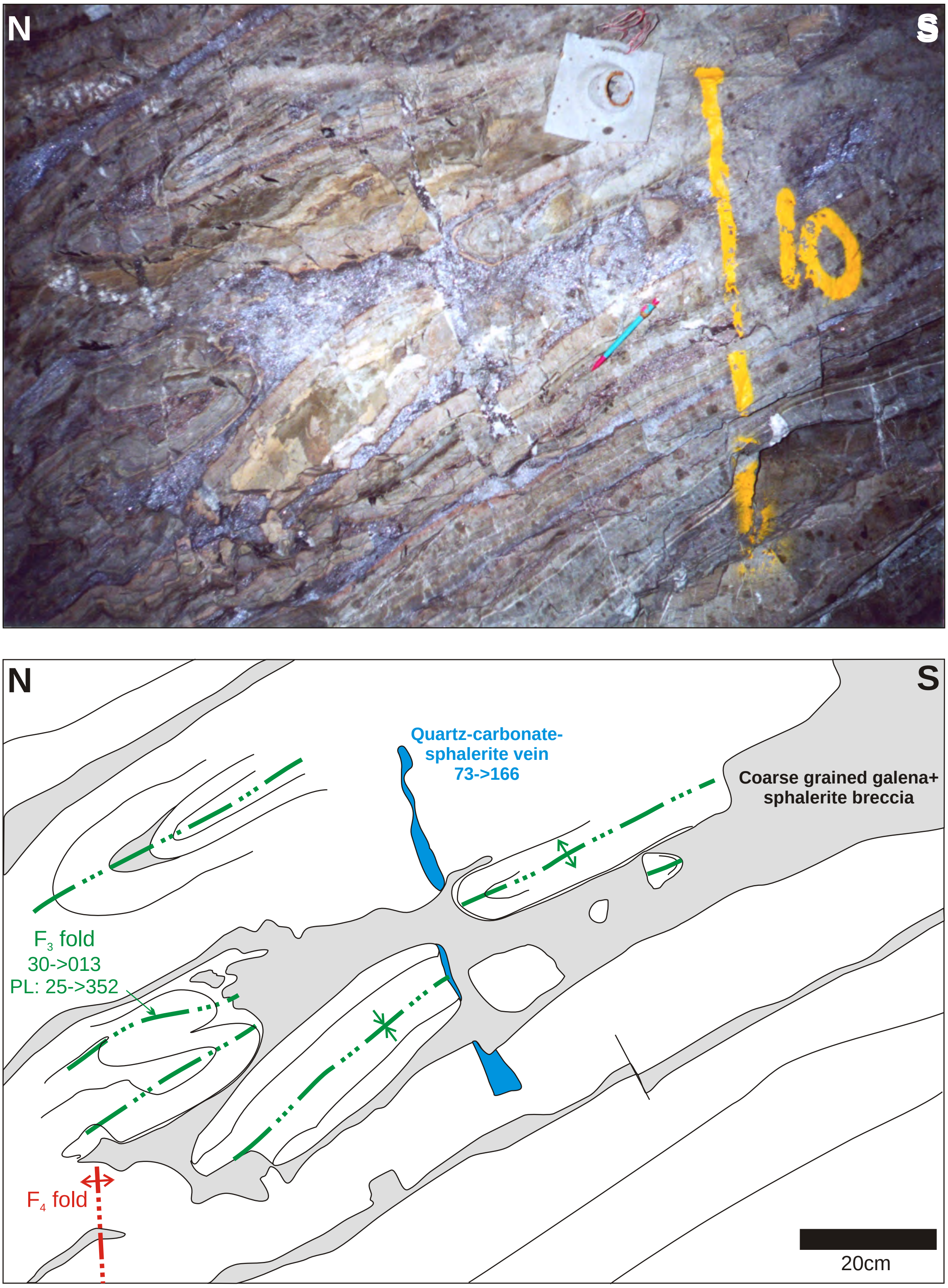

Figure 46. Photograph and line diagram illustrating the timing of coarse-grained galena+sphalerite mineralization relative to folding. A quartz-carbonate-sphalerite vein (blue) cross-cuts gently-dipping F_3 folds in the diagram. Both the folds and cross-cutting vein were subsequently brecciated by massive coarse-grained galena and sphalerite mineralization. Timing of the mineralization in this exposure is therefore interpreted as post-D_3.

Figure 47. Relict fold occurring as a clast within a galena-dominant coarse-grained galena breccia. This illustrates the preferential localization of galena breccia where pre-existing folds are brecciated during subsequent deformation.

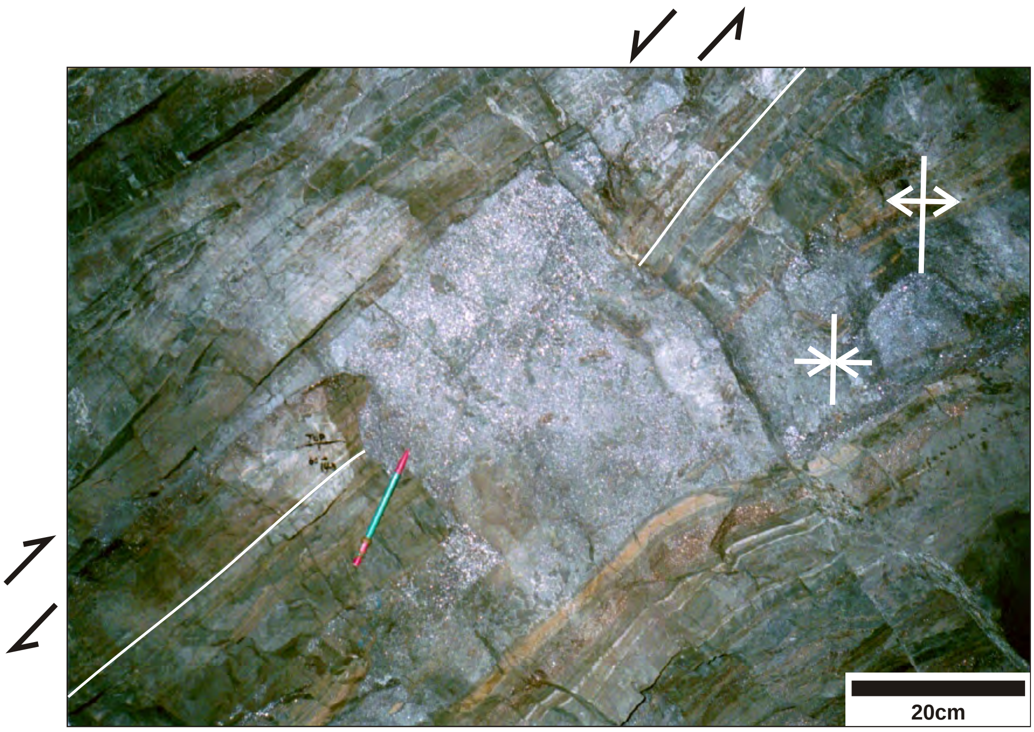

Figure 48. Coarse grained galena breccia in an apparent boudin neck formed during bedding-parallel extension. The thin white line indicates the continuation of a layer on opposite sides of the breccia. Black half-arrows indicate the apparent sense of shear required to create the dilatant site. There is no textural variation between the bedding-parallel and bedding-discordant galena breccia.

Coarse-grained galena breccia is more prevalent in buff-altered (Chapman, 1999) siltstones within C and D ore-horizons (Figures 47 and 48). The K-feldspar alteration has affected the rheological characteristics of the siltstone as indicated by more brittle fracturing and brecciation of the altered layers. The coarse nature of the breccia indicates that the galena has not undergone grainsize reduction due to dynamic recrystallization during deformation. Grainsize coarsening during recrystallization only occurs above 400°C (Stanton and Gorman-Willey, 1972), approximately 150-200°C higher than the temperatures attained at George Fisher. Temperature controlled grain-growth is therefore not considered to have created the observed coarse-grained texture in these breccias.

Coarse-grained galena-dominant breccias occur sporadically throughout intersections in the hangingwall section of the orebody sequence and this textural variety of galena mineralization accounts for approximately 9% of galena ore intersections in C, D, and G ore-horizon intersections (Figure 49a-c). Although of minor relative abundance, the breccia is dominantly massive sulphide and its thickness and distribution can significantly affect the average grade of intersections and interpolated grades in the resource model. A strong spatial relationship exists between the distribution of coarse-grained galena breccia and the F_1 short-limb zone (Figure 49). G ore horizon (Figure 49c) lacks significant coarse-grained galena mineralization. The spatial relationship between mineralization and the short-limb zone in C and D ore-horizons is attributed to the focussing of fluids into this region which was an area of low stress during D_4. Brecciation of pre-existing folds (Figure 46 and 47) also provided sites for deposition of sulphides during this deformation.

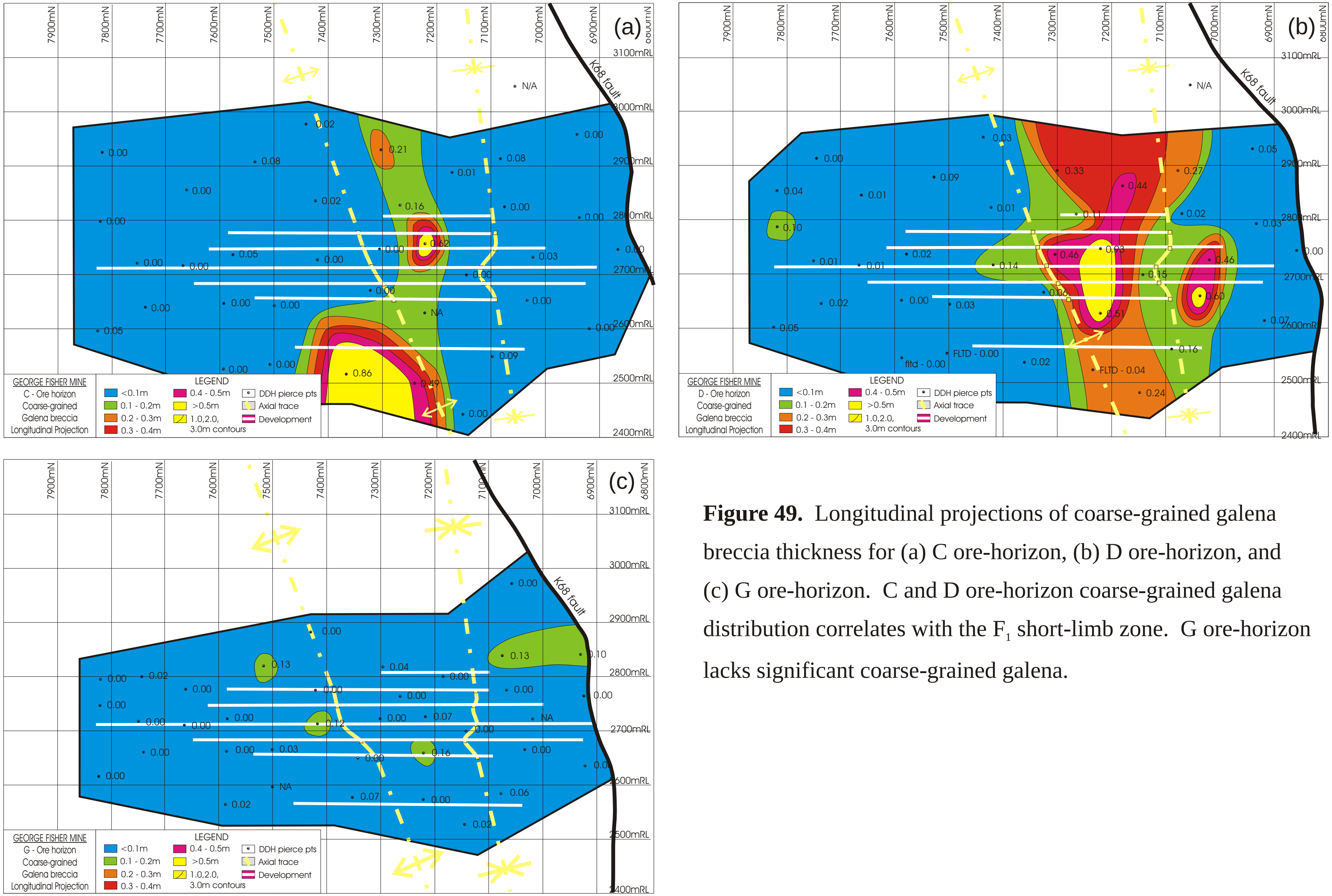

Figure 49. Longitudinal projections of coarse-grained galena breccia thickness for (a) C ore-horizon, (b) D ore-horizon, and (c) G ore-horizon. C and D ore-horizon coarse-grained galena distribution correlates with the F_1 short-limb zone. G ore-horizon lacks significant coarse-grained galena.

4. Discrimination of remobilized vs syntectonic mineralization based on analysis of grade populations

Assay data can be analyzed in order to determine the presence of more than one population of metal grades based on the average grade, range, and statistical distribution of the data. If more than one population is recognized, remobilization of the existing mineralization or overprinting by a later episode of mineralization may be inferred. Davis (2004) has interpreted the Pb-Zn ores at Mt Isa as the product of syntectonic replacement genetically related to the Cu mineralization which exists in close proximity. Remobilization at the scale of 100's of metres has been ruled out based on interpretation that only a single population of Pb and Zn grades exists (Davis, 2004). The frequency histogram of metal grades (sqrt) in figure 13 of Davis (2004) displays a strong correlation between the amounts of Pb and Zn (Figure 50). Both a higher and possible lower grade Zn and Pb population are interpreted to be associated with F_4 folding at the Mt Isa mine Davis (2004). The lower grade population was therefore not interpreted as a proto-ore occurrence (Davis, 2004).

Data from the D ore-body interval at George Fisher has been plotted on Figure 50a in a similar style to that of Davis (2004) and some significant differences between the Mt Isa and George Fisher data are observed. Zn grade distribution on the frequency histogram has a very similar pattern to that of Zn grades in the B orebody interval at Mt Isa (Davis, 2004). Potential lower and higher grade populations can be distinguished at approximately 6-7% Zn (dashed-dotted line at ~2.7% on the square root scale on Figure 50a) compared with ~1.6% Zn (Davis, 2004). The range of Zn grades is higher in the George Fisher deposit compared to Mt Isa. Pb grades which correlate with Zn grades at

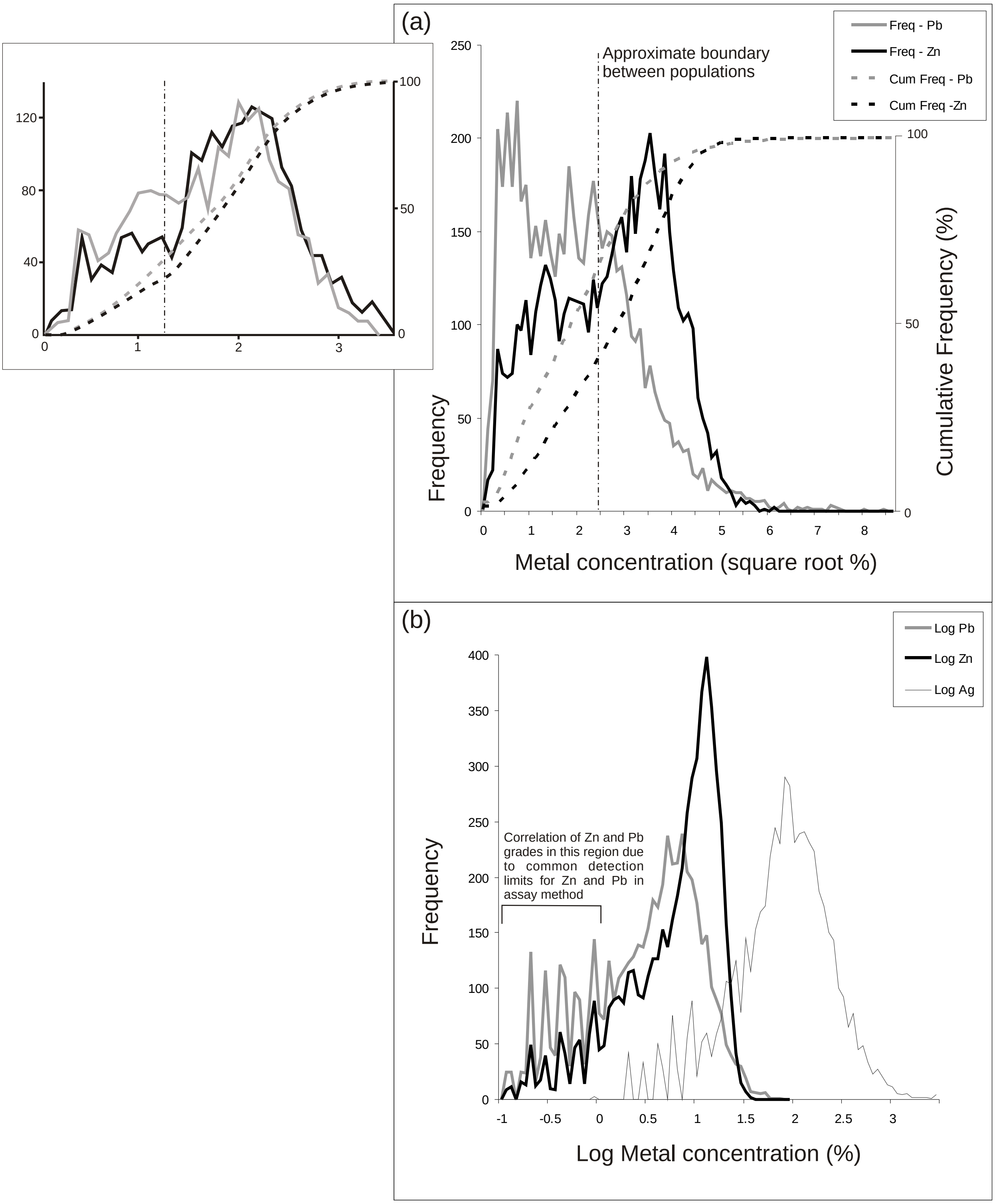

Figure 50. (a) Graph of the square root of metal concentration vs frequency for D ore body at George Fisher as used for B ore body at the Mt Isa deposit in Davis (2004) (inset). In contrast with the data presented by Davis (inset), Pb and Zn at George Fisher have different distributions as seen on this plot. High Zn have higher frequency yet the high Pb grades do not define a distinct population. (b) Distribution of Pb, Zn, and Ag a plot of Log(metal concentration) vs frequency for D orebody also show a more prounounced higher grade Zn component to the Zn distribution than seen in Pb. Ag has a near lognormal distribution.

Mt Isa (Davis, 2004) have a very different distribution at George Fisher (Figure 50a). Note that a positive correlation between Pb and Zn has been established (Part B – Figure 10) which is not evident in Figure 50a as this figure does not compare Zn and Pb values for individual samples but for bin sizes. A weak change in the slope of the cumulative frequency for Zn metal can be recognized at the equivalent of approximately 9.0% Zn in Figure 50a. This is comparable with a change in slope at a much lower grade of 2% Zn in Mt Isa data (figure 13a - Davis, 2004). The change at 9% coincides with the higher grade Zn population (Figure 50a) and may represent an upgrading effect due to remobilization.

Comparison of the logarithm of metal grades for each of the ore constituents in D ore-horizon on Figure 50b reveals that Pb and Zn have similar distributions at lower grades and are positively skewed. A significantly higher Zn grade population occurs above 6% (~0.75 on log scale). Note that Ag has a near bell-curve distribution indicating that it has a log-normal distribution. Figure 51a and c show the distribution of D ore-horizon Zn and Pb assays respectively in frequency histograms. Zn and Pb assays for the entire database are displayed on Figure 51b and d respectively. A difference in the distribution of Zn assays in D ore-horizon (Figure 51a) compared with the whole deposit (Figure 51b) occurs due to the presence of what may be interpreted as a higher grade population as indicated on the graph. This population has a median of approximately 12% Zn and is not prevalent throughout the whole of the deposit (compare Figures 51a and b). Pb assays do not show a trend of equivalent magnitude (compare Figures 51c and d). Normal probability plots for the whole dataset have been constructed using Ag (Figure 51e), Pb (Figure 51f), and Zn (Figure 51g) assay data. Log metal grade is plotted against the normal scores (number of matches that can be expected in a database of given size

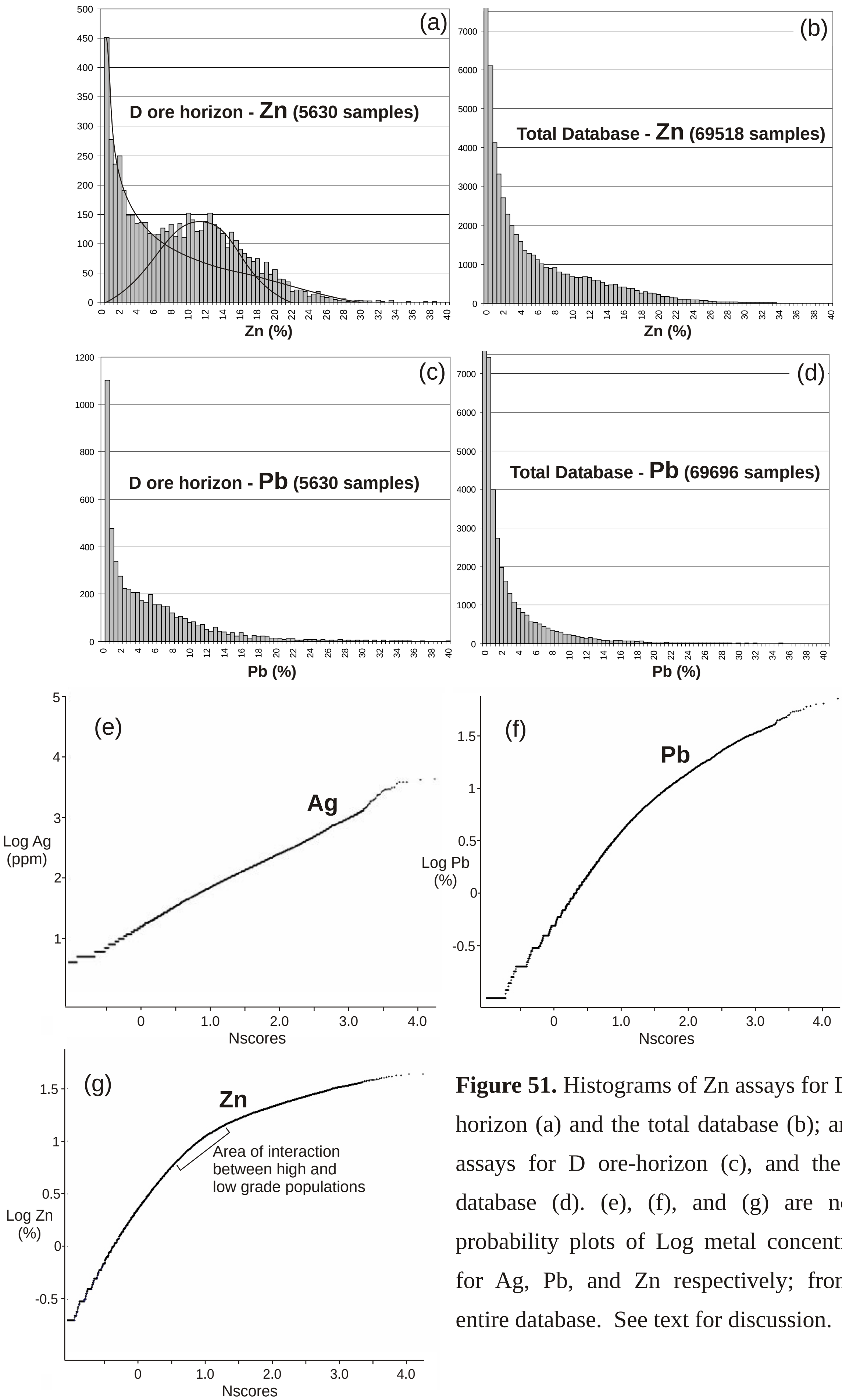

Figure 51. Histograms of Zn assays for D ore-horizon (a) and the total database (b); and Pb assays for D ore-horizon (c), and the total database (d). (e), (f), and (g) are normal probability plots of Log metal concentration for Ag, Pb, and Zn respectively; from the entire database. See text for discussion.

assuming a normal distribution and expressed in standard deviation units from the mean) of the dataset. Initial observations of the three diagrams are that Ag has an approximately straight line distribution (indicating a log-normal distribution as inferred from Figure 50b), Zn has two distinct trends, and Pb has an intermediate pattern between Ag and Zn. The two trends in Zn interact in the region of 4.5% Zn to 11% Zn which corresponds with the intersection of the hypothetical distributions drawn in Figure 51a. This observation supports the interpretation that remobilization or upgrading has been significant in developing the economic Zn ore-zones at George Fisher. The Pb distribution (Figure 51f) has a broad subtle curvature which doesn't allow for distinction of trends and Ag (Figure 51g) displays essentially a straight line trend from 10 to 1000ppm. This may reflect more advanced/efficient remobilization where Ag grades are homogenised and Pb grades again are at an intermediate position.

The variation in the population characteristics for Zn and Pb may be a factor of the differing structural controls on sites of deposition for the metals which ultimately affects the tenor of mineralization formed and therefore the possible grade populations.

5. Discussion

5.1 Relative timing of ore-types – integration with the structural history

Vein-hosted sphalerite and medium-grained galena breccia, the dominant Zn and Pb ore types, form shoots within and parallel the F_1 fold defined at George Fisher. Medium-grained galena breccia also forms a shoot parallel to F_2 folding in the northern part of the deposit. Less significant sphalerite breccia and coarse-grained galena breccia are also largely confined to the F_1 short-limb.

At hand-specimen to micro-scale, the vein-hosted Zn ores are interpreted to be only weakly deformed and are not pervasively recrystallized. Field relations described here indicate that some of the ore types post-date F_2 folding and that bedding-parallel migration of fluids along fracture networks has facilitated replacement of favourable layers. The combination of structurally controlled mine-scale distribution and general lack of deformation of the main sphalerite ore types is interpreted as indicating mineralization, in its present form occurred post-D_2 deformation, the main deformation episode in the region (Figure 52). This interpretation differs from those of Chapman (1999, 2004) and Valenta (1988, 1994) whereby the bulk of sphalerite mineralization was interpreted to occur pre-F_2 folding. Valenta (1988) inferred deformation of stratiform ores at all scales on the basis of:

- abrupt changes in the thickness of sulphide-rich layers,
- intense brecciation, and
- strong recrystallization of sulphides and gangue minerals.

However, changes in thickness of layers and the brecciated nature of ores are not exclusive observations of deformed ores as they can also occur where syntectonic ores are localized in angular jogs whose widths vary markedly. Strong recrystallization was not observed in the dominant sphalerite ore types at George Fisher. Valenta (1988) observed that recrystallized ore and gangue are spatially associated with abundant shear zones which occur within the Hilton Mine area. The bedded and finely banded nature of ores was interpreted to represent syngenetic to early diagenetic ore forming processes by Valenta (1988). Bedding parallelism of sulphides cannot be used as evidence for pre-

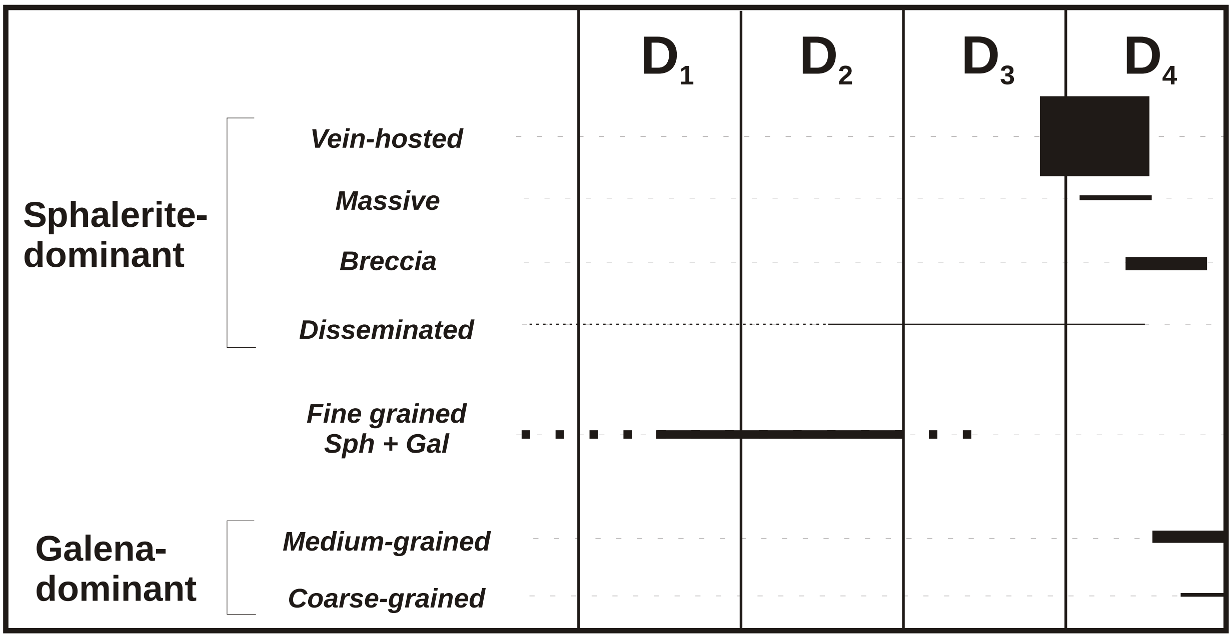

Figure 52. Relative structural timing of mineralization types at George Fisher. Thickness of line corresponds to relative abundance in studied drill-hole intersections across the deposit. Fine grained sphalerite mineralization is interpreted as pre-D_2 based upon the degree of deformation and recrystallization in this ore type which contrasts with all other textural varieties. Layer parallel disseminated sphalerite has also been interpreted as pre- to syn-D_2 through to D_4. The most abundant, and therefore most economically significant, ore types are situated in D_4 structures or earlier structures exploited during D_4. These include the main Zn ore: vein-hosted sphalerite, and main Pb ore: medium-grained galena breccia.

tectonic mineralization as Figures 4 to 15 demonstrate how syn- to post-tectonic mineralization can result in preferential replacement of layers and/or bedding parallel vein formation.

Chapman (1999, 2004) interprets the bulk of sphalerite mineralization to have occurred prior to regional deformation with some sphalerite emplaced as breccia during folding. Vein-hosted sphalerite mineralization was interpreted as the result of brecciation and infill/replacement after carbonate, quartz, and feldspar veining (Chapman, 1999, 2004). Vein-hosted mineralization in this study is a combination of this mechanism of syn-deformational vein-opening and infill of sphalerite, calcite, quartz, mica, and k-feldspar (Figures 10 - 13); as well as microbrecciation/fracturing of existing carbonate veins effecting replacement by sphalerite (Figures 4 - 9, 15). The major difference with the study by Chapman is in the timing of this mineralization relative to deformation episodes. Chapman (2004) interprets this dominant sphalerite ore-type to have formed prior to regional deformation as sphalerite+calcite+quartz+K-feldspar veins were observed with crenulated margins and intensification of cleavage along their margins (i.e. bedding). This phenomenon is addressed below.

Post-D_2 development of vein-hosted sphalerite mineralization is supported by observations of samples which indicate that sphalerite mineralization postdates D_3 fibrous micro-vein development. Chapman (2004) recognized brecciation and replacement of earlier-formed calcite-quartz-K-feldspar veins (Table 1) as a characteristic of vein-hosted sphalerite. Timing of the pre-ore bedding-parallel calcite-quartz veining is interpreted as dominantly syn-D_3 suggesting that mineralization occurred late to post-D_3. Crenulation of margins and S_2 intensification in the host rock at the margins to vein-hosted sphalerite layers was recognized by Chapman (1999, 2004) and interpreted as evidence for the vein predating D_2 deformation. Valenta (1988, 1989) interpreted relationships of veining and cleavage such that veins which occur sub-parallel to cleavage ($S_0||S_2$ in Chapman, 2004; refer to Part A, this study) and show irregular development of cleavage on vein margins, formed during ongoing cleavage development. An alternative interpretation of the phenomenon observed by Chapman is that prior to vein formation, S_2 was partitioned along weaker layers and bedding-parallel discontinuities (e.g. stylolitic contacts, shale horizons) in the F_1 short-limb zone where bedding is at a higher angle to the direction of shortening during D_2. A higher normal-stress will occur in this region of the F_1 short-limb where S_2 and S_0 are parallel. During D_3, bedding plane reactivation occurs (see Part A - Figure 25), intensifying S_2 adjacent to areas of enhanced slip and dilation is focussed into the higher strained layers and bedding planes (more-rich in graphitic material). Veining occurs with sub-horizontal fibres, consistent with D_3 strain. Note that Valenta (1988) also recognized a relationship between the incidence of F_3 folds and S_3 crenulations and bedding-parallel vein formation. Quartz+calcite+K-feldspar+sphalerite veins are inherently weaker than the host-rock due to the calcitic veins being weaker than the dolomitic siltstones and their localization on old bedding plane slip surfaces. This is shown in Figure 15 where F_3 folding preferentially occurs in the veined layer and not in the host siltstone. D_4 deformation dominantly causes bedding plane reactivation rather than folding and cleavage development due to the abundance of heterogeneities (e.g. F_2/S_2, F_3/S_3) already existing in the rock mass. Reactivation of bedding plane slip during D_4 causes brecciation of the D_3 vein thereby creating sites for fluid-rock interaction effecting replacement and 'new' vein development in areas conducive to dilation during

D_4. The result is a sphalerite-mineralized vein with bedding-parallel margins, replacive sphalerite and evidence for some open-space infill (euhedral quartz and carbonate crystals), relict calcite-quartz fibre vein material and intensification of the earlier S_2 cleavage in the host rocks immediately adjacent to the ore-vein. S_2 intensification is not considered characteristic of vein-hosted sphalerite samples observed in this study. The observed lack of significant deformation and recrystallization of sphalerite in vein-hosted sphalerite (as compared with other textural varieties discussed later in this paper) is consistent with the above interpretation.

Bedding reactivation during D_4 is therefore inferred to be responsible for the brecciation of pre-existing veins and creation of structurally enhanced permeability in the microveined layers thereby permitting the influx of sphalerite-bearing fluids. D_4 reactivation and resultant mineralization can be recognized in Part A – Figure 25 where sphalerite occurs at sites of brecciation of an earlier-formed vein during west-side-up slip on bedding/S_2. An intimate relationship between F_4 folds and the location of sphalerite deposition (Figure 11) also suggests a D_4 timing of vein-hosted sphalerite mineralization.

Pyrrhotite is a common accessory to vein-hosted sphalerite and occurs as intergranular inclusions. Pyrrhotite occurs late in the detailed paragenetic history during D_4 (Chapman, 1999) which is consistent with relative timing criteria discussed above.

Chapman (2004) also interpreted bitumens as intergrown with sphalerite in the vein-hosted mineralization. Vein-hosted mineralization was interpreted by Chapman (2004) to have occurred in at least semi-consolidated sediments or during brittle deformation prior to F_2 folding. The presence of bitumens in some of the vein-hosted sphalerite therefore does not preclude early-D_2 syntectonic development of this mineralization type. A key conclusion of Chapman (1999) was of the localization of celsian-hyalophane-K-feldspar-carbonate veining in the vicinity of fluid influx which preceded and structurally prepared the sedimentary sequence for precipitation of high-grade mineralization. The fluid influx region is interpreted to be the F_1 fold short-limb in this study which has preferentially focussed alteration, veining, and overall metal content in the deposit.

Chapman (1999, under review) recognized two chemically and isotopically distinct fluid-types at George Fisher interpreted to be responsible for diagenetic Zn-P-Ag and syntectonic Cu mineralization, respectively. The spatial coincidence of early hydrothermal calcitic alteration with Zn-Pb-Ag mineralization implies a genetic relationship (Chapman, 1999) whereas both calcitic alteration and Zn-Pb-Ag mineralization are spatially coincident with the F_1 fold. An alternative explanation may be that diagenetic fluids were focussed by the onset of F_1 folding and caused carbonate alteration that has been overprinted by veining and the ore-bearing fluid later in the deformation history possibly from D_2 onwards. This is discussed further in Part F.

Vein-hosted sphalerite is interpreted to be the result of fluid flow and metasomatism late in the structural history of the host rocks at George Fisher. Mineralization occurs in sites of structurally enhanced permeability where older structural features are reactivated and/or brecciated during late D_3 to D_4. Vein-hosted sphalerite occurs dominantly as replacement of older vein-fill material (quartz+carbonate) although evidence exists for infill-type veining on the microscale.

Galena occurs paragenetically later than sphalerite in each textural variety of sulphide ore at George Fisher (Chapman, 1999). Both the main sphalerite and galena mineralization types are interpreted to be located in sites that formed or were exploited during D_4. The separation of syn-D_4 galena and sphalerite into separate paragenetic sites implies two distinct phases of mineralization during D_4, both however, were derived from the same fluid reservoir, as discussed in Part E. Vein-hosted sphalerite described here, occurs as bedding-parallel replacement and micro-brecciation of veined layers. This is interpreted to have occurred during early D_4 when bedding reactivation dominated. Later in D_4, minor F_4 fold development occurred and bedding reactivation proceeds to the extent that F_2 – F_4 folds are brecciated. Galena mineralization occurs during this later phase of D_4 deformation and in the waning stages of D_4 where D_4 folds themselves are brecciated (e.g. Figure 40).

The distribution of galena mineralization at the mine scale correlates strongly with that of sphalerite (Part B – Figures 14a and b, and 17a and b). The relative timing of galena is less ambiguous at the exposure to hand-specimen scale than sphalerite ore types as the galena-breccias are more intimately associated with meso-scale to exposure-scale folding and a timing of syn- to post-D_4 is inferred. Galena microstructures indicate that it has recrystallized probably during late D_4 deformation, but does not generally preserve a foliation. Recrystallization may still preserve grain-shape preferred orientation (Clark and Kelly, 1973) and the absence of a pervasive preferred orientation is consistent with post-D_2 galena mineralization. Galena mineralization is focussed into sites of brecciation, commonly at the intersection of overprinting structural features.

Chapman (2004) interpreted galena mineralization as having a probable D_4 timing. The findings of this study confirm that the bulk of galena is situated in D_4 structural positions or in sites which focussed dilation during D_4.

The coincident sphalerite and galena distribution on the mine scale (Part B – Figures 14a and b, and 17a and b) suggests that both sulphide species were:

1. introduced at the same time, and/or
2. introduced via the same process, and/or
3. focussed by the same kinematic controls.

Intuitively, if the galena and sphalerite have the same distribution at the mine-scale then a similar timing might be expected. However, the first option is discounted based upon the observation that galena occurs paragenetically later than sphalerite (Chapman, 1999, 2004) and the disparity in textural styles between galena (breccia) and sphalerite (bedding-parallel vein/replacement) suggests that the second option does not account for deposition of Pb and Zn in contrasting structural sites at the exposure to hand-specimen scale. Part B – Figures 23 and 24 indicate how the kinematics during early D_4 may have caused dilation in the F_1 short-limb through slip on bedding. Later in D_4, further dilation was associated with minor fold development and brecciation of F_2/F_3 folds. This would account for the difference in sphalerite and galena mineralization styles, bedding-parallel (early D_4) sphalerite vs breccia-hosted, locally bedding-discordant (later D_4) galena and explains the observed steep, south-pitching and gentle, north-pitching ore shoot geometries. The kinematic regime during D_4 can therefore explain both the contrasting textural/structural characteristics of Pb and Zn mineralization while maintaining a strong correlation between the mine-scale distribution of galena and sphalerite mineralization.

Galena mineralization is interpreted by Chapman as the product of highly efficient remobilization, given that negligible galena can be interpreted as pretectonic (Chapman, 1999, 2004 – Table 5). The mine-scale correlation between sphalerite ore thickness and galena ore thickness, illustrated in Part B – Figures 17 a and b, is difficult to explain if sphalerite is dominantly pretectonic (diagenetic, ~1650Ma) and galena syntectonic (D_4, ~1500Ma) unless the remobilization of galena, although highly advanced/efficient, resulted in only metre-scale movement of Pb metal. Even still, the galena distribution would strongly correlate with the F_1 short-limb (Part B - Figure 17b). The interpretation of the bulk of sphalerite mineralization occurring in Post-D_3/D_4 sites preceding galena brecciation yet controlled by the same deposit scale architecture is more consistent with the observed distribution of metal at the deposit.

Within the limits of current development and drilling, the Hilton and George Fisher deposits lack a discordant feeder system associated with stratiform mineralization as recognized by both Valenta (1988, 1994) and Chapman (1999, 2004). At George Fisher, there is no appreciable change in sedimentary facies associated with higher or lower grade regions of the deposit and the distribution of metal is not associated with any fault (e.g. growth/synsedimentary fault or later) which occurs within the mine environs. While fluid flow in through unconsolidated sedimentary basins may negate the requirement for a feeder structure, Chapman (1999, 2004) interprets mineralization as occurring post-compaction (Table 1) and possibly during brittle deformation prior to regional folding.

Syndiagenetic models of mineralization are unable to explain why the deposits are situated at their current RL or northing within the Urquhart Shales. The syn-D_4 mineralization of the F_1 short-limb proposed in this study delineates a specific target consisting of overprinting structures within the Urquhart Shale which may be reproduced elsewhere in the Mt Isa valley and can be used as a prospectivity tool in conjunction with conventional exploration methods.

5.2 Pre-/early-D_2 mineralization at George Fisher?: Remobilization vs syntectonic orebody formation.

Features which indicate that small-scale mechanical remobilization has occurred are observed at George Fisher and include thickening of mineralization in fold hinges (cf. McDonald, 1970) and piercement structures (cf. Maiden et al., 1986; Marshall and Gilligan, 1989). At the George Fisher deposit, these structures are interpreted to affect metal distribution in the range of <2m and, if the material is mechanically remobilized, it remains texturally indistinct from the layer parallel mineralization from which it is sourced. The common plunge of mineralized shoots and folds and localization of thicker, high-grade mineralization in the F_1 short-limb imply redistribution of metal over greater distances and requires alternative explanation.

More strongly deformed fine-grained sphalerite+galena breccia mineralization with a mine-scale distribution unrelated to those folds that host the bulk of ore grade sulphide has been recognized and may represent a pre-deformational sulphide occurrence. The fine-grained sphalerite+galena mineralization type occurs as bedding-parallel layers generally in the order of 5-10cm thick. Folding can be preserved in the sulphide layers and microstructural observations of this ore-type indicate that significant recrystallization has occurred in response to deformation of the sulphides. Relict grains exhibit significant deformation including bent twins and rare deformation twins (Figure 28) and have recrystallized along their margins to a fine grained mosaic.

The thickness of fine-grained sphalerite+galena breccia is negligible to absent in the core of the deposit but increases toward the periphery. This relationship is the inverse of those ore-types containing economically significant quantities of metal. The relationship between fine-grained sphalerite+galena (Figure 30) and medium-grained galena (Figure 43) suggests that depletion of fine-grained galena is matched by increased thickness of medium-grained galena. An explanation for this may be that stratiform sphalerite+galena mineralization was deformed during D_2, grain-size reduction facilitating increase access and surface area for Zn and Pb to be removed from the rock mass by fluid-assisted remobilization, and migration of these fluids to sites of low stress with final deposition in areas of dilatancy during D_4. The dominant medium-grained galena breccia and vein-hosted sphalerite mineralization could therefore be interpreted as the product of remobilization from a proto-mineralization accumulation. Alternatively, deformation may be consistent with partitioning of strain during reactivation of bedding during D_4 and the fine-grained mineralization may therefore be of similar age to the other main ore types, however this has not been established during the course of this study. Chapman (1999, 2004) interpret the fine-grained galena+sphalerite breccia as being the same age as other galena mineralization styles but more deformed due to partitioning of D_4 strain into these layers. In this case, all mineralization bar some minor disseminated sphalerite can be interpreted as forming post-D_2 as determined by this study.

Pb isotopic age determinations are inconclusive for this mineralization style. The interpreted Pb isotope model age of 1653Ma (approx. age of host rocks) for all galena ore types (Chapman, 1999) using the methodology of Sun et al. (1994) is ambiguous as the same isotope data yields an age of approximately 1500Ma (approx. age of D_4) using the Cumming and Richards (1975) methodology (Figure 53). Sun et al. (1994) and Carr et al. (1996) have modified the single-stage model of Cumming and Richards (1975) using the HYC deposit (McArthur River) as a control point (Figure 53). This is based on the inference that the deposit is syngenetic in origin and therefore the same age as the host rocks (Hinman et al., 1994; Hinman, 1995). However, other interpretations of the timing of mineralization at this deposit include diagenetic (Williams, 1978) and formation late in the deformation history (Perkins and Bell, 1998). Aside from timing criteria, the consistent isotopic signature indicates a single source for the Pb in galena mineralization styles at George Fisher (Chapman, 1999) and this is supported by additional evidence in Part E.

It is unlikely a pre-deformational sulphide Zn+Pb accumulation, if dominated by the now fine-grained breccia, was of economic concentration as areas dominated by the fine-grained stratiform ore are found to be sub-economic (compare Figure 28 with Part B – Figures 11, 12, 13). This contrasts with interpretations by Smith (2000) where synsedimentary and diagenetic sulphides were considered to have formed in concentrations consistent with the present metal distribution at the Mt Isa Pb-Zn deposit. Other proposed models of syngenetic mineralization (Russell et al., 1981; Sawkins et al., 1984) also describe primary economic concentrations of sulphides. Chapman (1999) also interpreted the distribution of metal at George Fisher to represent the primary fluid flux at

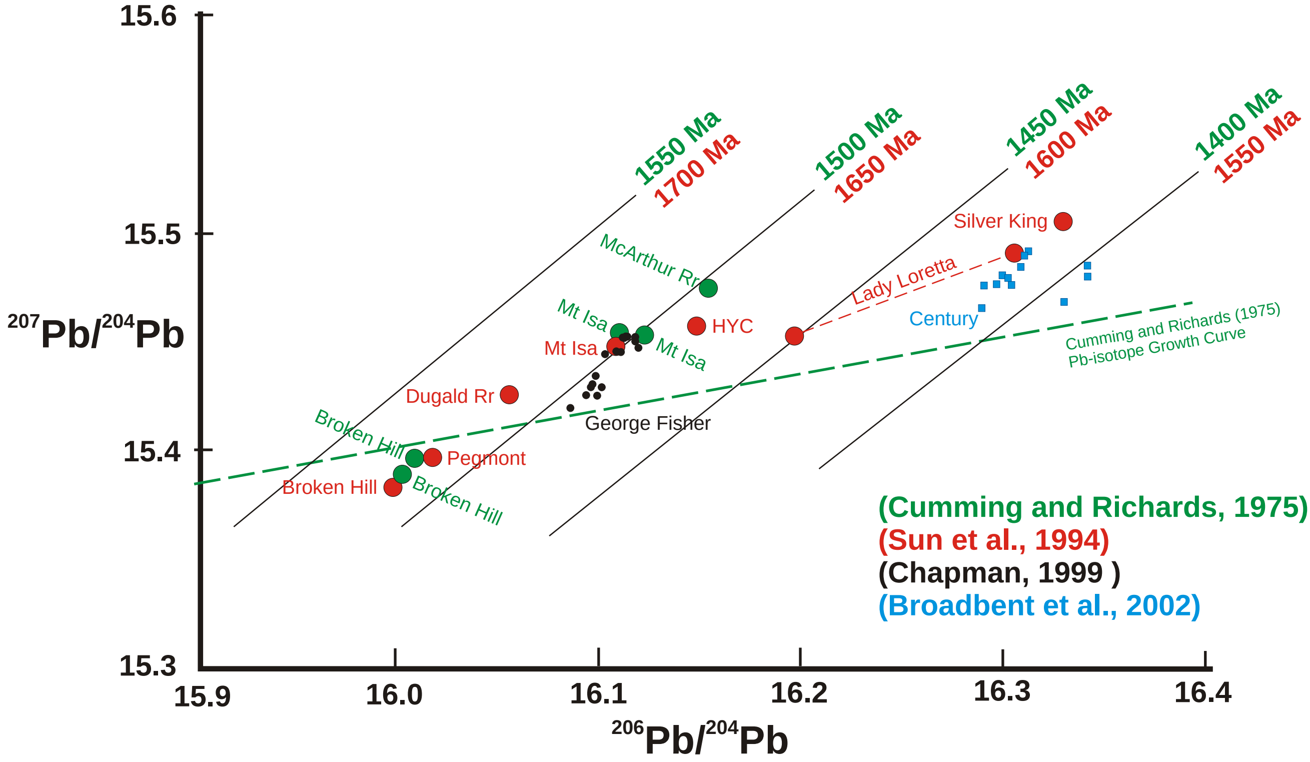

Figure 53. 207Pb/204Pb vs 206Pb/204Pb diagram showing the single-stage Pb evolution model ages (green) of Cumming and Richards (1975) and the same isochrons calibrated using zircon ages of tuffaceous horions from the HYC deposit (red) by Sun et al. (1994). The major base metal deposits of the Mt Isa and McArthur Inliers are also shown. Note that the Mt Isa deposit and data points from Chapman (1999) for the George Fisher deposit can be interpreted as either~1500Ma or ~1650Ma in the respective models.

the deposit and that remobilization has not been significant in the concentration of metal to ore grades. If mineralization was introduced during D_1 into the F_1 short-limb, ore-types would preserve strain associated with the main phase D_2 deformation (refer to Figure 9). Given that the bulk of mineralization types at George Fisher are interpreted to be at most weakly deformed, the mine-scale relationship of metal distribution to structural domains as observed in the ore-shoot geometries requires a large proportion of the metal in the deposit to be remobilized or introduced late in the structural history.

Analysis of Zn grade data at George Fisher has shown there are possibly two populations within the available data. A second population appears to be related to economic ore-horizons and this observation supports the interpretation that remobilization or upgrading has been significant in developing the economic Zn ore-zones at George Fisher. This differs from the interpretation of data from the Mt Isa Mine where remobilization is discounted based on the lack of a distinct second population of grades (Davis, 2004). Pb and Ag grades at George Fisher have a more uniform distribution either suggesting efficient remobilization or a single episode of galena mineralization.

6. Conclusions

Analysis of micro- and meso-scale textures and deformation features, exposure-scale relationships, and mine-scale distribution of each of the main ore types has enabled timing relative to one another and deformation.

Observations of microstructure in the dominant vein-hosted sphalerite and medium-grained galena breccia indicate that the ore is not significantly deformed.

Recrystallization is not pervasive in the dominant Zn mineralization types suggesting that the textures observed represent only minor modification of the original ore texture. Vein-hosted mineralization is interpreted as concomitant brecciation and replacement of pre-existing bedding parallel carbonate-quartz veins and syntectonic bedding-parallel vein formation. Medium and coarse-galena breccia occurs as replacement and brecciation of the paragenetically earlier vein hosted sphalerite.

At the exposure-scale, relative timing of bedding-parallel vein-hosted sphalerite is ambiguous; however observations of medium and coarse-grained galena breccia indicate that this mineralization occurs at sites where successive fold generations overprint one another effecting brecciation. The distribution of medium-grained galena is controlled by the location of earlier folding (F_2 and F_3) which have brecciated during D_4 due to unfolding and refolding processes.

Mine-scale distribution of the major sphalerite and galena ore-types correlate with structural trends and domains established in Part A. The F_1 short-limb is identified as the locus for brecciation and fluid flow during D_4 deformation and is preferentially mineralized forming what is now recognized as a steep, south-pitching shoot in longitudinal projections. While this subtle flexure in bedding has acted as the dominant heterogeneity for focussing sphalerite mineralization, galena mineralization occurs as brecciation in pre-existing fold corridors (F_2) modified during D_3. The deformed, fine-grained sphalerite+galena breccia is not spatially or genetically related to the F_1 short-limb zone and may represent deformed proto-mineralization and the source for metal deposited in later structural sites.

Analysis of assay data suggests that more than one population of Zn grades exists and that a higher-grade population is unique to the economic ore-horizons. This supports the interpretation of remobilization and upgrading of mineralization. However, this qualitative observation does not discriminate between upgrading of a pre-F_2 or post-F_2 sulphide accumulation during D_4.

The dominant ore types at George Fisher are interpreted to post-date the main phase of deformation (D_2) and are situated in sites consistent with emplacement during D_4. Remnants of a pre-deformational sulphide occurrence may have been identified, but it is unlikely that Pb and Zn concentrations were of ore-grade prior to remobilization, upgrading, and thickening of ore domains.

References

Atkinson, B.K., 1976. Deformation mechanism maps for polycrystalline galena: Earth and Planetary Science Letters, v. 29, p. 210-218.

Barber, D.J. and Wenk, H.-R., 1979. Deformation twinning in calcite, dolomite, and other rhombohedral carbonates: Physics and Chemistry of Minerals, v. 5, p. 141-165.

Blanchard, R. and Hall, G., 1942. Mt Isa ore deposition: Economic Geology, v. 32, p. 1042-1057.

Brebrick, R.F. and Scanlon, W.W., 1957. Chemical etches and etch pit patterns on PbS crystals: The Journal of Chemical Physics, v. 27, p. 607-608.

Carr, G.R., Sun, S-s., Page, R.W., and Hinman, M. 1996. Recent developments in the use of lead isotope model ages in Proterozoic terrains. In: Baker, T., Rotherham, J., Mark, G., and Williams, P.J. (eds), New Developments in Metallogenic research: The McArthur, Mt Isa, Cloncurry Minerals Province, p. 33-35. James Cook University Economic Geology Research Unit Contribution 55.

Chapman, L.H., 1999. Geology and genesis of the George Fisher Zn-Pb-Ag deposit, Mount Isa, Australia. (Unpublished PhD thesis – James Cook University, Townsville).

Chapman, L.H., 2004. Geology and mineralization styles of the George Fisher Zn-Pb-Ag deposit, Mount Isa, Australia: Economic Geology, v. 99, p. 233-255.

Clark, B.R. and Kelly, W.C., 1973. Sulfide deformation studies: I. Experimental deformation of Pyrrhotite and Sphalerite to 2,000 bars and 500°C: Economic Geology, v. 68, p. 332-352.

Clark, B.R. and Kelly, W.C., 1976. Experimental deformation of common sulphide minerals. In: R.G.J. Strens (ed), The physics and chemistry of minerals and rocks. p. 51-69.

Cooke, D.R., Bull, S.W., Large, R.R., and McGoldrick, P.J., 2000. The importance of oxidized brines for the formation of Australian proterozoic stratiform sediment-hosted Pb-Zn (Sedex) deposits: Economic Geology, v. 95, p. 1-18.

Cox, S.F., 1987. Flow mechanisms in sulphide minerals. In: B. Marshall and L.B. Gilligan (Eds), Mechanical and Chemical (Re)mobilization of Metalliferous Mineralization: Ore Geology Reviews, v. 2, p. 133-171.

Cumming, G.L. and Richards, J.R., 1975. Ore lead isotope ratios in a continuously changing Earth: Earth and Planetary Science Letters, v. 28, p. 155-171.

Davis, T.P., 2004. Mine-scale structural controls on the Mount Isa Zn-Pb-Ag and Cu orebodies: Economic Geology, v. 99, p. 543-559.

Durney, D.W. and Ramsay, J.G., 1973. Incremental strains measured by syntectonic crystal growths. In: De Jong and Scholten (eds), Gravity and tectonics. p. 67-96.

Finlow-Bates, T., 1979. Cyclicity in the lead-zinc-silver bearing sediments at Mount Isa Mine, Queensland, Australia, and rates of sulfide accumulation: Economic Geology, v. 74, p. 1408-1419.

Gilligan, L.B. and Marshall, B., 1987. Textural evidence for remobilization in metamorphic environments. In: B. Marshall and L.B. Gilligan (eds), Mechanical and chemical (Re)mobilization of metalliferous mineralization: Ore Geology Reviews, v. 2, p. 205-230.

Hinman, M.C., 1995. Base metal mineralization at McArthur River: Structure and kinematics of the HYC-Cooley zone at McArthur River. Australian Geological Survey Organization (AGSO) Record 1995/5.

Hinman, M.C., Wall, V.J., and Heinrich, C., 1994. The interplay between sedimentation, deformation and mineralization at the McArthur Pb-Zn(-Cu) deposit. Geological Society of Australia. Abstract No. 37, p. 176-177.

Lusk, J., Calder, B.O.E., and Freeman, T.E., 2002. Temperatures from triple-junction angles in sulfides: American Mineralogist, v. 87, p. 1390-1400.

Maiden, K.J., Chimimba, L.R., and Smalley, T.J., 1986. Cuspate ore-wall rpck interfaces, piercement structures, and the localization of some sulfide ores in deformed sulfide deposits: Economic Geology, v. 81, p. 1464-1472.

Marshall, B. and Gilligan, L.B., 1987. An introduction to remobilization: Information from ore-body geometry and experimental considerations. In: B. Marshall and L.B. Gilligan (eds), Mechanical and Chemical (Re)mobilization of metalliferous Mineralization: Ore Geology Reviews, v. 2, p. 87-131.

Marshall, B. and Gilligan, L.B., 1989. Durchbewegung structure, piercement cusps, and piercement veins in massive sulfide deposits: Formation and interpretation: Economic Geology, v. 84, p. 2311-2319.

Mathias, B.V., G.J. Clark, D. Morris, and R.E. Russell., 1971. The Hilton deposit – stratiform silver-lead-zinc mineralization of the Mount Isa type. In: Metallogenic Provinces and mineral deposition in the southwestern Pacific. Bureau of Mineral Resources Bulletin 141, p. 33-58.

McDonald, J.A., 1970. Some effects of deformation on sulfide-rich layers in lead-zinc orebodies, Mount Isa, Queensland: Economic Geology, v. 65, p. 273-298.

Myers, R., Ceremuga, C., Clark, D., McSkimming, D., Price, S., Tuesley, M., and Wilkinson, D. 1996. Mount Isa lead-zinc mineralization: What controversy? In: Baker, T., Rotherham, J., Mark, G., and Williams, P.J. (eds), New Developments in Metallogenic research: The McArthur, Mt Isa, Cloncurry Minerals Province, p. 85-89. James Cook University Economic Geology Research Unit Contribution 55.

Perkins, W.G., 1997. Mount Isa lead-zinc orebodies: Replacement lodes in a zoned syndeformational copper-lead-zinc system?: Ore Geology Reviews, v. 12, p. 61-110.

Perkins, W.G. and Bell, T.H., 1998. Stratiform replacement Lead-Zinc deposits: A comparison between Mount Isa, Hilton, and McArthur River: Economic Geology, v. 93, p. 1190-1212.

Ramsay, J.G. and Huber, M.I., 1987. The techniques of Modern Structural Geology, Volume 2: Folds and Fractures, 700p, Academic Press.

Russell, M.J., Solomon, M., and Walshe, J.C., 1981. The genesis of sediment-hosted, exhalative zinc and lead deposits: Mineralium Deposita, v. 16, p. 113-127.

Sawkins, F.J., 1984. Ore genesis by episodic dewatering of sedimentary basins: Application to giant Proterozoic lead-zinc deposits: Geology, v. 12, p. 451-454.

Siemes, H., 1977. Recovery and recrystallization of deformed galena: Tectonophysics, v. 39, p. 171-189.

Smith, W.D., 2000. Genesis of the Mount Isa base metal deposit: Australasian Institute of Mining and Metallurgy Proceedings, v. 305, p. 45-56.

Stanton, R.L. and Gorman, H., 1968. A phenomenological study of grain boundary migration in some common sulfides: Economic Geology, v. 63, p. 907-923.

Stanton, R.L. and Gorman-Willey, H., 1971. Recrystallization softening and hardening in sphalerite and galena: Economic Geology, v. 66, p. 1232-1238.

Stanton, R.L. and Gorman-Willey, H., 1972. Experiments on a specimen of galena from Coeur d'Alene, Idaho: Economic Geology, v. 67, p. 776-788.

Sun, S-s., Page, R.W., and Carr, G.R., 1994. Lead-isotope-based stratigraphic correlations and ages of Proterozoic sediment-hosted Pb-Zn deposits in the Mount Isa Inlier. Australian Geological Survey Organization (AGSO) Research Newsletter, 20, p. 1-2.

Valenta, R.K., 1988. Deformation, fluid flow and mineralization in the Hilton area, Mt Isa, Australia. (Unpublished PhD thesis – Monash University, Melbourne).

Valenta, R.K., 1989. Vein geometry in the Hilton area, Mount Isa, Queensland: implications for fluid behaviour during deformation: Tectonophysics, v. 158, p. 191-207.

Valenta, R.K., 1994. Deformation in the host rocks and stratiform mineralization in the Hilton Mine area, Mt Isa: Australian Journal of Earth Sciences, v. 93, p. 1119-1131.

Wenk, H.-R., 1985. Carbonates. In: H.-R. Wenk (ed), Preferred orientation in deformed metals and rocks: An introduction to modern texture analysis, p. 361-384.

Williams, N., 1978. Studies of the base metal sulfide deposits at McArthur River, Northern Territory, Australia: I. The Cooley and Ridge Deposits: Economic Geology, v. 73, p. 1005-1035.

PART E

Rhenium-Osmium isotopic analysis of mineralization at the George Fisher deposit, Northwest Queensland, Australia: Implications for the absolute age of mineralization and the source of metals.

Abstract

Analysis of the Re-Os isotopic signature of Pb and Zn sulfides and barren siltstones at the George Fisher Zn-Pb-Ag deposit indicates distinct Re/Os, $^{187}Re/^{188}Os$, $^{187}Os/^{188}Os$, and γOs isotopic ratios for sulfides compared to the barren host-rock. Sphalerite and Galena samples are isochronous, indicating a common source for the two metals at George Fisher. Barren siltstones are also broadly isochronous suggesting that the mineralizing fluids have affected the original Re-Os signature of the host-rocks. Eleven mineralized samples define an isochron and an age of 1423±130Ma has been calculated. This estimate for the age of mineralization is within error of the D_2 (1540Ma) and D_4 (1510Ma) deformation events of the Isan Orogeny but is significantly younger than the age of formation of host-rocks at George Fisher (1655Ma). An interpreted period of post-orogenic cooling (1392±85Ma/1482±52Ma) also correlates with the estimated age of mineralization that might alternatively record closure of the Re-Os system. A mantle source for the Pb and Zn is implied by the initial $^{187}Os/^{188}Os$ ratio of 0.077±0.071. This differs from previous models whereby metals have been leached from within the sedimentary basin. Proximity to regional faults which tap crustal scale shear-zones may therefore be more significant to exploration for Proterozoic stratiform base metal deposits

in the Mt Isa Inlier than the type or proportion of basin fill, although host-rock controls on mineralization exist. The Re-Os isotopic method has not distinguished between individual deformation events which may have been integral to ore formation but one interpretation of the obtained age suggests that mineralization postdates host-rock formation by >100My.

1. Introduction

Rhenium (^{187}Re) and Osmium (^{188}Os) are transition metals which occur within Groups VII (manganese family) and VIII (platinum family) of the periodic table, respectively. Both metals are siderophile and were preferentially concentrated into the Earth's Fe-metal-rich core during early differentiation and subsequently, the silicate mantle and crust are depleted in these elements compared to meteorites (Allegre and Luck, 1980). Morgan and Lovering (1967) showed that there are contrasting abundances of Re and Os in igneous rocks representative of the mantle and upper crust. Re and Os abundances for different rock types include:

Rock Type	Re (ppb)	Os (ppb)	Reference
Terrigenous sediments	0.43	46	Esser and Turekian (1993)
Quartz sandstone	0.03	0.06	Lovering and Morgan (1964)
Shale	0.05	0.45	Lovering and Morgan (1964)
Granite	0.56	0.06	Morgan and Lovering (1967)
Peridotite	0.05	5.9	Morgan and Lovering (1967)
Iron meteorite	1,470	19,000	Luck and Allegre (1983)

In a study by Hauri and Hart (1993), Re concentration in the crust was estimated at 10-100 times higher and Os concentration 10-10,000 times lower than that of mantle peridotites. Fractionation of platinum-group metals occurs in magma due to alteration, partial melting, and crystal fractionation (Barnes et al., 1985). The low solubility of Os in silicate magma (Barnes et al., 1985) means that Os is retained in the mantle, whereas Re is mildly incompatible during mantle melting and is enriched relative to Os, in the crust (Morgan et al., 1981; Shirey, 1991; Esser and Turekian, 1993).

Beta decay (loss of an electron but no change in atomic mass) of ^{187}Re to ^{187}Os occurs at a decay rate of 1.666 x 10^{-11} yr^{-1} (Smoliar et al., 1996) and the half-life of ^{187}Re is 42.3 billion years (Walker and Morgan, 1989). All ^{187}Os is radiogenic and given that the decay rate is known, the abundance of this isotope can therefore be used to derive the absolute age of the host minerals. Enrichment of ^{187}Os in the crust and ^{188}Os in the mantle means that the $^{187}Os/^{188}Os$ (initial) ratio can be interpreted as reflecting a dominant mantle source of platinum group elements if low (~0.1) and dominant crustal source of platinum group elements if high (~1-2). Note the high Os abundance reported for both terrigenous sediments and iron meteorites above. ^{187}Os is enriched in the crustal sample whereas ^{188}Os is significantly enriched in the meteorite sample ($^{187}Os/^{188}Os$ = 0.1215; Luck and Allegre, 1983). Large fractionation of Re and Os in the crust does not cause a measurable change in the Re/Os ratio of the mantle with time due to the significant abundance of Re and Os in the mantle relative to the crust (Allegre and Luck, 1980).

A parameter used in this study, γOs, indicates the percentage difference between the analyzed sample and the mantle at any specific time. The parameter has a high, positive value (~3000-5000) where the Osmium in the sample is radiogenic indicating a crustal source and low to negative where unradiogenic and related to a mantle fluid source (pers. comm., R. Keays, 2003). The γOs parameter is analogous to the ε_{Nd} parameter in the samarium-neodymium isotopic system.

As Re and Os are both siderophile and chalcophile they are preferentially concentrated into sulphides relative to silicate minerals (Shirey, 1991). The possibility therefore exists to date sulphide ores directly and compare both the absolute age and source of Os between ores and their silicate hosts. This is potentially useful where there is ambiguity concerning the timing of mineralization relative to the formation and deformation of the host-rocks as is the case with studies of sediment-hosted Zn-Pb-Ag deposits of the Mt Isa Inlier (compare Russell et al., 1981; Chapman, 1999, 2004; Perkins, 1997; Davis, 2004)

The Re-Os decay system has been used to analyze a range of deposit and commodity types including but not limited to:

- Molybdenum deposits (Stein et al., 1997)
- Porphyry copper-molybdenum deposits (McCandless and Ruiz, 1993; Freydier et al., 1997; Stein and Bingen, 2002).
- Orogenic gold (Arne et al., 2001)
- Epithermal silver (Levresse et al., 2002)
- Nickel sulfides associated with komatiites (Foster et al., 1996; Lesher et al., 2001) and the Sudbury igneous complex (Lightfoot et al., 2001)

- Pb-Zn sulfides from massive deposits of the Iberian Pyrite belt (Mathur et al., 1999), a Kuroko style deposit (Terakado, 2001), and volcanogenic massive sulfide (Hou et al., 2003).

The aim of this study is to determine the Re-Os isotopic characteristics of George Fisher Zn-Pb-Ag mineralization in order to constrain the absolute age and source of metals in the orebodies. This information is pertinent to the regional exploration for further sediment-hosted Zn-Pb-Ag deposits in the Western Fold Belt as structures of specific ages may be more prospective than others and proximity to potential source rocks my also increase prospectivity. The mineralization styles selected for analysis are the vein-hosted sphalerite and the medium-grained galena±sphalerite breccia; the main sources for Zn and Pb, respectively, at the George Fisher deposit.

2. Methodology

Representative samples of both vein-hosted sphalerite and galena±sphalerite breccia were selected for analysis as both mineral separates and whole-rock material. The samples are hand-specimens from the George Fisher workings or pieces of diamond-core. The following is a summary of the samples analyzed in this study.

Sample type	**Number**
Galena separate	2
Sphalerite separate	3
Galena-dominant whole-rock	3
Sphalerite-dominant whole-rock	5
Barren host siltstones	3
Total	**16**

Galena-dominant samples chosen for analysis include very fine-grained, medium-grained, and coarse-grained breccias (Figure1a-c, as described in Part D). Medium-grained breccia, the main ore of Pb at George Fisher, is the dominant galena-rich sample analyzed. Sphalerite dominant samples analyzed are bedding parallel sphalerite±pyrite±pyrrhotite bands (Figure 1d-f) described as vein-hosted sphalerite in Part D. Barren siltstone samples (Figure 1g and h) were obtained from stratigraphy approximately 200m into the footwall of the main body of mineralization at George Fisher. Dark and light beds reflecting variation in carbonaceous matter in a siltstone sample (Figure 1h) were analyzed individually.

Siltstone bands, barren clasts, and gangue sulfides (e.g. massive pyrite bands) were cut from whole-rock specimens of the mineralization. Mineral separates were obtained from the same samples as the whole-rock specimens.

The following is an abbreviated description of the process employed at the Rhenium-Osmium Laboratory at Monash University (Melbourne, Australia). Samples were crushed and milled using a ceramic jaw crusher and agate mill until a 200µm particle-size was achieved. Rhenium pre-determination of the samples was undertaken so as to optimize the Rhenium and Osmium spike used in the analysis. Mineral separation of sphalerite and galena from the gangue assemblage was accomplished using a Frantz separator as well as heavy mineral separation using tetrabromoethane. The sample, ^{185}Re and ^{190}Os spikes are digested in HCl in a carius tube and frozen to prevent reaction and volatilisation. The mixture is kept frozen while the open end of the carius tube is sealed using an oxy-LPG torch. Digestion of the sample occurs over 2 days heated at 200°C.

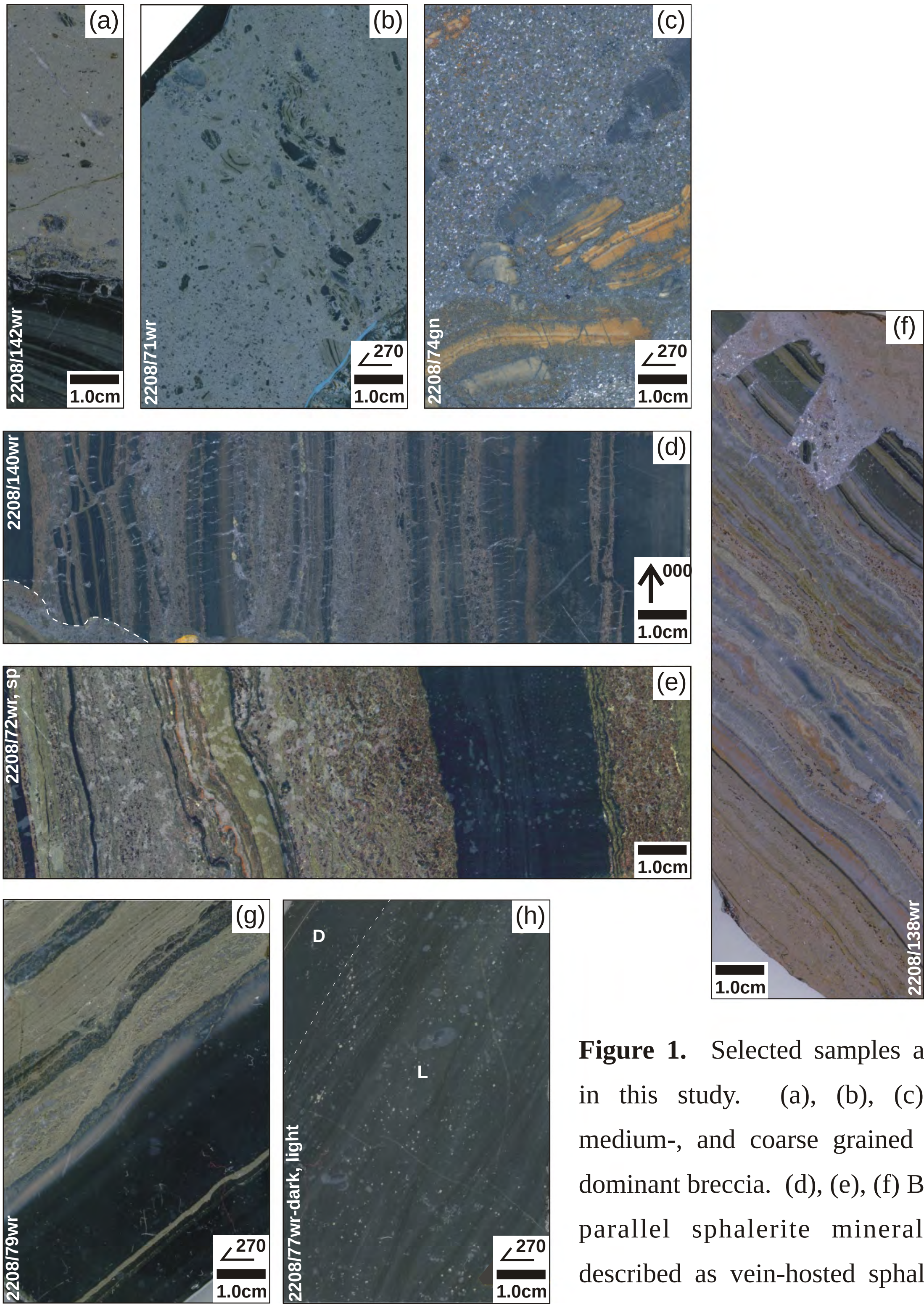

Figure 1. Selected samples analysed in this study. (a), (b), (c) Fine-, medium-, and coarse grained galena-dominant breccia. (d), (e), (f) Bedding-parallel sphalerite mineralization described as vein-hosted sphalerite in Part D. Medium-grained galena breccia cross-cuts bedding and sphalerite mineralization in the bottom left hand corner of (d). The sample illustrated in (e) is devoid of galena mineralization whereas medium-grained galena breccia occurs in apparent boudin necks formed by bedding-parallel extension in (f). (g) barren pyritic siltstone (only siltstone portion analysed) and (h) siltstone where lighter, ‘L’ and darker, ‘D’, layers were analysed individually (results in Table 1).

The homogenized sample is retrieved from the carius tube and divided in two subsequent to solvent extraction using CCl_4. The sample for Os analysis is dried and HBr is added during microdistillization. Os remains after evaporation of the HBr solution. The sample for Re analysis is digested in HNO_3 acid and Re is recovered through primary and secondary resin columns. Re and Os samples are electroplated onto platinum filaments for analysis on the 7-collector Finnigan MAT 262 Negative Thermal Ionisation Mass Spectrometer (NTIMS) at La Trobe University (Melbourne, Australia). The filament is inserted into the ion source of the mass spectrometer. A current is passed through the filament, which causes the Osmium isotopes in the sample to ionize. The ions are accelerated through a magnetic field, resulting in separation of the ions by mass. Detection limits for Osmium using the NTIMS process can be less than 10^{-14}g (Creaser et al., 1991). For all age calculations, a ^{187}Re decay constant of $1.666 \times 10^{-11} yr^{-1}$ was used (Smolar et al., 1996).

3. Results

Sphalerite and Galena from the George Fisher deposit contain an average of 0.77ppb Re and 0.13ppb Os and the barren siltstones contain 1.27ppb Re and 0.04ppb Os (Table 1). Barren siltstone and Pb-Zn sulfides can be distinguished isotopically according to Re/Os, ^{187}Re/^{188}Os, and ^{187}Os/^{188}Os ratios and the γOs parameter which is the percentage difference between the sample and the mantle at any specific time. The siltstone is higher in each case (Table 1). The higher Re content of siltstone is consistent with the high ^{187}Os/^{188}Os ratios (^{187}Os resulting from the beta decay of ^{187}Re). Radiogenic Osmium (^{187}Os) is dominant in the siltstone as expected in terrigenous rocks. The sulfides have a lower ^{187}Os/^{188}Os ratio which indicates that the Re in the sulfides has not undergone

Analysis N°	*Sample N°*	*Type*	*Re (ppb)*		*Os (ppb)*		*Re/Os*	*Com. Os*	*$^{187}Re/^{188}Os$*	*2 σ*	*$^{187}Os/^{188}Os$*	*2 σ*	*γOs*	*T Ma (Ma)*
2208/74 Gn	1712-3	Galena separate	**0.2440**		**0.2413**		1.01	0.2384	**4.9357**	0.0740	**0.2176**	0.0006	71	1,186
2208/140 WR	0103-1	Sphalerite whole rock	**0.4387**		**0.1881**		2.33	0.1822	**11.5985**	0.1740	**0.3719**	0.0015	193	1,298
2208/142 WR	960533	Sphalerite whole rock	**0.6839**		**0.1981**		3.45	0.1888	**17.4422**	0.2616	**0.4996**	0.0054	293	1,298
2208/73 Sp	3101-1	Sphalerite separate	**0.2676**		**0.0835**		3.21		**16.1835**	0.2428	**0.4609**	0.0012	263	1,256
2208/71 WR	1115-5	Galena whole rock	**0.8650**		**0.2095**		4.13	0.1985	**20.9822**	0.3147	**0.5424**	0.0028	327	1,199
2208/70 WR	0803-3	Galena whole rock	**1.1790**	**0.7724**	**0.1247**	**0.1296**	9.46		**52.7198**	0.7908	**1.3230**	0.0087	941	1,357
2208/70 Sp	0803-3	Sphalerite separate	**0.7900**		**0.1102**		7.17		**38.6297**	0.5794	**0.9931**	0.0019	681	1,345
2208/70 Gn	0803-3	Galena separate	**0.4910**		**0.0735**		6.68		**35.6954**	0.5354	**0.9323**	0.0037	634	1,354
2208/72 WR	960335	Sphalerite whole rock	**0.9360**		**0.1197**		7.82		**42.6659**	0.6400	**1.1364**	0.0044	794	1,417
2208/72 Sp	960335	Sphalerite separate	**0.4260**		**0.0674**		6.32		**33.1512**	0.4973	**0.7738**	0.0021	509	1,174
2208/138 WR	960839	Sphalerite whole rock	**1.5334**		**0.2073**		7.40	0.1831	**40.3161**	0.6047	**1.1218**	0.0068	783	1,478
2208/76 WR	0611-4	Sphalerite whole rock	**1.7041**		**0.0447**		38.14	0.0290	**287.1761**	4.3076	**4.2740**	0.0167	3263	862
2208/137 WR	2610-5	Sphalerite whole rock	**0.4821**		**0.0170**		28.40	0.0114	**202.3647**	3.0355	**3.7778**	0.0277	2,872	1,075
2208/77 dark	2710-4	Barren siltstone whole rock	**0.2415**		**0.0168**		14.41	0.0128	**91.7698**	1.3765	**2.4902**	0.0082	1859	1,533
2208/77 light	2710-4	Barren siltstone whole rock	**0.3520**	**1.2689**	**0.0132**	**0.0398**	26.73	0.0094	**181.5163**	2.7227	**3.1414**	0.0106	2372	991
2208/79 WR	2710-10	Barren siltstone whole rock	**3.2131**		**0.0893**		35.96	0.0469	**334.3507**	5.0153	**7.0858**	0.0308	5475	1,238

Table 1. Data from analyses of mineralized samples (both sphalerite and galena dominant) and barren siltstone samples representative of the host rocks. Mineralized samples with grey fill have isotopic characteristics more consistent with the barren siltstone than the other sphalerite samples. These samples are inferred to have incorporated some of the radiogenic osmium from the hostrocks during replacement.

significant beta decay to produce ^{187}Os, and is therefore of younger age.

Analyses are plotted on a graph of $^{187}Re/^{188}Os$ vs $^{187}Os/^{188}Os$ and an isochron is defined by a linear trend in the bulk of the data for sulfide samples (Figure 2a). Two sulfide analyses (annotated on Figure 2a) do not lie on the isochron defined by eleven sphalerite and galena samples. These samples are below the isochron and therefore represent samples whose Re/Os isotopic systematics have not behaved in a closed fashion since crystallization of the other samples. The anomalous sphalerite samples (2208/76 and 2208/137) have high Re/Os, $^{187}Re/^{188}Os$, and $^{187}Os/^{188}Os$ ratios which are more consistent with the siltstone rather than the Pb-Zn sulfide analyses, suggesting mixing of the two isotopic populations in these samples. The vein-hosted sphalerite (Part D) from which these samples were obtained is partly replacive mineralization and it is possible that the high Re and ^{187}Os of the replaced layer has been preserved in the mineralization in these samples during assimilation. However, other samples of this mineralization (Figure 2b) do not retain the isotopic signature of the host rock.

Sulfide samples and barren host-rock samples are broadly isochronous (Figure 2a). This suggests that the original Re-Os isotopic signature of the siltstones has been overprinted either by fluid associated with sulphide transport or some later thermal event. Note that the siltstones still retain a higher abundance of Re and radiogenic Osmium (^{187}Os) than the sulfide samples (Table 1). The siltstone therefore had some Re and Os (including ^{187}Os) prior to introduction of the later fluid. The host-rocks may never have defined an isochron due to heterogeneity of Re and Os. The Re/Os signature of the host-rocks must include the isotopic character of the source rocks, matrix cements, and one or more

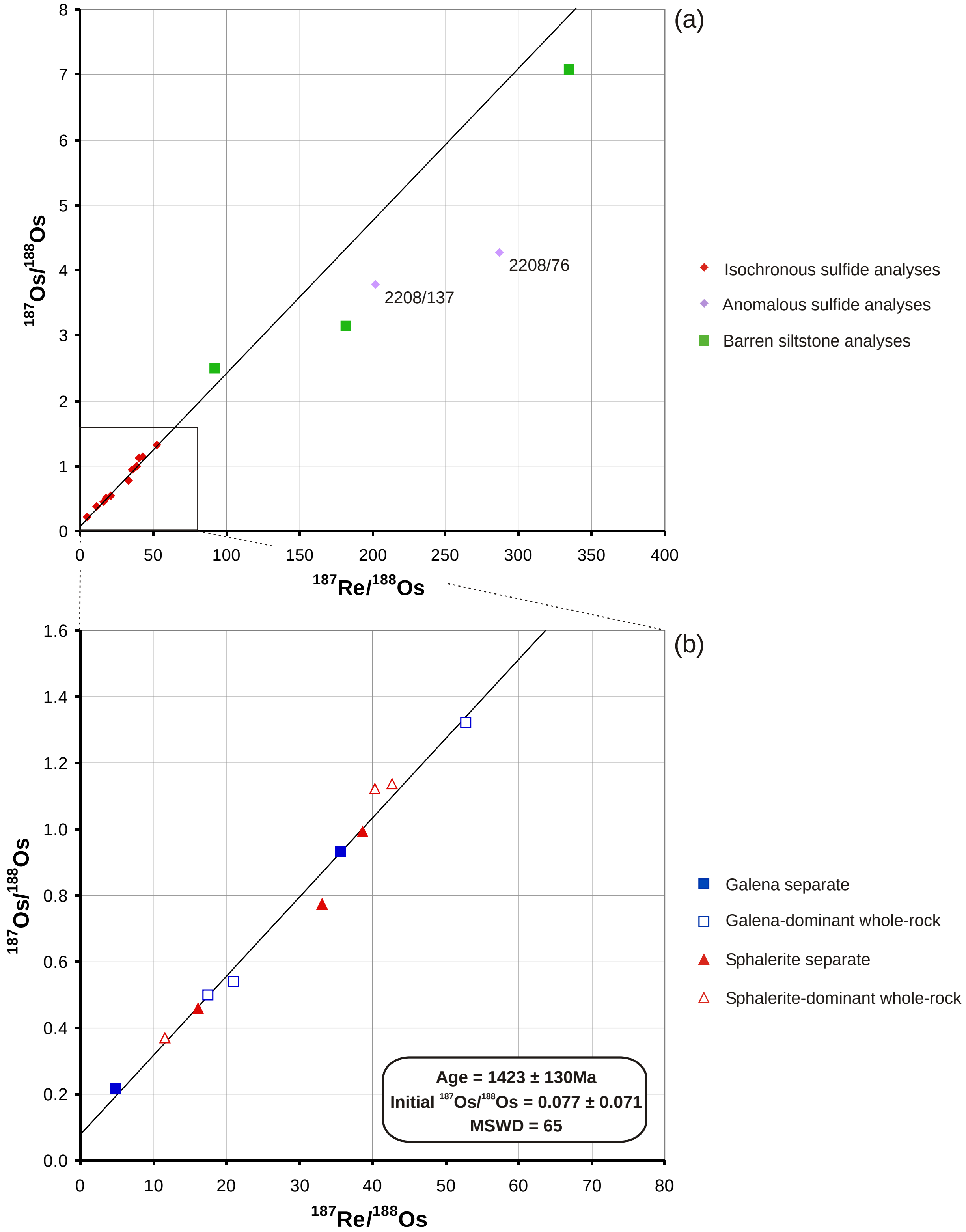

Figure 2. (a) Analyses of mineralized and barren samples displaying near isochronous behaviour of the siltstone samples. Analyses annotated 2208/137 and 2208/76 are bedding parallel sphalerite samples interpreted to have inherited the crustal signature from the host siltstones during replacive mineralization. The osmium is significantly more radiogenic in these two samples than the bulk of mineralized samples (see Table 1) (b) Eleven analyses from sphalerite and galena rich samples define an isochron and an age of 1423±130Ma has been calculated.

hydrothermal events which have affected the host-rocks prior to Zn-Pb-Ag mineralization. Therefore at least two populations of Re-Os isotopes are present in the barren siltstone samples and the analyses represent a combination of these populations. The analyses of the barren siltstone samples are therefore not representative of the original isotopic signature of the Urquhart Shale.

Eleven sphalerite and galena analyses form an isochron (model 3 or ‘errorchron’) with a large mean square of weighted deviations (MSWD) of 65 (Figure 2b). Sphalerite and galena mineralization is isochronous suggesting that the two sulfide species were deposited synchronously or within a timeframe not distinguishable using the Re-Os isotopic method (cf. mineralization paragenesis in Part D). Age estimates from iscochrons with high MSWD can have a small error depending on precision of analyses. In a study of komatiites, Gangopadhyay and Walker (2003) determined an isochron with MSWD=112 and an age estimate with ±3% error. An age estimate of 1423±130Ma has been derived from the gradient of the isochron from Figure 2a and using the decay constant of $1.666 \times 10^{-11} yr^{-1}$ (Smolar et al., 1996). The isochron yields an initial $^{187}Os/^{188}Os$ ratio of 0.077±0.071. Initial Osmium ratios between 0.8 and 1.4 indicate a crustal source (Hannah et al., 2001; Peucker-Ehrenbrink and Jahn, 2001) whereas initial $^{187}Os/^{188}Os$ ratios of ca. 0.12 indicate a mantle source (Walker et al., 1989; Schaefer et al., 2000). The initial $^{187}Os/^{188}Os$ ratio of carbonaceous chondrites, interpreted to be analogous to that of the mantle (Walker and Morgan, 1989; Walker et al., 1989) and iron meterorites (Luck and Allegre, 1983) is also in the order of 0.12. The sulfides at George Fisher therefore have an initial $^{187}Os/^{188}Os$ ratio reflecting mantle-derived osmium.

4. Discussion

4.1 Implications for the timing of mineralization at George Fisher

Re-Os dating of sulfides has provided a host rock independent absolute age for mineralization of 1423±130Ma at the George Fisher Mine. The large error associated with this age overlaps with age estimates for both the D_2 (1544±12Ma from Rb-Sr whole-rock analyses: Page and Bell, 1986; 1532±7Ma obtained from U-Pb SHRIMP analysis of zircons: Connors and Page, 1995) and D_4 (1510±13Ma from Rb-Sr whole-rock analyses: Page and Bell, 1986) deformation episodes. Relative timing of mineralization to deformation features is discussed in Part D and a conclusion of this work is that the majority of mineralization is located in sites which were dilatant during D_4 deformation. The Re-Os age is not within error of the age of deposition of the host rocks (1655±4Ma obtained from U-Pb SHRIMP analysis of zircons: Page et al., 2000) or diagenesis.

Rb-Sr dating of tuffs interbedded with the Urquhart Shale at Mt Isa has produced ages ~200-250my younger than the Urquhart Shale (Farquharson and Richards, 1975; Page, 1981). Farquharson and Richards (1975) analysed tuffs from the mine sequence at Mt Isa. Their suite of 8 whole-rock samples and 4 residues returned isochron ages of 1392±85Ma and 1346±48Ma respectively, and a combined whole-rock/residue (8 samples) isochron gave an age of 1341±21Ma. This young age was interpreted as the closure of isotopic exchange during post-tectonic cooling (Farquharson and Richards, 1975). Further analysis of the Mt Isa tuffs by Page (1981) resulted in a Rb-Sr isochron age of 1482±52Ma from 33 analyses. Having obtained 1480-1490Ma Rb-Sr biotite ages in basement volcanics 45km to the northeast (Page, 1978), 1482±52Ma was interpreted as the best estimate for the cessation of metamorphism (Page, 1981). Similarly, K-Ar analysis of biotites in the Sybella and Kalkadoon granites (which pre-dates the main phase of deformation: D_2) returned ages between 1363 and 1457Ma (Richards et al., 1963).

Little is known of the closing temperature of the Re-Os isotopic system and the 1423±130Ma age could represent the waning stages of metamorphism in the Leichardt River Fault Trough and not an indication of the age of the Zn-Pb-Ag mineralization event. Note that the temperature of deformation attained at George Fisher is only in the order of 200-250°C (Chapman, 1999; Part A-this study).

If the 'errorchron' age estimate is related to the closure of the Re-Os isotopic system at ca. 1450Ma and not the timing of mineralization, other indications of temporally distinct host-rock formation/diagenesis and mineralization can be inferred from the distinct isotopic signatures of the sulfides and barren siltstones. The siltstones contain significant radiogenic osmium compared to the sulfides and the $^{187}Os/^{188}Os$ ratios are 4.2391 and 0.7612 (excluding the two sphalerite samples where mixing is inferred, Table 1), respectively. The siltstones therefore had a higher initial Re content (Re is partitioned into crust) to the sulfides and have evolved accordingly as represented by the contrasting γOs (Table 1). The sulfides, although relatively enriched in Os, are dominated by the non-radiogenic ^{188}Os (Table 1). Correlation of both Re/Os ratio and abundance of ^{187}Os in PGE-enriched sulfide layers and host black shale in the Yukon Territory formed part of the argument for PGE-enrichment during sedimentation or early diagenesis (Horan et al., 1994). The sulfides and siltstones at George Fisher have distinct Re/Os ratios and contrasting ^{187}Os abundances, suggesting that they have evolved from separate Re-Os

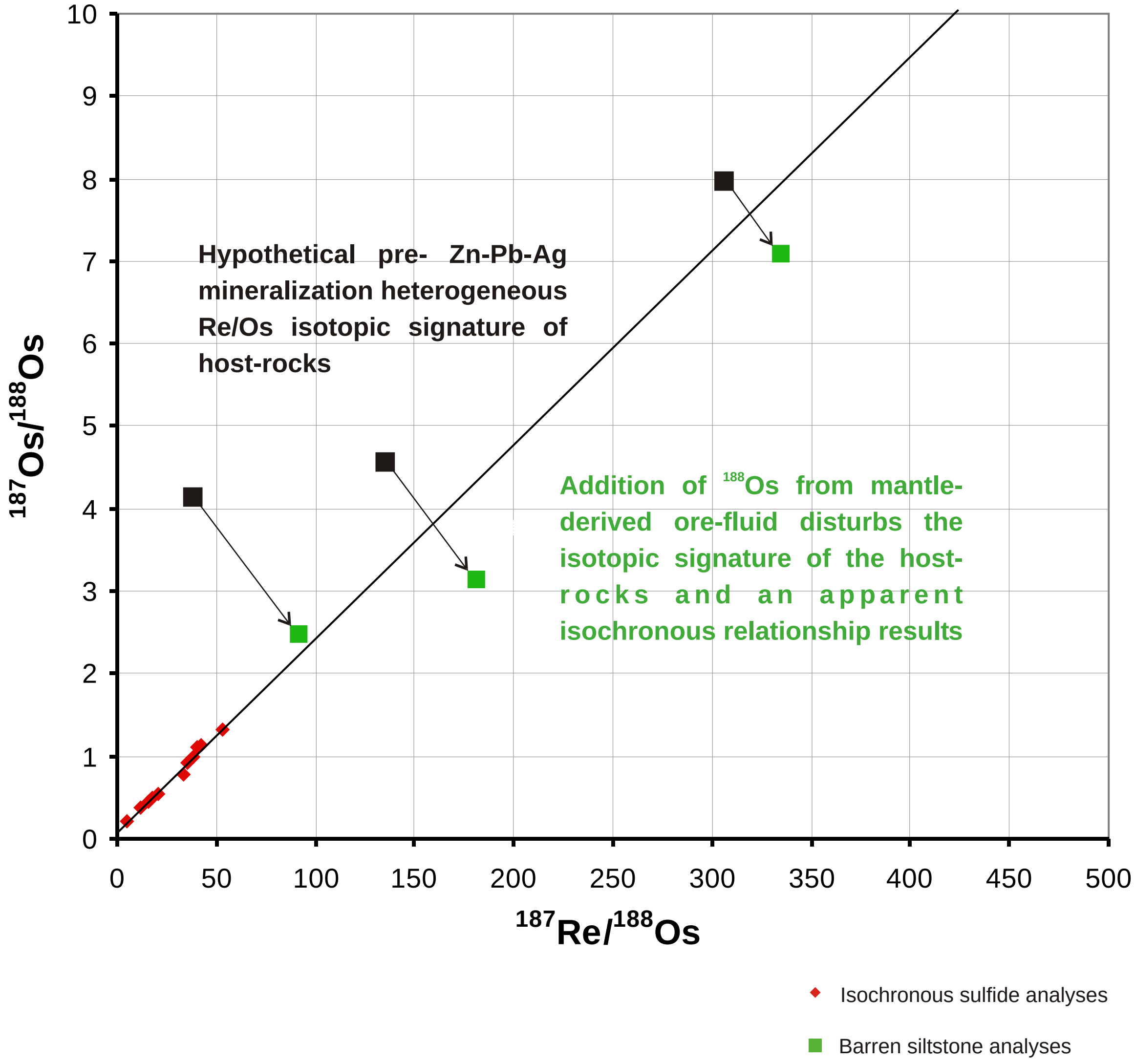

Figure 3. Possible scenario for resetting of the Re/Os isotopic signature of host-rocks at George Fisher during hydrothermal Zn-Pb-Ag mineralization. The Re/Os character of the host-rocks may have been heterogeneous prior to the disturbance as described in the text.

sources to the mineralization. The approximately isochronous behaviour of sulfide and siltstone analyses (Figure 2a) may reflect overprinting of the initial Re-Os isotopic signatures of the siltstone by fluids with different Re-Os characteristics that presumably contained the Zn and Pb (Figure 3). Preservation of a diagenetic signature in carbon and oxygen isotopes from carbonate alteration products (Chapman, in review) implies that resetting of the Re-Os signature has not significantly affected the carbonate alteration at George Fisher.

Fine-grained sulphide breccia interpreted to pre-date F_2 folding by qualitative means (refer to Part D) is indistinguishable from mineralization types interpreted to have formed later in the deformation history. This is possibly due to the large error of the age estimate (1423±130Ma) as this age range spans from ~1553-1293Ma. However, the oldest age of the span (~1553Ma) approximately correlates with D_2 deformation in the Mt Isa area (~1540Ma: Page and Bell, 1986). The effects of regional-scale hydrothermal activity and thermal peak (Chapman, 1999, 2004) associated with Cu mineralization during D_4 (~1510Ma: Page and Bell, 1986) may have resulted in similar isotopic evolution of a pre-deformational Zn-Pb-Ag sulphide occurrence as inferred for the host-rocks (Figure 3). However, the analyzed ore samples are likely to have contained more radiogenic Os if this were the case (see Table 1).

4.2 Source of metal at the George Fisher Zn-Pb-Ag deposit: comparison with previous models of Zn-Pb-Ag metallogeny in the Western Fold Belt of the Mt Isa Inlier.

The initial $^{187}Os/^{188}Os$ ratio can be used to discriminate between crustal and mantle sources of metals which comprise ore deposits. In studies of mineralization, sulfide ores were found to have initial ratios indicating crustal source of metal at the Tharsis and Rio Tinto massive sulfide deposits (0.37; Mathur et al., 1999), and at the Bendigo gold deposit (1.04; Arne et al., 2001). The sulfides analysed at these deposits were an order of magnitude more radiogenic than the ores at George Fisher. The average $^{187}Os/^{188}Os$ ratio for sulfides from Tharsis/Rio Tinto is 9.662 (Mathur et al., 1999) and 8.41 at Bendigo (Arne et al., 2001), compared with 0.7612 at George Fisher. The greater abundance of ^{187}Os corresponds with higher initial Re/Os ratio in the rock indicating a crustal source (Esser and Turekian, 1993). The initial ratio at George Fisher is 0.077±0.071which is within error of the $^{187}Os/^{188}Os$ ratio in the mantle of approximately 0.12 (Luck and Allegre, 1983; Walker and Morgan, 1989; Walker et al., 1989; Martin, 1991). A mantle source for the Re and Os and ore metals in the sulfide mineralization at George Fisher is therefore inferred. Metals have either been sourced from a mantle-fluid or from mantle-derived rocks of the same age as the sulfides, 1423±130Ma. Note that the basalts comprising the Eastern Creek Volcanics have an age of approximately 1770Ma (Blake and Stewart, 1992) and are therefore not the source rocks for Pb and Zn at George Fisher.

Previous models developed for Proterozoic stratiform Pb-Zn deposits in the Mt Isa Inlier have involved hypotheses of leaching of metals from within the sedimentary basin (e.g. Ord et al., 2002) and introduction of metals from fluids sourced externally (Perkins, 1997). Analogies drawn with modern basinal brine compositions and metal solubility criteria resulted in Cooke et al. (2000) concluding that the proportion and type of sedimentary basin fill are fundamental controls on the chemistry of metalliferous sedimentary brines interpreted to be responsible for stratiform Pb-Zn deposits. The oxidized basinal brines evolve from basins dominated by carbonates, evaporites, and hematitic sandstones and are reduced in anoxic sea-floor to sub sea-floor locations (Cooke et al., 2000). A model for compaction-driven flow whereby impermeable cap rocks are breached during faulting and underlying fluid reservoirs in porous clastic rocks are discharged onto the sea floor, has been proposed by Lydon (1983). Large et al. (2002) determined that this model is not applicable to deposits including Mt Isa, George Fisher/Hilton, and HYC, as thick porous clastic reservoir sequences are not present in the Mt Isa and McArthur basins and therefore there would be insufficient basinal fluid to form the 'super-giant' deposits. Compaction-driven dewatering is considered not to be a viable process in producing large base-metal deposits in carbonate-shale-sandstone basins as thermal and mass fluxes are inadequate (Bethke, 1985; Solomon and Heinrich, 1992).

Alternative models for deposits formed from metal sourced within the sedimentary basin include:

- Downward penetrating convective fluids leach Pb and Zn from strata within the sedimentary basin (Russell et al., 1981) and are deposited as stacked stratiform lenses through episodic dewatering of the basinal brines during rift basin evolution (Sawkins, 1984).
- Convection of fluids in sedimentary basins driven by high-heat producing granites (radioactive decay) within the basement (Solomon and Heinrich, 1992).

- Deformation-driven migration of basinal brines (Broadbent et al., 1998) is interpreted to have leached Pb and Zn from crustal rocks in the stratigraphic column subsequent to migration along faults in forming the Century Zn deposit late in the Isan orogeny (Ord et al., 2002).

However, Perkins (1997) inferred the involvement of a deep-seated metal source tapped by juvenile fluids. This is more consistent with the findings of this study of a mantle-source of Pb-Zn in sulfides at George Fisher. Adding to this argument, Chapman (1999, in review) interpreted $\delta^{18}O$ depletion haloes in the vicinity of economic Zn-Pb-Ag mineralization at George Fisher as zones of influx of mantle-fluid.

While Cooke et al. (2000) considered the amount and type of basin fill and the presence of growth faults as a guide to prospectivity for stratiform base metal mineralization, a mantle-source of Pb and Zn as suggested by this study requires host-rocks to be proximal to major faults linked with crustal-scale faults and shear-zones interpreted to have acted as fluid conduits. The Mt Isa-Paroo Fault system is proximal to the Mt Isa, Hilton and George Fisher Zn-Pb-Ag deposits. This fault zone is part of a network of faults linked to a major mid-crustal shear zone located at a depth of approximately 35km in the crust below the Western Fold Belt (MacCready et al., 1998).

5. Conclusions

Sphalerite and Galena mineralization at George Fisher have the same Re-Os isotopic signature and therefore have a common source. The near-isochronous behaviour of barren host-rocks, despite having distinct isotopic ratios from the sulfides suggests overprinting of host-rocks by the mineralizing fluid. Consistent Re-Os isotopic signature of host-rocks and mineralization in PGE mineralization in sulfidic black shales (Yukon, Canada) indicated a syn-sedimentary to diagenetic age of PGE enrichment (Horan et al., 1994). Distinct isotopic ratios in this study suggest temporally separate host-rock formation and mineralization events. An age of 1423±130Ma has been derived from an isochron consisting of eleven mineralized samples. The age of host-rocks at George Fisher is 1655Ma (Page et al., 2000) and is outside the error of this estimate for the age of mineralization.

The main deformation associated with the Isan Orogeny occurred from 1540 to 1510Ma (Connors and Page, 1995; Page and Bell, 1986). This period is within error of the age obtained from Re-Os analysis and is consistent with the inferred D_4 relative timing of the main mineralization styles at George Fisher (Part D-this study). The 1423±130Ma age is also temporally equivalent to a period of post-orogenic cooling dated at 1392±85Ma (Farquharson and Richards, 1975) and 1482±52Ma (Page, 1981). Re-Os dating of the sulfides at George Fisher has therefore not achieved the level of accuracy required to distinguish between individual deformation events and post-orogenic cooling but indicates that closure of the Re-Os isotopic system in the Zn and Pb sulphides significantly post-dates host-rock deposition.

Cross-cutting relationships of galena mineralization on sphalerite mineralization are common at George Fisher (e.g. Figure 1e) however the time lapse between the emplacement of the various mineralization styles is not distinguishable using the Re-Os method as they are isochronous (Figure 2b). Samples interpreted as pre-D_2 (fine-grained breccia, Figure 1a, refer to Part D) and syn-D_4 (medium-grained galena breccia which cross-cuts stratiform sphalerite, Figure 1b and e, refer to Part D) plot on the same isochron and have ages within the ±130Ma error.

A mantle source for the Pb and Zn is indicated by the initial $^{187}Os/^{188}Os$ ratio of 0.077±0.071. Proximity to a regional fault zone such as the Mount Isa-Paroo Fault system, interpreted to be part of a fault-network linked to a major mid-crustal shear zone (MacCready et al., 1998), is considered to be necessary to bring metal-bearing fluids from depth into contact with prospective host-lithologies at George Fisher.

References

Allegre, C.J. and Luck, J.M., 1980. Osmium isotopes as petrogenic and geological tracers: Earth and Planetary Science Letters, v. 48, p. 148-154.

Arne, D.C., Bierlein, F.P., Morgan, J.W., and Stein, H.J., 2001. Re-Os dating of sulfides associated with gold mineralization in central Victoria, Australia: Economic Geology, v. 96, p. 1455-1459.

Barnes, S-J, Naldrett, A..J., and Gorton, M.P., 1985. The origin of fractionation of platinum-group elements in terrestrial magmas: Chemical Geology, v. 53, p.303-323.

Bethke, C.M., 1985. A numerical model of compaction-driven groundwater flow and heat transfer and its application to the palaehydrology of intracratonic sedimentary basins: Journal of Geophysical Research, v. 90, p. 6817-6828.

Blake, D.H. and Stewart, A.J., 1992. Stratigraphic and tectonic framework, Mount Isa inlier: Australian Geological Survey Organization Bulletin 243, p. 1-11.

Broadbent, G.C., Myers, R.E., and Wright, J.V., 1998. Geology and origin of shale-hosted Zn-Pb-Ag mineralization at the Century deposit, Northwest Queensland, Australia: Economic Geology, v. 93, p. 1264-1294.

Chapman, L.H., 1999. Geology and genesis of the George Fisher Zn-Pb-Ag deposit, Mount Isa, Australia. (Unpublished PhD thesis – James Cook University, Townsville).

Chapman, L.H., 2004. Geology and mineralization styles of the George Fisher Zn-Pb-Ag deposit, Mount Isa, Australia: Economic Geology, v. 99, p. 233-255.

Chapman, L.H. Multiple episodes of hydrothermal carbonate formation in the Proterozoic Urquhart Shale and significance for the origin of Zn-Pb-Ag and Cu mineralization in the Mount Isa district, Australia: in review.

Connors, K.A. and Page, R.W., 1995, Relationships between magmatism, metamorphism and deformation in the western Mount Isa Inlier, Australia: Precambrian Research, v. 71, p. 131-153.

Cooke, D.R., Bull, S.W., Large, R.R., and McGoldrick, P.J., 2000. The importance of oxidized brines for the formation of Australian proterozoic stratiform sediment-hosted Pb-Zn (Sedex) deposits: Economic Geology, v. 95, p. 1-18.

Creaser, R.A., Papanastassiou, D.A., and Wasserburg, G.J., 1991. Negative thermal ion mass spectrometry of osmium, rhenium, and iridium: Geochimica et Cosmochimica Acta, v. 55, p. 397-401.

Davis, T.P., 2004. Mine-scale structural controls on the Mount Isa Zn-Pb-Ag and Cu orebodies: Economic Geology, v. 99, p. 543-559.

Esser, B.K. and Turekian, K.K., 1993. The osmium isotopic composition of the continental crust: Geochimica et Cosmochimica Acta, v. 57, p. 3093-3104.

Farquharson, R.B. and Richards, J.R., 1975. Isotopic remobilization in the Mount Isa tuff beds: Chemical Geology, v. 16, p. 73-88.

Foster, G.F., Lambert, D.D., Frick, L.R., and Maas, R., 1996. Re-Os isotopic evidence for genesis of Archean nickel ores from uncontaminated komatiites: Nature, v. 382, p. 703-706.

Freydier, C., Ruiz, J., Chesley, J., McCandless, T., and Munizaga, F., 1997. Re-Os isotope systematics of sulfides from felsic igneous rocks: Application to base metal porphyry mineralization in Chile: Geology, v. 25, no. 9, p. 775-778.

Gangopadhyay, A, and Walker, R.J., 2003. Re-Os systematics of the ca. 2.7-Ga komatiites from Alexo, Ontario, Canada: Chemical Geology, v. 196, p. 147-162.

Hannah, J.L., Schersten, A., and Stein, H., 2001. Re-Os behaviour in mafic magmas and terrestrial diagenetic materials: Extracting information from open systems. Abstracts of the Geological Society of America Annual Meeting.

Hauri, E.H. and Hart, S.R., 1993. Re-Os systematics of HIMU and EMII oceanic island basalts from the south Pacific Ocean: Earth and Planetary Science Letters, v. 114, p. 353-371.

Horan, M.F., Morgan, J.W., Grauch, R.I., Coveny JR., R.M., Murowchick, J.B., and Hulbert, L.J., 1994. Rhenium and osmium isotopes in black shales and Ni-Mo-PGE-rich sulfide layers, Yukon Territory, Canada, and Hunan and Guizhou provinces, China: Geochimica et Cosmochimica Acta, v. 58, p. 257-265.

Hou, Z., Wang, S., Du, A., Qu, X., and Sun, W., 2003. Re-Os dating of sulfides from the volcanogenic massive sulfide deposit at Gacun, Southwestern China: Resource Geology, v. 53, no. 4, p. 305-310.

Large, R.R., Bull, S., Selley, D., Yang, J., Cooke, D., Garven, G., and McGoldrick, P., with particular reference to the north Australian Proterozoic. In: Cooke, D.R., Pongratz, J. (Eds), Giant Ore Deposits – Characteristics, Genesis and Exploration. Codes Special Publication No. 4. Hobart Tasmania, pp. 107-149.

Lesher, C.M., Burnham, O.M., Keays, R.R., Barnes, S.J., and Hulbert, L., 2001. Geochemical discrimination of barren and mineralized komatiites associated with magmatic Ni-Cu-(PGE) sulphide deposits: Canadian Mineralogist, v. 39, p. 673-696.

Levresse, G., Cheilletz, A., Gasquet, D., Archibald, D., Reisberg, K., and Kyser, K., 2002. The Imiter silver deposit (Morocco): a giant Precambrian epithermal deposit. Abstracts of the SEG Meeting: Global Exploration 2002.

Lightfoot, P.C., Keays, R.R., and Doherty, W., 2001. Chemical evolution and origin of nickel sulfide mineralization in the Sudbury Igneous Complex, Ontario, Canada: Economic Geology, v. 96, p. 1855-1875.

Lovering, J.F. and Morgan, J.W., 1964. Rhenium and osmium abundances in tektites: Geochimica et Cosmochimica Acta, v. 28, p. 761-768.

Luck, J.M. and Allegre, C.J., 1983. ^{187}Re-^{187}Os systematics in meteorites and cosmochemical consequences: Nature, v. 302, p. 130-132.

Lydon, J.W., 1983. Chemical parameters controlling the origin and deposition of sediment-hosted stratiform lead-zinc deposits, Canada. In: Sangster, D.F. (ed.), Sediment-hosted stratiform lead-zinc deposits. Mineralogical Association of Canada Short Course Handbook, 9, 175-250.

MacCready, T., Goleby, B.R., Goncharov, A., Drummond, B.J., Lister, G.S., 1998. A framework of overprinting orogens based on interpretation of the Mount Isa deep seismic transect: Economic Geology, v. 93, p. 1422-1434.

Martin, C.E., 1991. Osmium isotopic characteristics of mantle-derived rocks: Geochimica et Cosmochimica Acta, v. 55, p. 1421-1434.

Mathur, R., Ruiz, J., and Tornos, F., 1999. Age and sources of the ore at Tharsis and Rio Tinto, Iberian Pyrite Belt, from Re-Os isotopes: Mineralium Deposita, v. 34, p. 790-793.

McCandless, T.E. and Ruiz, J., 1993. Rhenium-Osmium evidence for regional mineralization in Southwestern North America: Science, v. 261, p. 1282-1286.

Morgan, J.W. and Lovering, J.F., 1967. Rhenium and Osmium abundances in some igneous and metamorphic rocks: Earth and Planetary Science Letters, v. 3, p. 219-224.

Morgan, J.W., Wandless, G.A., Petrie, R.K., and Irving, A.J., 1981. Composition of the Earth's upper mantle: Trace elements in ultramafic nodules: Tectonophysics, v. 75, p. 47-67.

Ord, A., Hobbs, B.E., Zhang, y., Broadbent, G.C., Brown, M., Willetts, G., Sorjonen-Ward, P., Walshe, J.L., and Zhao, C., 2002. Geodynamic modelling of the Century deposit, Mt Isa Province, Queensland: Australian Journal of Earth Sciences, v. 49, p. 1011-1039.

Page, R.W., 1981. Depositional ages of the stratiform base metal deposits at Mount Isa and McArthur River, Australia, based on U-Pb Zircon dating of concordant tuff horizons: Economic Geology, v. 76, p. 648-658.

Page, R.W. and Bell, T.H., 1986, Isotopic and structural responses of granite to successive deformation and metamorphism: Journal of Geology, v. 94, p. 365-379.

Page, R.W., Jackson, M.J., and Krassay, A.A., 2000, Constraining sequence stratigraphy in north Australian basins: SHRIMP U-Pb zircon geochronology between Mt Isa and McArhur River: Australian Journal of Earth Sciences, v. 47, p. 431-459.

Peucker-Ehrenbrink, B., and Jahn, B., 2001. Rhenium-Osmium isotope systematics and platinum group element concenttrations: Loess and the upper continental crust: Geochemistry Geophysics Geosystems, v. 2.

Perkins, W.G., 1997. Mount Isa lead-zinc orebodies: Replacement lodes in a zoned syndeformational copper-lead-zinc system?: Ore Geology Reviews, v. 12, p. 61-110.

Richards, J.R., Cooper, J.A., and Webb, A.W., 1963. Potassium-Argon ages on micas from the Precambrian region of North-western Qld.: Journal of the Geological Society of Australia, v. 10, p. 299-312.

Russell, M.J., and Solomon, M., and Walshe, J.L., 1981. The genesis of sediment-hosted, exhalative zinc + lead deposits: Mineralium Deposita, v. 16, p. 113-127.

Sawkins, F.J., 1984. Ore genesis by episodic dewatering of sedimentary basins: Application to giant Proterozoic lead-zinc deposits: Geology, v.12, p. 451-454.

Schaefer, B.F., Parkinson, I.J., and Hawkesworth, C.J., 2000. Deep mantle plume osmium isotope signature from West Greenland Tertiary picrites: Earth and Planetary Science Letters, v. 175, p. 105-118.

Shirey, S.B., 1991. The Rb-Sr, Sm-Nd, and Re-Os isotopic systems: A summary and comparison of their applications to the cosmochronology and geochronology of igneous rocks. In: Heaman, L. and Ludden, J.N. (eds): Short course handbook on applications of radiogenic isotope systems to problems in geology, Mineralogical Association of Canada.

Smolar, M.I., Walker, R.J., and Morgan, J.W., 1996. Re-Os ages of group IIA, IIIA, IVA, and IVB iron meteorites: Science, v. 271, p. 1099-1102.

Solomon, M. and Heinrich, C.A., 1992. Are high-heat producing granites essential to the origin of giant lead-zinc deposits at Mount Isa and McArthur River, Australia?: Exploration and Mining Geology, v. 1, p. 85-91.

Stein, H.J., Markey, R.J., Morgan, J.W., Du, A., and Sun, Y., 1997. Highly precise and accurate Re-Os ages for molybdenite from the East Qinling Molybdenum Belt, Shaanxi Province, China: Economic Geology, v. 92, no. 7/8, p. 827-835.

Stein, H.J. and Bingen, B., 2002. 1.05-1.01 Ga Sveconorwegian metamorphism and deformation of the supracrustal sequence at Saesvatn, South Norway: Re-Os dating of Cu-Mo mineral occurrences. In: Blundell, D., Neubauer, F., and von Quadt, A. (eds), The Timing and Location of Major Ore Deposits in an Evolving Orogen: Geological Society, London, Special Publications, v. 204, p. 319-335.

Terakado, Y., 2001. Re-Os dating of the Kuroko ores from the Wanibuchi Mine, Shimane Prefecture, southwestern Japan: Geochemical Journal, v. 35, p. 169-174.

Walker, R.J., Carlson, R.W., Shirey, S.B., and Boyd, F.R., 1989. Os, Sr, Nd, and Pb isotope systematics of southern African peridotite xenoliths: Implications for the chemical evolution of subcontinental mantle: Geochimica et Cosmochimica Acta, v. 53, p. 1583-1595.

Walker, R.J. and Morgan, J.W., 1989. Rhenium-osmium isotope systematics of carbonaceous chondrites: Science, v. 243, p. 519-523.

PART F

Tectonostratigraphic setting and controls on stratiform base metal mineralization in the Western Fold Belt of the Mt Isa Inlier, Australia: Comparison of the Mt Isa, George Fisher - Hilton, Lady Loretta, and Century Zn-Pb-Ag deposits.

Abstract

The major Zn-Pb-Ag deposits of the Mt Isa Inlier are concentrated in the Western Fold Belt. The deposits are hosted by rocks deposited in the later stages of overprinting crustal extension events. Basin closure/inversion during the Isan Orogeny resulted in the reactivation of earlier formed basin-bounding faults and development of district scale folds. The Mt Isa, George Fisher/Hilton, Lady Loretta, and Century Zn-Pb-Ag deposits are hosted by variably carbonaceous and calcareous shale/siltstone which vary in age by approximately 60 million years. Therefore, the host-rocks to mineralization are not direct correlatives. However, deformation histories of the deposits and configuration of major structures are similar. D_1 faults and folds are implicated as potential fluid conduits or heterogeneities which have focussed dilation during later tectonism. Intersections of these faults reactivated during D_2-D_4 are considered to have focussed fluid to near surface sites of ore deposition. The D_1 structures may also have focussed fluid earlier in the diagenetic history of the rocks which resulted in hydrothermal alteration of carbonate mineral assemblages at George Fisher. The larger Zn-Pb-Ag deposits in the Western Fold

Belt are located at the intersection of D_1 faults and/or folds with D_2/D_4 structures in calcareous/carbonaceous siltstones and shales.

1. Introduction

The Western Fold Belt of the Mt Isa Inlier hosts globally significant resources of Zn-Pb-Ag mineralization including deposits at Mt Isa, George Fisher/Hilton, Lady Loretta, and Century, which comprise 62% of the Zn+Pb metal budget for the entire the Mt Isa Inlier. These deposits, while all stratiform in geometry and hosted by similar lithologies, have different metal contents, controls on high-grade mineralization, and interpreted geneses. An exploration strategy for stratiform Zn-Pb-Ag deposits in the Western Fold Belt must therefore accommodate several genetic models in accordance with the individual studies on each deposit.

The aim of this paper is to summarize the key aspects for each of the major deposits listed above, including the findings of this study of the George Fisher deposit, discuss correlations or contrasts in timing and interpreted genesis, and evaluate their implications for exploration for further Zn-Pb-Ag resources in the Western Fold Belt. Features considered significant in localizing mineralization at George Fisher will be compared to other deposits to determine whether there are regional similarities in the controls on Zn-Pb-Ag mineralization.

2. Geological evolution of the Western Fold Belt

The Proterozoic sedimentary basins of the Mt Isa Inlier are interpreted as intracratonic back-arc extension associated with subduction of the Arunta slab (1800Ma) in central

Australia and continental collision (1600Ma) on the southern margin of the North Australian Craton (O'Dea et al., 1997a,b; Betts et al., 1998; Jackson et al., 2000; Page et al., 2000; Southgate et al., 2000; Giles et al., 2001; Betts et al., 2002). The Proterozoic basins of the McArthur Basin, Georgetown Inlier, and Curnamona Craton are interpreted as correlative intracontinental back-arc basins with those of the Mt Isa Inlier (Betts et al., 2002a). The western part of the Mt Isa Inlier comprises two north-south striking terranes, the Leichardt River Fault Trough and Lawn Hill Platform (Figure 1). Together these terranes form the Western Fold Belt. Each represents sedimentary basins formed during intracontinental extension between 1780Ma and 1590Ma (Blake and Stewart, 1992; O'Dea et al., 1997a,b; Southgate et al., 2000; Betts and Lister, 2002). Extension and basin development terminated prior to the formation of oceanic crust due to the ensuing period of east-west directed shortening associated with the Isan Orogeny at ca. 1600-1500Ma (Blake et al., 1990). This orogenesis was related to docking of the North American plate with Eastern Australia ca. 1540Ma and comprised thin-skinned lateral translations/thrusting (ca. 1600-1550Ma) followed by thick-skinned shortening at deeper crustal levels (MacCready et al., 1998; Betts et al., 2000; Betts et al., 2002). Orogenesis in the Mt Isa and Georgetown Inliers (Isan Orogeny), Curnamona Craton (Olarian Orogeny), and northern Gawler Craton (Late Kararan Orogeny) are temporally equivalent episodes related to east-west directed continental collision (Betts et al., 2002).

Initial sedimentation in the Leichardt River Fault Trough occurred during the Leichhardt Rift Event (Betts and Lister, 2002) from 1790Ma (Page, 1983). This consisted of volcanics and conglomerate of the Bottletree Formation (Figure 2) and conglomerate, feldspathic sandstone, and quartz arenite of the Mount Guide Quartzite (O'Dea et al.,

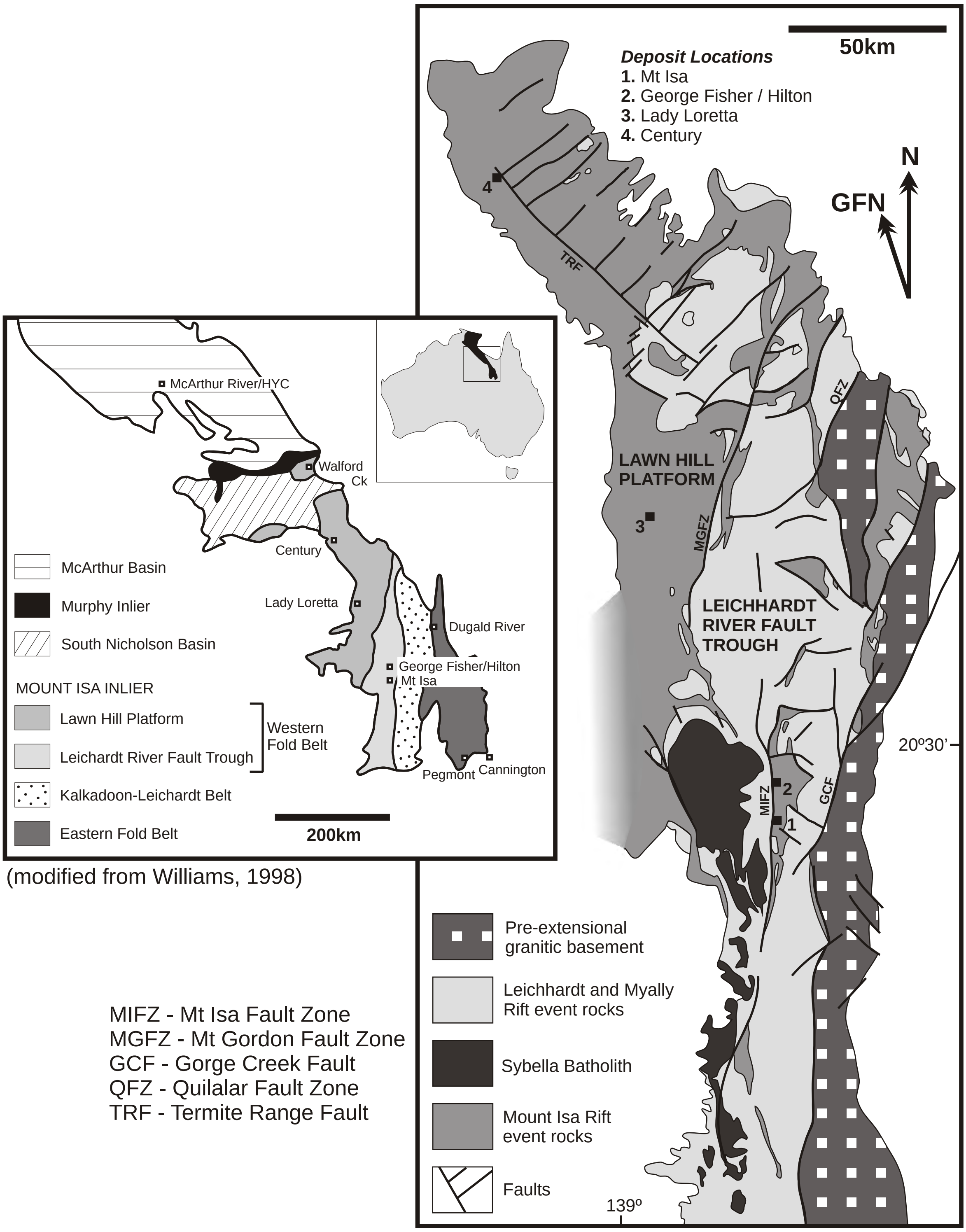

(modified from Williams, 1998)

(modified from Betts et al., 1998)

Figure 1. Tectonostratigraphic divisions of the Mt Isa Inlier (inset) and simplified geology of the Western Fold Belt (main diagram). The Leichhardt River Fault Trough and Lawn Hill Platform are elongate north-south trending basins bounded by regional fault systems. Deposit locations are indicated on both diagrams. In terms of metal content, the Mt Isa, George Fisher, Hilton, and Century Zn-Pb-Ag deposits represent four of the ten largest stratiform Zn-Pb-Ag deposits globally (Large et al., 2002) and the Western Fold Belt is therefore a globally significant Zn-Pb-Ag province.

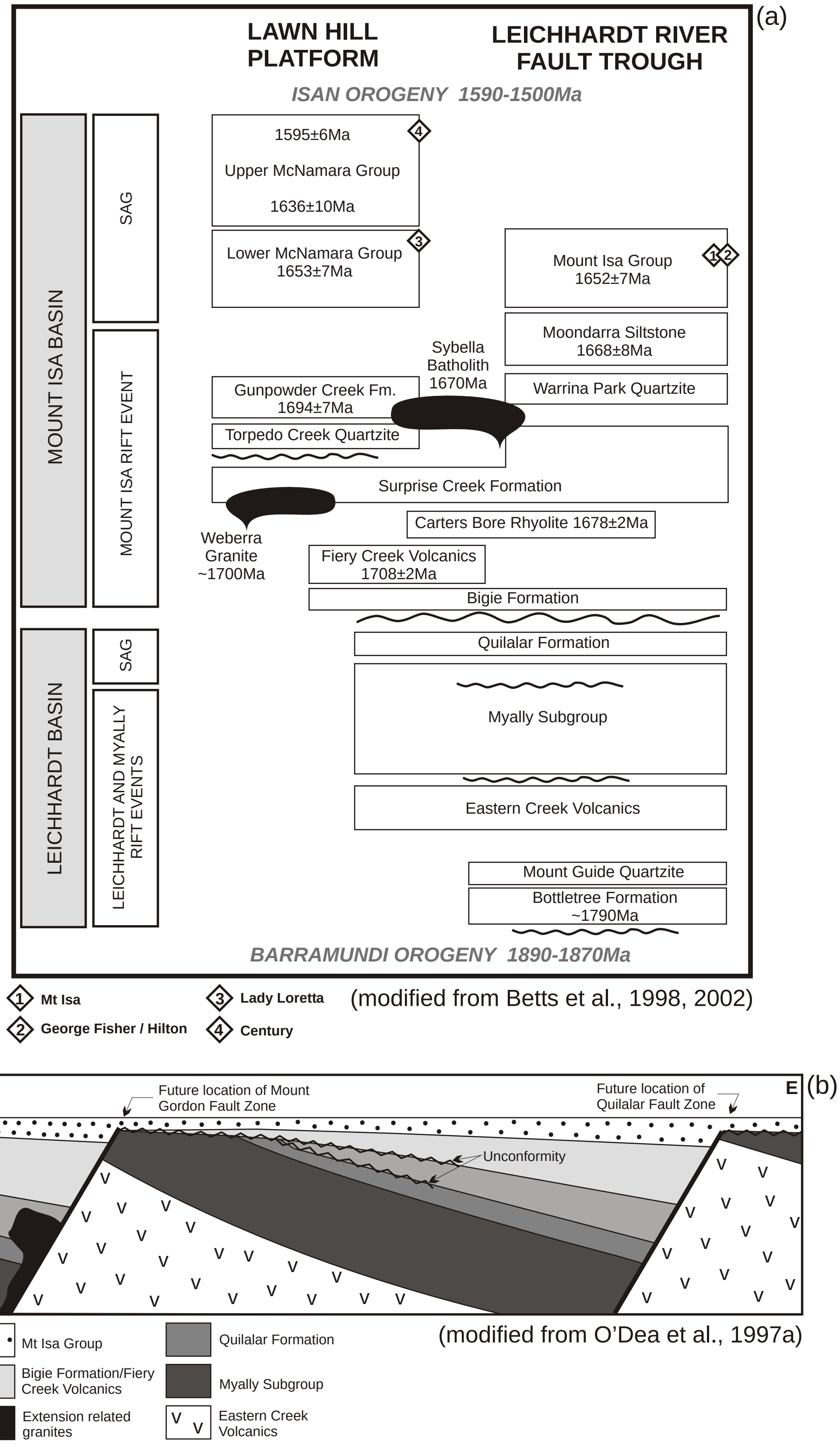

Figure 2. (a) Simplified tectonostratigraphic column for the Western Fold Belt. Temporal positions of host-rocks to Zn-Pb-Ag deposits are indicated. (b) Schematic cross-section through the Leichhardt River Fault Trough prior to basin inversion, district-scale folding and reverse movement on major faults. Refer to Figure 1 for fault locations.

These rocks are overlain by 4-6km of rift-related continental flood basalts and intercalated sediments termed the Eastern Creek Volcanics (Glikson et al, 1976). The next package of sediments, deposited during the Myally Rift Event (Betts et al., 1998), comprises the Myally Subgroup and Quilalar Formation which consist dominantly of quartzite and minor dolomite (O'Dea et al., 1997a). Thickness changes within the Myally subgroup across east-west striking faults suggest synsedimentary reactivation of basement faults (Smith, 1969; Derrick, 1982). Conglomerate and sandstone of the Bigie Formation lie unconformably on the Quilalar Formation and are intercalated with rhyolite flows in the Fiery Creek Volcanics (Betts et al. 1996) and Carters Bore Rhyolite.

The Mt Isa Rift Event occurred from 1708Ma (Page and Sweet, 1998) until 1653Ma (Page and Sweet, 1998). Temporally distinct rift sub-basins, each having similar dimensions and sharing bounding structures with the older Leichardt Rift, were superimposed onto the older Leichhardt basin (Figures 1, 2b) (Betts et al., 1998). The Mt Isa Rift developed under kinematic conditions distinct from the Leichardt Rift (Betts et al., 1988) and after termination of rifting at 1653Ma continued to develop as a 'sag' basin due to thermal subsidence until ~1595Ma (Page and Sweet, 1998). Sedimentary rocks of the Mt Isa Rift Event host all the known world class base-metal deposits in the Western Fold Belt. Within the Mt Isa Basin, the dominant sedimentary rocks deposited during the Mt Isa Rift Event include sandstones, siltstones, dolomitic siltstones and shale. The basal Surprise Creek formation was unconformably deposited upon the underlying rocks of the Leichhardt and Myally Rift Events and consists of channel-fill conglomerates, sandstones, and siltstone (O'Dea et al., 1997a). Intrusion of the Sybella Batholith occurred at 1670Ma (Page and Bell, 1986) and preceded deposition of the Mt Isa Group.

The Warrina Park Quartzite marks the base of the Mt Isa Group sedimentary rocks (O'Dea et al., 1997a). The Mt Isa Group consists dominantly of dolomitic and pyritic siltstones and shales and has a preserved thickness of approximately 3000m (Betts et al., 1998). In the Lawn Hill Platform, the lower member of the McNamara Group (~3000m thick) correlates with the Mt Isa Group in the Leichhardt River Fault Trough and also comprises dolomitic siltstones, sandstones and mudstones (Figure 2) (Betts et al., 1998). The deeper water sandstone, siltstone, and shale sequences of the Upper McNamara Group attained a thickness of 8km (Andrews, 1998) and are not preserved in the Leichhardt River Fault Trough (O'Dea et al., 1997a).

The Isan Orogeny, from 1600 to 1500Ma marks the end of sedimentation in the Lawn Hill Platform at 1595Ma (Page and Sweet, 1998). The Isan Orogeny involved components of both north-south and east-west shortening and sub-vertical extension causing crustal thickening (O'Dea et al., 1997b).

Deformation in the Mt Isa Inlier during the Isan orogeny was not associated with accretion of ophiolites, growth of magmatic arcs, or high-pressure metamorphism. Orogenesis was therefore not associated with an active subduction zone (O'Dea et al., 1997b). The distribution of deformation features in the basin fill of the Mt Isa Rift rocks has been interpreted to be partly controlled by reactivation of basement structures during mid-Proterozoic orogenesis (O'Dea et al., 1997b; MacCready et al., 1998). Reactivation of east-west striking basement faults during north-south crustal shortening (D_1) resulted in the development of localized east-west trending folds immediately adjacent to these faults (Figure 3) (O'Dea et al., 1997a,b; Betts and Lister, 2002). Apparently similar

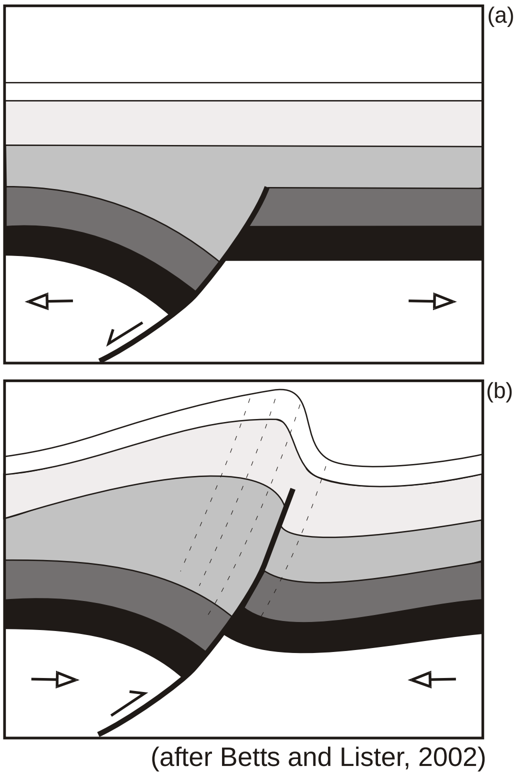

Figure 3. (a) East-west trending extensional faulting during the Leichhardt and Myally Rift Events formed half-grabens filled during synchronous and subsequent sedimentation. (b) North-south directed shortening caused buttressing of upper level sediments against basement rocks at the fault position. Reactivation of the fault and the resultant basin inversion created folds and zones of foliation development adjacent to and up-dip from the early formed faults. Note that the reactivation of the buried fault resulted in a fold in the overlying sediments.

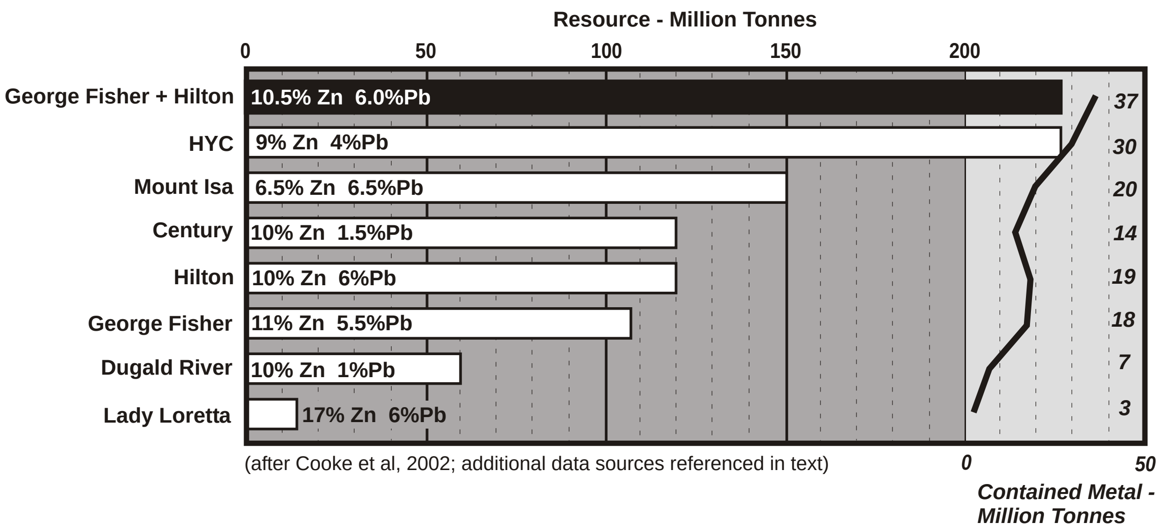

Figure 4. Summary of resource information for the major Zn-Pb-Ag deposits in the Mt Isa and McArthur Inliers (refer to Figure 1 for localities).

deformation partitioning in sedimentary rocks overlying a crystalline basement in the French Alps is interpreted to have occurred where basement blocks, formed during rifting, act as buttresses during subsequent deformation (Gratier and Vialon, 1980). East-west trending slaty cleavage and associated folding (Winsor, 1986) occurs in the vicinity of interpreted older growth faults in the underlying Leichardt Rift rocks (Derrick, 1982) resulting in a deformation style analogous with that inferred by Gratier and Vialon (1980). O'Dea and Lister (1995) interpret east-west striking high-strain zones in the hangingwall of normal faults as the effect of local strain in basin sediments buttressed against basement during deformation in the Crystal Creek area. Betts and Lister (2002) infer the formation of antiformal folds above reactivated basement faults near the Century deposit during half-graben inversion. Subsequent east-west shortening (D_2) produced crustal-scale north-south trending folds with a pervasive foliation (Bell, 1983; Blake, 1987). Further weak local deformations (D_3 – D_4+) associated with minor folds and sporadic cleavage development formed during subhorizontal east-west shortening (D_4) and intervening subhorizontal extension (D_3) (Valenta, 1988, 1994; Bell and Hickey, 1998; Chapman, 2004). These late minor deformations may not have regional analogs due to reactivation of earlier formed structures but are significant at the scale of Zn-Pb-Ag orebodies.

3. Characteristics of the setting of the Mt Isa, George Fisher-Hilton, Lady Loretta, and Century Zn-Pb-Ag deposits.

The Mt Isa, George Fisher/Hilton, Lady Loretta, and Century deposits will now be described in terms of their defining geological characteristics and setting in the context of the above mentioned tectonostratigraphic history.

3.1 Mt Isa

The Mt Isa Zn-Pb-Ag deposit is located in the Leichhardt River Fault Trough division of the Western Fold Belt (Figure 1). The Mt Isa Zn-Pb-Ag deposit had a pre-mining resource in the order of 150 million tonnes at 6.5% Zn, 6.5% Pb, and 149g/t Ag (calculated from data in: Forrestal, 1990) for approximately 19.5 million tonnes of contained metal (Figure 4). The deposit consists of stacked stratiform sulphide-rich packages of stratigraphy hosted within pyritic siltstones and shales of the Urquhart Shale formation in the Mt Isa Group (Figures 2 and 5a). The deposit is proximal to the Mt Isa-Paroo Fault system (Figure 5a). The Paroo Fault, implicated in the genesis of the Mt Isa Zn-Pb-Ag and Cu orebodies, is interpreted to represent a bounding fault to a half-graben formed during the Leichhardt Rift Event (Figures 1 and 2a and b) and subsequently reactivated during the Mt Isa Rift Event and basin inversion associated with the Isan Orogeny (Betts and Lister, 2002).

Fold zones with steeply dipping axial planes deform the sequence and are interpreted to be of D_4 age (Davis, 2004, Perkins 1997 (D_3: equivalent of D_4 in this study)). The main

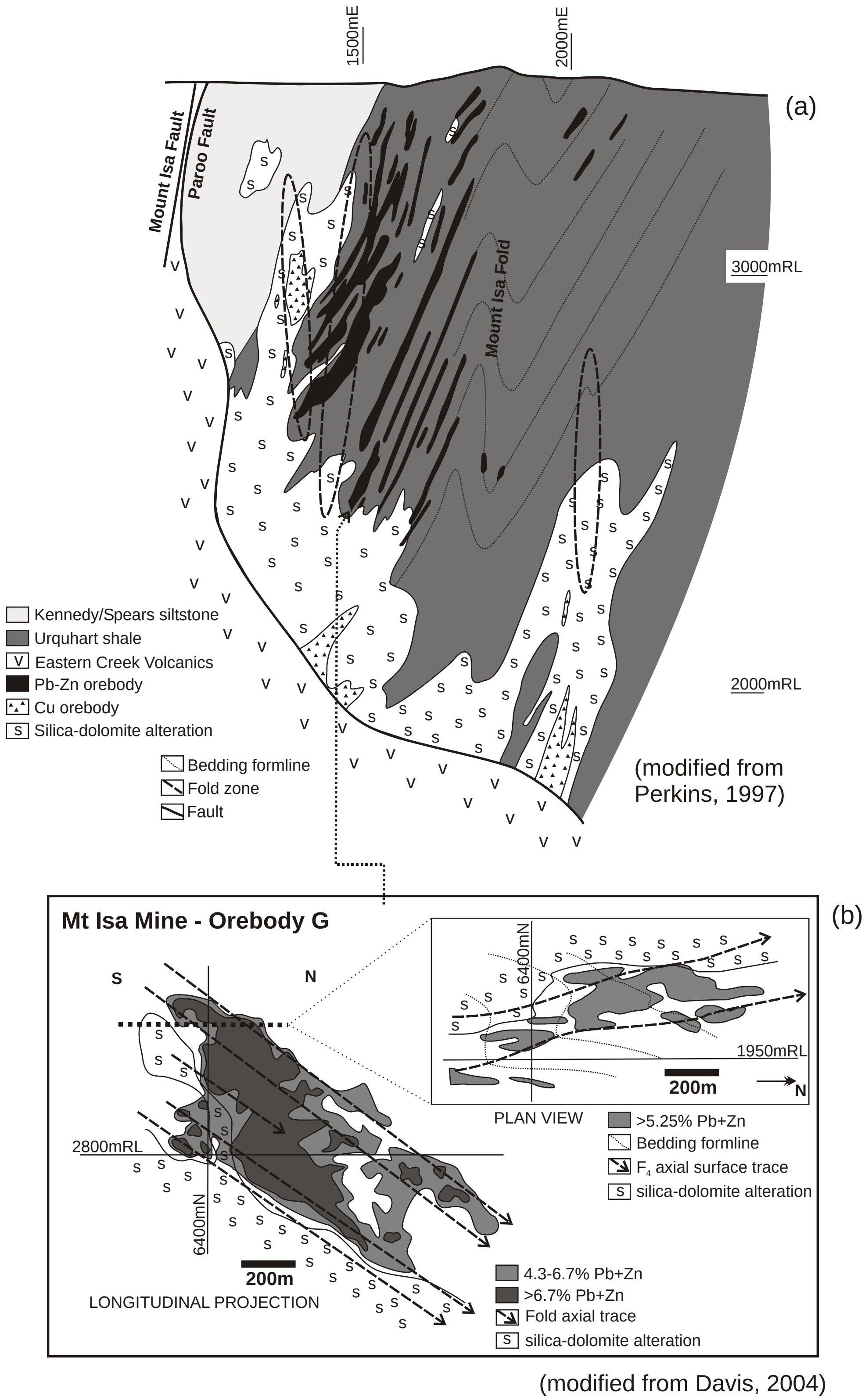

Figure 5. (a) Section at 6999N through the Mt Isa Mine showing orebody distribution and major zones of folding. The Zn-Pb-Ag orebodies have eastern terminations approximately coincident with the axial plane of the Mt Isa Fold. (b) Longitudinal projection and plan view of metal grades for G orebody in the Mt Isa deposit illustrating the parallelism of high-grade shoots and the F_4 fold axes and the apparent termination of mineralization along F_4 fold zones

fold zones control ore distribution such that the main body of mineralization is contained between the hinge zones (Figures 5a and b) (Wilkinson, 1995; Myers et al., 1996). This relationship is illustrated in Figure 5a where mineralization is less significant east of the Mt Isa Fold and in Figure 5b where the trend and plunge of F_4 fold axes is parallel with the plunge of high-grade Zn+Pb mineralization, and the folds mark the termination of the high-grade mineralization.

The replacive nature of sphalerite and galena mineralization at Mt Isa (Grondijs and Shouten, 1937; Perkins, 1997) terminating on post-lithification veins and fractures (Perkins, 1997) and the lack of mineralization in hemipelagic sediments (Neudert, 1986) indicate that the bulk of mineralization at Mt Isa attained its present distribution via processes other than exhalation onto the seafloor (cf. Finlow-Bates, 1979; Russell et al., 1981; Large et al., 2002). Introduction of ore sulphides is interpreted as syn- to late in the deformation history during differential shear on bedding surfaces (Blanchard and Hall, 1942; Perkins, 1997). Redistribution of early Pb-Zn mineralization during pervasive silica-dolomite alteration (Figure 5a) has been considered (Myers et al., 1996). However, steeply dipping F_3 (F_4 of Davis, 2004; this study) have more control over the termination of Pb-Zn mineralization and are not always spatially coincident with the obvious silica-dolomite alteration front (Myers et al., 1996), despite stable isotopic data indicating that associated hydrothermal activity extends regionally such that all Pb-Zn ore at Mt Isa is within the silica-dolomite Cu-related alteration halo (Chapman, 1999, in review). Davis (2004) infers that the homogeneity of the Zn-Pb-Ag grade populations at Mt Isa refutes the hypothesis of orebody formation by remobilization, instead invoking a model of syntectonic ore genesis. If remobilization was the ore forming process, Davis (2004) suggests that the proto-ore occurrence was distal to the current location of orebodies at the Mt Isa deposit. However, Chapman (1999, in review) inferred that the similar stable isotopic character of carbonate minerals interpreted to be associated with Pb-Zn mineralization and silica-dolomite alteration/Cu-mineralization at Mt Isa is the result of extensive remobilzation of a proto-ore during the Cu event. In areas distal from the intense silica-dolomite alteration at Mt Isa, Pb-Zn mineralization and incipient silica-dolomite alteration/Cu-mineralization are associated with compositionally and isotopically distinct carbonate mineral assemblages.

3.2 George Fisher - Hilton

The George Fisher and Hilton Zn-Pb-Ag ore deposits are located 22km north of the Mt Isa deposit in the Leichhardt River Fault Trough (Figures 1 and 2). The deposits have total resources of 108 million tonnes at 11.1% Zn, 5.4% Pb, and 93g/t Ag (MIM report to shareholders – 1998) and 120 million tonnes at 10% Zn, 5.5% Pb, and 100g/t Ag (Large et al., 2002); respectively (Figure 4). The two deposits occur along strike from one another with approximately 2km separation (Figure 6a). The deposits are essentially two shoots within the one mineralized system separated by younger faults (Figure 6a). Combined, the two deposits comprise over 37 million tonnes of contained Pb and Zn metal in a resource of approximately 228 million tonnes. The George Fisher – Hilton deposit is therefore the largest known Pb+Zn occurrence in the Mt Isa Inlier (Figure 4) and, globally, is the second largest stratiform Pb+Zn deposit after the Broken Hill deposit (52 million tonnes contained Pb+Zn metal: Large et al., 2002).

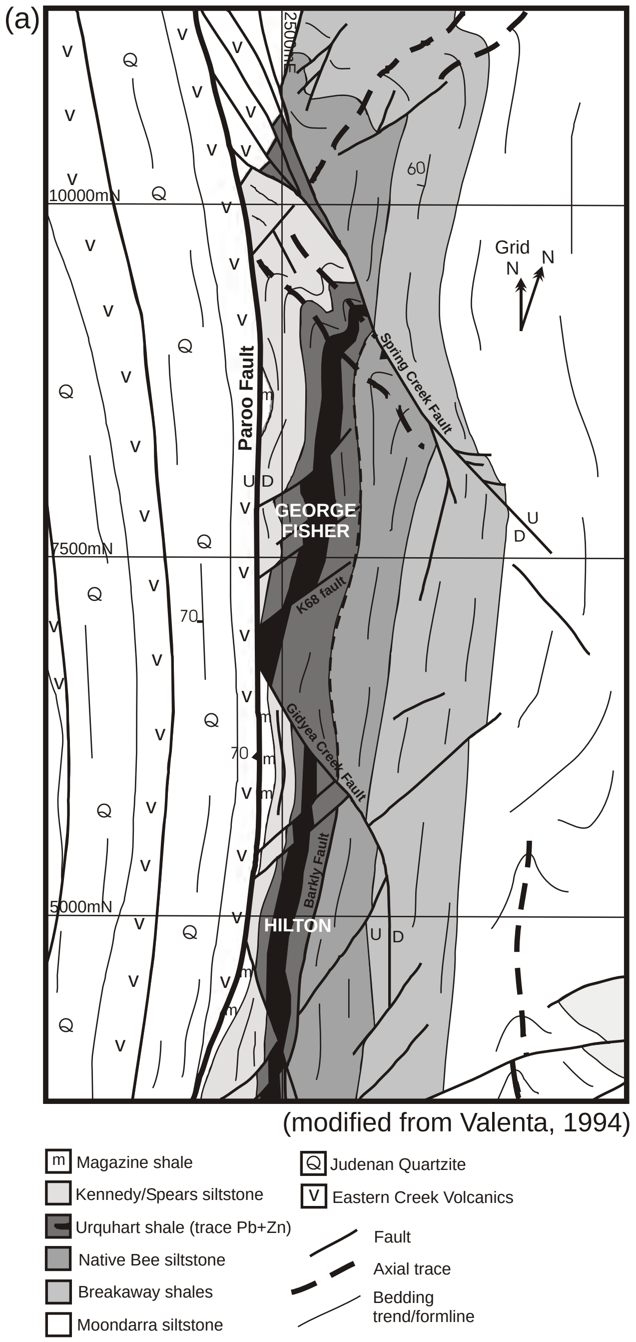

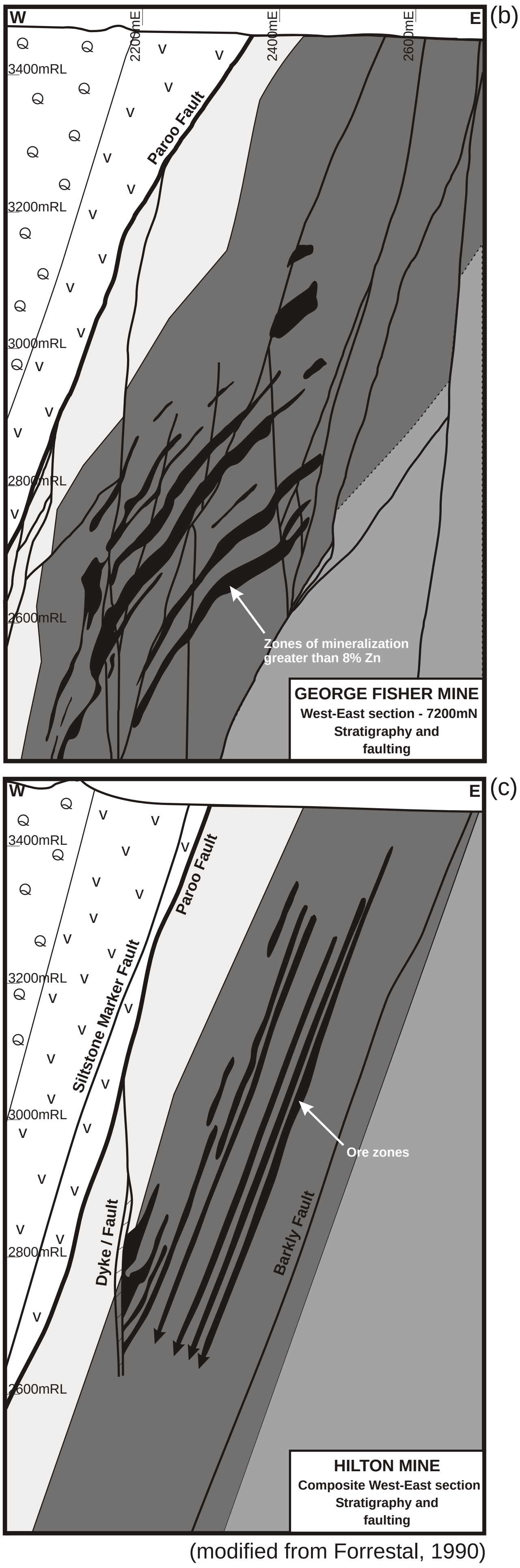

Figure 6. (a) Geological map illustrating the location of the George Fisher and Hilton deposits. The deposits appear to be part of a single hydrothermal system separated by later faulting. (b) Cross-section through the George Fisher deposit at 7200mN illustrating the distribution of mineralization greater than 8% Zn. (c) Composite cross-section of the Hilton deposit with orebody localities indicated.

The deposits consist of stacked stratiform sulphide-rich packages of stratigraphy hosted by siltstones and pyritic siltstones within the Urquhart Shale Formation in the upper Mt Isa Group (Figures 1,2 and 6a-c), proximal to the Mt Isa-Paroo Fault system (Figure 6a-c). Four deformation episodes are interpreted to have affected the host rocks at George Fisher and can be correlated with structural features in the Mt Isa deposit 22km to the south. The stratiform and stratabound nature of the sulphides has been interpreted as either syngenetic/SEDEX type mineralization (Mathias et al., 1971; Sawkins, 1984) or syn-diagenetic as the mineralization was interpreted to be overprinted by deformation features (Valenta, 1994; Chapman, 2004) and were spatially correlated with diagenetic calcite alteration (Chapman, 1999).

At George Fisher, the highest grade and thickest mineralization (Figures 7a and b) plunges steeply to the south-west within the short-limb of a deposit-scale F_1 fold (Figure 7a). The F_1 fold is represented by an s-shaped flexure in bedding in plan view (Figure 7b). Subsidiary ore shoots parallel to fold axes formed during D_2 and D_4 are discussed in Part B. Vein and breccia-hosted ore types which dominate the main steeply pitching ore shoot are here interpreted as post-D_2, the main phase of folding in the Leichhardt River Fault Trough. Formation of the present metal distribution is inferred to be controlled by the kinematics of D_4 whereby dilation was focussed within the F_1 short-limb zone thereby enhancing fluid flow in this region.

The distribution of diagenetic calcite alteration determined by Chapman (1999) also exhibits a spatial correlation with the F_1 fold short-limb (Figure 8). Calcite alteration occurs over wider intercepts and forms higher proportions of the rock within the F_1 short-

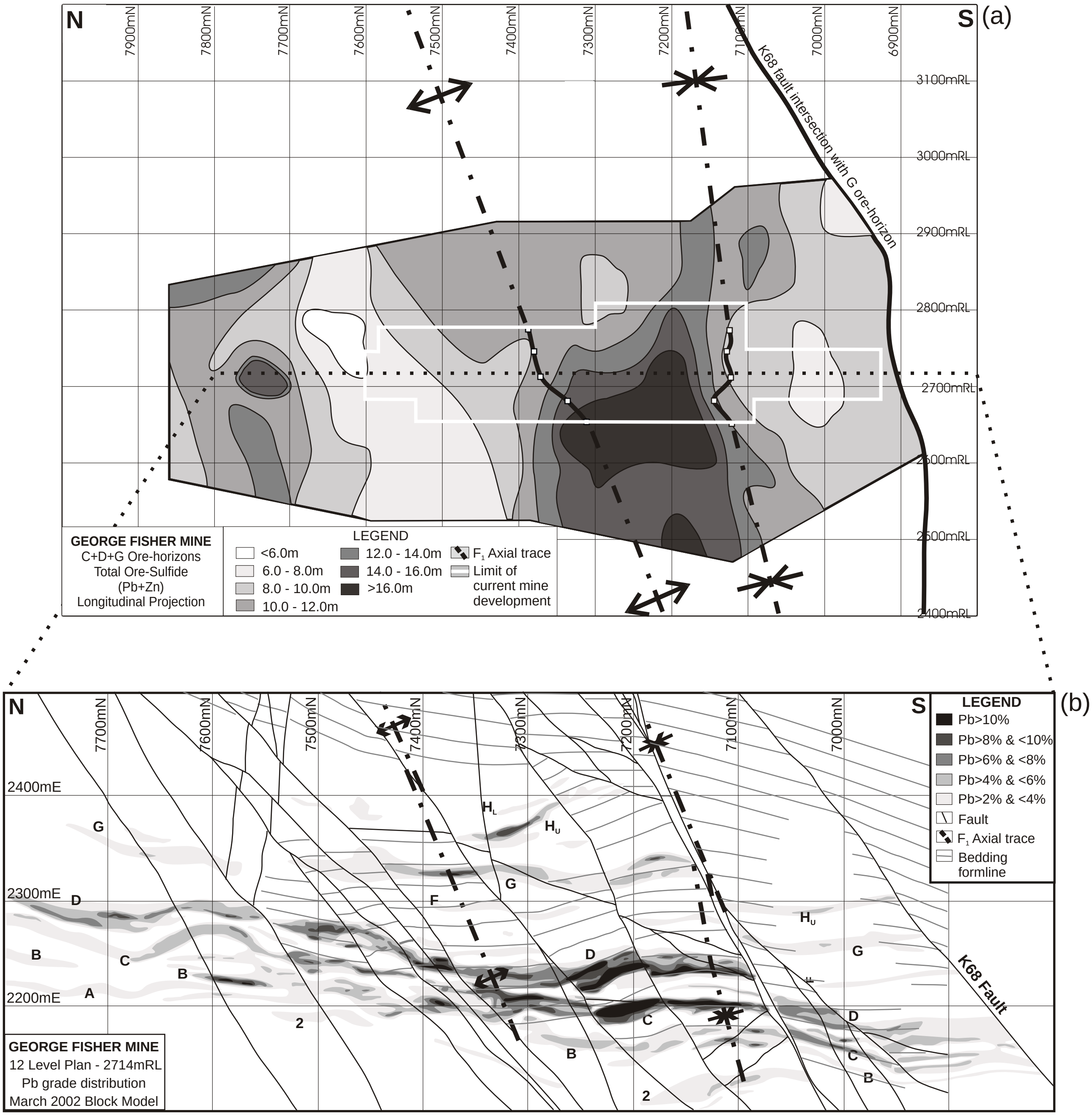

Figure 7. (a) Longitudinal projection of sulphide thickness measured from drill-hole intersections through the C, D, and G ore-horizons (relative positions of the ore-horizons is illustrated in (b)). The thickest ore-sulphides occur within the short-limb of the F_1 fold and the shoot plunges sub-parallel to the F_1 axes. (b) In plan view, contoured Pb grades demonstrate the preferential mineralization of the F_1 short-limb zone in adjacent ore-horizons.

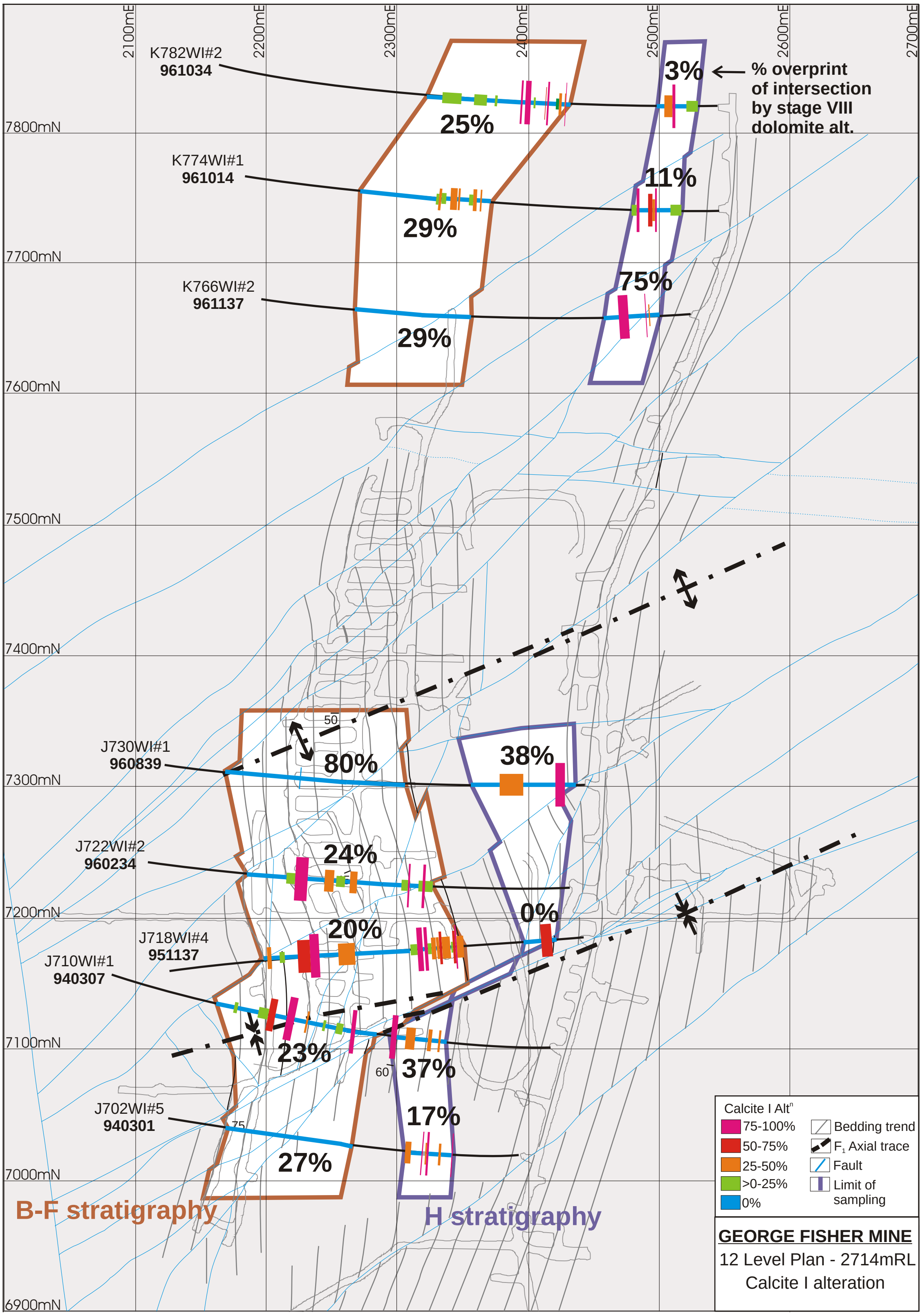

Figure 8. Plan view of 12 Level of the George Fisher Mine with traces of drill-holes analysed by Chapman (1999). Coloured bars indicate the approximate proportion of diagenetic calcitic alteration as indicated in *Part C figure1-3* of Chapman (1999). Percentages in black indicate the proportion of overprinting by later ferroan dolomite (Chapman, 1999). Calcite alteration is most prevalent in the F_1 short-limb suggesting that this structure may have focussed fluids during the early hydrothermal history of the deposit.

limb zone than in those rocks to the south and north of the F_1 short-limb. This implies that the fold has had some control over the development of the alteration and that both occurred during diagenesis and the onset of basin inversion. The east-west trending F_1 fold is interpreted to be related to folding and faulting of a similar orientation to the east of George Fisher in the Lake Moondarra area (Winsor, 1986). Folding of these structures by district-scale F_2 folds confirms their early relative timing (refer to Part A – Figure 2). The F_1 fold central to the George Fisher deposit may therefore have focussed fluid flow from as early as diagenesis through to the later stages of orogenesis recording a long-lived and complex hydrothermal system as described by Chapman (1999, 2004).

3.3 Lady Loretta

The Lady Loretta Zn-Pb-Ag deposit occurs within the Lawn Hill Platform (Figure 1). The deposit is stratiform and has a resource of 13.6 million tonnes at 17.1% Zn, 5.9% Pb, and 97g/t Ag (Noranda company report – 2000) with approximately 3 million tonnes of contained metal (Figure 4). Lady Loretta therefore represents the smallest and highest grade deposit of the Zn-Pb-Ag deposits in the Western Fold Belt discussed here. The deposit is hosted by siltstones and pyritic siltstones of the Lady Loretta Formation which occurs at the top of the Lower McNamara Group (Figure 2). The Lower McNamara Group correlates with the Mt Isa Group sediments (Betts et al., 1998) which host the Mt Isa and George Fisher-Hilton ore deposits. The age, geological setting, and ore characteristics of the Lady Loretta deposit are interpreted to be similar to that of the Mt Isa and George Fisher-Hilton deposits (Hancock and Purvis, 1990). The Lady Loretta orebody is located within a doubly-plunging F_2 syncline (Lee, 1972; Loudon et al., 1975) which is overprinted by minor F_3 folding with northwest trending axes (Lee, 1972)

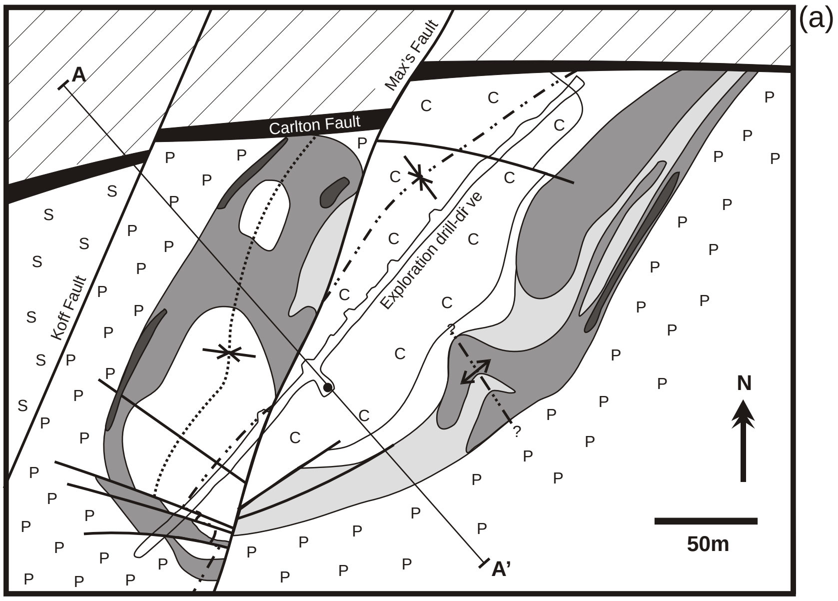

(modified from Hancock and Purvis, 1990)

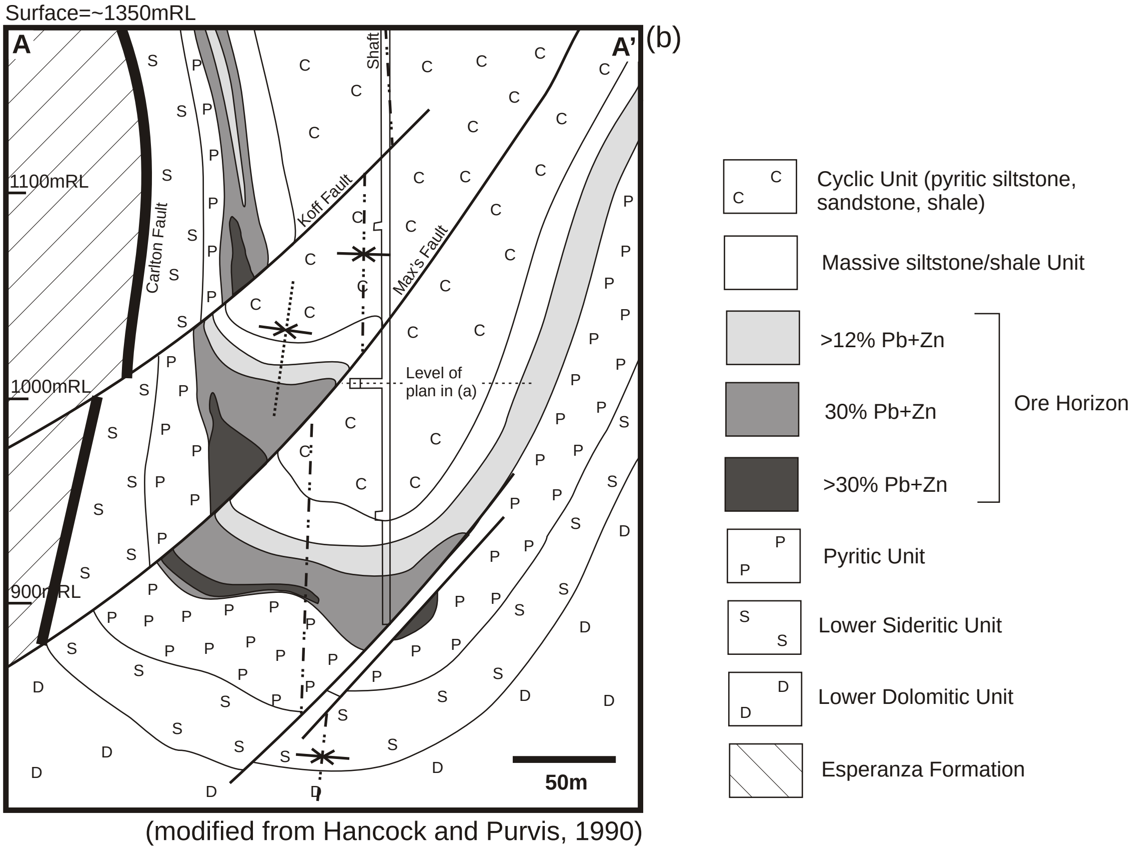

(modified from Hancock and Purvis, 1990)

Figure 9. (a) Plan view of the Lady Loretta deposit at the 100mRL illustrating the structural features that affect the distribution of Zn-Pb-Ag mineralization. The northeast trending F_2 syncline is cut by the Carlton Fault and overprinted by north-northeast striking reverse faults and associated drag- folding. (b) Section A-A' (see (a)): the north-northeast trending reverse faults correlate with significant changes in the thickness and distribution of high-grade mineralization. These faults postdate the F_2 syncline. Note that the distribution of ore is not symmetrical about the F_2 axial plane on this section.

(Figure 9a, b). The deposit is adjacent to the district-scale ENE striking Carlton Fault (Figure 9a), which attains a width of 200m of shearing and brecciation, and which brings older rocks of the Lower McNamara Group into contact with the ore sequence (Hancock and Purvis, 1990). The Carlton Fault cross-cuts the F_2 syncline and is not folded by the F_2 fold. The Carlton Fault therefore has a movement history which postdates the main phase of folding at Lady Loretta. This fault has previously been described as a possible conduit for mineralizing fluid (Lee, 1972; Hancock and Purvis, 1990). It has also been described as a growth fault with movement occurring during deposition of the ore sequence (Hancock and Purvis, 1990). The growth fault interpretation is disputed by Dunster and McConachie (1998) who found no evidence for unusual facies or thickness changes proximal to the fault and determined that features of the inter-ore breccias are not consistent with their formation during syn-sedimentary faulting. The fault was therefore considered to postdate mineralization (Dunster and McCDonachie, 1998). The F_2 syncline and Carlton Fault are offset by the reverse-sinistral NNE striking Max's and Koff Faults (Figure 9a, b). Displacement on these oblique-slip reverse faults is in the order of 15-30m laterally and 50-65m dip-slip (Figure 9a, b). The thickness and grade of the ore sequence increases where intersected by these faults (Figure 9b). The thickness and grade of the ore sequence does not correlate across these faults (Figure 9b). Max's Fault creates a synform in the ore sequence (Figure 9b) which parallels the strike of the fault (Figure 9a). From published geological interpretations, these faults, and associated folds appear to have the most significant affect on ore distribution (Hancock and Purvis, 1990).

Recrystallization of sulfides (Loudon et al., 1975; Hancock and Purvis, 1990; McGoldrick et al., 1996) is attributed to deformation of the deposit during fold-forming orogenesis. However, the timing of a tectonic fabric within the deformation history of the deposit is not established. Though deformation has produced pervasive recrystallization, remobilization and discordant sulphide veining appear uncommon (Hancock and Purvis, 1990). Thickening of the ore sequence and higher grade material has been interpreted to be related to the 'keel' or hinge of the F_2 syncline (Hancock and Purvis, 1990). However, the Max's and Koff reverse faults appear to correlate with a more significant change in grade distribution. The geographical centre of the high grade zone in the cross-section in Figure 9b is on the western limb of the F_2 syncline as opposed to the hinge.

Genetic models for the Lady Loretta deposit consist of variations on the syngenetic sedimentary exhalative hypothesis whereby sulphides precipitate from fluids expelled from a fault in the seafloor with contemporaneous infilling of pores in subsurface sediments (Loudon et al., 1975; Hancock and Purvis, 1990; McGoldrick et al., 1996). The Carlton Fault, or its pre-D_2 equivalent, is the most likely source of mineralizing fluid in the Lady Loretta deposit. Post-D_2 reverse faults appear to have significant controls on ore distribution despite previous interpretation that remobilization is insignificant.

3.4 Century

The Century Zn-Pb-Ag deposit is located in the northern reaches of the Lawn Hill Platform (Figure 1). This deposit comprises stratiform mineralization with a subhorizontal to gently dipping attitude. Century is zinc-dominant and has a total resource of 118 million tonnes at 10.2% Zn, 1.5% Pb, and 36g/t Ag (Broadbent et al.,

1998) for approximately 14 million tonnes of contained metal (Figure 4). The deposit is hosted within laminated siltstones and shales of the 1595±6 (Page et al., 1994) Lawn Hill Formation (Figure 2) which is approximately 60 million years younger than the host rocks to mineralization at the Mt Isa, George Fisher-Hilton, and Lady Loretta deposits. Sulphide mineralization is concentrated in the shale horizons (Broadbent et al., 1998). The Century deposit is situated in a region characterised by abundant F_1 folds and faults and later F_2 folds which have a near-orthogonal intersection angle with F_1 (Figure 10). This style of fold interference pattern has been described as 'dome and basin folding' (Broadbent et al., 1998), and represents a type 'A' interference pattern (Ramsay and Huber, 1987) (Figure 10).

Mineralization is interpreted to be spatially coincident with a hydrocarbon trap and liquid hydrocarbons are inferred to have facilitated thermochemical reduction of the ore fluid resulting in precipitation of sulphides (Broadbent et al., 1998). Ore fluid ingress was controlled by microfracture networks developed during repeated overpressuring of the sequence during basin inversion and regional deformation (Broadbent et al., 1998). Three sphalerite±galena mineralization stages are recognized at Century with post-compaction/pre-folding, syn-folding, and post-folding relative timing (Broadbent et al., 1998). The lead model age for the Century deposit is 1570±5Ma (Ord et al., 2002; Carr et al., 1996) which is 20my younger than the age of the host rocks (1595±6; Page et al., 1994). The formation of the Century deposit is therefore inferred to have initiated during late-diagenesis/post-compaction and continued during north-south (D_1) and east-west directed shortening (D_2) of the Isan Orogeny. Numerical modelling of fluid flow associated with both the D_1 and D_2 episodes indicates that hydrofracturing occurs during

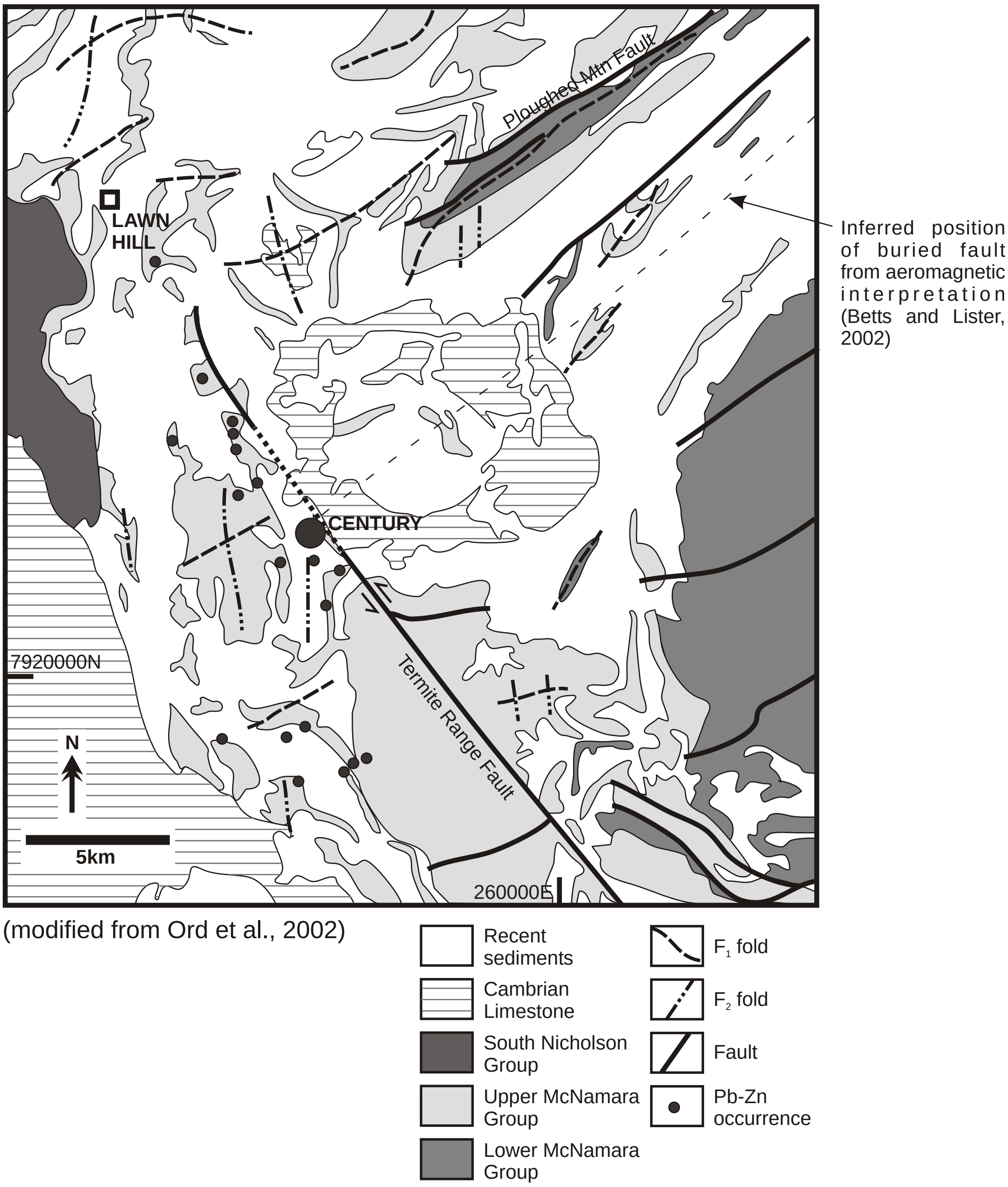

Figure 10. Geological map of the area encompassing the Century deposit. The Zn-Pb-Ag deposit is adjacent to the regional Termite Range Fault and occurs in the upper McNamara Group stratigraphy which has undergone 'dome and basin' folding (Broadbent et al., 1998). This is interpreted as the interference pattern produced by north-south oriented F_2 folding of east-northeast trending F_1 folds. Betts and Lister (2002) have interpreted a buried normal fault to the east of and intersecting the Termite Range Fault in the vicinity of the Century deposit. The intersection of these structures is interpreted as a region of enhanced fluid flow possibly supplying ore fluid in the formation of the deposit (Betts and Lister, 2002)

southeast-northwest shortening (D_1). However during D_2, hydrofracturing and related flow-focussing ceases (Ord et al., 2002). Despite this, increased topographic relief due to crustal thickening during the Isan Orogeny is implicated in driving fluid flow up faults normal to the Termite Range Fault to a locus of fluid mixing and sulphide precipitation (Ord et al., 2002). D_1 folding of fissile shales is considered a critical factor in exploration for Century-style mineralization (Ord et al., 2002).

4. Discussion

4.1 Common and contrasting features in the setting of the Zn-Pb-Ag deposits of the Western Fold Belt and implications for exploration

A key similarity between each of the deposits is the comparable host-lithologies comprising calcareous and variably carbonaceous siltstones, pyritic siltstones and shales. The Lady Loretta deposit differs in that barite is present in the ore-bearing stratigraphy but this is clearly not a requirement in the genesis of the larger base-metal deposits (Loudon et al., 1975; Large et al., 2002). Pyritic siltstone/shale are present at each deposit and interpretations of the formation of the fine grained pyrite range from syngenetic precipitation of pyrite with deposition of the host sequence (Finlow-Bates et al., 1977), synsedimentary to early diagenetic precipitation in H_2S producing micro-organisms (Love and Zimmerman, 1961), syndiagenetic replacement subsequent to compaction (Chapman, 1999), and post-diagenetic cleavage replacement (Perkins, 1998). Both syngenetic (Finlow-Bates et al., 1977) and syndeformational (Perkins, 1998) modes of formation are genetically related to the Pb+Zn mineralization system. However, syndiagenetic formation of the fine-grained spheroidal pyrite is inferred to have occurred during a distinct hydrothermal event from the base-metal mineralization (Williams, 1978a, b; Chapman, 1999). This is supported by sulfur (Smith and Croxford, 1973) and lead (Gulson, 1975) isotope studies which indicate that the fluids that formed the pyrite and Pb+Zn mineralization were derived from different sources (Schieber, 1990). Extensive pyritic shale horizons occur in Proterozoic basins in Montana, USA without significant Pb+Zn occurrences (Schieber, 1990). The pyritic siltstones show a striking resemblance to those of the Leichhardt River Fault Trough and Schieber (1990) concluded that the formation of pyritic shale/siltstone as microbial mats may be unrelated to the processes which form giant lead-zinc deposits. Pyritic rocks may however be preferential hosts to later-formed lead-zinc mineralization.

Another key element which links the stratiform Zn-Pb-Ag deposits discussed here is their proximity to district-scale faults which have long movement histories and have undergone reactivation throughout the Isan orogeny. The Mt Isa and George Fisher – Hilton Zn-Pb-Ag deposits are situated 200-300m from the Mt Isa – Paroo Fault system which may have been active during the Leichhardt Rift Event (from 1790Ma; Page, 1983) and therefore predates the formation of host-rocks to Zn-Pb-Ag mineralization (Betts and Lister, 2002). The Lady Loretta deposit is adjacent to the Carlton Fault, which may have predated deposition of the stratigraphy (1647Ma; Betts and Lister, 2002) hosting mineralization at the deposit (Hancock and Purvis, 1990). Both faults have subsequently been reactivated and now truncate stratigraphy and the ore sequence. The Century deposit is bounded by the Termite Range Fault which is interpreted to be the surface expression of reactivation of a deep-rooted shear zone which predates the Mt Isa Rift Event (Betts and Lister, 2002). Each of these faults are significant at the district-scale, may represent reactivation of a basement structure, and have a movement history which incorporates the entire diagenetic and deformation history of the host-rocks, although their movement histories cannot confidently be linked to the sedimentary history of the host sequences as reactivation during subsequent extensional and compressional events has obscured these relationships. At each deposit, the major fault which occurs in close proximity or bounds the deposit has been inferred as a conduit potentially supplying metal-bearing fluids to the site of mineralization.

There is at least an empirical relationship between the location of the Zn-Pb-Ag ore deposits and D_1 folds and/or faults. As discussed above, the Mt Isa – Paroo Fault system and Termite Range Faults are interpreted as pre-Mt Isa Rift structures and may therefore have been active during D_1 of the Isan Orogeny. The Century deposit is situated in a region characterized by the intersection of east-northeast striking D_1 folds and faults and the northwest striking Termite Range Fault. Dome and basin folding reported by Broadbent et al. (1998) and implicated in the genesis of the Century deposit, occurs where F_1 and north-south trending F_2 folds intersect at a high angle (Figure 10). Betts and Lister (2002) interpret the Century deposit to lie at the intersection between the Termite Range Fault and a buried east-northeast trending fault to the east of the Termite Range Fault (Figure 10). However, the Century deposit lies to the west of the Termite Range Fault and sinistral offset on the fault during the east-west horizontal shortening of the Isan Orogeny mean that the deposit and the 'buried fault' were not originally juxtaposed (Figure 10). The Lady Loretta deposit is located on the east-northeast striking Carlton Fault which was probably active during D_1 (Hancock and Purvis, 1990). At George Fisher, the deposit is centred on an open F_1 fold with an east-northeast striking axial plane. This fold has equivalent relative timing and parallels F_1 folds and faults mapped by Winsor (1986) in the lake Moondarra area to the east of George Fisher.

Each of the deposits occurs at a location where F_2 folding intersects earlier D_1 structures. This may not be such a useful tool for exploration given that the D_2 deformation is pervasive throughout the Mt Isa Inlier, however, it is probable that areas of F_2 folding focus later deformations and associated hydrothermal activity. The intersection of F_1 and F_2 folding may therefore help define prospective sites for structurally controlled mineralization.

The inferred genetic significance of F_4 folding at the Mt Isa deposit (Wilkinson, 1995; Myers et al, 1996; Perkins, 1997; Davis, 2004) is not replicated at the other deposits discussed in this paper. However, post-D_2 reverse faulting and associated drag-folds at Lady Loretta coincide with ore shoots of high grade and greater thickness. D_4 kinematics are inferred to have focussed ore fluid into structural sites at the George Fisher deposit. F_4 folding at the scale observed at the Mt Isa deposit (Figure 5a) is not recognized at the George Fisher – Hilton, Lady Loretta, or Century deposits. This is consistent with the association of D_4 structural elements with copper mineralization at Mt Isa (Perkins, 1997; Bell et al., 1988; Van Dijk, 1991), and the lack of associated extensive, high-grade copper mineralization similar to that found adjacent to the Mt Isa Zn-Pb-Ag deposit at the other deposits. However, studies of copper mineralization in the northern region of the Western Fold Belt by Van Dijk (1991) identified a relationship between D_1 structures and copper mineralization and infers that D_3 (D_4 – this study) extension at a high angle to D_1 structures optimized hydraulic brecciation through repeated cycles of dilation, resulting in alteration and mineralization replacing the brecciated host rock and progressing upward along steeply inclined bedding, cleavage, and earlier formed veining.

The Mt Isa, George Fisher – Hilton, Lady Loretta, and Century deposits are hosted by sedimentary rocks with ages that span approximately 60 million years. If sedimentary exhalative models were the main control on ore formation and an assumption that all of the Zn-Pb-Ag deposits formed in a similar manner, deposits should be hosted within a geological unit representing a more limited time span given that Finlow-Bates (1979) inferred sulfide deposition to occur at a rate of approximately 1cm/week. Exploration strategies based purely on stratigraphic correlation are therefore inadequate in the Western Fold Belt. The similar host-rock lithologies, proximity to district-scale faults, and shared early orogenic history enable prospectivity to be assessed based upon the broader setting of the giant ore deposits described in this study. An apparent trend in the timing of ore formation relative to deformation history from Century to George Fisher to Mt Isa (north to south) exists as: late-diagenetic/D_2 to late-diagenetic/post-D_2/D_4 to D_4 timing, respectively. Ambiguity in the interpretation of the timing of these deposits arises from the inference that structurally controlled mineralization may or may not be remobilized. At the George Fisher deposit it is apparent that the F_1 fold which focussed diagenetic hydrothermal activity and alteration also acted as a heterogeneity focussing dilation and final sites of mineralization. It is possible that diagenetic processes prepared the host-rock for later mineralization at George Fisher.

4.2 *Significance of D_1 (approximately east-west oriented) structures and implications for Zn-Pb-Ag metallogenesis in the Western Fold Belt of the Mt Isa Inlier*

D_1 folds and/or faults are implicated in each of the deposits discussed from focussing diagenetic fluid to focussing dilation during post-D_1 tectonism. These structures are interpreted as being related to reactivated basement faults (O'Dea et al., 1997a,b; Betts and Lister, 2002) and therefore it is likely that they or at least any related faults can tap fluids from deeper levels. Connectivity of these features with regional faults (e.g. the Termite Range Fault) enhances fluid flow to sites of near surface mineralization. At the regional scale, Betts and Lister (2002) propose that the intersections of the D_1 'cross-faults' and regional faults create dilational zones which channel ore fluid. Observations at individual deposits reveal that the effects of the D_1 deformation are subtle and partly obscured by overprinting deformation during the main phase of the Isan Orogeny.

Approximately east-west trending zones of D_1 deformation are not recognized in the vicinity of the Mt Isa deposit perhaps because of the particularly strong later F_4 folding. However, Betts and Lister (2002) interpret the Paroo Fault as a half-graben bounding structure during the Leichhardt Rift Event subsequently reactivated during the Mt Isa Rift Event. At the George Fisher deposit, an interpreted F_1 fold with east-northeast striking axial planes is spatially coincident with diagenetic alteration (Figure 8) and hosts the main ore shoot of higher grade Zn-Pb-Ag mineralization at the deposit (Figure 7a and b). Successive phases of hydrothermal activity responsible for calcite alteration, fine-grained pyrite formation, calcite+k-feldspar+hyalophane+celsian+quartz vein development, and sphalerite mineralization have been described at the George Fisher deposit (Chapman, 1999). Spatial coincidence of these events and the present day metal distribution, with the F_1 fold at George Fisher suggests that the F_1 fold has focussed fluid flow from diagenesis through to D_2-D_4 stages. The fold is a subtle feature, but if it is the upper level expression of a reactivated basement fault then the longevity of the hydrothermal system responsible for mineralization at George Fisher can be rationalized. The F_1 fold is considered a key element in the formation of mineralization at the George Fisher deposit. D_1 cross-faults (east-west striking in the Lake Moondarra area; refer to Part A – Figure 2) are interpreted to be related to the Myally Rift Event and when extrapolated along strike, these features intersect the Paroo Fault near the ore deposits on the western edge of the Mt Isa valley (Betts and Lister, 2002). Intersections of these fault systems have been inferred to be potentially important fluid conduits by Betts and Lister (2002). The configuration of fault systems produced throughout extensional basin formation is considered favourable for hydrothermal activity and passage of ore-fluids regardless of the timing of the hydrothermal event (Betts and Lister, 2002).

Similarly, the Carlton Fault at the Lady Loretta deposit (Figures 9a and b) has been interpreted as the fluid conduit which has supplied metals to the small but high grade Zn-Pb-Ag deposit.

At the Century deposit, results from fluid flow modelling infer that fluid was focussed into favourable layers during hydrofracturing associated with D_1 southeast-northwest directed shortening (Ord et al., 2002). Increased topographic relief due to crustal thickening during the Isan Orogeny is implicated in driving fluid flow up D_1 faults normal to the Termite Range Fault to a locus of fluid mixing and sulphide precipitation (Ord et al., 2002). D_1 folded carbonaceous shales are considered a key factor in exploration for Century-style mineralization (Ord et al., 2002).

5. Conclusions

The Zn-Pb-Ag deposits of the Western Fold Belt are hosted by sedimentary rocks deposited during the later stages of at least two overprinting extensional events. Mineralization occurs in calcareous and variably carbonaceous shales, siltstones, and pyritic siltstones. Host-rocks to the respective deposits vary in age by approximately 60 million years from 1655 to 1595Ma. Despite this, the structural history of the Mt Isa, George Fisher – Hilton, Lady Loretta, and Century deposits have similarities. Identification of similar structural histories in other prospects may be useful as exploration tools. Each of the deposits is proximal to a district to regional-scale fault which was active during D_1. These may be primary basin-bounding faults such as the Mt Isa – Paroo Fault system and Termite Range Fault or secondary reactivated basement faults such as the generally east-northeast to east-west striking faults and folds at Century, Lady Loretta, and George Fisher.

F_2 folding also occurs at each of the deposits and is likely to have influenced the development of later F_3 and F_4 fold episodes as inferred at George Fisher (refer to Part A). However, significant F_4 folding only occurs at the Mt Isa deposit, although D_4 kinematics are implicated in the focussing of dilation and potentially remobilized mineralization into the F_1 short-limb at the George Fisher deposit. At the George Fisher deposit it is apparent that the F_1 fold which focussed diagenetic hydrothermal activity and alteration also acted as a heterogeneity focussing dilation and final sites of mineralization.

The F_1 fold may be the upper level expression of a reactivated basement fault thereby accounting for the longevity of the hydrothermal system responsible for alteration and mineralization at George Fisher.

The spatial correlation of most larger stratiform Zn-Pb-Ag deposits in the Western Fold Belt with the intersection of D_1 faults and/or folds with D_2/D_4 structures in calcareous/carbonaceous siltstones and shales may be used as an indicator of prospectivity in the exploration for further deposits of this type.

References

Andrews, S.J., 1998. Stratigraphy and depositional setting of the Upper McNamara Group, Lawn Hill region: Economic Geology, v. 93, p. 1132-1152.

Bell, T.H., 1983. Thrusting and duplex formation at Mount Isa, Queensland, Australia: Nature, v. 304, p. 493-497.

Bell, T.H., and Hickey, K, A., 1998. Multiple deformations with successive subvertical and subhorizontal axial planes in the Mount Isa region: Their impact on geomtric development and significance for mineralization and exploration: Economic Geology, v. 93, p. 1369-1389.

Bell, T.H., Perkins, W.G., and Swager, C.P., 1988. Structural controls on development and localization of syntectonic mineralization at Mount Isa, Queensland: Economic Geology, v. 83, v. 69-85.

Betts P.G., Pound, K.S., and Lister, G.S., 1996. Episodic rift-sag sequences in Cover Sequence 3, northwestern Mount Isa Inlier: Geological Society of Australia Abstracts, v. 41, p. 32.

Betts, P.G., Lister, G.S., and O'Dea, M.G., 1998. Asymmetric extension of the middle Proterozoic lithosphere, Mount Isa terrane, Queensland, Australia: Tectonophysics, v. 296, p. 293-316.

Betts, P.G., Ailleres, L., Giles, D. and Hough, M., 2000. Deformation history of the Hampden Synform in the Eastern Fold Belt of the Mt Isa terrane: Australian Journal of Earth Sciences, v. 47, p. 1113-1125.

Betts, P.G. and Lister, G.S., 2002. Geodynamically indicated targeting strategy for shale-hosted massive sulfide Pb-Zn-Ag mineralisation in the Western Fold Belt, Mt Isa terrane: Australian Journal of Earth Sciences, v. 49, p. 985-1010.

Betts, P.G., Giles, D., Lister, G.S., and Frick, L.R., 2002. Evolution of the Australian lithosphere: Australian Journal of Earth Sciences, v. 49, p. 661-695.

Blake, D.H., 1987. Geology of the Mount Isa Inlier and environs, Queensland and Northern Territory: Bureau of Mineral Resources Bulletin 225.

Blake, D.H., Etheridge, M.A., Page, R.W., Stewart, A.J., Williams, P.R., and Wyborn, L.A.I., 1990. Mount Isa Inlier – Regional Geology and mineralisation, In: Hughes, F.E. (ed.), Geology of the Mineral Deposits of Australia and Papua New Guinea, Australasian Institute of Mining and Metallurgy Monograph 14, p. 915-925.

Blake, D.H. and Stewart, A.J., 1992. Stratigraphic and tectonic framework, Mount Isa Inlier, In: Stewart, A.J. and Blake, D.H. (eds), Detailed studies of the Mount Isa Inlier: Australian Geological Survey organization Bulletin 243, p. 1-11.

Blanchard, R. and Hall, G., 1942. Mt Isa ore deposition: Economic Geology, v. 32, p. 1042-1057.

Broadbent, G.C., Myers, R.E., and Wright, J.V., 1998. Geology and origin of shale-hosted Zn-Pb-Ag mineralization at the Century deposit, Northwest Queensland, Australia: Economic Geology, v. 93, p. 1264-1294.

Carr, G.R., Sun, S-S., Page, R.W., Hinman, M., 1996. Recent developments in the use of lead isotope model ages in Proterozoic terrains. In: Baker, T., Rotherham, J., Mark, G., and Williams, P.J. (eds), New Developments in Metallogenic research: The McArthur, Mt Isa, Cloncurry Minerals Province, p. 33-35. James Cook University Economic Geology Research Unit Contribution 55.

Chapman, L.H., 1999. Geology and genesis of the George Fisher Zn-Pb-Ag deposit, Mount Isa, Australia. (Unpublished PhD thesis – James Cook University, Townsville).

Chapman, L.H., 2004. Geology and mineralization styles of the George Fisher Zn-Pb-Ag deposit, Mount Isa, Australia: Economic Geology, v. 99, p. 233-255.

Chapman, L.H. Multiple episodes of hydrothermal carbonate formation in the Proterozoic Urquhart Shale and significance for the origin of Zn-Pb-Ag and Cu mineralization in the Mount Isa district, Australia: in review.

Cooke, D., McGoldrick, P., Large, R., and Bull, S., 2002. Stratiform sediment-hosted Zn-Pb-Ag deposits of northern Australia: Geological environments, characteristics and genesis. James Cook University Economic Geology Research Unit Short Course: Advances in Ore Genesis, March 2002.

Davis, T.P., 2004. Mine-scale structural controls on the Mount Isa Zn-Pb-Ag and Cu orebodies: Economic Geology, v. 99, p. 543-559.

Derrick, G.M., 1982. A Proterozoic rift zone at Mount Isa, Queensland, and implications for mineralisation: Bureau of Mineral Resources Journal of Geology and Geophysics, v. 7, p. 81-92.

Dunster, J.N. and McConachie, B.A., 1998. Tectono-sedimentary setting of the Lady Loretta Formation: synrift, sag, or passive margin?: Australian Journal of Earth Sciences, v. 45, p. 89-92.

Finlow-Bates, T., 1979. Cyclicity in the lead-zinc-silver bearing sediments at Mount Isa Mine, Queensland, Australia, and rates of sulfide accumulation: Economic Geology, v. 74, p. 1408-1419.

Finlow-Bates, T., Croxford, N.J.W., and Allan, J.M., 1977. Evidence for, and implications of, a primary FeS phase in the Lead-Zinc bearing sediments at Mount Isa: Mineralium Deposita, v. 12, p. 143-149.

Forrestal, P.J., 1990. Mount Isa and Hilton silver-lead-zinc deposits, In: Hughes, F.E. (ed.), Geology of the mineral deposits of Australia and Papua New Guinea, p. 927-934 (The Australian Institute of Mining and Metallurgy: Melbourne).

Giles, D., Betts, P.G., and Lister, G.S., 2001. A continental back-arc setting for early to middle Proterozoic basins of north-eastern Australia: Geological Society of Australia Abstracts, v. 64, p. 55-56.

Glikson, A.Y., Derrick, G.M., Wilson, I.H., and, Hill, R.M., 1976. Tectonic evolution and crustal setting of the middle Proterozoic Leichhardt River Fault Trough, Mount Isa region, northwestern Queensland: Bureau of Mineral Resources Journal of Australian Geology and Geophysics, v. 1, p. 115-129.

Gratier, J.-P. and Vialon, P., 1980. Deformation pattern in a heterogeneous material: Folded and cleaved sedimentary cover immediately overlying a crystalline basement (Oisans, French Alps): Tectonophysics, v. 65, p. 151-180.

Grondijs, M.F. and Shouten, C., 1937. A study of the Mount Isa ores: Economic Geology, v. 32, p. 407-450.

Gulson, B.L., 1975. Differences in Lead Isotope Compositions in the stratiform McArthur Zinc-Lead-Silver deposit: Mineralium Deposita, v. 10, p. 277-286.

Hancock, M.C. and Purvis, A.H., 1990. Lady Loretta Silver-Lead-Zinc Deposit, In: Hughes, F.E. (Ed.), Geology of the mineral deposits of Australia and Papua New Guinea. p. 943-948, (The Australasian Institute of Mining and Metallurgy: Melbourne).

Jackson, M.J., Scott, D.L., and Rawlings, D.J., 2000. Stratigraphic framework for the Leichhardt and Calvert Superbasins: review and correlations of the pre-1700Ma successions between Mt Isa and McArthur River: Australian Journal of Earth Sciences, v. 47, p. 381-404.

Large, R., Bull, S., Selley, D., Yang, J., Cooke, D., Garven, G., and McGoldrick, P., 2002. Controls on the formation of giant stratiform sediment-hosted Zn-Pb-Ag deposits: with particular reference to the north Australian Proterozoic. In: Cooke, D.R. and Pongratz, J. (eds), Giant Ore Deposits: Charactersitics, genesis, and exploration. p. 107-149. CODES Special Publication 4.

Lee, M.K., 1972. A fold study of the Lady Loretta area, NW Queensland, B.Sc. (Hons) Thesis, University of Adelaide (Unpublished).

Loudon, A.G., Lee, M.K., Dowling, J.F., and Bourn, R., 1975. Lady Loretta silver-lead-zinc deposit, In: Knight, C.L. (ed.), Economic geology of Australia and Papua

New Guinea, Vol. 1 Metals, p. 377-382, (The Australasian Institute of Mining and Metallurgy: Melbourne).

Love, L.G. and Zimmerman, D.O., 1961. Bedded Pyrite and micro-organisms from the Mount Isa Shale: Economic Geology, v. 56, p. 873-896.

Mathias, B.V., Clark, G.J., Morris, D., and Russell, R.E., 1971. The Hilton deposit – Stratiform silver-lead-zinc mineralization of the Mount Isa type, In: Fisher, N.D. (ed.), Metallogenic provinces and mineral deposits in the south western Pacific: Bureau of Mineral Resources – Geology and Geophysics Bulletin, v. 141, p. 33-58.

MacCready, T., Goleby, B.R., Goncharov, A., Drummond, B.J., Lister, G.S., 1998. A framework of overprinting orogens based on interpretation of the Mount Isa deep seismic transect: Economic Geology, v. 93, p. 1422-1434.

McGoldrick, P., Dunster, J., Cooke, D., and Aheimer, M., 1996. New observations from the Lady Loretta Zn-Pb-Ag deposit: towards a new genetic model, In: Baker, T., Rotherham, J., Mark, G., and Williams, P.J. (eds), New Developments in Metallogenic research: The McArthur, Mt Isa, Cloncurry Minerals Province, p. 81-84. James Cook University Economic Geology Research Unit Contribution 55.

Myers, R., Ceremuga, C., Clark, D., McSkimming, D., Price, S., Tuesley, M., and Wilkinson, D. 1996. Mount Isa lead-zinc minerlisation: What controversy? In: Baker, T., Rotherham, J., Mark, G., and Williams, P.J. (eds), New Developments in Metallogenic research: The McArthur, Mt Isa, Cloncurry Minerals Province, p. 85-89. James Cook University Economic Geology Research Unit Contribution 55.

Neudert, M.K., 1986. Sedimentology of the middle Proterozoic Mount Isa Group, NW Queensland, Australia and its constraints on lead-zinc ore genesis. Irish Association for Economic Geology – Annual Review, p. 43-44.

O'Dea, M.G., and Lister, G.S., 1995. The role of ductility contrast and basement architecture in the structural evolution of the Crystal Creek block, Mount Isa Inlier, Nw Queensland, Australia: Journal of Structural Geology, v. 17, p. 949-960.

O'Dea, M.G., Lister, G.S., Betts, P.G., and Pound, K.S., 1997a. A shortened intraplate rift system in the Proterozoic Mount Isa terrane, NW Queensland, Australia: Tectonics, v. 16, p. 425-441.

O'Dea, M.G., Lister, G.S., MacCready, T., Betts, P.G., Oliver, N.H.S., Pound, K.S., Huang, W., and Valenta, R.K., 1997b. Geodynamic evolution of the Proterozoic Mount Isa terrain, In: Burg, J.-P. and Ford, M. (eds), Orogeny Through Time. Geological Society Special Publication No. 121, p. 99-122.

Ord, A., Hobbs, B.E., Zhang, y., Broadbent, G.C., Brown, M., Willetts, G., Sorjonen-Ward, P., Walshe, J.L., and Zhao, C., 2002. Geodynamic modelling of the Century deposit, Mt Isa Province, Queensland: Australian Journal of Earth Sciences, v. 49, p. 1011-1039.

Page, R.W., 1983. Timing of superposed volcanism in the Proterozoic Mount Isa Inlier, Australia: Precambrian Research, v. 21, p. 223-245.

Page, R.W. and Bell, T.H., 1986. Isotopic and structural responses of granite to successive deformation and metamorphism: Journal of Geology, v. 94, p. 365-379.

Page, R.W., Sun, S-S, and Carr, G., 1994. Proterozoic sediment-hosted lead-zinc-silver deposits in northern Australia – U-Pb zircon and Pb isotope studies: Geological Society of Australia Abstracts, v. 37, p. 334-335.

Page, R.W. and Sweet, I.H., 1998. Geochronology of basin phases in the western Mount Isa Inlier, and correlation with the McArthur Basin: Australian Journal of Earth Sciences, v. 45, p. 219-232.

Page, R.W., Jackson, M.J., and Krassay, A.A., 2000. Constraining sequence stratigraphy in north Australian basins: SHRIMP U-Pb zircon geochronology between Mt Isa and McArthur River: Australian Journal of Earth Sciences, v. 47, p. 431-460.

Perkins, W.G., 1997. Mount Isa lead-zinc orebodies: Replacement lodes in a zoned syndeformational copper-lead-zinc system?: Ore Geology Reviews, v. 12, p. 61-110.

Perkins, W.G., 1998. Timing of formation of Proterozoic stratiform fine-grained pyrite: Post-diagenetic cleavage replacement at Mount Isa?: Economic Geology, v. 93, p. 1153-1164.

Ramsay, J.G. and Huber, M.I., 1987. The techniques of Modern Structural Geology, Volume 2: Folds and Fractures, 700p, Academic Press.

Russell, M.J., Solomon, M., and Walshe, J.C., 1981. The genesis of sediment-hosted, exhalative zinc and lead deposits: Mineralium Deposita, v. 16, p. 113-127.

Sawkins, F.J., 1984. Ore genesis by episodic dewatering of sedimentary basins: Application to giant Proterozoic lead-zinc deposits: Geology, v. 12, p. 451-454.

Schieber, J., 1990. Pyritic shales and microbial mats: Significant factors in the genesis of stratiform Pb-Zn deposits of the Proterozoic?: Mineralium Deposita, v. 25, p. 7-14.

Smith, W.D., 1969. Penecomteporaneous faulting and its likely significance in relation to Mt Isa ore deposition: Geological Society of Australia Special Publication, v. 2, p. 225-235.

Smith, J.W. and Croxford, N.J., 1973. Sulphur isotope ratios in the McArtur lead-zinc-silver deposit: Nature-Phys. Sci., v. 245, 10-12.

Southgate, P.N., Bradshaw, B.E., Domagala, J., Jackson, M.J., Idnurm, M., Krassay, A.A., Page, R.W., Sami, T.T., Scott, D.L., Lindsay, J.F., McConachie, B.A., and Tarlowski, C., 2000. Chronostratigraphic basin framework for Palaeoproterozoic rocks (1730-1575Ma) in northern Australia and implications for base-metal mineralisation: Australian Journal of Earth Sciences, v. 47, p. 461-483.

Valenta, R.K., 1988. Deformation, fluid flow and mineralization in the Hilton area, Mt Isa, Australia. (Unpublished PhD thesis – Monash University, Melbourne).

Valenta, R.K., 1994. Deformation in the host rocks and stratiform mineralization in the Hilton Mine area, Mt Isa: Australian Journal of Earth Sciences, v. 93, p. 1119-1131.

Van Dijk, P.M., 1991. Regional syndeformational copper mineralization in the Western Mount Isa Block, Australia: Economic Geology, v. 86, p. 278-301.

Wilkinson, D.L., 1995. Structural termination of 8 orebody and its implications for the genesis of lead-zinc-silver mineralisation, Mount Isa, Queensland: Unpublished Hons thesis, James Cook University, Townsville, Australia.

Williams, N., 1978a. Studies of the base metal sulfide deposits at McArthur River, Northern Territory, Australia: I. The Cooley and Ridge Deposits: Economic Geology, v. 73, p. 1005-1035.

Williams, N., 1978b. Studies of the base metal sulfide deposits at McArthur River, Northern Territory, Australia: II. The Sulfide-S and Organic-C relationships of the concordant deposits and their significance: Economic Geology, v. 73, p. 1036-1056.

Williams, P.J., 1998. Metallogeny of the McArthur River-Mount Isa-Cloncurry Minerals Province: Economic Geology, v. 93, p. 1119-1131.

Winsor, C.N., 1986. Intermittent folding and faulting in the Lake Moondarra area, Mount Isa, Queensland: Australian Journal of Earth Science, v. 33, p. 27-42.

CONCLUSIONS

Key conclusions of this study of the George Fisher deposit are as follows:

1. Deformation history of the George Fisher host-rocks

The effects of four ductile deformations are preserved in the host-rocks to Zn-Pb-Ag mineralization. The earliest, D_1, is manifest as an open deposit-scale fold (F_1) with an east-west striking axial plane. D_2 is regionally extensive and F_2 folding dominates the structural grain of the George Fisher – Lake Moondarra area. The majority of mesoscale to exposure-scale folds at George Fisher are of D_2 age and have north-northwest striking axial planes and a pervasive slaty/solution cleavage (S_2) parallel to the F_2 axial planes. Following this main phase of sub-horizontal shortening, an episode of sub-vertical shortening/sub-horizontal extension (D_3) formed folds with sub-horizontal axial planes and gently-dipping crenulations of the S_2 cleavage and bedding. D_3 features are overprinted by sub-vertical crenulations (S_4) and minor folds (F_4) with sub-vertical north-northeast striking axial planes. Faults in the deposit and surrounding environs range in age from syn-D_1 or older faults that have been reactivated during subsequent deformations, through to late faults formed during late or post-D_4 which cut the ore-bearing sequence.

Within the short-limb of the deposit-scale F_1 flexure, S_2/F_2 are parallel to bedding whereas north and south of the F_1 short-limb, S_2/F_2 are oblique to bedding. However, S_4/F_4 are markedly discordant to bedding and S_2 within the F_1 short-limb, but approximately parallel to bedding outside the F_1 short-limb. The higher angle of S_4 to bedding in the F_1 short-limb coincides with the location of more intense development of S_4 crenulations.

A swap in the foliation vergence relationships between S_4 and S_0/S_2 occurs between the Mt Isa and George Fisher deposits. The district-scale orientation of S_4/F_4 features sub-parallels the margins of the Sybella Batholith and implies that the batholith has acted as a buttress during later deformation and thereby resulted in heterogeneous development of D_4 strain.

2. Geometry of George Fisher ore shoots and location within the structural architecture of the deposit

Shoots of high-grade and thicker mineralization parallel the plunge of the F_1 fold and are largely confined to the short-limb of this fold. Subsidiary ore shoots are coincident with areas of more intense F_2 folding and high-grade mineralization parallels both F_2 and F_4 fold axes in longitudinal projection.

An empirical relationship exists whereby areas of more intense S_3 and S_4 foliation development in the F_1 short-limb are coincident with areas of higher-grade mineralization.

High-grade mineralization at George Fisher is constrained both in plunge and strike extent such that it occurs between ~600m and 1000m below surface. Both F_1 and F_2 folds are recognized at surface and weaker Zn-Pb-Ag mineralization occurs near surface. The high-grade mineralization at depth is interpreted to be related to the intersection of the earlier folds with a discrete zone of higher D_4 strain which does not outcrop at surface due to truncation by the Paroo Fault. The kinematics during D_4 are considered to have focussed dilation on the intersections between the F_1 short-limb, F_2, and F_3 folds which were favourably oriented relative to the regional palaeostress field.

3. Application of fractal analysis to analysis of sphalerite microstructures

A quantitative method of microstructural analysis has been developed to assist in determination of the extent of deformation and recrystallization in sphalerite ores in order to distinguish between those ore-types that may have formed earlier and later in the deformation history. A relationship between the fractal dimension of sphalerite grain boundaries and the degree of deformation and recrystallization is recognized for samples deformed at temperatures between 200-300°C. Undeformed, deformed, and recrystallized grains have mean fractal dimensions and 95% confidence intervals of $1.0126 \pm 5.5x10^{-3}$, $1.0948 \pm 1.3x10^{-2}$, and $1.0485 \pm 4.3x10^{-3}$ respectively. The three categories of undeformed, deformed, and recrystallized sphalerite grains can be completely discriminated when grain diameter is plotted against fractal dimension on a log-normal plot.

4. Timing of mineralization types relative to the deformation history of the host-rocks

Qualitative determination of the timing of both sphalerite and galena-dominant mineralization types within the deformation history has been determined from exposure and hand-specimen scale cross-cutting relations, and microstructural development. The two dominant sources of Zn and Pb metal at the deposit, vein-hosted sphalerite and medium-grained galena breccia, respectively; are interpreted to comprise only weakly deformed sulphides and contain clasts of host-rock and earlier remnant vein material which preserve more intense deformation. This suggests that these mineralization types postdate a phase of more intense deformation, most likely D_2.

The deposit-scale distribution of the main ore types correlates with the location of ore shoots inferred to have formed during D_4 and described in earlier stages of the study. The inferred D_4 timing is supported by the interpretation of dominantly syn-D_4 vein-hosted sphalerite and medium-grained galena breccias.

Mineralization types inferred to have formed pre- to syn-D_2 include minor disseminated sphalerite and strongly deformed fine-grained sphalerite±galena breccia. These potential pre-F_2 mineralization types do not currently constitute economic mineralization and any pre-F_2 proto-mineralization is therefore likely to have been sub-economic.

Zn assay data suggests that more than one population of Zn grades exists and that a higher-grade population is unique to the economic ore-horizons. This supports the interpretation of remobilization and upgrading of mineralization during D_4. However, this qualitative observation does not discriminate between upgrading of a pre-F_2 or syn-/post-F_2 sulphide accumulation during D_4.

5. Re-Os isotopic analysis of George Fisher Zn-Pb-Ag mineralization

Sphalerite and galena mineralization types at George Fisher have the same Re-Os isotopic signature and are therefore interpreted to have a common source. Eleven samples of mineralization from George Fisher define a linear trend which approximates an isochron. An age of 1423±130Ma has been derived from the isochron. The age estimate spans from ~1553-1293Ma which incorporates D_2 (1540Ma), D_4 (1510Ma), and a period of post-orogenic cooling dated at 1392±85Ma to 1482±52Ma. Re-Os dating of the sulfides at George Fisher has therefore not achieved the level of accuracy required to distinguish between individual deformation events, different styles of mineralization inferred to have formed pre-/syn-D_2 and syn-D_4, and post-orogenic cooling but indicates that closure of the Re-Os isotopic system in the Zn and Pb sulphides significantly post-dates host-rock deposition.

A mantle source for the Pb and Zn is indicated by the initial $^{187}Os/^{188}Os$ ratio of 0.077±0.071. This differs from other studies of Proterozoic Zn-Pb-Ag deposits in the Western Fold Belt which infer scavenging of metal from within the sedimentary basin or from the basement rocks immediately underlying the sedimentary basin. Proximity to a regional fault zone such as the Mount Isa-Paroo Fault system, interpreted to be part of a fault-network linked to a major mid-crustal shear zone, is therefore considered necessary to bring metal-bearing fluids from depth into contact with prospective host-lithologies at George Fisher.

6. Implications for metallogenesis in the Western Fold belt

Proximity to a major fault is a characteristic shared by all major Zn-Pb-Ag deposits in the Western Fold Belt. A spatial coincidence also exists between deposits and broadly east-west trending D_1 faults and folds except at the Mt Isa deposit where more intense D_4 strain may have obscured earlier deformation features. More intense D_4 strain at Mt Isa is associated with formation of the giant syntectonic Cu system adjacent to the Zn-Pb-Ag orebodies. An apparent evolution of mineralization at George Fisher is inferred from Zn to Pb dominant however conditions have not been favourable for the later Cu dominant phase. Sphalerite mineralization, which dominantly occurs as bedding-parallel replacement and micro-brecciation of veined layers, is interpreted to have occurred early in D_4 when bedding reactivation dominated. Later in D_4, minor F_4 fold development occurred and bedding reactivation proceeded to the extent that F_2 – F_4 folds are brecciated. Galena mineralization occurs during this later phase of D_4 deformation and in the waning stages of D_4 where D_4 folds themselves are brecciated. D_4 strain at George Fisher is comparatively weak and Cu mineralization occurs only at anomalous levels.

The spatial coincidence of diagenetic carbonate alteration and Zn-Pb-Ag mineralization with the deposit-scale F_1 fold at George Fisher suggests that this F_1 fold has focussed fluid flow from diagenesis through to the D_4 stage.

At the George Fisher deposit it is apparent that the F_1 fold which focussed diagenetic hydrothermal activity and alteration also acted as a heterogeneity focussing dilation and final sites of mineralization. The F_1 fold may be the upper level expression of a reactivated basement fault thereby accounting for the longevity of the hydrothermal system responsible for alteration and mineralization at George Fisher. It is possible that diagenetic processes prepared the host-rock for later mineralization at George Fisher.

APPENDIX I

Sample Catalogue

JCU Sample #	T.E.M. Sample #	Description	Location				Analysis type				
				X	Y	Z	HS	TS	PS	Re-Os	EMP
71937	1111-4	Mudstone with stylolitic seams	CN71, 11Level	2217	7098	2780	X	X			
71938	0512-3	foliated siltsone	739D X/C, 12C	2278	7397	2750	X	X			
71939	1412-3	foliated siltsone with nodules	FWD, 11Level	2330	7115	2777	X	X			
71940	1311-2	foliated siltsone	747D X/C, 13C	2260	7490	2687	X	X			
71941	2810-1	foliated siltstone	FWD, 12C	2308	7309	2747	X	X			
71942	1012-6	foliated siltstone with vein-hosted sphalerite	739D X/C, 12C	2282	7402	2748	X	X			
71943	1012-2	foliated siltstone with vein-hosted sphalerite	739D X/C, 12C	2286	7402	2748	X	X			
71944	1012-3	foliated siltstone with vein-hosted sphalerite	739D X/C, 12C	2282	7402	2748	X	X			
71945	1012-4	foliated siltstone with vein-hosted sphalerite	739D X/C, 12C	2282	7402	2748	X	X			
71946	1012-5	foliated siltstone with vein-hosted sphalerite	739D X/C, 12C	2282	7402	2748	X	X			
71947	1012-7	foliated siltstone with vein-hosted sphalerite	739D X/C, 12C	2282	7402	2748	X	X			
71948	1012-8	foliated siltstone with vein-hosted sphalerite	739D X/C, 12C	2282	7402	2748	X	X			
71949	H748EH1-5.45m	vein-hosted sphalerite terminating on cross-cutting vein	G orebody	2324	7480	2718	X		X		
71950	1311-6	foliated siltstone with vein-hosted sphalerite	733D X/C, 13C	2206	7346	2685	X	X			
71951	960519-91.2m	vein-hosted sphalerite	G orebody	2343	7222	2729	X		X		X
71952	2710-7	crenulated siltstone	7200 X/C, 12Level	2223	7203	2714	X	X			

71953	1311-14	foliated siltstone	GN69, 13C	2232	7014	2684	X	X			
71954	1311-10	crenulated siltstone	719D X/C, 13C	2226	7210	2683	X	X			
71955	0902-3	crenulated siltstone	723DX/C, 12Level	2215	7251	2716	X	X			
71956	0103-1	vein-hosted sphalerite	FWD, 12Level	2326	7400	2718	X		X	X	
71957	Silverspur	sphalerite mineralization							X		
71958	Rammelsberg	massive sulphide							X		
71959	los minas dos ingleses	sphalerite crack-infill in quartz							X		
71960	gf late vein	vughy sphalerite infill in quartz-carbonate vein							X		
71961	961233-80.8m	deformed fine-grained sphalerite-galena breccia	G orebody	2496	7741	2790	X		X		
71962	2603-1	vein-hosted sphalerite	12C	2409	7410	2745	X		X		
71963	1212-1	vein-hosted sphalerite	12C	2359	7499	2750	X		X		
71964	J754WD1-220.15m	vein-hosted sphalerite terminating on cross-cutting vein	C orebody	2263	7560	2708	X		X		
71965	1311-5	vein-hosted sphalerite with quartz-carbonate fibres	737D X/C, 13C	2238	7386	2685	X	X			
71966	3010-1	vein-hosted sphalerite with quartz-carbonate fibres	12Level	2388	7068	2731	X	X			
71967	1311-7	vein-hosted sphalerite	730D X/C, 13C	2215	7316	2684	X	X			
71968	0203-3	vein-hosted sphalerite heterogeneously developed around mesofold	12Level	2331	7400	2717	X		X		
71969	1011-2	planar vein-hosted sphalerite	737D X/C, 12C	2267	7345	2748	X		X		
71970	1011-7	vein-hosted sphalerite in fold zone	737D X/C, 12C	2259	7345	2747	X		X		
71971	0803-1	massive sphalerite	12Level	2322	7401	2717	X		X		
71972	960436-296.5m	sphalerite breccia		2152	7222	2624	X		X		

71973	951033-221.05m	sphalerite breccia	G orebody	2209	7080	2586	X		X			
71974	2610-6	disseminated sphalerite in fractures	12C	2358	7304	2745	X	X				
71975	960355-389.8m	fine-grained sphalerite breccia	A orebody	2412	7451	3076	X		X			
71976	0803-3	medium-grained galena breccia with clasts of vein-hosted sphalerite	739D X/C, 13C	2223	7387	2684	X			X		
71977	960817-256.6m	medium-grained galena breccia cross-cutting vein-hosted sphalerite	D orebody	2287	7751	2724	X					
71978	960932-178.7m	medium-grained galena breccia cross-cutting vein-hosted sphalerite	G orebody	2344	7663	2714	X					
71979	951033-319.65m	medium-grained galena breccia	C orebody	2119	7096	2551	X		X			
71980	2102-3	medium-grained galena breccia	723D X/C, 12Level	2242	7245	2715	X		X			
71981	2602-2	bedding-discordant medium-grained galena breccia vein	723D X/C, 12Level	2226	7246	2770	X		X			
71982	1302-2	medium-grained galena breccia	12Level	2217	7252	2770	X		X			
71983	960313-380.9m	medium-grained galena breccia	C orebody	2118	7240	2502	X		X			
71984	960436-289.6m	foliated medium-grained galena breccia	D orebody	2158	7222	2626	X		X			
71985	0512-6	folded sphalerite bands in medium-grained galena breccia	720D X/C, 12C	2267	7208	2745	X					
71986	0412-1	foliated medium-grained galena breccia	723D X/C, 12C	2269	7240	2746	X		X			
71987	960313-380.35m	coarse-grained galena breccia	C orebody	2118	7240	2502	X		X			
71988	1712-3	coarse-grained galena-sphalerite breccia	723D X/C, 12C	2265	7240	2746	X		X	X		
71989	1112-6	coarse-grained galena-sphalerite breccia	12C	2275	7396	2748	X		X			

71990	960533-322.3m	fine-grained sphalerite breccia	D orebody	2174	7362	2535	**X**			**X**	
71991	3101-1	vein-hosted sphalerite breccia	13C	2184	7175	2656	**X**			**X**	
71992	1115-5	medium-grained galena breccia	CN71, 11Level	2217	7098	2780	**X**			**X**	
71993	960335-596m	vein-hosted sphalerite	G orebody	2512	7431	2898	**X**			**X**	
71994	960839-201.05m	vein-hosted sphalerite	D orebody	2244	7305	2734	**X**			**X**	
71995	0611-4	vein-hosted sphalerite	742D X/C, 12C	2219	7415	2745	**X**			**X**	
71996	2610-5	vein-hosted sphalerite	12C	2334	7249	2721	**X**			**X**	
71997	2710-4	barren siltstone	12Level	2566	7249	2721	**X**			**X**	
71998	2710-10	barren siltstone	12B	2537	7403	2727	**X**			**X**	

X = Easting, Y = Northing, Z = R.L., HS = Hand specimen, TS = Thin-section, PS = polished thin-section, Re-Os = sample analyzed as part of Re-Os isotopic study, EMP = sample analyzed with electron microprobe

APPENDIX II

Structural Data

THIN SECTION MEASUREMENTS																			
Sample	**S_0**		**S_1**		**S_2**			**S_3**			**S_4**			**S_5**			**S_6**		
	dip	dipdir	dip	dipdir	dip	dipdir	Int	dip	dipdir	Int	dip	dipdir	Int	dip	dipdir	Int	dip	dipdir	Int
1512-1	34	253	73	190	66	268	w	32	148	cw	81	290	cw						
0902-3	19	270			40	258	s	29	119	cs	82	280	cs						
0312-1	71	277			60	265	m	16	314	icw	88	108	sw						
1412-4	60	283			69	256	m	10	231	cm	64	125	cw						
3011-1	57	266			73	262	w	8	36	cm	70	115	cm						
1512-2	65	287			68	217	w												
1512-3	50	270			60	246	w	17	345	sw	86	94	sw						
0512-2	51	270			61	280	w												
0312-2	60	261			76	245	m	30	W	cw	84	280	sw						
1412-3	59	294			64	240	m	36	344	icw	89	265	sm						
0512-3	43	273			78	253	s	28	157	sw	88	89	sw						
1012-3	67	266			45	254	s	26	325	icw									
1012-4	81	76			36	261	w	26	334	icw									
1012-5	1	160			44	250	s												
1012-6	28	283			46	248	m	14	W	icw	84	277	icw						
1012-7	18	281			42	270	s	53	E	icm									
1012-8	73	96			83	253	m												
0512-1	55	264			64	244	w	5	69	icw	88	292	icw						
1803-2	60	39			54	246	s												
1212-2					71	228	s												
1203-4	40	289			61	249	m												
2510-1	69	286			88	260	m				83	122	sw						
2510-2	74	259			86	252	m												
2510-3	70	267			90	250	m												
2510-4	60	254			67	260	m				78	294	sm						
2510-5	58	270			89	74	w												
2510-6	48	300			79	276	w												
2510-7	58	269			84	254	w												
2610-1	33	260			71	257	s												
2610-2	62	270			70	253	m												
2610-3	48	226			75	213	w												
2610-4	52	289			68	270	m												
2610-5	38	247			71	285	m												
2610-6	43	270	75	330	77	248	m												
2610-7	64	210			80	260	w												
2610-8	22	335			60	256	m												
2610-9	40	253			73	112	w												
2610-10	37	254			63	242	m												
2610-11	65	271			83	259	m												
2710-1	42	253			77	238	m												
2710-2	78	268			65	76	m												
2710-3	63	280			80	284	s												
2710-4	60	275			87	280	s												
2710-5	59	234			75	246	s												

2810-1	42	270			71	273	m												
2810-3	37	254			63	273	w	24	139	icw	84	98	icw						
2710-10	41	251			66	232	m												
2710-11	43	284			67	260	w												
2710-12	43	269			66	232	w												
2710-13	41	287			68	260	m				63	90	sm						
1311-1	57	283			67	277	m	28	303	sw									
1311-2	48	250			67	270	m												
1311-13	76	250			83	79	w												
1311-14	70	250			90	241	m												
1311-12	62	246			78	236	m												
1311-3	56	284			68	270	w												
1311-4	52	277			83	257	w				65	114	sm						
1311-5	69	276			83	266	w												
1311-6	56	227			72	218	m	36	162	cm	71	104	cm						
1311-7	65	269			80	278	m	15	150	cm	54	119	cm						
1311-8	48	309			78	240	m												
1311-9	24	253			45	248	m	51	141	cs	78	290	cw						
1311-10	34	260			59	244	m	36	158	cs	80	100	cs	56	131	cw	89	321	cs
2910-7	79	252			85	67	m	13	180	cs	56	98	cs	54	337	cw			
2710-7	43	258			60	251	m	42	150	cs	70	100	cs	12	W	cm			
2710-6	56	294			67	268	w	8	146	icw	72	112	icw						
2610-12	67	292			74	95													
2610-13	71	280			80	81													
2910-4	65	281			80	86													
1203-1	86	294			73	88													
3010-1	76	275			78	71													
3010-2	57	272			74	74													
3010-3	54	280			88	92													
3010-4	61	273			84	80													
2910-5	56	262			80	260													
2910-8	58	262			80	236													
2910-2	47	252			59	249		37	116		66	96							
3010-5	62	292			76	274													
3010-6	80	96			63	79		63	330										
3010-7	80	274			72	60		51	288		16	71							
3010-8	45	275			63	246													
2810-4	55	323			87	93													
2810-6	62	295			80	270													
2810-7	53	312			77	231													
2810-8	50	296			86	256													
2810-9	53	258			77	250													
2810-5	46	273			63	260													
2810-10	51	264			73	251													
2810-11	50	275			77	254													
2710-9	68	259			87	253													
2910-1	56	276			78	252													
0411-2	43	271			66	248		20	132		82	108							

dipdir = dip direction, Int. = relative intensity of foliation (w, weak; m, moderate; s, strong; and prefixes: s, seamy; ic, incipient crenulation; c, crenulation)

MAPPING MEASUREMENTS

S_0				F_2				F_3				F_4				Late Kinks			
dip	dipdir	dip	dipdir	dip	dipdir	pl.	pl.dir.	dip	dipdir	pl.	pl.dir.	dip	dipdir	pl.	pl.dir.	dip	dipdir	pl.	pl.dir.
25	263	60	262	74	279	42	184	14	249	-	-	84	94	-	-	34	320	28	246
16	261	58	287	51	265	55	314	19	188	-	-	83	95	35	357	55	171	32	238
34	245	62	275	70	255	41	335	10	185	10	185	82	276	14	190	75	200	46	280
77	259	59	265	65	257	30	352	33	105	15	185	85	110	38	183	59	126	26	215
59	276	66	277	35	239	35	324	30	94	18	185	85	91	2	173	64	110	5	11
50	245	59	268	66	250	40	151	10	182	10	170	89	260	48	179	58	164	64	225
40	256	59	280	88	79	12	9	25	115	25	17	72	295	35	14	70	185	47	273
26	226	60	265	76	249	37	344	19	0	25	354	89	89	-	-	87	183	66	276
42	278	60	278	70	54	29	320	21	323	11	4	82	104	49	198	83	193	60	277
25	279	66	292	64	274	24	4	17	9	19	342	83	105	44	308	60	211	60	255
50	284	61	273	58	292	50	207	34	18	36	354	84	90	-	-	88	28	61	294
62	254	52	280	65	300	23	221	29	86	30	0	85	120	26	220	50	217	55	218
55	277	42	254	57	266	0	348	37	85	10	356	84	286	13	195	89	147	38	234
66	275	41	253	76	279	49	213	44	14	30	318	89	95	34	8				
49	158	44	258	77	276	30	9	17	307	18	324	84	262	5	350				
20	240	46	284	35	283	12	202	0	204	29	288	86	267	6	180				
68	242	57	295	10	82	10	170	12	349	16	345	89	103	18	194				
67	269	64	257	80	285	16	12	10	260	12	332	88	125	42	227				
27	256	50	270	60	267	20	347	10	252	10	158	76	105	14	24				
65	292	37	263	60	305	3	358	11	89	5	172								
38	270	40	265	69	294	31	348	10	84	5	181								
51	270	35	250	76	290	37	14	10	252	10	166								
67	278	43	282	66	263	19	5	5	104	10	190								
42	283	50	267	76	243	33	333	20	206	20	206								
72	275	60	223	30	228	31	305	20	319	20	319								
25	258	50	263	60	285	19	347												
40	306	54	246	64	247	52	322												
70	277	43	279	60	231	40	320												
38	252	34	268	83	240	35	322												
54	56	39	253	72	222	48	301												
89	248	30	232	80	257	15	174												
85	95	34	258	33	260	10	175												
72	274	47	237	74	259	20	164												
35	272	58	262	65	256	11	349												
84	134	48	275	73	273	20	3												
49	260	48	286	64	267	38	342												
59	262	44	275	64	258	63	313												
46	238	49	263	55	243	25	328												
52	278	56	280	78	289	7	14												
58	248	34	253	30	282	10	13												
42	261	19	270	49	243	22	313												
65	273	71	277	18	272	10	357												
59	263	60	283	53	260	28	338												
64	263	57	266	53	254	12	172												
50	260	65	287	46	250	17	323												
58	287	50	270	27	240	17	323												
32	277	51	270	63	238	17	325												
65	263	60	261	73	247	20	335												
69	88	59	294	66	240	37	310												
56	284	43	273	70	262	35	340												

78	274	67	266	84	236	39	320
30	308	81	76	63	284	27	357
42	280	1	160	55	283	26	354
44	274	28	283	64	288	33	1
59	269	18	281	42	250	25	190
46	260	73	96	33	237	17	303
30	260	55	264	72	256	39	341
34	255	60	39	49	255	31	313
76	241	40	289	34	277	41	352
60	260	69	286	35	261	10	322
48	267	74	259	43	268	24	354
39	271	70	267	60	260	15	336
40	282	60	254	77	273	15	194
41	276	58	270	21	273	23	336
68	347	48	300	44	273	12	4
54	264	58	269	46	286	10	205
47	275	33	260	44	236	37	202
48	261	62	270	59	225	55	294
76	268	48	226	57	278	20	358
61	287	52	289	61	262	20	201
84	265	38	247	72	258	20	340
58	287	43	270	65	257	30	328
65	261	64	210	56	260	17	190
52	276	22	335	54	267	7	356
77	292	40	253	65	285	50	338
72	273	37	254	75	245	20	323
66	280	65	271	75	260	17	345
48	268	42	253	72	260	24	338
64	265	78	268				
48	281	63	280				
48	263	60	275				
45	263	59	234				
59	265	42	270				
56	256	37	254				
61	290	41	251				
50	255	43	284				
35	247	43	269				
50	252	41	287				
50	265	57	283				
57	269	48	250				
55	264	76	250				
61	273	70	250				
56	262	62	246				
58	262	56	284				
47	252	52	277				
62	292	69	276				
80	96	56	227				
80	274	65	269				
45	275	48	309				
55	323	24	253				
62	295	34	260				
53	312	79	252				
50	296	43	258				
53	258	56	294				
46	273	67	292				
51	264	71	280				
50	275	65	281				

68	259	86	294																
56	276	76	275																
43	271	57	272																
		54	280																

dipdir = dip direction, pl. = plunge of fold axes, pl.dir. = direction of plunge of fold axes.

Type	**Fault**		**Slickensides**		**Observations**
	dip	dipdir	pitch	pitch dir.	
east-west striking faults	87	168	10	e	
	77	196			
	80	202			south-block-up drag
	64	182	90		
	37	210	85	e	
	70	195			south-block-up drag
	83	195			truncated by bedding-parallel shear
	66	185			
	74	196	10	w	10cm gouge, north-block-up and west
	78	168	25	sw	earlier ss
	78	168	42	ne	later ss
	85	142			
northeast striking faults	62	294	75	s	
	87	146			
	86	143	26	ne	north-block-down and east
	83	329			
	86	326	24	ne	
	74	335			
	68	340	30	ne	north-block-down and east
	70	338	60	w	
	64	340			
	70	340	75	ne	drag indicates north-block-down
	68	308	70	sw	
	74	309			
	68	343	80	ne	
	79	345	5	ne	drag indicates strike-slip
	76	322			
	80	298	72	w	stepping indicates north-block-east
	82	122	25	sw	
	87	313	19	ne	
	89	322			
	77	303	70	sw	
	84	333			
	85	325	2	ne	
	89	305			
	80	312			north-block-down and east
	84	145			north-block-down and east

	72	315			
	87	320			
North-northeast striking faults	78	135			reverse drag, east-side-up
	73	144	7	sw	
	89	105			
	82	106	60	sw	
	81	299	43	n	
	82	292	30	nne	east-block-down and north?
	65	60	5	n	
	81	74			
	88	134	10	s	
	78	123	5	s	
	71	131			
	83	111			
	80	104			east-block-up
	78	75	87	ne	east-block-up
	89	108	85	ne	
Northwest striking	48	227	90		
	64	224	75	w	
	57	220	85	w	
	57	220	5	w	
	63	220	61	s	
Bedding-parallel	60	267	40	s	
	59	275			folding and veining indicate reverse movement
	56	284			

APPENDIX III

Electron Microprobe Analyses

	defd Vein 1	defd Vein 2	defd Vein 3	defd Vein 4	defd Vein 5	defd Vein 6	defd Vein 7	defd Vein 8	defd Vein 9	defd Vein 10	defd Vein 11	defd Vein 12
SiO2	0.35	0.42	0.36	0.62	0.31	0.46	0.65	0.33	0.33	0.37	0.21	0.47
TiO2	0.06	0.01	0	0	0.01	0.01	0.05	0	0	0	0	0.05
Al2O3	0	0	0	0.27	0	0.19	0	0	0.04	0	0.5	0.16
FeO	4.92	6.81	5.06	4.34	5.47	8.41	7.93	7.75	7.95	4.7	7.98	7.14
MnO	1.46	1.83	1.45	1.53	1.24	1.79	1.6	1.77	1.55	1.32	1.38	1.45
MgO	16.19	15.25	16.51	17.72	16.51	14.79	13.55	14.7	14.84	17.49	16.68	15.1
CaO	27.41	27.62	28.57	28.16	28.32	29.03	27.69	28.03	27.62	28.19	29.63	28.02
Na2O	0	0	0	0	0	0	0	0	0	0	0	0
K2O	0	0.07	0	0.05	0.04	0.04	0	0	0.01	0.11	0.09	0
Cl	0	0	0.04	0.03	0	0.02	0	0.03	0	0	0.02	0.02
TOTAL	50.38	52.01	51.99	52.73	51.9	54.74	51.49	52.61	52.35	52.18	56.48	52.41
	late vein 1	**late vein 2**	**late vein 3**	**late vein 4**	**late vein 5**	**late vein 6**	**late vein 7**	**late vein 8**	**late vein 9**	**late vein 10**	**late vein 11**	**late vein 12**
SiO2	0.33	0.67	0.58	0.44	0.44	0.51	0.3	0.5	0.36	0.35	0.47	0.47
TiO2	0.16	0	0	0	0	0.01	0	0	0	0	0	0
Al2O3	0.05	0.22	0.43	0	0.12	0.04	0.16	0.22	0.07	0	0	0
FeO	0.17	0.47	0.07	0.24	0.76	0.11	0.31	0.47	0.21	0	0.15	0.43
MnO	0.3	0.1	0.97	0.35	0.35	0.67	0.24	0.56	0.76	0.39	0.39	0.48
MgO	0.05	0.24	0.28	0.12	0.09	0.04	0.1	0.07	0.32	0.14	0	0
CaO	58.19	57.77	56.02	56.39	55.88	55.79	55.76	54.04	54.81	55.44	56.75	56.14
Na2O	0	0.01	0	0.05	0	0	0	0.16	0	0	0	0.07
K2O	0	0	0.02	0.02	0	0	0	0	0.05	0.01	0.04	0
Cl	0.06	0	0.11	0	0.12	0.02	0	0	0.03	0.09	0.1	0.17
TOTAL	59.32	59.47	58.48	57.61	57.76	57.2	56.87	56.01	56.61	56.42	57.9	57.76
	min vein 1	**min vein 2**	**min vein 3**	**min vein 4**	**min vein 5**	**min vein 6**	**min vein 7**	**min vein 8**	**min vein 9**	**min vein 10**	**min vein 11**	**min vein 12**
SiO2	0.18	0.59	0.52	0.27	0.34	0.64	0	0	0.34	1.65	0	0
TiO2	0.01	0	0.07	0.03	0	0	0.08	0.09	0	0	0.01	0
Al2O3	0	0	0.11	0	0.16	0	0	0	0.15	1.13	0	0
FeO	0	0.59	0.99	5.7	1.2	0.08	0.52	0.49	1.04	0.25	0.16	0
MnO	0.17	0.46	0.53	1.23	0.12	0.03	0	0	0.12	0.29	0	0.03
MgO	0	0.33	0.97	15.26	2.03	0	0	0	2.34	0	0	0.16
CaO	54.55	55.76	49.25	27.58	52.71	51.74	51.59	51.54	49.19	50.23	52.38	53.27
Na2O	0	0	0	0	0	0	0	0	0	0	0	0.32
K2O	0.07	0	0.05	0.03	0	0.02	0.25	0.24	0.11	0.47	0	0.15
Cl	0	0.16	0.05	0.04	0	0	0	0	0.01	0	0	0.09
TOTAL	54.99	57.88	52.54	50.13	56.57	52.51	52.44	52.37	53.31	54.02	52.56	54.02

	hr 2	hr 3	hr 4	hr 5	hr 6
SiO2	33.03	31.08	44.29	35.7	46.83
TiO2	0.22	0.37	0.13	0.26	0.27
Al2O3	6.58	5.74	4.83	8.89	9.9
FeO	3.78	2.92	2.85	3.67	2.37
MnO	0.59	0.81	0.64	0.68	0.48
MgO	8.7	9.62	7.71	8.56	5.88
CaO	15.79	16.85	14.04	14.75	10.37
Na2O	0	0	0	0	0
K2O	3.14	2.6	2.26	3.44	4.47
Cl	0	0	0	0.04	0
TOTAL	71.83	69.99	76.76	75.99	80.57

defd vein = deformed vein, min vein = vein-hosted sphalerite mineralization, late vein = youngest vein cross-cutting all earlier vein types, hr = host-rock

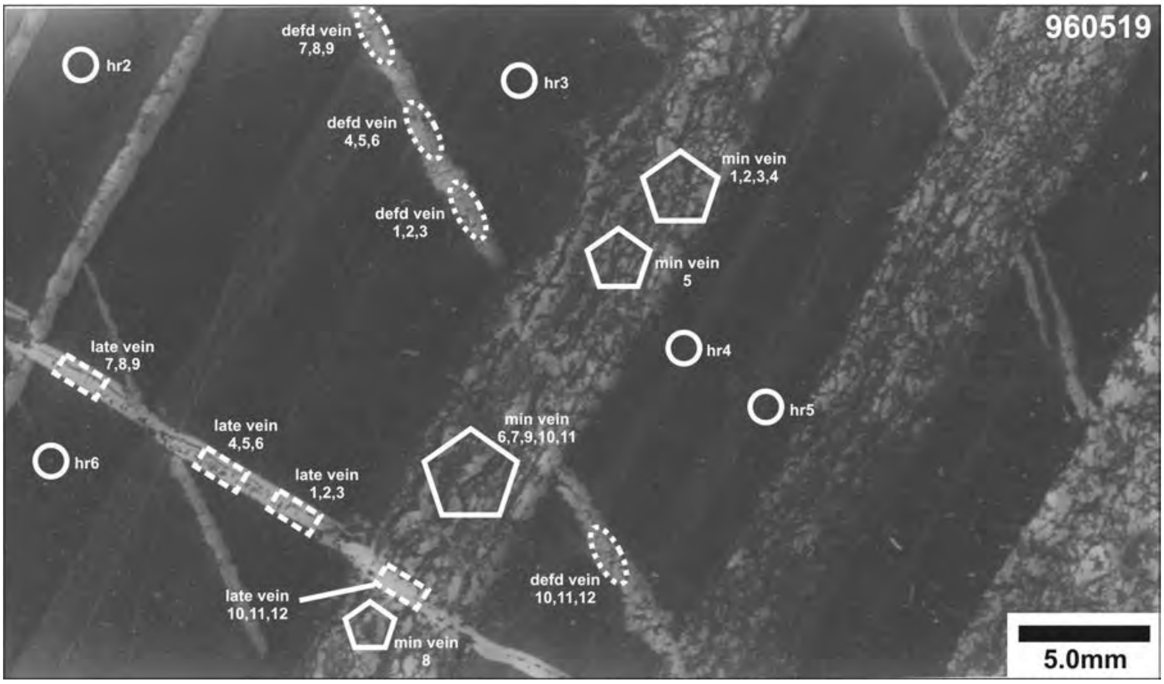

Location of probe analyses (Refer to Part A - Figure 19).

APPENDIX IV

(a) Fractal Method

Some of the following steps taken in the fractal analysis are specific to equipment used at JCU or certain software, however the following is intended as a general guide for users of other equipment and software also:

- Digital photomicrograph taken at 50x magnification and opened in Corel Draw
- Set scale (1.2628:1) and check that the long axis of the image is 280µm
- Digitize the grain boundary in 1µm segments using a dark grey 0.1pt line
- Draw a scale bar (10µm long) and position in top left hand corner of area to be exported and close as possible to the digitized boundary
- To minimize the pixel area it may be necessary to drag the boundary and scale bar to ~ 1000,0.
- Export the selected boundary and scale bar only, at 1000dpi and greyscale to the desktop as a .TIF file
- Split boundary into several segments and export individually if large (i.e. >25mb once exported)
- Open in Scion (NIH)
- Set scale by selecting 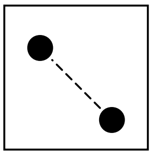 and digitizing a straight line across the scale bar
- Go to analyze > set scale and set unit to micron. In ‘known distance’ enter 10
- Digitize a line across the scale bar to check the measurement (10µm) in the information window
- Zoom to ~ 8x/16x
- Draw a 0.25µm line at the start of the line as a gauge for digitizing points
- Copy measurements to an Excel spreadsheet after every 100 points, do not exceed 256
- Reset measurements after copying to Excel
- Leave the first row blank in Excel
- Open fractal program (written by T. Blenkinsop) and run in visual basic in Excel. At the relevant place in the program the script should be either ‘chord’ or an estimate of the diameter of the grain (in µm) if a closed polygon has been used.
- Plot a scatterplot of columns f vs g and j vs k
- Change data points to size 2
- Set Y-scale minimum to 0
- Determine fractal limits to the data by visually fitting a straight line
- Using Tools > Data Analysis, preform regression of the data (columns f and g) between these limits
- Repeat for reverse data (column j and k)
- The x-variable coefficient is the gradient of the data and add 1 to calculate the Fractal Dimension (D)
- The forward and reverse calculations are averaged to give the final result for D

(b) Data from Fractal Analysis

Sample	D	95% Conf. Interval	R	Std Error	Coast line Error	Lower fractal limit	Upper fractal limit	Diam-eter	No. of points	Interpret-ation
						µm	µm	µm		
gf_late_1	1.0057	(1.0071,1.0181)	-0.92	2.2E-04	1.1E-04	1.00	31.75	980.0	3783	undef
gf_late_2	1.0189	(1.0071,1.0181)	-0.94	6.0E-04	1.2E-04	1.00	31.75	806.0	4644	undef
ertsberg_1	1.0192	(1.0071,1.0181)	-0.95	5.6E-04	4.5E-04	1.00	31.75	840.0	3044	undef
ertsberg_2	1.0255	(1.0071,1.0181)	-0.97	5.5E-04	4.2E-04	1.00	31.75	193.5	2915	undef
brazil_1	1.0049	(1.0071,1.0181)	-0.93	9.6E-05	5.9E-05	1.00	100.00	2200.0	6068	undef
brazil_2	1.0048	(1.0071,1.0181)	-0.93	1.0E-04	3.0E-05	1.00	100.00	982.0	4782	undef
welcome_1	1.0102	(1.0071,1.0181)	-0.96	2.5E-04	6.5E-06	1.00	31.75	570.0	4635	undef
welcome_2	1.0078	(1.0071,1.0181)	-0.98	8.6E-05	3.4E-04	1.00	100.00	4223.0	8776	undef
welcome_3	1.0089	(1.0071,1.0181)	-0.97	1.1E-04	3.1E-04	1.00	100.00	1690.0	3763	undef
mtmuro_1	1.0066	(1.0071,1.0181)	-0.89	3.1E-04	1.9E-04	1.00	31.75	565.0	3215	undef
mtmuro_2	1.0257	(1.0071,1.0181)	-0.89	1.2E-03	6.0E-05	1.00	100.00	388.5	1926	undef
gf_0103_1_bv	1.0342	-	-0.91	1.4E-03	1.7E-03	1.00	31.75	125.0	863	undef/wk
gf_0103_1_bv_2	1.0308	-	-0.93	1.0E-03	1.9E-03	1.00	31.75	81.5	615	undef/wk
silverspur_1_a	1.0303	(1.0463,1.0557)	-0.93	2.0E-03	7.3E-04	1.00	10.00	25.0	366	recrys
silverspur_1_b	1.0266	(1.0463,1.0557)	-0.89	2.5E-03	4.9E-04	1.00	8.75	25.0	376	recrys
silverspur_1_c	1.0172	(1.0463,1.0557)	-0.83	2.1E-03	1.2E-04	1.00	8.75	28.0	406	recrys
silverspur_1_d	1.0241	(1.0463,1.0557)	-0.82	3.2E-03	1.6E-04	1.00	7.75	20.0	288	recrys
silverspur_2_p	1.0500	(1.0463,1.0557)	-0.79	6.8E-03	1.5E-03	1.00	10.00	18.5	271	recrys
silverspur_2_q	1.0465	(1.0463,1.0557)	-0.85	4.9E-03	1.7E-04	1.00	10.00	18.5	258	recrys
silverspur_2_r	1.0469	(1.0463,1.0557)	-0.88	4.3E-03	4.2E-04	1.00	10.00	19.0	273	recrys
silverspur_2_s	1.0216	(1.0463,1.0557)	-0.82	2.4E-03	1.3E-03	1.00	10.00	23.0	341	recrys
mtmolloy_1_q	1.0644	(1.0463,1.0557)	-0.82	1.0E-02	1.4E-02	1.00	8.75	12.0	160	recrys
mtmolloy_1_r	1.0610	(1.0463,1.0557)	-0.84	7.2E-03	7.8E-03	1.00	7.00	12.0	166	recrys
mtmolloy_1_u	1.0450	(1.0463,1.0557)	-0.84	6.0E-03	5.3E-03	1.00	5.75	13.5	152	recrys
mtmolloy_2_p	1.0221	(1.0463,1.0557)	-0.81	2.5E-03	1.4E-03	1.00	10.00	35.5	339	recrys
mtmolloy_2_q	1.0224	(1.0463,1.0557)	-0.87	2.2E-03	8.6E-04	1.00	10.00	32.0	341	recrys
rammelsberg_1_p	1.0794	(1.0463,1.0557)	-0.81	1.2E-02	9.8E-03	1.00	6.00	11.0	140	recrys
rammelsberg_1_q	1.0750	(1.0463,1.0557)	-0.77	1.4E-02	1.3E-02	1.00	4.75	11.0	127	recrys
rammelsberg_1_r	1.0535	(1.0463,1.0557)	-0.88	5.5E-03	1.1E-02	1.00	5.50	12.5	132	recrys
rammelsberg_1_s	1.0602	(1.0463,1.0557)	-0.84	6.7E-03	1.5E-03	1.00	10.00	14.0	194	recrys
rammelsberg_1_t	1.0631	(1.0463,1.0557)	-0.85	9.0E-03	4.4E-03	1.00	6.75	13.0	157	recrys
rammelsberg_1_u	1.0528	(1.0463,1.0557)	-0.87	5.3E-03	3.5E-03	1.00	10.00	18.0	221	recrys
ramms_recryst_in_strshad_p	1.0338	(1.0463,1.0557)	-0.92	2.4E-03	4.8E-04	1.00	10.00	22.0	301	recrys
ramms_recryst_in_strshad_q	1.0316	(1.0463,1.0557)	-0.94	1.9E-03	9.3E-04	1.00	11.25	23.5	288	recrys
ramms_recryst_in_strshad_r	1.0365	(1.0463,1.0557)	-0.80	6.2E-03	2.1E-03	1.00	5.50	14.0	178	recrys
ramms_recryst_in_strshad_s	1.0627	(1.0463,1.0557)	-0.95	4.8E-03	1.4E-03	1.00	6.25	20.0	231	recrys
ramms_recryst_in_strshad_t	1.0602	(1.0463,1.0557)	-0.89	6.2E-03	3.9E-03	1.00	6.50	12.5	159	recrys
ramms_recryst_in_strshad_u	1.0379	(1.0463,1.0557)	-0.89	3.5E-03	2.7E-03	1.00	10.00	19.0	212	recrys
ramms_dyn_recrys_p	1.0564	(1.0463,1.0557)	-0.89	5.1E-03	4.8E-03	1.00	7.75	12.0	143	recrys
ramms_dyn_recrys_q	1.0725	(1.0463,1.0557)	-0.90	8.7E-03	5.7E-03	1.00	5.75	13.0	142	recrys
ramms_dyn_recrys_r	1.0714	(1.0463,1.0557)	-0.90	8.8E-03	4.3E-03	1.00	5.75	14.0	177	recrys
ramms_dyn_recrys_s	1.0658	(1.0463,1.0557)	-0.86	9.7E-03	3.3E-03	1.00	5.75	16.0	185	recrys
ramms_dyn_recrys_t	1.0634	(1.0463,1.0557)	-0.90	7.2E-03	3.1E-03	1.00	6.00	14.5	179	recrys
ramms_dyn_recrys_u	1.0349	(1.0463,1.0557)	-0.87	4.2E-03	5.3E-04	1.00	7.00	13.0	154	recrys
gf_recrys_away_from_shear_a	1.0371	(1.0463,1.0557)	-0.92	2.0E-03	2.9E-03	1.00	15.00	48.0	684	recrys

gf_recrys_away_from_shear_b	1.0362	(1.0463,1.0557)	-0.85	2.9E-03	1.1E-03	1.00	15.75	30.5	411	recrys
gf_recrys_away_from_shear_c	1.0299	(1.0463,1.0557)	-0.86	3.7E-03	1.3E-03	1.00	7.75	20.5	275	recrys
gf_recrys_adjacent_to_shear_p	1.0359	(1.0463,1.0557)	-0.84	3.6E-03	6.7E-04	1.00	11.25	20.0	286	recrys
gf_recrys_adjacent_to_shear_q	1.0514	(1.0463,1.0557)	-0.91	5.0E-03	1.9E-03	1.00	6.50	15.5	191	recrys
gf_recrys_adjacent_to_shear_r	1.0508	(1.0463,1.0557)	-0.86	5.5E-03	2.4E-03	1.00	10.00	16.0	194	recrys
gf_recrys_adjacent_to_shear_s	1.0371	(1.0463,1.0557)	-0.73	8.2E-03	2.4E-03	1.00	5.25	10.0	128	recrys
gf_recrys_adjacent_to_shear_t	1.0644	(1.0463,1.0557)	-0.66	1.8E-02	6.6E-03	1.00	4.75	12.5	172	recrys
gf_recrys_adjacent_to_shear_u	1.0342	(1.0463,1.0557)	-0.75	4.6E-03	7.5E-03	1.00	8.00	17.5	236	recrys
gf_recrys_adjacent_to_shear_v	1.0611	(1.0463,1.0557)	-0.86	6.9E-03	3.3E-03	1.00	9.25	16.0	196	recrys
gf_dyn_recrys_p	1.0531	(1.0463,1.0557)	-0.85	6.2E-03	1.3E-03	1.00	7.75	14.0	216	recrys
gf_dyn_recrys_q	1.0573	(1.0463,1.0557)	-0.85	8.6E-03	1.3E-03	1.00	5.50	11.5	162	recrys
gf_dyn_recrys_r	1.0393	(1.0463,1.0557)	-0.92	2.8E-03	1.2E-03	1.00	10.00	24.5	349	recrys
gf_dyn_recrys_s	1.0607	(1.0463,1.0557)	-0.77	1.1E-02	4.0E-03	1.00	6.25	13.0	174	recrys
gf_dyn_recrys_t	1.0581	(1.0463,1.0557)	-0.91	5.0E-03	7.6E-04	1.00	7.75	14.0	192	recrys
gf_dyn_recrys_u	1.0468	(1.0463,1.0557)	-0.91	3.6E-03	1.6E-03	1.00	11.25	19.5	259	recrys
gf_dyn_recrys_v	1.0532	(1.0463,1.0557)	-0.92	5.8E-03	7.0E-03	1.00	5.75	12.0	167	recrys
gf_dyn_recrys_w	1.0511	(1.0463,1.0557)	-0.86	5.8E-03	1.7E-03	1.00	8.00	17.0	261	recrys
gf_dyn_recrys_x	1.0655	(1.0463,1.0557)	-0.93	6.2E-03	2.4E-03	1.00	6.25	13.5	192	recrys
gf_dyn_recrys_y	1.0589	(1.0463,1.0557)	-0.74	1.7E-02	4.6E-03	1.00	4.25	10.0	126	recrys
gf_dyn_recrys_z	1.0506	(1.0463,1.0557)	-0.89	5.3E-03	3.2E-04	1.00	7.25	18.5	254	recrys
mtmolloy_1_v	1.1066	-	-0.91	7.9E-03	5.7E-03	1.00	10.00	25.0	423	recrys>def
mtmolloy_1_w	1.0458	-	-0.95	2.5E-03	2.0E-03	1.00	10.00	29.5	327	recrys>def
mtmolloy_1_x	1.0904	-	-0.93	7.1E-03	4.0E-04	1.00	7.50	12.5	150	recrys>def
mtmolloy_1_y	1.0641	-	-0.87	6.1E-03	9.4E-04	1.00	10.00	18.5	241	recrys>def
mtmolloy_1_s	1.1122	-	-0.96	5.8E-03	4.2E-04	1.00	10.00	19.0	240	recrys>def
mtmolloy_1_t	1.1449	-	-0.93	1.1E-02	1.3E-02	1.00	10.00	19.5	333	recrys>def
mtmolloy_1_p	1.0610	-	-0.91	4.5E-03	1.4E-03	1.00	10.00	22.5	249	recrys>def
gf_961233_4_dr_h	1.0491		-0.91	3.8E-03	7.9E-04	1.00	10.00	25.0	346	recrys>def
gf_961233_4_dr_i	1.0725		-0.93	5.6E-03	4.2E-03	1.00	9.00	21.0	341	recrys>def
gf_961233_4_dr_j	1.0686		-0.96	4.0E-03	8.9E-04	1.00	8.25	21.5	286	recrys>def
gf_961233_4_dr_k	1.0892		-0.94	5.8E-03	1.3E-03	1.00	9.00	27.0	408	recrys>def
gf_961233_4_dr_l	1.1042		-0.94	7.6E-03	1.2E-03	1.00	7.75	21.5	283	recrys>def
Clark_and Kelly_1973_a	1.1713	(1.0816,1.1080)	-0.95	1.0E-02	1.1E-02	1.00	10.00	340.0	522	defd
Clark_and Kelly_1973_b	1.1730	(1.0816,1.1080)	-0.97	3.8E-03	3.7E-04	1.00	31.75	340.0	1521	defd
mtmolloy_1_a	1.0768	(1.0816,1.1080)	-0.99	1.1E-03	2.1E-04	1.00	31.75	185.5	3871	defd
mtmolloy_1_b	1.1145	(1.0816,1.1080)	-0.95	6.2E-03	6.9E-03	1.00	10.00	76.0	521	defd
mtmolloy_2_a	1.1107	(1.0816,1.1080)	-0.98	1.5E-03	2.5E-03	1.00	63.25	201.0	1505	defd
mtmolloy_2_b	1.0836	(1.0816,1.1080)	-0.97	3.3E-03	6.8E-05	1.00	10.00	201.0	1112	defd
mtmolloy_2_c	1.0883	(1.0816,1.1080)	-0.94	2.9E-03	1.7E-03	1.00	31.75	254.0	1068	defd
mtmolloy_3_a	1.0921	(1.0816,1.1080)	-0.94	5.5E-03	1.3E-03	1.00	10.00	50.0	993	defd
mtmolloy_3_b	1.0975	(1.0816,1.1080)	-0.95	2.9E-03	2.9E-03	1.00	31.75	70.0	1180	defd
mtmolloy_4	1.0625	(1.0816,1.1080)	-0.95	1.6E-03	2.2E-03	1.00	40.75	80.0	1184	defd
rosebery	1.0755	(1.0816,1.1080)	-0.97	9.9E-04	1.8E-03	1.00	100.00	266.0	3482	defd
silverspur_2_a	1.0707	(1.0816,1.1080)	-0.89	4.5E-03	5.1E-03	1.00	19.25	113.5	915	defd

961233_1_a	1.0891	(1.0816,1.1080)	-0.98	1.7E-03	2.0E-03	1.00	31.75	105.5	2425	**defd**
961233_2_a	1.1391	(1.0816,1.1080)	-0.96	7.1E-03	8.3E-04	1.00	10.00	45.0	1048	**defd**
961233_3_a	1.0928	(1.0816,1.1080)	-0.98	1.9E-03	1.1E-03	1.00	31.75	117.0	2430	**defd**
961233_4	1.1116	(1.0816,1.1080)	-0.96	5.4E-03	9.1E-04	1.00	10.00	75.0	1838	**defd**
rammelsberg_1_a	1.1137	(1.0816,1.1080)	-0.96	3.3E-03	4.2E-04	1.00	25.25	55.5	1049	**defd**
gf_defgrain_away_from_shear	1.0645	(1.0816,1.1080)	-0.93	2.4E-03	7.5E-04	1.00	31.75	180.5	2665	**defd**
gf_defgrain_adjacent_to_shear_a	1.1013	(1.0816,1.1080)	-0.94	3.3E-03	2.9E-03	1.00	31.75	148.0	3061	**defd**
gf_defgrain_adjacent_to_shear_b	1.0780	(1.0816,1.1080)	-0.93	3.4E-03	3.8E-03	1.00	22.00	52.0	847	**defd**
rammelsberg_dyn_recryst_a	1.0698	(1.0816,1.1080)	-0.95	3.5E-03	3.7E-03	1.00	12.00	38.5	506	**defd**
rammelsberg_dyn_recryst_b	1.0576	(1.0816,1.1080)	-0.95	2.6E-03	2.2E-04	1.00	16.00	36.0	455	**defd**
rammelsberg_dyn_recryst_c	1.0843	(1.0816,1.1080)	-0.89	8.1E-03	1.1E-04	1.00	8.50	28.0	416	**defd**
gf_0803_1_bv_1a	1.0579	(1.0816,1.1080)	-0.95	3.1E-03	1.3E-04	1.00	10.00	73.5	1217	**defd**
gf_0803_1_bv_1b	1.1195	-	-0.97	2.9E-03	9.5E-04	1.00	31.75	115.5	942	**wk defd**
sullivan_a	1.0592	-	-0.94	1.9E-03	1.1E-03	1.00	31.75	120.0	1580	**wk defd**
sullivan_b	1.0508	-	-0.96	5.6E-04	1.2E-03	1.00	31.75	165.0	1933	**wk defd**
sullivan_c	1.0208	-	-0.95	1.6E-03	1.0E-04	1.00	31.75	226.5	2076	**wk defd**
sullivan_d	1.0554	-	-0.92	2.2E-03	1.3E-03	1.00	31.75	111.5	1363	**wk defd**
century_1	1.0331	-	-0.93	1.7E-04	3.6E-04	1.00	100.00	559.0	4580	**wk defd**